NUREG/CR-5642
EGG-2618

Light Water Reactor Lower Head Failure Analysis

Prepared by
J. L. Rempe, S. A. Chávez, G. L. Thinnes, C. M. Allison, G. E. Korth,
R. J. Witt, J. J. Sienicki, S. K. Wang, L. A. Stickler, C. H. Heath, S. D. Snow

Idaho National Engineering Laboratory
EG&G Idaho, Inc.

Prepared for
U.S. Nuclear Regulatory Commission

NUREG/CR-5642
EGG-2618

Light Water Reactor Lower Head Failure Analysis

Manuscript Completed: September 1993
Date Published: October 1993

Prepared by
J. L. Rempe, S. A. Chávez, G. L. Thinnes, C. M. Allison, G. E. Korth,
R. J. Witt[1], J. J. Sienicki[2], S. K. Wang[3], L. A. Stickler, C. H. Heath, S. D. Snow

Idaho National Engineering Laboratory
Managed by the U.S. Department of Energy

EG&G Idaho, Inc.
Idaho Falls, ID 83415

Prepared for
Division of Systems Research
Office of Nuclear Regulatory Research
U.S. Nuclear Regulatory Commission
Washington, DC 20555-0001
NRC FIN D2029
Under DOE Contract No. DE-AC01-76ID01570

---

[1]University of Wisconsin-Madison, 1500 Johnson Drive, Madison, WI 53706
[2]Argonne National Laboratory, 9700 South Cass Avenue, Argonne, IL 60439
[3]Commonwealth Edison Company, One First National Plaza, Chicago, IL 60690-0767

ABSTRACT

This document presents the results from a U.S. Nuclear Regulatory Commission-sponsored research program to investigate the mode and timing of vessel lower head failure. Major objectives of the analysis were to identify plausible failure mechanisms and to develop a method for determining which failure mode would occur first in different light water reactor designs and accident conditions. Failure mechanisms, such as tube ejection, tube rupture, global vessel failure, and localized vessel creep rupture, were studied. Newly developed models and existing models were applied to predict which failure mechanism would occur first in various severe accident scenarios. So that a broader range of conditions could be considered simultaneously, calculations relied heavily on models with closed-form or simplified numerical solution techniques. Finite element techniques were employed for analytical model verification and examining more detailed phenomena. High-temperature creep and tensile data were obtained for predicting vessel and penetration structural response.

CONTENTS

LIST OF FIGURES

LIST OF TABLES

EXECUTIVE SUMMARY

This document presents the results from a U.S. Nuclear Regulatory Commission (USNRC)-sponsored research program to investigate the mode and timing of vessel lower head failure. Major objectives of the analysis were to identify plausible failure mechanisms and to develop a method for determining which failure mode would occur first in different light water reactor (LWR) designs and accident conditions. Failure mechanisms, such as tube ejection, tube rupture, global vessel failure, and localized vessel creep rupture, were studied. Newly developed models and existing models were applied to predict which failure mechanism would occur first in various severe accident scenarios. So that a broader range of conditions could be considered simultaneously, calculations relied heavily on models with closed-form or simplified numerical solution techniques. Finite element techniques were employed for model verification and examining more detailed phenomena. High-temperature creep and tensile data were obtained for predicting vessel and penetration structural response.

Thermal Analysis Results

Thermal analyses were performed to obtain boundary conditions, such as event timing and temperature distributions, for failure analyses. Order-of-magnitude estimates for pressurized water reactor (PWR) and boiling water reactor (BWR) response indicate that a PWR transient will proceed more rapidly (by as much as a factor of two) than a BWR transient. These results were attributed to higher ratios of BWR structural mass per heat generation rate, larger initial BWR water inventories, and thicker BWR lower heads.

Scoping calculations were performed to investigate the state of the melt and arrival conditions upon the lower head for situations involving localized release of a melt stream from a crust-confined molten pool in the core region. Although several computer codes are available for predicting melt/water interactions, there is considerable uncertainty in code results because of limited data for validating these models. Hence, calculations concentrated on the effects of lower plenum geometry and structures in plant designs. In PWR designs, the presence of flow plates was found to affect jet impingement strongly. For Babcock & Wilcox (B&W) plants, the flow plates accumulate the melt and form multiple jets, which reduces the jet velocity and the fraction of initial jet energy that can impinge on the vessel lower head. Unlike the flow plates in a B&W plant, flow plates in Westinghouse and Combustion Engineering (CE) plants do not generally accumulate melt, allowing "straight shot" jets to occur through any horizontal structural plates. Although relocating melt is not impeded by any horizontal plates, the General Electric (GE) BWR lower head is protected by a water pool that is deeper than water pools in PWR lower plena.

Thermal analysis results emphasize the importance of geometrical parameters and material composition in predicting in-vessel tube ablation and melt migration through failed tubes. In-vessel tube melting is governed by the tube-to-debris mass ratios in the lower head, and most penetrations are predicted to reach melting temperatures rapidly if surrounded by molten debris. Melt penetration distances through failed tubes or tubes with no in-vessel structures were estimated by applying two models: (a) a conduction model, where a crust is assumed to form along the tube surface, so that conduction heat transfer through this crust dominates melt behavior, and (b) a modified bulk freezing model, where turbulence within the melt is assumed to preclude crust formation, so that turbulent heat transfer dominates melt behavior. The bulk freezing model applied in these calculations was modified to consider the effects of coolant that is

present in some lower head penetration flow paths. Results for a case with gravity-driven melt flow indicate that melt penetration distances predicted by the conduction model are considerably longer than those predicted by the modified bulk freezing model. In fact, melt is predicted to travel below the lower head through all LWR penetrations if the conduction model is applied; whereas melt is predicted to travel below the lower head only for penetrations having larger effective areas for melt flow and/or penetrations that are ablated near the vessel inner surface if the modified bulk freezing model is applied. Experimental data are needed to determine which of these models is appropriate for severe accident analysis.

Failure Analysis Results

As noted above, this study concentrated on four vessel failure mechanisms: tube ejection, tube rupture, global vessel failure, and localized vessel creep rupture. Other failure mechanisms, such as vessel ablation from a coherent jet relocating to the lower head and thermal shock following external flooding in a containment cavity, and interactions between various failure mechanisms were not considered because of uncertainties related to their potential for occurring. For example, the formation of a crust between the lower head and the jet or the formation of a relatively deep molten pool may preclude vessel ablation, and external flooding has not yet been accepted as an accident management strategy.

For depressurized reactor vessels, ex-vessel tube failure was assessed by applying thermal equilibrium calculations to provide order-of-magnitude estimates for minimum debris requirements, such as the debris relocation temperature and the debris heat flux, necessary to induce ex-vessel tube failure. Results indicate that tube geometry and material are important parameters in predicting tube failure. Although additional data are needed to quantify ultimate strength behavior for the SA105/SA106 material used in BWR drain lines, results indicate that this lower head penetration is more susceptible to ex-vessel tube rupture than other LWR penetrations. Results indicate that heat fluxes characteristic of a mostly ceramic slurry (i.e., in excess of 0.05 MW/m^2) are needed to induce failure in a BWR drain line tube, which is composed of SA105/SA106 steel and has a relatively large cross-sectional area for melt flow. However, higher heat fluxes characteristic of a high temperature and molten ceramic debris (i.e., as high as 0.2 MW/m^2) were not predicted to fail any of the other LWR penetrations.

For higher pressures (between ~0.1 and 16 MPa), analytical models with closed-form solutions were applied to compare the potential for tube ejection, tube rupture, and global vessel rupture. Failure maps were generated that indicate relative pressure bearing capacities of vessel heads and their penetrations based on ultimate strength. Failure maps considered three types of debris beds: a primarily metallic debris, a primarily ceramic slurry, and a primarily ceramic molten pool. Failure curves for tube ejection and tube rupture plot at the same location, near the tube material's melting temperature. For the case of a molten ceramic pool in a BWR vessel, model results indicate that tube failures will occur at lower temperatures than vessel failures for any system pressure. Except for the BWR case with a molten ceramic pool, model results indicate that global rupture is the controlling failure mode in BWRs or PWRs with system pressure above approximately 2 MPa. Although model results indicate that penetration tube failures control failures below 2 MPa, uncertainties in the ultimate strength data at high temperatures for penetration materials do not allow a clear distinction of the controlling failure mode in this pressure range.

A new model, based upon Reissner's theory of shells with finite deformation, was applied to the problem of localized creep rupture on a corium-loaded lower head. This new model was applied to determine how localized debris heat sources impact vessel failure times and what conditions are necessary for the formation and failure of a localized bulge or cusp to occur. Two types of thermal loads were investigated. The first set of loads used contrived, steady-state temperature profiles to demonstrate the range of behaviors possible under localized hot spots. It was found that a localized hot spot does not always produce a bulge or cusp as it fails. The failure geometry depends on the creep rate of the balance of the shell relative to the hot spot. If the magnitude of the peak temperature is small, the failure geometry is elliptical, and the hot spot assists or accelerates a failure that looks like global failure. If the magnitude of the peak temperature is large, the hot spot is punched out of a comparatively stiff vessel, and the failure geometry is cusped. The second set of problems used transient thermal loads from applied heat fluxes associated with different debris characteristics. All failure geometries in these problems were localized because it was assumed that the background heat flux was benign and that the balance of the vessel remained cool. As with the contrived problems, times to failure were very strong functions of applied pressure and peak heat flux.

Finite Element Thermal and Structural Analysis Results

More detailed numerical methods were applied to a BWR design to gain insight into the importance of two-dimensional effects in special geometries where simplified analytical techniques may be insufficient to study the roles of thermal stress plasticity and creep in vessel failure. To complete this analysis, an interface was created so that temperatures from the COUPLE thermal analysis model of SCDAP/RELAP5 could be input into the structural analysis code, ABAQUS. Analyses considered the effects of debris composition, debris porosity, debris-to-surface gap resistance, reactor coolant pressure, and heat transfer conditions on the outer surface of the drain line and vessel.

If melt travels through the drain line to locations below the vessel outer surface, thermal analysis results indicate that drain line failure will not occur in cases where metallic debris relocates to the lower head. In cases where ceramic debris relocates to the lower head, drain line temperatures peak near values where failure may occur within the first few minutes of the transient; whereas vessel failure temperatures do not occur until several hours into the transient. Sensitivity study results indicate that high porosity in a debris bed or high heat removal rates from the vessel and drain line outer surface, such as might occur in a flooded containment cavity, can significantly affect predictions for peak drain line and vessel temperatures. In fact, neither drain line nor vessel failure temperatures are predicted to occur in the ceramic debris cases that assume high porosity debris or high exterior drain line and vessel surface heat removal rates.

In the event that drain line failure does not occur, structural analysis results indicate that vessel creep rupture can occur as early as 4 hours after debris relocation. For ceramic debris with a 7-MPa pressure, creep strains and accumulated creep damage remain relatively low for the first 2 hours, after which both increase quite dramatically until failure is predicted between 3.5 and 4 hours. In the case of metallic debris at lower pressures, failure was not predicted for more than 24 hours because effective creep strains were less than 0.5%. In both cases, plastic deformation was minimal (less than 0.5%).

Application of Models to Various Debris Conditions and Reactor Designs

Although a detailed analysis is required to obtain quantitative answers about event progression, results documented in this report were used to make qualitative judgements about which failure mechanisms are possible and which failure mechanism will occur first during severe accidents. Three types of debris configurations were studied: a metallic slurry; a primarily ceramic slurry; and a high temperature, molten ceramic material that relocates to form a molten pool. Results for four representative plant designs are summarized in Table ES-1. Failure analysis results are presented as a function of vessel inner surface temperature and system pressure. *However, it is emphasized that these temperatures and pressures should only be considered as approximate values because there is considerable uncertainty associated with these values.*

Results in this document indicate that most debris will relocate incoherently in a B&W plant because of lower plenum flow plates that accumulate melt and form multiple jets. Calculational results indicate that all types of melt may lead to in-vessel tube ablation. If conduction heat transfer dominates, all types of melt are predicted to travel through an instrument tube to locations below the lower head. However, if turbulent heat transfer dominates, melt is not predicted to travel below the lower head. Thermal analysis results indicate that peak vessel and penetration temperatures following relocation of a metallic slurry remain below values where vessel or penetration failure occurs. Hence, neither vessel nor penetration failure is predicted to occur following relocation of a primarily metallic slurry in any of the LWRs considered. At pressures above approximately 2 MPa, both global and localized vessel failures are possible in the B&W plant for either the ceramic slurry or the high temperature ceramic melt that forms a pool. However, additional information about relocation mass, debris bed configuration, and accident pressure history are needed to determine if a localized failure will occur before a global vessel failure. At pressures below 2 MPa, tube failures are possible if the vessel inner surface temperature exceeds 1600 K.

Westinghouse plant results in Table ES-1 are similar to those for the B&W plant with the exception of debris arrival state. In a Westinghouse plant, "straight shot" paths for relocating material are possible. Hence, higher fractions of melt are estimated to arrive as a coherent jet for this plant. The potential for larger fractions of ceramic debris to arrive coherently upon the lower head in the Westinghouse plant suggests that a local failure might occur before a global vessel failure. However, additional scenario-specific information, such as relocation mass, debris bed configuration, and accident pressure history, are required before more definitive conclusions can be drawn concerning these failure modes.

Results for the CE plant in Table ES-1 differ from the B&W plant for two reasons. First, the CE plant has no lower head penetrations. Hence, tube failures are not possible. Second, as observed in the Westinghouse plant, "straight shot" paths for relocating material are also possible in this plant. Hence, higher fractions of melt are also estimated to arrive as a coherent jet for this plant.

Results for the GE BWR in Table ES-1 differ from any of the PWR plant results for several reasons. Some melt is predicted to arrive coherently on the BWR lower head because relocating melt is not impeded by any horizontal plates. However, the GE BWR lower head is protected by coolant in the lower head, which is deeper than the coolant level in PWR lower plena. Hence, coherent melt fractions listed in Table ES-1 for the BWR are much smaller than those predicted

Table ES-1. Dominant failure modes for various debris conditions and reactor designs.

Reactor type	Debris composition	Debris arrival state	Failure mode
PWR			
B&W	Metallic	Incoherent, coolable	None
	Ceramic Slurry	Incoherent	Localized or global failure for pressures above ~1.5 MPa and vessel inner surface temperatures above ~1000 K; tube failure for pressures less than ~1.5 MPa and vessel inner surface temperatures above ~1600 K.[a]
	Ceramic Pool	Coherent (10-20%)[b]	Localized or global failure for pressures above 2.5 MPa and vessel inner surface temperatures above 1200 K; tube failure for pressures less than 2.5 MPa and vessel inner surface temperatures above 1600 K.
Westinghouse	Metallic	Coherent	None
	Ceramic Slurry	Coherent	Localized or global failure for pressures above 1 MPa and vessel inner surface temperatures above 1000 K; tube failure for pressures less than 1 MPa and vessel inner surface temperatures above 1600 K.
	Ceramic Pool	Coherent (15-40%)	Localized or global vessel failure for pressures above 2.5 MPa and vessel inner surface temperatures above 1200;[c] tube failure for pressures less than 2.5 MPa and vessel inner surface temperatures above 1600 K.
CE	Metallic	Coherent	None
	Ceramic Slurry	Coherent	Localized or global vessel failure
	Ceramic Pool	Coherent (45-60%)	Localized or global vessel failure
BWR			
GE	Metallic	Coherent (<5%)	None
	Ceramic Slurry	Coherent (<7%)	Localized or global failures for pressures above 2 MPa and vessel inner surface temperatures above 1100 K; tube failure for pressures less than 2 MPa and vessel inner surface temperatures above 1600 K.[d]
	Ceramic Pool	Coherent (<10%)[e]	Tube failure (via ejection and/or rupture) for all pressure ranges and vessel inner surface temperatures above ~1200 K.

a. Temperature and pressure values are approximate because temperature distributions depend on assumptions related to accident pressure history, exterior surface heat transfer to the containment, debris-to-vessel heat transfer, etc.

b. Approximately 10% of the material arrives as a coherent jet if a central relocation path is assumed, and less than 20% of the material arrives as a coherent jet if a peripheral relocation path is assumed.

c. Vessel inner surface temperatures are higher in the ceramic pool case because failure is predicted to occur during the initial transient heatup stages of the accident.

d. Because there is considerable uncertainty in the ultimate strength of drain line SA106 material, analyses suggest that it may be possible for drain line tube failure to occur earlier than global or localized vessel failures at high pressures.

e. No coherent jet reaches the lower head if a central relocation path is assumed; less than 10% of the material relocates as a coherent jet if a peripheral relocation path is assumed.

for the CE and Westinghouse PWRs. Second, the effective diameter for melt flow is relatively large in the BWR drain line and instrument tube penetrations. Hence, melt is predicted to travel below the lower head regardless of whether conduction or turbulent conditions dominate heat transfer from the debris to the tube. BWR failure mode results for the high-temperature, ceramic pool also differ from the other plants because tube failures are predicted to occur before either local or global vessel failures for all pressures if the vessel inner surface temperature exceeds approximately 1200 K. Tube failures control failure in this case because the BWR vessel is nearly twice as thick as a PWR vessel. Hence, tube failure temperatures occur before the thermal front penetrates the vessel.

ACKNOWLEDGMENTS

The authors would like to express their gratitude to several individuals who contributed to this report. First, we would like to thank Thomas J. Walker, our USNRC technical monitor, for his helpful suggestions and guidance on this research project. Contributions from A. W. Cronenberg assisted in the completion of sections pertaining to tube heatup and melt penetration. Review comments and information from colleagues at other national laboratories, Westinghouse, and the Yankee Atomic Electric Company were also instrumental in the completion of this work. In particular, we would like to thank Larry Ott and Steve Hodge of Oak Ridge National Laboratory for their comments and assistance in addressing questions related to boiling water reactors. We would also like to thank Larry Hochreiter of Westinghouse and Ramu Sundaram and Kevin St. John of Yankee Atomic Electric Company for their assistance in obtaining plant data. We are also indebted to colleagues at the Idaho National Engineering Laboratory. In particular, we would like to thank Larry Seifken and Ken Katsma for their assistance in applying SCDAP/RELAP5 and Paul Jacobs for writing the interface between the SCDAP/RELAP5 and ABAQUS codes. In addition, we would like to thank Jill White, Judy Gordon, and Julie Steffes for their editing assistance through the drafts to the final document and Gerry Reilly and Christine White for their graphics support.

Light Water Reactor Lower Head Failure Analysis

1. INTRODUCTION AND METHODOLOGY

1.1 Introduction and Objective

The mode and timing of reactor vessel lower head failure during a severe accident have a controlling effect on subsequent consequences, in particular, direct containment heating (DCH) for pressurized water reactors (PWRs) and meltthrough of the containment shell for boiling water reactor (BWR) Mark-I containment designs. Consequently, the mode and time of lower head failure have been identified by the U.S. Nuclear Regulatory Commission (USNRC) as important tasks (Task 2.5 and Task 3.1) in the *Revised Severe Accident Research Program Plan*.[1-1]

Previous evaluations of potential lower head failure for selected lower head designs and accident conditions have been performed in support of the USNRC-sponsored NUREG-1150,[1-2] *Revised Severe Accident Research Program Plan*,[1-1] risk studies, the U.S. Department of Energy (DOE)-sponsored Three Mile Island Unit 2 (TMI-2) Accident Evaluation Program, and the industry-sponsored Industry Degraded Core Rulemaking (IDCOR) Program. These evaluations and other analyses have included the study of molten jet impingement, flow and freezing of molten corium into tube penetrations, penetration tube ejection, and creep rupture failure. Both experimental and analytical studies were performed. However, a review of the literature indicates that an integrated assessment should be performed to determine which failure mechanism will occur first under a wide range of vessel designs and debris conditions.

This document presents results from an integrated assessment of reactor vessel lower head failure analyses for the full range of reactor vessel designs presently used in the U.S. commercial nuclear power industry and for a wide range of corium melt progression and debris characteristics. Specific objectives of this research are to

1. Identify dominant lower head failure mechanisms

2. Develop models needed to predict when it is possible for these failure mechanisms to occur

3. Apply models to determine which failure mechanisms are possible and the relative time when each possible mechanism occurs in different LWR designs for various debris and accident conditions.

All major types of vessels used in U.S. light water reactors (LWRs) are considered, and both high- and low-pressure conditions are addressed for each reactor type. As part of this assessment, creep and tensile tests on LWR pressure vessel steels and lower head penetration materials at high temperatures have been performed because such data were typically not available for temperatures above 1000 K.

The remainder of this section describes (a) the dominant mechanisms identified as having the potential to cause lower head failure, (b) the methodology used for determining what failure mechanism will occur first in a wide range of accident conditions and reactor designs, and (c) high-temperature material property testing performed to supplement this research. Section 2 provides a review of previous research pertaining to lower head failure mechanisms, and Section 3

describes the thermodynamic and geometric parameters considered in this study. Section 4 presents results obtained from lower head thermal and failure mechanism analyses methods that use closed-form or simplified numerical solution techniques. Section 5 presents numerically obtained results for vessel thermal and structural response. A nomenclature list is located in Appendix A. Results from creep-rupture and tensile tests on pressure vessel steels and penetration materials at high temperatures are presented in Appendix B. Appendices C through E provide additional information on two models used in these calculations. Appendix F contains material property data and geometric dimensions used to perform calculations for these analyses. A summary of comments received at an international peer review meeting held to review the contents of a draft version of this document is included in Appendix G.

1.2 Mechanisms Having the Potential to Cause Lower Head Failure

There are several possible mechanisms or combinations of mechanisms that could lead to lower head failure during a severe accident. Because this study represents the first endeavor to perform an integrated assessment of lower head failure for a range of plant designs and severe accident conditions, the report is focused on mechanisms that appeared to be dominant failure mechanisms for existing LWR plant designs undergoing a severe accident. Furthermore, the potential for interactions between mechanisms was not included in this assessment. An initial review resulted in the following four mechanisms being identified as dominant failure mechanisms for consideration:

- *Penetration Tube Heatup and Rupture.* Corium melt attack on lower head penetrations may result in melt entering a penetration channel and refreezing, thus causing tube blockage and potentially tube rupture.

- *Penetration Tube Ejection.* Corium melt attack and sustained heating from accumulated debris may lead to tube penetration weld failure and subsequent penetration tube ejection.

- *Lower Head Global Rupture.* Stress induced by elevated system pressure and/or the core and structure weight, in conjunction with sustained heating from accumulated debris, may lead to lower head global failure.

- *Localized Effects/Jet Impingement.* Nonuniform heat sources within the debris bed or a coherent jet of debris impinging directly onto the lower head can cause localized thermal and mechanical loads on the lower head. In addition to lower head failure from the thermal and mechanical loads, there is also the potential that a coherent jet can ablate the vessel head.

This research project considers all of the above mechanisms to provide a comprehensive assessment of mechanisms leading to lower head failure.

It should be noted that a later, more-detailed literature review of previous analyses (see Section 2.4) indicated that one of the above mechanisms, the potential for a coherent jet to ablate the lower head, was limited by phenomena such as the formation of a ceramic crust on the vessel surface and the formation of molten pools with relatively large depths. Hence, jet impingement analyses in this report concentrate on the potential for a coherent jet to relocate and transfer energy to the lower head and the subsequent potential for the vessel to experience a localized creep failure.

Some failure mechanisms, such as the potential for thermal shock following external flooding in the containment cavity, were not included in this study because external flooding has not been accepted as an accident management strategy in existing LWR designs. It is recognized that this mechanism may need further evaluation if external flooding is used in existing reactors or if it is adopted for advanced reactor designs.

1.3 Methodology

1.3.1 Major Tasks Completed to Evaluate Lower Head Failure

Figure 1-1 illustrates major tasks performed in this program to study vessel failure mechanisms under a wide range of accident and reactor conditions. As denoted in the first block in the upper left corner, the range of accident conditions and vessel design parameters having the potential to result in vessel failure were reviewed to select reactor design and accident scenario parameters that are representative, albeit somewhat idealized, conditions for the analysis. Output from this block (such as the debris decay heat load or the system pressure) provides the basis for the next task, a thermal analysis to characterize parameters, such as the lower head structure temperature, for a range of representative reactor designs.

In defining this research program, it was recognized that the database for creep and tensile properties of pressure vessel steel and vessel penetration materials at high temperatures was insufficient (see Section 1.4). Hence, as shown in the upper right corner of Figure 1-1, a task was defined to obtain high-temperature creep and tensile data for these materials.

The new creep and tensile data and results from the thermal analyses, such as the time- and spatially-dependent vessel temperature distributions, provide input for the next five blocks, which represent the models used to predict vessel failure phenomena, such as localized effects, jet impingement, tube ejection, tube heatup and rupture, and global vessel failure. Because many combinations of debris conditions, lower head design, and accident conditions could result in vessel lower head failure, this research relies heavily on analytical models with closed-form solution or simplified number solution techniques. Results from these models are developed in terms of dimensionless parameters, which are varied to determine failure maps that illustrate the sensitivity to these dimensionless parameters.

Results from these failure maps are compared to determine which failure mechanism will occur first during a particular set of reactor accident and design conditions (the box in the lower left corner of Figure 1-1). Finally, in cases where more detailed analyses are needed, finite element numerical analyses are applied to evaluate the sensitivity of previous results to nonidealized geometry and debris conditions.

1.3.2 Application of Lower Head Failure Models to Predict Failure

Figure 1-2 illustrates the procedure for applying lower head failure models to determine which failure mechanism will occur first during a specific accident scenario. Shaded boxes in this figure represent analyses that must be performed using models documented in Section 4 of this report. The user must travel each path starting at the left and working toward the right. If there are lower head penetrations in the vessel, such as in the Babcock & Wilcox (B&W), Westinghouse, and General Electric (GE) vessels, all paths are considered. If there are no lower head penetrations in the vessel, such as in most Combustion Engineering (CE) vessels, only the paths including the "CE" designation are considered. If the user reaches a box containing a failure

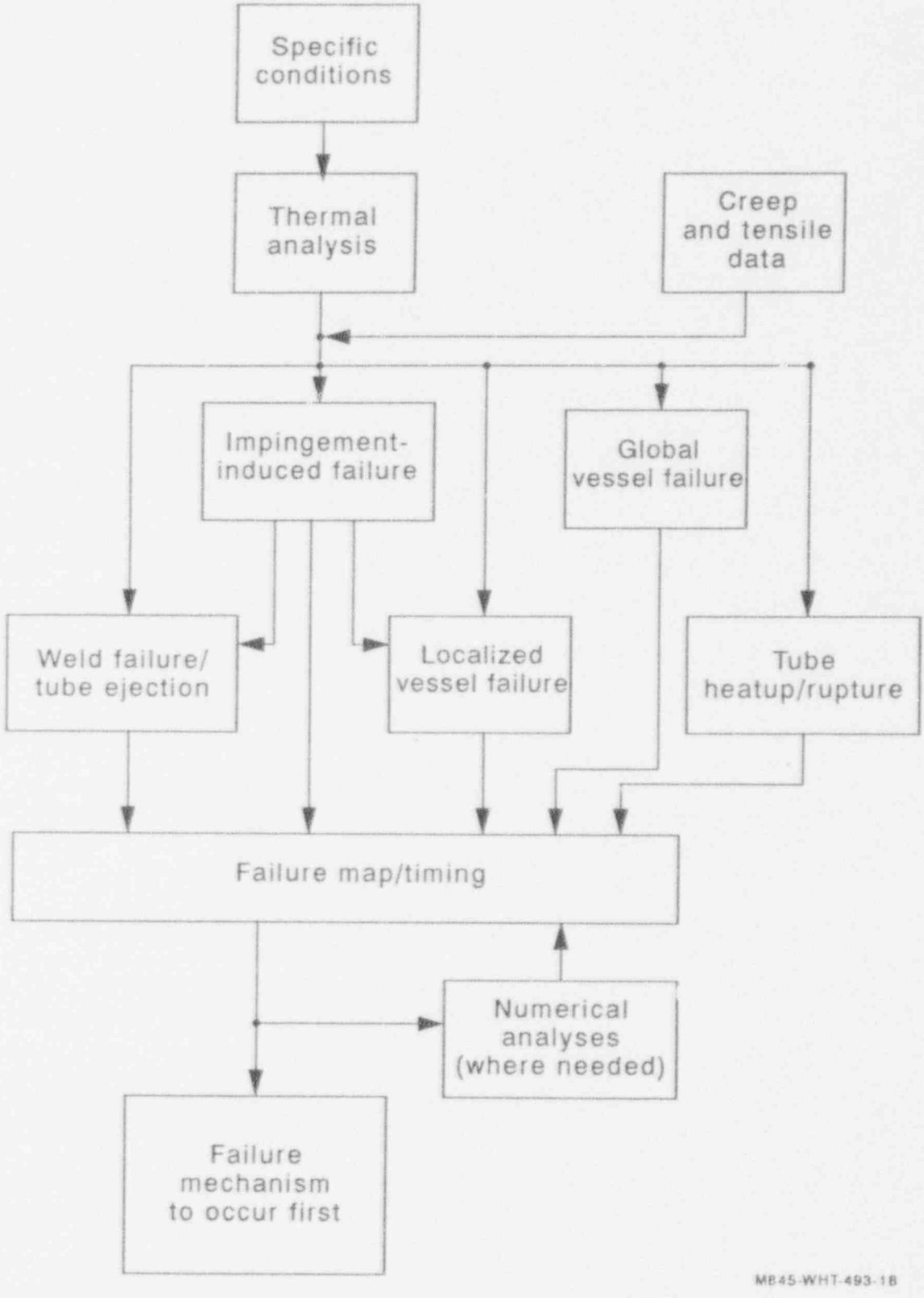

Figure 1-1. Major tasks performed in the lower head failure research program.

Figure 1-2. Methodology for predicting lower head failure.

mechanism and determines that it is not possible for a failure mechanism to occur, the user is directed toward the right along the "no" path (labeled with an "N"). If the user determines that it is possible for a failure mechanism to occur, the appropriate model is applied to determine the time at which failure is predicted to occur. Then, the user is directed to continue in the flow diagram with a "GO TO" statement. After each appropriate failure mechanism has been evaluated for a particular scenario, failure times are compared to determine which failure mechanism occurs first and the properties of the debris in the lower plenum at the time of failure.

Starting with the time-dependent results from a code capable of determining the manner in which debris relocates to the lower head, the user first considers whether the debris relocates as a coherent jet. If the debris does relocate as a coherent jet (and if the plant has lower head penetrations), the user then considers whether the penetration weld will remain intact. If the weld has reached temperatures where failure is predicted, the user then applies the tube ejection model to determine the time of failure via this mechanism. Proceeding along this path, the user reaches the "GO TO 1" direction and returns to Point 1.

From this point, the user considers if it is possible for the coherent jet to induce a thermal load to a localized region of the vessel and cause a localized creep failure of the vessel. If the thermal load is sufficient, the user evaluates the time of failure via a localized creep failure from an impinging jet. Proceeding along this path, the user reaches the "GO TO 2" direction and returns to Point 2.

From Point 2, the user considers whether the consolidated debris is in a coolable geometry in the lower head. If the debris bed is coolable, the user stops. If the debris bed is not coolable, the user then applies the global vessel failure model to predict the time at which vessel failure occurs. Proceeding along this path, the user reaches the "GO TO 3" statement.

From Point 3, the user considers whether there are nonuniform heat sources present in the debris bed. If the "hot spot" in the debris is determined to be sufficient to induce a localized vessel failure, the localized creep vessel failure model is applied to predict a failure time. Proceeding along this path the user is directed to "GO TO 4."

At Point 4, the user is directed to stop if the plant contains no lower head penetrations. Otherwise, the user considers whether the debris contains sufficient heat to induce in-vessel tube failure or the debris is capable of traveling through failed penetrations to locations below the vessel lower head. In cases where debris is not predicted to travel below the lower head, the user evaluates the potential for the consolidated, uncoolable debris to induce weld failure and tube ejection.

In cases where debris is predicted to travel below the lower head, the user evaluates the potential for the debris within the tube to weaken the surrounding vessel and induce a localized vessel failure. After determining the time of a localized vessel failure, the user then proceeds to evaluate the potential for an ex-vessel tube rupture to occur. After determining the time of an ex-vessel tube rupture, the user proceeds to evaluate the potential for weld failure and tube ejection to occur.

For cases in which failure mechanisms are predicted to occur, failure times are compared. The failure mode is selected based upon which mechanism is predicted to occur earlier. The failure time estimated with the model for this mechanism is used to estimate the mass, composition, and temperature of the melt at vessel failure. The method depicted in Figure 1-2 is applied to several examples in Section 6.

1.4 Material Creep and Tensile Tests of Pressure Vessel Steel and Penetration Materials at High Temperatures

Calculations of a vessel or penetration material's response to the presence of molten debris requires knowledge of a material's structural properties at temperatures up to the material's melting point. In the past, structural properties of materials used in nuclear reactors were typically determined for use up to reactor operating and design temperatures, leaving a gap in the temperature-dependent data between those levels and the melting temperatures. High-temperature creep and tensile tests were performed for these materials so that structural analyses can be made in much higher temperature regimes than previously possible. Results from these tests are summarized in Appendix B.

The lower heads of commercial power reactor pressure vessels are generally fabricated from the plate material SA533B1 or its predecessor, SA302B, which has very similar structural properties. Before the tests described in Appendix B, no creep and tensile data existed for the SA533B1 material at temperatures above 922 K. Because this material undergoes a ferritic to austenitic phase change at temperatures near 1000 K, it was recognized that higher temperature data were needed to accurately predict vessel response. Creep tests were completed up to 1373 K, and tensile tests were completed up to 1473 K. Relationships were developed for using these data in simpler models with closed-form or simplified numerical techniques and in finite element structural analysis codes.

Lower head penetrations, such as instrument tubes, control rod guide tubes, and the drain nozzle are constructed of Inconel 600, 304 stainless steel, or SA105/SA106B carbon steel. Creep tests were performed for Inconel 600 and stainless steel material for temperatures up to 1366 and 1350 K, respectively. Tensile tests were performed for these materials at temperatures up to 1373 K. For the SA106B material, creep tests were completed up to 1050 K, and tensile tests were completed up to 1150 K. Relationships were developed for using these data in simpler models with closed-form or simplified numerical techniques and in finite element structural analysis codes.

Although the new data are beneficial because they extend into temperature regions where data were previously unavailable, the data are limited and additional tests are needed to reduce the range of uncertainty associated with these data. In particular, data were not previously available for the SA106 material at temperatures above 811 K, and extrapolation of previously available data indicated that the ultimate strength of this material became negligible at 1000 K. However, test results indicate that the ultimate strength of SA106B material is considerably stronger than indicated by previous data. Hence, additional SA106B tests are needed so that the ultimate strength of this material can be predicted at temperatures above 1150 K.

1.5 References

1-1. U.S. Nuclear Regulatory Commission, *Revised Severe Accident Research Program Plan*, NUREG-1365, August 1989.

1-2. U.S. Nuclear Regulatory Commission, *Severe Accident Risks: An Assessment of Five U.S. Nuclear Power Plants*, NUREG-1150, June 1989.

2. REVIEW OF PREVIOUS RESEARCH APPLICABLE TO LOWER HEAD FAILURE ANALYSES

A literature search was conducted to review previous experimental and analytical analyses that are applicable to the lower head failure mechanisms considered in this document. Sections 2.1, 2.2, 2.3, and 2.4 summarize the major results from previous analyses pertaining to tube heatup and plugging, tube ejection and rupture, global rupture, and jet impingement. No work was found in the available literature on models for predicting localized vessel failure.

2.1 Tube Heatup and Failure

During a severe accident, one postulated vessel failure mode results from in-vessel tube heatup and failure from relocated melt in the lower plenum. As shown in Figure 2-1, the melt is postulated to enter the failed tube and travel down the penetration annulus below the vessel lower head. In predicting the likelihood of such a failure mechanism, several questions are of interest, such as the debris temperatures required to cause tube melting and the melt penetration distance within a penetration prior to plugging. This section reviews prior research related to analyzing this failure mechanism.

2.1.1 Tube Heatup Analyses

Two references were found in the literature that consider the potential for relocated debris to ablate through nozzles in the vessel. Both analyses were performed to evaluate the integrity of the TMI-2 nozzles following debris relocation. Reference 2-1 reports results from one-dimensional scoping calculations that were performed to investigate the debris thermal properties needed to induce in-vessel tube melting. The calculations assumed that a tightly packed debris bed, with essentially no coolant ingress into the bed, surrounded a penetration nozzle. Assuming perfect contact between the debris and the nozzle, the one-dimensional heat conduction was solved to determine the peak debris temperature needed to induce nozzle melting. Results indicate that debris with temperatures in excess of 1600 K can induce nozzle melting.

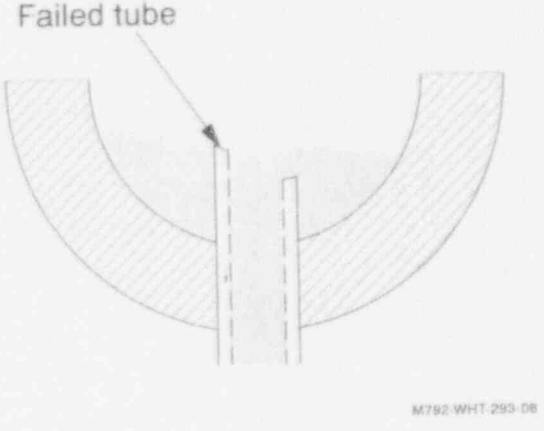

Figure 2-1. Melt penetration through failed penetration.

Reference 2-2 reports results from two-dimensional calculations scoping, which were performed to evaluate the integrity of the TMI-2 lower head and in-core instrument nozzles. Numerical calculations were performed with the FELCON code,[2-3] assuming an axisymmetric nodal model based on the following configuration:

- A cylindrical column of corium 10.2 cm in diameter and 17.8 cm high was assumed to surround an in-core instrument nozzle 1.746 cm in diameter by 25.4 cm high.
- The corium in the lower head is solid. The surface of the corium in contact with the lower head was assumed to be initially at 2477 K, and the remainder of the corium was initially at 3033 K.
- A corium heat generation rate of 1.48 MW/m^3 was assumed with a debris-to-vessel conductance of 1140 WM/m^2K.
- The only cooling was by radiation and by water boiling on the corium outside surface.
- The initial temperature of the nozzle and lower head was assumed to be 608 K, which corresponds to the coolant saturation temperature at 15.2 MPa.

Figure 2-2 shows the physical configuration assessed. The nozzle region was assumed to be in perfect contact with the corium and lower head. Inside cooling of the nozzle by water was neglected, with an adiabatic boundary condition at the inner nozzle surface. Water cooling was assumed to occur at the outer surface of the corium region (see Figure 2-2). In the calculation, heat transfer from the water-cooled surface was either by nucleate boiling or by a combination of film boiling and radiation, depending on the temperature difference between the surface and the water. Heat transfer from the bottom of the corium region was by conduction into the lower head. Contact between the lower head and the corium was conservatively assumed to have a conductance of 1140 W/m^2K.

Figure 2-3 presents calculational results. Although the FELCON code[2-3] does not consider the corium heat of fusion, which will result in calculated nozzle temperatures peaking more rapidly at a lower temperature than in more detailed calculations, the upper in-core instrument nozzle reaches temperatures well above melting. These temperatures result from the nozzle being surrounded by hot corium without any cooling except axial conduction into the lower head. However, results also show that portions of the nozzle near the lower head are cooler, because conductive heat transfer to the head provides sufficient cooling to keep the nozzle from melting.

2.1.2 Melt Penetration Distance

Most analytical and experimental work for predicting melt penetration distance a tube was performed in support of the liquid-metal fast-breeder reactor (LMFBR) program during the 1970s and early 1980s. This extensive research into molten fuel freezing phenomena was performed to understand recriticality potential following a core disruptive accident in the Clinch River Breeder Reactor. This section describes aspects of LMFBR research that may be applicable to predicting melt behavior within a failed LWR lower head penetration. Table 2-1 summarizes the conditions tested in melt penetration distance experiments.

2.1.2.1 Ostensen and Jackson Bulk Freezing Model and Experiment. This research, documented in References 2-4 and 2-5, was performed to assess penetration distances of molten fuel ejected into LMFBR subassembly structures following a core disruptive accident. An

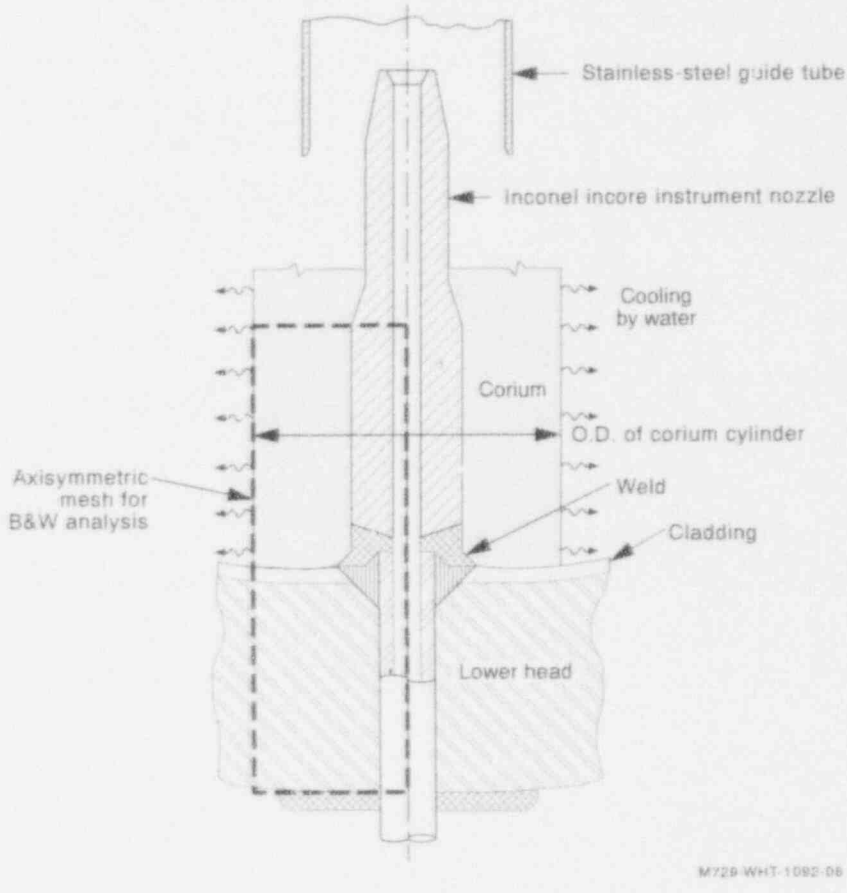

Figure 2-2. Configuration for assessing TMI-2 penetration tube heatup and failure potential.[2-2]

experiment was performed in which 200 to 300 g of molten UO_2 were injected horizontally into a seven-pin steel test bundle at ~3500 K and ~1,500 cm/s. The analytical model proposed assumed that fuel turbulence would preclude freezing at the wall (i.e., the bulk freezing model described in Section 4.1.2.4). Thus, the melt penetration distance was calculated by determining the length of travel required to remove sensible and latent heat from the leading edge of the molten slug. The analytical model used a turbulent drag correlation to calculate fuel velocity[2-6] and Deissler's correlation[2-7] for convective heat transfer between the fuel and steel. Analytically predicted penetration distances in the pins were found to range between 14% longer and 25% shorter than the measured results.

2.1.2.2 Cheung and Baker Experiments. Parametric experiments were performed to study the transient freezing of liquids in circular tubes.[2-8] These studies included no simulation of wall melting or fuel-coolant interaction. Liquids with Prandtl numbers ranging from 10^{-2} to 10^{3} (water, Wood's metal, naphthalene, paraffin wax, and olive oil) were used as the simulant

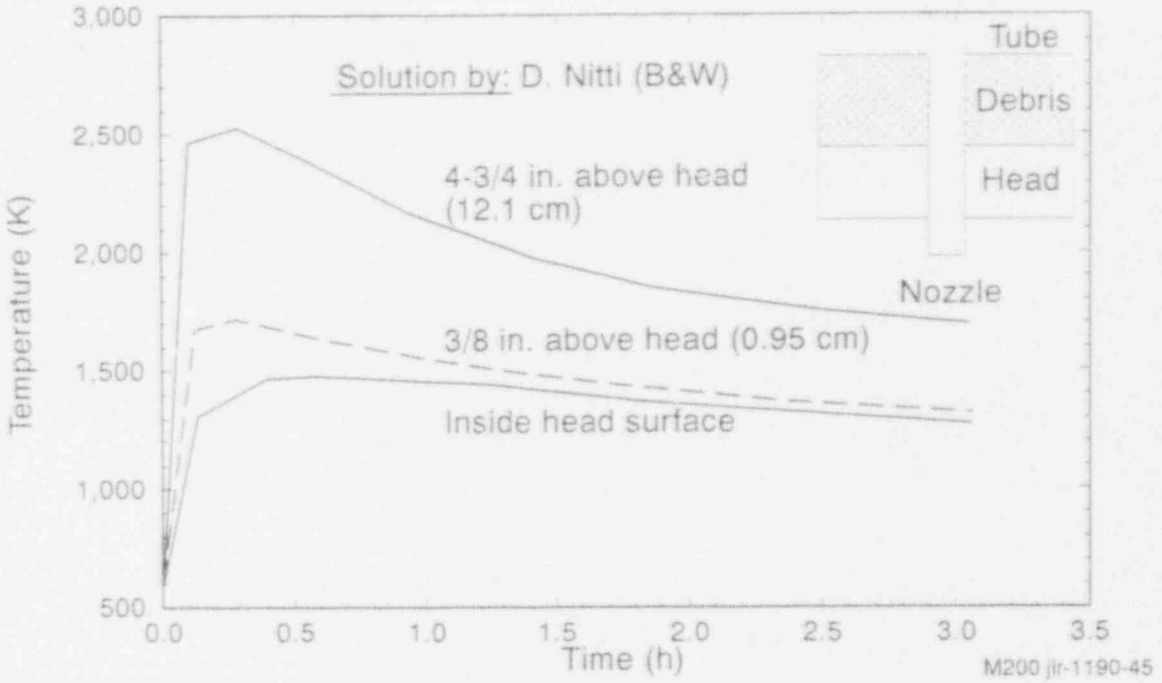

Figure 2-3. FELCON predictions for TMI-2 nozzle temperature.[2.2]

materials. Simulant and wall temperatures were varied to test the melt latent heat, sensible heat, and wall temperature effects on freezing. These studies bracket the estimated Prandtl number of molten fuel and steel from a disrupted reactor core. Flow velocities varied from 10 to 150 cm/s. The experimental apparatus consisted of a copper coil immersed in a bath of liquid coolant. The effect of tube diameter on freezing was studied by using copper tubing with two different diameters (0.47 and 0.79 cm).

An empirical correlation of the transient freezing data was obtained, and results were compared with melt distances predicted assuming domination by either conduction heat transfer (a conduction heat transfer model based upon information in References 2-10 and 2-11) or turbulent convective heat transfer (a bulk freezing model based on References 2-4 and 2-5). For a fuel velocity of ~100 cm/s, the bulk freezing model penetration distances were shorter by at least an order of magnitude than those distances obtained from the empirical correlation; whereas the conduction model distances were within a factor of two of the distances obtained from the empirical correlation. However, as noted in Reference 2-8, applicability of the empirical correlation to melt velocities greater than 150 cm/s is uncertain.

2.1.2.3 Epstein Analytical and Experimental Analysis. In Reference 2-19, results from the conduction and bulk freezing model were compared with experimental data. A velocity criterion to determine conditions necessary for fuel crust breakup was derived. The experimenters proposed that once crust removal occurs, melting of the tube steel wall becomes dominant, resulting in rapid fuel freezing in a bulk manner via turbulent mixing between the steel wall and hot molten fuel. In fact, they suggested that bulk freezing occurs only after the fuel crust growth process is transformed to a steel ablation process. The shiny, frozen debris observed at the conclusion of fuel freezing experiments in Reference 2-5 substantiated this suggestion because the shiny portions indicate the presence of entrained steel.

Table 2-1. Summary of melt penetration experiments.

Experiment	Material		Melt characteristics				Tube characteristics		
	Melt	Tube	T(K)	Velocity (m/s)[a]	Re	Flow	T(K)	Diameter (cm)	ΔP(MPa)
Ostensen and Jackson[2-4,2-5]	UO_2	SS	3500	15	—	—	1300	0.3[a]	1.2
Cheung and Baker[2-8]	H_2O Wood's metal Naphthalene Paraffin Olive oil	Cu	300–400[b]	0.1–1.5	—	Down	80–270	0.47–0.8[c]	—
Sienicki[2-9]	SS, nickel	SS	—	1.95–12	>30000	Up and down	—	0.33–0.64[b]	—
Epstein[2-10]	H_2O, freon, benzene	Cu	—[d]	—	>2100	—	—	—	0.2
Epstein[2-11]	Thermite	SS	3500	5	—	—	970–1170	0.3[b]	3–10
Kölig and Grigull[2-12]	Sn, Pb, Zn, Al, Inconel, Fe, and sand	Inc	—[e]	<2	—	Horizontal	—[f]	0.05	0.0
Spencer[2-13]	Thermite	SS	3500	25	—	Up	570–1300	0.3[b]	3–7
TRAN Series B Tests									
B-1[2-14]	UO_2	SS	3600	13–16	—	Up	775	0.58/0.88[f]	1.0
B-2[2-15]	UO_2/SS	SS	3600	50	—	Up	760	0.3	1.0
B-3[2-16]	UO_2	SS	3600	13–16	—	Up	1175	0.58/0.88	0.5
GEYSER[2-17]	UO_2	SS	3280	~1–3	—	Up	290	0.4/0.6	0.3
	UO_2	SS	3280	~4		Up	1270	0.4	0.3
	SS	SS	2100			Up	290	0.4	0.3
BLOKKER-II[2-18]	UO_2	SS	3280	3–7	—	Down	670	0.4/0.5/0.6	0.62

a. Ex-tube flow in and around seven-pin assembly; d_h = 0.3 cm.

b. Melt materials heated above their freezing point.

c. In-tube flow with varying inner diameter.

d. Melt Biot numbers ranged from 0.4 to 1.6.

e. Melt was superheated so that the ratio of the difference between the initial melt and wall temperature over the ratio of the melt solidification temperature and the wall temperature was $\leq$1.8.

f. Annular melt flow; d_h = 0.3 cm.

In Reference 2-10, an analytical expression for penetration distance of a saturated liquid through a horizontal tube was developed by using an approximate method for the form of the instantaneous shape of the frozen layer along the tube wall. In the limit of negligible liquid inertia, a closed-form expression for the liquid penetration length was derived and found to compare well with experimental results documented in References 2-4, 2-5, and 2-10. Although the expression developed in Reference 2-10 incorporates crust hydraulic effects on melt penetration distance, it is not applicable to cases with either superheated liquid or tube wall melting.

In a subsequent experimental study, Epstein simulated the Ostensen experiments with prototypic, fast-reactor steel-clad pins at ~1200 K.[2-11] Two different injector inventories were used in this experiment to assess the influence of thermite mass on penetration behavior. The molten thermite penetration results using a 0.5-kg thermite load were similar to those obtained in References 2-4 and 2-5. However, when the thermite injector inventory was increased to 2.0 kg, the flow front penetrated much longer distances. As in previous tests, the penetrating thermite mixture was observed to ablate the steel pins. Inspection of the frozen front revealed solid steel plugs containing only trace amounts of thermite, compared with the rough, clinker-like debris observed at the conclusion of the 0.5-kg injections. The experimenters concluded that the observed penetration behavior was incompatible with a bulk freezing mechanism and that, while steel ablation rapidly leads to fuel freezing in a bulk manner, bulk freezing does not provide significant containment capability. Instead, frozen steel is required to stop the flow, and fuel penetration is conduction controlled.

2.1.2.4 Köllig and Grigull Experiments and Analyses. In Reference 2-12, a two-dimensional, finite element model was used to determine the behavior of melts penetrating a horizontal cylinder. The model accounts for a crust developing along the outer surface of the melt and an air gap between this crust and the tube wall, resulting from thermal contraction of the solidified annulus.

Casting experiments with pure metals, such as tin, lead, zinc, and aluminum, were performed for a range of melt superheats. Experimental results were found to agree with the numerical model.

In Reference 2-12, a closed-form expression to predict melt penetration distance was derived from the two-dimensional, finite element model described above. This closed-form expression includes key dimensionless groups related to the melt superheat; melt and tube capacitance and thermal resistance; solidification enthalpy; and melt Prandtl, Reynolds, and phase change numbers. Constants and exponents for these dimensionless groups were obtained by fitting the expression to numerical model results from Reference 2-12 with a 10% tolerance.

2.1.2.5 Spencer Experiments and Analyses. Reference 2-13 reports results from thermite injection tests in which two injector sizes, capable of delivering 0.5 and 2.0 kg of melt, were employed. In one of these tests, 2.0 kg were injected into the steel pins at 1200 K, and the leading edge of the molten material was observed to travel a distance of 140 cm, which agrees with the observations reported in Reference 2-11 under similar conditions. However, a much shorter penetration distance (40 cm) was observed in two other tests in which the bundle temperature was initially 570 K. Such a short distance could not be explained by the conduction model and was nearly a factor of two larger than distances predicted by the bulk freezing model.

2.1.2.6 Sandia TRAN Experiments and PLUGM Calculations. The TRAN series experiments were conducted at Sandia National Laboratories (SNL) to investigate the

characteristics of fuel removal and freezing through the upper axial blankets of an LMFBR during the transition phase of a hypothetical core-disruptive accident.

The first series of TRAN experiments (TRAN Series I)[2-20] investigated basic phenomena between superheated, pure UO_2 melts injected upward into thick-walled steel cylindrical channels. Although the experiments confirmed certain features (e.g., stable crust growth and minimum steel tube temperatures required for tube ablation), simple models could not be directly applied to predict melt penetration phenomena, such as penetration length. In the TRAN B (blanket) series experiments,[2-14,2-15,2-16] whose results provided the most applicable data for PWR lower head failure analyses, molten UO_2 and UO_2/316 stainless steel mixtures were injected into channels with complex geometries to investigate the effects of molten steel and complex geometries on fuel relocation and crust formation. The TRAN G series (GAP series) of experiments investigated pure UO_2 and UO_2/ stainless steel mixture freezing and ablation behavior in subassemblies with various gap dimensions.

The TRAN B-1 experiment was performed to investigate the effects of curvature on crust stability. An annular geometry was selected, because both convex and concave surfaces could be tested (previous analyses had tested only concave surfaces in which the crust was held in compression). The TRAN B-2 experiment was performed to investigate the effects of molten steel on melt relocation. The third of these experiments, TRAN B-3, was similar to the TRAN B-1 experiment, except that the steel wall temperature was raised 400 K to investigate the impact of steel tube melting on crust formation.

TRAN B experiments were analyzed using the PLUGM code.[2-21] The code features include the following:

- Hydrodynamic analysis of the pressure-driven molten-fuel slug, accounting for inertial effects, area-change pressure drops, and friction losses
- Bulk-melt/wall heat transfer that accounts for stable, conduction-limited crust growth on both channel surfaces
- Calculation of molten fuel depletion by crust growth and liquid-film deposition at the trailing edge of the fuel flow
- Calculation of enhanced film deposition by Taylor instabilities, using the correct Taylor wavelength in both tube (melt chamber) and annulus (flow channel)
- The ability to model both tube geometry (melt chamber) and annular geometry (flow channel) in the same problem.

Direct examination and PLUGM calculations of the crust thickness and the penetration distance during the TRAN B-1 and TRAN B-3 experiments indicate that fuel flow and fuel/wall heat transfer were characterized by stable fuel crusts on both inner and outer channel surfaces. However, the experimental data indicate that crust formation is less stable on the outside of a rod than on the inside of a cylinder at later times. Results from the B-2 experiments indicate that fuel/steel mixtures with a low steel content behave similarly to pure UO_2 melt.

2.1.2.7 Sienicki Experiments and Analyses. A series of scoping experiments was performed to investigate the freezing and plugging behavior of molten structural materials or metal alloy fuel during severe accidents in liquid metal reactors.[2-9] Penetration phenomena for

molten metals are of interest because many metals do not wet the flow channel walls. For these experiments, molten stainless steel and nickel (superheated to between 9 and 200 K) were injected downward and upward (with various driving pressures and velocities from 195 to 1200 cm/s) into stainless steel tubes (6.4- and 3.3-mm ID) initially at room temperature.

Complete plugs were formed in all the experiments, halting the continued injection of melt. Neither the molten stainless steel nor the molten nickel were found to have wetted the solid stainless steel tube walls. However, quite different behavior was observed in the downward and upward injection tests. In the downward injection test, 71 g of the 110 g of melt injected traveled the entire 95-cm tube length. Posttest examination revealed that 13 g of the injected steel were located near the tube entrance, forming a solid plug, followed by a crust. The remaining 30 g of melt comprised four slugs at distances of 39, 43, 51, and 70 cm into the tube. This behavior is explained by the continuing acceleration under gravity of a draining liquid stream in a tube, in the absence of wetting. Once liquid slugs form, they can fall through the tube without undergoing significant heat loss (<10 K, based upon thermal radiation from the slugs to the wall).

In contrast, melt did not penetrate the entire tube length in any of the upward directed tests. Also, the injected metal in these tests consisted of a relatively long slug encompassing the tube inlet and plugging the channel, followed by a shorter "downstream region" composed of a number of slugs. The shorter penetration distances observed during these tests may be explained by noting that gravity acts to decelerate the liquid stream, causing it to fill the channel cross-sectional area such that conduction heat transfer can occur at the wall, resulting in stable crust formation upon the wall.

Analysis of the injected mass and plug formation was performed using the EMF-C (Experiment Modeling Freezing-Conduction) coupled fluid dynamic/heat transfer computer code, which calculates the conduction freezing controlled penetration of a melt within a freezing channel. Freezing is assumed to take place with the growth of a stable solidified layer, or crust, upon the channel wall (using the stable crust growth/conduction model),[2-10,2-11] and plugging occurs when the crust at some location completely occludes the channel. It should be noted that this analysis assumes that the thermal contact between the crust and the wall is perfect, even though the melt does not actually wet the tube wall. The agreement between model predictions and experimental results for the amount of injected mass that is limited by plugging justifies this calculational assumption. An analytical expression for predicting steel-ablation-induced freezing penetration distances is derived and compared with experimental data. Results were similar to distances observed in the Ostensen experiments.[2-5]

2.1.2.8 CENG GEYSER Experiments and Analysis. A series of tests was performed for the CEA by CENG (Centre D'Etudes Nucleaires de Grenoble) in the GEYSER facility to investigate the behavior of molten UO_2 as it travels through penetrations.[2-17] Results are reported from nine tests performed in the GEYSER facility during the first year of operation. Test sections of stainless steel tube were used in all these tests, although the inner diameter of the test sections varied between 0.4 and 0.6 cm. Most of the tests used a pure UO_2 source melted to an initial temperature of 3273 K, although one test used stainless steel melted to an initial temperature of 2073 K. The source was injected into the tube at the base so that the penetration distance was the distance that the melt traveled upward before freezing. A pressure difference of 0.3 MPa was applied during all the tests reported.

Experimentally measured penetration distances were found to be smaller than one calculated by the conduction freezing model and larger than one obtained with the classical bulk freezing model. Microstructure analysis of the solidified melt found equiaxed grains at the leading edge,

implying that the temperature of the fluid at the leading edge was uniform and less than the fusion temperature. Thus, results indicate that supercooling of the fluid occurred without tube ablation because of the resistance between the melt and the tube. Columnar grains were found in solidified melt in the tube, which indicated competition between the two types of grain growth.

Results from the tests indicate that the flow velocity of the melt was fairly constant; thus, the classical conduction freezing approach is not applicable. Heat transfer coefficients were obtained using experimental data and compared with heat transfer coefficients obtained using a Dittus-Boelter correlation ($Nu_D = 0.023\ Re^{0.8}\ Pr^{0.3}$), which is typically used in bulk freezing model correlations. Results indicate that the experimentally obtained heat transfer coefficients were an order of magnitude smaller than those obtained from the Dittus-Boelter correlation. Hence, the results also indicate that the bulk freezing approach also falls short for describing experimental results.

The authors postulate that nucleation theory is necessary to describe melt penetration distances accurately in these cases because of the following:

- High cooling rates and disequilibrium associated with the high Reynolds numbers that occur for melt traveling in such tubes
- Turbulence
- Interfacial resistance that develops following contact between the high Reynolds number melt and tubes.

More recent calculations by CENG are documented in Reference 2-22. The analysis considers the potential for three materials, steel, UO_2-ZrO_2, and silver, to travel through instrument tube penetrations at driving pressures up to 18 MPa. To maximize melt penetration distances, it was assumed that there was no coolant or instrument strings within the tubes. Results indicate that the melt can travel through an instrument tube from 3 to 28 m, depending upon assumptions related to melt initial temperature, melt composition, and driving pressure.

2.1.2.9 ISPRA BLOKKER II Experiments. Melt penetration tests were performed in circular and rectangular channels in the FARO BLOKKER II facility at Ispra.[2-18] For the circular channel tests, seven stainless steel tubes were tested with diameters ranging from 0.4 to 0.6 cm. In these tests, 3270 K UO_2 melt was injected downward into the stainless steel tubes at an initial temperature of 670 K and a pressure difference of 0.6 MPa.

Penetration distances for each tube in the array are listed in Reference 2-18. Experimentally obtained penetration distances were found to be longer than distances predicted with the bulk freezing model and shorter than distances predicted with the conduction model.

2.1.3 Tube Heatup Failure Analysis Summary

Few analyses of melt attack on LWR lower head penetrations were found in the literature. The only analyses of melt attack on LWR lower head penetrations reviewed in this section were performed to evaluate the integrity of the TMI-2 lower head and in-core instrument nozzles. Although in-vessel nozzle melting was predicted in these calculations, results from a two-dimensional analysis indicate that portions of the nozzle near the lower head were cooler because conductive heat transfer to the head provided sufficient cooling to prevent nozzle and

weld melting. However, these two-dimensional calculations assumed that the vessel outer surface was cooled by water.

A considerable amount of research related to melt relocation through LMFBR penetrations exists in the literature. However, this review of experimental and analytical calculations related to melt penetration in steel tubes indicates that the behavior of molten fuel freezing in tubes and rod bundles is still not completely understood. The conduction model appears to reasonably predict the behavior of simple materials injected into initially empty channels (e.g., initially without water or other materials present) with non-melting walls. However, significantly shorter distances have been observed in certain experiments with thermite entering tubes. It appears that experimentally observed distances are bounded by the values predicted with conduction and bulk freezing models.

Previous research did indicate that such factors as melt/tube geometry, material properties system pressure, initial melt velocity, initial melt superheat, and observed interactions between the melt/tube interface provide clues as to which model should be applied to predict melt penetration distance during a severe LWR accident. In Reference 2-1, scoping calculations were performed to apply some of the models for predicting melt penetration distance to the instrument tubes in the TMI-2 vessel. Large uncertainties in input parameters, such as debris composition and heat transfer properties, resulted in melt penetration distances ranging from 0.3 to 3 m. Furthermore, the analysis was performed to maximize melt penetration distances by assuming that the melt occupied the entire area within the instrument tube, neglecting the presence of coolant and an instrument string inside the tube. Data from TMI-2 nozzle examinations, such as the melt/tube interface conditions and observed melt penetration behavior, may provide insight into whether the bulk freezing or conduction model is more applicable to severe accident scenarios.

2.2 Tube Ejection of a Lower Head Penetration

If relocated core debris rests on the lower head, the resulting thermal attack on tube penetrations can fail the attachment welds. The operating system pressure can then produce a driving force that could possibly overcome the binding force resulting from differential thermal expansion of the penetration tube and lower head and eject the tube. That binding force, however, depends on the mean coefficient of thermal expansion (CTE), which varies as a function of temperature and material, for carbon steel of the lower head and Inconel or stainless steel of the nozzle penetration tube. A schematic illustration of this failure mechanism is presented in Figure 2-4. Prior research to investigate the potential for ejection of a lower head tube penetration has been performed and reported by SNL and Oak ridge National Laboratory (ORNL).

2.2.1 SNL Tube Ejection Research

Scoping calculations performed by SNL[2-23] have indicated that the material shear strength of a PWR instrument guide tube penetration weld need only be on the order of 7 MPa to withstand an operating system pressure of 17.2 MPa. However, because the inner wall temperatures of the lower head of the reactor pressure vessel during the severe accident could be as high as the melting temperature of the weld material, the effects of differential thermal expansion between the tube and lower head materials were also evaluated to see if the tubes would bind in the holes of the lower head. A lower bound estimate of the coefficient of friction between the tube and vessel hole surface was combined with differential thermal expansion calculations to conclude that the tubes could not eject under accident pressure conditions unless global sagging of the vessel

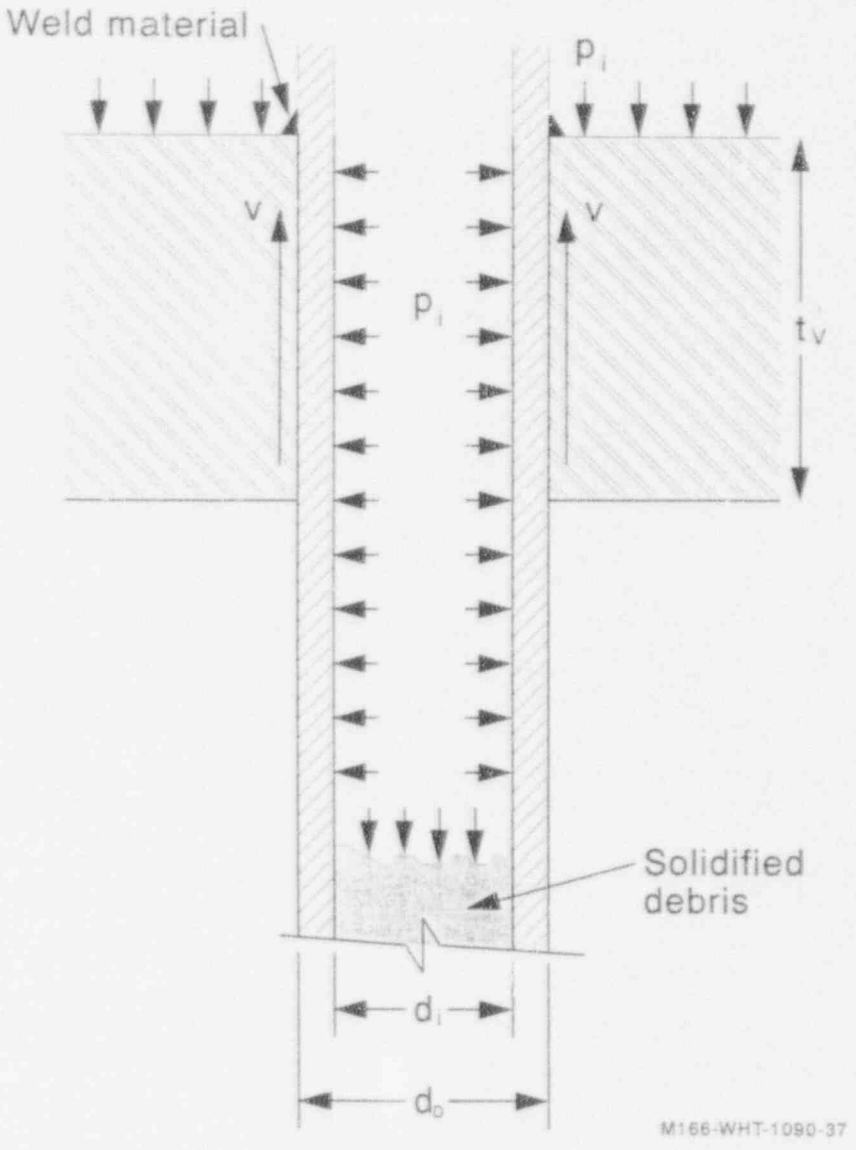

Figure 2-4. Lower head failure via tube ejection.

head occurred. An 8-mm sagging displacement of the vessel at the centerline was calculated. The displacement resulted from global creep rupture to offer sufficient dilation of the holes to allow tube ejection. This analysis suggested that differential thermal expansion might be a dominant mechanism that prevents ejection of the penetration nozzles.

A series of experiments was performed at SNL[2-24] to substantiate these analytical calculations. A prototypic instrument tube penetration was set up with the dimensions shown in Figure 2-5. The experiment apparatus consisted of a press frame, a 12-ton hydraulic ram, an induction heating coil, and the tube penetration assembly of Figure 2-5. The "zero clearance" penetration assembly was heated to steady-state temperatures ranging from 473 to 1473 K, and the required ejecting force was recorded.

In the experiments performed in this facility, the instrument tube was made of SA316 stainless steel and the metal block representing the vessel head was made of a mild steel. Results

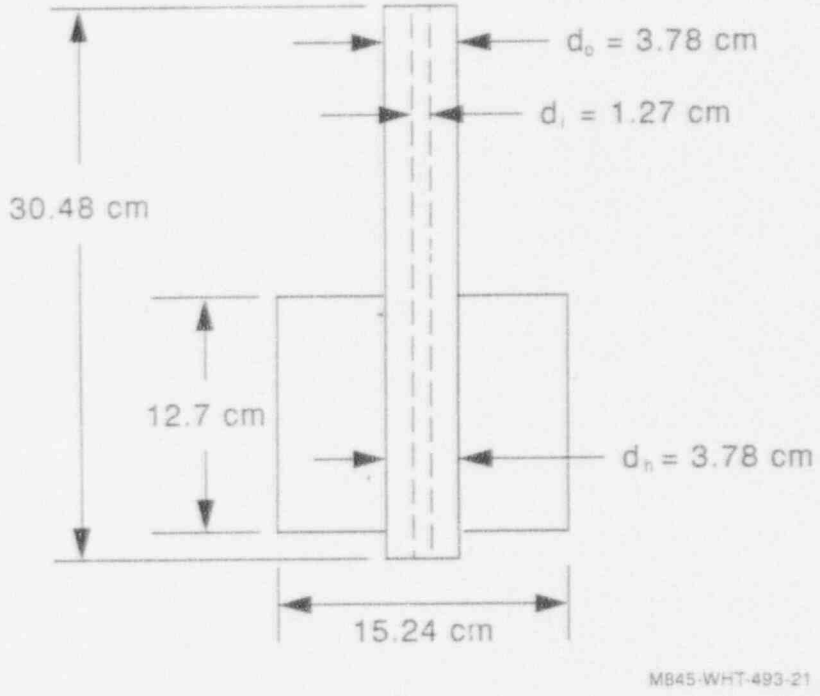

Figure 2-5. SNL tube ejection experiment geometry.

indicated that the force required to punch out the tube when the assembly was heated to 683 K was equivalent to an internal ejecting pressure of about 107 MPa. This is about 8 to 10 times greater than the operating system pressure after the core relocation at TMI-2. It is expected that tubes of Inconel, which have a lower coefficient of thermal expansion, would require a lower ejecting force.

2.2.2 ORNL Penetration Tube Failure Analysis

ORNL[2-25] has studied the failure of bottom head penetrations in BWRs. A failure scenario was proposed that included dryout of the accumulated debris bed on the lower head. This dryout would be followed by thermal attack on the control rod drive (CRD) guide and instrument tube penetrations. Failure of the CRD guide tubes would result in the collapse of the core structure onto the lower head because it is supported by the CRD guide tubes. Failure of the stub tube welds that support the CRD guide tubes is expected to occur before failure of the instrument guide tube welds at the vessel wall because these welds are above the inner surface of the vessel wall. However, it is postulated that ejection of the CRD guide tubes would not occur because the CRD housing support under the vessel limits downward displacement to about 3 cm, whereas the vessel wall thickness is more than 20 cm. Thus, instrument guide tube failure was evaluated.

A transient heat transfer model of the melt, vessel wall, instrument tube wall, and structures interacting with the instrument tube beneath the vessel has been developed for calculating temperature distributions in the tube. For a case in which it is assumed that metallic melt relocates to the lower head with no superheat or internal heat generation, temperatures above 1478 K are predicted in the tube. Creep rupture from the combined weights of the ex-vessel portion of the tube, the solidified debris, and the instrument string is expected within tens of seconds.

2.2.3 TMI-2 Instrument Tube Analysis

The Babcock & Wilcox investigation[2-2] discussed in Section 2.1.1 also studied the ability of the in-core instrument nozzles to carry axial, bending, torsion, and internal pressure loads after the TMI-2 accident. The instrument nozzle-to-vessel welds were assumed to be degraded, in that only a portion of the original weld remained. Simple hand calculations using the material ultimate strength were employed. Required remaining weld thickness for given temperatures and load levels were calculated.

The results show that the minimum weld thickness required to hold the in-core instrument nozzle in the lower head, given a 13.8-MPa vessel internal pressure difference, was 0.0178 to 0.076 cm at head temperatures of 590 to 1580 K. A minimum weld thickness of 0.076 cm was shown to support 24 kN of axial load, 158 N-m of bending moment, or 655 N-m of torque at defueling temperature conditions. The report indicated that results have some uncertainties because of a lack of material properties for Inconel-600, which is the material used in instrument nozzles for temperatures above 1140 K.

2.2.4 Summary of Tube Failure Evaluations

Only a limited set of preliminary calculations and experimental efforts on nozzle ejection were found in the open literature. Assumptions concerning different material properties and tube geometries for the various bottom head penetrations have resulted in conflicting conclusions concerning penetration tube ejection. In the SNL studies, an assumption of no gap between the penetration tube and vessel hole resulted in conclusions of no ejection. In reality, gaps do exist at ambient temperature to allow insertion of the tubes into the holes under field fabrication conditions. Tolerances on the tube outer diameter and the vessel hole diameter contribute to the bounding gap dimensions.

In competition with the failure mechanism of tube ejection is the possibility of ex-vessel tube rupture. Once melt is in the tube, certain conditions allow melt to penetrate down the tube and past the vessel wall before plugging. An assumption of hydrostatic conditions in the melt above the plug result in a tube loaded by operating system pressure and degraded in structural strength because of very high temperatures. Because of this competition, a simultaneous assessment of both failure mechanisms considering material properties and tube and hole geometries is necessary.

2.3 Lower Head Global Rupture

When temperature and stress levels in a significant portion of the vessel lower head wall exceed a certain limit, the lower head may fail immediately by ultimate strength failure or over time by global creep rupture. A schematic illustration of a vessel lower head collapsing from creep rupture failure is presented in Figure 2-6.

This section provides a review of research by SNL, Electric Power Research Institute (EPRI), Idaho National Engineering Laboratory (INEL), and ORNL that investigated the potential for global lower head failure from creep rupture. The SNL investigations indicated that thermally induced strains do not significantly affect the time of vessel failure. The EPRI analyses indicated that global failure of a PWR vessel could occur between 10 minutes and 1 hour for an accident having a molten debris pool in a PWR. The INEL calculations focused on the impact of

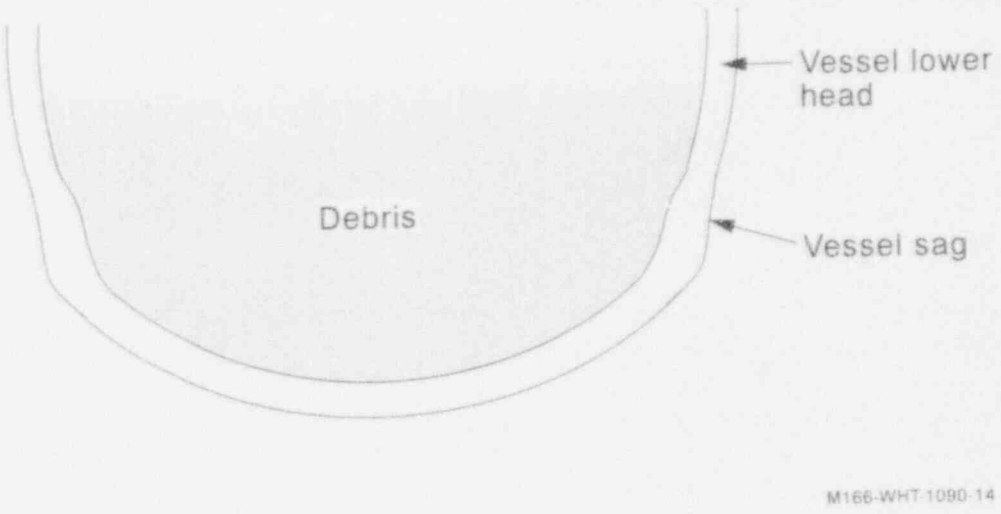

Figure 2-6. Global collapse of the lower head.

debris configuration and coolability on creep rupture failure during a TMI-2 type event. The ORNL studies concentrated on the likelihood of creep rupture in BWR designs, where it is more likely that the vessel will be depressurized and dry prior to vessel failure.

2.3.1 SNL Analysis

A finite-element analysis of a pressurized vessel was performed at SNL by Chambers,[2-24,2-26] who used finite-element computer codes to develop temperature distributions that were then used in a finite-element thermal stress analysis: COYOTE[2-27] for a two-dimensional heat conduction solution and JAC[2-28] for stress analysis. Creep effects were not included in the model.

This analysis examined the importance of thermally induced strains on lower head failure. Calculational results indicated that even though thermal strains increase the magnitude of the sag in the vessel head and alter the stress distribution throughout the vessel thickness, they have no significant effect on the time of vessel failure. Results indicated that the rupture of the vessel occurs when the hot inner portion of the vessel wall degrades in strength, and the vessel fails when the cooler outer portion cannot withstand the pressure stress.

Reference 2-29 documents results from a one-dimensional model that considers melt progression in the debris as well as the thermal and mechanical response of the vessel lower head. The study was performed in order to identify the parameters that most affect the plenum debris and vessel failure times resulting from creep rupture.

The thermal model considers a corium bed composed of UO_2, ZrO_2, and stainless steel. The model includes the effects of melt relocation. A uniformly mixed debris bed and a stratified bed were compared, as were an insulated boundary and a radiative vessel boundary. Debris bed porosity and particle diameter were varied. The initial temperature of the debris was set equal to the saturation temperature of the coolant at the pressure of interest for all cases investigated. The vessel internal pressure was varied from 2 to 15 MPa.

The creep-rupture failure mode was investigated by using the Larson-Miller[2-30] correlation. This approach is based on sets of equations that give the time to rupture, given a constant stress and temperature level. The material data used to develop the Larson-Miller equations were based on extrapolated lower temperature data.[2-31] Because the stress states of the material in the lower head are transient during accident conditions, a life fraction rule was used to account for the varying stress and temperature. The life fraction rule assumed that damage to the lower head was cumulative.

Results of the analysis indicate vessel failure times from 3,300 to 6,000 seconds (with an insulated boundary) or 3,600 to 7,900 seconds (with a radiative boundary), for system pressures of 2 to 15 MPa. Pressure and boundary conditions had the greatest effect on failure times. Competing effects were found to reduce the sensitivity of analysis results to assumptions related to debris bed porosity. Vessel temperatures initially increased more slowly for higher porosity debris beds because of the reduced effective conductivity. However, this effect is offset when temperatures in the debris bed reach melting because there is more space available for melt relocation in a higher porosity debris bed. Likewise, the competing effects of effective conductivity and flow resistance during melt relocation made analysis results less sensitive to particle size assumptions. A stratified debris composition substantially increased the failure times over the uniformly mixed bed times reported above.

2.3.2 EPRI Analysis

EPRI's IDCOR Program sponsored a creep rupture analysis of a PWR lower head with no penetrations.[2-32] Thermal response was calculated for an instantly formed molten debris pool on the vessel lower head using an axisymmetric finite difference model with General Electric's Transient Heat Transfer Program.[2-33] The MARC finite element structural analysis code[2-34] was used to calculate the thermal stresses. Structural material properties for SA533B1 were extrapolated beyond existing test data at 922 K, constant internal pressures were varied from 100 to 2500 psi, and a constitutive creep law modeled the visco-plastic response of the lower head to the thermal transient. The corium pool's depth, initial temperature, decay heat generation rate, sink temperature at the free surface, and the film coefficient of the vessel outer surface were varied to offer a qualitative estimate of the expected temperatures and resulting structural response of the lower head.

Typically, the stress distribution in the wall started with a uniform stress resulting from internal pressure. The temperature of the hot inner region of the wall increased from 533 to 1473 K a few seconds after the beginning of the transient, and within a few minutes the entire vessel wall temperature was above 700 K. As time progressed, the cooler material nearer the outer surface carried an increasing proportion of the load because the capacity of the inner region was degrading with the increasing temperature. Finally, collapse occurred when the head could no longer support the internal pressure load.

An approximate solution for calculating times to creep rupture was developed based on the phenomena discussed above. This solution simply evaluated the ultimate strength at various locations through the wall for a spatial temperature distribution at a given time, integrated those strength values over the entire wall thickness, and compared that maximum membrane load carrying capacity to the pressure-induced membrane load. When the head's membrane capacity was exceeded, the time at which the evaluated temperature distribution occurred in the transient was considered as the time of rupture. Estimations of rupture time from this simplified calculation procedure compared very well with the structural finite-element analysis for internal

pressures from 4.2 to 17.5 MPa. For internal pressures near 0.7 MPa, a caution was made that complete melt-through of the head may be a competing failure mode.

2.3.3 INEL Analysis

Studies at INEL[2-35 through 2-41] addressed characteristics of the relocated core debris bed and the vessel response in the TMI-2 accident. In References 2-39 and 2-41, finite-element analyses are described in which the COUPLE/FLUID[a] code was applied to model postulated configurations of the debris bed and their interaction with the vessel wall. Transient temperature distributions were developed and input into lower head stress calculations,[2-41] which were performed with the ABAQUS structural analysis code.[2-42]

The heat-transfer analysis consisted of an axisymmetric model of the relocated debris bed and vessel wall. Because of uncertainties regarding the heat transfer properties between the debris and vessel wall, three possible debris states were considered:

1. *Upper-Bound Configuration*. This depicted an upper-bound thermal challenge to the vessel. A layer of porous debris was assumed to settle onto the lower head. The interstices between the debris particles were assumed to be filled with molten control rod and/or core structural materials, resulting in a consolidated (zero porosity) layer of metallic/ceramic material adjacent to the vessel. This layer transmitted heat to the vessel more rapidly than the ceramic material. A porous debris bed was assumed to be supported on the frozen upper crust of the consolidated region.

2. *Lower-Bound Configuration*. This represented a lower-bound thermal challenge to the vessel. It consisted of a porous debris bed separated from the vessel by a layer of solidified control rod material assumed to have relocated and frozen before the major relocation event. In this case, the frozen control rod layer acted as a heat sink and added thermal resistance to heat flow from the debris to the vessel wall.

3. *Intermediate Configuration*. This consisted of a porous debris bed similar to that of the lower-bound case; however, control rod material was absent from the debris.

In addition to uncertainties in the debris configuration, uncertainty existed relative to the coolability of the various types of debris. Combining debris configuration with coolability produced six possible debris states.

Lower head rupture was estimated for the various combinations of assumed debris bed configuration and quench status[2-41] using an average value of the operating system pressure, which was measured throughout the accident, a maximum midwall temperature calculated by COUPLE/FLUID, and a creep rupture criterion developed in Reference 2-40. This creep rupture criterion was developed from Larson-Miller parameters for SA533B1 and pressure stresses in a hemispherical head of the TMI-2 dimensions. Table 2-2 summarizes rupture times estimated in Reference 2-41.

---

a. E. C. Lemon, unpublished research concerning *COUPLE/FLUID*, a two-dimensional finite-element thermal conduction and convection code at EG&G Idaho, Inc. Note that the COUPLE model was later incorporated into SCDAP/RELAP5, which was applied in the Section 5 finite element analysis.

Table 2-2. Estimated TMI-2 vessel creep rupture times.

Debris configuration	Debris cooling	Average reactor system pressure (MPa)	Maximum vessel mid-wall temperature (K)	Estimated time for creep rupture (h)
Upper bound	Dry	9.5	1481	<0.1
Upper bound	Quenched	9.5	1366	<0.1
Intermediate	Dry	9.5	1366	<0.1
Intermediate	Quenched	9.5	907	100
Lower bound	Dry	9.5	1023	<0.1
Lower bound	Quenched	9.5	825	No rupture

Because the TMI-2 vessel did not fail, and, as indicated in Table 2-2, the dry bed scenarios would have failed the head within an hour, the next most stringent condition, the intermediate quenched case, was selected for the detailed creep rupture analysis. An axisymmetric finite-element model of the lower head with no penetrations was developed for the stress analysis. Thermal creep and plastic material properties were used in the model. Time-varying operating system pressure, which had been measured during the accident, was applied to the model in conjunction with the temperature distribution history provided by the COUPLE/FLUID calculation. Operating system pressure was the predominant mechanical load during the accident. The maximum total strain (elastic + plastic + creep) developed in the model for the scenario selected was about 1%, which is considerably less than the 25 to 30% required to rupture the pressure vessel steel at the corresponding temperature levels.

2.3.4 ORNL Analysis

ORNL has considered lower head failure in BWRs.[2-25] Because the BWR Owner's Group Emergency Procedures Guidelines[b] direct reactor operators to manually depressurize the reactor vessel very early in a severe accident sequence, the wall membrane stress in a BWR lower head is expected to be only about 1 MPa. This stress results only from the weight of the debris and the head itself. At this low stress level, vessel wall temperatures would have to be near the melting point of the vessel material for vessel failure to occur. The vessel penetrations are expected to fail long before this. As an example, a short-term station blackout scenario resulted in penetration failure within 10 minutes after debris bed dryout, and global failure of the head about 3-1/2 hours later.

ORNL has recently completed a study to evaluate several strategies for management of postulated BWR severe accidents.[c] Drywell flooding, vessel skirt venting, and vessel depressurization were considered. The vessel lower head analysis used the Larson-Miller correlation[2-30] to evaluate creep-rupture failure. The Larson-Miller parameters were based on the

b. Available from the General Electric Company and the BWR Owner's Group.

c. S. A. Hodge, Oak Ridge National Laboratory.

high-temperature SA533B1 steel data documented in Appendix B of this report. The Hodge ORNL results showed that a flooded well, with venting of the vessel skirt (to eliminate an air pocket at the vessel lower head), significantly increased the time to failure of the vessel. Vessel depressurization also increased the time to failure.

2.3.5 GRS Analysis

The German Bundesminister für Forschung und Technologie (BMFT) supported an effort by the Gesellschaft für Reaktorsicherheit (GRS) to compare three analysis methods for predicting PWR lower head failure.[2-43] The load case employed, which simulated a core meltdown scenario, defined interior pressure and inner-vessel-wall-temperature versus time envelopes. The first analysis method involved a modified elastic-plastic approach that used temperature independent values for parameters, such as Young's modulus, Poisson's ratio, and the coefficient of thermal expansion, at high temperatures. These properties were developed from average values of these properties at lower temperatures. Creep effects were not included. The second method used a finite-element solution that included the plastic material behavior as well as creep effects. The third method consisted of a simple analysis that employed the Larson-Miller[2-30] correlation and a life fraction rule.

The results gave failure times for all three analysis methods from 1,800 to 2,450 seconds. The modified elastic-plastic method gave the shortest failure time (1,800 seconds), which was considered to be conservative. However, in accident scenarios where creep effects are more significant (where the entire vessel bottom head is above 1000 K), this method would be excessively conservative. The finite-element model with creep properties and the Larson-Miller evaluation predicted failure in the middle and upper end of the time envelope.

2.3.6 BCL MARCH2 Vessel Strength Model

The MARCH code,[2-44] developed at Battelle Columbus Laboratories (BCL), describes the physical processes governing the progression of core meltdown accidents. It includes a bottom head failure model that compares applied stresses, calculated using a mechanics of materials approach, with the tensile (ultimate) strength of the vessel. Creep failure is not considered. The MARCH2 model also includes an option to allow leakage of gases and water, but not of debris. Leakage starts when the head temperature at a user-specified thickness exceeds 891 K (1144°F).

The applied stresses include the effects of dead loads and are calculated at four locations: (a) the junction of cylindrical and hemispherical parts of the vessel; (b) the point of the vessel corresponding to the debris top surface; (c) the maximum longitudinal stress in the cylindrical part of the vessel; and (d) the maximum circumferential stress in the cylindrical part of the vessel. The tensile strength is calculated assuming either a linear temperature distribution through the wall thickness or a bilinear distribution; melted portions are subtracted from the thickness. The bilinear distribution has a limited definition. The outside wall temperature must be the head temperature at the start of the calculation. Traversing inward, the temperature distribution must be flat to a point in the interior, where the temperature increases linearly to the maximum temperature (below melt) on the inside wall.

The MARCH models are particularly useful in cases with low pressure and large debris or water volume, where stresses induced by dead loads would be significant compared with stresses induced from pressure. However, significant error may be introduced in the MARCH calculation of temperature-dependent tensile strength, given the limitations on allowable through-wall

temperature distributions and the temperature sensitivity of tensile strength in the 600–1000 K range.

2.3.7 INEL SCDAP/RELAP5 Vessel Creep Model

The SCDAP/RELAP5 code,[2-45] developed at the INEL, gives best-estimate transient simulation of LWR systems during a severe accident. It includes a bottom head failure model based on creep rupture theory. Applied stresses resulting from pressure loads are calculated using a thin-walled, mechanics of materials approach. Through-wall vessel temperatures from the finite-element thermal analysis are averaged over user-specified elements. The fraction of the life "used" for a given stress or temperature calculation is calculated using either the Larson-Miller parameter[2-30] or the Manson-Haferd parameter.[2-46] Damage is accumulated using the time damage model.

This model is particularly useful for cases where temperatures are above half the vessel material's melting temperature, but pressures are not high enough to cause immediate failure. Here, time-dependent creep rupture is possible, whereas calculations based only on tensile strength would not predict failure.

2.3.8 Summary of Global Rupture Analyses

Study of the prior efforts in global head failure indicates that stress conditions in the vessel lower head tend to be complex and time varying during a general heatup that results from the decay heat of a debris bed. However, observations of the macroscopic trend in vessel wall response to such heatup tends to indicate that a much simpler, analytic model of structural capacity may be possible. This simpler model would then allow simultaneous evaluation of global failure with the tube penetration failure mechanisms discussed previously.

Tying the evaluation of these failure mechanisms together in simple analytic solutions offers an evaluation of the failure sequence and the development of easily understood failure maps. This development is discussed in Section 4.

2.4 Jet Impingement

The localized attack caused by jet impingement onto the lower head of a reactor vessel is a potential failure mechanism. Relocating molten material, such as corium or in the early stages of a severe accident, metals, can fall to the bottom of the vessel and may ultimately lead to its failure. The failure can be brought about by an active erosion process of the relocating material in the form of a jet or by localized heating of the vessel from the mass of relocated material. Several experiments and analyses have been performed to determine the breakup of the jet material by a fluid and the erosion or ablation rate of a molten jet on the solid vessel wall. Some of the analyses also consider the effects of breakup and dispersion by a fluid, such as water or gas, that could be present in the lower vessel during melt relocation.

The review of this research has been broken down into two parts. The first part will present the analyses that pertain to the erosion and heat transfer processes associated with a jet impinging onto a solid surface, such as steel, representing the vessel lower head. The second part will discuss mixing and breakup analyses used to determine the behavior of a molten jet when it enters and travels through a fluid such as air or water.

2.4.1 Jet Impingement and Heat Transfer Analyses

The exact composition of a molten jet that could be produced in a severe accident is both reactor and reactor-accident dependent. Experiments have used varying simulant mixes of metals as well as corium mixtures of ceramic UO_2, ZrO_2, and stainless steel for the jet. Depending on the plate and jet composition, a liquid melt layer from the plate, a solid crust from the jet, or both can form and significantly affect the rate of heat transfer from the jet to the solid plate material, possibly insulating the jet from the solid and preventing any significant plate erosion. Despite the predicted presence of insulating layers, evidence for the erosion of vessel metal by both corium and metal mixtures exists. Figure 2-7 is an example of a vertical jet impinging on a horizontal solid surface with a crust and a melt layer formed at the interface.

2.4.1.1 Cronenberg Analytical Calculations. Reference 2-47 presents analyses performed to understand melt relocation behavior of and damage progression to TMI-2 vessel components. The potential for vessel ablation due to jet impingement was also assessed. The study found that heatup of the lower head is largely controlled by the time over which jet impingement takes place and the heat transfer characteristics at the contact surface. It assessed jet impingement heat-transfer characteristics for two limiting conditions. The first condition was for a weak jet with conduction-limited heat transfer (through stratified liquid layers), while the

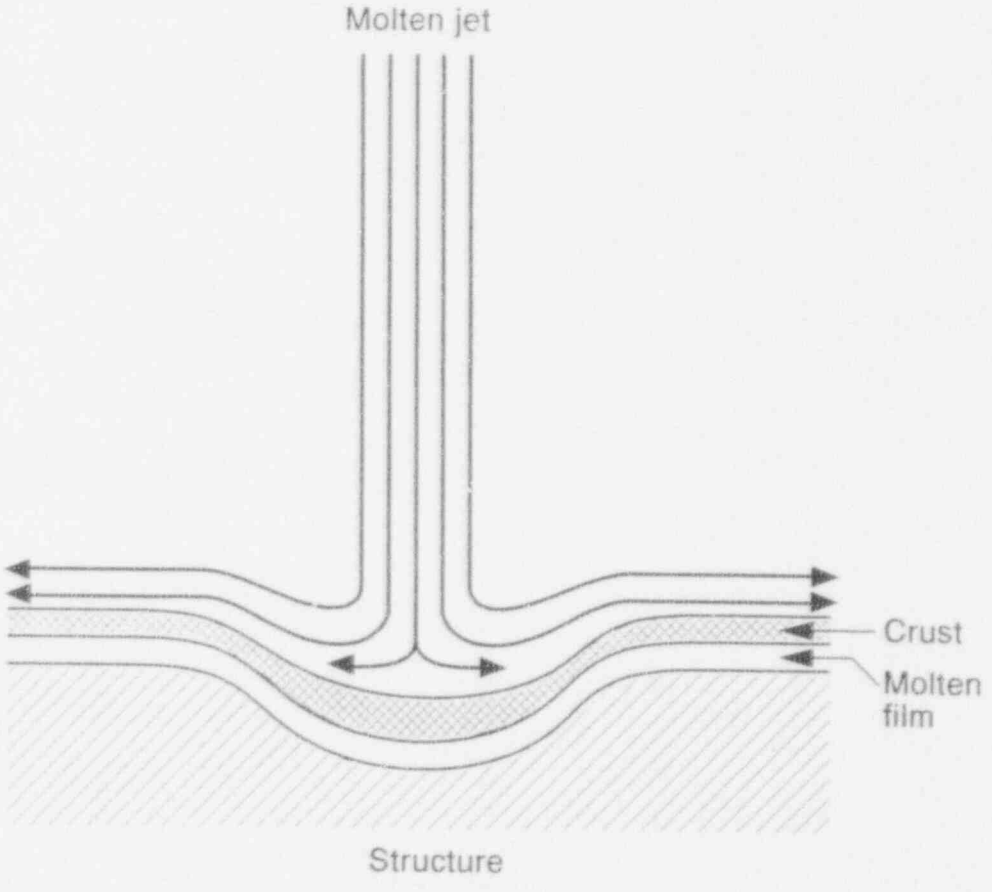

Figure 2-7. Configuration for analyzing a vertical jet impinging on a horizontal surface.

second condition was for strong jet forces, where turbulent mixing and mass transfer effects at the impact surface led to convection-controlled heat transfer. No ablation of the lower head is expected for the conduction-controlled heat transfer because of the relatively low conductivity of the molten ceramic material (corium) and the high thermal capacity of the large vessel head. Some ablation is predicted from convection-controlled heat transfer calculations. These calculations assumed a flow diameter equal to the hydraulic diameter of the flow area in a single undegraded fuel assembly and 20,000 kg of molten material. For a molten core relocation time of 75 seconds, a 0.5-inch penetration depth is calculated for the 5.5-inch head thickness. Furthermore, based on similar calculations, it was predicted that the lower vessel head for the TMI-2 reactor was probably not close to failure from ablation. It should be noted that these calculations treat jet impingement in a simplistic fashion, neglecting jet/coolant interactions and jet/lower plenum structure effects.

2.4.1.2 Powers High Temperature Melt Experiments. References 2-48 and 2-49 discuss results of the MC and PLATE experiments performed at SNL and supported by the NRC. The three MC experiments were large-scale tests consisting of 207 to 222 kg of molten type 304 stainless steel at 1978 to 2003 K impinging upon steel plates. The PLATE experiments were small-scale tests with high-temperature melts consisting typically of 3 kg of molten 55 wt% iron and 45 wt% alumina at approximately 2673 K impinging upon steel, stainless steel, and urania coated steel. One PLATE experiment (PLATE 16) was performed with 5 kg of molten corium consisting of 54 wt% UO_2, 16 wt% ZrO_2, and 30 wt% stainless steel at ~3053 K impinging upon a steel plate. Most of the experiments showed rapid erosion of the plates by the impinging jets. The exceptions were the plates with the urania coatings. The plate with the thickest coating of urania (2 mm) showed no ablation, which has been attributed to the combined effects of urania's thermal resistance and higher melting temperature. The velocities of the melt streams were varied for several experiments, and the rate of erosion was determined at the point of melt contact. Thermocouple behavior indicated that a cool layer of steel was present until just before penetration. Thus, a thermal ablation process appeared to be responsible for plate erosion and perforation.

2.4.1.3 Sienicki and Spencer Reactor Material Experiment Studies. Reference 2-50 presents results of three reactor material experiments: Corium-Structure Thermal Interaction (CSTI)-1, CSTI-3, and Corium-Water Thermal Interaction (CWTI)-11. These corium interaction experiments impinged a mixture of 60 wt% UO_2, 16 wt% ZrO_2, and 24 wt% stainless steel at an initial temperature of 3080 K (160 K above the liquidus temperature of the oxide phase) onto a stainless steel plate 1.27 cm thick. The corium for these three experiments fell 35 cm to the plates. The velocity was increased for CSTI-3, and even more for CWTI-11, by pressurizing the feed volume. The results of these experiments were studied to investigate the basic mechanisms of corium-structure interactions, particularly the effect of a crust forming at the interface that could insulate the structure from the hot molten corium. No significant ablation occurred, but some pitting of the plates was apparent. This supports the possible existence of a crust because calculations predict that the plate should not melt in the presence of a crust. The CSTI tests are similar to the PLATE 16 experiment, where significant ablation was reported. The corium for that experiment was at a slightly lower temperature (3053 K versus 3080 K), but had 6% less UO_2 (and consequently 6% more stainless steel) in the jet mixture. The higher steel content increases jet thermal conductivity and the amount of heat transferred from the molten pool to the steel structure (with or without the presence of a crust). Also, 5 kg of corium relocated in the PLATE experiment compared with 2.4 to 3.3 kg for the reactor material experiments. Other possible variations that may explain the conflicting erosion results are differing velocities (and flow conditions), differing jet diameters, and differing grades of plate steel.

2.4.1.4 Epstein Model and Experiments. Reference 2-51 presents a laminar-axisymmetric flow model developed to describe melting heat transfer in the presence of jet solidification (crust formation) during impingement. When molten jet and walls are immiscible liquids and the fusion temperature of the jet material is greater than the wall's, simultaneous melting of the wall and freezing of the flow can occur. This behavior is expected for molten corium jets impinging on steel vessel walls with lower melting points. The supporting experiments were performed with hot water impinging upward and melting the bottom of octane and mercury rods. From the experiments it was determined that the melting rate of the solid is a function of the difference between the liquid jet temperature and the freezing temperature of the solid; and consequently, the melting rate goes to zero as the impinging jet approaches its freezing temperature. The melting rates observed in the experiment agreed well with the simple axisymmetric melt flow model predictions that a circular disk of frozen jet material would separate the water jet from the melt layer. Such a disk of ice was readily observed at the interface of a melting rod and water for a water jet around 5 K.

2.4.1.5 Swedish Model and Experiments. Reference 2-52 discusses theoretical and experimental investigations of a hot water jet impinging on a melting solid surface of ice, octane, P-xylene, and olive oil. A laminar stagnation flow model was successfully used to describe melting heat transfer in the jet impingement region despite turbulent jet conditions, and the melting rate measurements were found to agree reasonably well with model predictions. Results are believed to be useful for determining the rate of ablation of low melting point solids subjected to hot liquid jets of normal incidence. It was shown that an approximate analytic solution that treats the melt layer as a thin film is useful for predicting melting rates over a range of jet velocities and temperatures. Despite highly turbulent jet flow, experimental data indicate that a melt layer is always present and insulates the melting surface from an impinging jet.

2.4.1.6 Furutani Experiments. Reference 2-53 presents a series of experiments that study the effect of a molten layer on plate erosion during jet impingement. The experiments were performed with plates made of Wood's metal and two types of paraffin. The liquid jet consisted of hot water ranging from 333 to 363 K. An analytical solution for predicting erosion was developed assuming that a thin film of molten material existed at the interface of the jet and solid plate. The solution was found to be reasonably accurate except where large (deep) pools of molten material collected above the plate's surface. Several effects from the impingement experiments with these materials were noted. The erosion rate was observed to increase with both jet temperature and jet velocity, as expected. Erosion rates lowered with increasing ratios of erosion depth to jet diameter because of the effects of the molten pools formed on the plates. The decrease in erosion was more significant for cases with higher viscosities of the molten plate and higher density ratios of the molten plate to the liquid jet. Inclined plate experiments showed that the erosion rates increased with plate inclination and were close to thin film model predictions because of continuous removal of molten material allowing no pool buildup. The results of these experiments and the thin film model developed for predicting erosion rates are not applicable to the case of corium impingement onto solid plates where a thin crust of jet material was determined likely to develop in addition to the thin film of molten plate material.[2-51] However, these results are significant for the scenario where molten metal may precede relocation of the molten corium and impinge on the metal vessel, forming a thin film but no crust. Additional experiments are planned for jets of molten steel by the Power Reactor and Nuclear Fuel Development Corporation in Japan to validate the thin film model.

2.4.1.7 Saito Model and Experiments. Saito et al. developed a turbulent jet flow model[2-54] analogous to Epstein's laminar jet flow model discussed in Section 2.4.1.4. However, in addition to calculating the erosion rate, the Saito model predicts the crust thickness, molten layer

thickness, and threshold jet temperature for crust formation. Both freezing of the jet and melting of the solid are possible when the interfacial temperature is between the freezing point of the jet and the melting point of the solid plate (a considerable range for typical corium and vessel wall steel). The model was developed from and compared with results from two sets of experiments. In one set of experiments, molten salt (NaCl) was impinging perpendicular to a tin plate. An initial set of experiments using an Al_2O_3 jet and stainless steel plate was performed, which helped check the effects of thermo-physical properties on erosion behavior. Results of the study emphasized that crust and melting film layers significantly affect erosion rates. It was also observed that when the ratio of erosion depth to jet diameter exceeded four, the erosion rate tends to substantially decrease from the interaction between the jet and the stagnant molten pool effect. This phenomenon was labeled "pool effect" and, though related, it should not be confused with the pooling of molten material above the plate, which does not necessarily lead to the same results.

2.4.1.8 FARO facility and BLOKKER I Experiments. Reference 2-55 provides a brief description of the FARO facility and the state of test programs for LMFBR safety research conducted there. FARO is a large, multipurpose test facility used to study simulated accident conditions through out-of-pile experiments. Test programs discussed are the ablation tests for fuel impact and erosion against stainless steel (BLOKKER I), the metal freezing and blockage in channels and clusters (BLOKKER II, which are discussed in Section 2.1.2.9), and UO_2-sodium interaction tests for jet stability and fragmentation (TERMOS, which are discussed in Section 2.4.2.7).

Additional discussion of the BLOKKER I test results and analyses can be found in Reference 2-18. The BLOKKER I series of plate erosion experiments impinged around 100 kg of UO_2 onto preheated stainless steel plates. The inclination angle of the plates was varied for the series covering 5, 45, and 90 degrees with respect to the vertical jet. No ablation occurred for the 45- or 90-degree inclined plate. However, there was moderate ablation of the nearly vertical 5-degree inclined plate, suggesting that a large melt-mass exposure of plates to pure UO_2 (at grazing incidences) could lead to substantial erosion. A crust at the interface was found for all cases, with the thinnest crust occurring for the 5-degree inclined plate and, naturally, the thickest for the 90-degree plate. Apparently, the poorly conductive crust of the pure UO_2 for the horizontal 90-degree plate prevented ablation unlike that found for the similar PLATE 16 experiment with the more conductive corium mixture (Section 2.4.1.2).

2.4.1.9 KfK Experiments. Experiments were performed at the Kernforschungszentrum Karlsruhe (KfK) to investigate the erosive effect of oxide material impinging upon a horizontal steel plate. In the tests, an Al_2O_3 thermite stream, 20 mm in diameter, impinged upon a 40 mm thick horizontal stainless steel plate through an air atmosphere. Tests were run for initial plate temperatures of 1173 and 1473 K. Test results, which are documented in Reference 2-56, indicate that the erosion area on the surface of the plate was increased in the higher temperature test. However, no macroscopic increases were observed in the erosion depth in the higher temperature test.

2.4.1.10 Pessanha and Podowski Analysis of Inclined Jets. Reference 2-57 summarized analyses of vertically oriented ablation from inclined impinging jets. The authors have developed two-dimensional theoretical models of simultaneous flow and heat convection in inclined jets combined with heat transfer across the moving layer of melted wall material. Model calculations showed good agreement for impingement angles greater than 45 degrees for two sets of experiments. The developed model uses an approximate solution technique to calculate such parameters as wall ablation rates and jet to wall heat transfer coefficients as a function of jet

inclination angle. While the model developed for this study is more applicable to the ablation of vertically oriented structures such as core baffle plates, it is useful for extending ablation behavior to geometries where pooling would not immediately occur. This category might include the perimeter of the lower head vessel wall, which is sloped.

2.4.1.11 United Kingdom Atomic Energy Authority Analyses. Results from scoping calculations to investigate the potential for vessel ablation following debris relocation are documented in Reference 2-58. The analysis assumes that the debris relocates as a coherent jet and an empirical correlation for laminar gas jets is applied to predict the maximum heat flux. Both the case in which a thin, stable crust of debris forms at the vessel wall and the case that the vessel is directly attacked by the molten debris are considered. Crust growth and vessel thermal response were predicted using models from the MELTPV code[2-59]. Results from a case in which the lower head is protected by a ceramic crust indicate that the maximum ablation depth is insignificant (less than 0.60 cm of the ~14 cm thick vessel). In cases without crust formation, ablation is still insufficient to fail the vessel (less than 7.2 cm), although the welds holding lower head instrumentation tubes may be ablated sufficiently to cause vessel failure via tube ejection. It should be noted that these results were obtained for cases in which a coherent jet attacks the lower head without any heat losses to coolant or structures that are typically present in the lower plenum.

2.4.1.12 Ablation Analyses Conclusions. Experiments have shown that a potential exists for significant erosion by molten reactor materials such as corium and stainless steel under certain circumstances. Experimental data also indicate that several phenomena will limit the potential for jet erosion, such as the formation of a ceramic crust on the vessel surface and the formation of molten pools with relatively large depth to jet diameter ratios.

Experiments indicate that important parameters for predicting ablation behavior include jet temperature and velocity, erosion-depth-to-jet-diameter ratio, pool depth of accumulated melt, melt composition, and plate and jet inclination angle. Extensive models describing both heat-transfer and ablation (erosion) rates have been developed from non-reactor materials. Because experimental melt results indicate that ablation is dependent on material properties, models need to be developed in terms of dimensionless parameters, and experimental data should be used to validate the analytic solutions for model parameters, such as the heat transfer coefficient from high temperature jets. Then, it will be possible to adequately describe and predict the jet impingement stage of a severe accident in LWRs.

2.4.2 Jet Mixing and Breakup Analyses

Jet breakup and mixing behaviors are important parameters for determining the ultimate magnitude of concern for jet impingement as a vessel failure mechanism. As mentioned, some studies have indicated that certain metals and corium mixes have the potential to ablate vessel wall materials. The ability of the vapor and liquid, which exists between the effective nozzle (likely to be the lowest core former as in the TMI-2 accident) and the lower head liner surface, to break up a molten jet could significantly affect the final accident outcome. In terms of localized lower head vessel failure, three potential effects arise from the presence of a fluid, such as a vapor or water. First, the presence of a fluid could have little effect on the jet, which then has the potential to ablate the lower head, as previously discussed. Second, the fluid may cause some breakup leading to an uncoolable pile of debris with the potential to melt through the vessel wall. Third, the fluid could lead to significant breakup of the jet into coolable fragments with no concern for ablation or heating through the vessel.

One indicator used to describe breakup is the jet breakup length, which is the depth where the jet is completely fragmented. The breakup length is frequently scaled in terms of jet diameter. It is suspected that much of the base core support structures will remain intact up to and past the time when core melt relocates to the lower vessel head and, therefore, the jet diameters will be limited by holes in these structures (about 3 to 10 cm for TMI-2). Thus, for a 10-cm diameter jet draining into a 1.0-m pool, the relocation distance would have to be more than 10 jet diameters to prevent a coherent portion of the jet from reaching the wall.

Another important measure of breakup is the droplet size formed from jet fragmentation. Studies indicate that the fragmented droplet diameter and, consequently, the erosion rate are functions of the instability wavelengths along the interface of the jet and surrounding pool, so a considerable emphasis has been placed on determining the exact role of instabilities, such as Kelvin-Helmholtz, Rayleigh-Taylor, and boundary layer, in erosion and droplet formation. For situations where the breakup length is greater than the depth of the water, one should be able to determine the form of the resultant jet impinging on the base from the initial mass rate and the erosion rate. However, many breakup phenomena models have been formulated from experiments where the water depth was greater than the breakup length; and the exact effect of a water depth near the breakup length has not been isolated. Figure 2-8 is an example of a jet penetrating into a liquid pool, illustrating both the representative jet breakup length and the reduction in jet diameter due to erosion and droplet formation.

2.4.2.1 Epstein and Fauske Analysis. Reference 2-60 reports the results of a linear Kelvin-Helmholtz instability analysis used to examine the stability of a steam sheet (film) generated when molten reactor core material is poured into water. Using thin and thick steam films as the bounding cases, the breakup and mixing of a hypothetical corium melt jet in a water pool is modeled. Droplet size dimensions and erosion velocity equations are derived based on instabilities; and ultimately, two jet penetration distance formulas are developed for thin and thick film limiting cases. The penetration distance for the thin film case is a function of the jet diameter and the corium to water density ratio. The penetration distance for the thick film case is similar, but the density ratio is for corium to steam. It was noted that the assumption of surface instabilities being in phase results in maximum jet breakup rates, and therefore, should underestimate the molten jet penetration lengths. However, the model neglects any effects of vapor velocity that could result in underestimating the jet breakup rate.

The report concluded that the surface stability of high-temperature, large molten jets falling through water is increased by the presence of a thick steam film layer. The variances in results for each film thickness indicate that parameters, such as pool subcooling that affects the amount of steam generated to surround the jet, also affect the penetration lengths.

2.4.2.2 Wang, Bloomquist, and Spencer (ANL) THIRMAL Code Development and Validation. In Reference 2-61, jet erosion was analyzed assuming that Kelvin-Helmholtz type instabilities dominate the length scale and growth rate of jet/coolant interfacial disturbances. An analysis was performed considering the bounding cases of a purely viscous and an inviscid vapor phase. Calculational results were found to agree well with CWTI experimental results (the CWTI experiments are discussed in Section 2.4.2.5). Hence, it is concluded in Reference 2-61 that Kelvin-Helmholtz interfacial instabilities must be considered in modeling molten jet breakup.

Reference 2-62 describes the development of the THIRMAL (Thermal- Hydrodynamic Interaction and Reaction of Melt and Liquid) code, which is a phenomenological model designed to describe the thermal and hydrodynamic behavior of a high-temperature molten jet when it interacts with a pool of water in a film boiling regime. The nature of the film boiling regime

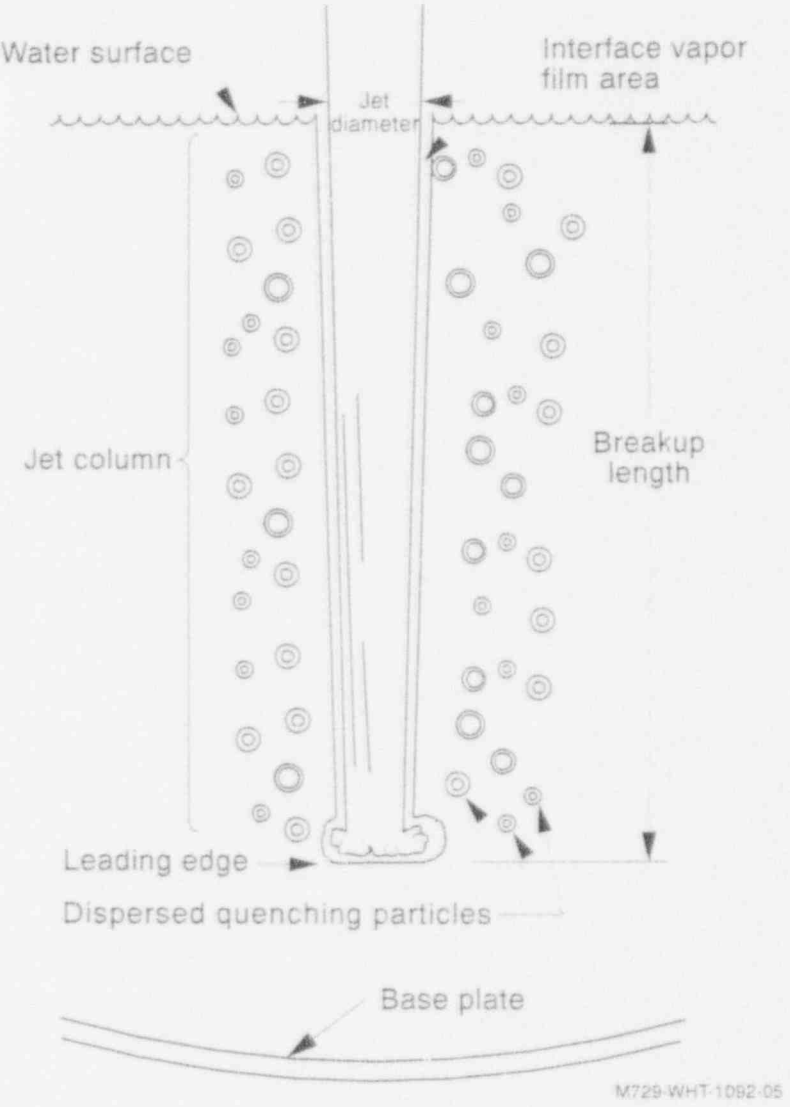

Figure 2-8. Configuration for analyzing a jet penetrating into a liquid pool.

characteristics, as well as two other common modes of liquid-to-liquid heat transfer considered for reactor situations, can be found in Reference 2-63. The model solves analytically for the heat-transfer coefficient, vapor film thickness, and net steam generation that are affected by breakup. It was determined from the analysis that the jet breakup is sensitive to initial jet temperature, water subcooling, and the physical state of the pool (i.e., agitated versus placid). The model was compared with mixing experiments performed by Gabor et al. at ANL.[d] The reference experiments consisted of high-temperature molten jet pours of Wood's metal into water. Model predictions agreed reasonably well with the experimental values for high-temperature jets (i.e., >600 K), below which film thickness and related calculations broke down. Model results were also compared with results from some of the CWTI experiments (Section 2.4.2.5) for particle debris size, and no major discrepancies were observed. It should be noted that the analytical

d. Argonne National Laboratory, August 1987.

solutions for parameters, such as the heat-transfer coefficient for a high temperature jet, are necessary to validate the model.

Currently, the THIRMAL code is the only code that models Kelvin-Helmholtz induced droplet erosion and considers the effects of steam vapor velocity. Although additional validation is needed, the code has undergone some validation and has been applied to predict the strong influence of lower plenum melt/water and melt/structure interactions in mitigating the effects of melt impingement on the lower head for the TMI-2 system.[2-64] For the perceived (at the time) best-estimate relocation path that involved meltthrough into the former core region and drainage of a large number of jets from the lowermost former core plate, the corium jets were predicted to completely break up into molten droplets that froze while settling through the lower plenum water.

An updated version of the THIRMAL code[c] has been applied to predict the potential for jet impingement for a range of debris conditions in lower plenum configurations that are representative of each of the U.S. reactor vendor vessel designs. Results from these calculations are found in Section 4. A more detailed description of the THIRMAL code is found in Appendix C of this report.

2.4.2.3 Saito et al. Experiments and Analyses. Analyses reported in Reference 2-65 investigated fundamental physical phenomena on penetration behavior of large molten jet pours into coolant pools. Experiments were performed with relatively hot water jets pouring into Freon-11 and liquid nitrogen. The experiments and analyses tried to examine the effects of the density difference between jet and coolant on jet penetration behaviors (vital for applying results of non-reactor material experiments and resultant correlations to actual reactor accident situations). It was determined that the penetration or breakup length increases with jet velocity, jet diameter, and the density ratio between the jet and coolant. Relative penetration lengths can be correlated well with the Froude number (Fr) and the jet-to-coolant density ratio, i.e., $L/D_j = 2.1(\rho_j/\rho_c)^{.5}Fr^{.5}$. The jet velocity dependence is present in the Froude number. The correlation also successfully predicted the behavior noted in similar experiments reported by Spencer et al.[2-66] using Wood's metal injected into a water pool. Though these last comparison experiments are closer to the actual reactor accident scenarios of corium or heavier metals poured into water, they still do not verify the applicability of the correlation for the typical LWR accident situations. The lack of a velocity dependance for later experiment analyses using corium and water may indicate that it has not been sufficiently tested to date.

2.4.2.4 SNL Experiments and Analyses. As part of a report on Reactor Safety Research, Reference 2-67 reports results from molten fuel-coolant interaction (MFCI) experiments. Experiments were performed to address the following four phenomena of liquid jet mixing:

1. Jets of molten iron-alumina and air
2. Jets of water falling through air
3. Jets of molten iron-alumina falling through water
4. Isothermal Freon jets falling through water.

---

c. S. K. Wang and J. J. Sienicki, Argonne National Laboratory, September 1991.

Experimental results indicate that for jet temperatures well above the pool liquid saturation temperature, jet breakup is affected by the generation of steam and related heat-transfer phenomena associated with a vapor film interface. Water subcooling was also observed to affect the time when a jet mixing region forms and the extent of jet fragmentation. Hence, it is recommended that neither the liquid-gas and isothermal liquid-liquid jet data be directly extrapolated in predicting corium and water mixing. Unfortunately, the only large-scale tests performed in this series considered isothermal liquid mixing. Reference 2-67 also reports on initial development of the Integrated Fuel-Coolant Interaction (IFCI) code being developed at SNL to model interactions observed in these experiments.

2.4.2.5 CWTI Experiments and Analyses. The corium-water thermal interaction (CWTI) tests performed at ANL are reactor material experiments with a strong emphasis on ex-vessel phenomena (i.e., in the reactor cavity). Many of the experiment processes are important for reactor vessel as well as reactor cavity accident progression issues, such as the mixing of jets and water. Reference 2-68 summarizes five of the CWTI experiments. In Reference 2-69, ANL presents the results of reactor material experiments CWTI-1 to -10. The report provides a complete description of the Corium Ex-vessel Interaction (COREXIT) facility and a full discussion of the objectives for the CWTI test program. Several models were discussed to assist in interpreting the experimental data on heat-transfer processes, including a quenching model.

Reference 2-70 presents detailed results of two CWTI tests (9 and 10) where molten corium with a composition of 60 wt% UO_2, 16 wt% ZrO_2, and 24 wt% stainless steel at 3080 K (~160 K above liquidus oxide phase) was poured at roughly 4 m/s into a pool of water about 32 cm deep. The subcooling for these tests was varied (6 and 74 K for CWTI-9 and -10, respectively) to determine the mixing behavior, corium-to-water heat-transfer rates, and characteristic sizes of the debris bed particles. The different degrees of subcooling greatly affected the outcome for the two different experiments, with vigorous steam generation causing boilup of the pool and considerable agitation for the low subcooling experiment (CWTI-9). Consequently, more quenching occurred during the fall stage (~41% versus 22%), and a smaller resultant debris size (0.1 to 1 mm versus 1 to 5 mm diameter) for the CWTI-9 experiment as opposed to the CWTI-10 experiment. Pressurization and water heatup data indicate two distinct quench and heat-transfer rates for the jet fall stage and the debris bed stage, with the former being far greater. For both experiments, most of the corium collected as a melt layer on the base. Along with only a partial quenching of the jet and the results of boundary case analyses performed, the melt layer indicates that neither jet was entirely eroded or broken up. Therefore, the corium breakup length, for a 2.2 cm diameter jet, was shown to be greater than 15 diameters for both pour experiments into water. Finally, it was observed that, despite penetration of the reduced jet through the water, no pitting or erosion of the steel base was apparent.

2.4.2.6 CCM Experiments and Analyses. The objective of the Corium-Coolant Mixing (CCM) experiments, which were performed at ANL, was to establish a data base using actual reactor materials to study the fragmentation and quench behaviors of corium melts in water, which are similar to the postulated events from the TMI-2 accident, as then perceived. The three important scaling parameters considered for the CCM tests were the coolant-depth-to-jet diameter ratio, the fuel-to-coolant-mass ratio, and the vessel ambient pressure.

Reference 2-71 reports on the CCM-1 through -6 experiment descriptions, test results, and recent analyses. Attempts were made in the analyses to explain some of the differing results between the CCM tests and related liquid-liquid mixing analyses, including Epstein and Fauske's film analysis (Section 2.4.2.1) and Saito et al.'s study of hot water jets entering Freon-11 and liquid nitrogen (Section 2.4.2.3) for breakup-length-to-jet-diameter ratio model predictions.

For the CCM tests, breakup length was determined from the depth at which the penetration velocity slowed to a value consistent with free falling drops. The values found for the breakup-length-to-diameter ratio for the CCM tests ranged from 10 to more than 25, with the lowest ratio values possibly limited by the mass poured. For the jet mass and diameters investigated in the CCM-5 and CCM-6 experiments, the jet length was apparently comparable to, if not less than, the breakup length.

The CCM test studies provided several important conclusions. For the most precise experiment data, the jet breakup length ranged from approximately 10 to 19 jet diameters, with at least the lower values being determined by the mass of jet material poured. The quench fraction was higher for greater subcooling. Quench fractions for the corium fall stage of 55 to 72% were measured for the subcooled experiments; and quench fractions of 20 to 45% were measured during the saturated water experiments.

Again, vessel pressurization data indicate a two-stage quench process with high heat transfer occurring in the jet fall stage and considerably lower heat removal from the debris layer. The multi-jet geometry test (CCM-2) showed a reduced quench fraction. The jet surface area in film boiling contact with the water appears to have been reduced as a result of the volume between the jets being highly voided. However, the shallowness of the pool for this test may also have contributed to the lower quench fraction. Except for CCM-2, a debris bed of solidified and substantially quenched particles was formed on the vessel bottom. These particles were characteristically from 1 to 5 mm in diameter and showed a log-normal distribution by mass.

Ultimately, the CCM test results report concluded that the most important parameters for corium stream breakup and quenching are (a) jet geometry (i.e., single versus multiple jets), (b) water subcooling, and (c) depth of water. The effect of multiple jets is also important because multiple paths are available for relocating corium once it reaches the lower support structure in an LWR. More recent studies by ANL indicate that the total mass of debris relocating may also impact results because both the CWTI and CCM experiments used smaller amounts of corium than expected to relocate during a severe accident.

2.4.2.7 FARO/TERMOS Experiments and Analyses. Reference 2-55 includes reports of a TERMOS test involving a stream of 110 kg of UO_2 falling into 130 kg of sodium. The results were compared with computer code JENA[f] calculations to describe jet-sodium interaction phenomena. The code was found to show reasonable qualitative agreement, but was quantitatively imprecise, indicating a need for improved modeling to describe hydrodynamic heat-transfer phenomena. These jet interaction studies may prove useful for LWR type interactions because sodium is near the density of water, and density appears to be a dominant parameter for describing breakup lengths. However, another important parameter is the vapor film formed at the interface that requires heating the sodium to around 1273 K, which is much higher than the boiling point for water.

Reference 2-72 provides additional experimental data on the above-mentioned TERMOS test and on a similar test that had slightly more UO_2 injected (140 versus 110 kg) with a greater jet diameter (8 versus 5 cm) and, consequently, twice the mass delivery rate. The penetration for both experiments measured under 1 m, resulting in breakup lengths less than 20 and 12.5 jet diameters for the two experiments, respectively.

---

f. L. Biasi and L. Castellano, Joint Research Centre, Ispra, Italy, March 1986.

Additional LWR accident sequence tests planned under the FARO/TERMOS program should prove more relevant than the previous experiments, which used molten fuel and sodium. The primary objective of these experiments is to measure the effects of molten fuel-coolant thermal interactions, specifically, melt quenching and fuel-structure interactions under conditions in which the water depth is of scale (although the mass poured into the water is much lower than predicted for severe accidents). The FARO/TERMOS facility currently has the capability of melting and heating a urania/zirconia mixture of 150 kg to 3200 K and combining it with zirconium for delivery into a pool of water up to 2.5 m deep at pressures up to 100 bar.

2.4.2.8 Jet Mixing and Breakup Conclusions. The breakup and mixing of a jet in a pool has been found to be a function of many parameters. The jet-to-coolant-density ratio, the jet diameter, and the degree of subcooling have been shown to be the dominant parameters controlling the degree of mixing and breakup for film boiling heat-transfer regimes. Other parameters, which have been shown to be of influence, or are related to the above, are the jet velocity, state of motion for the pool, the depth of water (i.e., greater or less than the physical breakup length for the jet), and jet temperature, particularly with respect to superheat. One of the less understood phenomena for mixing is the depth of water with respect to the ideal jet breakup length. Another parameter requiring more understanding is the state of the pool when mixing is occurring. The state of the pool is particularly important when multiple jets enter the pool (the expected event in an LWR relocation accident stage) because these multiple jets can significantly enhance agitation, as observed in the CCM-2 experiment.

2.4.3 Conclusions

Research has indicated that ablation of steel walls by molten core material is possible; and furthermore, that for many common reactor dimensions, a jet can penetrate limited depths of water for a reduced chance of vessel ablation. For cases where the depth of water is greater than the jet breakup length, it is expected that the jet will be broken up into fragments and droplets, which appear to be on the order of millimeters in diameter, removing the threat of erosion of the pool base plate. Most of the experiments and model predictions for the breakup length have been under 20 diameters. This implies, for a maximum jet diameter of 10 cm as in the TMI-2 case, that a depth of water greater than 2 m would prevent jet erosion of the vessel head. Depths of water greater than 2 m from the lower vessel head to the bottom of the active core region are common for typical LWRs. However, the depth of water above the lower head varies in different reactor designs and accident situations. Also, in the experiments reviewed, the resultant jet fragments were sufficiently quenched and dispersed to prevent any immediate threat to the pool base (lower vessel) by heatup. For cases where the pool depth is less than the jet breakup length, and a coherent jet reaches the base, no erosion (such as pitting or ablation) was detected. However, extensive research has not been performed for cases where the pool is significantly less than the jet breakup length or for cases where large quantities of corium relocate.

From the tests and analyses performed, it appears that the major parameters describing both the erosion and mixing phenomena have been defined. Furthermore, it may be possible from current models to determine how jet impingement can lead to localized lower vessel head failure. However, some discrepancies in testing results and modeling, particularly for mixing phenomena, may prevent a complete definition of the role of jet impingement for vessel failure. These impediments may be removed by the results of ongoing and planned experiments, such as the expanded FARO/TERMOS experiments (Section 2.4.2.7). This progress would then lead to a more complete assessment of jet impingement failure.

2.5 References

2-1. A. W. Cronenberg, S. R. Behling, and J. M. Broughton, *Assessment of Damage Potential to the TMI-2 Lower Head due to Thermal Attack by Core Debris*, EGG-TMI-7222, EG&G Idaho, Inc., June 1986.

2-2. D. A. Nitti, *Evaluation of the Structural Integrity of the TMI-2 Reactor Vessel Lower Head*, 77-1158426-00, Babcock & Wilcox, June 1985.

2-3. *FELCON - A General Purpose Program for Solving Thermal Conduction Problems*, NPGD-TM-268 (Revision I), Babcock & Wilcox, April 1984.

2-4. R. W. Ostensen, *Extended Fuel-Motion Study*, ANL-RDP-18, 7.4, Argonne National Laboratory, July 1973.

2-5. R. W. Ostensen et al., "Fuel Flow and Freezing in the Upper Subassembly Structure Following an LMFBR Disassembly," *Transactions of the American Nuclear Society, 18*, 1974, p. 214.

2-6. R. Bird, W. Stewart, E. Lightfoot, *Transport Phenomena*, New York: John Wiley & Sons, 1960, p. 182.

2-7. R. Bird, W. Stewart, E. Lightfoot, *Transport Phenomena*, New York: John Wiley & Sons, 1960, p. 402.

2-8. F. B. Cheung and L. Baker, Jr., "Transient Freezing of Liquids in Tube Flow," *Nuclear Science and Engineering, 60*, 1976, pp. 1–9.

2-9. J. J. Sienicki et al., "Freezing Controlled Penetration for Molten Metals Flowing through Stainless Steel Tubes," CONF-85081028, *ANS Proceedings of the 1985 ANS/ASME/AIChE National Heat Transfer Conference, Denver, CO, August 1985*, pp. 245–254.

2-10. M. Epstein et al., "Freezing-Controlled Penetration of a Saturated Liquid into a Cold Tube," *Journal of Heat Transfer, 66*, May 1977, p. 233.

2-11. M. Epstein et al., "Analytical and Experimental Studies of Transient Fuel Freezing," *Proceedings of the International Meeting on Fast Reactor Safety and Related Physics, Chicago, IL, October 5–8, 1976*, Vol. IV, U.S. ERDA Conference Number 761001, pp. 1788–1798.

2-12. M. Köllig and U. Grigull, "Unsteady Heat Transfer with Solidification Applied to the Fluidity of Pure Metals," *Wärme- und Stoffübertragung, 14*, 1980, p. 231.

2-13. B. W. Spencer et al., "Results of Fuel Freezing Tests with Simulated CRBR-Type Fuel Pins," *Transactions of the American Nuclear Society, 30*, 1978, p. 446.

2-14. D. A. McArthur and P. K. Mast, *TRAN B-1: Experimental Investigation of Fuel Crust Stability on Surfaces of an Annular Flow Channel*, NUREG/CR-3484, SAND83-1916, 1984.

2-15. D. A. McArthur and P. K. Mast, *TRAN B-2: The Effect of Low Steel Content on Fuel Penetration in Non-Melting Cylindrical Flow Channels*, NUREG/CR-3757, SAND84-0814, 1985.

2-16. D. A. McArthur and P. K. Mast, *TRAN B-3: Experimental Investigation of Fuel Crust Stability on Melting Surfaces of an Annular Flow Channel*, NUREG/CR-3944, SAND84-1646, 1985.

2-17. G. Berthoud and B. Duret, "The Freezing of Molten Fuel: Reflections and New Results," *Proceedings of the Fourth International Topical Meeting on Nuclear Reactor Thermal-Hydraulics (NURETH-4), Vol. 1, Karlsruhe, FRG, October 10-13, 1989.*

2-18. D. Magellon, R. Zeyer, H. Hohmann, "100 Kg-Scale Molten UO_2 Out-of-Pile Interactions with LMFBR Structures: Plate Erosion and Fuel Freezing in Channels," *International Conference on Fast Reactor Core and Fuel Structural Behavior, Inverness, Scotland, June 4-6, 1990.*

2-19. M. Epstein et al., "Transient Freezing of a Flowing Ceramic Fuel in a Steel Channel," *Nuclear Science and Engineering, 61*, 1976, pp. 310–323.

2-20. D. A. McArthur, N. K. Hayden, P. K. Mast, *In-Core Fuel Freezing and Plugging Experiments: Preliminary Results of the Sandia TRAN Series I Experiments, Technical Report October 1980–December 1983*, NUREG/CR-3675, SAND81-1726, 1984.

2-21. M. Pilch and P. K. Mast, *PLUGM: A Coupled Thermal-Hydraulic Computer Model for Freezing Melt Flow in a Channel*, NUREG/CR-3190, SAND82-1580, 1982.

2-22. B. Duret, *Etude du Gel De Corium et du Risque de Percement des Tubes d'Instrumentation en Fond de Cuve, (A Study of Corium Freezing and the Risk of Rupture in Lower Head Instrument Tubes)*, CEA report STT/LETM/89.07.C/BD, May 1989.

2-23. *Reactor Safety Research Semiannual Report July-December 1986*, NUREG/CR-4805, SAND86-2752 (Vol. 2), 1987.

2-24. *Reactor Safety Research Semiannual Report July-December 1987*, NUREG/CR-5039, SAND87-2411 (Vol. 2), 1988.

2-25. S. A. Hodge, *BWR Reactor Vessel Bottom Head Failure Modes*, Dubrovnik, Yugoslavia, CONF-890546-3, December 1989.

2-26. R. S. Chambers, *A Finite Element Analysis of a Pressurized Containment Vessel during Core Melt Down*, NUREG/CR-5046, SAND87-2183, 1989.

2-27. D. K. Gartling, *COYOTE—A Finite Element Computer Program for Nonlinear Heat Conduction Problems*, SAND77-1332, Sandia National Laboratory, 1982.

2-28. J. H. Biffle, *JAC—A Two-Dimensional Finite Element Computer Program for the Nonlinear Quasistatic Response of Solids With the Conjugate Gradient Method*, SAND81-0998, Sandia National Laboratory, April 1984.

2-29. S. S. Dosanjh and M. Pilch, "Lower Head Creep-Rupture Sensitivity Studies," *Nuclear Science and Engineering, 108*, 1991, pp. 172–183.

2-30. F. R. Larson and J. Miller, "A Time-Temperature Relationship for Rupture and Creep Stresses," *Transactions of ASME 74*, No. 5, 1972.

2-31. G. V. Smith, "Evaluations of the Elevated Temperature Tensile and Creep-Rupture Properties of C-Mo, Mn-Mo, and Mn-Mo-Ni Steels," ASTM-DS 47, American Society for Testing and Materials, 1971.

2-32. L. E. Anderson et al., *Effects of a Hypothetical Core Melt Accident on a PWR Vessel with Top-Entry Instruments*, EPRI, IDCOR Program Technical Report 15.2A, June 1983.

2-33. *Transient Heat Transfer Program Description and Applications*, (available through General Electric, Vallecitos Nuclear Center, Vallecitos, CA), 1983.

2-34. *MARC-CDC General Purpose Finite Element Analysis Program*, (available through Control Data Corporation), 1983.

2-35. A. W. Cronenberg and E. L. Tolman, *Thermal Interaction of Core Melt Debris with the TMI-2 Baffle, Core-Former, and Lower Head Structures*, EGG-TMI-7811, EG&G Idaho, Inc., September 1987.

2-36. D. W. Golden and P. Kuan, "Summary of Recent TMI-2 Accident Scenario Development Work," *Proceedings of the 16th Water Reactor Safety Information Meeting, Gaithersberg, MD, October 1988*, NUREG/CR-0096.

2-37. M. Epstein and H. K. Fauske, *The TMI-2 Core Relocation - Heat Transfer and Mechanism*, EGG-TMI-7956, EG&G Idaho, Inc., July 1987.

2-38. R. L. Moore and E. L. Tolman, "Estimated TMI-2 Vessel Thermal Response Bounds Based on the Lower Plenum Debris Configuration," *Proceedings of the 1988 ANS/ASME/AIChE National Heat Transfer Conference, Houston, TX, July 24–27, 1988.*

2-39. R. L. Moore, *TMI-2 Reactor Vessel Lower Head Heatup Calculations*, EGG-TMI-7784, EG&G Idaho, Inc., August 1987.

2-40. G. L. Thinnes, *TMI-2 Lower Head Creep Rupture Analysis*, EGG-TMI-8133, EG&G Idaho, Inc., August 1988.

2-41. G. L. Thinnes and R. L. Moore, "Comparison of Thermal and Mechanical Responses of the Three Mile Island Unit 2 Reactor Vessel," *Nuclear Technology, 87*, 4, December 1989.

2-42. *ABAQUS User's Manual*, Version 4.6, Hibbitt, Karlsson & Sorensen, Inc., Providence, RI, 1987.

2-43. P. Gruner and H. Schulz, "Investigations on the Primary Pressure Boundary within Risk Analyses of German PWRs," Transactions of the 10th International Conference on Structural Mechanics in Reactor Technology, SMIRT-10/M, 1989.

2-44. MARCH 2 (Meltdown Accident Response Characteristics) Code Description and User's Manual, NUREG/CR-3988, BMI-2115, 1984.

2-45. C. M. Allison and E. M. Johnson (eds.), *SCDAP/RELAP5/MOD2 Code Manual, Volumes 1, 2, and 3*, NUREG/CR-5273, EGG-2555, 1989.

2-46. S. S. Manson and A. M. Haferd, "A Linear Time-Temperature Relation for Extrapolation of Creep and Stress Rupture Data," NACA TN 2980, March 1953.

2-47. A. W. Cronenberg and E. L. Tolman, *Thermal Interaction of Core Melt Debris with TMI-2 Baffle, Core-Former, and Lower Head Structures*, EGG-TMI-7811, EG&G Idaho, Inc., September 1987.

2-48. D. A. Powers, "Erosion of Steel Structures by High-Temperature Melts," *Nuclear Science and Engineering, 88*, 1984, pp. 357–366.

2-49. D. A. Powers and F. E. Arelleno, *High Temperature Melt Attack on Steel and Urania-Coated Steel*, NUREG/CR-3366, SAND83-1350, 1984.

2-50. J. J. Sienicki and B. W. Spencer, "Analysis of Reactor Material Experiments Investigating Corium Crust Stability and Heat Transfer in Jet Impingement Flow," CONF-850810-9, *ANS/ASME/AIChE National Heat Transfer Conference, Denver, CO, August 4–7, 1985*, p. 255.

2-51. M. Epstein et al., "Simultaneous Melting and Freezing in the Impingement Region of a Liquid Jet," *AIChE Journal, 26*, September 1980, p. 743.

2-52. M. J. Swedish et al., "Surface Ablation in the Impingement Region of a Liquid Jet," *AIChE Journal, 25*, July 1979, p. 630.

2-53. A. Furutani et al., "Erosion Behavior of Solid Plate by a Liquid Jet-Effect of a Molten Layer," *26th ANS/ASME/AIChE National Heat Transfer Conference, Philadelphia, PA, August 6–10, 1989.*

2-54. M. Saito et al., "Melting Attack of Solid Plates by a High Temperature Liquid Jet-Effect of Crust Formation," *Nuclear Engineering and Design, 121*, 1990, p. 11.

2-55. H. Hohmann et al., "Results of the FARO Programme," *Reactor Safety Research—the CEC Contribution*, CONF-891139, EUR-12343-3N, Varesa, Italy 1990, pp. 837–854.

2-56. B. H. Stuka et al., *Versuche zur Untersuchung der erosiven Wirkung oxidischer Gießstrahlen auf Strukturen, (Experiments to Study the Erosive Effect of Oxide Casting Streams on Structures)*, KfK 18.02.05P03A, Kernforschungszentrum Karlsruhe, FRG, August 1991.

2-57. J. A. Pessanha, and M. Z. Podowski, "Ablation of Solid Walls Subjected to Impinging Inclined Jets," *ANS Proceedings of the 1989 ANS/ASME/AIChE National Heat Transfer Conference, Philadelphia, PA, August 6–9, 1989.*

2-58. B. D. Turland and J. Morgan, "Progression of a PWR severe Accident from Core Melt to Cavity Interactions," *Preliminary Proceedings of Sixth Information Exchange Meeting on Debris Coolability, Los Angeles, CA, November 7–9, 1984.*

2-59. B. D. Turland and J. Morgan, "Thermal Attack of Core Debris on a PWR Reactor Vessel," *Proceedings from the International Meeting on Light Water Reactor Severe Accident Evaluation, Cambridge, MA, August 28–September 1, 1983.*

2-60. M. Epstein and H. K. Fauske, "Steam Film Instability and the Mixing of Core-Melt Jets and Water," *ANS Proceedings of the 1985 ANS/ASME/AIChE National Heat Transfer Conference, Denver, CO, 1985.*

2-61. S. K. Wang, C. A. Blomquist, and B. W. Spencer, "Interfacial Instabilities Leading to Bubble Departure and Surface Erosion During Molten Jet/Water Interaction," CONF 890819-22, *26th ANS/ASME/AIChE National Heat Transfer Conference, Philadelphia, PA, August 6–9, 1989.*

2-62. S. K. Wang, C. A. Blomquist, and B. W. Spencer, "Modeling of Thermal and Hydrodynamic Aspects of Molten Jet/Water Interaction," CONF-890819-22, *26th ANS/ASME/AIChE National Heat Transfer Conference, Philadelphia, PA, August 6–9, 1989.*

2-63. H. K. Fauske, "Some Aspects of Liquid-Liquid Heat Transfer and Explosive Boiling," *Proceedings of the First Conference on Fast Reactor Safety, Beverly Hills, CA, April 2–4, 1974*, p. 992.

2-64. S. K. Wang, J. J. Sienicki and B. W. Spencer, "Assessment of the Integrity of TMI-2 Lower Head during Core Relocation," *Fifth Proceedings of Thermal Hydraulics, 1989 ANS Winter Meeting, San Francisco, CA, 1989*, p. 36.

2-65. M. Saito, K. Sato, and S. Imahori, "Experimental Study on Penetration Behaviors of Water Jet into Freon-11 and liquid Nitrogen," *ANS Proceedings 1988 National Heat Transfer Conference, Houston, TX, July 24–27, 1988*, pp. 173–183.

2-66. B. W. Spencer, J. D. Gabor, and J. C. Cassulo, "Effect of Boiling Regime on Melt Stream Breakup in Water," *4th Miami International Symposium on Multi-phase Transport and Particulate Phenomena, Miami, FL, 1986.*

2-67. B. W. Marshall, Jr., and M. Berman, "Molten Fuel/Coolant Interactions," *Reactor Safety Research Semiannual Report July-December 1986*, NUREG/CR-4805, SAND86-2752, (Vol. 2), 1987.

2-68. B. W. Spencer, et al., "Overview and Recent Results of ANL/EPRI Corium-Water Thermal Interaction Investigations," *Proceedings of the International Meeting on Light Water Reactor Severe Accident Evaluation, Cambridge, MA, August 28–September 1, 1983*, Vol. 2, American Nuclear Society, La Grange Park, IL, 1983.

2-69. B. W. Spencer, J. J. Sienicki, and L. M. McUmber, *Hydrodynamics and Heat Transfer Aspects of Corium-Water Interactions*, EPRI/NP-5127, Electric Power Research Institute, 1987.

2-70. B. W. Spencer et al., "Corium Quench in Deep Pool Mixing Experiments," CONF 850810-10, *ANS Proceedings of the 1985 ANS/ASME/AIChE National Heat Transfer Conference, Denver, CO, August 4–7, 1985.*

2-71. S. K. Wang et al., "Experimental Study of the Fragmentation and Quench Behavior of Corium Melts in Water," CONF-891103-53, *Proceedings of Fifth Reactor Thermal-Hydraulics Conference, San Francisco, CA, 1989.*

2-72. D. Magallon, H. Hohmann, H. Schins, "Pouring of 100 kg-Scale Molten UO_2 into Sodium," *ANS 1990 International Fast Reactor Safety Meeting, Snowbird, UT, August 12–16, 1990.*

3. THERMODYNAMIC AND GEOMETRIC CONDITIONS FOR CONSIDERATION

A literature search was conducted to determine the range of thermal-hydraulic conditions and geometric parameters that should be considered in lower head failure analyses. Results from this literature search, which corresponds to the first step in Figure 1-1, provide input to subsequent aspects of lower head failure analyses, such as appropriate values for reactor pressure that are input into thermal and mechanical response analyses. Section 3.1 reviews vessel thermal-hydraulic conditions predicted in previous severe accident analyses. Of particular interest in reviewing these accident analyses was the reactor pressure and power history, the water inventory, the lower head thermal history, the debris state during the transient, and design features within and external to the vessel that could impact heat transfer from the vessel. Material and geometrical properties of structures within and external to various reactor designs are compared in Section 3.2. Appendix F summarizes the geometric parameters for the lower head failure analyses described in this document.

3.1 Reactor Coolant System Thermal-Hydraulic Conditions

A review of literature describing scenarios leading to vessel meltthrough revealed that a wide range of conditions has been evaluated. The types of internally initiated transients considered may typically be grouped into the following categories:

- Station blackout (SBO)
- Anticipated transients without scram (ATWS)
- Steam generator tube rupture (SGTR)
- Loss-of-coolant accidents (LOCA) (small and large break).

Table 3-1 summarizes characteristic thermal-hydraulic parameters predicted for these categories from some reactor analyses results found in the literature. More detailed descriptions of these conditions are found in the following sections.

3.1.1 Pressure

Reactor system pressure prior to vessel meltthrough is important because it impacts vessel internal loading prior to failure (and thus, the likelihood of global creep or tube ejection failure) and the manner in which debris is ejected following failure (and thus, the likelihood of phenomena such as direct containment heating). The system pressure predicted prior to vessel failure is dependent upon the reactor type, the scenario, and the phenomena considered in the analysis. This section describes the pressure response predicted in several analyses for various reactor types and scenarios. Differences observed when certain phenomena were included in the analyses are noted where possible.

Results from NUREG-1150, *Severe Accident Risks: An Assessment for Five U.S. Nuclear Power Plants*,[3-1] indicate that during SBO and ATWS scenarios, it is more likely for one of the BWR plants considered (the Peach Bottom Unit 2 BWR/4 plant) to fail at pressures above 1.4 MPa (200 psia). In the remaining BWRs considered (the Grand Gulf Unit 1 BWR/6) and the PWR power plants considered (the Zion Unit 1 four-loop plant, the Surry Unit 1 three-loop

Table 3-1. Scenario summary description.

Scenario	Power level[a]	Pressure[b]	Water inventory[c]	Reactor type	Section 3 references
Station blackout (SBO)					
Without depressurization	Full	High	High	APWR-CE[d]	7
				BWR-GE	17,20,21,23,25,41
				PWR-W	1,3,4,5,9,10,11,12,13,21
	Low	High	—	PWR-B&W	22
				BWR-GE	23
				PWR-B&W	22
With depressurization	Full	Low	Low	APWR-CE[d]	7
				BWR-GE	1,16,18,19,21
				PWR-W	1,3,4,8,13,14
				PWR-B&W	22
Anticipated transient without scram (ATWS)	Full	Low	Low	APWR-CE[d]	7
				BWR-GE	21
		High	High	BWR-GE	1,12,21
				PWR-W	1
	Low	High	High	BWR-GE	23
		Low	Low	BWR-GE	23,25,26
Steam generator tube rupture (SGTR)	Full	High	High	APWR-CE[d]	7
Loss-of-coolant accident (LOCA)					
Large break	Full	Low	Low	APWR[d]	7
				BWR-GE	1
				PWR-W	1,21
	Low	Low	Low	BWR-GE	23
Small break	Full	High	High	APWR-CE	7
				BWR-GE	1
				PWR-W	1,21
	Low	Low	Low	BWR-GE	23

a. The power level at the time of accident initiation.

b. The pressure at the time of vessel meltthrough: high is greater than ~1.4 MPa (~200 psia); low is less than or equal to 1.4 MPa (200 psia).

c. Water inventory at the time of melt relocation.

d. Calculations performed as part of the Advanced Reactor Severe Accident Program (ARSAP) indicate that hot leg nozzle failure or a manually initiated reactor coolant system (RCS) depressurization should occur prior to reactor vessel lower head failure via creep rupture for an Advanced PWR (APWR), although both cases were analyzed.

plant, and the Sequoyah Unit 1 four-loop plant), the results in Reference 3-1 indicate that a higher probability exists for the vessel to fail at pressures below 1.4 MPa (200 psia).

The relative likelihood of a pressurized BWR vessel failure differed between the two BWR plants considered in Reference 3-1 because plant-specific differences increase the likelihood of long-term station blackout for the Peach Bottom plant. During a long-term station blackout, the vessel is predicted to fail at high pressure because the diesel power needed to recharge batteries is unavailable. These batteries provide the dc power required to maintain the automatic depressurization system (ADS) relief valves open. In the Peach Bottom ATWS scenario, high-pressure vessel failure is predicted in cases where the operator fails to open the ADS relief valves (after the operator has previously inhibited the ADS and actuated the standby Liquid Control System for an inadequate high-pressure core cooling event). However, it should be noted that these results are specific to the Peach Bottom plant. As discussed by Hodge,[a] design features of the Grand Gulf plant, as well as features in many other BWR plants, result in a greater likelihood of vessel failure at low pressures.

For each of the accident scenarios considered in Reference 3-1, a substantial fraction of the PWR vessels were predicted to fail at low (<1.4 MPa) pressures because it was considered more likely that the vessel would first depressurize via mechanisms such as a stuck-open relief valve, an operator depressurizing the reactor system, or failures of hot leg piping, pressurizing surge line, or coolant pump seal. Recently performed PWR severe accident analyses[3-2,b] support this conclusion. However, the reactor system pressure at the time at which vessel failure is predicted has been found to be dependent upon pilot-operated relief valve (PORV) capacity, reactor coolant system (RCS) pump design, and assumptions related to melt relocation phenomena.

Results from the Seabrook Station probabilistic safety assessment[3-3] by Pickard, Lowe, and Garrick, Inc. (PLG) show that for a total core melt frequency of 2.7×10^{-4} per reactor-year (based on mean values), about 99% of the scenarios are at moderately high [2.07 to 6.89 MPa (300 to 1,000 psia)] to high [6.89 to 16.55 MPa (1,000 to 2,400 psia)] pressure at the time of core melt. Most of these, 82% of the total, occur at moderate pressure with successful steam generator cooling. However, a later PLG evaluation[3-4] of the Seabrook Station during a TMLB' [loss of both on- and off-site ac power, with early (immediate) failure of the steam-driven auxiliary feedwater pump] sequence, which is a dominant contributor to core melt, concluded that it is more likely that the primary system is depressurized during this event. This new result was attributed to the inclusion of additional phenomena, such as pump seal LOCAs and the operator acting to open the pressurizer PORVs, in their analysis.

The TMLB' sequence in the Seabrook plant was also investigated at the INEL.[3-5] Results indicate that depressurization by the PORV will reduce the time to the onset of core damage, but expedite accumulator injection. Hence, it was concluded that depressurization has the potential to delay the time to core relocation.

Analyses with the DOE version of the Modular Accident Analysis Program (MAAP) computer code[3-6] for vessel meltthrough events have been performed for the Advanced Pressurized Water Reactor (APWR).[3-7] Although the geometry and size of the reactor vessel

---

a. S. A. Hodge, unpublished report on accident management for critical BWR severe accident sequences, Oak Ridge National Laboratory, 1990.

b. D. Knudsen and C. Dobbe, "Assessment of the Potential for High Pressure Melt Ejection Resulting from a Surry Station Blackout Transient (Draft)," NUREG/CR-5949, EGG-2689, November 1992.

cavity differ in the APWR design suggested by ARSAP, the internal vessel configuration is similar to that of existing PWRs. For SBO and ATWS events, it was predicted that the vessel is more likely to be depressurized, via hot leg failure or operator-initiated RCS depressurization, prior to bottom head meltthrough. For example, in an SBO event, the hot leg nozzle was predicted to fail 30 minutes after reactor trip when the vessel reaches 1000 K. Thus, the vessel would depressurize prior to the predicted vessel meltthrough time of 2.5 to 3 hours.

Several analyses performed for the Surry Unit 1 PWR during an SBO event using MELPROG/TRAC, MARCH-2, and the Source Term Code Package (STCP) with MARCH-3 have been documented.[3-8,3-9,3-10,3-11,3-12] MARCH-2 analyses predict reactor vessel bottom head failure in about 3 hours if the reactor is pressurized. MELPROG/TRAC analyses indicate that the event was dramatically changed when depressurization was included as a result of a pump seal LOCA. The time to vessel failure was increased to 10 hours, and the pressure at vessel failure decreased from 16 MPa to 0.27 MPa.

Sensitivity studies[3-13,3-14] were also performed using the SCDAP/RELAP5 code[3-15] to determine the effects of natural circulation and induced depressurization by a surge line failure upon core damage progression following a TMLB′ event in the Surry Unit 1 plant. Analyses in Reference 3-14, which include the effects of natural circulation on plant response, indicate that the transient will progress more slowly than indicated in NUREG-1150 calculations and that localized reactor coolant system pipe heating from natural circulation flows will result in failure outside of the vessel prior to bottom head failure. Creep rupture of the surge line was analyzed in Reference 3-13 because it was found to be the most probable failure for the plant under these conditions, failing the vessel between 160 and 170 minutes. Although the time for core damage initiation was shortened by ~45 minutes in cases where the reactor was depressurized, the lower pressure caused the accumulators to actuate, delaying further cladding heatup by 200 minutes. Relocation of molten core materials into the lower plenum was calculated to occur between 6.5 and 7.5 hours after the loss of power. The size of the molten pool varied from 49 to 77% of the core, depending on the assumptions made concerning core behavior.

Several MELCOR, Source Term Code Package (STCP) with MARCH-2, and BWRSAR[c] analyses for BWRs undergoing SBO events have been documented.[3-16,3-17,3-18,3-19,3-20,3-21] BWRSAR analyses indicate that the Peach Bottom vessel will be depressurized prior to global vessel failure during both long-term and short-term SBO events. BWRSAR results predict that failure of lower head penetrations (such as the 185 control rod guide tubes, the 55 instrument guide tubes, or the drain nozzle) will result in steam and debris exiting the vessel before the time that the vessel bottom head wall failure is predicted. However, debris is not predicted to exit the vessel via the control rod guide tubes because the catcher devices, approximately 2.54 cm (1 in.) beneath the vessel, would prevent the mechanisms from clearing the vessel wall even if the welds holding them in place failed and the assembly length broke near the debris bed. The BWRSAR code predicts a longer time for BWR vessel failure than for other BWR analyses. This longer predicted time for BWR vessel failure results from the BWRSAR modeling assumption that the water in the lower head will be boiled away before penetration welds are heated to failure temperatures.

In summary, more recent PWR and BWR analyses indicate that low pressures are more likely to exist within the vessel at the time of failure because it seems more likely that the vessel

---

c. Unpublished report of S. A. Hodge and L. J. Ott, Oak Ridge National Laboratory, February 1, 1989.

first depressurizes via mechanisms such as operator action, pump seal failure, hot leg piping, pressurizer surge line failure, or lower head penetration failure. However, the potential for high vessel pressure during certain sequences, such as long-term SBO BWR events, requires that both high- and low-pressure conditions be considered in these preliminary vessel failure analyses. Note that on-going individual plant examination (IPE) endeavors should guarantee the availability of ADS and thereby preclude high-pressure BWR vessel failure events. Hence, high-pressure BWR scenarios could be omitted if plant modifications make their probability negligible.

3.1.2 Power Level

Although most severe accident calculations are performed for reactors that are at full power at the accident initiation, several analyses for reactors operating at low power (~25% power) were also identified in the literature.[3-22,3-23,3-24,3-25,3-26] Generally, the lower power level tended to reduce the severity of the event. For example, analyses for the Shoreham BWR operating at low power[3-23,3-25] were generally found to have less severe consequences because capacities of mitigating systems were significantly greater than the amounts required for a 25% power case and because more time was available for the operator to diagnose the accident correctly and implement restorative actions. However, Reference 3-25 predicted that somewhat higher amounts of hydrogen [836.36 kg (1,840 lbm) for a 25% power case versus 736.36 kg (1,620 lbm) for a 100% power case] would be generated in the Shoreham reactor during a loss of injection event. This prediction resulted from the calculated result that the zircaloy channel boxes are heated more slowly with the reactor at 25% power, which, allowed more time for the channel boxes to oxidize before melting temperatures were reached and relocation occurred according to the models used in these calculations. However, more recent data from experiments, such as SFD 1-3 and DF-4, indicate that relocated material and material in partially blocked channel boxes will continue to oxidize.[3-27,3-28]

Sensitivity of melt progression to power level during a TMLB′ event in the Bellefonte PWR was tested by Chambers[3-22] using an early version (the SCDAP/MOD1/V0) of the SCDAP/RELAP5 Code.[3-15] For this event, it was predicted that higher temperatures, hydrogen production rates, and fission product release rates occur at higher power levels. However, the increases observed were much smaller than the increases observed in cases with increased amounts of available steam.

3.1.3 Water Level/Inventory

The presence of water influences the manner in which the debris exchanges energy, the debris oxidation, and the formation of hydrogen. This section describes the quantities and effects of water present in the vessel for the accident analyses reviewed. Water volumes that are contained in different LWR vessel designs during normal operation are discussed in Section 3.2, and estimates are listed in Appendix F.

In the BWR analyses of TMLB′ events reviewed,[3-1,3-16,3-17,3-18,3-19,3-25] the large quantity of water in the bottom head of a BWR is expected to be more than sufficient to quench an entire mass of molten core and associated structural material. However, calculations using the BWRSAR code differ from previous analytical approaches because of the consideration that the water in the lower head will be boiled dry before vessel penetration weld failure will occur. Hence, in the BWRSAR analyses, the lower head is dry at the time of vessel failure.

Reference 3-26 presents results from sensitivity runs performed with MAAP 2.0 to investigate the impact of actions to control core water level on core damage progression. Results

confirm that operator actions, such as throttling of the emergency core cooling system (ECCS) pumps, can significantly delay or avert core damage.

The impact of water level was also assessed by Chambers[3-22] and by Bayless et al.[3-29] for the Bellefonte PWR plant during a TMLB′ event. In Reference 3-22, an early version (SCDAP/MOD1/V0) of the SCDAP/RELAP5 code[3-15] was used to predict fuel bundle response during TMLB′ events with and without steam. Results indicate that the temperature, hydrogen production rate, and fission product release rate increase significantly; and melting and material relocation occur earlier in cases with steam available for cladding oxidation. Integral calculations of system thermal-hydraulic response and core damage[3-29] were performed using the SCDAP/RELAP5 code.[3-15] In the calculations that considered the addition of liquid through failed pump seals and natural circulation, steam starvation was not predicted to occur; and, in a case where a high-pressure injection pump was able to provide coolant, no core damage was predicted.

3.1.4 Lower Head Thermal History

In most of the analyses reviewed in this section, water is predicted in the lower head at the time debris melts and relocates downward through lower support structures into the vessel bottom head. Hence, the lower head temperatures are initially cool, corresponding to the temperature of the water, which in turn is dependent upon thermal-hydraulic conditions within the reactor vessel.

Analyses using the BWRSAR code for SBO, ATWS, and loss of injection events[3-16,3-17,3-18,3-19,3-25] predict that temperatures within the lower head increase as the transient progresses. In these BWR analyses, it is predicted that the debris would cause the water in the lower head to boil dry. Hence, molten debris would be in contact with dry structures within the vessel lower head, eventually causing the penetration weld to heat to failure temperatures.

The configuration, quantity, and composition of the debris also impacts lower head temperature. Sensitivity studies[3-30] illustrate the importance of debris configuration on long-term vessel temperature response during the TMI-2 event. In cases using more conservative assumptions related to the configuration and quantity of the debris and the presence of water in the debris, the vessel temperatures were predicted to reach failure temperatures within one hour. (Additional discussion of the analyses from Reference 3-30 is found in Section 2.3).

3.1.5 Expected Debris States

The quantity of heat transferred from the molten debris to the reactor vessel is dependent on factors such as the amount of decay heat in the debris, the debris composition, particle size, and configuration. This section reviews observed debris states and postulated debris states during meltdown accidents. In addition, this section discusses calculations performed for the TMI-2 PWR accident and an SBO event in the Shoreham BWR/4.

Video inspection[3-31] of the TMI-2 lower head region indicates that ~15 to 20 metric tons of previously molten core material relocated to the lower head in an irregular configuration with various particle sizes. The height of the TMI-2 debris bed on the lower head is estimated between 0.7 and 0.9 m.[3-32,3-33] Particles less than 1 cm have been observed near the center of the vessel; larger pieces of debris (up to 0.2 m) have been observed at the periphery of the debris bed in the south quadrant of the vessel; and a wall of lava-like, consolidated debris exists at the north quadrant. Samples have been found to consist primarily of previously molten ceramic $(U,Zr)O_2$, with transition metal oxides in the grain boundaries. Based on the presence of the previously

molten $(U,Zr)O_2$, it is estimated that the material in the lower plenum reached temperatures of about 2800 K prior to relocation.[3-34,d]

The decay power in the debris is related to the fission products retained in the core material. During the TMI-2 accident, significant release of the volatile fission products (noble gases, cesium, iodine, and tellurium) occurred. For example, in the lower plenum, it is estimated that only 3% of the iodine and 13% of the cesium were retained.[3-35] The reductions in total core decay power as a result of the release fraction of volatile fission products are shown in Figures 3-1 and 3-2 for a generic PWR (33,800 MWd/tU) and the TMI-2 fuel inventory, respectively.[e]

As discussed in Section 2.3, References 3-30, 3-36, and 3-37 describe scoping calculations that were performed using bounding assumptions pertaining to debris configuration in the TMI-2 lower vessel head. Results indicate that global vessel failure occurs in cases where the debris is not quenched or in cases where a consolidated mass of core and molten control rod material exists on the bottom head without water or penetrations between the consolidated mass or the vessel wall. Because the vessel did not fail at TMI-2, the analysis concludes that it is more likely that the debris was porous or that solidified material existed below molten debris, insulating the vessel from decay heat produced in the fuel.

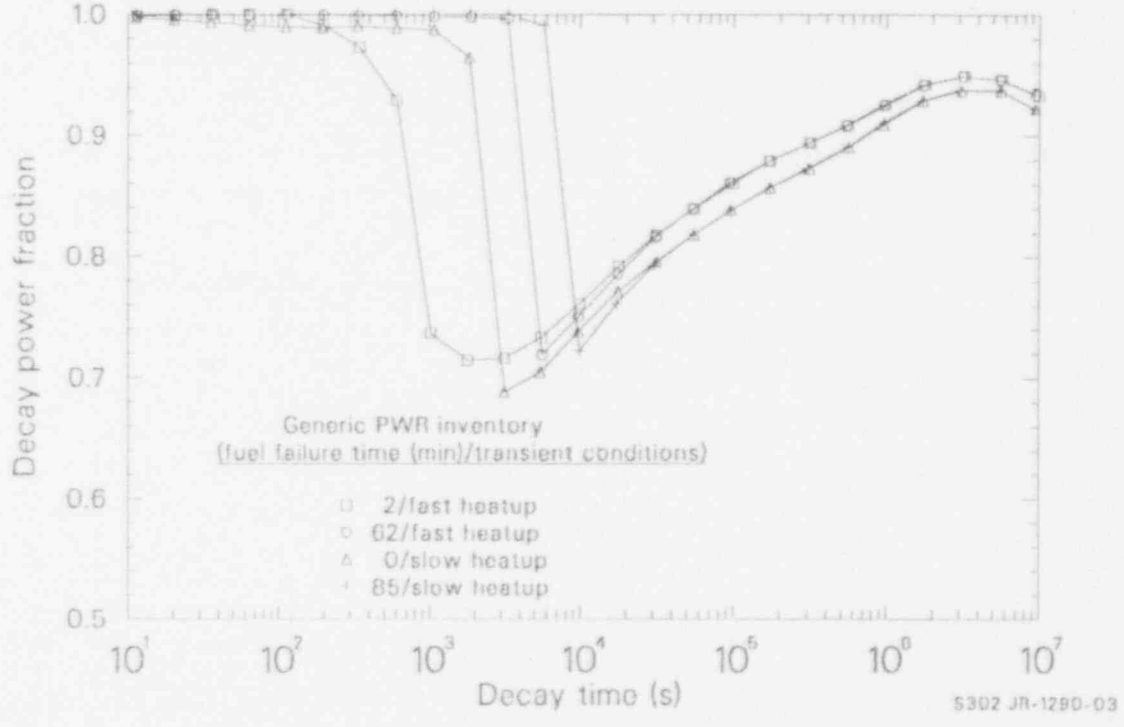

Figure 3-1. Reduction in total core decay power as a result of volatile fission product release fraction for a generic PWR.

d. C. S. Olsen et al., unpublished results from the examination of debris from the lower reactor head of the TMI-2 reactor, EG&G Idaho, Inc., April 1987.

e. B. G. Schnitzler, unpublished research concerning the fission product decay heat modeling for disrupted fuel region (FDECAY), EG&G Idaho, Inc., December 1981.

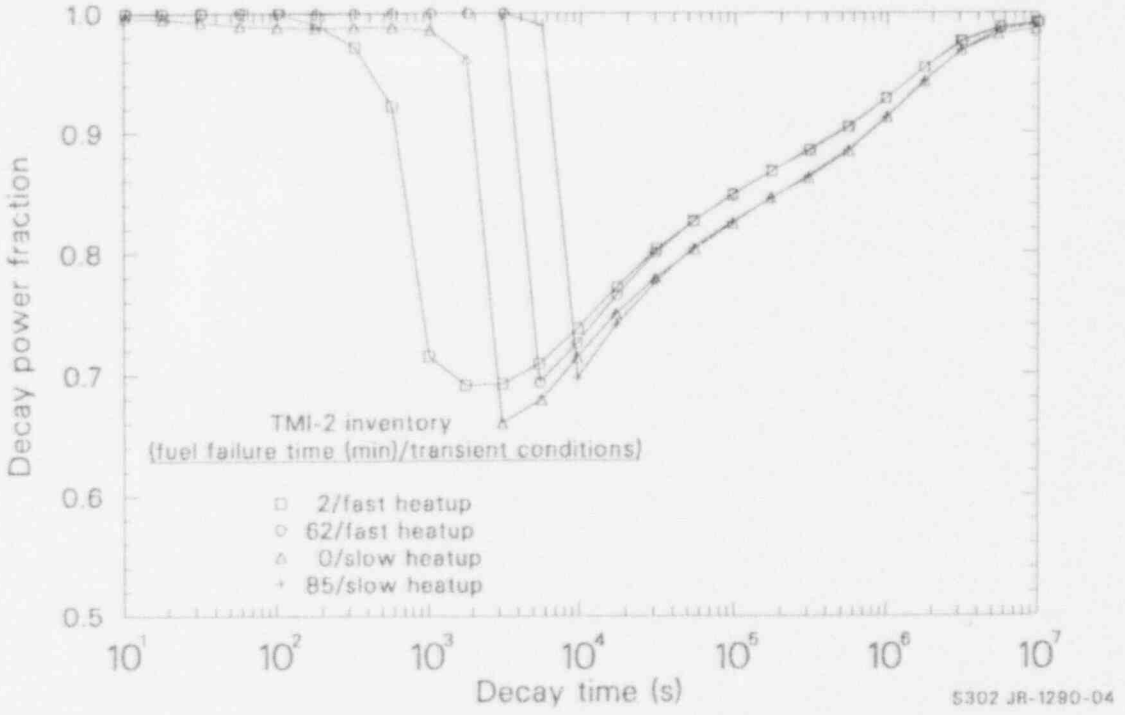

Figure 3-2. Reduction in total core decay power as a result of volatile fission product release fraction for TMI-2.

The coolability of a debris bed is also dependent on its porosity. Reference 3-38 discusses modeling considerations for analyzing porous debris bed thermal characteristics. Reference 3-38 also recommends using a porosity of 0.4 in debris bed thermal analyses.

Reference 3-39 presents results from MAAP 2.0 simulations of the TMI-2 accident. Results from times prior to core reflood were found to agree well with accident data. However, for times after core reflood, calculational results were found to be extremely dependent on debris and core configuration assumptions.

The composition of a debris bed in the Shoreham and Peach Bottom BWR vessels after an SBO event has been postulated.[3-17,3-40,3-41] As discussed previously, these BWR analyses assume that the debris would enter the lower head as a solid because core plate failure subsequent to vessel depressurization and dryout of the core region would preclude retention of a large molten mass within the core region before relocation. The composition of the quenched debris bed was predicted to vary with height, which was typically assumed as ~0.1 m. Lowermost in the bed would be mostly metallic debris (control blades, canisters, candled cladding, and dissolved fuel) that had either accumulated on the core plate before local core plate failure or subsequently relocated downward above the core plate failure locations before fuel pellet stack collapse.[3-41] The collapsed fuel and ZrO_2 from the central region of the core would be higher near the middle regions of the bed.

3.1.6 Summary

Information in this section illustrates that a wide range of accident thermal-hydraulic conditions and debris configurations has been studied to determine the progression of core melt

and timing of vessel failure. Table 3-2 summarizes key parameters characterizing melt progression for some severe accident analyses that were found in the literature. As shown in Table 3-2, the analyses tend to concentrate on a limited number of events (such as SBO, ATWS, and small LOCA) and plants (such as Surry and Peach Bottom). Furthermore, as discussed in this section, the results for a particular event in a particular reactor may vary because of differences in the phenomena modeled and assumptions related to the event's progression (e.g., the failure of a pump seal or vessel penetration, the inclusion of natural circulation, operator response, and debris bed composition and configuration). For example, the time predicted for vessel failure can vary significantly if phenomena, such as penetration tube failure and pump seal failure, are included in the analysis. Hence, even for a particular event or reactor type, it is difficult to draw general conclusions from existing literature related to reactor thermal-hydraulic conditions prior to and during vessel failure.

3.2 Important Plant Design Features

Design features within and surrounding the reactor vessel affect the response during a severe reactor accident. Hence, a review of plant-specific features affecting vessel failure, such as vessel internal structures, vessel penetrations, and vessel cavity configuration, has been performed to characterize the heat-transfer resistances and the likelihood of various vessel failure mechanisms during severe reactor accidents.

To compare design features of reactor vessels, typical designs were reviewed from each of the four major U.S. vendors: Babcock & Wilcox, General Electric, Combustion Engineering, and Westinghouse. This section emphasizes plant design features that are important in assessing the likelihood of vessel lower head failure during severe reactor accidents. Areas where vendor plant designs differ are noted, where possible. This section is primarily based on information found in vendor Final Safety Analysis Reports (FSAR), plant design drawings, Reference 3-42 (a detailed plant configuration comparison), and conversations with plant personnel. In addition, vendor reports describing other plants with similar designs have been used. This section provides plant parameters typical of each vendor's design to elucidate the discussion. A detailed list of plant parameters used in lower head analyses can be found in Appendix F.

3.2.1 Reactor Vessel Lower Head Design

The following sections discuss the geometry and material composition of each reactor vessel and the major internal structures through which the molten debris would pass prior to contacting the lower reactor vessel. Estimates are provided for the mass and material composition of corium that could reach the lower vessel head during a complete meltdown and the water inventories in the reactor vessel at heights of interest for lower head analyses.

3.2.1.1 Babcock & Wilcox Lower Head Design. The principal design parameters of the reactor vessel for the TMI-2 plant, which has been selected as a typical B&W reactor, are summarized in Appendix F-2. The reactor vessel consists of a cylindrical shell, a cylindrical support skirt, a spherically dished bottom head, and a ring flange to which a removable reactor closure head is bolted. The reactor closure head is a spherically dished head welded to a matching ring flange. The cylindrical shell is composed of three shell courses: upper, intermediate, and lower. Three 120-degree steel plate segments are welded together to form each shell course. Full thickness welding is used to assemble the shell courses. The bottom head is constructed of several peel segments and a dome section, all formed from plate material, which are welded together to form an elliptical head. Typical weld locations for a PWR vessel are illustrated in Figure 3-3.

Table 3-2. Summary of key parameters in previous severe accident analyses.

Reactor/ vendor	Event	Initial power level[a]	Vessel pressure[b]	Event timing (h)				Temperature (K)					Methodology	Section 3 reference
				Core uncovery	Corium relocation	RCS dryout	Vessel failure	Debris	Vessel	Tube	Bldg	Coolant		
Shoreham (BWR/4)/GE	ATWS	Low-25%	Low	1.7	—	—	—	—	—	—	—	—	BWRSAR	25
		Full	Low	—	—	—	—	—	—	—	—	—	BWRSAR	25
Peach Bottom (BWR4)/GE	SBO-ST	Full	Low	0.7	2.21	4.3	7.8	—	561-1225	>1478	>330	—	BWRSAR	16
	SBO-ST	Full	High	0.5	1.7	4.1	4.6	—	—	—	380	—	MELCOR	20
	SBO-LT	Full	High	7.8	9.6	12.8	13.5	—	—	—	—	—	MELCOR	20
	SBO-LT	Full	Low	8.8	11.6	11.7	12.2	2550	—	—	310	570	STCP	21
	ATWS	Full	Low	1.3	—	—	2.9-5.0	—	—	—	>330	—	MAAP 2.0B	26
	ATWS	Full	High	0.6	1.5	—	2.1	2550	—	—	310	630	STCP	12
	ATWS	Full	Low	1.6	2.2	3.3	3.8	2550	—	—	310	—	STCP	21
	ATWS	Full	High	1.0	1.4	1.9	2.1	>2550	—	—	310	—	STCP	21
Susquehanna (BWR/4)/GE	SBO-ST	Full	—	0.6	1.5	3.2	4.1	—	—	—	340-700	—	BWRSAR	18
		Full	—	0.6	2.1	4.4	4.4	—	—	—	340-420	—	BWRSAR	18
Grand Gulf (BWR/6)/GE	SBO-ST	Full	Low	0.7	1.8	3.6	3.6	—	—	—	330-333	—	BWRSAR	19
		Full	Low	0.9	1.8	2.6	3.0	2550	—	—	310	—	STCP	21
	SBO-LT	Full	High	8.0	10.9	11.3	11.7	2550	—	—	310	—	STCP	21
Bellefonte/ B&W	SBO	Full	—	0.6	0.7-0.8	—	—	—	—	—	—	—	SCDAP/ MOD1	22
		Full	High	0.5	1-10	—	—	2000-3000	—	—	—	—	SCDAP and SCDAP/ RELAP5	29

Table 3-2. (continued).

Reactor/ vendor	Event	Initial power level[a]	Vessel pressure[b]	Event timing (h)				Temperature -- (K)					Methodology	Section 3 reference
				Core uncovery	Corium relocation	RCS dryout	Vessel failure	Debris	Vessel	Tube	Bldg	Coolant		
Seabrook (4 Loop)/W	SBO	Full	High	2.0	–	–	3.5	–	650-1000	–	400-800	600-1050	MAAP 3.0B	4
	SBO	Full	High	1.8	3.2	2.2-2.5	–	2900	–	–	–	>565	RELAP5/ MOD2 & SCDAP/ MOD1	5
Sequoyah (4 Loop)/W	Small LOCA	Full	–	1.3	–	2.7-3.3	–	–	–	–	–	–	MAAP 2.0B	26
	Small LOCA	Full	High	4.5	6.5	–	6.8	2550	–	–	310	–	STCP	21
	SBO	Full	Low	8.6	13.1	14.3	16.4	2550	–	–	310	–	STCP	21
	SBO	Full	High	1.6	2.3	2.5	2.5	2550	–	–	310	610	STCP	12
Surry (3 Loop)/W	SBO	Full	High	2.2	2.4-2.8	2.8	2.9	–	480-1000	–	–	–	MARCH-2	11
		Full	Low	2.2	8.3	6.5	10	1650-2900	–	–	–	–	MELPROG/ TRAC	8
		Full	High	2.2	3.3	3.6	4	–	–	–	–	–	MELPROG/ TRAC	9,10
		Full	High	1.8	2.8	2.9	2.9	2550	–	–	310	630	STCP	12
		Full	Low	2.3	6.5-7.5	–	–	1000-3500	–	–	–	–	SCDAP/ RELAP5	13
		Full	Low	2.2	2.7-3.0	–	–	–	–	–	–	–	SCDAP/ RELAP5	14

Table 3-2. (continued).

Reactor/ vendor	Event	Initial power level[a]	Vessel pressure[b]	Event timing (h)				Temperature (K)					—	
				Core uncovery	Corium relocation	RCS dryout	Vessel failure	Debris	Vessel	Tube	Bldg	Coolant	Methodology	Section 3 reference
Advanced PWR (SYS80)/ CE[c]	SBO	Full	High	—	—	—	2.7	—	—	>1000	320-1080	—	MAAP-DOE	7
		Full	Low	—	—	—	3.6	—	—	>1000	320-900	—	MAAP-DOE	7
TMI-2/B&W		Full	Low	1.7-1.9	—	—	—	581-2800	—	—	—	550-922	SCDAP/ RELAP5, Analytical, COUPLE/ FLUID, MAAP 2.0	30,33,36, 37,39

a. Power level at initiation of accident.

b. Pressure at time of global vessel failure or end of analyses: high is greater than −1.4 MPa; low is less than or equal to 1.4 MPa.

c. Design evaluated in ARSAP program.

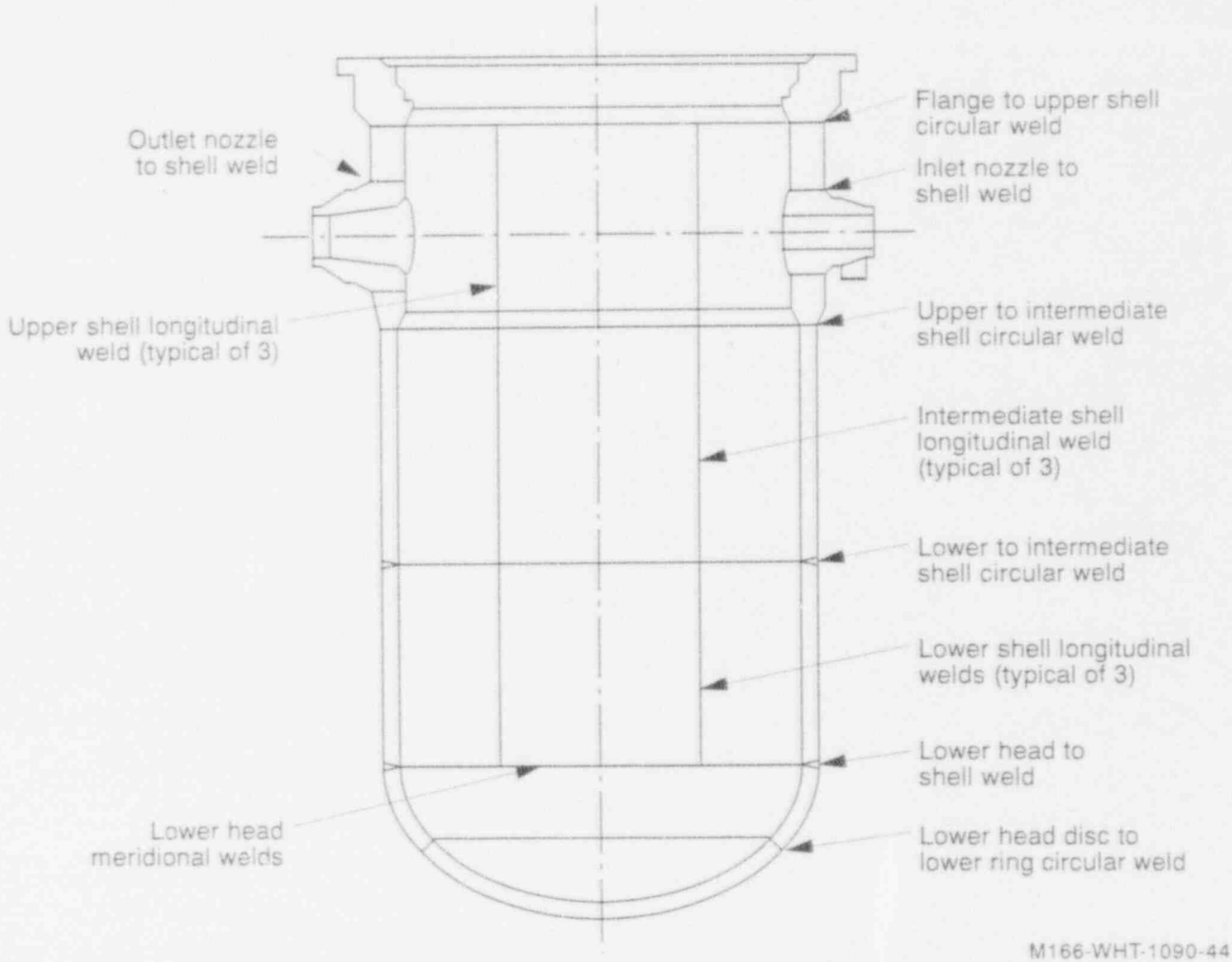

Figure 3-3. Weld location on a typical B&W PWR reactor vessel.

The TMI-2 vessel is composed of manganese-molybdenum-nickel steel plates (SA533B1) and manganese-molybdenum-nickel-chromium steel forgings (SA508-64, Class 2). These materials are typical of those found in reactor vessels constructed after 1970.[3-43] During the mid-1960s, the increasing size of nuclear components required that vessel materials have increased hardenability. Hence, nickel was added in quantities between 0.4 and 0.7 wt%. Before this time, vessels were composed of either carbon-silicon or manganese-molybdenum alloys.

Figure 3-4 illustrates the arrangement of components in the reactor vessel. This arrangement is typical of vessels used in B&W lowered-loop plant designs, in which the steam generators extend to a elevation lower than the reactor vessel lower head. Later B&W plants, featuring raised-loop designs, have larger vessels and omit the internal vent valves, which are opened during a cold leg break accident to vent steam from the core and promote rapid core reflooding. Based on information from References 3-42 and 3-44, the volume of water required to reach selected heights has been estimated for the TMI-2 vessel. These volumes are listed in Appendix F-2.

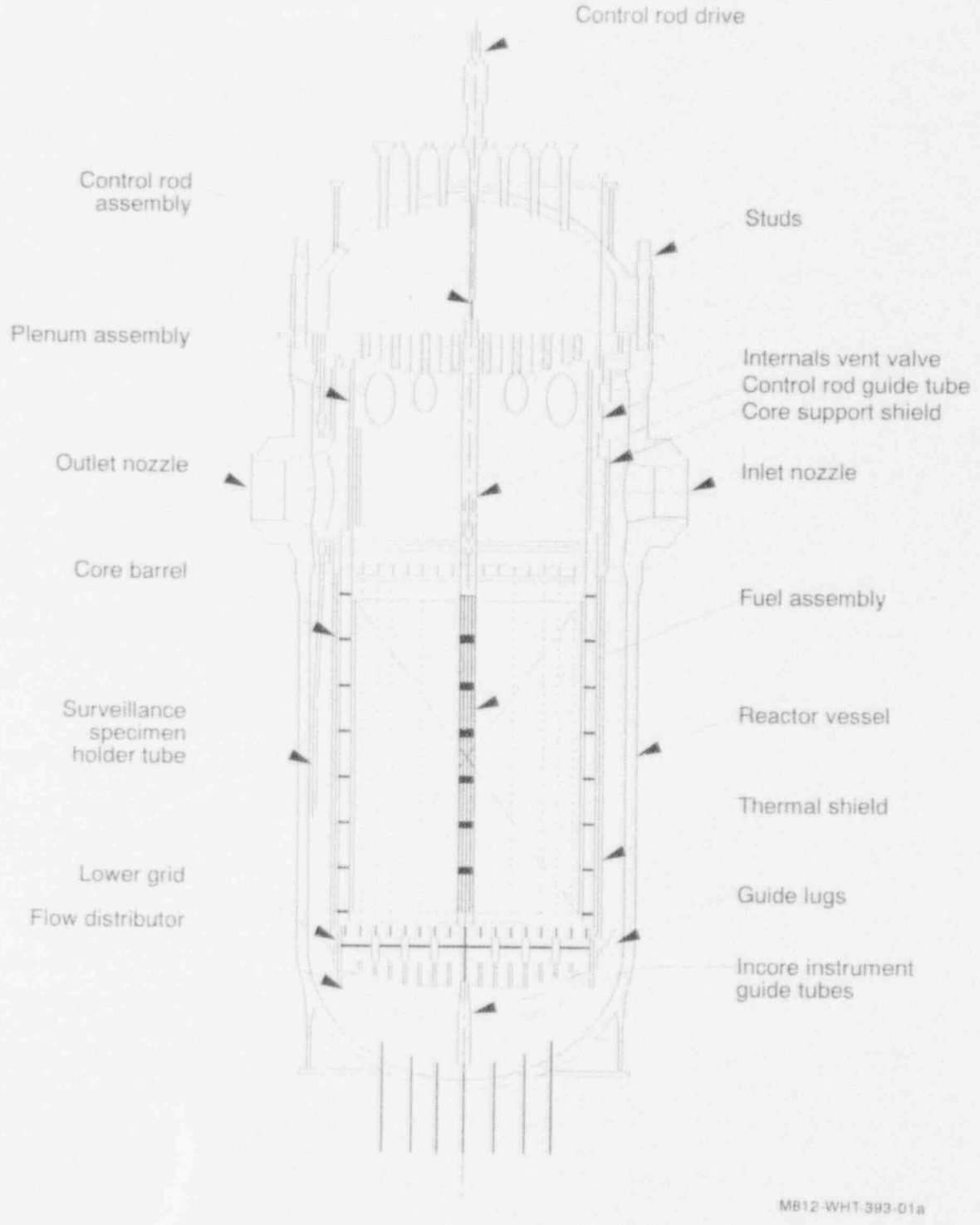

Figure 3-4. Arrangement of reactor vessel components in a typical B&W.

As shown in Figure 3-4, internal components of the TMI-2 reactor vessel include the plenum assembly and the core support assembly. The core support assembly consists of the core support shield, internal vent valves, core barrel, lower grid, flow distributor, 52 in-core instrument guide tubes, a 0.05-m (2-in.)-thick thermal shield, and three surveillance holder tubes. To minimize

lateral deflection of the core support assembly from horizontal seismic loading, integral weld-attached, deflection-limiting guide lugs have been welded on the reactor vessel inside wall. These lugs are also designed to limit core vertical drop to less than 0.01 m (0.5 in.) if a flange, circumferential weld, or bolted joint fails.

The fuel assemblies with stainless steel end fittings are supported on each end by support plates. A baffle wall with horizontal support plates maintains the sides of the assemblies. The support plates are welded to the core barrel and baffle wall and extend around the baffle wall perimeter.

An enlargement of the configuration for the lower plenum support structure is shown in Figure 3-5. The uppermost plate of the lower grid plate supports the fuel assemblies and is estimated to have a diameter of 2.56 m (140 in.), with 0.15-m (6-in.)-square openings through 0.18 m (7.2 in.) of stainless steel. Debris originating within the fuel assemblies, after passing through the slotted lower end fitting, would pass through this plate that provides for major coolant passage.

The grid plate is itself supported by columns that are approximately 0.10 m (4 in.) in diameter and 0.30 m (12 in.) high. At the column's half-height, between the two grid plate

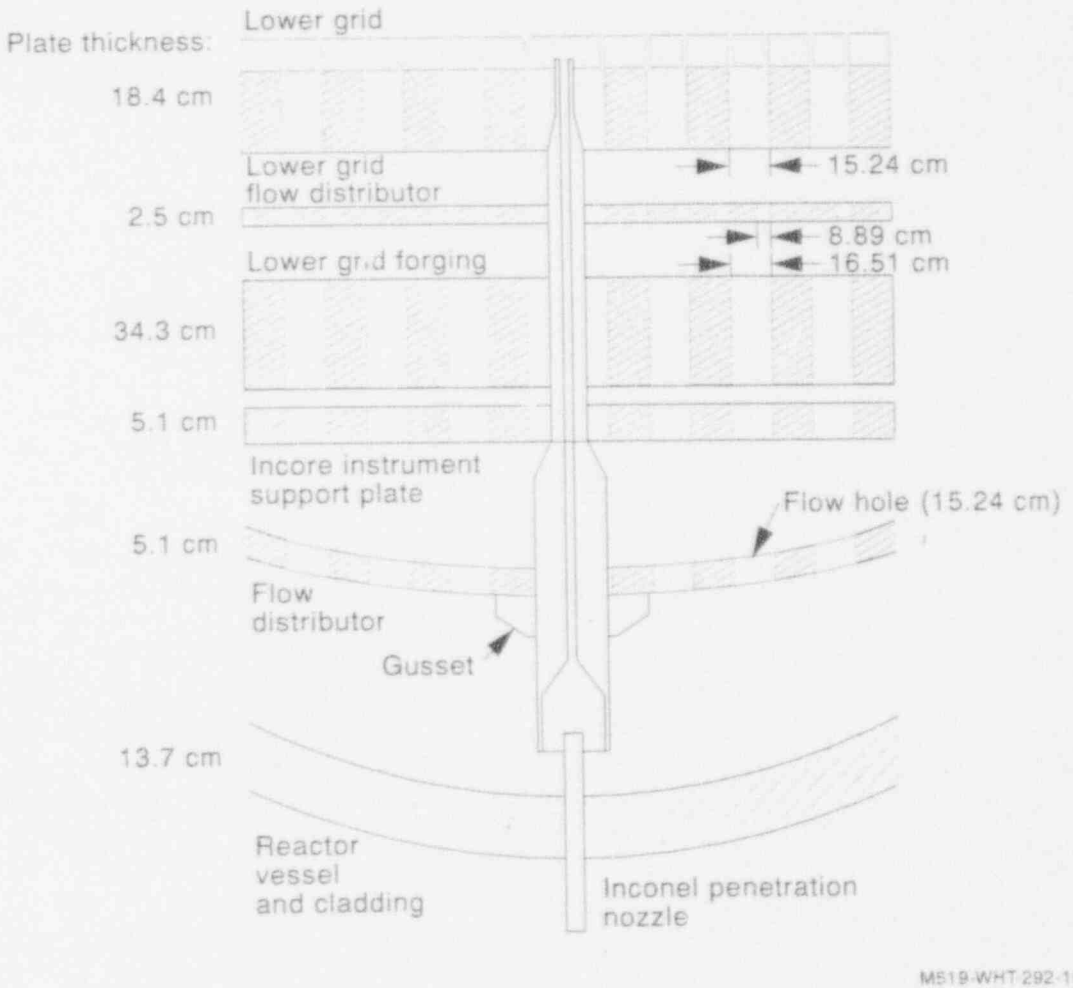

Figure 3-5. Lower head structures in a typical B&W PWR.

structures, is the lower grid distributor plate, which is approximately 0.03 m (1.0 in.) thick with 0.09-m (3.5-in.)-diameter holes. The columns are welded to a 0.34-m (13.5-in.)-thick lower grid forging and a 0.05-m (2-in.)-thick in-core instrument support plate, which has square channel openings with sides that are 0.17 m (6.5 in.). The flow distributor, consisting of a flat plate and a dished head, is below this lowest grid plate. The flow distributor is approximately 0.05 m (2 in.) thick, with 0.15-m-(6 in.)-diameter holes. Additional information on B&W lower plenum structures can be found in Section 4.2.1.

In Reference 3-42, the mass of material that could enter the lower head during a complete core meltdown accident for the TMI-2 plant was estimated. Appendix F.2 compares the values obtained for the TMI-2 plant with other vendor plant results. The TMI-2 vessel meltdown masses included the thermal shield, the core barrel, baffle wall and former plates, support ring, end fittings, distributor and grid plates, support columns, fuel, cladding, control rod poison, and Inconel spacer grids.

3.2.1.2 Combustion Engineering Lower Head Design. The major design features of a typical CE PWR reactor vessel are also summarized in Appendix F.2. The construction and material composition of this vessel are similar to those described above for the TMI-2 vessel. Figure 3-6 illustrates the arrangement of structures in the reactor vessel. Noticeable differences between the B&W design and the internal structure of a CE vessel are the lack of a thermal shield and lower head nozzles for instrumentation tubes in the CE vessel. Reference 3-42 indicates that although most CE vessel designs are similar to this vessel design, certain variations exist. For example, the Maine Yankee vessel includes a thermal shield and instrumentation guide tubes that penetrate the vessel lower head. Water inventories required to reach heights of interest within a typical CE reactor vessel have been estimated, using information from References 3-42 and 3-45. Results in Appendix F-2 indicate that the estimated volumes of water are similar to those values estimated for the TMI-2 vessel.

The components of the reactor internals are divided into two major parts: the upper guide structures assembly and the core support structure. The flow skirt, although functioning as an integral part of the coolant flow path, is separate from the internals and is affixed to the bottom head of the pressure vessel.

The core support structure consists of the core support barrel and the lower support structure. The 0.08-m (3-in.)-thick core support barrel rests on a ledge within the pressure vessel. In turn, the core support barrel supports the lower support structure upon which the fuel assemblies rest. The lower support structure supports the core by means of a 0.05-m (2-in.)-thick stainless steel core support plate, which rests on columns mounted on support beams that transmit the load to the core support barrel lower flange. The core support plate supports and orients the lower ends of the fuel assemblies and contains flow distribution holes. The core shroud, which provides a flow path for the coolant and lateral support for the fuel assemblies, is also supported and positioned by the core support plate. The lower end of the core support barrel is restricted from excessive radial and torsional movement by six snubbers that interface with the pressure vessel wall. Additional information on CE lower plenum support structures can be found in Section 4.2.1.

The flow skirt is a right-circular, Inconel cylinder, perforated with flow holes and reinforced at the top and bottom with stiffening rings. The skirt is supported by nine equally spaced machined sections that are welded to the bottom head of the pressure vessel.

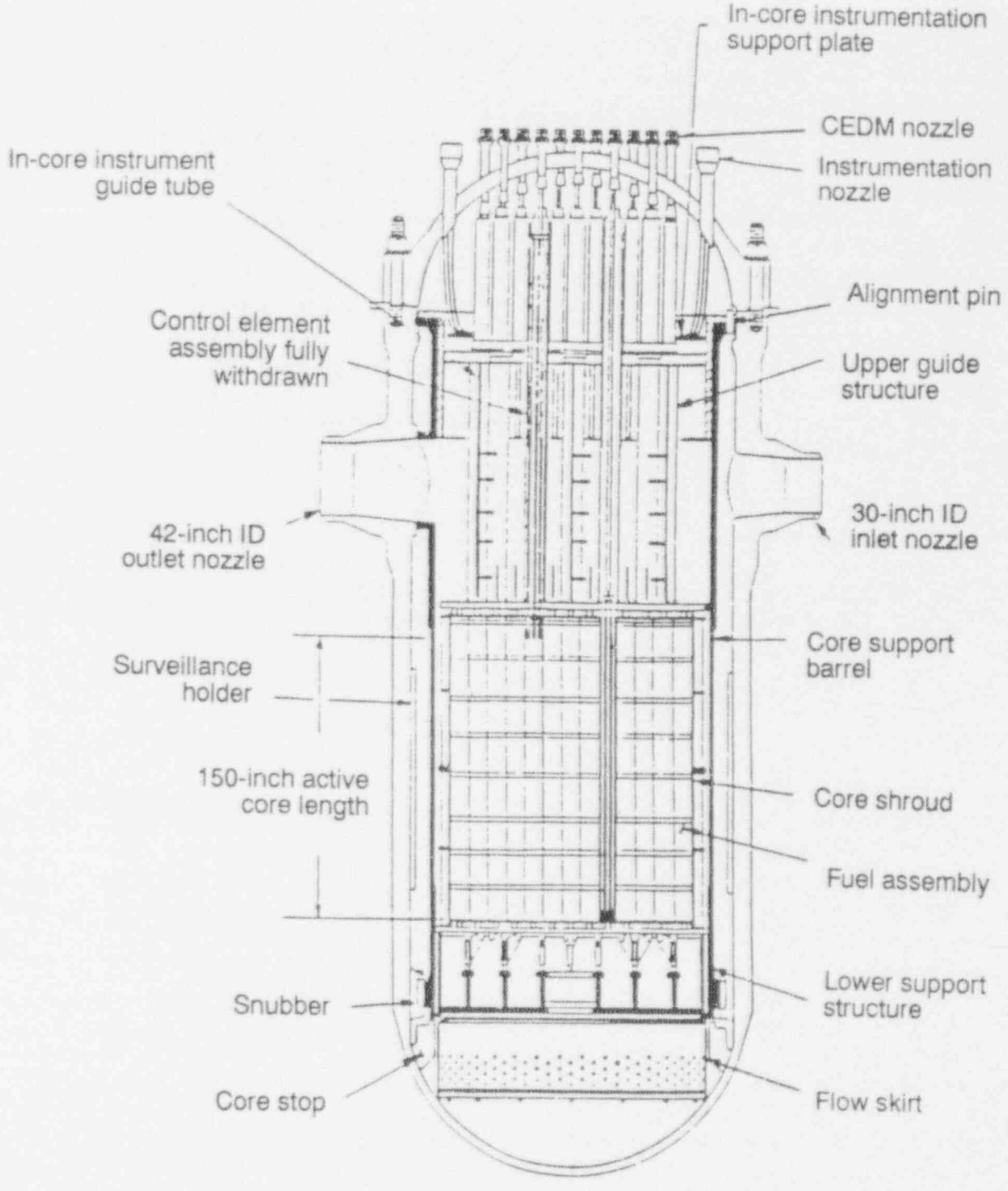

Figure 3-6. Arrangement of reactor vessel components in a typical CE PWR.

Masses of vessel materials that may be included in a major meltdown of a typical CE plant are listed in Appendix F-2.[3-42] Included in this estimate are masses of the fuel, cladding, control rod material, guide tubes, flow skirt, and the structural support steel, including the core barrel.

lower cylinder, and lower support plates (Table F-2.1 includes the masses of all structural items below the upper core support plate).

3.2.1.3 General Electric Lower Head Design. Major design parameters for two reactor vessels from GE-designed BWR nuclear power stations are listed in Appendix F-2. The construction and material composition of these vessels are similar to those described above for the TMI-2 vessel. However, the BWR vessels are larger than the PWR vessels listed in Appendix F-2 because BWR vessels must accommodate steam separators, dryers, and (in the case of most BWRs) jet pumps, in addition to the reactor core. The inventories required to reach heights of interest in both BWR plants have been estimated from information found in References 3-42, 3-46, 3-47, and 3-48. The water volumes listed in Appendix F-2 indicate that the water required to cover the core in BWR reactor vessels is at least four times that required for the reference PWR designs.

The BWR vessel cylindrical wall [0.13 m (~5 in.)] is generally thinner than a PWR wall [0.23 m (~9 in.)] because a BWR operates at a lower pressure [typically 6.9 MPa (1000 psia)] than a PWR [typically 15.5 MPa (2250 psia)]. However, a BWR lower head thickness is greater [0.2 m (~8 in.)] because the lower head must accommodate over 200 penetrations, some of which are significantly larger than the penetrations found in a PWR vessel (see Section 3.2.2).

The different BWR designs are classified into product lines, designated BWR/1 through BWR/6. The differences in the product lines are basically in the nuclear steam supply system (NSSS) and engineered safety features (ESFs) and include variations in water volumes, coolant flow, reactor vessel dimensions, and emergency core cooling systems (ECCS). However, there are different sizes of reactors and vessels within the same class. For example, Duane Arnold (a 538-MWe plant with a 4.65-m-ID reactor vessel), HATCH 1 (a 753-MWe plant with a 5.54-m-ID vessel), and Peach Bottom 2 (a 1051-MWe plant with a 6.38-m-ID vessel) are all of the BWR/4 design. A major difference between the BWR/4 and later plant designs is the addition of recirculation valve flow control. The majority of operating BWRs are BWR/4 designs. The newest generation of BWRs is the BWR/6, which was introduced in 1972. There are two standard BWR/6 designs, 238 and 251, where the number refers to the reactor vessel diameter in inches. The BWR/6 incorporates numerous changes in design, including improved ECCS performance and solid-state electronics in protection systems. The BWR/1 and BWR/2 reactors are similar to the BWR/3, except that they have recirculation loops instead of jet pumps.

Internal structures in the reactor vessel are shown in Figures 3-7 and 3-8. The BWR core support structure consists of the shroud, shroud support, core support, fuel support pieces, and control rod guide tubes. The 0.05-m (2-in.)-thick core shroud is a stainless steel, cylindrical assembly that provides a partition to separate the upward flow of coolant through the core from the downward recirculation flow. The lower shroud is welded to the reactor pressure vessel shroud support, which is a circular plate welded to the vessel wall. The shroud support is designed to carry the weight of the shroud, shroud head, peripheral fuel elements, neutron sources, core support plate, top guide, steam separators, and jet pump diffusers; it also laterally supports the fuel assemblies.

The core plate consist of a 0.05-m (2-in.)-thick, stainless steel plate with 185 large holes [0.28-m (11-in.) ID] to accommodate the passage of the control rod guide tubes and 55 smaller holes [0.05 m (2 in.)] to accommodate the in-core instrument guide tubes. Unlike PWRs, a BWR core plate provides only vertical support to the 24 outermost fuel assemblies (of the 764 assemblies that make up the core). Four-lobed and orificed fuel support pieces are used by each of the 185 control rod guide tubes to support most of the fuel assemblies (four fuel

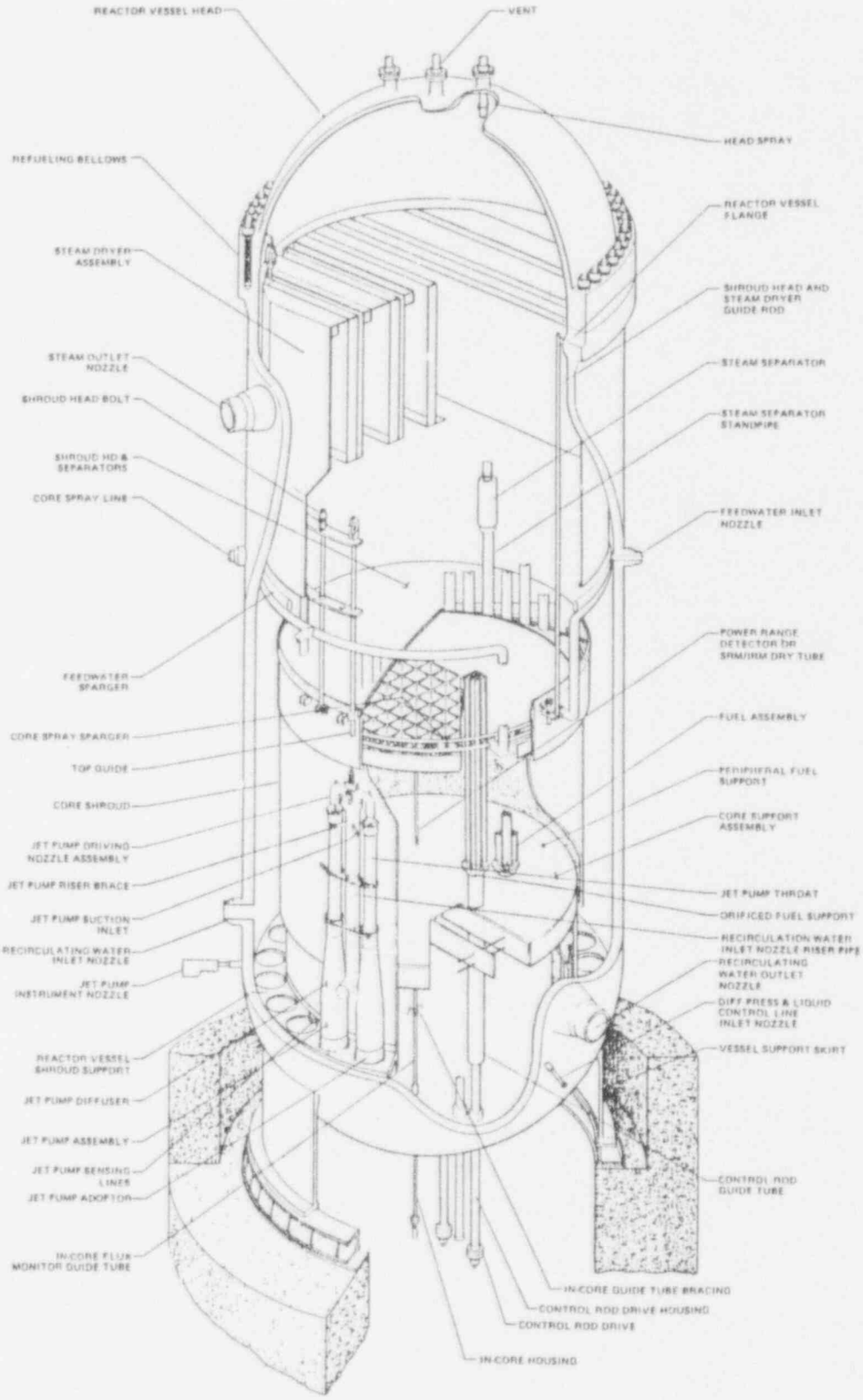

Figure 3-7. Arrangement of reactor vessel components in typical GE BWR/4, BWR/5, and BWR/6 plants.

assemblies are supported by each control rod guide tube). In contrast, the peripheral fuel support pieces are seated in the core plate. S. A. Hodge[f] at Oak Ridge National Laboratory investigated the role of a BWR core plate during normal and accident conditions.

The core plate is supported around the outer periphery (bolted to a ledge on the core shroud)., In addition, significant central support is provided by the stiffener plates and stiffener rods (see Figure 3-8). Additional information on GE lower plenum configuration is found in Section 4.2.1.

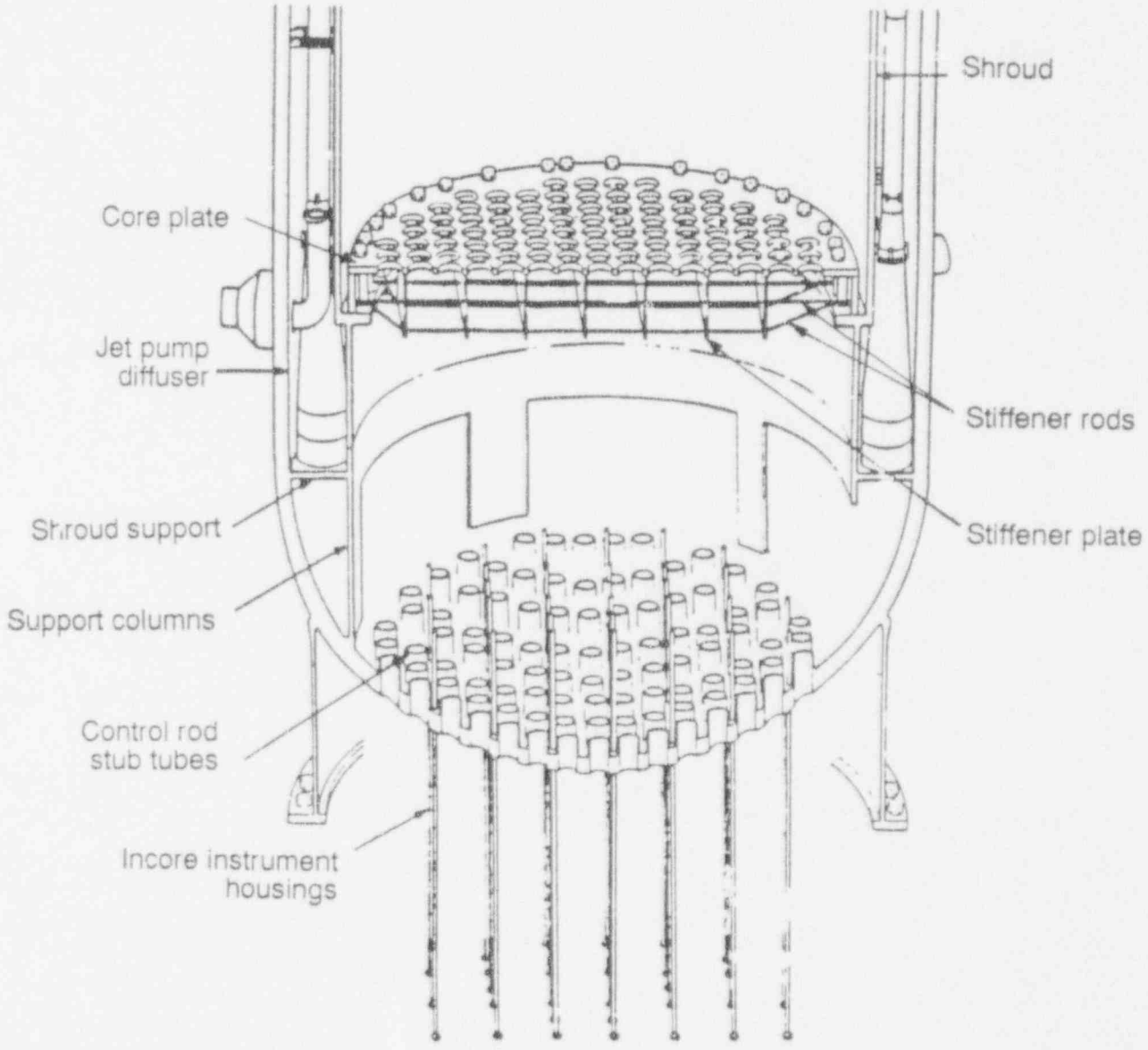

Figure 3-8. Structures in a typical GE BWR.

f. Unpublished research, Oak Ridge National Laboratory, 1990.

Masses of material that may melt during a complete core meltdown accident in BWR plants are compiled in Appendix F-2.[3-16,3-42] Major components included in this estimate are the UO_2 fuel, zircaloy cladding and channel enclosures, Inconel springs and clips, control rod poisons, and steel materials below the active fuel height, such as support plates; control rod structures (guide tubes, drive housings, etc.); supports for the fuel, core, and shroud; jet pumps; and the shroud below the top of the active fuel. As shown in Appendix F-2, approximately twice as much zircaloy is available for relocation in a GE BWR than in a PWR. This increase is from the zircaloy associated with the BWR fuel assembly channel enclosures.

3.2.1.4 Westinghouse Lower Head Design. Appendix F-2 lists the major design parameters for the vessel of a typical Westinghouse four-loop PWR plant. The construction and material composition of this vessel are similar to those described above for the TMI-2 vessel. Figure 3-9 illustrates the lower core support structures found in this reactor vessel. Comparisons of Westinghouse plants in References 3-42, 3-43, 3-49, and 3-50 indicate that most of the reactor vessels are similar in design, although the size of the vessel increases with the number of coolant loops, and some earlier Westinghouse plants do not have instrumentation guide tubes penetrating the bottom head. The inventories of water required to reach heights of interest in this Westinghouse vessel have been estimated from information found in References 3-42, 3-49, and 3-50. As shown in Appendix F, the estimated inventories are similar to the values estimated for the other reference PWR vessels.

The major components of the Westinghouse vessel's lower core support structure are neutron shield pads, the core barrel, the core baffle, the lower core plate and support columns, and the core support, which is welded to the core barrel. These structures are primarily composed of 304 stainless steel. The thermal shield pad assembly consists of four pads that are bolted and pinned to the outside of the core barrel. These pads are approximately 1.23 m (48 in.) wide by 3.79 m (148 in.) long by 0.07 m (2.8 in.) thick. Within the core barrel are an axial baffle and a lower core plate, both of which are attached to the core barrel wall and form the enclosure periphery of the assembled core. The 0.05-m (2-in.)-thick lower core plate, through which flow distribution holes for each fuel assembly are machined, is positioned at the bottom level of the core below the baffle plates and supports, and orients the fuel assemblies. The lower core support structure is supported at its flange by a ledge in the reactor vessel head flange, and its lower end is restrained in its traverse movement by a radial support system attached to the vessel wall.

The in-core instrumentation support structures consist of an upper system to convey and support thermocouples penetrating the vessel through the head and a lower system to convey and support flux thimbles penetrating the vessel through the bottom. Reactor vessel bottom port columns carry the retractable, cold-worked, stainless steel flux thimbles that are pushed upward into the reactor core. Section 4.2.1 provides additional information on Westinghouse lower plenum structures.

Masses of material (including fuel, cladding, control rod material, burnable poisons, guide tubes, in-core and lower core support structures) that could melt during a complete meltdown accident in the Westinghouse reactor are also listed in Appendix F-2.[3-42]

3.2.2 Reactor Vessel Lower Head Penetrations

The size, type, and number of penetrations may also impact the probability of vessel failure during a core melt accident. The parameters for penetrations in the vessel lower heads vary from

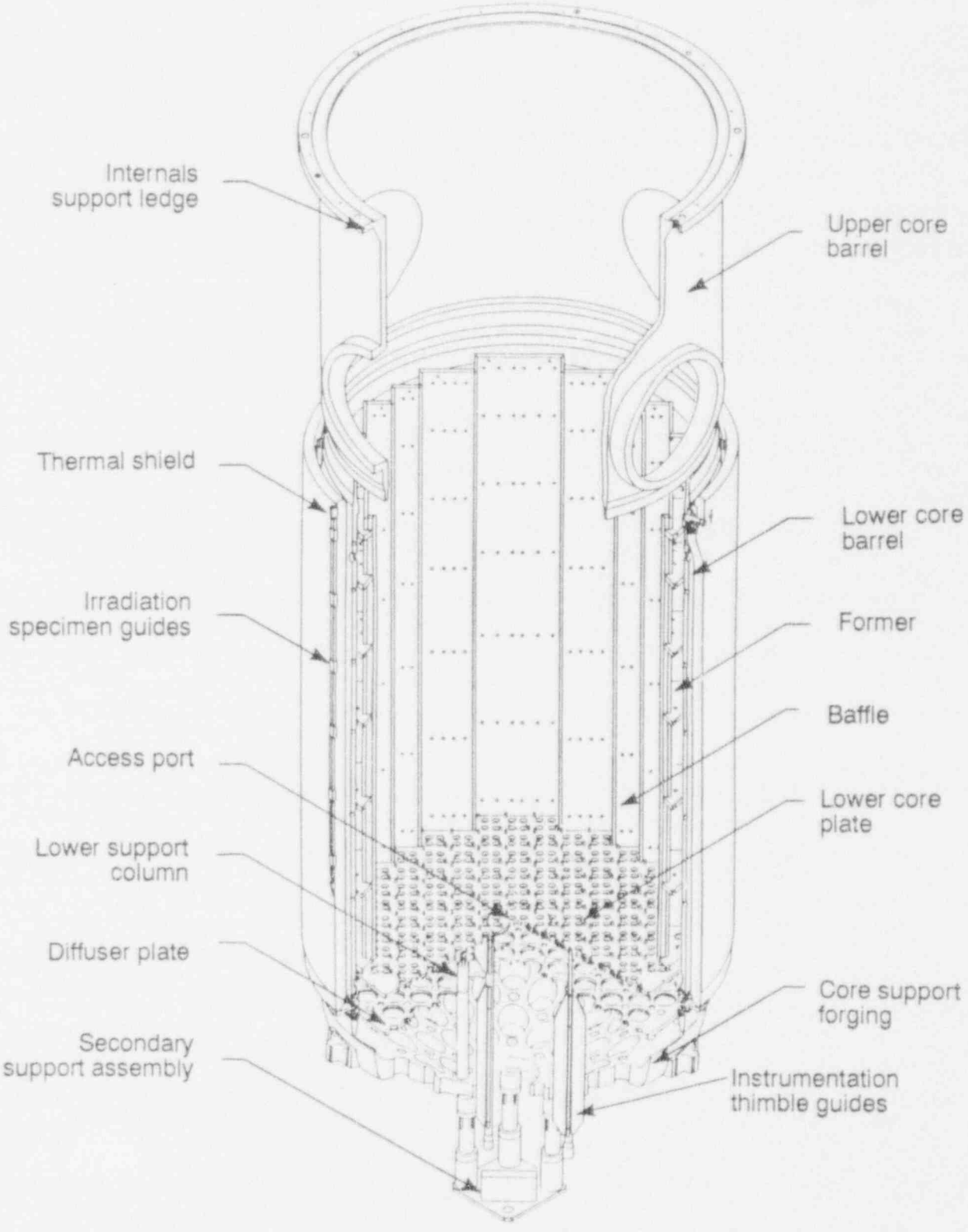

Figure 3-9. Arrangement of reactor vessel components in a typical Westinghouse PWR.

vendor design to design. For example, the number of bottom head penetrations varies from none in typical CE PWRs to over 200 penetrations in typical GE BWRs. Penetrations for each vendor's vessel lower head are discussed in the following sections. A detailed list of penetration dimensions is located in Appendix F-2.

3.2.2.1 B&W Vessel Penetrations. All vessels in B&W plants have instrumentation tube penetration nozzles that penetrate the vessel through the lower head. Figure 3-10 illustrates the general arrangement of an instrumentation tube nozzle penetrating the B&W TMI-2 vessel. Made of Inconel-600, 52 in-core tube instrumentation nozzles 0.02 m (0.75 in.) in diameter penetrate this reactor vessel.

Instrument guide tube penetrations are made by boring vertical holes into the vessel lower head, inserting a tube through the hole, and welding a nozzle to the tube and vessel inner surface. To facilitate the insertion of the tubes into the holes in the vessel head, tolerances for the outer diameter of each penetration tube and the diameter of each hole in the vessel head are set by design. These dimensions result in a radial gap range that must be considered in penetration failure analyses. Typically, instrument tubes are mounted between 2 to 3 m below the exterior of the vessel. Then, these tubes are curved along their horizontal run toward the seal table in the containment cavity.

An instrumentation string, whose cross section is shown in Figure 3-10, is inserted into instrumentation tubes. The inner channel of this string through which a thermoluminescent dosimeter probe or miniature ion chamber is inserted, is filled with containment air at atmospheric pressure. The outer diameter of this string is approximately 0.7 cm smaller than the inner diameter of the instrument tube. Thus, in addition to the air-filled channel within the string, there is also an annulus filled with RCS water at system pressure available for melt flow if an in-vessel tube failure occurs during a severe accident.

3.2.2.2 CE Vessel Penetrations. Although some of the operating CE plants (such as the Maine Yankee plant) and the new CE APWR System 80 design use bottom-entry instrumentation tubes, most CE reactor vessels have in-core detector assemblies that pass through the upper reactor vessel head. Hence, there are no vessel lower head penetrations in most operating CE plants.

3.2.2.3 GE Vessel Penetrations. The BWR is the only LWR system that employs bottom-entry control rods. A GE BWR vessel is also penetrated by guide tubes for in-core flux monitors and a drain nozzle. Both reference GE plants have vessel lower heads with 185 stainless steel control rod penetrations 0.15 m (6 in.) in diameter, 55 stainless steel in-core guide tube penetrations 0.05 m (2.0 in.) in diameter, and one carbon steel drain nozzle 0.05 m (2.0 in.) in diameter. Figure 3-11 illustrates the arrangement of typical BWR penetrations.

A BWR instrument tube, whose cross section is shown in Figure 3-11, is inserted in each 304 stainless steel BWR instrument guide tube. Similar to a PWR instrument tube penetration, RCS coolant fills the 2.0 cm gap between the outer diameter of a BWR instrument tube and the inner diameter of a BWR instrument guide tube, and air at atmospheric pressure surrounds monitors within the instrument tube.

The drain penetration, which is located in the bottom of the reactor vessel 15.24 cm off the centerline, directs flow to the reactor water cleanup system to aid in the removal of suspended solids, to provide a temperature measurement of water in the bottom head area, and to minimize cold water stratification in the bottom head area. It consists of a SA105 Class II carbon steel

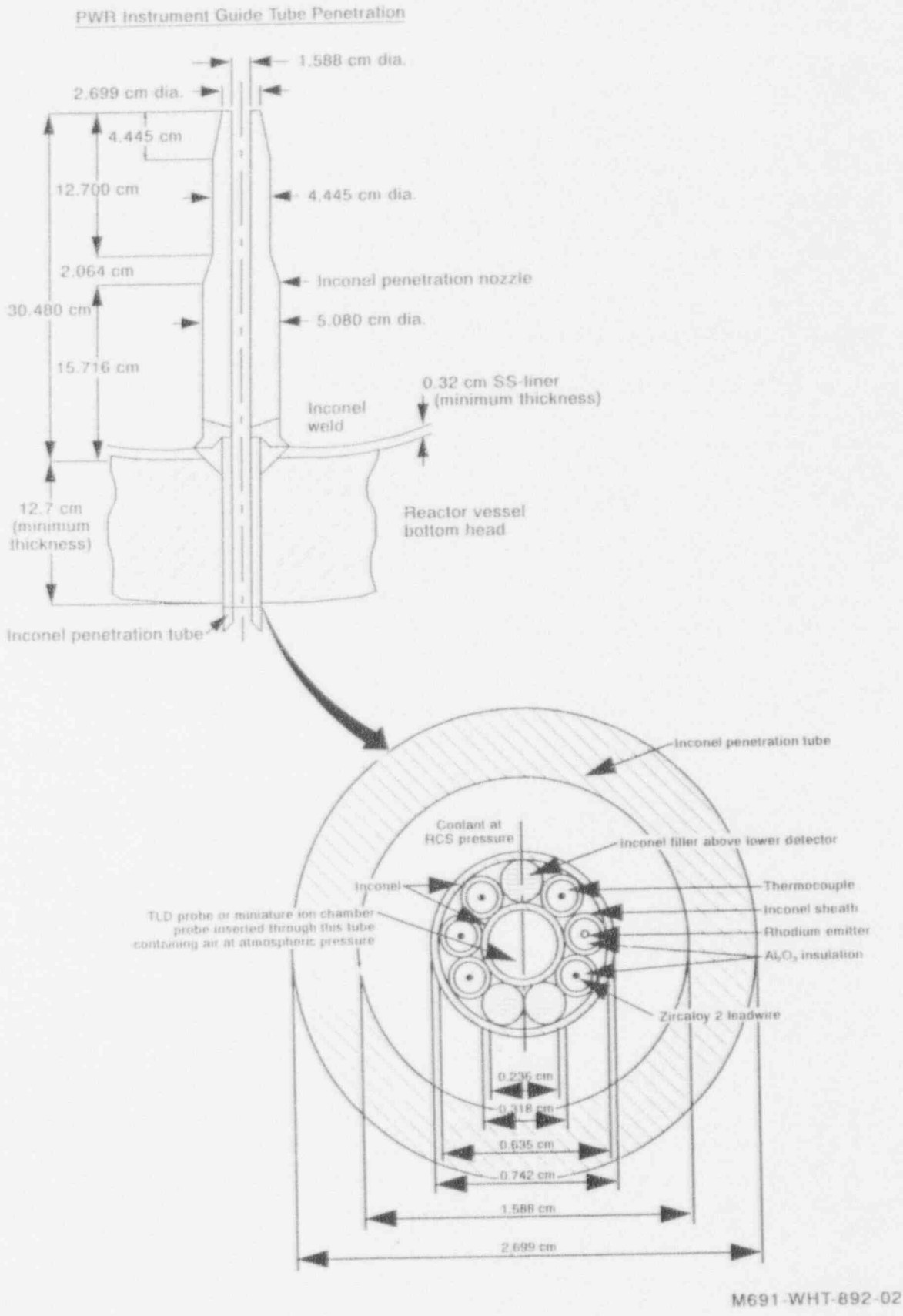

Figure 3-10. Arrangement of instrument penetration tube in a typical B&W reactor vessel.

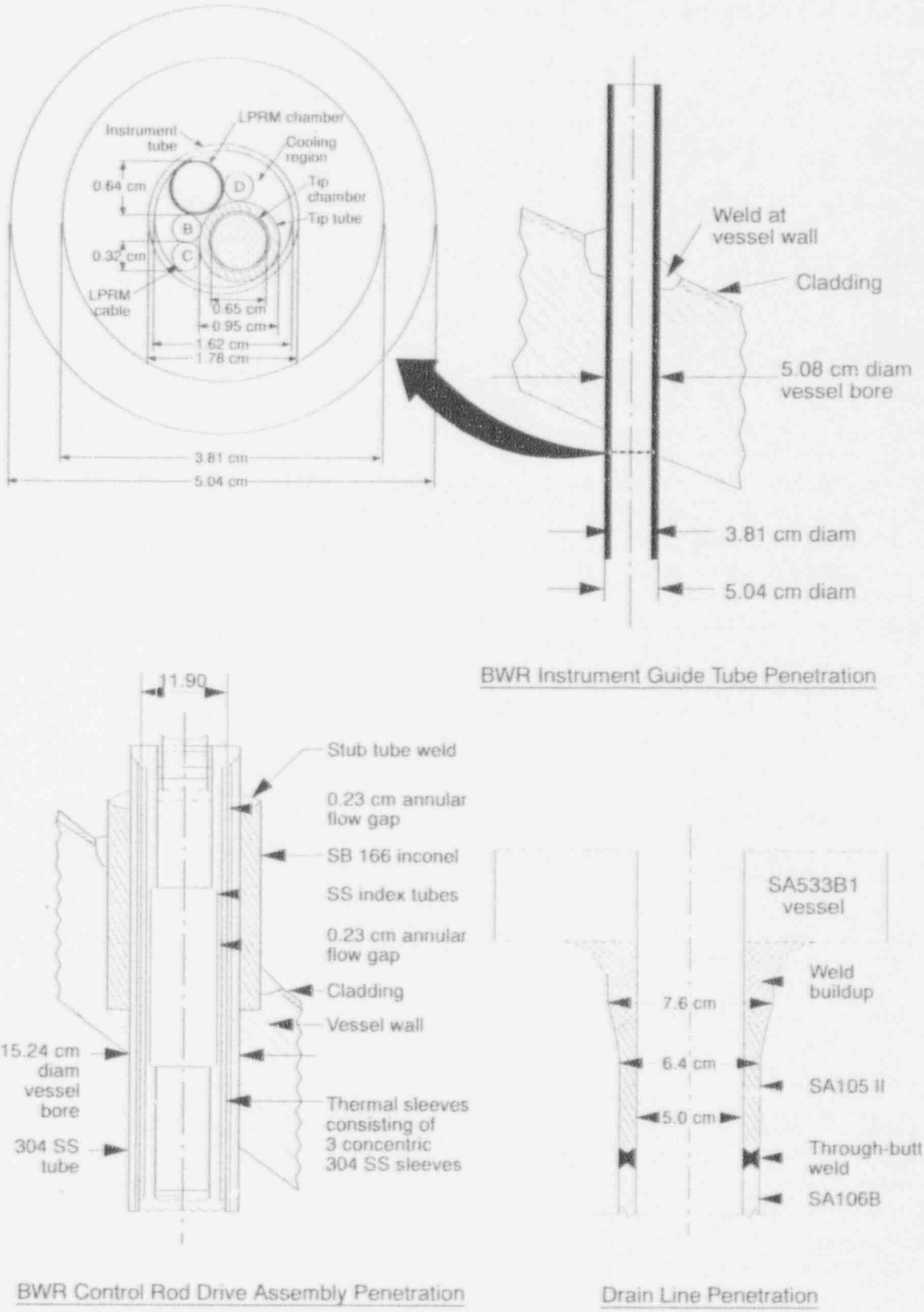

Figure 3-11. Arrangement of penetrations in a typical GE reactor vessel.

nozzle and SA106 mating pipe. Unlike BWR control rod and instrument guide tube penetrations, the drain line does not have any in-vessel structures nor contain any internal structures.

The 304 stainless steel BWR control rod guide tube penetrations are formed by boring the hole for the guide tube, drilling a countersink for a stub tube that surrounds the guide tube on the vessel inner surface, inserting the guide and stub tubes, and welding the guide tube to the stub tube. The control rod drive system within each guide tube consists of a cylinder containing several tubes. As illustrated in Figure 3-11, cooling water flows between these tubes.

3.2.2.4 Westinghouse Vessel Penetrations. Most Westinghouse vessel lower heads are penetrated by instrumentation tubes. The type, size, manufacturer, and number of bottom-mounted instrumentation tubes found in Westinghouse plants are compared in Reference 3-51. As discussed in this reference, the number of bottom instrumentation tube penetrations in the Westinghouse reactor vessels, which were produced by five different vendors, varied from none (in the Yankee Rowe and San Onofre Unit 1 plants) to 55 (which is typical of more recently designed plants).

For the reference Westinghouse plant, there are 55 instrumentation tube penetrations through the lower vessel head, which are 0.05 m (2.0 in.) in diameter. These penetrations are for port columns that carry the retractable, cold-worked stainless steel flux thimbles. (Thermocouples are routed through port columns on the upper head of the reactor vessel.) Each penetration nozzle consists of a tubular member made of Inconel. Each tube is attached to the inside of the bottom head by a partial penetration weld. Figure 3-12 illustrates the general arrangement of a typical Westinghouse in-core penetration tube. As shown in the figure, an Inconel pad is sometimes placed along the vessel outer surface to aid in instrument guide tube repair. However, this pad is not attached to the instrument guide tube. Instrument strings, similar to the geometry shown in Figure 3-10 and described in Section 3.2.2.1, are inserted in these instrument guide tube penetrations.

3.2.3 Radiative/Convective Boundary Conditions

This section describes structures and conditions exterior to the vessel that may influence heat transfer from the reactor vessel during a core meltdown accident. The geometry of the containment and reactor vessel cavity is described to provide an estimate of the heat transfer conditions that would be present outside the vessel during a core melt accident. Parameters important for predicting heat transfer rates from the vessel, such as the insulation thickness and distance between the insulation and the reactor vessel, are summarized in Appendix F-2. Descriptions of the reactor vessel cavity geometries and surfaces within the cavity are found in the following sections.

3.2.3.1 B&W Boundary Conditions. The containment building used for the B&W reference plant, TMI-2, is a reinforced concrete structure lined with carbon steel designed by the plant's architect-engineer, Bechtel Group Incorporated. Below the reactor vessel is a 3.69-m (12-ft)-diameter cylindrical volume with a height of 3.23 m (10.5 ft). The net free volume of the lower reactor cavity (i.e., the net free volume from the cavity floor up to the basemat floor) is estimated as approximately 124.52 m^3 (4400 ft^3). The in-core instrumentation tubes pass through sleeves consisting of steel tubes that penetrate through the primary shield wall (the concrete cylinder that surrounds the reactor vessel). Annular openings in the primary shield wall between each guide tube and its sleeve allow seepage of water into the cavity. These openings would allow water to enter the cavity if the containment floor were flooded.

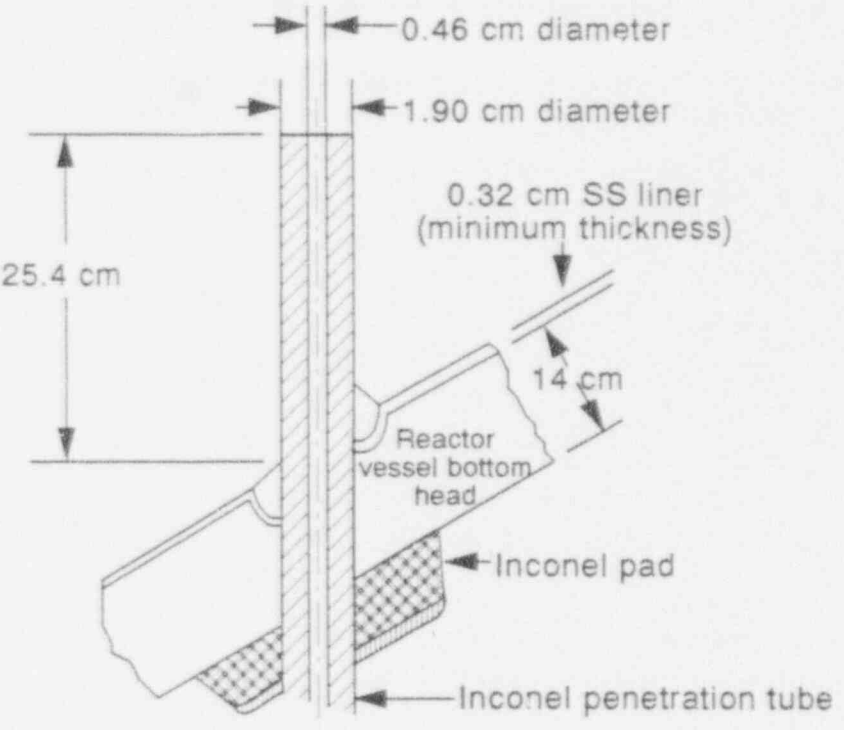

Figure 3-12. Arrangement of instrument penetration tube in a typical Westinghouse reactor vessel.

The majority of the B&W plants examined had cavity designs similar to that of the TMI-2 plant with the cavity floor levels being close to the same elevation as the basemat floor. This similarity was attributed to the fact that Bechtel was the architect-engineer for many of the B&W plants. However, some of the B&W plant containment buildings were designed to prevent water flow into the cavity.

The TMI-2 reactor pressure vessel is a skirt-supported vessel. The skirt, located around the bottom head, is 0.05 m (2 in.) thick. The vessel-skirt junction is constructed of SA508-64 Class 2 material. Reactor coolant system components are insulated with 0.08-m (3-in.)-thick, stainless steel, metal reflective type insulation units.

3.2.3.2 CE Boundary Conditions. The containment system of the reference CE plant was designed by the plant's architect-engineer, Ebasco Services Incorporated. The reactor building for this plant was designed so that water will enter the vessel cavity during accident conditions. The lack of instrumentation tubes penetrating the lower vessel head (see Section 3.2.2.2) affects the way in which lower cavities of plants are designed. The reactor vessel rests closer to the floor than in designs with in-core instrumentation through the reactor vessel lower head because clearance for the bending instrumentation tubes is not required. For example, the reactor vessel rests about 1.83 m (6 ft) above the cavity floor; whereas in CE designs with lower head in-core instrumentation penetrations the vessel is located approximately 4.58 m (15 ft) above the cavity

floor. Consequently, the net free volume of the reference plant reactor cavity, estimated as 45.19 m^3 (1,614 ft^3) in Reference 3-42, is 20% smaller than the cavity of a CE plant with lower head in-core instrumentation penetrations. Furthermore, most CE reactor buildings do not have the instrumentation tunnels that are included in designs with lower head instrumentation.

The CE reference plant reactor vessel uses supports under each of the four reactor cold leg nozzles. However, newer CE System 80 vessel designs use keys at the bottom of the vessel, as well as supports under the cold leg nozzles.

Reflective insulation, built of stainless steel panels, surrounds the reactor vessel. The reference plant FSAR[3-45] provides an estimate of 213.9 m^2 (2,300 ft^2) for the surface area of insulation surrounding the reactor vessel, including the head and supports.

3.2.3.3 GE Boundary Conditions. BWRs are also characterized by the containments. Most operating BWR plants use multibarrier pressure suppression type containments, designated Mark I, II, III.[g] All three types have dual barrier systems that are designated as the primary and secondary containments. The primary containment, which is of concern in analyzing lower head boundary conditions, includes the drywell that encloses the reactor vessel and recirculation system, a pressure suppression chamber that stores a large volume of water, and a connecting vent system between the drywell and the suppression chamber. The reference BWR/4 plant in this section uses a Mark I design, and the reference BWR/5 uses a Mark II design. The Mark III containment design is the most recent GE product line and is used only in conjunction with BWR/6 reactors.

All BWR/2, BWR/3, and most BWR/4 plants use a Mark I containment design. This design is shaped like an inverted light bulb with a torus-shaped suppression pool. For the reference BWR/4 Mark I design, the in-pedestal region has an inside diameter of 6.2 m. The reactor pressure vessel sits approximately 8.6 m above the floor, giving the in-pedestal region a volume of ~260 m^3. The in-pedestal region is connected to the drywell by a 2-m-high doorway. During a severe accident it is possible for the in-pedestal region to fill with water up against the trapped air pockets within the vessel support skirt. The drywell (portion outside the reactor pedestal) can be filled to the level of the vent lines.

The Mark II primary containment is an over-and-under, steel-lined, post-tensioned pressure suppression system. The Mark II containment reactor cavity is designed to remain dry during normal operation. However, it is possible for water to enter the drywell during a pipe break accident. The area beneath the reactor is separated into two areas: (a) the control rod drive (CRD) area, which is in direct contact with the 0.08-m (3-in.)-thick pressure vessel insulation plate, and (b) the pedestal area, which is the area inside the reactor pedestal in the suppression pool. A concrete floor about 1.2 m (4 ft) thick separates the CRD area from the pedestal area. The net free volume within the CRD area of the BWR/5 Mark II reference plant containment is estimated to be ~129 m^3 (~3200 ft^3).

The Mark III containment systems are the only BWR containments that are not inerted. Although two types of secondary containment designs are found in the Mark III systems, the primary containment designs of these plants are similar. The Mark III drywell is a cylindrical shell of reinforced concrete. Large-diameter horizontal vent openings penetrate through the lower section of the drywell. These openings are used to conduct steam during a loss-of-coolant

---

g. The one exception is Big Rock Point (BWR/1, 67 MWe).

accident to the suppression pool. The reactor pressure vessel is ~0.71 m above the cavity, which has a net free volume of 249 m^3. CRD openings and a CRD access doorway are located in this cavity at a lower elevation than the weir wall. Hence, it is likely that the cavity will fill with water during a pipe break accident.

Each of the BWR reference plant reactor vessels is mounted on a support skirt. As shown in Figure 3-7, this skirt is bolted to a concrete-and-steel cylindrical vessel pedestal that is integral with the reactor building foundation. Hence, only the portion of the BWR bottom head that is below the support skirt would be in tension (and subject to creep rupture) during a depressurized severe accident.

All lower head BWR reactor vessel insulation is of the stainless steel reflective type. According to plant personnel from the BWR/4 Mark I plant, there is a minimum of 0.038-m (1.5-in.) annular clearance between the reactor vessel and the insulation. The bottom head insulation, which encloses the volume immediately below the reactor vessel, is bounded by flat horizontal panels [0.076 m (3.0 in.) thick] that are connected to a cylindrical shell [0.076 m (3.0 in.) thick] covering the inside of the reactor support skirt.

3.2.3.4 Westinghouse Boundary Conditions. A carbon-steel-lined, prestressed concrete containment designed by the plant's architect-engineer, Sargent & Lundy, is used in the reference Westinghouse plant. The vessel is located about 4.27 m (14 ft) above the cavity floor. The reactor vessel cavity leads to an instrumentation tunnel. The net free volume in the reactor cavity and instrumentation tunnel (from the cavity floor to the containment basemat) is estimated to be 254.7 m^3 (9,000 ft^3) for this plant.[3-42]

The primary shield wall, which is the circular cylindrical structure surrounding the reactor vessel, forms the reactor vessel cavity. The reactor vessel is supported at the coolant nozzles by steel pads that rest on steel base plates in the primary shield. Above the reactor support, the shield wall is 1.37 m (4.5 ft) thick; and below the reactor support, the shield wall is 2.57 m (8.5 ft) thick.

A review of containment and cavity designs[3-42] identified several other designs used in Westinghouse plants; for example, a flat-bottom, steel-lined, prestressed concrete containment was used in the South Texas Project (STP) plant. This flat-bottom containment is similar to the TMI-2 containment, except that the STP containment was designed to prevent water contacting the bottom of the reactor vessel during an accident.

Reactor coolant system components are insulated with a minimum of 0.076-m (3-in.)-thick stainless steel, metal-reflective-type insulation consisting of two 0.038-m (1.5-in.) layers. The insulation is self-supporting from the reactor vessel nozzles. Discussions with Westinghouse plant personnel indicate that insulation panels are placed at angles that follow the curvature of the lower head, with a minimum distance of 0.024 m (0.94 in.) between the lower head and the insulation.

3.2.4 Summary

In summary, a BWR vessel is larger and heavier than a PWR vessel because a BWR vessel must accommodate steam separators, dryers, and, in most cases, jet pumps, in addition to the reactor core. Data for the reference plants indicate that more water is required to reach heights of interest (e.g., the top of the core) in a BWR vessel. A PWR wall [~0.23 m (~9 in.)] is typically thicker than a BWR wall [0.13 m (~5 in.)] because a PWR operates at a higher pressure [typically

15.2 MPa (2250 psia)] than a BWR [typically 6.8 MPa (1,000 psia)]. However, the lower head for a BWR vessel is thicker because it must accommodate over 200 penetrations, some of which are significantly larger than the penetrations found in the PWR vessels.

Support structures in the lower vessel varied between vendor designs as well as within the different plants offered by a vendor. These differences may impact melt progression, as illustrated by results from jet impingement calculations documented in Section 4.2.1.

To illustrate the maximum amount of mass that could relocate during a severe accident, scoping calculations were performed using characteristics of each vendor's design. Results indicate that the material composition entering the lower plenum would be similar for the reference plants if the maximum amount of mass were to relocate during a severe accident (indicating that the corium will contain approximately 40–50% UO_2, 30–40% 304 stainless steel, 10-20% zircaloy, and less than 2% Inconel).[h] Higher quantities of zircaloy were found in the BWR design because of the fuel assembly channel enclosures. The amount and type of control rod and burnable poisons were found to be dependent upon reactor design, although they were estimated as <4%.

The number and type of penetrations of the lower head also varied significantly between and within vendor vessel designs. However, the penetrations of the BWR vessel are generally larger and more numerous because there are control rod drive tubes and a drain nozzle in addition to penetrations for in-core monitoring guide tubes.

The geometry of the reactor containment cavities also varied. Although many plant-specific differences exist among containment cavity designs, there are three major types of PWR reactor cavities: flat-bottomed, sunken cavities, and sunken cavities with an instrumentation tunnel. Likewise, three types of BWR reactor vessel cavities were identified, corresponding to the Mark I, II, and III types of containments, although many variations exist within each of these types. Two additional design features, which were found to differ between the plants and may impact heat removal from the vessel during a severe reactor accident, are the ability of a vessel cavity to become flooded and the close proximity of steel support structures and stainless steel insulation material to the reactor vessel.

In conclusion, various plant-specific features will impact heat transfer during a severe reactor accident. To simulate phenomena properly, such as heat transport occurring within the vessel and from the vessel to the containment surroundings and the likelihood of vessel failure at a penetration, design-specific features must be considered. Section 4 presents results obtained by applying the approach described in Section 1.2 to reduce the large number of parameters characterizing these design-specific features and the range of heat-transfer conditions into a workable set of parameters that can be incorporated into a simplified approach for modeling the vessel lower head during a core melt accident.

3.3 References

3-1. U.S. Nuclear Regulatory Commission, *Severe Accident Risks: An Assessment for Five U.S. Nuclear Power Plants*, NUREG-1150, 1989.

h. Note that these scoping results represent a maximum amount of stainless steel because they include all stainless steel within the core region and in the core support structures. Experimental data indicate that a much smaller fraction of steel may be incorporated into the corium.

3-2. D. A. Brownson et al., *Intentional Depressurization Accident Management Strategy for Pressurized Water Reactors*, NUREG/CR-5937, EGG-2688, 1993.

3-3. Pickard, Lowe, & Garrick, Inc., *Seabrook Station Probabilistic Safety Assessment*, PLG-0300, (Main Report Vol. 1-6: PB84-186949; Summary Report: PB84-18693) Pickard, Lowe, & Garrick, Newport Beach, CA, December 1983.

3-4. K. N. Flemming et al., *Risk Management Actions to Assure Containment Effectiveness at Seabrook Station*, PLG-0550, Pickard, Lowe, & Garrick, July 1987.

3-5. P. Bayless and R. Chambers, *Analysis of a Station Blackout Transient at the Seabrook Nuclear Power Plant*, EGG-NTP-6700, EG&G Idaho, Inc., September 1984.

3-6. Fauske and Associates, Inc., *User's Manual for the Modular Accident Analysis Program*, AIF, 1987. (Available through Fauske and Associates, Inc.)

3-7. J. C. Carter et al., *Prevention of Early Containment Failure Due to High Pressure Melt Ejection and Direct Containment Heating for Advanced Light Water Reactors*, DOE/ID-10271, March 1990.

3-8. T. J. Heames and R. C. Smith, "Integrated MELPROG/TRAC Analyses of a PWR Station Blackout," *Proceedings of the 1989 ANS/ASME/AIChE National Heat Transfer Conference, Philadelphia, PA, August 1987.*

3-9. J. E. Kelly et al., *MELPROG/PWR-MOD1 Analysis of a TMLB' Accident Scenario*, NUREG/CR-4742, SAND86-2175, 1987.

3-10. R. Henninger et al., "Integrated MELPROG/TRAC Analysis of a PWR Station Blackout," *AIChE Symposium Series, 83*, 257, 1987 p. 326.

3-11. R. L. Ritzman et al., *Surry Source Term and Consequence Analysis*, NP-4096, Electric Power Research Institute, June 1985.

3-12. E. Cazzoli et al., *Independent Verification of Radionuclide Calculations for Selected Accident Scenarios*, NUREG/CR-4629, BNL-NUREG-51998, 1986.

3-13. R. Chambers et al., "Depressurization to Mitigate Direct Containment Heating," *Nuclear Technology, 88*, December 1989, p. 239.

3-14. P. Bayless, *Analyses of Natural Circulation During a Surry Station Blackout Using SCDAP/RELAP5*, NUREG/CR-5214, EGG-2547, 1988.

3-15. C. M. Allison and E. M. Johnson (eds.), *SCDAP/RELAP5/MOD2 Code Manual, Volumes 1, 2, 3, and 4*, NUREG/CR-5273, EGG-2555, 1989.

3-16. S. A. Hodge, *BWR Reactor Vessel Bottom Head Failure Modes*, CONF-890546-3, Dubrovnik, Yugoslavia, December 1989.

3-17. S. A. Hodge, *Primary Containment Response Calculations for Unmitigated Short-term Station Blackout at Peach Bottom*, NUREG/CR-5418, ORNL/TM-11058, 1988.

3-18. S. R. Green et al., *Response of BWR Mark II Containments to Station Blackout Severe Accident Sequences*, NUREG/CR-5565, ORNL/TM-11548, 1991.

3-19. S. R. Greene et al., *Response of BWR Mark III Containments to Term Station Blackout Severe Accident Sequences*, NUREG/CR-5577, ORNL/TM-11549, 1991.

3-20. S. E. Dingman et al., *MELCOR Analyses for Accident Progression Issues*, NUREG/CR-5331, 1991.

3-21. R. S. Denning et al., *Radionuclide Release Calculations for Selected Severe Accident Scenarios*, Volume 1–6, NUREG/CR-4624, BMI-2139, 1986.

3-22. R. Chambers, *Analysis of Core Behavior During a Station Blackout Transient (TMLB') for the Bellefonte Pressurized Water Reactor*, EGG-2342 (Draft, available from EG&G Idaho, Inc.), August 1984.

3-23. Long Island Lighting Company, *Request for Authorization to Increase Power to 25%*, Docket No. 50-322-0L, April 1987.

3-24. D. R. Buttermer, *Analysis of Postulated Accidents During Low Power Testing at the San Onofre Nuclear Generating Station, Unit 2*, PLG-0199, Pickard, Lowe, and Garrick, Newport Beach, CA, September 21, 1981.

3-25. S. A. Hodge and R. M. Harrington, "Considerations Regarding Certain Aspects of Severe Accident Mitigation Afforded by Operation of Shoreham at Reduced Power," Letter Report from ORNL to the U.S. Nuclear Regulatory Commission, Docket No. 50-322-OL, June 12, 1987.

3-26. Z. T. Mendoza and J. M. Hall, *Structured Sensitivity Study using the MAAP 2.0 Computer Code*, EPRI NP-4437, Electric Power Research Institute, October 1986.

3-27. A. W. Cronenberg, *In-vessel Zircaloy Oxidation/Hydrogen Generation Behavior During Severe Accidents*, NUREG/CR-5597, 1990.

3-28. Z. R. Martinson et al., *PBF Severe Fuel Damage Test 1-3 Test Results Report*, NUREG/CR-5354, 1989.

3-29. P. D. Bayless, C. A. Dobbe, and R. Chambers, *Feedwater Transient and Small Break Loss of Coolant Accident Analyses for the Bellefonte Nuclear Plant*, NUREG/CR-4741, EGG-2471, 1987.

3-30. R. L. Moore and E. L. Tolman, "Estimated TMI-2 Vessel Thermal Response Based on the Lower Plenum Debris Configurations," *Proceedings of the 1988 ANS National Heat Transfer Conference, Houston, TX, July 24-27, 1988*, Vol. 3, p. 11.

3-31. J. P. Adams et al., *TMI-2 Lower Plenum Video Data Summary*, EGG-TMI-7429, EG&G Idaho, Inc., July 1987.

3-32. E. L. Tolman et al., *TMI-2 Accident Scenario Update*, EGG-TMI-7489, EG&G Idaho, Inc., December 1986.

3-33. P. Kuan, *Core Relocation in the TMI-2 Accident*, EGG-TMI-7402, EG&G Idaho, Inc., November 1986.

3-34. E. L. Tolman et al., *TMI-2 Core Bore Acquisition Summary Report*, EGG-TMI-7385, Rev. 1, EG&G Idaho, Inc., February 1987.

3-35. R. R. Hobbins et al., "Fission Product Release as a Function of Chemistry and Fuel Morphology," *International Seminar of Fission Product Transport Processes in Reactor Accidents, Dubrovnik, Yugoslavia, May 22-26, 1989.*

3-36. G. L. Thinnes and R. L. Moore, "Comparison of Thermal and Mechanical Responses of the Three Mile Unit 2 Reactor Vessel," *Nuclear Technology, 87*, December 1989.

3-37. G. L. Thinnes, *TMI-2 Lower Head Creep Rupture Analysis*, EGG-TMI-8133, EG&G Idaho, Inc., August 1988.

3-38. G. E. Mueller and A. Sozer, *Thermal-Hydraulic and Characteristic Models for Packed Debris Beds*, NUREG/CR-4689, ORNL/TM-10117, 1986.

3-39. M. Kenton et al., *Simulation of the TMI-2 Accident using the MAAP Modular Accident Analysis Program, Version 2.0*, NP-4292, Electric Power Research Institute, January 1986.

3-40. A. M. Kolaczkowski et al., *Analysis of Core Damage Frequency: Peach Bottom, Unit 2 Internal Events, Vol. 4*, NUREG/CR-4550, Rev. 1, SAND86-2094, 1986.

3-41. G. Parker and S. Hodge, "Small Scale Melt Layer Experiments," *Proceedings of the 16th Water Reactor Safety Information Meeting, Gaithersburg, MD, October 1988*, NUREG/CP-0096.

3-42. G. Jaross, J. Maneke, T. Stoodt, *A Study on the Configuration and Safety Features of U.S. Nuclear Power Plants*, ANL/LWR/SAF 82-2, Volumes I-IV, Argonne National Laboratory, July 1982.

3-43. R. Rungta, J. D. Gilman, W. H. Bamford, "Performance and Evaluation of Light Water Reactor Pressure Vessels," *1987 Pressure Vessels and Piping Conference, San Diego, CA, June 1987*, PVP - Vol. 119.

3-44. Metropolitan Edison Company, *Three Mile Island Unit 2 Final Safety Analysis Report*, Docket No. 50-320, 1974.

3-45. Louisiana Power and Light, *Waterford Steam Electric Station Unit 3 Final Safety Analysis Report*, (through Amendment 36), Docket No. 50-382, May 1984.

3-46. Cincinnati Gas and Electric Company, *William M. Zimmer Nuclear Power Station Unit 1 Final Safety Analysis Report*, Docket No. 50-358, 1975.

3-47. Long Island Lighting Company, *Shoreham Nuclear Power Station Unit 1 Final Safety Analysis Report*, (through Amendment 52), Docket No. 50-322, November 1984.

3-48. L. J. Ott, Advanced Severe Accident Response Models for BWR Application, *Nuclear Engineering and Design, 115*, 1989, pp. 289-303.

3-49. Commonwealth Edison, *Byron/Braidwood Station Units 1 and 2 Final Safety Analysis Report*, (through Amendment 49), Docket Nos. 50-454, -455, -456, and -457, November 10, 1987.

3-50. Commonwealth Edison Company, *Zion Station Units 1 and 2 Final Safety Analysis Report*, Docket Nos. 50-295 and 50-304, 1992.

3-51. S. L. Abbott et al., "The Westinghouse Reactor Vessel Life Extension Variance Study," *Proceedings of the ANS/ENS Atomic Energy Society of Japan Topical Meeting on Nuclear Power Plant Life Extension, Snowbird, UT, July 1988.*

4. CLOSED-FORM AND LESS-DETAILED NUMERICAL TECHNIQUES FOR PREDICTING LOWER HEAD FAILURE

The procedure used in this study for determining which failure mode will occur first during a severe accident is depicted in Figure 1-2. Questions related to debris relocation and vessel response in Figure 1-2 may be answered by applying methods described in this section. A brief description of these models, along with key assumptions used in the models, is provided in Table 4-1. Note that models consider both the thermal and structural response of the vessel and lower head penetrations. In addition to describing these simpler methods, this section also presents results obtained from these methods and summarizes general insights into vessel failure that have been gained from applying these models.

As discussed in Section 1, these methods use closed-form and less-detailed numerical solution techniques because of the large number of reactor design and severe accident parameter combinations that can result in lower head failure. Thus, a major uncertainty in model results is due to some of the simplifying assumptions required to obtain solutions for these models. Other uncertainties in model results are discussed in Table 4-1.

Models are discussed this section based on their solution technique. Models that use closed-form solution techniques are discussed in Section 4.1, and models that use simplified numerical solution techniques are discussed in Section 4.2. Within each of these categories, models that consider thermal response are discussed first. General insights obtained from applying the models are summarized in Section 4.3.

4.1 Models Using Closed-form Solution Techniques

Because of the large number of reactor design and severe accident parameter combinations that can lead to lower head failure, this study has relied heavily on models that use closed-form solution techniques. As illustrated in this section, these models allow a larger number of cases to be considered more rapidly and provide general insights into how different reactor designs respond to different accident conditions.

4.1.1 Event Timing and Vessel Heatup

Thermal analyses provide boundary conditions, such as event timing and temperature distributions, for lower head failure analyses. By applying mass and energy equations to simplified geometries, closed form solutions have been obtained in this section to predict event timing and one-dimensional vessel temperature distributions.

4.1.1.1 Application of Energy and Mass Conservation Equations to Predict Event Timing. A nondeformable control volume, representing the corium and coolant in the reactor vessel at the calculation initiation, is shown in Figure 4-1. Conservation of energy and mass were applied to this control volume from an arbitrary beginning state (denoted by the superscript b) to an end state (denoted by the superscript e) to obtain the following equations:

$$M_d^e - M_d^b = \Delta M_d \quad . \tag{4-1}$$

Table 4-1. Summary of models discussed in Section 4.

Model description	Assumptions	Range of applicability	Uncertainties
Relocation time as a function of melt relocation temperature	• No coolant in core region • Heat losses from core to coolant are negligible • Oxidation energy is negligible • Heat losses from vessel to environment are negligible • No coolant leaves or enters the vessel • Constant decay heat equal to one percent of the initial core power level	Applicable for cases with • no coolant in the core region • near adiabatic heatup • heat losses from the corium to the coolant and from the vessel to the environment are much less than the decay heat in the corium.	Model is expected to give order of magnitude estimates for melt relocation times. Uncertainties in model results are due to uncertainties in corium material properties and corium composition.
Coolant boiloff time as a function of coolant volume	• No coolant makeup water available • Unrestricted mass loss from the vessel • Oxidation energy is negligible • Heat losses from vessel to environment are negligible • Debris and coolant are in perfect thermal contact • Debris quenches during relocation • Coolant boiloff can be modeled assuming isothermal and isobaric conditions • Constant decay heat equal to one percent of the initial core power level	Applicable for cases where • near perfect thermal contact between the debris and the coolant exists • changes in coolant properties over the range in pressures and temper-atures that occur during depressurization are negligible • heat losses from the corium to the coolant and from the vessel to the environment are much less than the decay heat in the corium.	Model is expected to give order of magnitude estimates for coolant boiloff times. Uncertainties in model results are primarily attributed to assumptions, such as isobaric and isothermal conditions and the debris being in perfect contact with the coolant.
One-dimensional time-dependent vessel temperature distribution	• Constant heat flux • One-dimensional heat conduction equation is applicable • Heat removal from the vessel to the containment by a constant heat transfer coefficient • Vessel thermal properties remain constant	Applicable for cases where • a nearly uniform and constant heat source is applied to the entire vessel lower head • heat removal from the vessel to the containment is nearly constant	Model is expected to give order of magnitude estimates for vessel thermal response. Uncertainties in model results are primarily attributed to assumptions, such as constant vessel material properties, constant and uniform heat source, and constant heat removal.

Table 4-1. (continued).

Model description	Assumptions	Range of applicability	Uncertainties
Tube heatup time (time for thermal front penetration and time for tube melting)	Good debris-to-tube surface contact • Isothermal tube and debris • Tube thermal response can be modeled one-dimensionally • No coolant in the lower head	Applicable for cases where • good thermal contact exists between the debris and the tube • no coolant is in the lower head	Models are expected to give order of magnitude estimates for tube thermal response times. Uncertainties in model results are primarily attributed to uncertainties in estimates for the tube phase change constant.
Debris thermal requirements to induce in-vessel tube melting	• Good debris-to-tube thermal contact • Isothermal debris and tube • No coolant in the lower head • Zero porosity in relocated debris	Applicable for cases where • debris completely surrounds the tube • debris has zero porosity • good thermal contact exists between the debris and the tube • no coolant is in the lower head	Model is expected to give order of magnitude estimates for debris thermal requirements to induce tube melting. Note that results from this model will be minimum values because it is assumed that there is no coolant in the lower head and an infinite time is available for heat transfer. Uncertainties in model results are primarily attributed to the assumption of isothermal debris.
Terminal melt velocity from a penetration as a function of pressure, tube effective diameter for melt flow and in-vessel tube length	• Melt flow is steady • No heat is transferred from the debris to the tube (adiabatic flow) • The melt velocity outside the tube is much less than the tube exit velocity • Constant debris thermal properties • Melt flow is turbulent • Melt flow area can be characterized by an effective diameter	Applicable for cases where • melt velocity is steady • heat losses from the debris to in-vessel tube structures is negligible • melt flow through a tube is turbulent (analysis indicated that this is true for all the cases considered)	Model is expected to give order of magnitude estimates for melt velocity through a penetration tube. Uncertainties in model results are primarily attributed to uncertainties in estimates for melt thermal properties, the Fanning friction factor, and entrance loss coefficient.

Table 4-1. (continued).

Model description	Assumptions	Range of applicability	Uncertainties
Melt penetration distance through a tube (modified bulk freezing model and conduction model)	• Constant thermal properties • Melt flow area can be characterized by an effective diameter • Melt flow area within a tube is constant (i.e., debris does not thin or "neck down" as it travels) Conduction Model • transient freezing is governed by crust buildup at the channel wall, where conduction heat transfer governs melt solidification • the melt velocity is constant as it travels through the tube • no convective heat exchange occurs at the melt-crust interface	The conduction model is applicable for cases where • debris is near its melting point • changes in thermal properties are negligible • good thermal contact between the debris and the tube exists	Models are expected to give order of magnitude estimates for the upper and lower bounds that melt will travel through lower head penetrations. Uncertainties in the conduction model are primarily attributed to uncertainties in the melt solidification constant and the impact of coolant within the tubes.
	Modified Bulk Freezing Model • turbulence within the melt precludes a stable crust from forming along tube walls • coolant within the tube can escape as it is heated • heat is transferred from the debris to the coolant only in the radial direction • changes in the average temperature of the debris are negligible as the melt proceeds down the channel	The modified bulk freezing model is applicable for cases where • the initial temperature difference between the debris and its melting point is much less than the initial temperature difference between the debris and the tube • changes in thermal properties are negligible • good thermal contact exists between the debris, tube, and coolant • melt flow is turbulent	Uncertainties in modified version of the bulk freezing model are primarily attributed to uncertainties in heat transfer correlations between the debris and the tube.

Table 4-1. (continued).

Model description	Assumptions	Range of applicability	Uncertainties
Ex-vessel tube rupture at low pressure (tube equilibrium temperature and tube steady-state temperature)	• Good debris-to-tube thermal contact • One-dimensional heat transfer from the melt to the tube • Melt fills the entire area available for melt flow within a tube • Thermal properties remain constant • An infinite time is available for heat transfer • Effects of insulation around the vessel have negligible impact on heat losses from penetrations	Applicable for cases where • changes in thermal properties are negligible • good thermal contact exists between the tube and the debris • a long time is available for heat transfer • melt fills entire flow area available within the tube	Models are expected to give order of magnitude estimates for lower bound debris thermal requirements to induce ex-vessel tube rupture. Uncertainties in model results are primarily attributed to uncertainties in estimates for melt thermal properties, tube emissivity, and tube material ultimate strength behavior at high temperatures.
Ex-vessel tube rupture at high pressure	• Creep effects are negligible • Molten debris has traveled within a penetration to distances below the lower head • Tube end effects are negligible • A steady-state or transient temperature distribution exists in the vessel • The tube midwall temperature at the inner surface of the vessel wall is equal to the vessel inner surface temperature • The difference between the tube temperature at the inner surface of the vessel and the tube temperature at the outer surface of the vessel is much smaller than the difference between the vessel inner and outer surface temperatures	Results for a wide range of temperature levels are included in Section 4.1.3. The appropriate failure map should be selected based upon the expected vessel temperatures at the inner wall surface, pressures, and the conditions (debris decay heat flux to the vessel and vessel-to-containment heat transfer coefficient) required to produce vessel temperatures. Because creep effects are neglected, model results will be more accurate for cases where tubes rapidly reach failure temperatures.	Model is expected to give order of magnitude estimates for upper bound values of pressure and temperature combinations where tube rupture will occur. Uncertainties in model results are primarily attributed to uncertainties in high temperature tube material properties.

Table 4-1. (continued).

Model description	Assumptions	Range of applicability	Uncertainties
Tube ejection			Model is expected to give order of magnitude estimates for upper bound values of pressure and temperature combinations where tube ejection will occur. Uncertainties in model results are primarily attributed to uncertainties in estimates for high temperature tube and vessel material properties.
a. Weld failure	• Weld temperature is constant with location • Base metal material ultimate strength properties are used for the weld • Weld area associated with weld buildup above the cladding is ignored • Weld dimensions are ASME code minimum, except for the B&W design, where lengths were obtained from plant drawings • Weld defects are not considered	Because creep effects are neglected, model results are more accurate for cases where the vessel rapidly reaches failure temperatures.	
b. Binding	• Creep effects are negligible • Molten debris has traveled within a penetration to distances below the lower head • The weld holding the tube to the vessel has failed • Sufficient heat has been lost from the leading edge of the melt to cap the debris or there is a bend in the tube • No support outside of the vessel resists tube ejection • A steady-state or transient spatial temperature distribution exists in the vessel • The tube midwall temperature in the radial direction is constant and equal, near the vessel wall inner surface, to the vessel inner surface temperature • The difference between the tube temperature at the inner surface of the vessel and the tube temperature at the outer surface of the vessel is much smaller than the difference between the vessel inner and outer surface temperatures	Results for a wide range of temperature distributions are included in Section 4.1.3. The appropriate failure map should be selected based upon the expected vessel inner wall temperatures, system pressures, and the conditions (debris decay heat flux to the vessel and vessel-to-containment heat transfer coefficient) required to produce vessel temperatures.	

Table 4-1. (continued).

Model description	Assumptions	Range of applicability	Uncertainties
Global vessel rupture	• Creep effects are negligible • Thermal stresses are self relieving • Successive inner layers lose strength as temperatures elevate • Collapse predicted when membrane strength capacity is exceeded by pressure stress	Results for a wide range of temperature distributions are included in Section 4.1.3. The appropriate failure map should be selected based upon the expected vessel inner surface temperatures, system pressure, and conditions (debris decay heat flux to the vessel and vessel-to-containment heat transfer coefficient) required to produce vessel temperatures. Because creep effects are neglected, model results are more accurate for cases where the vessel rapidly reaches failure temperatures.	Model is expected to give order of magnitude estimates for the pressure and temperature combinations where global vessel rupture will occur. Uncertainties in model results are primarily attributed to uncertainties in high temperatures, vessel material properties, and the accuracy of predicting failure stress progression.
Debris relocation through lower plenum structures (jet impingement)	The ANL-developed THIRMAL0 model used in this study assumes: • melt is released from the core as a coherent circular stream • surface erosion of the melt stream is driven by Kelvin-Helmholtz instabilities • the diameter of eroded droplets and particles is equal to the inverse of the fastest growing wave number • eroded droplets/particles interact with coolant inside a finite-radius cylindrical interaction zone • multiphase flow inside the interaction zone can be modeled with one-dimensional axial, mass, and energy conservation equations together with drift flux correlations	Applicable for cases where • a localized failure occurs in a solid crust that surrounds a molten pool within the core region • melt is released from the core as a coherent circular stream that is not small enough (e.g., about 0.5 cm) to cause breakup from capillary effects or large enough (e.g., tens of centimeters) to cause the melt break up from Taylor instabilities	Model is expected to give order of magnitude estimates for comparing the effects of lower plenum geometry and structures on melt relocation in different plant designs. Characterization of uncertainties requires comparisons with experiment data to provide useful information on melt stream breakup and particle formation.

Table 4-1. (continued).

Model description	Assumptions	Range of applicability	Uncertainties
Localized vessel failure	Algorithm solves displacement-based, finite deformation equilibrium equations, allowing for creep, plastic, and thermal strains, but assuming • radial stresses are negligible compared with membrane stresses • normal strains vary linearly through the thickness • shear strains vary parabolically through the thickness	Valid for finite deformations, but based on engineering (rather than true) strains. Errors will grow as strains exceed 10–20%.	Model predictions are very sensitive to Larson-Miller parameter correlations and failure criteria.

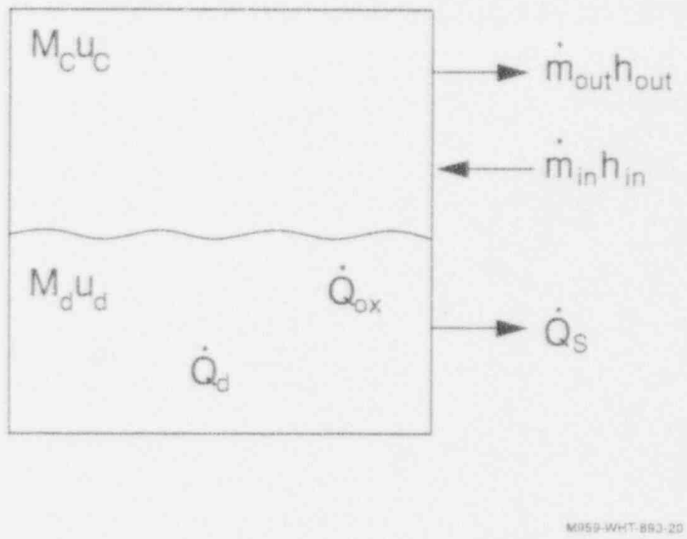

Figure 4-1. General control volume for modeling conditions prior to vessel failure.

$$M_c^e - M_c^b = \int_b^e (\dot{m}_{in} - \dot{m}_{out})dt \quad . \tag{4-2}$$

$$M_d^e u_d^e - M_d^b u_d^b + M_c^e u_c^e - M_c^b u_c^b =$$

$$\int_b^e (\dot{Q}_d + \dot{Q}_{ox} - \dot{Q}_s)dt + \int_b^e (\dot{m}_{in} h_{in} - \dot{m}_{out} h_{out})dt \quad . \tag{4-3}$$

Each of the variables in the above equations, which are identified in Table 4-2,[a] is a function of one or more accident and/or reactor design parameters, as indicated in Table 4-2.[b] Because of this complexity, it is not possible to directly obtain an analytical solution to these equations for the severe accident scenarios reviewed in Section 3. However, by identifying all possible variables and eliminating variables based on assumptions for specific accident scenario conditions, it is possible to reduce these equations into a series of parametric curves, as illustrated in the following examples. Results from these analyses should be viewed as order-of-magnitude estimates, and assumptions used in the analyses should be reviewed before assuming that the results are applicable to a particular accident scenario.

4.1.1.1.1 Time Until Corium Relocation During a Dry Adiabatic Heatup—To illustrate the application of the process described, a simple case was considered in which a reactor, initially operating at full power, has depressurized such that the core region is dry and the decay heat goes entirely toward structure heatup. The control volume and assumptions used for this case are illustrated in Figure 4-2. Makeup water is assumed to be unavailable, and the mass

---

a. A complete nomenclature list is provided in Appendix A.

b. Note that enthalpy is used in describing the energy from mass entering and leaving the system, but internal energy is used in describing initial and final system states. This simplification is allowed because the control volume has a constant volume (see Reference 4-1).

Table 4-2. Parameters impacting variables within system energy balance.

Symbol	Description[a]	Parameters impacting value
$\dot{Q}_d(t)$	Power produced by debris fuel decay heat (J/s)	Material composition of corium debris (melt fuel fraction), initial core power level, fraction of fission products released from debris, debris geometry
$\dot{Q}_{ox}(t)$	Energy production rate from oxidation (J/s)	Transient system temperature, pressure, water inventory
$\dot{Q}_s(t)$	Energy loss rate from the vessel (J/s)	Transient ability of steam generator to remove heat, vessel exterior structural geometry (floodable cavity configuration, insulation location and thickness)
u_d	Corium internal energy (J/kg)	Initial reactor power (for beginning conditions); debris composition and temperature (for end conditions)
u_c	Coolant internal energy (J/kg)	Initial reactor power (for beginning conditions); system temperature and pressure (for end conditions)
h_{in}	Coolant inlet enthalpy (J/kg)	Initial reactor conditions, design specifications
h_{out}	Coolant exit enthalpy (J/kg)	Transient system pressure and temperature
M_d	Debris mass (kg)	Reactor design specifications, vessel internal structure geometry
M_c	Coolant mass (kg)	Reactor design specifications (for beginning conditions); transient loss of coolant (for end conditions)
$\dot{m}_{in}$	Coolant inlet mass flowrate (kg/s)	Ability of emergency systems to provide coolant, RCS makeup
$\dot{m}_{out}$	Coolant exit mass flowrate (kg/s)	Depressurization area, transient system pressure, RCS letdown

a. A complete list of nomenclature is provided in Appendix A.

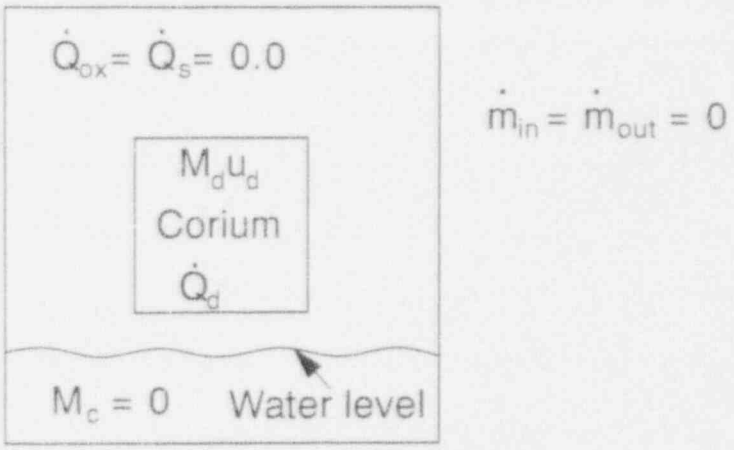

Figure 4-2. Control volume for modeling adiabatic heatup.

loss from the vessel is negligible (i.e., $\dot{m}_{in} = \dot{m}_{out} = 0.0$). Furthermore, the energy from fuel oxidation and the energy loss from the vessel are negligible (i.e., $\dot{Q}_{ox} = \dot{Q}_s = 0.0$). For the duration of the analysis, the rate of decay heat production is assumed constant and equal to 1% of the initial reactor power level (i.e., $\dot{Q}_d = 0.01\ \dot{Q}_o$).[c] The fraction, 0.01, was obtained by iterating between the calculated times until relocation and a time versus decay power level curve from Reference 4-2.

Given the above conditions, Equation (4-3) reduces to

$$M_d(u_d^e - u_d^b) = \int_b^e 0.01\,\dot{Q}_o\,dt \qquad (4\text{-}4)$$

and the time until corium debris relocation, t_{rel}, can be estimated using

$$t_{rel} = \frac{M_d(u_d^e - u_d^b)}{0.01\,\dot{Q}_o} = \frac{M_d\,\Delta u_d}{0.01\,\dot{Q}_o} \quad , \qquad (4\text{-}5)$$

which is simply a ratio of the change in corium (fuel and structure) internal energy to the decay power produced in the system.

The initial average corium temperature was assumed as 825 K. Because the temperature at which relocation of corium occurs is not known precisely, Equation (4-5) was evaluated for a range of corium end-state temperatures using material property data and design information from Appendix F. Results, which are shown in Figure 4-3, indicate that the time until corium relocation for the reference BWRs is nearly a factor of two longer than for the reference PWRs.

c. Although the decay power varies somewhat over the solution times predicted, a constant value was assumed so that an order-of-magnitude answer could be obtained using a closed-form solution technique.

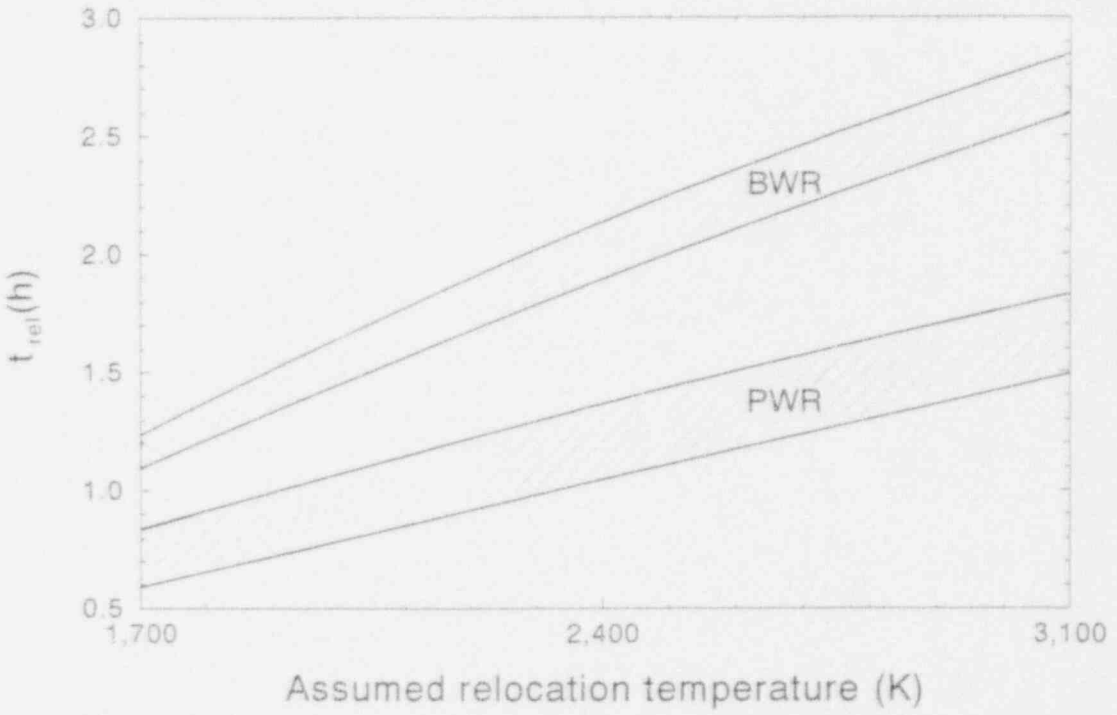

Figure 4-3. Time until melt relocation, assuming a dry adiabatic heatup.

This time difference results from the higher ratio of the structural mass to the initial power level of the reference BWRs (typically over 100 kg/MWt for the reference BWRs versus less than 76 kg/MWt for the reference PWRs).

4.1.1.1.2 Boiloff Time Assuming Relocated and Quenched Debris—As a second example, this process was applied to determine the impact of transient and design parameters on vessel dryout times. The control volume and assumptions used for this case are illustrated in Figure 4-4. As in the first example, the reactor is assumed to be initially operating at full power. Makeup water is assumed to be unavailable (i.e., $\dot{m}_{in} = 0.0$). However, mass loss from the vessel is unrestricted. As in the previous example, the energy from fuel oxidation and the energy loss from the vessel are neglected (i.e., $\dot{Q}_{ox} = \dot{Q}_{s} = 0.0$). Because the analysis is concentrating on the effects of transient thermal hydraulic conditions and reactor design parameters on coolant boiloff time predictions, the debris and coolant are assumed to be in perfect thermal contact for all cases. The debris is assumed to quench during relocation; and for the duration of the analysis, the rate of decay heat production is assumed to be a constant value equal to 1% of the initial power level (i.e., $\dot{Q}_{d} = 0.01\ \dot{Q}_{o}$).[d] The fraction, 0.01, was obtained by iterating between the calculated boiloff times and a time versus decay power level curve from Reference 4-2.

d. Although the decay power varies somewhat over the solution times predicted, a constant value was assumed so that an order-of-magnitude answer could be obtained using a closed-form solution technique.

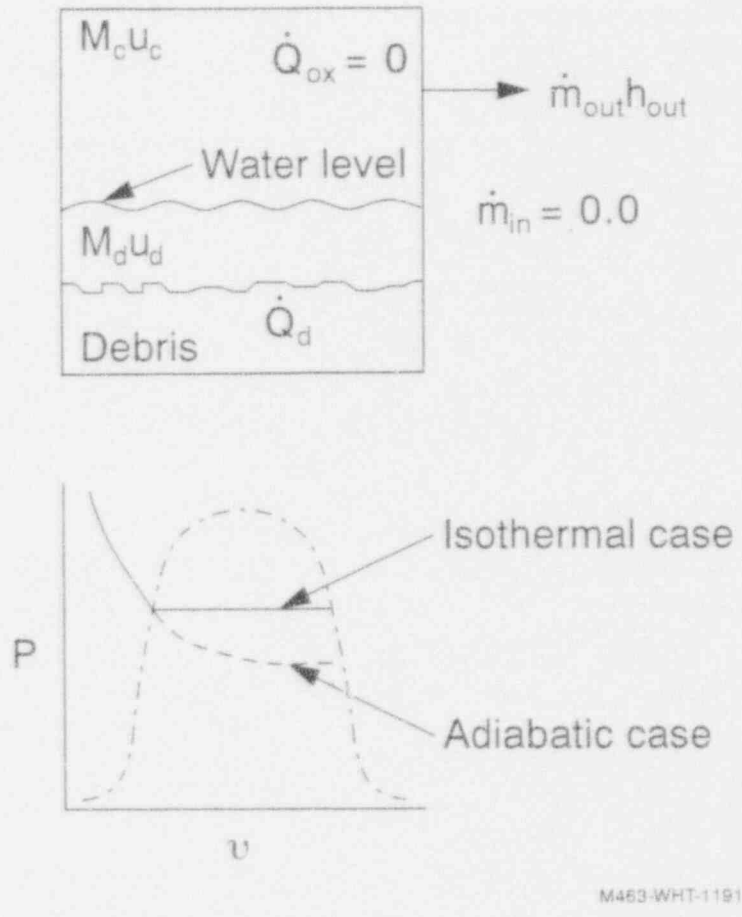

Figure 4-4. Control volume and Pv diagram for modeling boiloff times, assuming debris has initially relocated to the lower plenum.

Given the above conditions, Equation (4-2) reduces to

$$M_c^e - M_c^b = \int_b^e \frac{-0.01\dot{Q}_o dt}{h_{fg}(t)} \tag{4-6}$$

where h_{fg} represents the enthalpy change as coolant transfers from a fluid to a gaseous state. From the above relationship, it can be deduced that the coolant boiloff time, t_{bo}, is dependent on the change in coolant mass, the change in coolant thermodynamic conditions, and the decay energy produced by the fuel. Although the actual depressurization time is dependent on the initial and final pressures within the system (see Figure 4-4), if an isothermal and isobaric process is assumed in Equation (4-6), the following equation for estimating boiloff can be obtained

$$t_{bo} = \frac{-(M_c^e - M_c^b)h_{fg}}{0.01\dot{Q}_o} = \frac{V_c\left(\frac{1}{v_f} - \frac{1}{v_g}\right)h_{fg}}{0.01\dot{Q}_o} \tag{4-7}$$

where the ratio of the coolant volume to the coolant fluid or vapor-specific volume, V_c/v_f or V_c/v_g, has been substituted for the initial liquid mass and final steam mass, respectively.

Results for Equation (4-7) are plotted in Figure 4-5, assuming the reference BWR/4 and B&W PWR coolant inventories from Appendix F and an initial pressure equal to each reference plant's relief valve setpoint pressure. In addition, Equation (4-6) was evaluated for cases in which the final pressure was lower than the initial pressure. Results for all cases indicate that the BWR/4 boiloff times are longer, which is primarily a result of the larger initial water inventory in the BWR/4 plant (416.6 m^3 of liquid is in the BWR/4 versus 335.4 m^3 in the B&W PWR).[e] However, the lower operating BWR coolant temperatures and pressures in BWRs (typically, 550 K/6.9 MPa for the BWRs versus 580 K/15.5 MPa for the PWRs) also impact the results shown in Figure 4-5, since more energy is required to vaporize water at lower temperatures and pressures. Shorter dryout times are predicted for transients approaching isothermal conditions at full pressure because less energy is required to vaporize water at higher temperatures and pressures.

4.1.1.2 Transient Vessel Temperature Distribution Assuming Constant Debris Heat Flux. Although more complex methods are required to determine detailed transient temperature distributions, an analytical solution to the one-dimensional form of the conduction equation can be used to compare the effect of parameters, such as debris heat flux to the vessel and the heat

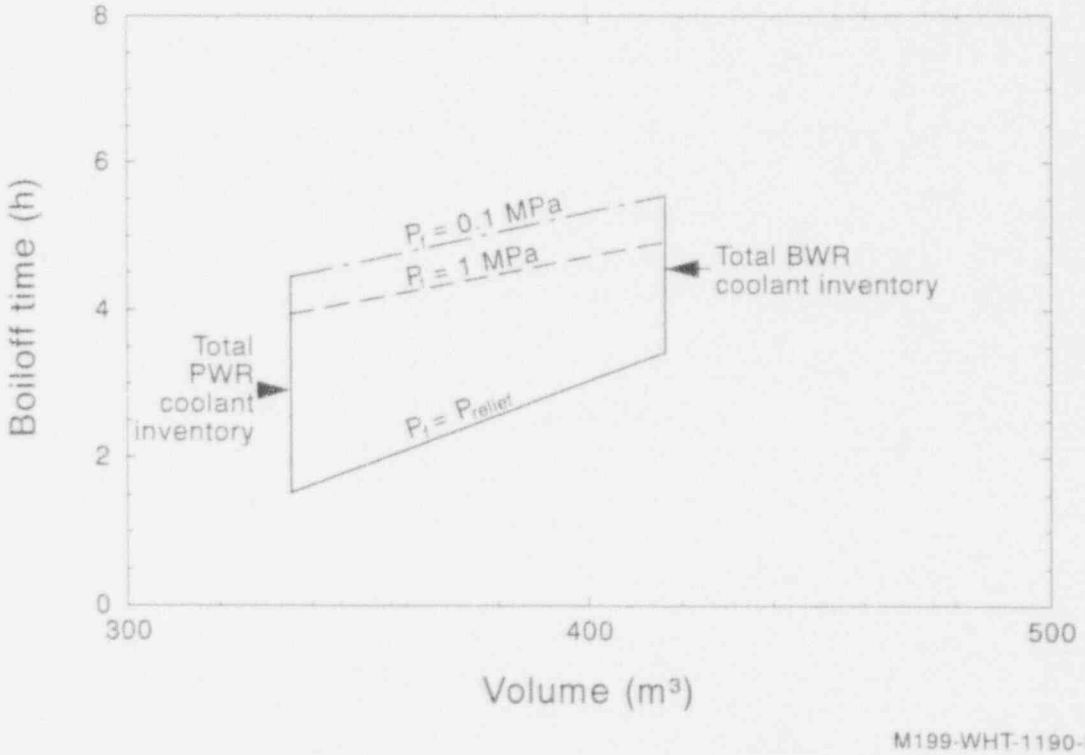

Figure 4-5. Boil-off time, assuming relocated debris.

e. Reactor system coolant inventories neglect water available in plant emergency core coolant systems. For example, if PWR accumulator inventories are included, PWR boiloff times could increase by 20 to 30% (see Reference 4-3).

transfer coefficient from the vessel to the containment. The method for obtaining this solution is documented in this section and several sample temperature distributions are provided. These temperature distributions are input to failure analyses in Sections 4.1.3 and 4.1.4.

For the vessel geometries shown in Figure 4-6, the applicable form of the one-dimensional transient heat conduction equation for predicting the vessel temperature, $T_v(x,t)$, at distance, x, and time, t, is

$$\frac{\alpha_{tv}\partial^2 T_v}{\partial x^2} = \frac{\partial T_v}{\partial t} \tag{4-8}$$

where α_{tv} is the vessel thermal diffusivity. To obtain analytical solutions to the one-dimensional transient heat conduction equation for the vessel geometries shown in Figure 4-6, the transient was divided into two regimes: (a) the period required for the temperature front to penetrate through the vessel and (b) the period required for the vessel temperatures to reach steady-state.[4-4] Solutions to each regime are described in the following sections.

4.1.1.2.1 Period Prior to Temperature Front Penetrating Vessel—Using Leibnitz's Rule[4-5] and integral solution techniques with appropriate boundary conditions, the following vessel temperature distribution, $T_v(x,t)$, at distance, x, and time, t, is obtained from Equation (4-8)

$$T_v(x,t) = T_{vo}(0) + \frac{\dot{q}_d(0)(\delta - x)^2}{2k_v\delta} \tag{4-9}$$

where $T_{vo}(0)$ is the initial outer vessel wall temperature, k_v is the vessel conductivity, $\dot{q}_d$ is the debris heat flux, and δ is the thermal front penetration distance. The temperature distribution becomes directly dependent upon time when the following relationship between time, vessel thermal diffusivity, α_{tv}, and thermal front penetration distance[4-4] is applied:

$$\delta = \sqrt{6\alpha_{tv}t} \quad . \tag{4-10}$$

Equations (4-9) and (4-10) are used to obtain representative PWR and BWR temperature distributions in Section 4.1.1.2.3.

Using the following dimensionless groups

$$T^*_{vl} = \frac{T_v(0,t) - T_{vl}}{\dot{q}_d(0)t_v/2k_v} \text{ and } \quad t^*_l = 6t\alpha_{tv}/t_v^2 \quad ,$$

a dimensionless vessel temperature distribution can be obtained. At x = 0, this distribution is

$$T^*_{vl} = \sqrt{t^*_l} \quad . \tag{4-11}$$

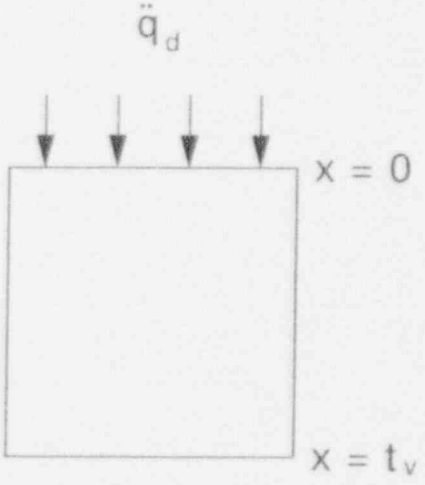

(a) Configuration for predicting time for temperature front to reach vessel outer wall.

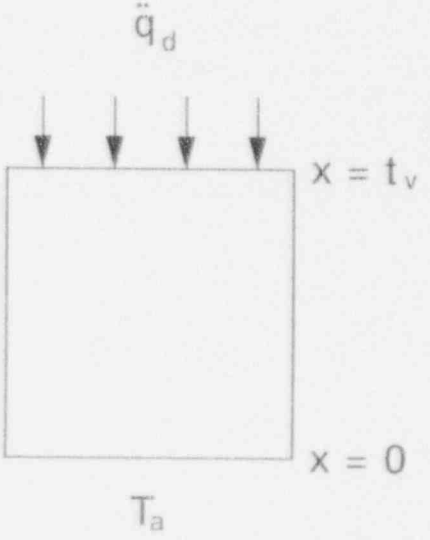

(b) Configuration for predicting time for vessel wall temperature to reach a steady-state distribution.

M577-WHT-492-04

Figure 4-6. Vessel and debris configurations for analytically predicting vessel transient temperature distributions.

As shown in Figure 4-7, removal of plant-specific material and geometrical parameters from Equation (4-11) allows multiple plant vessel distributions to be collapsed into one curve. By inputting appropriate parameters for a specific plant, this curve can be used to estimate a parameter, such as the time required for a thermal front to penetrate a vessel, the maximum temperature difference through a vessel, or the decay heat flux, when all the remaining parameters are known.

4.1.1.2.2 Period Prior to Steady-State Temperature Distribution—Applying Leibnitz's Rule[4-5] and integral solution techniques with appropriate boundary conditions, the following temperature distribution is obtained from Equation (4-8)

$$\frac{T_v(x,t) - T_a}{\ddot{q}_d(0)t_v/k_v} = \left[\frac{x}{t_v}\left(1 - \frac{x}{2t_v}\right) + \frac{1}{Bi_v}\right]\left\{1 - \exp\left[-\frac{(t - t_{vp})}{\tau_v}\right]\right\} + \frac{1}{2}\left(\frac{x}{t_v}\right)^2 \qquad (4\text{-}12)$$

where t_v is the vessel thickness, T_a is the containment temperature, Bi_v is the vessel Biot number ($h_{tv}t_v/k_v$), h_{tv} is the convective heat transfer coefficient between the vessel outer surface and the containment atmosphere, t_{vp} is the thermal front penetration line [(Equation (4-10) with $\delta = t_v$], and τ_v is the time constant, given by

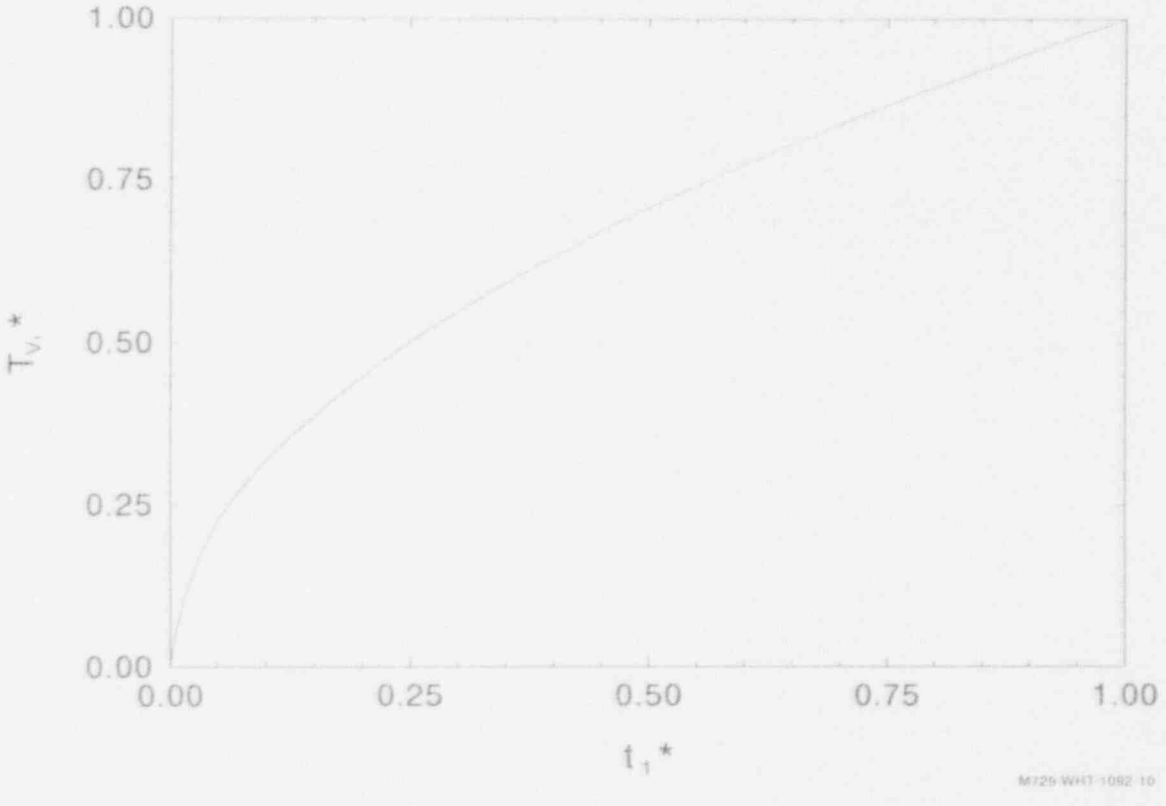

Figure 4-7. Normalized difference between the vessel inner and outer wall temperatures before the thermal front reaches the vessel outer surface.

$$\tau_v = \frac{1 + Bi_v/3}{h_{tv}/\rho_v c_{pv} t_v} \quad .$$

Equation (4-12) is used to obtain representative PWR and BWR temperature distributions in Section 4.1.1.2.3.

A dimensionless temperature distribution can also be obtained from Equation (4-12), using the following dimensionless groups:

$$T^*_{v2} = \frac{T_v(0,t) - T_a}{\dot{q}_d(0)/h_{tv}} \text{ and } \quad t^*_2 = (t - t_{vp})/\tau_v \quad .$$

At x = 0, this distribution is

$$T^*_{v2} = \left[1 - \exp(-t^*_2)\right] \quad . \tag{4-13}$$

Equation (4-13) has been used to obtain the dimensionless plot shown in Figure 4-8, that may be applied to a wide range of vessel geometries and debris conditions to obtain quick estimates for a parameter, such as the time required for a steady-state temperature distribution, the maximum temperature difference in a vessel, the debris decay heat flux, or the heat transfer coefficient, when all the remaining parameters are known.

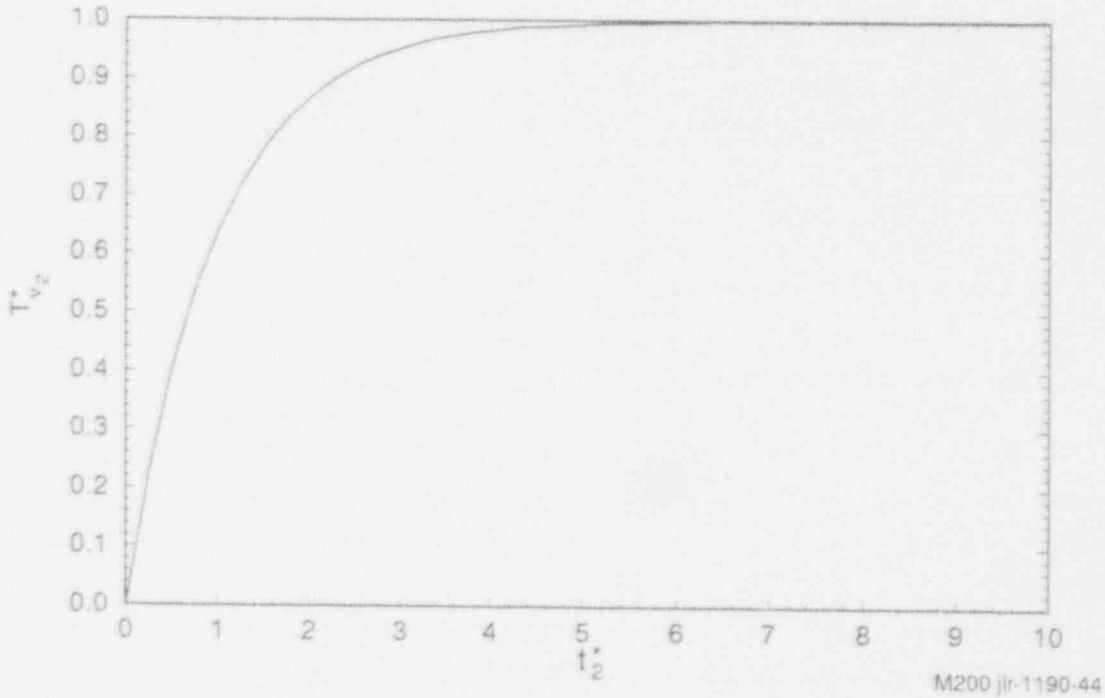

Figure 4-8. Normalized difference between the vessel inner and outer wall temperatures before steady-state vessel wall temperatures occur.

4.1.1.2.3 Comparison of Vessel Thermal Response—Sample temperature distributions are provided in this section using the equations derived in Sections 4.1.1.2.1 and 4.1.1.2.2. In these examples, melt is assumed to relocate to the lower head as a noncoherent jet and form a homogeneous debris bed. The thermal responses of a B&W PWR and a GE BWR/4 are compared for three postulated debris conditions. Case I debris properties were selected to represent material that is a primarily metallic slurry; Case II debris properties were selected to represent material that is a primarily ceramic slurry; and Case III debris properties were selected to represent a molten pool of primarily ceramic debris. Typical debris heat fluxes for each of these cases were estimated based upon SCDAP/RELAP5 results from Section 5 and Reference 4-6. Initial calculations were performed assuming a vessel-to-containment heat transfer coefficient of 50 W/m^2K, which is representative of the combined convective and radiative heat transfer expected to occur for cases in which the containment cavity is not flooded. However, sensitivity calculations were performed to consider upper and lower bound estimate; namely, heat transfer coefficients of 1 W/m^2K and 100 W/m^2K.

Results for Cases I through III, shown in Figures 4-9 through 4-11, indicate that the time for thermal front penetration and the time for a steady-state temperature distribution to occur is shorter in the PWR than in the BWR. BWR vessel response time predictions, which are typically twice as long as values predicted for the PWR vessel, are primarily a result of the larger BWR lower head thickness. As indicated in Figures 4-9 through 4-11, the magnitude of the heat flux from the debris also impacts vessel response time. For example, the factor of four increase in the heat flux between Case II and Case III is predicted to cause more than an order of magnitude decrease in the time for the vessel inner surface to reach melting. Figure 4-12 illustrates that assumptions related to heat removal from the vessel to the containment significantly impact vessel thermal response, because melting temperatures are predicted for Case II within 4 hours for the nearly adiabatic 1 W/m^2K case (Figure 4-12a); whereas vessel temperatures are predicted to remain below 1200 K for the 100 W/m^2K case where high heat losses are assumed (Figures 4-12c).

4.1.1.3 Summary. Section 4.1.1 discusses analytical models that can be used for estimating the thermal response of the vessel during a severe accident. These models were developed by applying mass and energy equations to simplified geometries for which analytical closed-form solutions may be obtained to predict the relative timing for PWR and BWR severe accident progression. Models were applied to obtain order-of-magnitude estimates for PWR and BWR vessels using values typical of depressurized severe accident conditions. Results from these models, which are summarized in Table 4-3, indicate that a PWR transient will proceed more rapidly (by as much as a factor of two) than a BWR transient. These results were attributed to higher ratios of BWR structural mass per heat generation rate, larger initial BWR water inventories, and thicker BWR lower heads. When results from analytical solutions were plotted in terms of nondimensional groups, curves were obtained that can be applied to any PWR or BWR, given that the appropriate reactor- and accident-specific parameters within the dimensionless groups are specified.

4.1.2 Penetration Tube Heatup and Failure

Analyses have been performed to calculate characteristic tube heatup times, melt velocity and penetration distance, and in-vessel and ex-vessel tube failure. The results represent a range of melt compositions (bounded by a metallic melt based on stainless-steel properties and a ceramic melt based on UO_2 properties) and penetration geometrical parameters (based upon PWR and BWR penetrations described in Section 3). Material properties and penetration dimensions used for these calculations are given in Appendix F.

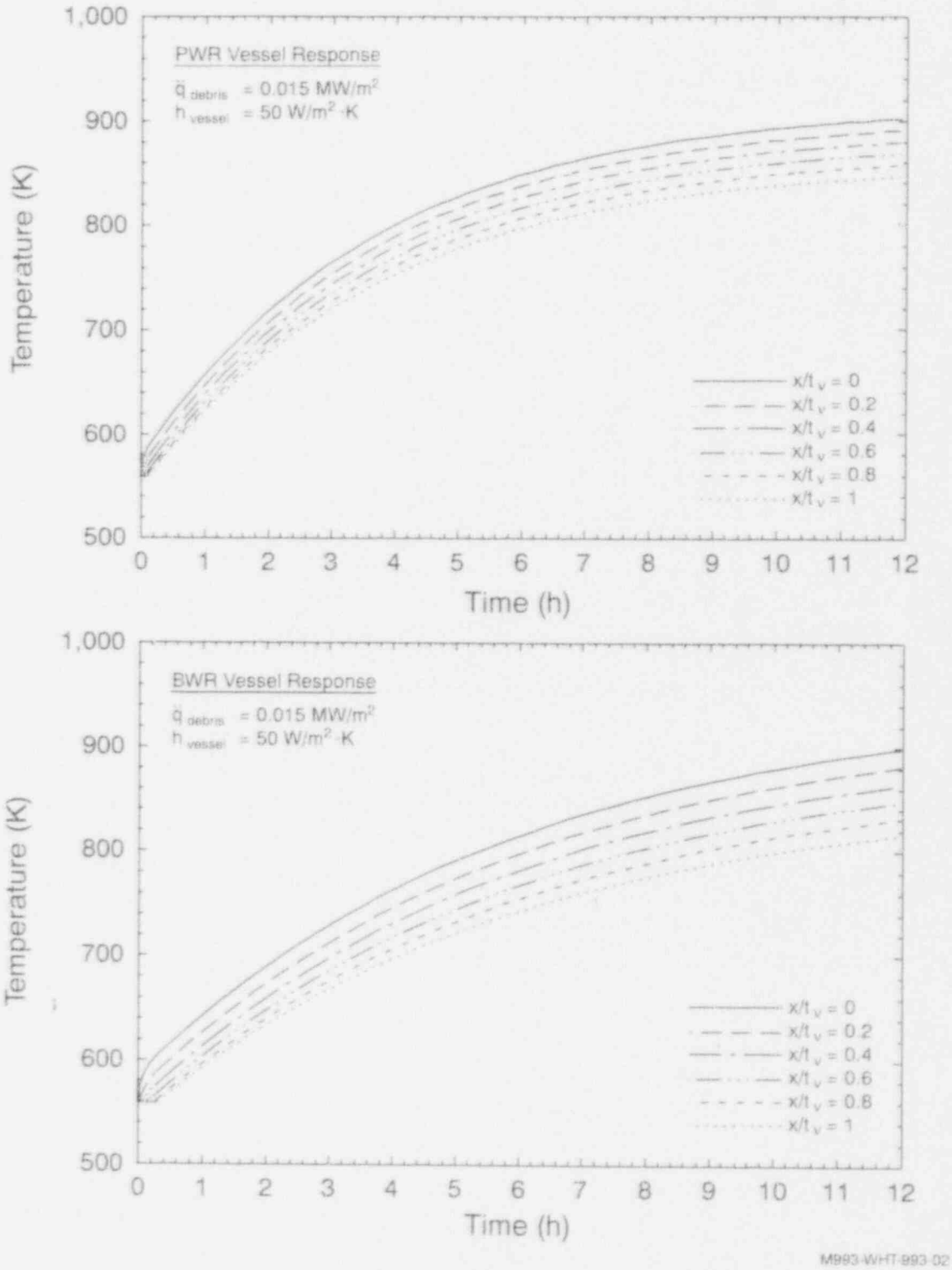

Figure 4-9. Case 1 thermal analysis results.

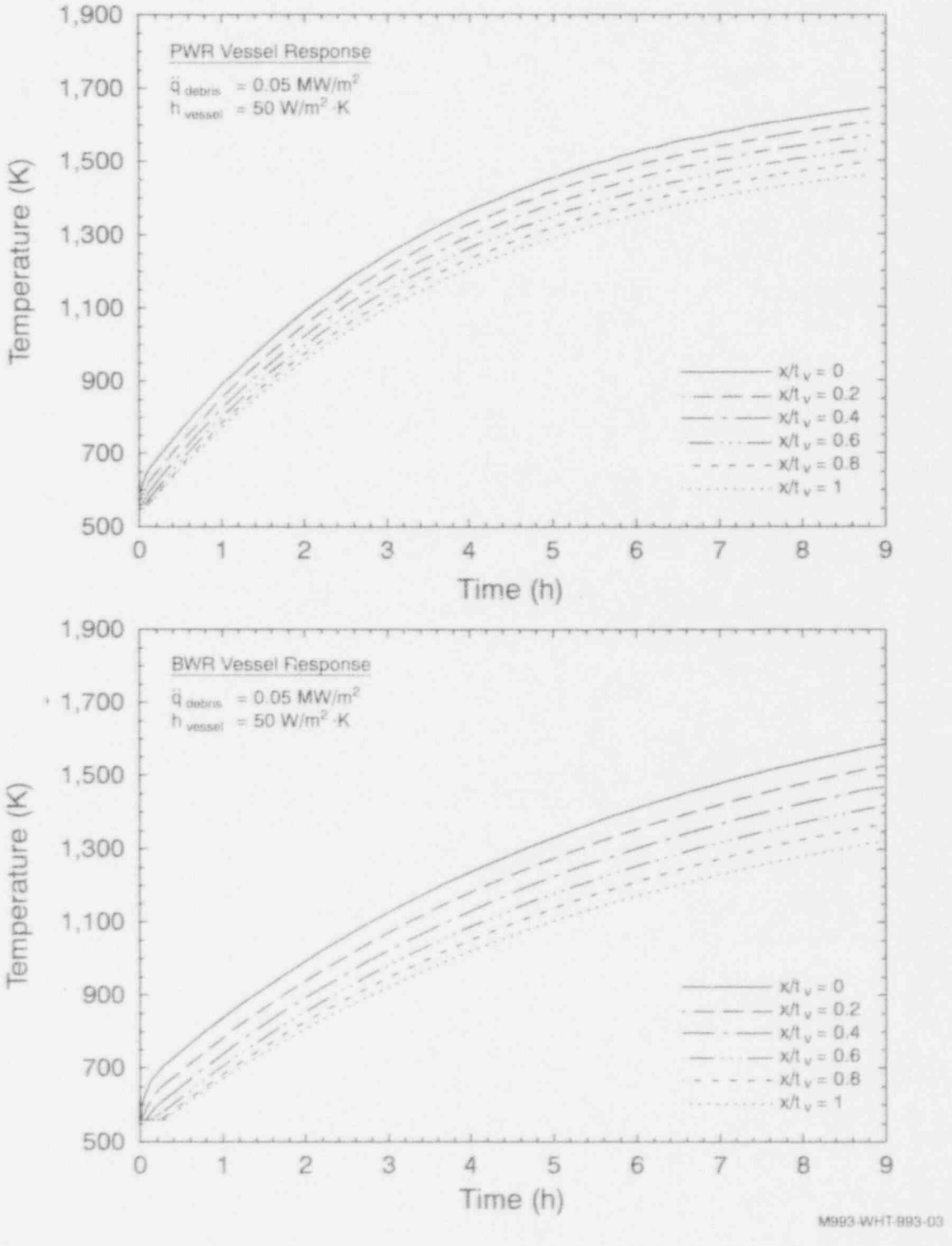

Figure 4-10. Case II thermal analysis results.

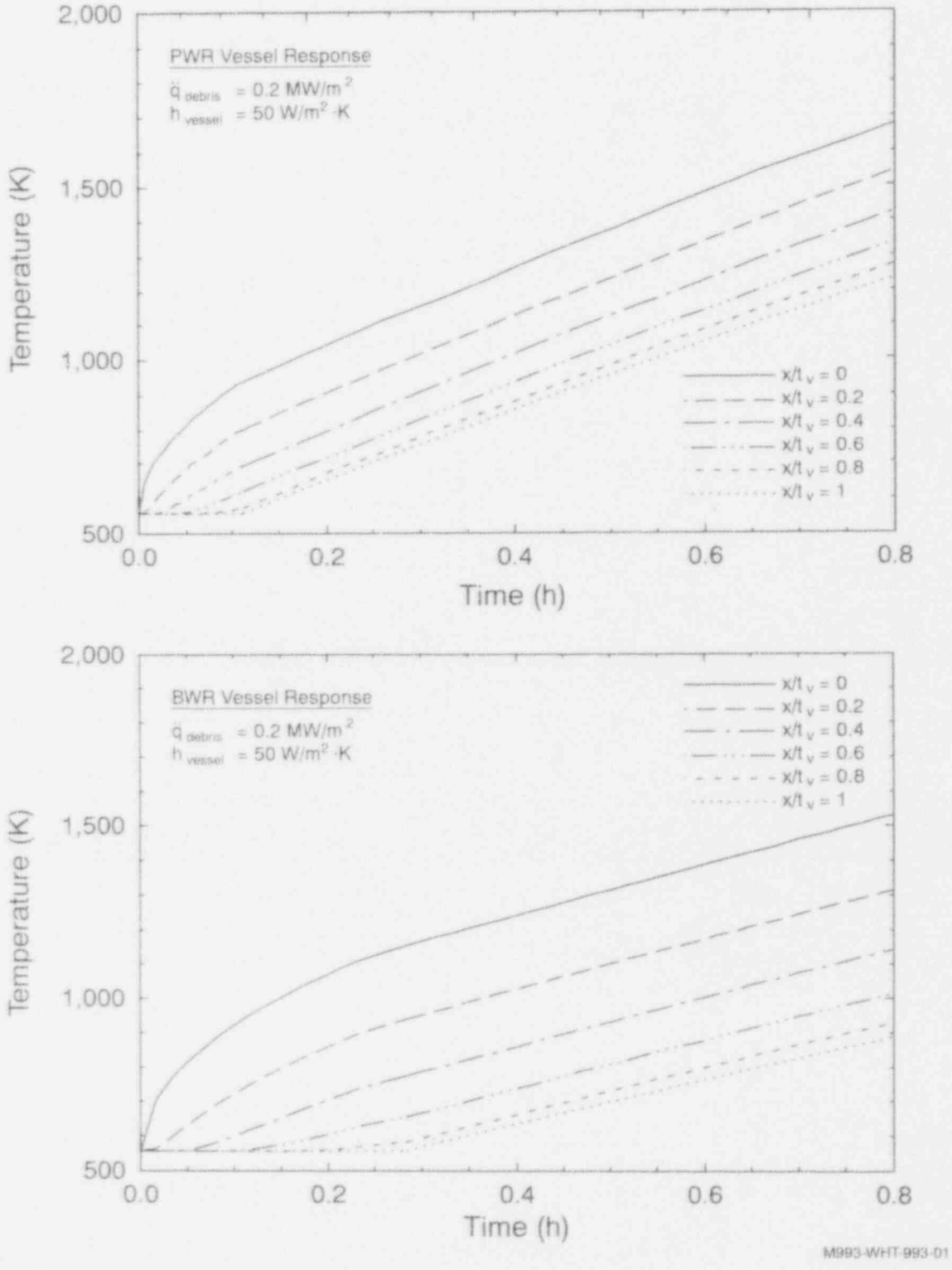

Figure 4-11. Case III thermal analysis results.

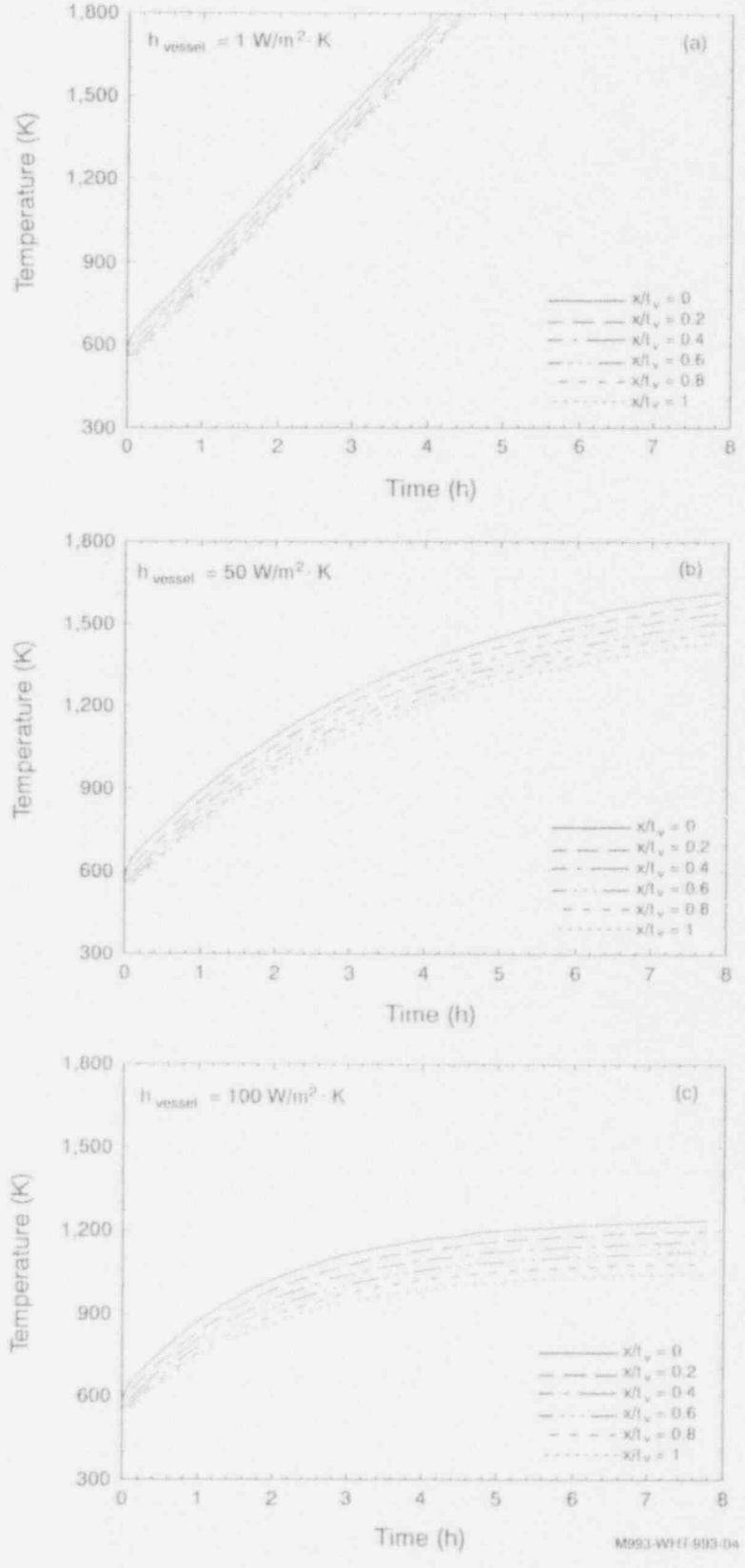

Figure 4-12. Sensitivity of Case II thermal analysis results to vessel outer surface heat transfer assumptions.

Table 4-3. Summary of Section 4.1 analyses results.

Event	Incremental time required for event to occur (hours) PWR	BWR
Melt relocation (assuming T_{rel} = 2400 K	1.0–1.4	1.9–2.1
Coolant boiloff (assuming P_f = 0.1013 MPa and all RCS coolant is released)	4.4	5.5
Temperature front penetrates vessel[a]	0.1	0.3
Steady-state vessel temperature distribution[a]	11.0	18.0

a. Values are quoted for a case in which it is assumed that a ceramic slurry relocates to the lower head with a debris decay heat flux of 0.05 MW/m^2 and that the vessel-to-containment heat transfer coefficient is 50 W/m^{2}K.

4.1.2.1 Tube Thermal Heatup Time. An order-of-magnitude estimate for in-vessel tube heatup time can be obtained by applying the expression for thermal relaxation time.[f] For conditions of good debris-tube surface contact and conduction heat transfer, the time for thermal front penetration (t_{tp}) through the tube wall thickness (t_t) is given by[4-7]

$$t_{tp} = \frac{t_t^2}{4\,\alpha_{tt}} \tag{4-14}$$

where α_{tt} is the thermal diffusivity ($k_t/\rho_t c_{pt}$) of the penetration tube. In cases where the instantaneous debris-to-tube contact temperature exceeds the tube material's melting temperature, the tube latent heat of fusion (L_t) must be taken into account. The thermal relaxation time for tube melting (t_{tm}) is approximated using a solution for two semi-infinite regions,[4-7]

$$t_{tm} = \frac{t_t^2}{4\,\alpha_{tt}\,\lambda_t^2} \tag{4-15}$$

where λ_t is the tube phase change constant, which is dependent upon the material properties and initial temperatures of the debris and the tube. The solution for λ_t largely depends on system

f. Thermal relaxation time, t_{tp}, is defined as the time required to transmit a temperature-forcing function at the surface of a heat-conducting body through the tube wall thickness, t_t.

boundary conditions and the number of regions that may experience phase change. A system of transcendental equations was developed in Reference 4-8 to determine the melting and solidification constants for a solid in contact with a molten material. Applying the material data for either ceramic or metallic melt in contact with PWR Inconel-600 and BWR stainless steel penetrations, tube melting constants for both materials are nearly identical, although assumptions related to melt conditions cause the tube melting constants to range from 0.05 to 0.2.

Assuming an average tube melting constant of 0.1, Figure 4-13 illustrates relaxation times for thermal front penetration and for tube melting calculated for debris in contact with the range of lower head penetrations with in-vessel structures: a GE instrument tube (GE IT); a GE control rod guide tube (GE C/R); a B&W instrument tube (BW IT); and an instrument tube from two Westinghouse plants, W IT 1 and W IT 2). As shown in Figure 4-12, all thermal front penetration times are short, ranging from 1 second for GE BWR stainless steel instrumentation penetrations to 17 seconds for the thicker portion of a B&W Inconel instrumentation tube nozzle (see Figures 3-10 through 3-12 for penetration tube diagrams). Tube melting times are longer,

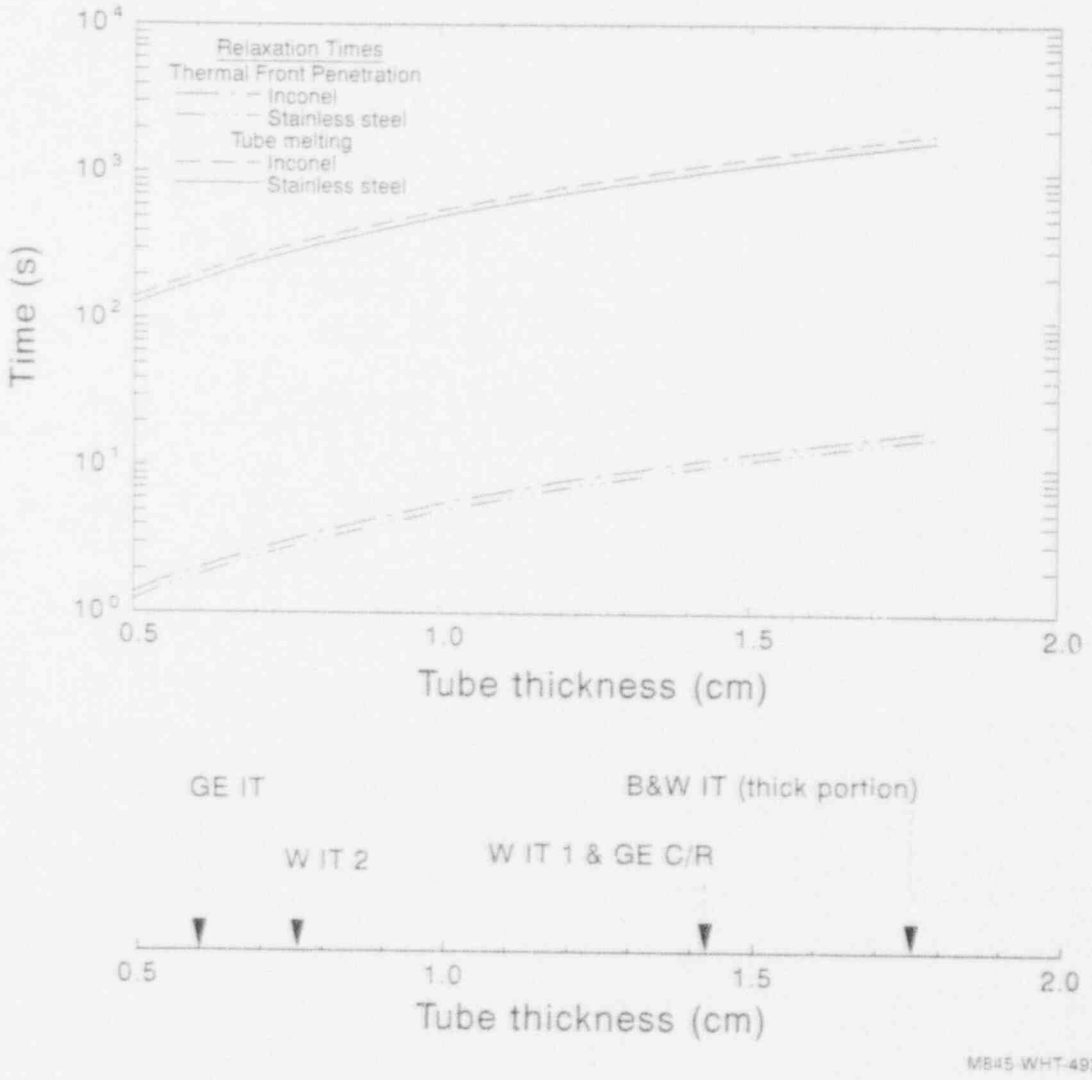

Figure 4-13. Estimated thermal response time for lower head penetrations in contact with debris.

ranging from 3 minutes for a GE BWR stainless steel instrumentation tube to 25 minutes for the thicker portion of a B&W Inconel penetration tube. The response times for Inconel tubes are somewhat longer than those for stainless steel tubes because of Inconel's lower conductivity and thermal diffusivity.

4.1.2.2 Debris Thermal Requirements to Induce In-vessel Tube Melting. The short time constants estimated in Section 4.1.2.1 indicate that rapid tube heatup can be expected when lower head penetrations are in contact with corium melt. However, these analyses do not consider the thermal requirements necessary for tube melting. A detailed calculation for predicting tube melting requires knowledge of convective heat transfer as melt travels past a penetration, conduction heat transfer through any solidified debris that forms outside the penetration, and the magnitude of decay heat within the debris. However, an order-of-magnitude estimate of the minimum debris thermal requirements to induce tube melting may be obtained by neglecting the presence of coolant in the lower head and applying a heat balance to a penetration tube surrounded by a constant temperature, nonporous debris using the idealized geometry shown in Figure 4-14, as follows:

$$A_d \rho_d c_{pd} \theta_d = A_t \rho_t c_{pt} \theta_t \tag{4-16}$$

In this equation the variables θ_d and θ_t represent effective temperatures for the debris and tube, which are given by

$$\theta_d = T_d(0) - T_{mp/t} \quad \text{for solid debris with } T_{mp/t} \le T_d(0) < T_{mp/d}; \text{ or}$$

$$\theta_d = T_d(0) - T_{mp/t} + \frac{L_d}{c_{pd}} \quad \text{for molten debris with } T_d(0) \ge T_{mp/d} \text{ and}$$

$$\theta_t = T_{mp/t} - T_t(0) + \frac{L_t}{c_{pt}};$$

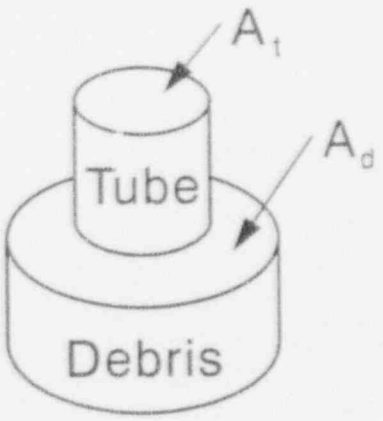

M792-WHT-283-13

Figure 4-14. Idealized geometry of penetration surrounded by corium for predicting minimum debris temperature requirements to induce tube melting.

where c_p represents the specific heat capacity, ρ represents the density, A represents the area, L represents the latent heat of fusion, and T_{mp} represents the tube melting point of the debris or tube (denoted by the subscript d or t).

Equation (4-16) may be rewritten as follows:

$$\frac{\theta_d}{\theta_t} = \frac{c_{pt}\,\rho_t\,A_t}{c_{pd}\,\rho_d\,A_d} = \frac{c_{pt}}{c_{pd}}\,\frac{M_t}{M_d} \qquad (4\text{-}17)$$

where M_t represents the mass of tube material buried in debris of mass, M_d. The above relationship indicates that lower temperature debris is capable of causing tube melting when the ratio of tube-to-debris mass per unit length is low. Although the presence of coolant was neglected in this analysis, the debris temperatures required to induce tube melting for cases with coolant would increase because heat would be lost to the coolant.

Curves in Figure 4-15 represent Equation (4-17) evaluated for several debris and tube material combinations. The region above the boundary lines separating the failure and intact regions corresponds to cases where the effective debris-to-tube temperature ratio can induce tube melting. Mass ratios are plotted on the lower x-axis for reference PWR and BWR lower heads. These ratios were calculated using a unit cell approach, where the area without penetrations is assumed to be full of debris. A range is specified because the penetration pattern is irregular in lower heads. Because the length of the debris is equal to the length of the tube surrounded by the debris, mass ratios were then obtained by multiplying the area ratios by appropriate densities for the debris and tubes. Bounding values for the mass ratios, M_t/M_d, were found to range from 0.0039 to 0.053 for a PWR and from 0.15 to 0.30 for a BWR. BWR values are significantly higher because BWR lower heads are penetrated by instrument tubes and control rod guide tubes; whereas PWR lower heads are penetrated only by instrument tubes.

As shown in Figure 4-15, relatively low debris temperatures may cause tube melting in PWRs, such as the B&W plant, which have only instrument tube lower head penetrations. For example, ceramic debris temperatures in excess of 1700 K are required to induce melting of the B&W Inconel penetration tubes, whereas ceramic debris temperatures in excess of 2000 K are required to induce tube melting in GE stainless steel penetration tubes. The curves in Figure 4-15 also show that somewhat lower debris temperatures can cause melting if the melt is primarily metallic material or if the penetrations are stainless steel.

Figure 4-15 was generated assuming a debris that is either ceramic or metallic with zero porosity. Temperature independent values for tube and debris thermal properties were assumed (the debris is at its solidus temperature and the tube is initially at 560 K) using data in Appendix F. However, similar failure maps could be generated for other initial reactor thermal hydraulic conditions and for porous debris beds by appropriately modifying the tube and debris thermal properties. Figure 4-15 considers Inconel and stainless steel tube materials because these materials are the only ones present in LWR penetrations with in-vessel structures (i.e., the BWR carbon steel drain line does not have any in-vessel structures).

Horizontal cross-hatched bands corresponding to θ_d/θ_t for an initial tube temperature of 560 K and initial debris temperatures of 3113 K (the melting temperature of UO_2) and 2400 K (the average of UO_2 and stainless steel melting temperatures) are included in Figure 4-15. Bars are required, rather than individual lines because the bars consider both Inconel and stainless

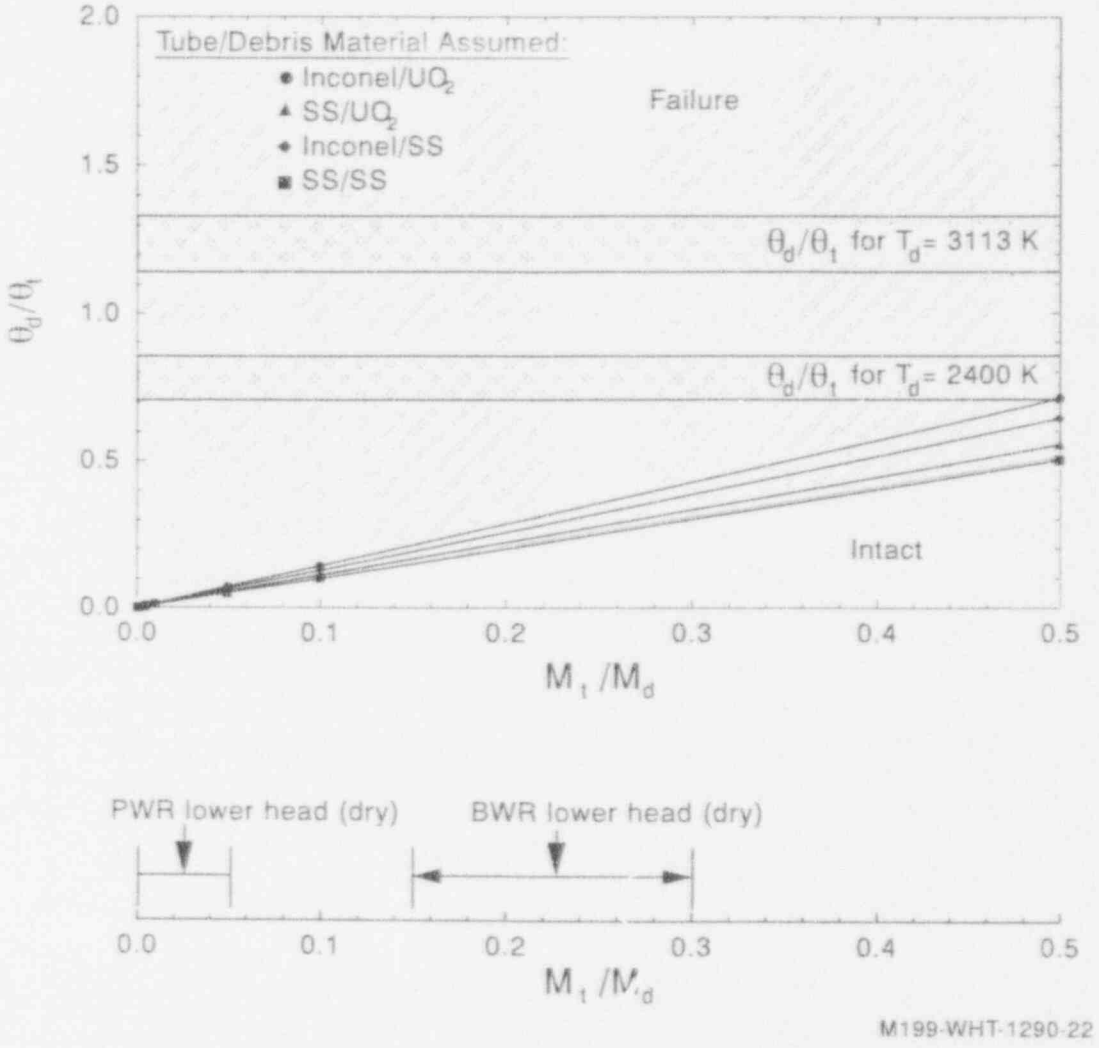

Figure 4-15. Debris thermal requirements to induce penetration melting.

steel tube material properties. As shown in Figure 4-15, both reactors' penetrations are predicted to melt at these temperatures for cases where coolant or voids are absent from the lower head debris bed.

4.1.2.3 Melt Velocities for Gravity and Pressure Driven Flow. The preceding calculations indicate that in-vessel tube melting is possible if bottom entry penetrations are in thermal contact with corium debris. Penetration tube failure can create an open pathway for melt relocation through the lower head via the breached penetration tubes. A governing parameter that affects ex-vessel melt/tube interaction is melt flow velocity. The section provides estimates for characteristic values for terminal melt velocities.

Figure 4-16 illustrates the geometry used to model viscous melt drainage in an open channel. As discussed in Section 3.2.2, most flow paths through LWR penetrations contain RCS coolant at system pressure, so there is no pressure difference between locations 1 and 2 affecting melt flow. However, the inner channel within LWR instrument tubes contains air at containment pressure. Hence, there are some melt pathways through LWR penetrations where a pressure gradient will

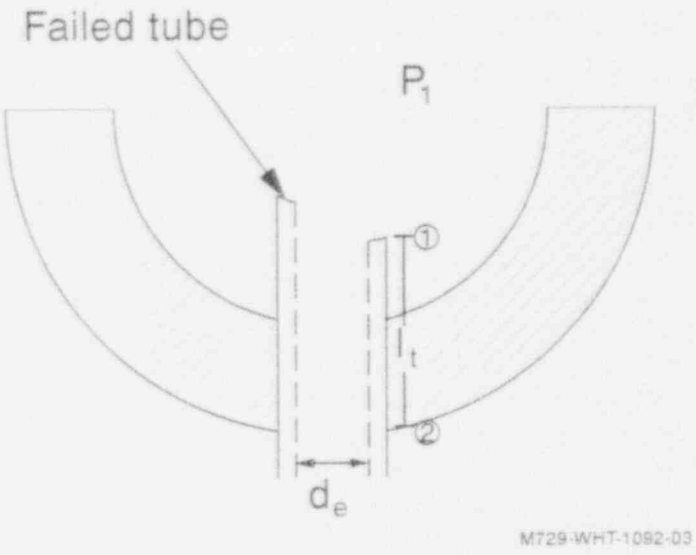

Figure 4-16. Illustration of melt flow through a penetration.

exist. Neglecting any decay heat that may be present in molten debris traveling through a lower head penetration, the energy equation for steady, adiabatic flow in a tube gives

$$\frac{P_1}{\rho_d} + \frac{v_{d1}^2}{2} + g y_1 = h_L + \frac{P_2}{\rho_d} + \frac{v_{d2}^2}{2} + g y_2 \tag{4-18}$$

where P represents the pressure, v_d represents the velocity, and y represents the vertical location of the debris at the tube entrance and exit (denoted by a subscript 1 and 2, respectively). The loss due to friction, h_L, is calculated by applying

$$h_L = \left[4 f_f \frac{l_t}{d_e} + K \right] \frac{v_{d/avg}^2}{2} \tag{4-19}$$

where f_f represents the Fanning friction factor, l_t represents the distance required for melt to travel to locations within the tube below the vessel lower head (i.e., the distance from the break location to the vessel outer surface), K represents the entrance loss coefficient, and $v_{d/avg}$ represents the average velocity across the tube area at the exit. Note that an effective flow diameter for melt, d_e, is used in Equation (4-19) so that annular flow paths within penetrations, such as the flow path between LWR instrument guide tubes and instrument strings (see Figures 3-10 and 3-11), can be considered. Recognizing that $v_{d2} >> v_{d1}$, and that $y_1 - y_2 = l_t$, Equation (4-18) can be simplified to

$$\frac{\Delta P}{\rho_d} + g l_t = \left[4 f_f \frac{l_t}{d_e} + K + 1 \right] \frac{v_{d2}^2}{2} \tag{4-20}$$

which can be solved for v_{d2} to obtain

$$v_{d2} = \sqrt{\frac{2\,\Delta P/\rho_d + 2\,g\,l_t}{4\,f_f\,l_t/d_e + K + 1}} \quad (4\text{-}21)$$

The Fanning friction factor and entrance loss coefficient are dependent on Reynolds number. The solution to Equation (4-21) requires iteration between f_f and v_{d2}; a friction factor must be assumed to calculate the velocity, and then the Reynolds number is calculated to confirm that the appropriate friction factor and loss coefficient were selected using a Moody diagram[4-9] and an entrance loss coefficient diagram.[4-10]

Figure 4-17 compares terminal melt velocities for the range of pressure gradients possible in BWR and PWR reactor vessels. Pressure gradients were selected to compare maximum melt velocities

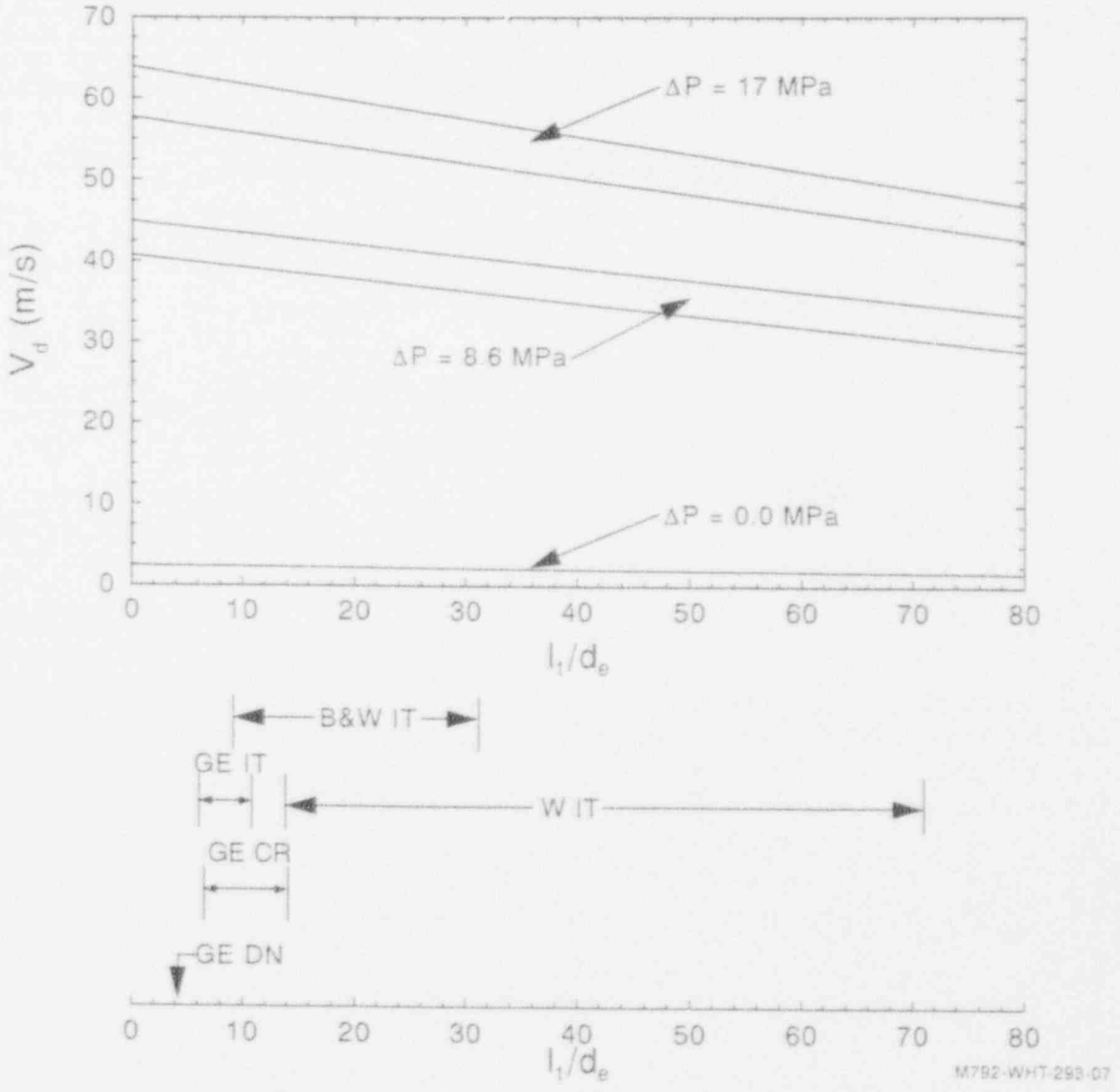

Figure 4-17. Velocities for melts driven by gravity and pressure.

through penetrations of depressurized reactors (0 MPa) and the vessel design pressure for BWRs (8.6 MPa) and PWRs (17 MPa). Ceramic and metallic melt compositions were bounded by using thermal properties for UO_2 and stainless steel evaluated at the liquidus temperature for each material (see Appendix F).

The lower x-axis in Figure 4-17 displays appropriate ranges for the tube length over the tube effective diameter of the LWR penetrations listed in Appendix F: a GE instrument tube (GE IT), a GE control rod guide tube (GE C/R), a GE drain line nozzle (GE DN), a B&W Instrument Tube (B&W IT), and instrument tubes from the two Westinghouse vessels (combined into the range indicated by W IT). A lower bound for the value of l_1 in each of these ratios was estimated by recognizing that the minimum distance that the melt must travel is the vessel thickness. Upper bounds were estimated by considering the point where debris is more likely to ablate through each penetration tube. These estimates were obtained by considering points where tube narrowing occurred (such as where the B&W instrument tube nozzle narrows) and by considering where the hotter portion of debris beds would occur (in cases where no tube narrowing occurs).[g] Note that only a single value is displayed for the drain line because there is no in-vessel structure associated with this penetration.

Results indicate that system pressure has the most influence on melt velocity predictions. At higher pressures, results are displayed as velocity ranges and melt velocities are approximately 10% higher if the melt is metallic rather than ceramic. At lower pressures, the influence of melt composition becomes negligible because the density dependence is tied to the pressure difference term in Equation (4-21). In fact, for a depressurized severe accident, melt velocities are predicted to range between 1.8 and 2.6 m/s for the LWR lower head penetrations listed in Appendix F. Hence, gravity-driven melt velocity predictions are relatively low for all of the melt material properties and penetration geometries included.

4.1.2.4 Melt Penetration Distance. As discussed in Section 2.1.2, previous LMFBR experimental analyses did not prove conclusively that melt penetration was governed by turbulent heat transfer (as predicted with the "bulk freezing" model first advanced by Ostensen and Jackson[4-11, 4-12]) or conduction heat transfer through the crust which forms along the channel wall (as predicted with the "conduction layer" model of Epstein[4-13, 4-14]). However, experimental data indicate that melt penetration distances are bounded by the distances predicted by the bulk freezing and conduction layer models. Although more complex models have been developed to simultaneously evaluate convective and conduction heat transfer phenomena and other phenomena affecting melt solidification, a modified version of the bulk freezing model and an original version of the conduction model are applied in this section to obtain upper and lower bounds for order-of-magnitude estimates of the melt penetration distances. Figure 4-18 illustrates the geometry assumed for applying each model.

Although the entire area within some LWR penetrations, such as the BWR drain line, is available for melt flow, many penetrations contain inner structures, such as LWR instrument tubes (see Figures 3-11 and 3-12), creating an annular area for melt flow. In order to consider both types of melt flow paths in these models, an effective diameter has been incorporated, which for an LWR instrument tube is given by

---

g. Upper bounds for debris bed heights in previous severe accident analyses were based upon information reviewed in Section 3.

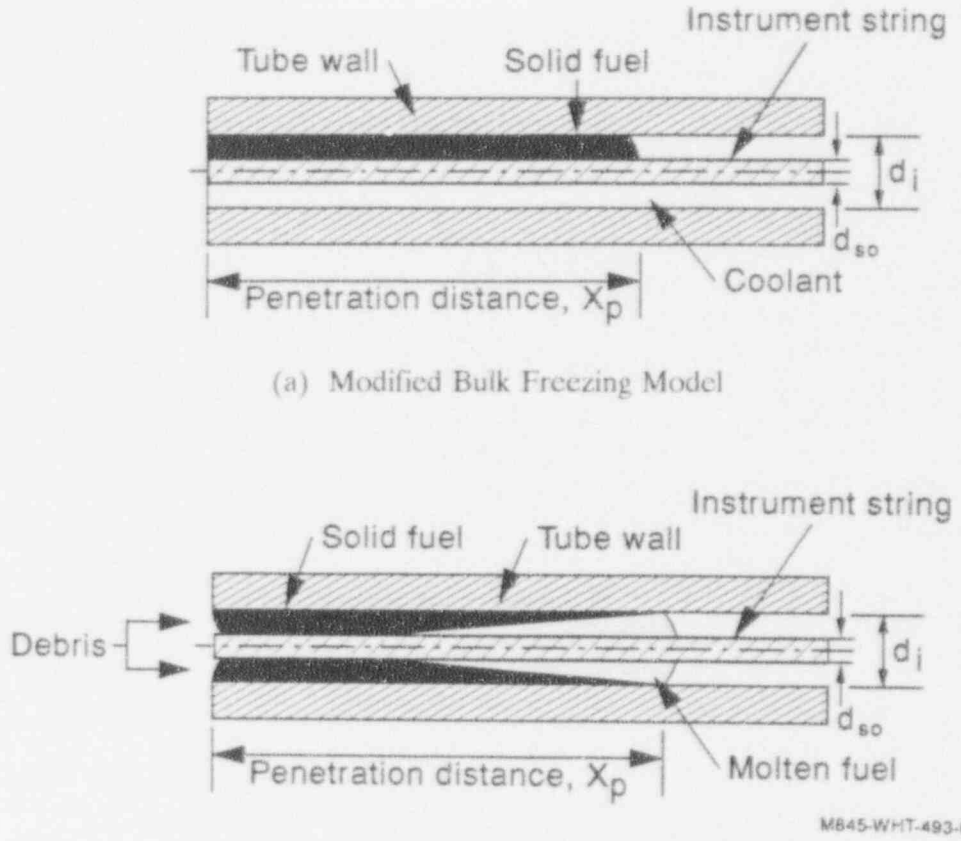

Figure 4-18. Comparison of the "bulk freezing" and "conduction layer" models for the prediction of melt penetration distance through a cold tube.

$$d_e = \sqrt{d_i^2 - d_{so}^2}$$

where d_i is the inner diameter of the tube and d_{so} is the outer diameter of the instrument string. For a channel without any internal structures, d_{so} is set equal to zero, and the effective diameter reduces to the tube inner diameter.

A modified version of the bulk freezing model is used to estimate the penetration distance of molten debris into vessel penetrations containing coolant. The model assumes that turbulence in the flowing melt prevents a stable crust from forming at the channel wall (see Figure 4-18a).

In this study, heat transfer coefficient correlations for turbulent liquid metal flow are used to model both metallic and ceramic debris. Because the Prandtl number for either metal or ceramic melt is less than 0.4 and the Reynolds number for either metallic or ceramic debris in even the lower velocity, gravity-driven cases, is well above 2300, these correlations are considered to be appropriate. A conservative turbulent liquid metal heat transfer coefficient correlation for flow in long circular tubes is [4-15]

$$Nu = \frac{h_t d_e}{k_d} = 0.625\ Pe^{0.4}$$

An appropriate correlation for turbulent liquid metal flow in concentric annuli is[4-1]

$$Nu = 5.25 + 0.0188\ Pe^{0.8}\left(\frac{d_i}{d_{so}}\right)^{0.3} .$$

The Peclet number, Pe, in both of the above equations is defined as

$$Pe = \frac{d_e v_d \rho_d c_{pd}}{k_d} . \qquad (4\text{-}22)$$

The penetration distance is conservatively estimated by assuming that the melt stops when the entire amount of debris in the tube has solidified. The model uses a heat balance to equate the amount of heat removed as the debris solidifies with the convective heat transfer between the melt and the tube wall and between the melt and the coolant. Assumptions made in the derivation of the equation include allowing coolant to escape from the tube as vapor upon heating and limiting heat exchange between the debris and the coolant to the azimuthal direction. Heat transfer from the leading edge in the axial direction is neglected. A separate heat balance around the coolant in contact with the debris allows the debris-coolant heat transfer coefficient in the first heat balance to be replaced by terms accounting for the change of energy stored in the coolant.

Because several final coolant conditions are possible, three cases are considered. At the time of solidification the coolant in radial contact with the debris is modeled as either subcooled liquid, saturated vapor, or superheated vapor. Letting a lower case x represent the fraction of the available effective area containing melt, the dimensionless penetration distances for a case in which the final coolant temperature is subcooled (i.e., T_{l_f} = subcooled, but at a temperature above the initial temperature, T_{l_i}) are given by the following relationships

Circular tubes

$$\frac{X_p}{d_i - d_{so}} = 0.4\ Pe^{0.6}\ \frac{\left[\rho_d\left\{c_{pd}\left(T_d - T_{mp/d}\right) + L_d\right\} - \left(\frac{1}{x} - 1\right)\rho_{l_{sub}} c_{pl}\left(T_{l_{sub}} - T_{l_i}\right)\right]}{\rho_d c_{pd}\left(T_d - T_{l_i}\right)} \qquad (4\text{-}23)$$

Annular Tubes

$$\frac{X_p}{d_i - d_{so}} = 0.25\ Pe\ \frac{\left[\rho_d\left\{c_{pd}\left(T_d - T_{mp/d}\right) + L_d\right\} - \left(\frac{1}{x} - 1\right)\rho_{l_{sub}} c_{pl}\left(T_{l_{sub}} - T_{l_i}\right)\right]}{\rho_d c_{pd}\left(T_d - T_{l_i}\right)\left(5.25 + 0.0188\ Pe^{0.8}\left(\frac{d_i}{d_{so}}\right)^{0.3}\right)} \qquad (4\text{-}24)$$

For the case where the coolant in contact with the debris becomes saturated vapor, the relations are

Predicting Lower Head Failure

Circular tubes

$$\frac{X_p}{d_i - d_{so}} = 0.4\,Pe^{0.6}\,\frac{\left[\rho_d\left\{c_{pd}\left(T_d - T_{mp/d}\right) + L_d\right\} - \left(\frac{1}{x} - 1\right)\left\{\rho_{l_{sat}} c_{pl}\left(T_{l_{sat}} - T_{l_i}\right) + \rho_{g_{sat}} h_{fg}\right\}\right]}{\rho_d\, c_{pd}\left(T_d - T_t\right)} \tag{4-25}$$

Annular tubes

$$\frac{X_p}{d_i - d_{so}} = 0.25\,Pe\,\frac{\left[\rho_d\left\{c_{pd}\left(T_d - T_{mp/d}\right) + L_d\right\} - \left(\frac{1}{x} - 1\right)\left\{\rho_{l_{sat}} c_{pl}\left(T_{l_{sat}} - T_{l_i}\right) + \rho_{g_{sat}} h_{fg}\right\}\right]}{\rho_d\, c_{pd}\left(T_d - T_t\right)\left(5.25 + 0.0188\,Pe^{0.8}\left(\frac{d_i}{d_{so}}\right)^{0.3}\right)} \tag{4-26}$$

If the coolant becomes superheated the equations are modified as,

Circular tubes

$$\frac{X_p}{d_i - d_{so}} =$$

$$0.4\,Pe^{0.6}\,\frac{\left[\rho_d\left\{c_{pd}\left(T_d - T_{mp/d}\right) + L_d\right\} - \left(\frac{1}{x} - 1\right)\left\{\rho_{l_{sat}} c_{pl}\left(T_{l_{sat}} - T_{l_i}\right) + \rho_{g_{sat}} h_{fg} + \rho_{g_{sup}} c_{pg}\left(T_{g_{sup}} - T_{l_{sat}}\right)\right\}\right]}{\rho_d\, c_{pd}\left(T_d - T_t\right)} \tag{4-27}$$

Annular tubes

$$\frac{X_p}{d_i - d_{so}} =$$

$$0.25\,Pe\,\frac{\left[\rho_d\left\{c_{pd}\left(T_d - T_{mp/d}\right) + L_d\right\} - \left(\frac{1}{x} - 1\right)\left\{\rho_{l_{sat}} c_{pl}\left(T_{l_{sat}} - T_{l_i}\right) + \rho_{g_{sat}} h_{fg} + \rho_{g_{sup}} c_{pg}\left(T_{g_{sup}} - T_{l_{sat}}\right)\right\}\right]}{\rho_d\, c_{pd}\left(T_d - T_t\right)\left(5.25 + 0.0188\,Pe^{0.8}\left(\frac{d_i}{d_{so}}\right)^{0.3}\right)} \tag{4-28}$$

For the case where no coolant is present, the heat balances yield

Circular tubes

$$\frac{X_p}{d_i - d_{so}} = 0.4\ Pe^{0.6}\ \frac{\left[\left(T_d - T_{mp/d}\right) + \dfrac{L_d}{c_{pd}}\right]}{\left(T_d - T_t\right)} \tag{4-29}$$

Annular tubes

$$\frac{X_p}{d_i - d_{so}} = 0.25\ Pe\ \frac{\left[\left(T_d - T_{mp/d}\right) + \dfrac{L_d}{c_{pd}}\right]}{\left(T_d - T_t\right)\left(5.25 + 0.0188\ Pe^{0.8}\left(\dfrac{d_i}{d_{so}}\right)^{0.3}\right)} \tag{4-30}$$

In the above equations, changes in the mean temperature of the melt are neglected as the melt proceeds down the channel. This assumption is valid provided[4-13]

$(T_d - T_{mp/d})/(T_d - T_t) << 1.0$.

Typically, this ratio is around 0.25.

The "conduction layer" model assumes that transient freezing is governed by crust buildup at the channel wall, where conduction heat transfer governs melt solidification. Once the frozen layer closes at the channel center, flow ceases and the remaining melt inside the channel freezes. The model also assumes a constant penetration melt velocity into a thick-walled channel. Because the molten material is assumed to be at or near its melting point, no convective heat exchange occurs at the melt-crust interface, and crust solidification is assumed to be independent of melt flow dynamics. For all times, t, the crust thickness is zero at the leading edge and maximum at the channel inlet (see Figure 4-18b).

The conduction model predicts a square root dependence for the crust thickness, σ_c, as a function of time, t, in a semi-infinite wall channel[4-13]

$$\sigma_c(t) = 2\ \lambda_c(\alpha_{td}\ t)^{0.5} \tag{4-31}$$

where λ_c represents the solidification constant for the debris and α_{td} represents the debris thermal diffusivity. As discussed in References 4-8, 4-13, and 4-16, the solidification constant is found from different approximations of boundary conditions and the number of regions that may experience phase change. Using the methodology described in Reference 4-8, the solidification constant for molten ceramic debris in contact with either Inconel-600 or stainless steel penetrations is estimated to have a value of ~0.75. Likewise, the solidification constant for molten metallic debris in contact with either Inconel-600 or stainless steel penetrations is estimated to have a value of ~0.2. There are no data for quantifying the solidification constant

for melt contacting coolant. Hence, it is not currently possible to use the conduction model to quantify the effect that coolant within a tube has on melt penetration distances.

Substituting the criteria for melt freezing ($\sigma_c = d_e/2$) and the relationship between time and penetration distance ($t = X_p/v_d$) into Equation (4-31), the following relationship is obtained for predicting a dimensionless melt penetration distance:

$$\frac{X_p}{d_e} = \frac{1}{16\lambda_c^2} Pe \quad . \tag{4-32}$$

This equation may be rearranged in terms of the difference of the diameters in place of the effective diameter to obtain

$$\frac{X_p}{d_i - d_{so}} = \frac{Pe}{16\lambda_c^2}\sqrt{\frac{d_i + d_{so}}{d_i - d_{so}}} \quad .$$

Figure 4-19 compares the results from the modified bulk freezing and conduction models for ceramic and metallic debris compositions at their respective liquidus temperatures. Dimensionless penetration distances are plotted as a function of Peclet number, which is dependent upon the melt velocity, the melt thermal diffusivity, and the effective diameter for melt flow. The modified bulk freezing model takes debris superheat into consideration, along with the state of the coolant, if present, at the time of debris solidification. The conduction model curves are independent of debris temperature, but account for debris solidification. Debris was assumed to fill the entire effective area available for melt flow in both models.

The penetration distances predicted by each model are given as ranges for each model to account for the various types of penetration tubes. Debris penetration in a GE control rod guide tube represents the upper bound for the conduction model, and the GE drain line represents the lower bound. However, the GE drain line represents the upper bound for the modified bulk freezing model, and a GE instrumentation tube produces the lower bound. Conduction model results indicate that for a given penetration diameter, metallic melts travel further than ceramic melts; whereas similar penetration lengths are predicted for ceramic and metallic melt with the modified bulk freezing model. Because of its larger thermal diffusivity ($k/\rho c_p$), metallic melt has a smaller Peclet number for a given velocity and temperature in a given penetration. However, the smaller Peclet number for the metallic melt is overshadowed by a much smaller melt solidification constant in conduction model predictions, and is balanced by superheat effects in modified bulk freezing model predictions. Hence, the ability of metallic debris to conduct heat more rapidly is offset by its smaller solidification constant and by its much higher superheat for a given temperature.

Locations on the secondary horizontal axes of Figure 4-19 indicate the Peclet number for various penetrations based on a velocity of 1 m/s. As discussed in Section 4.1.2.3, this velocity is an order-of-magnitude prediction for melt traveling through penetrations with no pressure head. The penetration distances corresponding to the Peclet numbers on these grids represent minimum values; longer distances would be predicted for pressure-driven cases. The horizontal region labeled $l_i/(d_i-d_{so})$ in Figure 4-19 represents the upper and lower bound for the distance that must be traveled by debris to reach the vessel outer surface through a gap of d_i-d_{so}, based on various reactor lower head thicknesses and possible ablation heights of lower head penetrations. The

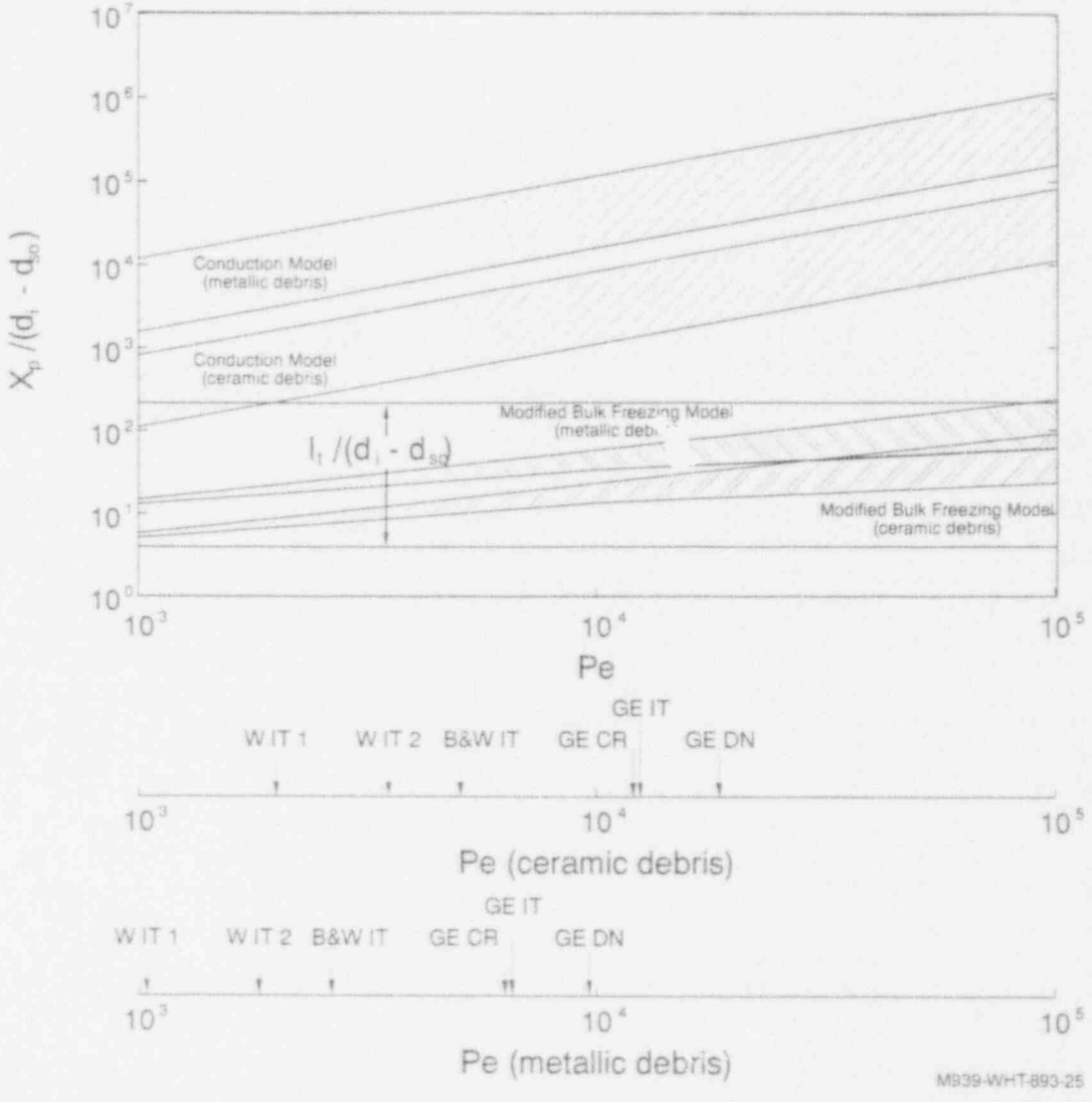

Figure 4-19. Comparison of dimensionless penetration distance $[X_p/(d_i-d_{so})]$ versus Peclet number $(d_e v_d \rho_d c_{pd}/k_d)$ predicted by the modified bulk freezing and conduction layer models. (Locations on lower x-axes assume a melt velocity of 1.0 m/s and an initial melt relocation temperature of 2400 K.)

minimum for this range corresponds to a GE drain line nozzle, which has no in-vessel structure, and the BWR vessel thickness; whereas the maximum for this range corresponds to the maximum debris height expected in a lower head during a severe accident and a Westinghouse instrument tube gap thickness.

Results from the conduction model calculations show that for a Peclet number range of 10^3 to 10^5, debris will flow out of the lower head regardless of the penetration type. However, debris modeled with the modified bulk freezing equations is predicted to flow out of the lower head only for cases where the tube is ablated near the vessel/tube interface and where the tube has a relatively large effective diameter for melt flow. For example, melt is predicted to travel below the lower head through a GE drain line penetration that has no in-vessel structures and a

relatively large effective diameter for melt flow. Note that Figure 4-19 results were obtained assuming that there was no pressure head driving the melt flow. Higher velocity melts would be predicted to travel to distances below the lower head through more of these penetrations.

As discussed above, Figure 4-19 shows that distances predicted with the conduction model are orders of magnitude greater than distances predicted with the modified bulk freezing model, even without considering the effects of coolant. The presence of coolant within a tube, coupled with a reduced flow area, would lower the penetration distances predicted by both models. The effect of coolant in the conduction model would be incorporated through differences in values for the solidification constant. However, the solidification constant, which typically has a value <1,[4-8] would have to increase by an order of magnitude before the conduction model would predict distances comparable to results of the modified bulk freezing model.

The effect of coolant on modified bulk freezing model predictions is illustrated in Figure 4-20. This figure presents dimensionless penetration distance predictions for the modified bulk freezing model as a function of the ratio of the Peclet number to the Nusselt number. Calculating penetration distance based on a Pe/Nu ratio enables both annular and non-annular types of penetrations to be analyzed with one set of curves. Both ceramic and metallic debris are represented in Figure 4-20. For the cases that involved coolant, debris was assumed to fill one-quarter of the effective area available for melt flow in the tube.

The initial temperature of both melt compositions was assumed to be 200 K above their respective solidification temperatures. The tube wall temperature was assumed to equal the initial temperature of the coolant. The final temperature of the coolant in the subcooled state was set 50 K above the initial temperature, which would allow the temperature to remain below saturation. A superheated temperature 200 K above saturation was selected because this temperature difference allowed results to be distinguished from the penetration distances predicted with saturated vapor in the tube. The curves in Figure 4-20 show that debris travels farthest if the tube is void of coolant. The presence of coolant decreases the penetration distance because of the heat transferred from the debris to the coolant.

A range of Pe/Nu for each tube is given on the secondary x-axes of Figure 4-20. The low end of each range corresponds to debris filling one-quarter of the effective area. The high end corresponds to a cross section filled with debris. A velocity of 1 m/s is used to determine the ratio of Peclet number to Nusselt number for each penetration tube. The upper and lower bounds for the distance that the debris must travel to exit the vessel lower head are also represented in Figure 4-20 by the horizontal region labeled $l_t/(d_i-d_{so})$. Thus, modified bulk freezing model results indicate that debris inside both Westinghouse instrument tubes and the GE control rod guide tube will remain within the lower head for the two debris compositions considered in Figure 4-20. Tubes with larger effective diameters for melt flow will allow debris to flow out of the lower head if the tubes are ablated close to the surface of the vessel.

A number of parameters affect the penetration distance, including the coolant condition, the melt composition, effective area, initial temperature, and velocity. The debris composition appears to have the greatest impact on penetration depth, as shown in Figures 4-19 and 4-20. As the area of debris increases, effects of coolant state decrease. The initial temperature of the debris greatly influences the distance predicted if coolant is absent from the tube. However, debris temperature effects decrease with the introduction of coolant and as more heat is transferred to the coolant. A change in coolant state from subcooled to superheated for debris encompassing one quarter of the effective area has less effect on penetration distance than changing the debris effective area from one-half to one-quarter.

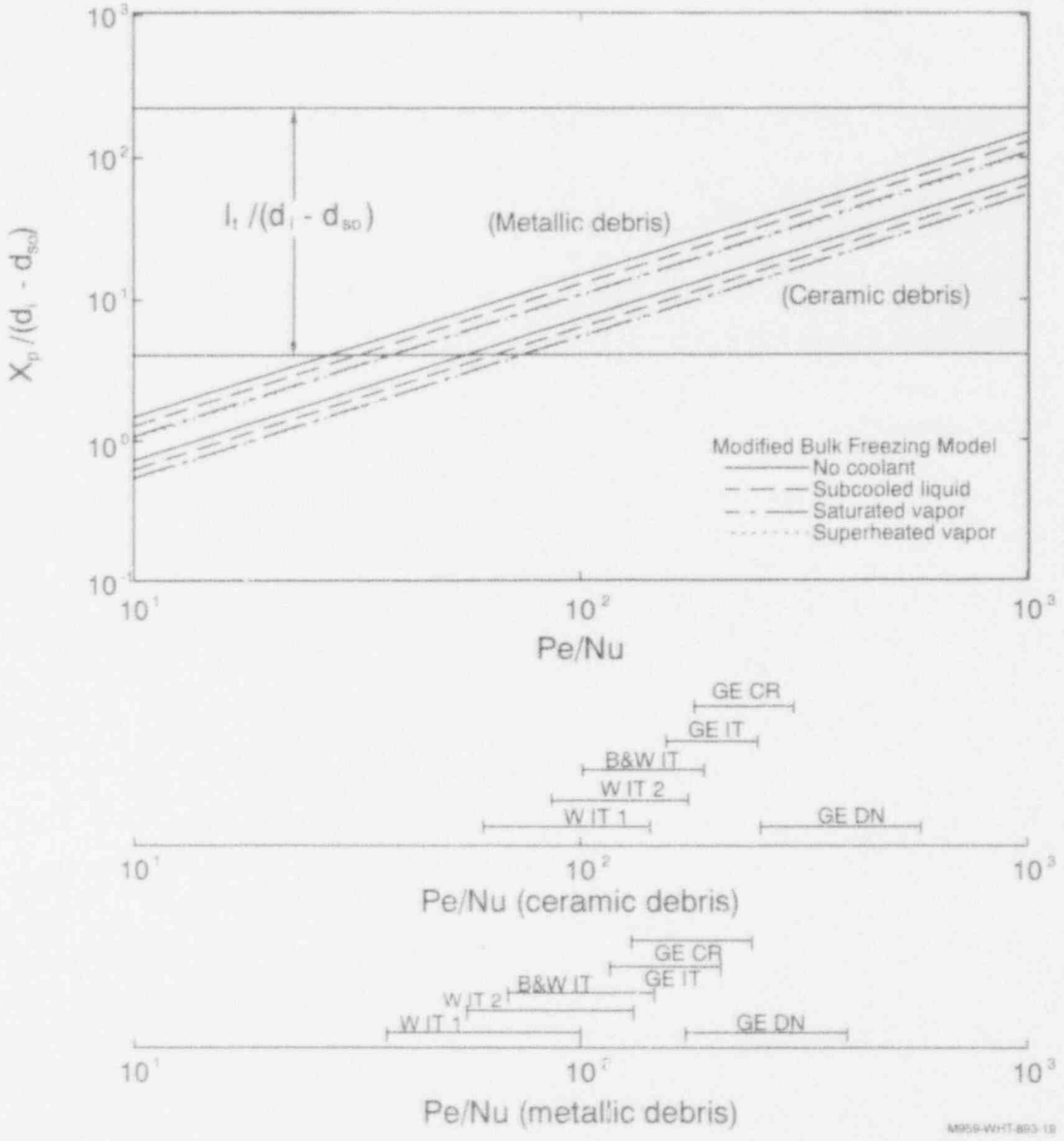

Figure 4-20. Modified bulk freezing model results illustrating the effects of coolant on the dimensionless penetration distance $[X_p/(d_i-d_{so})]$ predictions as a function of the ratio of Peclet to Nusselt number $(v_d\rho_d c_{pd}/h_i)$. (Locations on lower x-axes assume a melt velocity of 1.0 m/s and an initial melt relocation temperature of 2400 K.)

As discussed in Section 2.1, previous LMFBR work did not prove conclusively which of these two models is more appropriate. However, previous work did show that penetration distances were bounded by these two models. There are large discrepancies between the two models' predictions. For the low pressure cases considered in Figure 4-19, melt is predicted to travel below the lower head if the conduction model is applied; whereas, if the modified bulk freezing model is applied, melt is predicted to travel below the lower head only for penetrations having larger effective areas for melt flow and/or penetrations that are ablated near the vessel inner surface. Experimental data are needed to determine which of these models is appropriate for severe accident analysis.

4.1.2.5 Thermal-Induced Ex-vessel Tube Mechanical Failure. Using the geometry shown in Figure 4-21, two methods were applied to assess the potential of ex-vessel thermal-induced tube failure:

1. A heat balance between melt heat loss and melt/tube wall heat transfer

2. A steady-state heat transfer model that considers melt decay heat and tube wall radiative heat loss.

These methods are examined to define the heat transfer parameters influencing thermal-induced mechanical failure in ex-vessel tubes. Both methods assume one-dimensional heat transfer from the melt, which is assumed to fill the entire effective flow area, to the tube. Thermal properties are evaluated at the initial temperatures assumed for the debris and tube. An infinite time is assumed to be available for heat transfer. Thus, these analyses provide a lower bound for conditions, such as debris relocation temperature and debris heat flux, necessary to induce ex-vessel tube failure. The appropriateness of assumptions utilized in these analyses is evaluated using finite element techniques in Section 5.

To determine if tube failure by thermal means is possible, a simple heat balance was written for the geometry illustrated in Figure 4-21, where the sensible and latent heat transferred from a molten melt plug is equated to the heat gained by the tube wall

$$\frac{\theta_d}{\theta_t} = \frac{A_{tx}}{A_{eff}} \frac{\rho_t c_{pt}}{\rho_d c_{pd}} \tag{4-33}$$

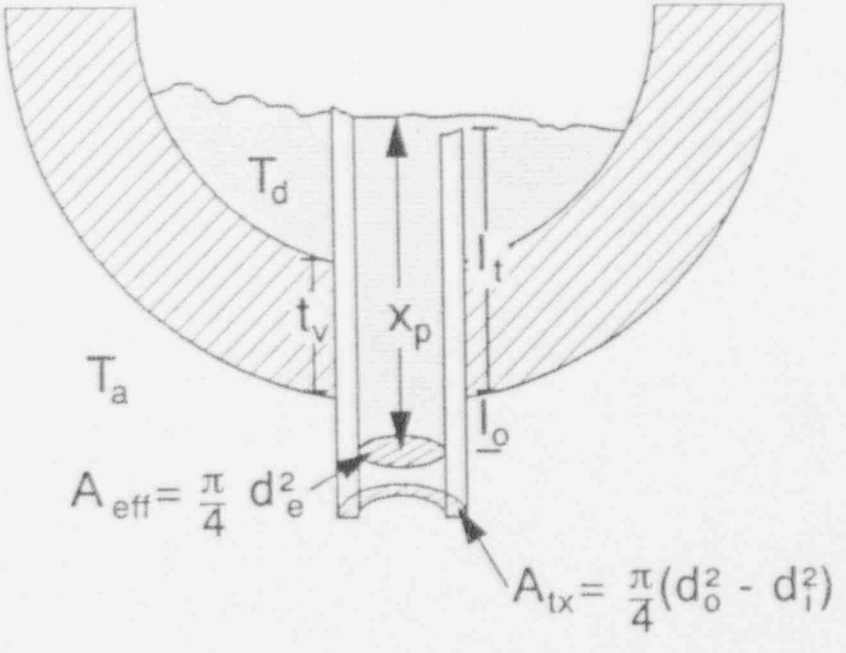

Figure 4-21. Melt flow and refreezing through lower head via breached penetration tube.

where θ_d is equal to the effective debris temperature, which is defined as

$\theta_d = T_d(0) - T_{t/f}$ for solid debris with $T_{t/f} \le T_d(0) < T_{mp/d}$; or

$\theta_d = T_d(0) - T_{t/f} + L_d/c_{pd}$ for molten debris with $T_d \ge T_{mp/d}$

and θ_t designates the temperature increase from the initial tube temperature to the tube failure temperature, $T_{t/f}$, which for ex-vessel failure calculations is assumed to occur when the temperature of the tube reaches the point at which the tube's ultimate strength is less than the average stress in the tube from the system pressure. Ultimate strength behavior of penetration tube material (Inconel, stainless steel, and SA105/SA106 carbon steel) is not well defined at high temperatures. In fact, before the NRC Lower Head Failure Program, high-temperature data for these materials were limited, if nonexistent, for temperatures above 1000 K. As discussed in Appendix B, a small number of high-temperature tests for penetration tube materials were completed. Although results from these tests are limited, calculations were performed using the new data to estimate ultimate strength behavior at high temperatures. Curves illustrating the ultimate strength behavior assumed in these calculations are found in Appendix F.

Equation (4-33) was evaluated for metallic (stainless steel) and ceramic (UO_2) based melt debris in contact with the reference plant penetrations. Figure 4-22 presents results obtained when the initial tube temperature is assumed at 550 K and the final tube temperature is assumed equal to the temperature where the ultimate strength of the tube material is less than the stress in the tube from system pressure. Results in Figure 4-22 illustrate that a higher debris temperature is required to induce failure if the debris is metallic. This phenomenon may be understood by noting that for the temperatures of interest, UO_2 has a higher heat capacitance (for example, 2400 K values in Appendix F indicate that ρc_p for UO_2 is 4.2 MJ/m^{3}K; whereas ρc_p for stainless steel is 3.9 MJ/m^{3}K).

Horizontal bands corresponding to θ_d/θ_t for debris temperatures of 3113 K (the melting temperature of UO_2) and 2400 K (the average of UO_2 and stainless steel melting temperatures) are included in Figure 4-22. As shown in Figure 4-22, ex-vessel tube failure is predicted for only the BWR drain line and some of the instrument tube penetrations because of their larger effective diameters for melt flow and their relatively thin walls.

To determine an order-of-magnitude estimate of the debris heat flux required to induce tube failure, a heat balance can be applied between the containment at temperature, T_a, and the tube with exterior surface area, $\pi d_o l_o$, containing debris with ex-vessel length, l_o, equivalent diameter, d_e, and heat flux, $\ddot{q}_d$. Writing the resulting expression in nondimensional terms yields

$$\left[\frac{\ddot{q}_d}{\varepsilon_t \sigma T_a^4}\right] = \left[\frac{1}{d_e/d_o}\right]\left[\frac{T_{t/f}^4 - T_a^4}{T_a^4}\right] \quad (4\text{-}34)$$

Assuming a containment temperature of 400 K and using tube material properties in Appendix F, Equation (4-34) was evaluated to construct the failure map shown in Figure 4-23. The failure region is separated from the intact region in Figure 4-23 by boundaries that are dependent upon tube material composition. As previously discussed, there are limited data for predicting tube material ultimate strength at high temperatures. Hence, subregions in Figure 4-23 indicate possible lower boundaries for each tube material's failure region. Note that uncertainty related to the boundary for SA105/SA106 is largest in this figure because there are no data for this material

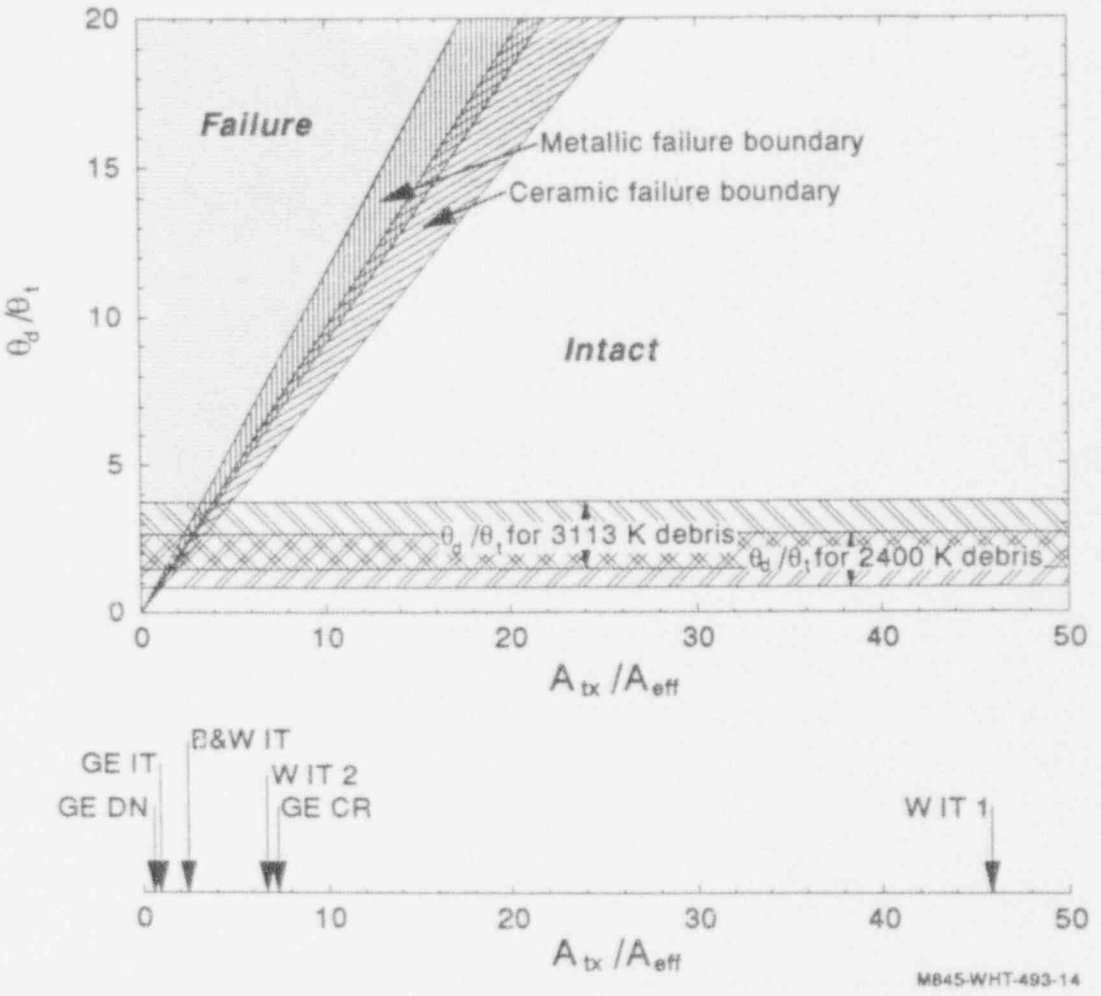

Figure 4-22. Dimensionless temperature plot from heat balance between penetration and debris.

above 1150 K.[h] Hence, there is more uncertainty in predicting the ultimate strength of this material at high temperatures than for stainless steel and Inconel, for which tests at 1373 K were performed. Upper bounds for estimating failure boundaries are based on tube material melting temperatures. On the lower x-axis, the ratio, d_e/d_o, has been evaluated using the penetration dimensions from Appendix F. As shown in Figure 4-23, larger heat fluxes are required to fail thicker walled tubes with smaller effective diameters for melt flow, such as instrument guide tubes in Westinghouse plants and the BWR control rod guide tube. Furthermore, results in Figure 4-23 indicate that the BWR drain line may be more susceptible to ex-vessel tube failure because of its relatively high d_e/d_o ratio and because of uncertainty related to ultimate strength behavior for the drain line SA105/SA106 carbon steel.

h. INEL SA106 tests were not performed for temperatures above 1150 K. This temperature was well above the 1000 K value where previous data indicated that the ultimate strength of this material becomes negligible. However, test results (see Appendix B) indicate that the ultimate strength of SA105/SA106 material is 60 MPa at 1150 K. Although there was no higher temperature data available for the SA105/SA106 steel, its ultimate strength was extrapolated based on some data for SA533B steel.

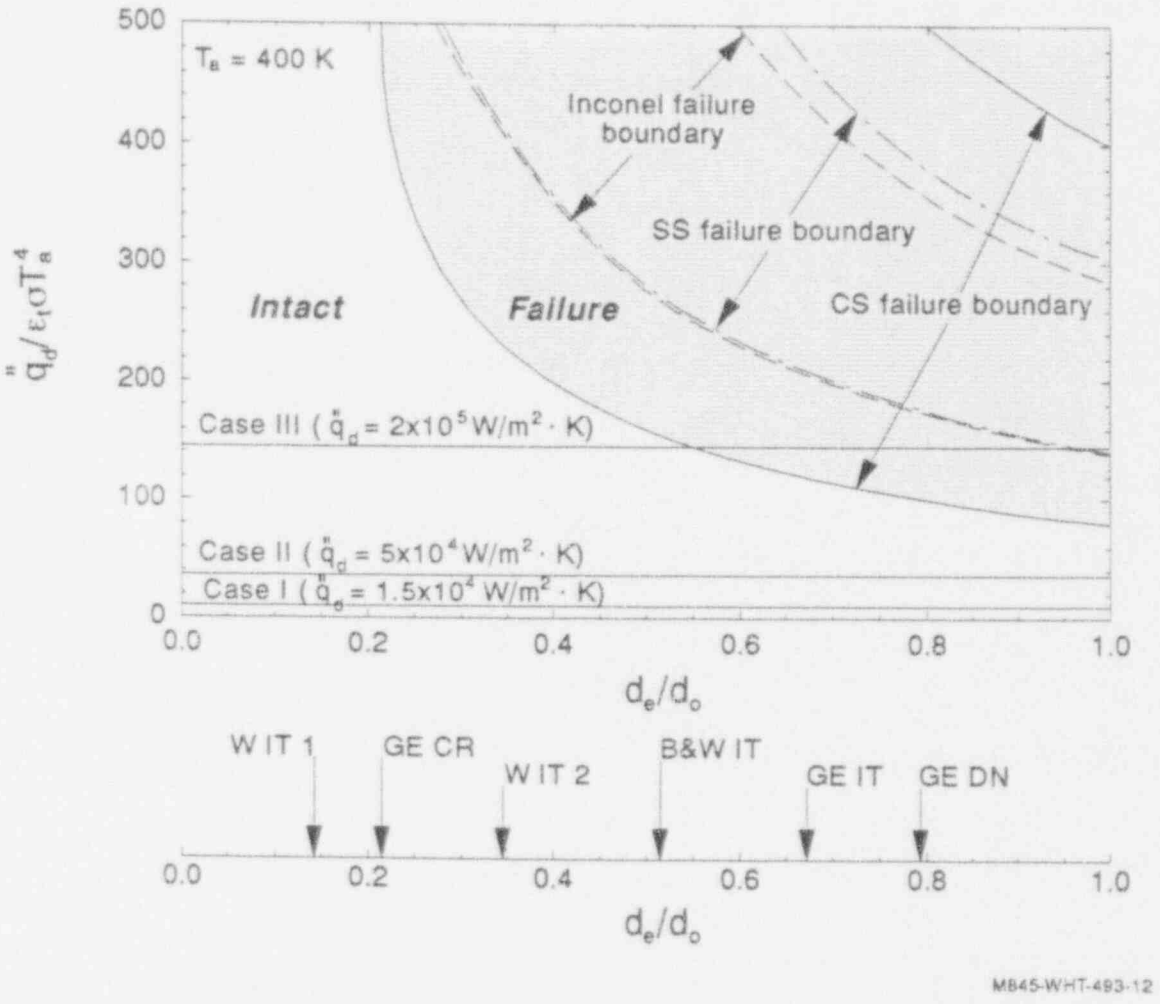

Figure 4-23. Dimensionless plot illustrating melt heat fluxes required to induce tube failure.

Horizontal lines are plotted in Figure 4-23 that correspond to the three postulated debris conditions considered in Section 4.1.1.2.3: (a) Case I debris properties were selected to represent material that is a primarily metallic slurry; (b) Case II debris properties were selected to represent material that is a primarily ceramic slurry; and (c) Case III debris properties were selected to represent a molten pool of primarily ceramic debris. Typical debris heat fluxes for each of these cases were estimated based upon SCDAP/RELAP5 results from Section 5 and Reference 4-6. Results in the failure map indicate that penetration failure is predicted only for the GE drain line penetration and for cases with heat fluxes higher than Case II (i.e., heat fluxes must exceed 5×10^4 W/m^2).

4.1.2.6 Penetration Tube Heatup and Failure Analysis Summary. The thermal response of lower head penetrations in contact with molten corium debris has been characterized using simplified models and closed-form solutions to assess governing thermal conditions. Analyses were performed to identify important trends and governing conditions leading to in-vessel tube failure. Although results are preliminary, they do provide insight into the timing of in-vessel tube failure, melt velocity, penetration distance through a failed tube, and requirements for ex-vessel tube failure. Reactor-specific differences in the potential for tube failure have been identified, where possible.

Based upon these analyses, the following conclusions can be drawn:

- *Thermal Relaxation and Tube Melting Times.* The time required for the thermal front from the hot debris in a tube to penetrate lower head tube walls is less than ~20 seconds. Tube melting times are somewhat longer, ranging from 3 to 25 minutes, depending on tube thickness.

- *In-Vessel Tube Melting.* The ratio of the tube-to-debris mass in the lower head governs in-vessel tube melting. Since BWR vessels have a larger number of penetrations, higher temperature debris is needed to cause in-vessel tube failure. For example, in cases where no coolant is present in the reactor vessel lower head, ceramic debris temperatures greater than 1700 K are required to induce tube melting in a PWR, where only instrumentation tubes penetrate the lower head; whereas ceramic debris temperatures in excess of 2000 K are required to induce tube melting in a BWR lower head.

- *Gravity- and Pressure-Driven Melt Velocities.* For cases in which only gravity forces act upon melt in a penetration tube, melt velocities between 1 and 3 m/s are predicted, with higher velocity melts being predicted for a BWR drain line penetration tube because of its larger effective diameter available for melt flow. For cases where a pressure gradient exists such as in the air-filled channel at atmospheric pressure within a BWR instrument tube, velocities of nearly 45 m/s are predicted to occur.

- *Melt Penetration Distance.* Two models were used to predict melt penetration distance: a modified bulk freezing model, which assumes that melt flow is sufficiently turbulent to preclude crust formation so that convection heat transfer dominates; and a conduction model, which assumes crust formation occurs along the tube outer wall so that conduction heat transfer dominates. Model results differ for certain cases. For cases where melt velocities are affected only by gravity, the conduction model predicts that melt will travel below the lower head for all LWR lower head penetrations; whereas the modified bulk freezing model predicts that melt will not travel below the lower head unless the tube has a fairly large effective diameter for melt flow and/or the tube has been ablated within the vessel at the point near the vessel inner surface. However, both models predict that melt will travel below the lower head for the GE drain line penetration, which has a fairly large effective diameter for melt flow and no in-vessel structures. Furthermore, both models may predict that melt travels below the lower head through other penetrations if the tubes are ablated near the vessel and if the melt is driven by a large pressure gradient, such as the pressure difference between RCS operating pressure and the inner channel within instrument tubes.

- *Ex-Vessel Tube Failure.* For depressurized conditions, thermal equilibrium calculations indicate that thin-walled penetrations with larger effective diameters for melt flow, such as the GE BWR drain line penetration, are more susceptible to failure after melt penetrates beyond the vessel outer wall. Higher debris temperatures are required to induce tube failure if the debris is metallic rather than ceramic. Although additional data are needed to quantify ultimate strength behavior for the SA105/SA106 material used in BWR drain lines, longer term steady-state temperature estimates indicate that this lower head penetration is more susceptible to ex-vessel tube rupture than other LWR penetrations. Results indicate that heat fluxes characteristic of primarily ceramic debris (i.e., in excess of 0.05 MW/m^2) are needed to induce failure in a BWR drain line tube, which is composed of SA105/SA106 steel and has a relatively large cross-sectional

area for melt flow. Heat fluxes characteristic of molten ceramic debris (i.e., as high as 0.2 MW/m^2) were not predicted to fail any of the other LWR penetrations.

In summary, models with closed-form analytical solutions have proved successful in predicting trends for melt progression and tube heatup. Section 5 presents results from finite element calculations, that were performed to determine if simplifying assumptions used in these analytical models are adequate for predicting penetration response. Examples illustrating the application of these failure maps are also presented in Section 5.

4.1.3 Penetration Tube Ejection and Rupture

Penetration tube failure can be divided into the two categories: tube ejection out of the vessel lower head and rupture of the penetration tube outside the vessel. Tube ejection (see Figure 4-24) begins with degrading the penetration tube weld strength to zero as the weld is exposed to temperatures that range up to melting and then overcoming any binding in the hole in the vessel wall that results from differential thermal expansion of the tube and vessel wall. Tube rupture, (see Figure 4-25) assumes the debris bed has melted the instrument tube inside the reactor and melt migrates down into the tube to a location outside the vessel wall where a pressure rupture can occur, thus breaching the pressure boundary.

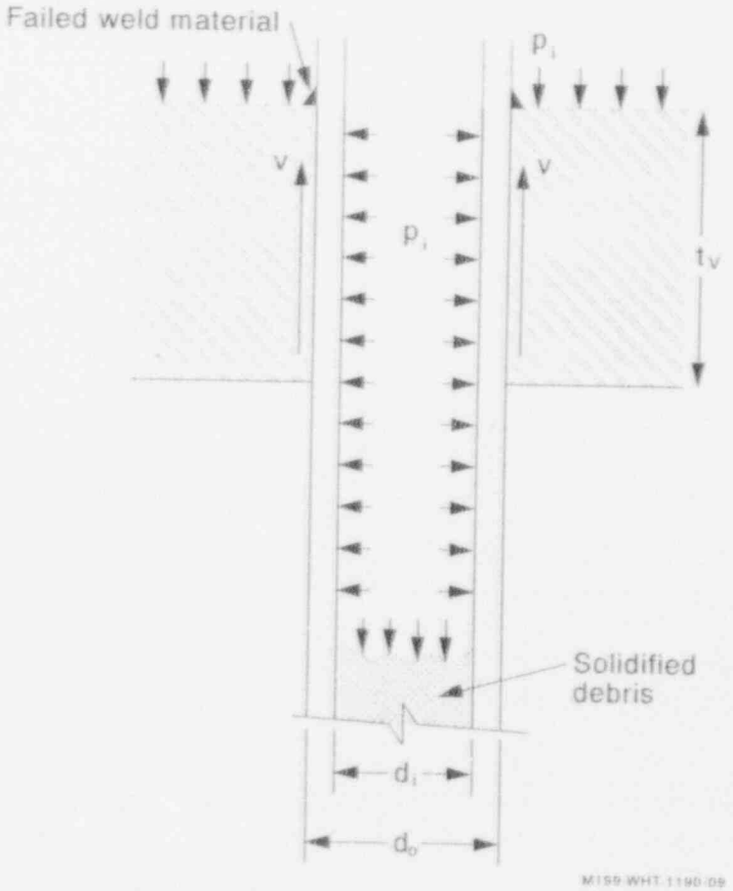

Figure 4-24. Penetration tube ejection mechanism.

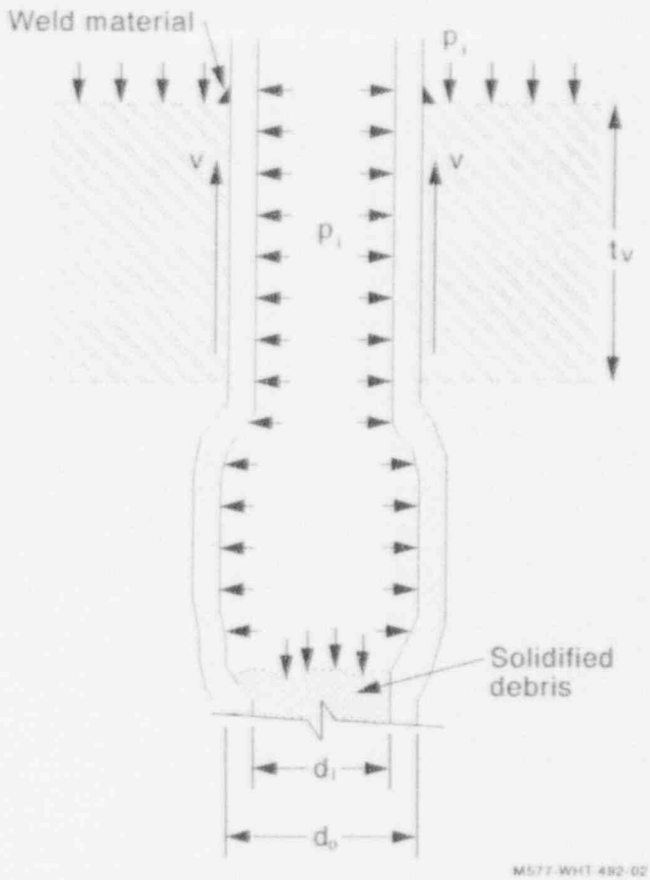

Figure 4-25. Penetration tube rupture mechanism.

This section looks at the conditions required to achieve these failure modes based on the temperature-dependent degradation of the tube material's ultimate strength. Both of these failure modes are caused by exposure of the penetration tube concurrently to molten debris bed temperatures and reactor system pressure. Since consideration of material creep under these conditions can result in lower failure capacities that are dependent on particular scenarios of time duration at elevated temperature levels, this analysis should be considered an upper bound on component failure capacity and should be used to offer general insight into the relative pressure/temperature failure levels of these penetrations and the vessel itself.

4.1.3.1 Methodology. Most reactor pressure vessels (RPVs) designed by three major nuclear steam supply system (NSSS) vendors (Westinghouse, B&W, and GE)[i] have penetrations in their lower heads. All three designs have in-core instrument guide tube penetrations, while GE's BWR vessels also have control rod guide tube penetrations and a small external nozzle that is attached to a drain line outside the vessel. Figures 3-10 through 3-12 show sections of lower head penetrations.

Typically, the instrument guide tube penetrations consist of a tube inserted through a vertical hole in the lower head and welded to the vessel at the inner surface of the RPV. In the

i. As discussed in Section 3, most CE reactor vessels have no lower head penetrations.

case of B&W plants, a thickened internal nozzle is welded to the penetration tube at this weld location while the other plant designs have a continuous tube extending up into the lower plenum region of the vessel.

Control rod guide tube penetrations in BWRs are typically formed by boring the hole for the guide tube, drilling a countersink for a stub tube that surrounds the guide tube on the inner surface of the vessel, inserting the guide and stub tubes, and welding the guide tube to the upper end of the stub tube. Control rod guide tubes provide much of the support of the BWR reactor core. Ejection of these tubes is precluded by a support system below the reactor that is engaged once the tube has displaced about 3 cm. Thus, ex-vessel tube rupture is the only failure mode to be considered for the control rod guide tubes.

A BWR drain line nozzle is welded on the outside of the vessel. Hence, ex-vessel tube rupture is also the only failure mode to be considered for the drain line nozzle.

To facilitate the insertion of the tubes into the holes in the vessel head, tolerances are set by design for the outer diameter of each penetration tube and the diameter of each hole in the vessel head. The resulting radial gap range must, therefore, be considered in tube ejection analyses. Typically, the instrument guide tubes for PWRs are Inconel, while those of BWRs are stainless steel. The BWR control rod guide tubes are also stainless steel, and the drain line is SA105/SA106 carbon steel. Geometric and material data used in the model are included in Appendix F.

Figure 4-26 illustrates the thermal and mechanical loading and the generalized geometry of the tube and vessel wall. It is assumed that the tube is breached and that internal pressure acts on the tube walls. Downward axial loads are imposed from pressure acting on solidified debris, a tube elbow or tube end. In order for the tube to eject, this downward force must first overcome the resistance of the weld connecting the penetration to the vessel. Assuming the weld fails, the downward force must then overcome frictional resistance from the interference fit between the tube and the vessel for ejection to take place.

Instantaneous weld failure occurs when the weld effective stress exceeds its ultimate strength. It should be noted that time-dependent creep rupture can occur at lower loads than ultimate strength. Because the pressure area for a downward tube load is small and the tube weld is relatively large, low stresses are expected in the weld, making instantaneous failure most likely at very high temperatures in a region where structural material data must be extrapolated.

Initially, resistance to tube ejection arises from the penetration weld. It is assumed that the weld carries this downward load in shear. Figure 4-27 shows a schematic of the weld geometry, applied loads, and resultant shear stresses in the weld. Here, it is conservatively assumed that the tube melts off at the inside surface of the vessel inside cladding. As such, pressure area calculations use the outer diameter of the tube, and shear area calculations neglect the material associated with the weld buildup above the vessel cladding surface. Weld dimensions in the axial direction, which are taken from plant drawings[j] or from ASME code minimums,[4-17] are listed in Appendix F.

---

j. Babcock & Wilcox drawing, October 4, 1991.

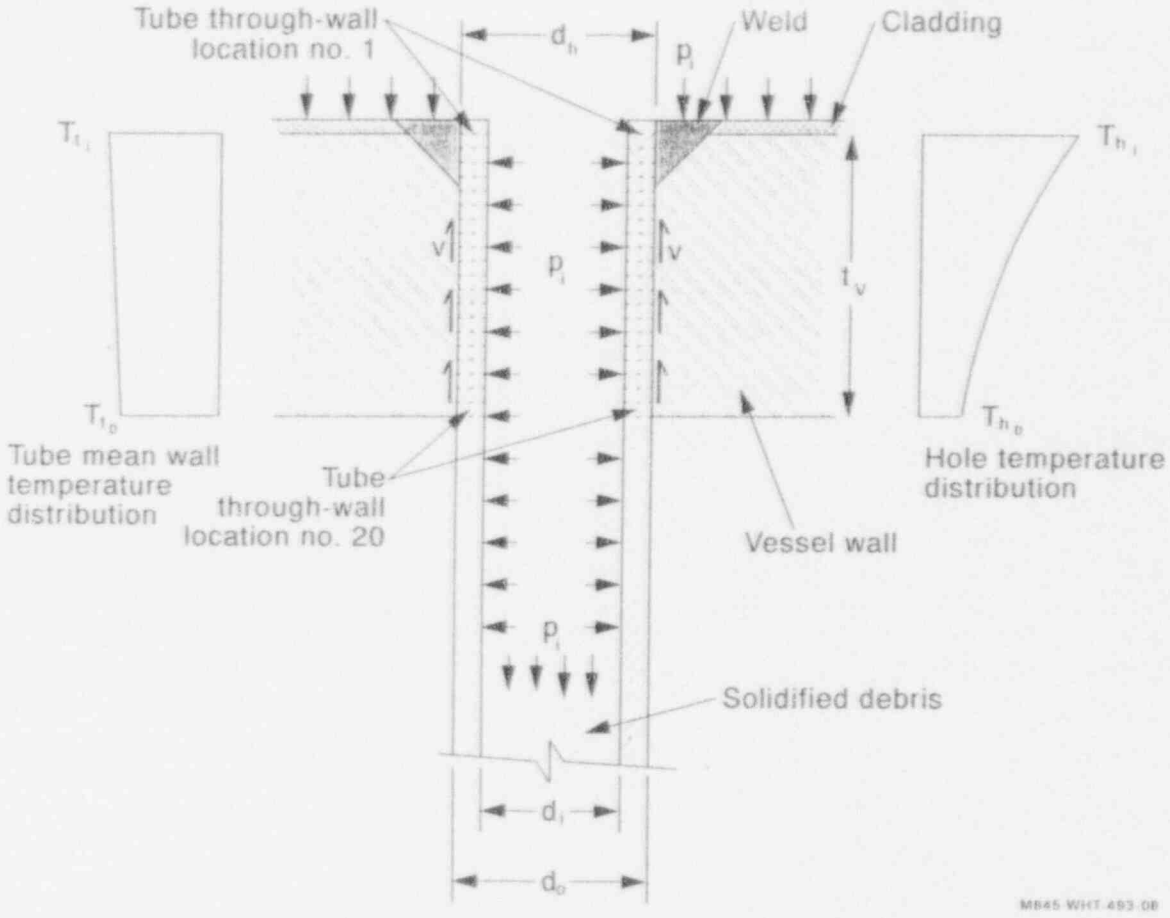

Figure 4-26. Idealized penetration tube and RPV wall with temperature.

In Table 4-4, Equations (1) through (3) are applicable to the weld failure analysis. Shear stress is calculated from the pressure, pressure area, and shear area. Effective, or Mises, stress (σ_e) is calculated assuming pure shear and compared with the temperature-dependent ultimate strength. If weld failure does not occur, penetration ejection is precluded. However, if it is concluded that the weld fails, then the only mechanism resisting the ejection is the expansion of the tube in the hole, which causes a friction force buildup through the vessel wall.

Figure 4-28 illustrates the free body diagram of the ejection forces acting on the tube. The resulting equilibrium equation provides a means of measuring ejection, which is achieved when the following inequality is true:

$$p_i \pi r_o^2 > V_t \qquad (4\text{-}35)$$

where

$$V_t = \int_0^{t_v} v\,dx \quad .$$

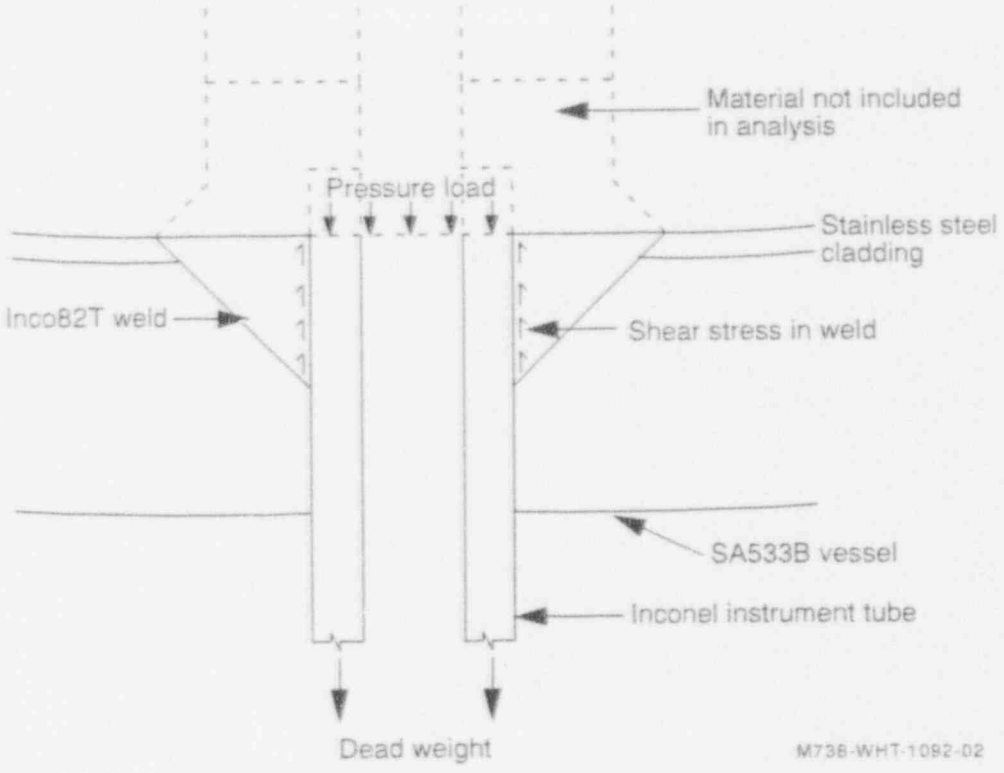

Figure 4-27. Schematic of instrument tube penetration showing applied loads, shear stress and weld buildup material.

Table 4-4. Equations of the tube ejection/rupture and lower head global rupture models.

Weld Failure Equations

1. Shear stress on the weld

$$\tau_w = \frac{p_i \pi r_o^2}{2\pi r_o L_w} = \frac{p_i r_o}{2L_w}$$

2. Effective stress

$$\sigma_e = \sqrt{3}\ \tau_w$$

3. Weld Failure

$\sigma_e \geq \sigma_u$ (failure)

Table 4-4. (continued).

Tube Ejection Equations

4. Free thermal expansion of tube and hole[a]

a. $\Delta r_o^T = r_o \cdot \alpha_t \cdot (T_t - T_{ref})$ $\quad T_{ref} = 294\ K\ (70°F)$

b. $\Delta r_h = r_h \cdot \alpha_h \cdot (T_h - T_{ref})$ $\quad T_{ref} = 294\ K\ (70°F)$

5. Pressure expansion of tube[a]

$$\Delta r_o^P = \frac{p_i}{E} \frac{r_o \cdot r_i^2 \left(2 - \nu_t\right)}{\left(r_o^2 - r_i^2\right)}$$

6. Total expansion of tube

$$\Delta r_o = \Delta r_o^T + \Delta r_o^P$$

7. Tube-hole radial gap at temperature and pressure

$$\delta_i = \left(r_h + \Delta r_h\right) - \left(r_o + \Delta r_o\right)$$

where + ⇒ gap

− ⇒ interference

8. Tube-hole interface pressure[a]

$$\delta_i < 0 \quad P_{th} = \text{lesser of} \begin{cases} \dfrac{\delta_i \cdot E \left(r_o^2 - r_i^2\right)}{r_o \left[r_o^2 \left(1 - 2\,\nu_t\right) + r_i^2 \left(1 + \nu_t\right)\right]} \\ \dfrac{2}{\sqrt{3}}\, \sigma_u \ln\left(\dfrac{r_o}{r_i}\right) \end{cases}$$

$$\delta_i \geq 0 \quad P_{th} = 0$$

9. Incremental thermal binding shear[a]

$$(\Delta v)_n = (f_t \cdot P_{th} \cdot 2\,\pi\, r_o \cdot \Delta l_t)_n$$

Table 4-4. (continued).

10. Total thermal binding shear

$$V_T = \sum_{n=1}^{20} (\Delta v)_n$$

11. Ejecting pressure force

$$F_p = p_i \pi r_o^2$$

12. Ejection

$$F_p > V_T$$

Tube rupture equation

13. Tube rupture[b]

$$p_i \geq \frac{2}{\sqrt{3}} \sigma_u \ln\left(\frac{r_o}{r_i}\right)$$

Global head rupture equations

14. Ultimate membrane capacity for vessel wall

$$N_c = \sum_{n=1}^{20} (\sigma_u \Delta t_v)_n$$

15. Membrane load on vessel wall caused by internal pressure, p_i

$$N_p = p_i \frac{R_m}{2}$$

16. Lower head global rupture

$$N_p > N_C$$

a. Material properties are evaluated for the temperature of the component (tube or vessel head) at the radial location of the increment, n. The incremental in-vessel length of the penetration tube is Δl_t.

b. Ultimate strength evaluated at the extreme outer increment of the vessel wall, n = 20.

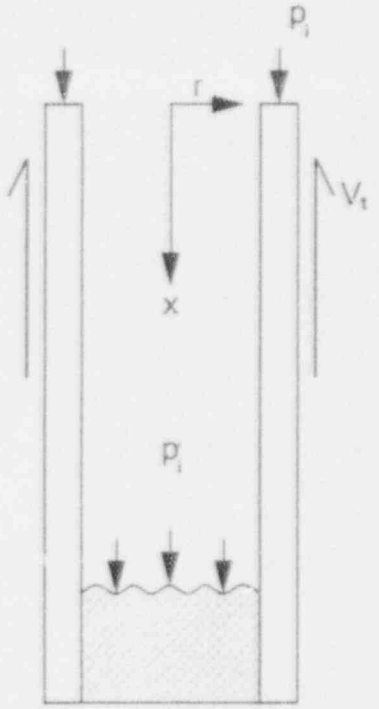

M519-WHT-292-12

Figure 4-28. Ejection model free body diagram.

Here the frictional shear, v, is a function of internal pressure, hole and tube temperature, hole radius, tube inner and outer radius, friction coefficient between the tube and hole, coefficients of thermal expansion, Poisson's ratios, and elastic moduli of the head and tube materials. Some of these parameters vary significantly with temperature, which varies radially through the vessel wall and, therefore, causes the frictional shear function to vary radially. Because instrument guide tubes are quite long and flexible outside the reactor vessel, no support of the tube outside the vessel wall is assumed to resist nozzle ejection. Control rod guide tubes, which cannot totally eject, are not considered for this mechanism. The total frictional shear force available to resist tube ejection, V_t (MPa) in Figure 4-28, is the integral of differential shear forces, vdx, across the vessel wall thickness.

This differential shear force is simplistically assumed to be the result of an interference pressure developed between a short length of thick-walled cylinder (the tube) and a surrounding rigid jacket (the vessel wall). Each expands separately because of the local temperature and, for the tube, pressure loads. Penetration hole dilation resulting from pressurization of the lower head is not considered here because its effect on the results, as will be seen, is small. Closed-form solutions[4-18] are then used to calculate interface pressures required to force the outer diameter of the tube to conform to the diameter of the hole in the vessel wall after free expansion. However, this pressure is limited to the pressure required to cause compression failure of the tube material throughout its wall thickness.[4-19] When this pressure limit is reached in a given segment of the tube (calculations are made at 20 segment locations along the axis of the tube in this model), that segment is no longer assumed to contribute to the tube's resistance to the ejection force. Pertinent equations used in the model are listed in Table 4-4.

Ambient temperature (294 K) dimensions are used as reference values for calculations of thermal expansion on each increment. This assumption is equivalent to slicing the tube into 20 short segments, or rings, and determining the total force required to push those rings out through the hole in the vessel wall. Expansion calculations at each increment are based on mean wall temperatures in the tube and the local vessel temperature at the corresponding wall depth. Although the model will allow these two component temperatures to be distributed in any fashion along the axis of the tube, the calculations for developing the failure maps in this section used a linear distribution for the tube temperatures, T_t, and a radial distribution representative of steady-state heat transfer out of the head, T_h, for the vessel wall material. From the thermal analyses described in Section 4.1.1 for the anticipated range of accident conditions, it is seen that the ratio of the inner wall to the outer wall temperature of the vessel, T_{ho}/T_{hi}, remains somewhat constant over the duration of the accident history. With this in mind, this analysis varies the inside vessel wall temperature and defines an outside wall temperature such that T_{ho}/T_{hi} remains constant and characteristic for the given accident addressed. Failure maps in this section were developed using T_{ho}/T_{hi} characteristic of the molten pool, ceramic slurry, and metallic debris bed temperature distributions obtained in Section 4.1.1. Those ratios are listed in Table 4-5.

The ultimate strength and elastic modulus of the tube material and coefficients of thermal expansion of the tube and vessel are temperature-dependent material properties. These material properties are not always available for elevated temperatures. The model linearly extrapolates from known property values, when necessary, to estimate those at elevated temperatures. For example, the ultimate strength data are extrapolated linearly to zero strength at melting from highest known temperature data points. The frictional coefficient is not a function of temperature, but is related to the roughness of the sliding surface. This parameter is highly variable, but one source[4-20] indicates that it could be about 0.27 for high-temperature, oxidized conditions.

The model calculates any radial gap (+) or interference (-) between the outer radius of the tube and the hole radius, calculates the pressure at the interface required to make the tube conform to the final hole radius, and multiplies that pressure by the incremental surface area of the interface and the assigned friction coefficient for that increment to arrive at an incremental friction force. Checks made at each increment show if the compressive interface pressure is greater than that required to cause complete plasticity throughout the tube wall. Interface pressures are not allowed to exceed that value. Finally, all 20 incremental forces are summed and compared with the force resulting from internal pressure acting on the outside surface of the tube.

The tube rupture equation is Equation (13) in Table 4-4. The model calculates the internal pressure required to rupture a cylinder, the tube with end effects ignored, whose material ultimate strength is evaluated at the local tube temperature near the outer radius of the vessel lower head,

Table 4-5. T_{ho}/T_{hi} ratios used to develop failure maps.

Debris bed	PWR	BWR
Molten pool	0.73	0.63
Ceramic slurry	0.88	0.83
Metallic	0.94	0.91

T_{to}, in Figure 4-26. This rupture pressure is then compared with the system operating pressure, which is an input parameter for the model, to determine whether conditions are sufficient to rupture the tube outside the vessel wall.

4.1.3.2 Tube Ej :tion/Rupture Failure Map Development. Penetration failure modes can be subdivided into two categories: (a) penetration tube ejection and (b) ex-vessel rupture of the penetration tube. Because the tube ejection failure mode requires that the penetration weld fail first, an evaluation of that weld's capacity was performed first. Weld failure curves were developed for typical instrument guide tubes designed by B&W, Westinghouse, and GE. Because drawings were readily available for TMI-2, the specified weld length was used on the B&W weld analysis, while minimum ASME code weld lengths, which are listed in Appendix F, were used for the Westinghouse and GE plant calculations.[4-17] Calculations for constructing weld failure curves were performed using the equations listed in Table 4-4 and temperature-dependent ultimate strength data listed in Appendix B of this report. The entire weld was conservatively assumed to be at the inner vessel wall temperature.

Once weld failure bounds were evaluated, the ability of the tube to bind in the vessel penetration hole was considered to see if ejection could be restrained beyond those limits. Failure curves were developed using the equations in Table 4-4 and the methodology discussed in the previous subsection for typical in-core instrument guide tubes designed by B&W, Westinghouse, and GE. The weld failure curve and the tube binding curve were then compared to determine the upper envelope of the two. This upper envelope, which composes the instrument tube ejection curve, was then compared with the failure curve of instrument tube rupture. The lower envelope of tube ejection and tube rupture then became the instrument guide tube failure curve that is compared with vessel global rupture in the following section.

The failure maps were developed by assuming a radial temperature distribution (with respect to the vessel head) in the vessel head just outside the tube that represents a steady-state heat transfer distribution through the head for the metallic melt and the ceramic slurry debris bed conditions and a transient distribution for the molten pool condition, given some wall inner surface temperature. Concurrently, that same inner surface temperature was assumed to be the average radial temperature of the penetration tube wall at the inner radius of the vessel, T_{ti} (Figure 4-26). A linear distribution along the length of the tube through the vessel wall was assumed with the temperature in the tube at the outside radius of the head being 30 K lower (see Figure 4-26). Given this combination of temperature profiles, operating system pressure and temperature at the vessel inner wall were varied until the tube was ejected according to the inequality in Equation (4-35) and the tube ruptured according to Equation (13) in Table 4-4. Tube rupture was evaluated at temperatures corresponding to those in the tube at the outer radius of the vessel head. Instrument guide tube failure curves have been plotted with lower head global rupture curves for each corresponding reactor type and, for the BWR vessel, the drain line and the control rod guide tube failure curves. As discussed in Section 4.1.3.1, failure will occur only via tube rupture for these latter two penetrations. This comparison of failure curves maps the failure and safety regions in terms of the vessel wall inner surface temperatures and the operating system pressure, which are the critical parameters affecting all these failure modes. Further discussion for these failure maps is deferred to the following section on global rupture.

During the course of this analysis, several observations from parameter studies indicate the sensitivity of the problem to various parameters involved in the calculation. Before this exercise, tube ejection was expected to be highly sensitive to the coefficient of friction used in the analysis. However, variation of this parameter from 0.27 to 0.6 typically changed the positions of ejection failure curves less than 5% along the temperature axis of the failure map. All tube failure modes

are insensitive to vessel head thickness. Tube weld failure has little or no dependence on head thickness because the temperatures in the weld analysis were those of the inner surface of the vessel wall only. Because of the small axial temperature differential assumed in the tube for the ejection analysis (30 K), temperatures in the tube closely tracked the inner vessel wall surface temperature, no matter what the vessel thickness. For the same reason, tube rupture analysis temperatures also closely tracked the vessel inner surface temperatures and desensitized vessel thickness effects on the failure curve.

Tube failures occur as a result of the ultimate strength reducing, because of the higher temperatures, to a point at which it is exceeded by the, albeit low, pressure-induced stresses. There is some uncertainty in the actual ultimate strength values to be used at these high temperatures. It is estimated that strength data could vary enough to result in an uncertainty band of 200 K about the tube failure curves developed. The GE tubes show the most sensitivity to pressure, which can be attributed to their lower r_o/r_i (values for this parameter are listed in Table 4-6). Variation of the gap size within the tolerance ranges affects only the temperature at which tubes can wedge in the vessel. Because the weld has to melt before binding need be considered, the relevant tube binding analysis temperatures are very high. Small gaps are closed, but tube strength is degraded by temperature so severely by then that very little margin is gained by considering binding in the hole.

Tube ejection does not seem to vary with respect to the shape of the radial temperature distribution in the vessel wall. Figure 4-29 indicates the shape of the temperature distributions for the vessel wall, or hole. The profile was modified to that shown in Figure 4-30 to reflect the shape expected in the wall at some time before steady-state heat transfer conditions are reached in the lower head. Comparison of failures developed with these two sets of conditions indicated little change in the tube failure curves. This is because the binding force is caused primarily by the thermal and pressure expansion of the tube. Axial tube temperature was assumed to vary little because the debris temperature inside the tube was not expected to vary significantly over the length of tube penetrating the vessel wall. The most sensitive parameters in these tube ejection calculations are the lower head inner wall temperature and the ultimate strength of the tube material, which limits the binding force between the tube and vessel head.

For this analysis, Young's modulus and ultimate strength values (which are temperature dependent) were linearly extrapolated beyond existing test data to zero at material melting temperatures. Plots of these data are included in Appendix F. The tube ejection curves and the tube rupture curves tended to form near the tube material melting temperatures.

Table 4-6. Dimensionless parameters for penetration tubes analyzed.

	Vendor	Material	r_o/r_i
In-core instrument guide tube	B&W	Inconel	1.71
	W	Inconel	4.16
	GE	Stainless steel	1.32
Control rod guide tube	GE	Stainless steel	1.23
Drain line nozzle at safe end	GE	Carbon steel	1.41

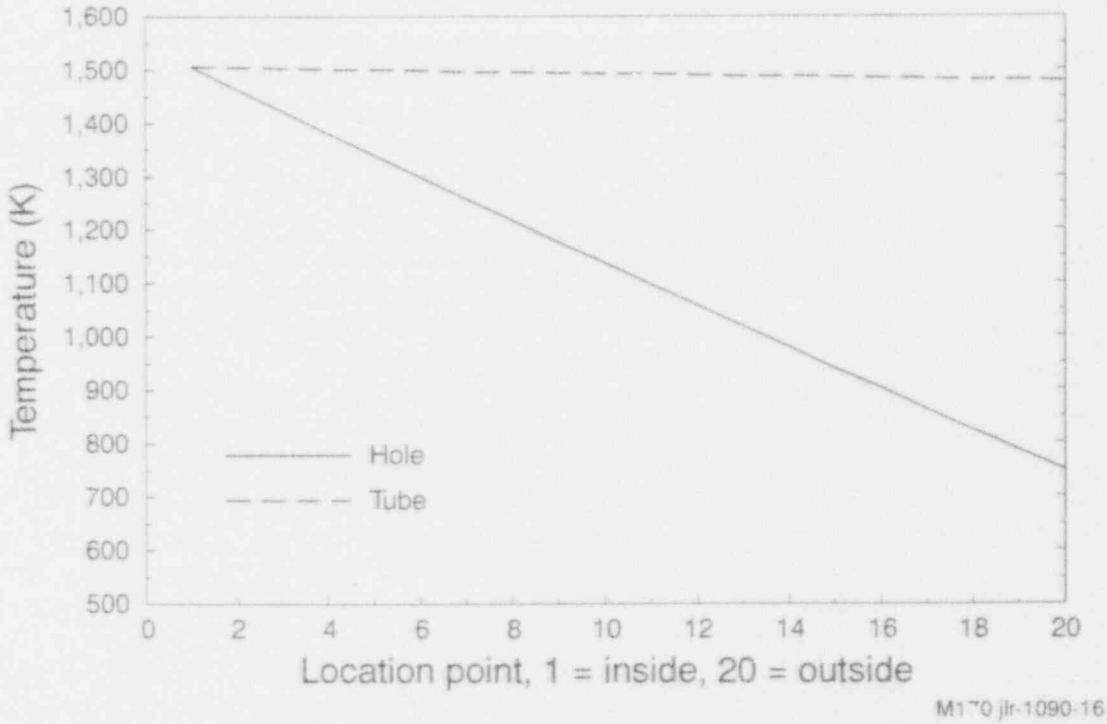

Figure 4-29. Penetration tube and vessel hole temperature profiles for steady-state heat transfer conditions.

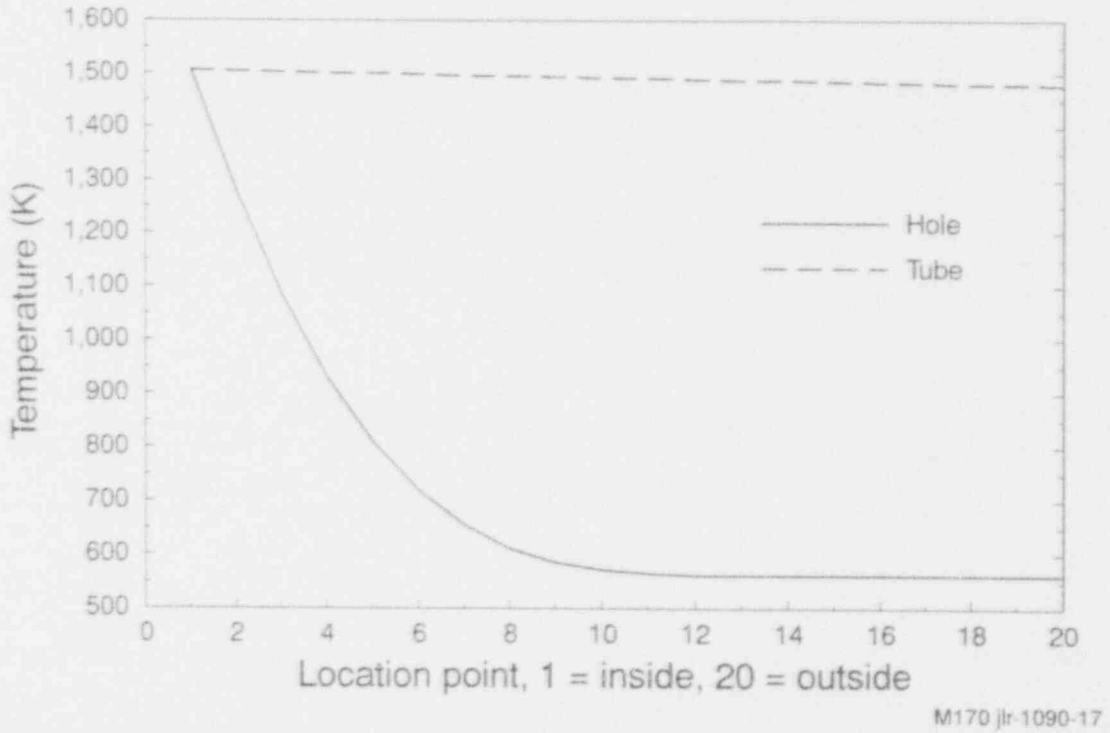

Figure 4-30. Penetration tube and vessel hole temperature profile representative of transient heat transfer conditions in the head.

4.1.4 Lower Head Global Rupture

Previous severe accident analyses for lower heads, in which plastic and creep response of vessel lower heads were calculated with finite element models, have suggested a simpler approach to calculate vessel rupture based solely on radial temperature distribution in the vessel wall and the ultimate strength of the head material at temperature. This simplified approach, discussed in Section 2.3, is incorporated into a model of global head failure to provide some means of comparison between the penetration tube ejection/rupture failure modes and the global head failure mode.

4.1.4.1 Methodology and Failure Map Development. Chambers performed a finite element calculation[4-21] of the vessel lower head to assess the effects of thermal stresses on global head rupture. This calculation did not include creep effects that would affect vessel rupture times. However, Chambers concluded that the failure from sagging and rupture of the lower head could be characterized as a progressive degradation of the hotter inner portions of the vessel wall until the cooler outer portions could no longer withstand the operating system pressure. An EPRI creep rupture study[4-22] discussed in Section 2.3, made this same observation when a creep law was included in its finite element analysis. The EPRI study also suggested a simple approach to estimating time-to-rupture based solely on radial temperature distribution in the vessel wall and the ultimate strength of the head material at temperature. This simplified approach was discussed in Section 2.3 and incorporated into this model of global head failure to compare the penetration tube ejection/rupture failure modes and the global head failure mode.

Three debris configurations are analyzed with parameters from Table 4-5. Because the molten pool reaches temperatures beyond the failure levels for the penetrations in the transient phase of the accident scenario, transient temperature distributions are used in the molten pool calculations. Steady-state heat transfer temperature distributions are used in the other two debris bed configuration analyses. The ultimate strength for SA533B1, as a function of temperature, and the radial temperature profile are used to determine the ultimate membrane load capacity of each of 20 increments of the wall thickness. All incremental ultimate load capacities are then summed to develop a total membrane load capacity for the vessel. This load capacity is then compared with the membrane load generated by the internal pressure, which is an input parameter for the tube ejection/rupture calculation.

The ultimate strength curve for the SA533B1 material comes from an ASTM test[4-23] with additional INEL high-temperature data reported in Appendix B and a linear extrapolation beyond that data to a value of zero at the melting point. Figure 4-31 compares these ultimate strength data with extrapolations used in an IDCOR RPV analysis.[4-22] Note that the ASTM data show higher material ultimate strengths at temperatures below 800 K than assumed in the IDCOR analysis. However, the INEL high-temperature (950–1473 K) ultimate strength drops off much faster than the IDCOR assumptions. Therefore, at high temperatures the RPV lower head has a lower membrane ultimate load capacity than calculated in the IDCOR analysis.

4.1.4.2 Comparison of Global Rupture and Penetration Tube Failure Maps. Global rupture failure curves are compared with the tube ejection/rupture failure curves in Figures 4-32 through 4-34. Three failure curves are plotted for each vessel considered, using the temperature distribution parameters outlined in Table 4-5 that simulate conditions for a molten pool, ceramic slurry, and a metallic based debris bed. Global failure is predicted by this model in the temperature region above each failure curve.

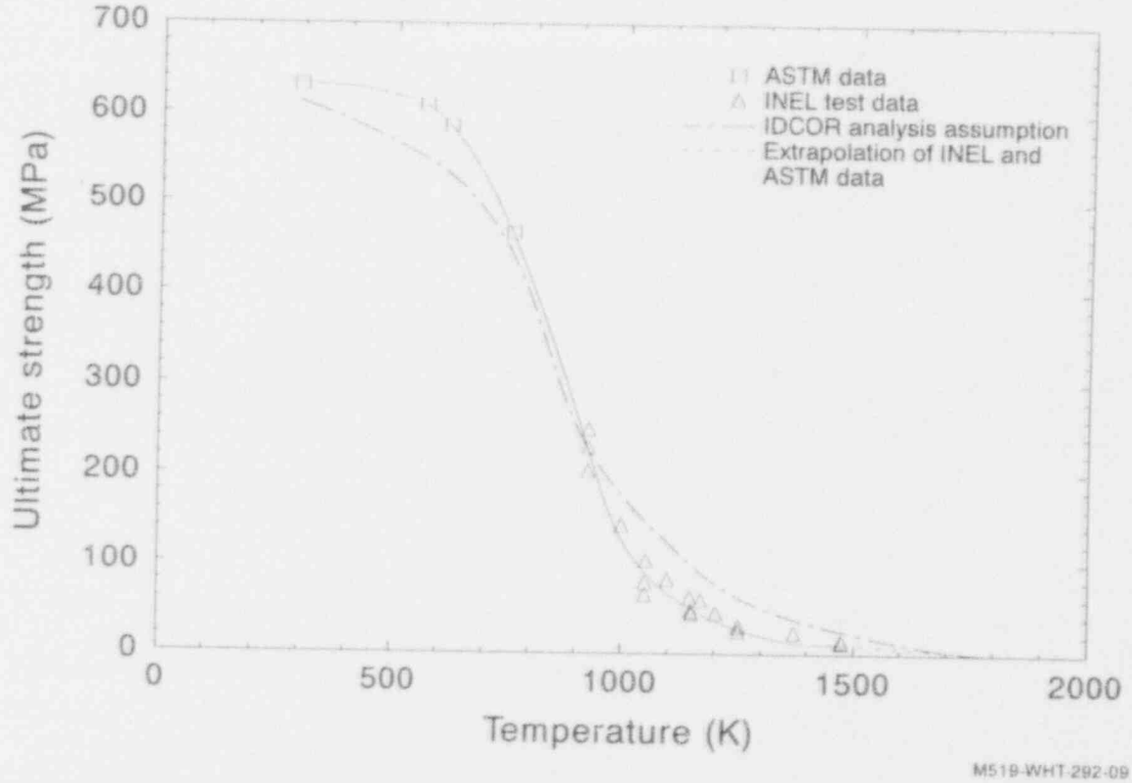

Figure 4-31. Comparison of SA533 ultimate strength data.

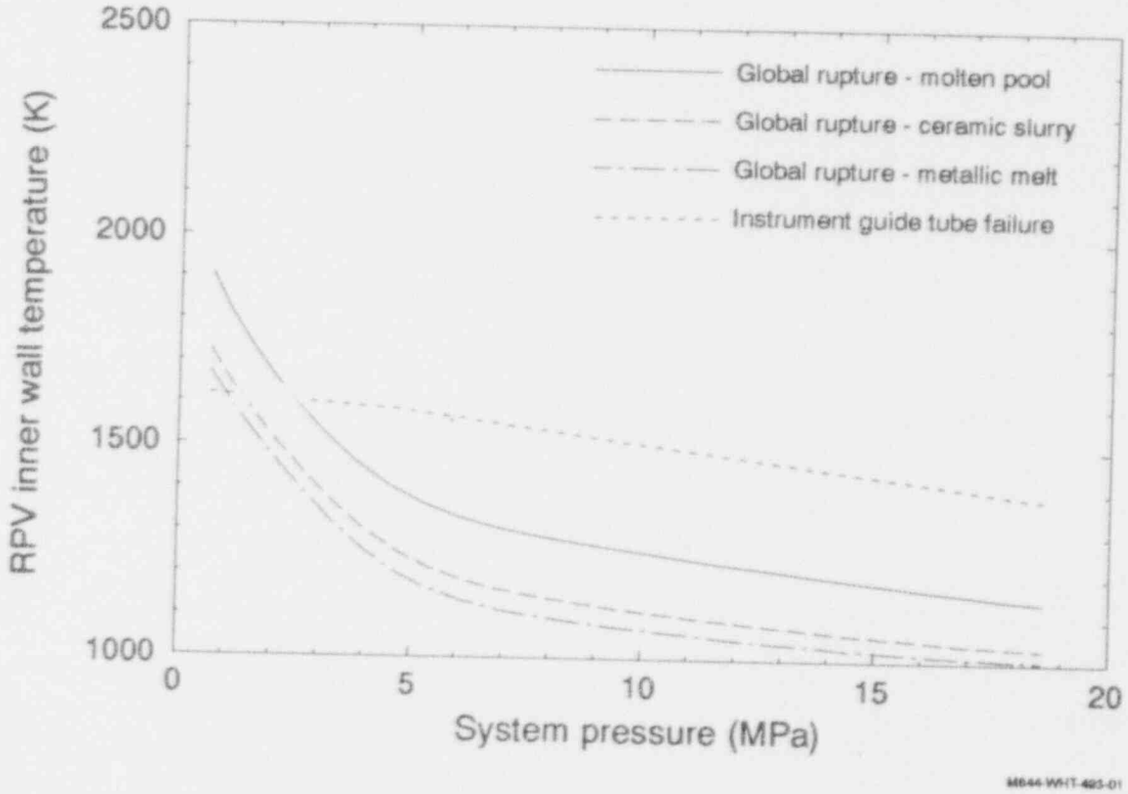

Figure 4-32. Comparison of B&W global rupture and instrument guide tube failure maps.

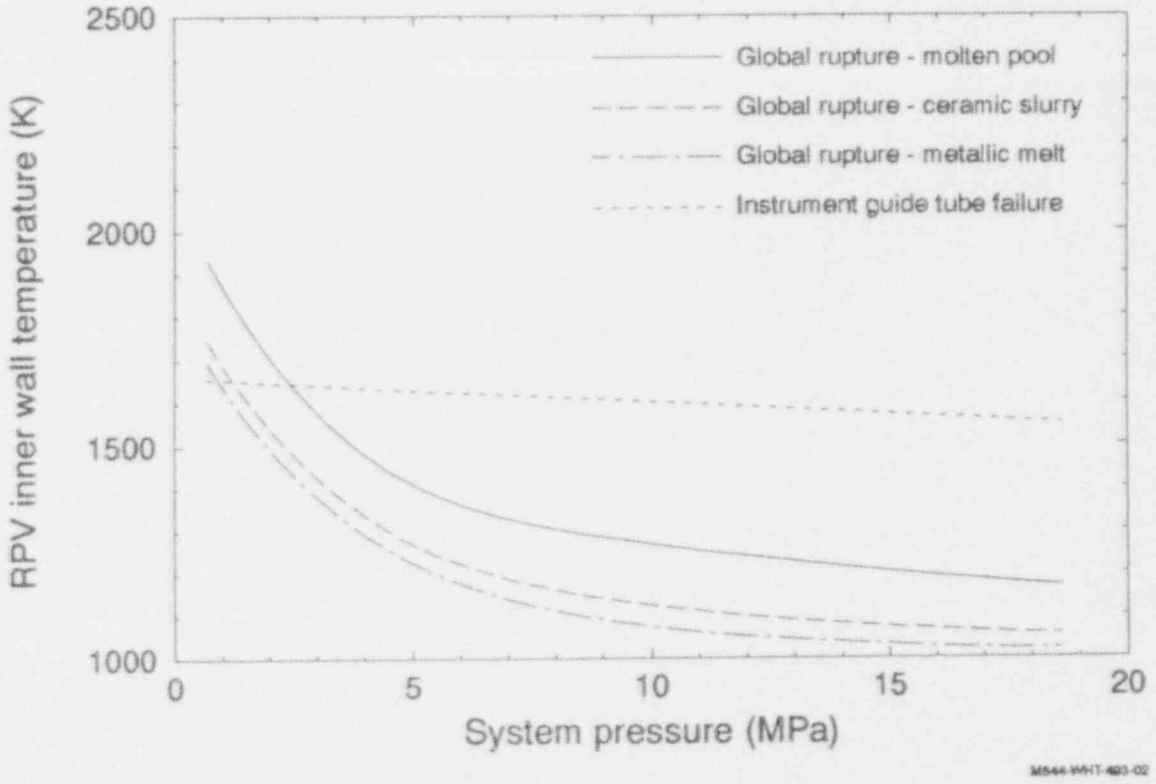

Figure 4-33. Comparison of Westinghouse global rupture and instrument guide tube failure maps.

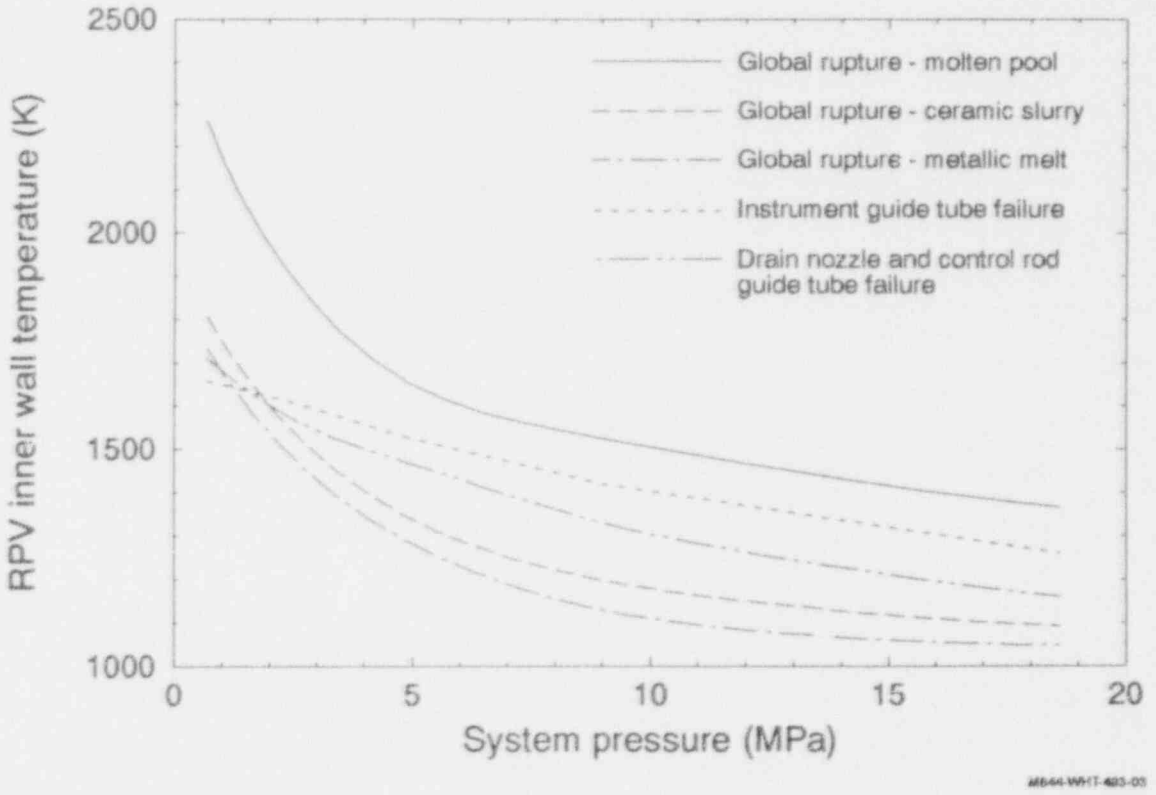

Figure 4-34. Comparison of GE BWR global rupture and instrument guide tube failure maps.

For the PWRs the global rupture failure mode dominates for all but the lowest of system pressures (2 MPa or less), as can be seen in the B&W and Westinghouse failure maps in Figures 4-32 and 4-33. At higher pressures, all three postulated debris conditions result in global rupture of the vessel head. At failure, steady-state wall temperatures, of the inner vessel wall at failure range from about 1600 K at 2 MPa to 1050 K at 14 MPa. To offer a time frame for achieving these inner vessel wall temperatures during the three accidents considered, the molten pool thermal analysis predicted a temperature of 1600 K within 0.7 hour, the ceramic slurry analysis, 1000 K at 1.5 hours and 1600 K within 8 hours, and the metallic debris bed analysis reached a maximum of 900 K at 11 hours.

Instrument tube rupture and ejection failures tended to occur within a 100 K range at low temperatures and to be dominated by the material strength near the tube material melting temperature. However, it should be noted that the estimated uncertainty band in this analysis indicates that no failure mode clearly dominate at the lower pressures.

Comparison of the penetration tube and global failure curves for the three different debris conditions in the GE BWR indicates a different picture of the dominant failure mode. Control rod guide tube and drain nozzle failures map quite closely to one another throughout the system pressure range. Therefore, a mean of those two curves is plotted here for map simplicity. Except for a slightly lower level at the lowest pressures (less than 2 MPa), failure of the penetrations does not control for the ceramic slurry and the metallic debris bed conditions. Weld failure of the instrument tube controls at the low pressures; however, the uncertainty in the analysis would indicate no clear dominant tube failure mode here. For the molten pool debris bed condition, failure is controlled by penetrations throughout the pressure range. However, for the other two debris bed conditions, global rupture of the vessel would dominate.

To offer some sense of timing of the temperature levels reached at the inner surface of the vessel, the molten pool thermal analysis predicted a temperature of 1600 K within 1 hour; the ceramic slurry analysis, 1200 K at 4 hours and 1600 K at 9 hours; and the metallic debris bed analysis reached a maximum of 950 K at 30 hours.

4.1.4.3 Conclusions and Recommendations from Failure Map Analysis. Simple models for global failure of the lower head and penetration tube failure have been analyzed to offer an estimate of vessel and tube capacity in terms of anticipated accident temperature distributions. The failure maps for tube ejection/rupture and global rupture of the lower head provide insight into predicting lower head failure in severe accidents. From analysis of these maps the following conclusions can be made:

1. The failure maps indicate relative pressure-bearing capacities of vessel heads and their penetrations based on ultimate strength. These are expressed as safe operation regions based on reactor system pressure and the inner wall temperature to which a lower head can be exposed in an accident.

2. Except for the molten pool debris bed configuration in a BWR vessel head, global rupture is the controlling failure mode for accidents of higher system pressures (above 2 MPa) in both PWRs and BWRs. While the analyses indicate that penetration tube failure controls below 2 MPa, uncertainties in the analyses do not allow a clear distinction of the controlling failure mode in this pressure range.

3. Tube rupture and tube ejection are highly dependent on the temperature at which the ultimate strength of the tube material reduces to zero, or at least a very small strength

value. The maximum safe temperature for the inner surface of the vessel wall ranges from 1500 to 1700 K for vessel penetration tubes.

4.2 Models Using Simplified Numerical Solution Technique

The phenomena of melt relocation through lower plenum structures and of localized creep rupture have been considered in this study using models with simplified numerical solution techniques. Although these phenomena were considered too complex to consider using closed-form solution techniques, the models described in this section are sufficiently simple that a large number of plant design and reactor thermal condition combinations could be rapidly evaluated.

4.2.1 Jet Impingement

Molten corium is often envisioned to be released from the core region in the form of a cylindrical jet. Melt draining from the core region in a jet mode will break up, disperse, and quench because of interactions with water and the structure present inside the lower plenum. As a jet penetrates through water, it will progressively break up into droplets as a result of hydrodynamic instabilities arising from melt interactions with the surrounding water. This change in form will decrease the amount of melt relocating in a jet mode. In specific instances, the jets may break up completely. The droplets formed by the breakup processes lose energy as they fall through the water and may freeze to become solid particles.

In addition to melt/water interactions, the state and conditions of relocating melt are dependent on melt interactions with the structures found in the lower plenum. The lower plenum region of a light water reactor contains steel structures that distribute the coolant flow, support the weight of the core, and protect in-core instrument lines or control rod drive lines. Pressurized water reactors incorporate perforated horizontal plates that span across all or a significant fraction of the width of the core. Depending on the particular plate hole size, melt will be intercepted and collected by the plate. As the local depth of melt on the plate builds up, melt may spread horizontally and drain through nearby flow holes in the plate thickness (see CCM test results discussed in Section 2.4.2.6). As a consequence, melt that is collected by a plate largely as a single jet can drain from the plate in the form of several jets. The formation of multiple jets in this manner can further enhance the breakup of melt as a result of the formation of greater jet surface area. This process will also modify the jet diameter. Boiling water reactors do not use plates inside the lower plenum, but contain numerous vertical control rod guide tubes and control rod drive housings. Thus, it is possible for melt to relocate from the core pool to the lower head without directly interacting with the guide tubes and housings. However, their presence might still influence arrival conditions by restricting the lateral flow of coolant into the interaction region immediately surrounding the melt and by providing surface area for melt freezing.

Of special interest are situations in which a portion of the released melt impinges upon the lower head in a jet mode. The high forced-convection heat fluxes realized in the impingement zone of a melt jet could potentially result in heatup and melting-induced erosion of weld or lower head wall material located beneath the impingement zone. The impingement heat flux is dependent on the impinging melt jet temperature, diameter, velocity, and composition. These conditions, in turn, reflect the effects of the various melt/water and melt/structure interactions undergone by the melt in the process of relocating from the core region to the lower head.

As discussed in Section 2.4, the strong influence of lower plenum melt/water and melt/structure interactions in mitigating the effects of melt impingement on the lower head were

first demonstrated by analyses of the TMI-2 accident.[4-24] That analysis was carried out using the THIRMAL/0 melt/water interaction code developed at Argonne National Laboratory.[4-25,4-26] The TMI-2 THIRMAL/0 analysis was performed for melt release conditions representative of the TMI-2 core relocation event as determined from plant data recorded during the accident and subsequent modeling of the accident. However, the analyses documented in this section consider a broader range of potential melt release conditions. The lower plenum interactions are also dependent on the particular lower plenum configuration, which is a reactor design-specific feature. Given the multiplicity of LWR designs employed in the U.S., the effects of lower plenum melt/water and melt/structure interactions must be investigated for specific reactor system designs. To analyze the lower head thermal and mechanical response to jet impingement, it is necessary to have a basis for the selection of impingement conditions to determine the thermal loading applied to the lower head wall. The THIRMAL/0 code, which has been further improved since its original application to the TMI-2 accident, can calculate melt arrival conditions and jet impingement conditions that account for lower plenum interactions in the various reactor systems, given the conditions of melt release from the core as a coherent jet.

Scoping calculations were performed to investigate melt arrival conditions for situations involving a localized release of melt from a crust-confined molten pool in the core region. There are several computer codes available for predicting melt/water interactions. However, there is considerable uncertainty in code results because of limited data for validating these models (see Section 2). In light of this uncertainty, calculations documented in this section used the THIRMAL/0 code to investigate the effects of plant lower plenum geometry rather than to study differences in models for predicting jet/water interactions.

The objectives of this work are to

1. Provide calculations of melt arrival conditions on the lower head that accounts for melt breakup and quenching resulting from melt interactions with water and structure inside the lower plena of representative U.S. LWRs

2. Investigate the dependency of the melt arrival conditions on the conditions of melt assumed to be released from the core region

3. Identify those conditions of melt release for which a portion of the melt is calculated to impinge on the lower head surface in a jet mode and characterize the conditions of the impinging jets

4. For those cases involving jet impingement, estimate the heat flux and energy delivered to the lower head surface inside the impingement zone

5. Provide results in a non-dimensional fashion, where possible, recognizing the inherent complexity of the lower plenum interaction processes.

The calculations investigated the effectiveness of water in the lower plenum together with the lower internal structures in breaking up and quenching the melt such that corium typically collects at the head as a high-solid fraction slurry or particle bed. The potential for the lower plenum water and structures to avert the threat of a melt stream's impinging directly on the lower head or, if impingement occurs, decreasing the impingement liquid mass, was also investigated. Calculations did not investigate phenomena such as steam explosions, debris crust formation upon contact with the lower head, or the heatup and remelting of debris particles upon the lower head. Although results from these calculations could be used to estimate the potential for vessel

ablation, which may subsequently enhance the potential for vessel failure, the relatively large upper bound of relocation masses assumed (100% of the corium material) in these scoping calculations in conjunction with the omission of investigating debris bed behavior after relocation would make the results from such calculations somewhat unrealistic.

4.2.1.1 Methodology. The THIRMAL/0 code was applied to calculate lower plenum melt/water and melt/structure interactions and to predict melt arrival conditions on the lower head over a broad range of core release conditions. To assist the reader in understanding the scope of THIRMAL/0 and the modeling incorporated therein, a description of the code is provided in Appendix C.

Four reference plants were selected as representative of the various lower plenum configurations used in U.S. reactor designs. For each individual reference system, melt release conditions from the core region were defined. Although a broad range of melt relocation paths and compositions were considered, most analyses concentrated on conditions that enhanced the likelihood that melt would impinge on the lower head as one or more jets. These conditions were generally defined to enhance the likelihood that melt would be calculated to impinge on the lower head as one or more jets. In particular, in all cases, melt is assumed released as a single coherent jet. This would apply to situations where a molten pool surrounded and insulated by a solid crust forms in the core region followed by localized crust failure or melt through, giving rise to release of melt into the lower plenum as a single jet. The present analysis does not consider other melt release modes. As noted earlier, during the TMI-2 accident the melt has also been assumed to subsequently enter the former core region and drain into the lower plenum as a large number of small diameter jets from flow holes in the former lowermost core plate. Although less likely because of its multiple supports, the structure immediately below the core pool might also be envisioned to fail and allow the molten pool mass to fall downward suddenly in a global sense over its lateral extent rather than drain by means of a localized release. Failure of the structure immediately below the core pool might also be envisioned to allow the molten pool mass to suddenly fall downward in a global sense over its lateral extent rather than drain by means of a localized release. However, the analysis of these other release modes lies beyond the scope of the current work, which is focused on jet impingement.

Because of the uncertainty associated with the size of the stream draining from the core pool, it has been postulated in the analyses performed here that this draining stream size may be represented by an equivalent circular stream with a 10-cm diameter. This 10-cm diameter is considered representative. Obviously, in cases where impingement is predicted for a 10-cm jet, impingement would also be predicted for larger diameter jets. Furthermore, if it is possible for smaller diameter jets of a given superheat to impinge on the lower head coherently, the heat flux for the smaller diameter jet will be higher than the heat flux from a jet with an initial diameter of 10-cm. Thus, the energy transferred to the vessel from a 10-cm jet is expected to be representative of the energy transferred from a broader range of jet diameters.

A reference melt mass equal to the total mass of molten core material was assumed to be distributed over the core cross-sectional area. The resulting melt depth was used to define the reference jet initial velocity as the velocity corresponding to the initial gravity head. The velocity was assumed to remain constant without decrease throughout the calculation. Most cases were carried out for melt having the reference proportions, 80 wt% UO_2 - 20 wt% ZrO_2. This pure oxide composition has a high liquidus temperature of 2860 K. A reference initial molten superheat of 250 K was assumed representative of the magnitude of superheat nominally predicted for released melt during the TMI-2 core relocation event. In the reference melt release, melt was assumed released from the periphery of the core region where the total water

depth to the lower head is lowest relative to central release locations. The reference water state was also assumed saturated, thereby minimizing the enhanced quenching effects associated with water subcooling. Finally, the reference primary system pressure was taken equal to the nominal operating value. Melt thermophysical properties were based on data found in Appendix F.

For the GE and B&W reference systems, a large number of cases were calculated investigating the sensitivities to the initial jet diameter, jet velocity, melt composition, melt superheat, water depth (i.e., release location), water subcooling, and system pressure. In particular, the consequences were determined for: reducing the jet diameter from 10 to 5 cm; reducing the jet velocity to values representative of a molten pool height reduced to 50 and 10% of a total core pool; changing the melt composition to successively 20 wt% UO_2 - 80 wt% stainless steel and 100% stainless steel; raising the melt superheat to 400 K; moving the melt release location from the core periphery to the core centerline; increasing the water subcooling to a value equivalent to the nominal operating cold leg inlet value; and decreasing the primary system pressure down to one atmosphere. In specific instances, the effects of varying two variables, such as release location and melt composition, were examined. In addition, consistent with the approach of defining conditions that would enhance the likelihood of impingement, a case was defined that combined all of the single variations of conditions that were found to enhance the potential for impingement.

For the Westinghouse and CE reference systems, few cases were calculated. The conditions for these cases were defined as those expected to most likely result in impingement based on the results of the B&W system calculations.

Key results from these analyses consist of the proportions of melt arriving on the lower head as molten jets, molten droplets, and solid particles, as well as the temperature of each of these phases. For cases involving jet impingement, the number of impinging jets, jet temperature, diameter, and velocity were determined. Additionally, the local impingement heat flux corresponding to the jet impingement conditions was calculated using an appropriate impingement heat transfer correlation. In calculating the heat flux, frozen core material was assumed to be present as a solid crust layer between the impinging melt and underlying lower head substrate. Plots showing the disposition of melt at successive times as it relocates through the water and collects upon the lower head were also produced.

An attempt was made to display selected results in a non-dimensional format. A rough preliminary correlation for the jet breakup length non-dimensionalized by the initial jet diameter was studied and compared with the results of the THIRMAL/0 calculations. Results for the impingement zone heat flux and energy deposition were also presented in a non-dimensional fashion.

The remainder of this section is organized as follows. Section 4.2.1.2 presents detailed THIRMAL/0 calculation results for two scoping cases. Section 4.2.1.3 summarizes the major conclusions from sensitivity studies. Non-dimensional studies of the jet breakup length and impinging heat flux are presented in Section 4.2.1.4. Appendix C provides a description of the THIRMAL/0 code.

4.2.1.2 Results for Scoping Cases. Two scoping cases based on the GE and B&W reactor configurations were first defined and carried out assuming the conditions shown in Table 4-7. The dimensions of the lower plenum configurations assumed for these two plants are found in Appendix F.

Table 4-7. Melt release conditions of scoping cases.

	Scoping Case GE1	Scoping Case BW1
Reactor type	GE BWR/4	B&W (TMI-2)
Melt composition	Ceramic (80% UO_2-20% ZrO_2)	Ceramic (80% UO_2-20% ZrO_2)
Melt superheat, K	250	250
Melt mass, kg	3.14×10^5	1.70×10^5
Molten pool cross-sectional area, m^2	17.8 (100% of core cross-sectional area)	9.9 (100% of core cross-sectional area)
Jet diameter, m	0.1	0.1
Initial jet velocity, m/s	6.2	6.1
Relocation path	Central vessel region	Central vessel region
Water depth, m	5.3	2.2
Water subcooling, K	0	0
Vessel pressure, MPa	6.94 (full system pressure)	14.9 (full system pressure)

4.2.1.2.1 Scoping Case GE1—The arrangement of the lower head structures for the reference GE BWR/4 reactor vessel is shown in Figure 4-35. A large portion of the flow area in the lower head region is occupied by control rod guide tubes and control rod drive housings, as shown in Figures 4-35 and 4-36. An effect of the closely-packed control rod guide tubes is to limit the lateral propagation of the dispersed melt droplets and particles during the melt jet/water interaction. As a result, the water region in the midst of the control rod guide tubes is more likely to become void because of a higher melt droplet concentration. When the void fraction in this region becomes large enough, a continuous liquid coolant phase may not exist near the jet and the jet surface erosion could be reduced. Thus, a longer jet penetration distance and, possibly, jet impingement could occur. The effects of the instrument tubes on the jet/water interaction are neglected because of their smaller diameter.

In the THIRMAL/0 code, the lateral inhomogeneity of the flow conditions, such as the radial void distribution, is accounted for by using a mixing zone representation (see Appendix C). The mixing zone is roughly a cylindrical volume that contains the jet column, dispersed droplets,

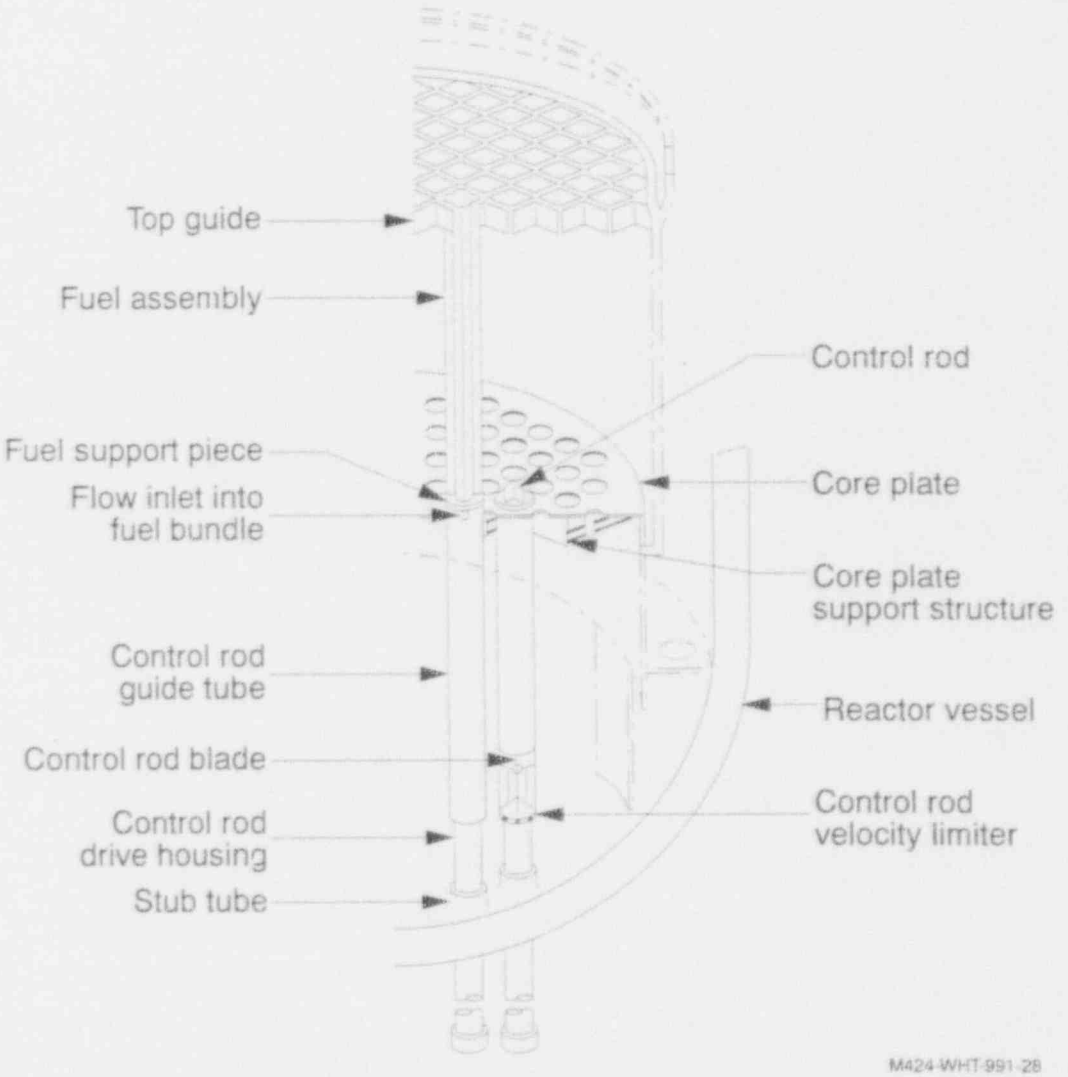

Figure 4-35. Arrangement of BWR/4 core, core plate, control rod guide tubes, and supporting components.

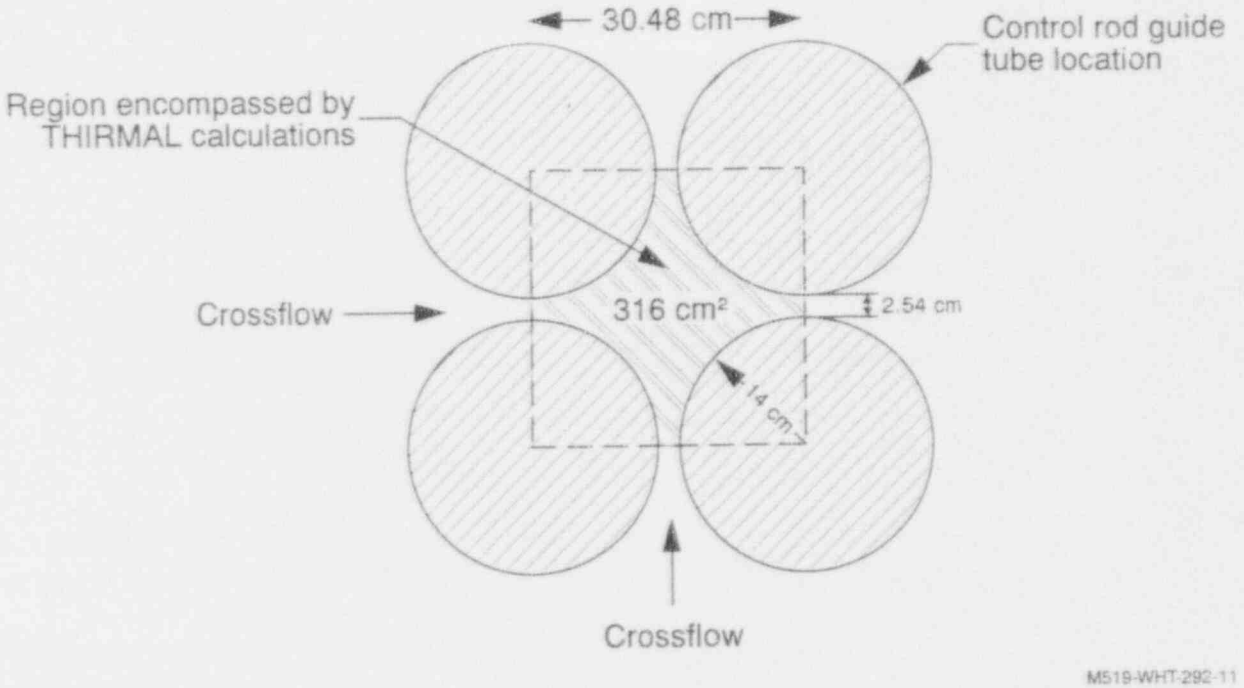

Figure 4-36. Cross-sectional flow area beneath BWR/4 core.[4-27]

steam, and water. Outside the mixing zone, the flow is assumed to consist of single-phase water without any melt or steam. The volume of the mixing zone is determined based upon the lateral migration of the dispersed droplets/particles. In Scoping Case GE1, the cross-sectional area of the water region in the middle of the control rod guide tubes (and the control rod drive housing) is treated as a circular area with an equivalent diameter that yields the same cross-sectional area. During the interaction, the mixing zone may expand or shrink depending on the variation of the steam generation rate. The code allows water to flow into the region between the control rod guide tubes through the gaps between the guide tubes and housings when the steam generation decreases and the pressure drops as a result of the different gravity heads that cause the mixing zone to shrink.

In the THIRMAL/0 code, a correlation based on the experiment data of Sato et al.[4-28] is applied to evaluate the heat flux when jet impingement occurs. As shown by Sato et al., the Nusselt number for a turbulent jet impinging upon a melting substrate surface can be represented by

$$Nu = 0.0155\ Re^{0.917}\ Pr^{0.8}. \tag{4-36}$$

This correlation was obtained using data valid for $0.095 < Pr < 0.20$ and $4.1 \times 10^4 < Re < 4.9 \times 10^5$.

The results of the melt/water interaction calculations of Scoping Case GE1, as predicted by the THIRMAL/0 code, are shown in Table 4-8. The following is a brief discussion of the results.

The jet breakup length is defined as the depth at which a coherent jet column ceases to exist as a result of dispersion or fragmentation of the corium stream. Jet breakup length is usually

Table 4-8. Results of THIRMAL calculations for scoping cases GE1 and BW1.

		Case GE1	Case BW1
Jet impingment		No	Yes
Extent of jet breakup	Breakup length, L/D	44.6	–
Aspects of heat transfer if jet impingement occurs on lower head	Number of jets	–	4
	Max. impinging jet diameter, m	–	0.026
	Max. impinging jet superheat, K	–	176
	Max. impinging jet velocity, m/s	–	2.28
	Duration of impingement, s	–	380
	Max. heat transfer coefficient, MW/m^2K	–	0.077
	Maximum heat flux, MW/m^2	–	13.6
	Integrated heat flux, MJ/m^2	–	5.2×10^3
Melt accumulation state upon lower head	Impinging jet, %	0	10.0
	Molten droplets, %	0	4.7
	Solid particles, %	100	85.3
Temperature of accumulated melt on lower head	Impinging jet, K	–	3036
	Molten droplets, K	–	3000
	Solid particles, K	1598	1700
Debris particle size distribution			
	Median diameter, mm	3.5	3.2
	Standard deviation, σ	2.0	2.0

expressed in terms of the jet diameter. The volume fractions of the jet column and the melt droplets/particles in the mixing zone during the interaction are shown in Figure 4-37. Thus, the physical state of the accumulated melt on the vessel bottom can be predicted. As shown in Figure 4-37, the deepest distance that the jet can penetrate without being completely fragmented is predicted to be around 45 initial jet diameters (i.e., 4.5 m) below the core support plate, which occurs ~2 seconds after the commencement of jet flow. After ~2 seconds, a quasi-steady breakup behavior is attained when a roughly constant melt dispersion rate, as well as a coherent jet column of a constant length, is achieved. For the reference Case GE1, jet impingement is not predicted to occur because the depth of the water in the lower head is greater than the predicted jet breakup length.

Corresponding to Figure 4-37, the variations of temperature for each phase in the mixing zone at successive times are shown in Figure 4-38. The melt superheat of the jet column is predicted to decrease ~30 K. It is predicted that all the dispersed droplets are solidified when they collect on the lower head with an average temperature of ~1600 K. Note that the solid particle temperatures do not vary linearly with elevation from the lower head (e.g., a temperature drop in particles occurs at 4.5 m for 0.5 seconds and at 0.2 m for 2.0 seconds in Figure 4-38). These discontinuities result from variations in heat removal and particle travel time that are associated with particle size. For example, a larger particle will fall more rapidly to the lower head at a higher temperature because such particles have smaller surface area to mass ratios and smaller travel times for heat removal. The size of the mixing zone (i.e., the melt/water/steam mixture) is shown in Figure 4-39. The mixing zone expands radially and vertically until a stable size is obtained after ~2 seconds and a quasi-steady state is reached.

The local void fraction averaged over the mixing zone is shown in Figure 4-40 at different times. In general, the void fraction in the mixing zone is high, especially when jet breakup occurs. According to the THIRMAL/0 predictions, flow dispersion always occurs from the core plate to ~3 m below. Therefore, the dominant breakup mechanism is the melt erosion from steam flow in the mixing zone in the region where water is dispersed.

As predicted by THIRMAL/0, the melt starts to collect on the vessel bottom at ~1.5 seconds, and 100% of the accumulation is composed of solid particles. The prediction of the dispersed particle size distribution for Scoping Case GE1 is shown in Figure 4-41 on a logarithmic probability graph. A log-normal distribution plots as a straight line on a log probability graph. As shown in Figure 4-41, the debris of Scoping Case GE1 is predicted to show a roughly log-normal size distribution with a mass median particle size of ~3.5 mm. The standard deviation, σ, of the particle diameter characterizes the range over which the particles are distributed around the median. In particular, 68% of the total debris mass is composed of particles ranging from $\bar{d}/\sigma$ to $\sigma\bar{d}$, where $\bar{d}$ is the median diameter.

4.2.1.2.2 Scoping Case BW1—The B&W reference reactor vessel contains various core structures in the lower plenum, such as the flat distributor plate, grid forging, instrument support plate, and elliptical flow distributor plate, as shown in Figure 4-42. The effects of the structures on the melt jet breakup are mainly to collect the melt on the plates and to form multiple jets after the accumulated melt drains through each plate. As illustrated in Figures 4-42 and 4-43, the relocated melt jet would interact with water in Regions I, II, III, and IV. A "straight-shot" jet of significant diameter cannot exist in this geometry.

During the relocation, melt is assumed to accumulate on the flat flow distributor plate, the grid forging, and the elliptical flow distributor plate. A quasi-steady flow situation is assumed to

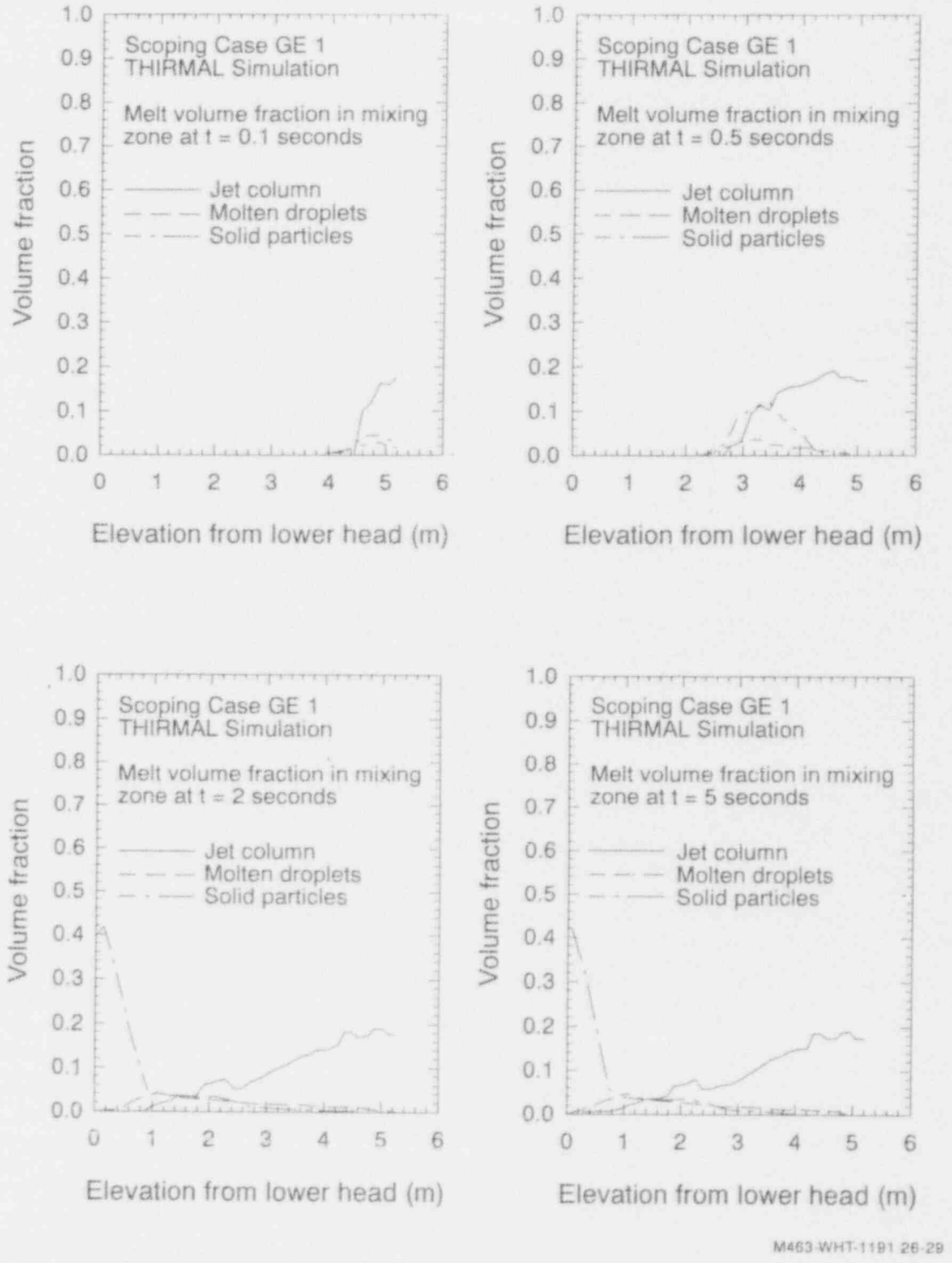

Figure 4-37. Melt volume fractions in mixing zone for reference case GE1 at 0.1, 0.5, 2, and 5 seconds (void and water fractions are not included in figures).

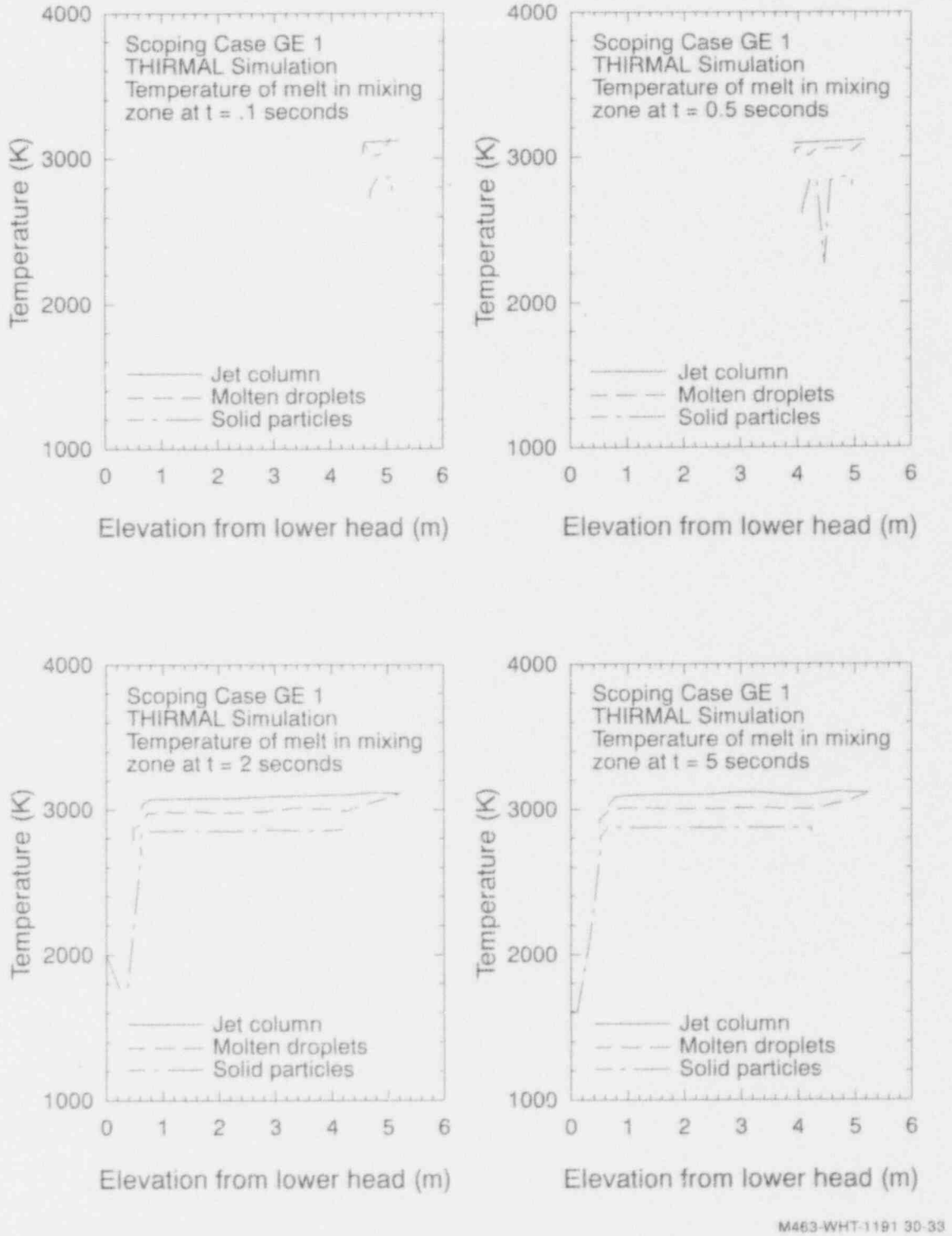

Figure 4-38. Temperature variations of melt in mixing zone for reference case GE1 at 0.1, 0.5, 2, and 5 seconds.

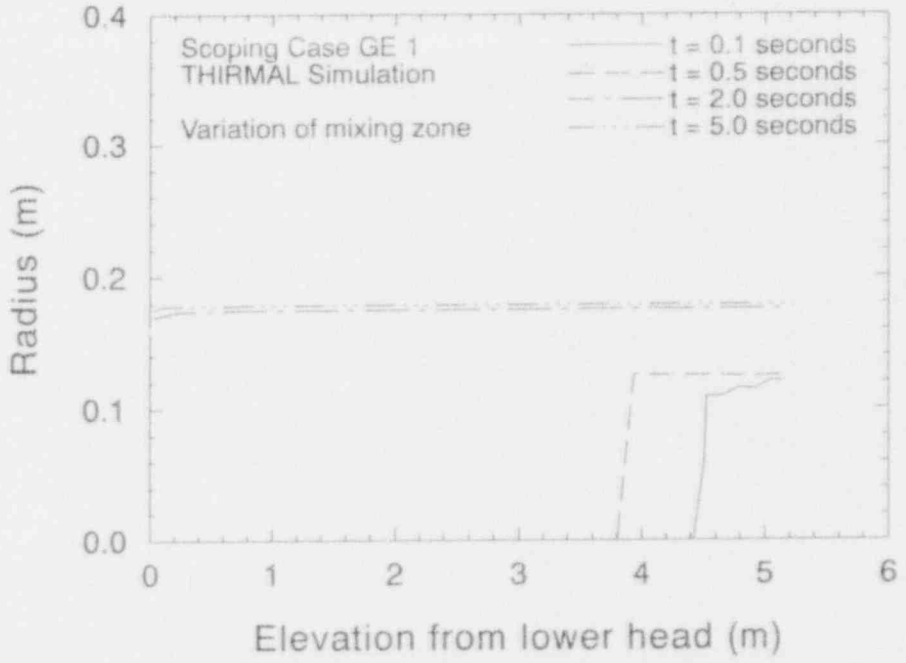

Figure 4-39. Variation of mixing zone for Scoping Case GE1.

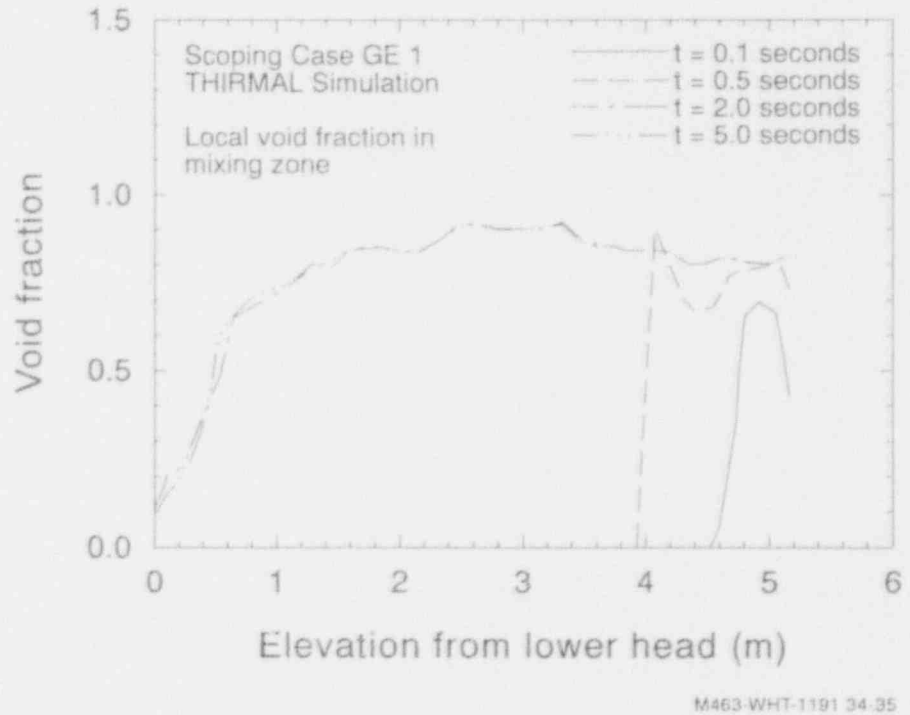

Figure 4-40. Local void fraction in mixing zone for Scoping Case GE1.

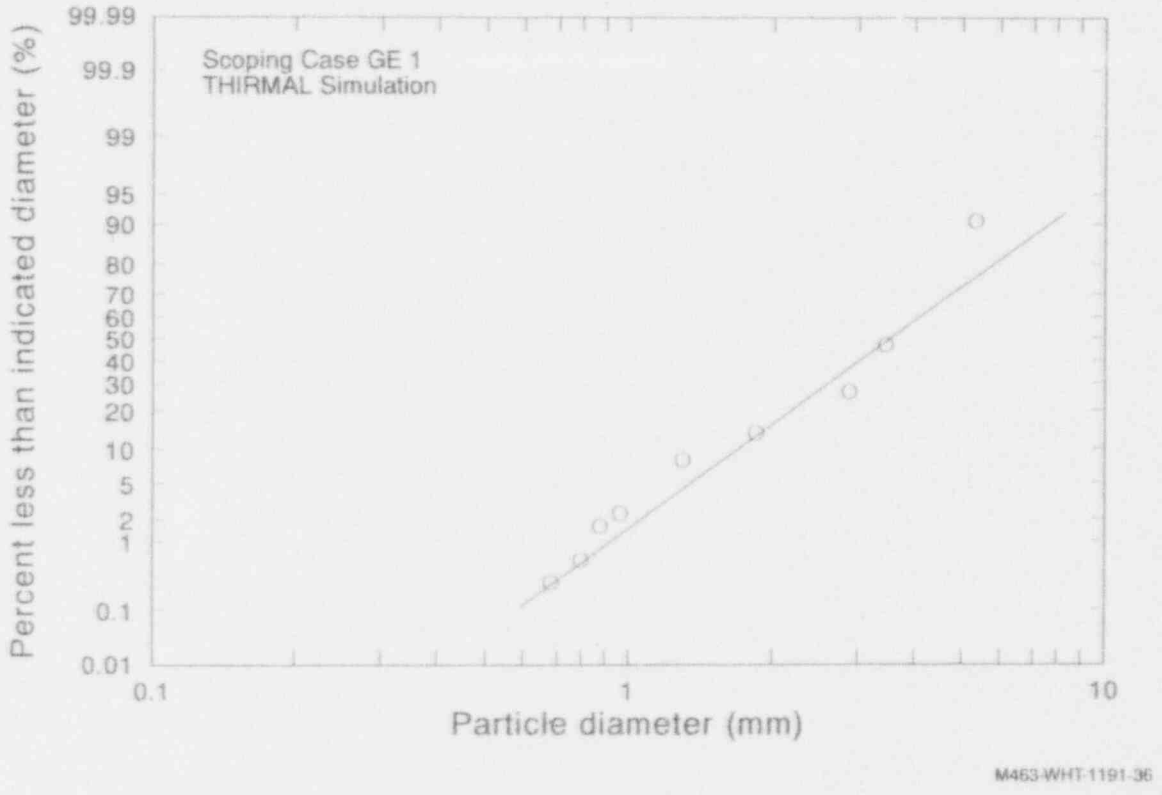

Figure 4-41. Dispersed particle size distributions for Scoping Case GE1.

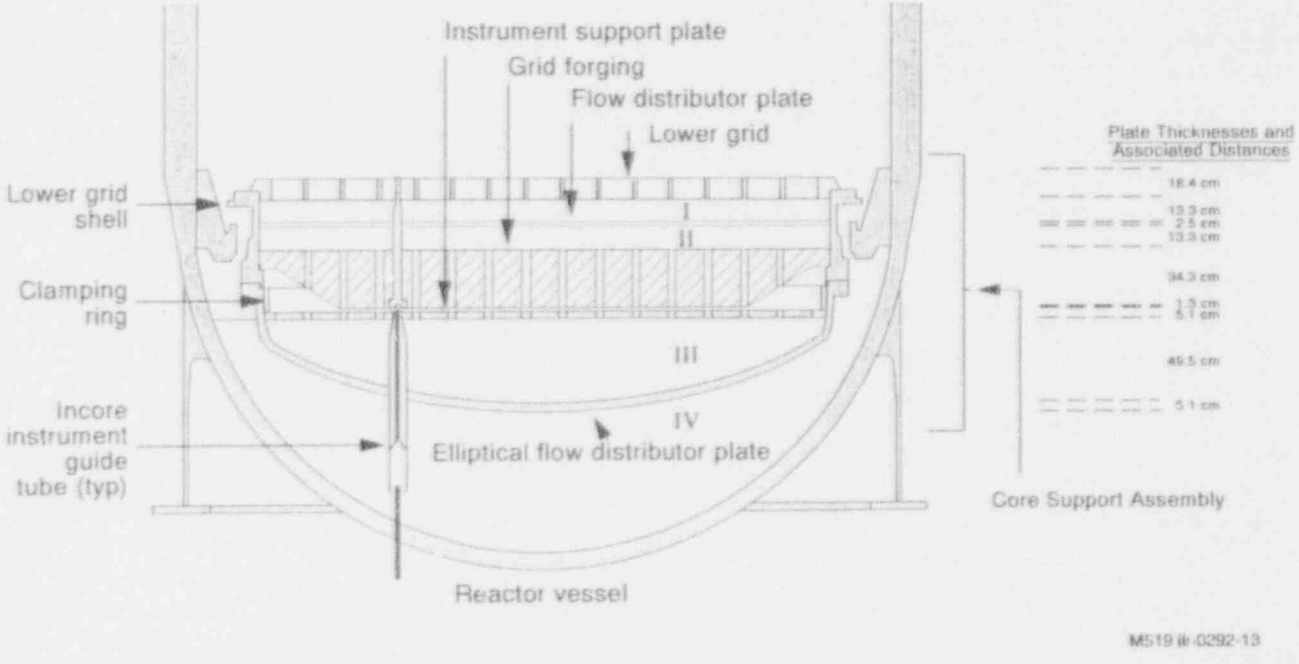

Figure 4-42. Details of reference B&W core support assembly.

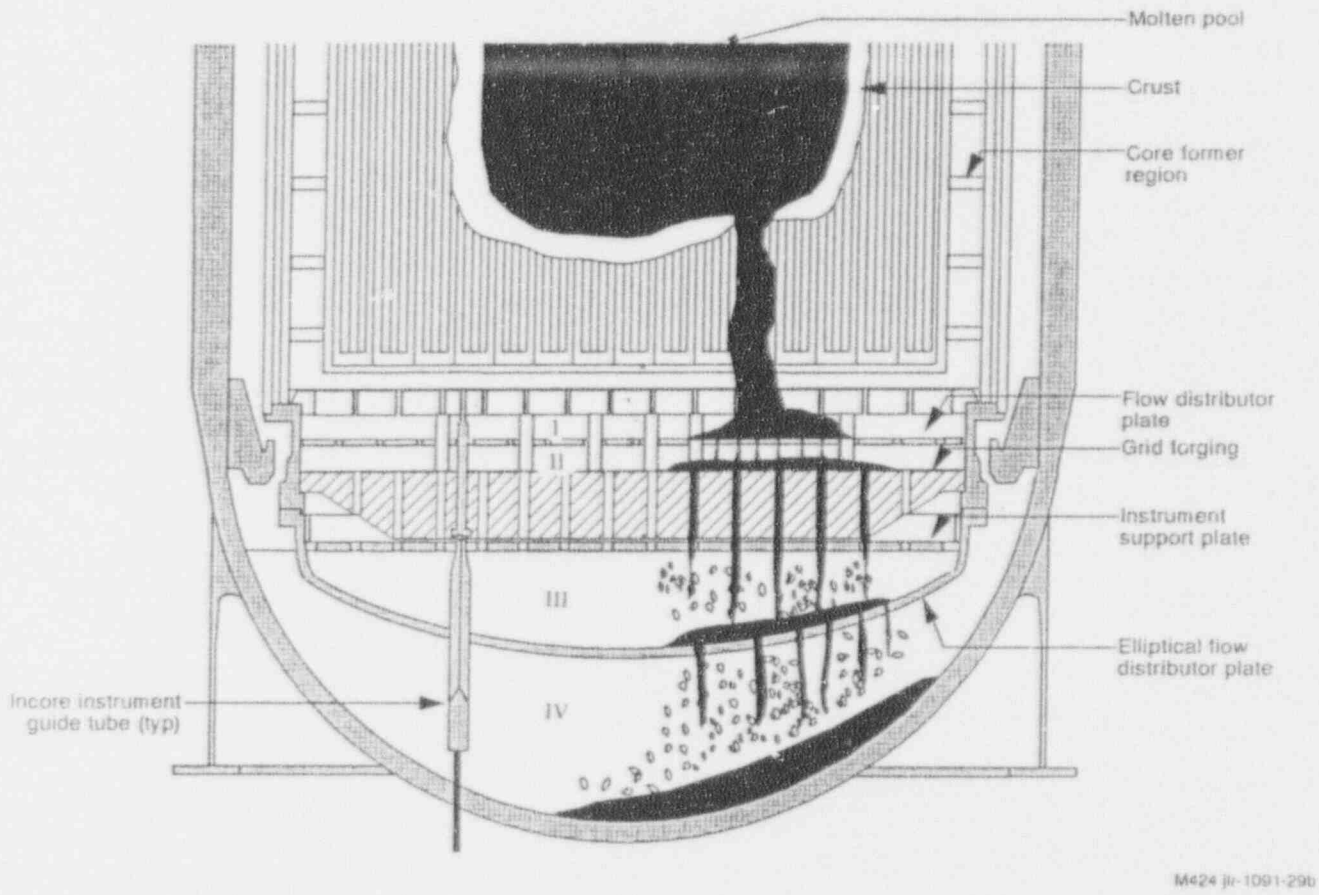

Figure 4-43. Schematic configuration of melt relocation and breakup inside lower head.

develop where the rate of corium arrival upon each plate is equal to the rate of drainage through the various plate openings. The freezing of melt on the plate steel is neglected, as this is expected to represent only a small portion of the released mass. The potential melting and erosion of the plate steel by the impinging corium is also neglected. The diameters of the jets draining from a plate reflect the size of the holes passing through the plate thickness. For a sufficiently small hole size relative to the arriving melt, the new jets formed will have diameters initially equal to the hole size. However, in many instances, the hole size exceeds the diameters of the arriving corium jets. In this case, the size of the newly formed jets depends on the nature of the melt flow surrounding the various openings. As melt collects on the plates, it will flow toward the nearby openings and freely fall into them. Thus, how the melt flows over the upper surface of the plate and freely falls into the holes is of interest.

Assuming that the arriving, spreading, and draining melt has reached a quasi-steady state, the drainage conditions of the melt passing through each plate are assumed to satisfy the following equation:

$$\dot{m} = \rho_J N_{hole} \pi d_{hole} U_c h_c \qquad (4\text{-}37)$$

where

$\dot{m}$ = melt relocation rate

N_{hole} = number of holes covered by the accumulated melt on each plate

d_{hole} = diameter of holes

h_c = critical depth of melt flowing horizontally and draining through hole

$U_c = \sqrt{gh_c}$ = critical velocity of melt flowing towards the edge of holes

ρ_J = melt density.

Figure 4-43 illustrates the formation of multiple jets on the flow plates. The melt flowing into each hole is modeled as a free overfall in open channel flow. The free overfall can be described in terms of the depth at the brink and the subsequent form of the freely falling nappe (see Figure 4-44). The depth must pass through the critical depth, h_c, at which the flow velocity is U_c, as the flow accelerates into the supercritical free fall. From Reference 4-29, the flow depth at the brink is a fraction (0.715) of the critical depth, h_c, for a level channel.

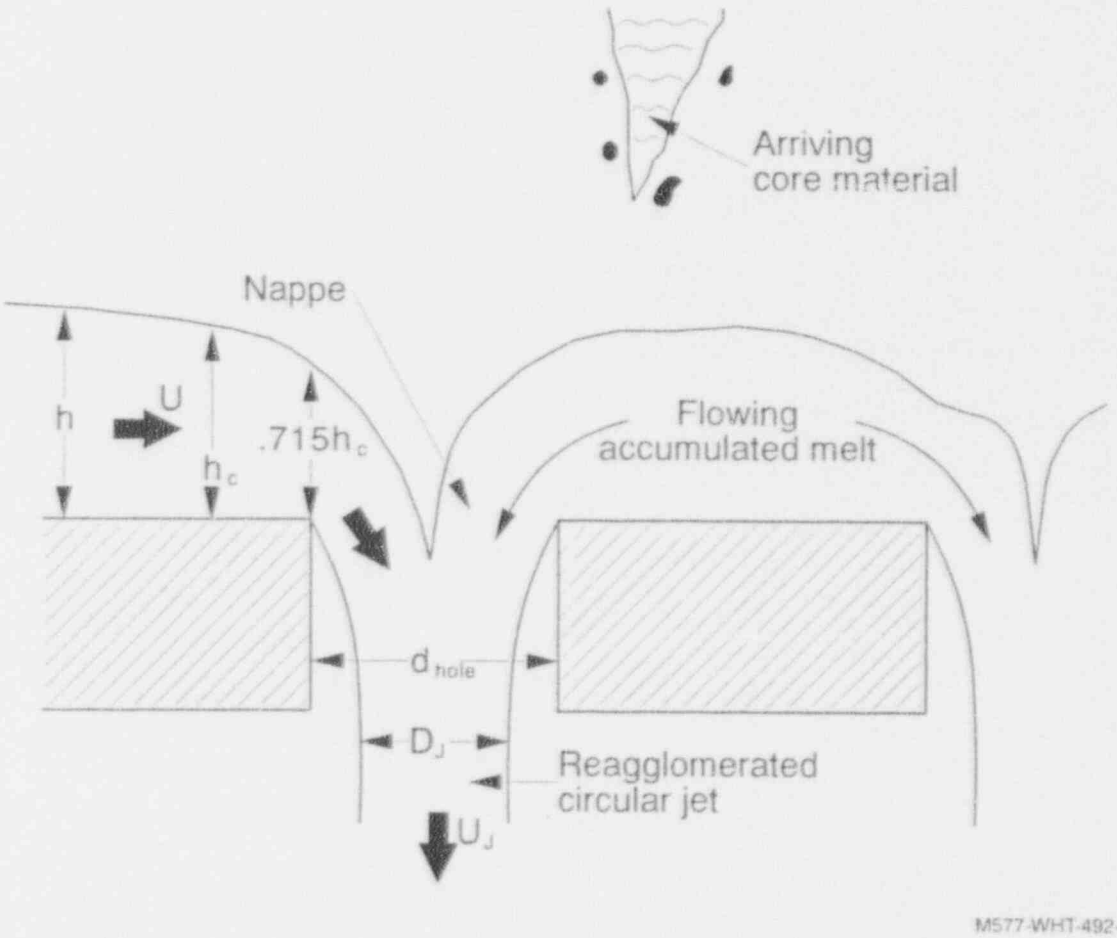

Figure 4-44. Illustration of formation of multiple jets through flow holes in core support structure.

Resulting from the acceleration of the melt flowing to the holes between the location of critical flow and the rims of the holes, the melt jet velocity at the exit of the hole increases by a factor of 1/0.715 such that

$$U_J = 1.4\ (gh_c)^{1/2} \quad .$$

The melt flowing into each hole is assumed to reagglomerate to form a circular jet in the center of each hole. From conservation of the flow rate, the diameter of the multiple jets formed by each plate satisfies the following equation:

$$\dot{m} = \rho_J\ N_{hole} \pi\ D_J^2\ U_J/4 \qquad (4\text{-}38)$$

where

D_J = diameter of multiple jets

U_J = jet velocity.

Combining Equations (4-37) and (4-38), the diameter of each jet immediately below the plate can be expressed as

$$D_J = 1.155\ d_{hole}^{1/6} \left(\frac{\dot{m}}{\rho_J\ N_{hole}\ g^{1/2}} \right)^{1/3} . \qquad (4\text{-}39)$$

A straight-shot pathway through the central part of the lower plenum structure does not exist in the B&W reference configuration. Thus, melt draining vertically downward from the flat distributor plate will impinge on and collect on the underlying grid forging steel (i.e., melt jets will not pass directly through the large holes in the grid forging). Similarly, jets draining vertically downward from the grid forging will be intercepted by the steel of the elliptical flow distributor plate without passing directly through its large holes.

For the purpose of evaluating the potential for jet impingement, it is conservative to assume that only the holes near the impinging jet are covered by the melt spreading on the plate. Therefore, four jets are assumed to form when a single jet impinges on the first plate (i.e., the flat flow distributor plate). It is possible that more than four jets could be formed on the grid forging as a result of the impingement of four jets from the flow distributor plate on the vessel lower head, but the number is limited to four in the current analysis. This choice is expected to represent a conservative assumption with regard to impingement on the lower head. Again, note that the initial melt accumulation on each plate is ignored. Instead, a quasi-steady melt drainage is assumed to occur immediately after melt relocation starts. Thus, the melt thickness on each flow plate is assumed to have reached a constant value, and the flow rate if the melt mass is conserved at each plate.

Based on the melt release rate (i.e., 440 kg/s in Scoping Case BW1), Equation (4-39) yields a jet diameter of 0.12 m for the four jets formed from the flat distributor plate. This is larger than the diameter of the holes on this plate. Therefore, the flat distributor plate hole size of 0.089 m (3.5 in.) determines the jet diameter. Assuming that four jets drain from the grid forging, Equation (4-39) again predicts a jet diameter of 0.12 m. However, this is smaller than the hole

size such that the jets form with a 0.12 m initial diameter. Similarly, assuming that four jets drain from the underlying elliptical flow distributor plate, an initial jet diameter of 0.12 m is calculated.

The results of Scoping Case BW1 are shown in Table 4-8. In Scoping Case BW1, the melt/water interaction is assumed to be composed of four stages (see Figure 4-43): (I) a single jet of 0.1 m diameter relocates from the bottom of the molten core to the flat flow distributor plate; (II) four jets of 0.089-m (3-1/2 in.) diameter relocate from the flat flow distributor plate to the grid forging; (III) four jets of 0.12-m diameter relocate from the grid forging to the elliptical flow distributor plate; and (IV) four jets of 0.12-m diameter relocate from the elliptical plate to the vessel lower head.

In Stage I, the melt impinges and starts to collect on the flat flow distributor plate shortly after of relocation begins from a high initial jet velocity (i.e., 6.1 m/s) and a short travel distance of 0.32 m through water. As predicted by the THIRMAL/0 code, the melt jet reaches the flow distributor plate at ~0.1 sec. The melt/water interaction quickly reaches a quasi-steady state, as shown in Figure 4-45 where the melt volume fractions (in terms of coherent jet, molten droplets, and solid particles) are plotted after the system has reached a quasi-steady state. In general, only a small fraction of the relocated melt has been dispersed into molten droplets, and ~79% of the accumulated material on the flat distributor plate is composed of the melt of the impinging jet column. Also shown in Figure 4-45 are the variations of the melt volume fraction, void fraction, and the radius of the mixing zone when a quasi-steady state is reached. The average temperature of the jet column is predicted to be 3108 K (~248 K superheat) when it impinges and accumulates on the flat distributor plate. Therefore, an initial temperature of 3108 K is assumed for the multiple jets formed from the bottom of the flat distributor plate.

In Stage II, the initial velocity of the four jets is calculated to be 1.04 m/s based on a critical melt thickness of 0.056 m, as predicted by Equation (4-37). The water depth in this region is 0.133 m, as illustrated in Figure 4-42. As a result of the short traveling distance between the flat distributor plate to the top of the grid forging (0.133 m), the multiple jets quickly reach and start to collect on the grid forging at ~0.2 second. Similar to the interaction in Stage I, the melt dispersion and quenching reach a quasi-steady state after ~1 second. The melt volume fractions, melt temperatures, void fraction, and the mixing zone boundary for each of the multiple jets are shown in Figure 4-46. Also similar to Stage I, the portion of the melt impinging in a jet mode consists of ~61% of the accumulated material on the grid forging. This reflects a short travel distance for a significant melt jet erosion process to occur. The average temperature of the jet columns is 3101 K (241 K superheat) when they impinge and collect on the grid forging. Thus, an initial temperature of 3101 K is assumed for the multiple jets formed from the bottom of the grid forging. Here, the heat loss and the melt dispersion are neglected when the melt relocates through the 0.165-m (6.5-in.) diameter, 0.41-m (16 in.) long openings in the grid forging to yield a conservative energy and mass content for the multiple jets formed at the grid forging.

In Stage III, the diameter of the four jets formed from the bottom of the grid forging is estimated to be 0.12 m, as discussed above, and the initial velocity is calculated to be 1.06 m/s based on Equation (4-38). The water depth in this region (i.e., Region III of Figure 4-43) is 0.5 m. Compared to Stages I and II, the multiple jets suffer more heat loss and melt dispersion because of a longer vertical distance of travel. The multiple jets are predicted to reach and start to accumulate on the elliptical flow distributor plate at ~0.5 second. After ~1 second, the system reaches a quasi-steady state for melt dispersion and quenching. Figure 4-47 shows the melt volume fractions, melt temperatures, void fraction, and the mixing zone radius when a quasi-steady state is reached. The impinging jet consists of only 36% of the material that collects on the elliptical flow distributor plate because more breakup and dispersion occurs in the greater

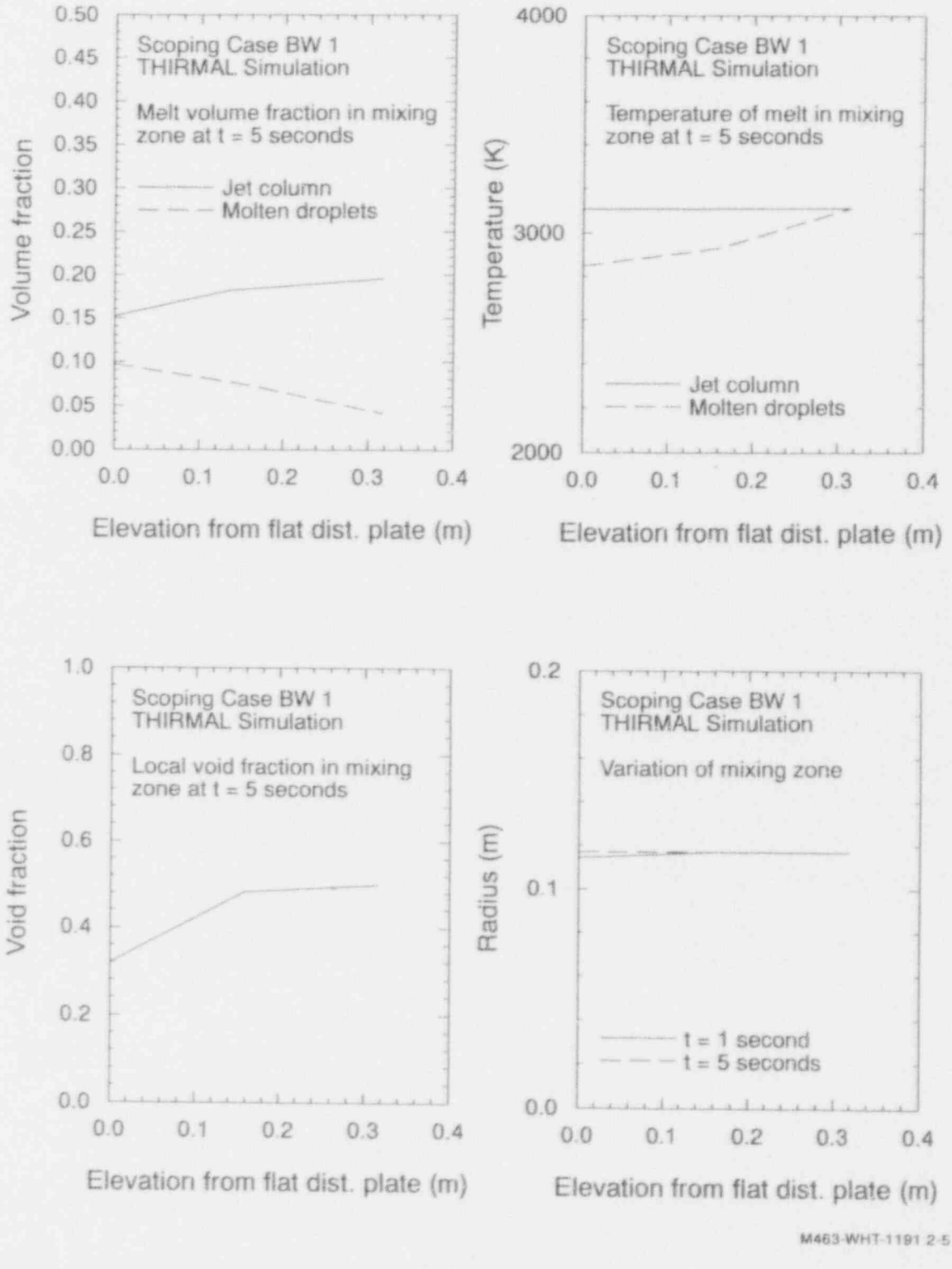

Figure 4-45. Melt volume, fractions, melt temperatures, and void fraction in mixing zone and radius of mixing zone for Stage 1 of Scoping Case BW1.

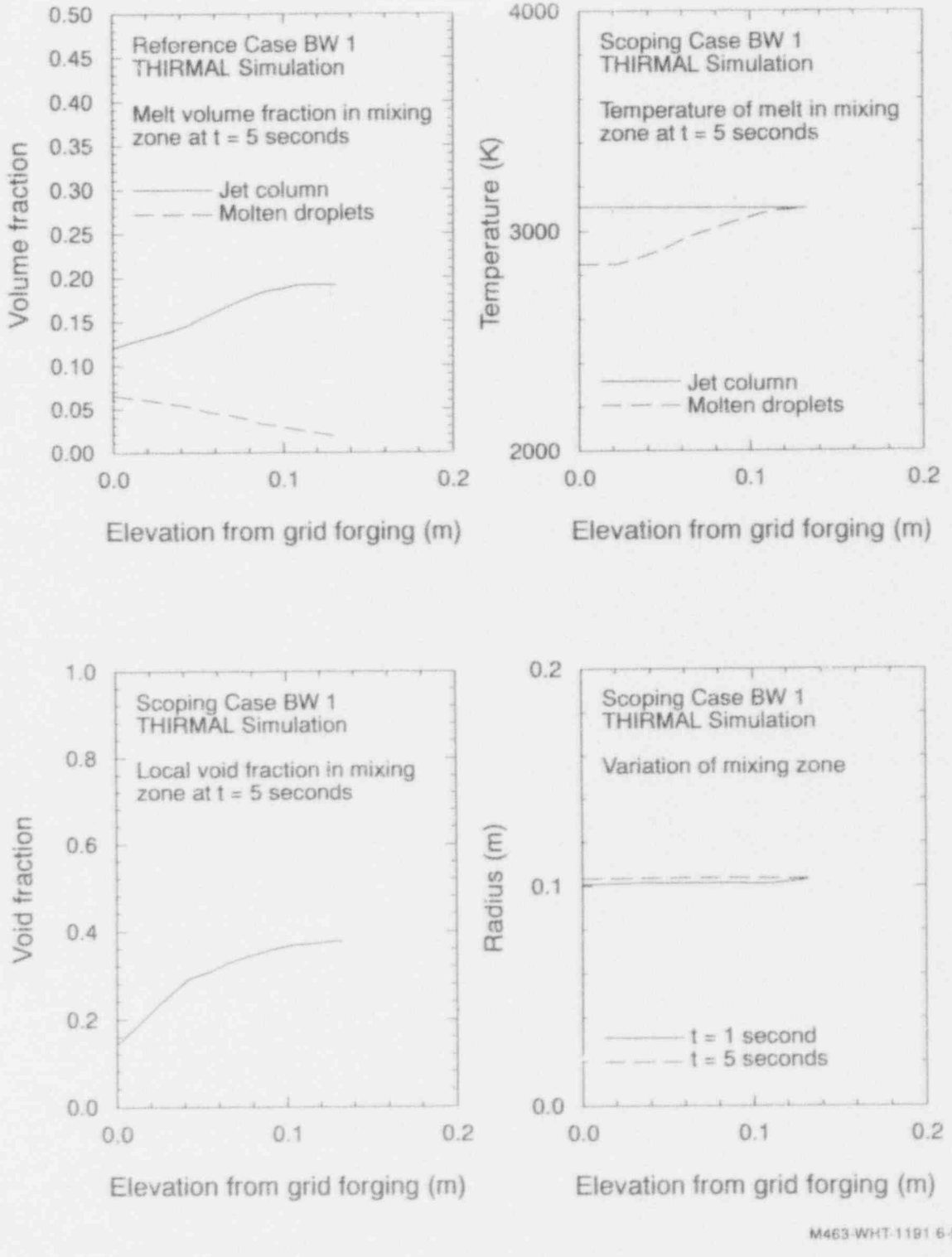

Figure 4-46. Melt volume fractions, melt temperatures, and void fraction in mixing zone and radius of mixing zone for Stage II of Scoping Case BW1.

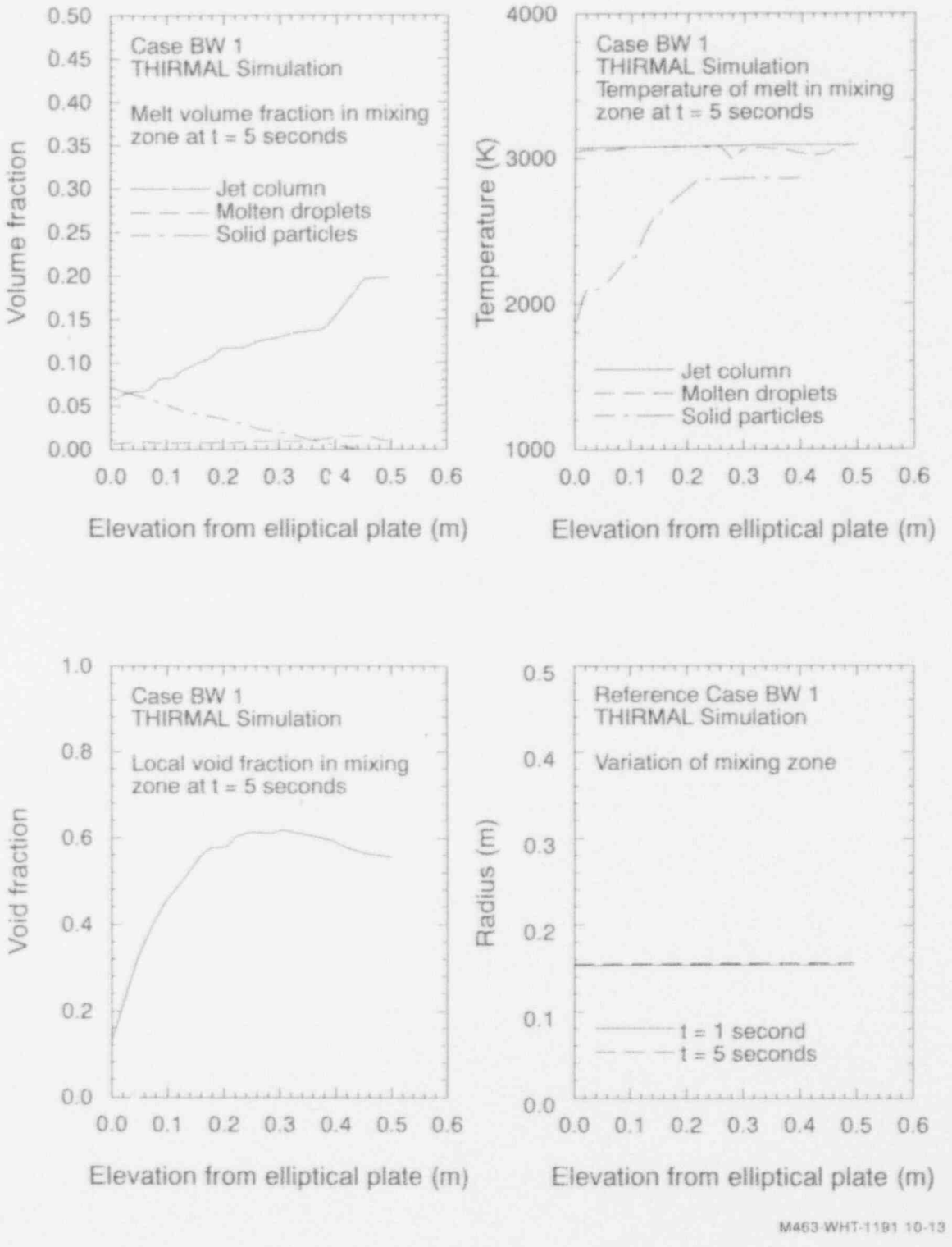

Figure 4-47. Melt volume fractions, melt temperatures, and void fraction in mixing zone and radius of mixing zone for Stage III of Scoping Case BW1.

distance of water. The average temperature loss of the jets is 15 K in this stage. Thus, the initial temperature of the multiple jets formed from the bottom of the elliptical flow distributor plate is assumed to be 3084 K.

In Stage IV (i.e., in the region below the elliptical flow distributor plate), the four jets suffer significant breakup and heat loss because of the greater water depth of 0.74 m. Similar to Stage III, the initial velocity and diameter of the multiple jets are 1.06 m/s and 0.12 m, respectively. Jet impingement is predicted to begin at ~0.8 second. The melt volume fractions, melt temperatures, void fraction, and the mixing zone radius when a quasi-steady state is reached are shown in Figure 4-48. In general, a superheat of 176 K is predicted for the jets when they impinge on the lower head. The impinging heat transfer coefficient, as correlated by Equation (4-36), is predicted to have a maximum value of 0.077 MW/m^2K. If a melt crust with a freezing temperature equal to the oxide melting temperature is formed on the lower head immediately after the jet impingement occurs, the impinging heat flux from the jet to the "crust" is 13.6 MW/m^2 in the impinging zone. Over the duration of melt relocation, the integrated heat flux is predicted to be 5.2×10^3 MJ/m^2.

The accumulated melt on the lower head is predicted to arrive with ~10% in the form of four impinging jets, 4.7% as molten droplets, and 85.3% as solid particles with average temperatures of 3036 K, 3000 K, and 1700 K, respectively. The particle size distribution is shown in Figure 4-49. The median size is about 3.5 mm. As discussed in Section 3.1.5, TMI-2 debris contained particles less than 1 cm diameter as well as larger pieces of rubble nearly 20 cm in diameter. However, larger pieces of debris may have been generated during reflood or defueling operations.

4.2.1.3 Sensitivity Studies. In order to evaluate the effects of melt release conditions on the melt arrival and jet impingement conditions, a series of calculations with variations in the release conditions was carried out. Twelve additional cases for the GE and B&W plants were performed to determine the effects of melt composition, melt superheat, jet diameter, release location (i.e., water depth), jet velocity, water subcooling, and system pressure. The initial and boundary conditions of Cases GE2 to GE13 and BW2 to BW13 are listed in Tables 4-9 and 4-10, respectively. The results of the melt/water interaction calculations of Cases GE2 to GE13 and BW2 to BW13 are summarized in Tables 4-11 and 4-12. Sections 4.2.1.3.1 and 4.2.1.3.2 contain a brief discussion of the results for these two plants. The plots of the melt volume fractions, melt temperatures, void fractions, and mixing zone are presented in Reference 4-30. Selected calculations were also performed for plants designed by the other U.S. LWR vendors: Westinghouse and Combustion Engineering. Results are discussed in Sections 4.2.1.3.3 and 4.2.1.3.4.

4.2.1.3.1 Results for General Electric Cases—Results from sensitivity studies for the GE plant design are summarized below. Since no jet impingement is predicted to occur for scoping case GE1, in which it is assumed that corium relocates through the central core region, Cases GE2 through GE13 are compared to a case with melt and reactor conditions similar to GE1, but with relocation occurring through a peripheral core region (Case GE6).

Mixed Oxide Melt Composition (Case GE2)

In Case GE2, a metal-oxide melt mixture material is assumed using material thermophysical properties from Appendix F. This material represents a melt that is at a higher temperature than pure metal because it contains some ceramic fuel and a melt that is able to conduct almost as well

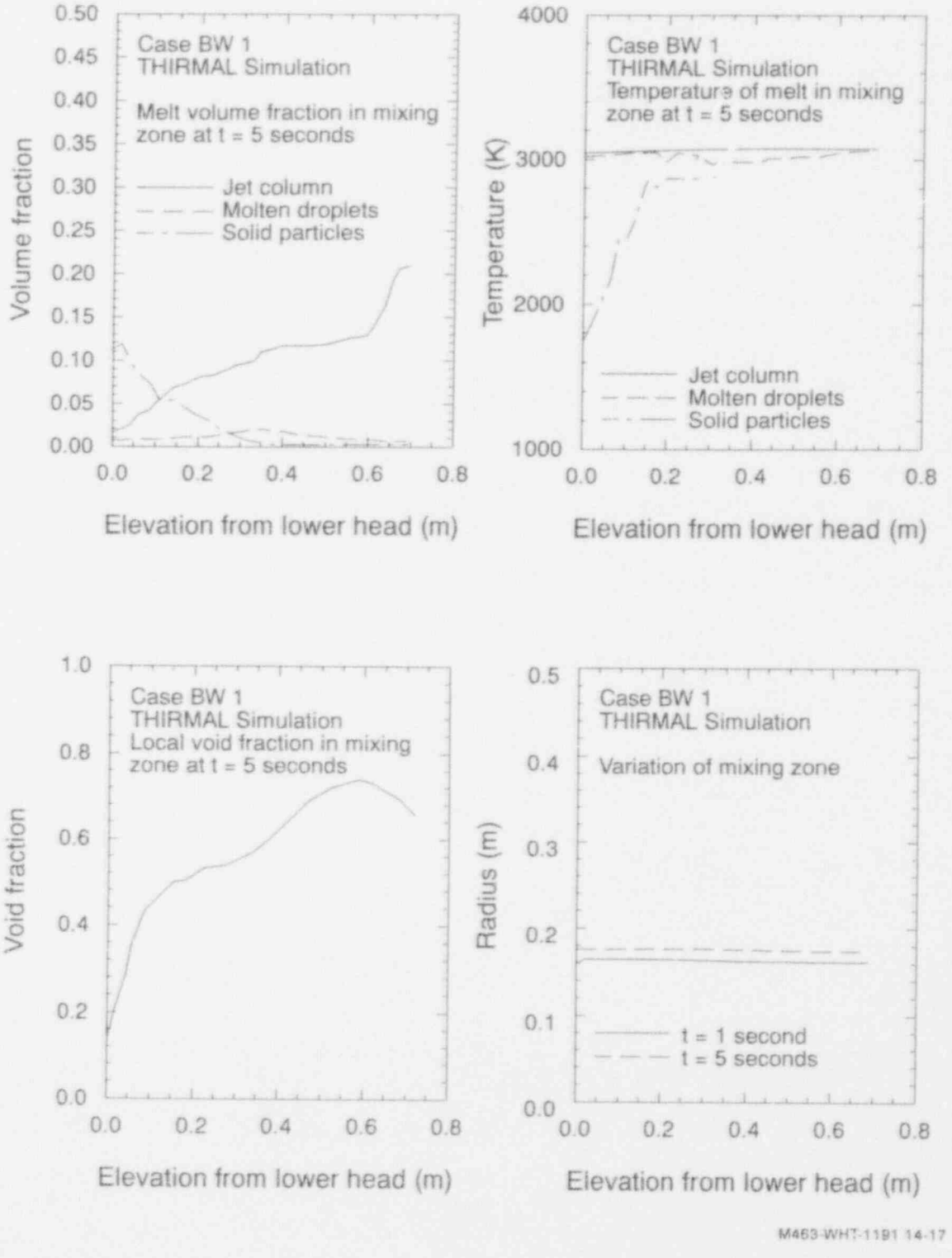

Figure 4-48. Melt volume fractions, melt temperatures, and void fraction in mixing zone and radius of mixing zone for Stage IV of Scoping Case BW1.

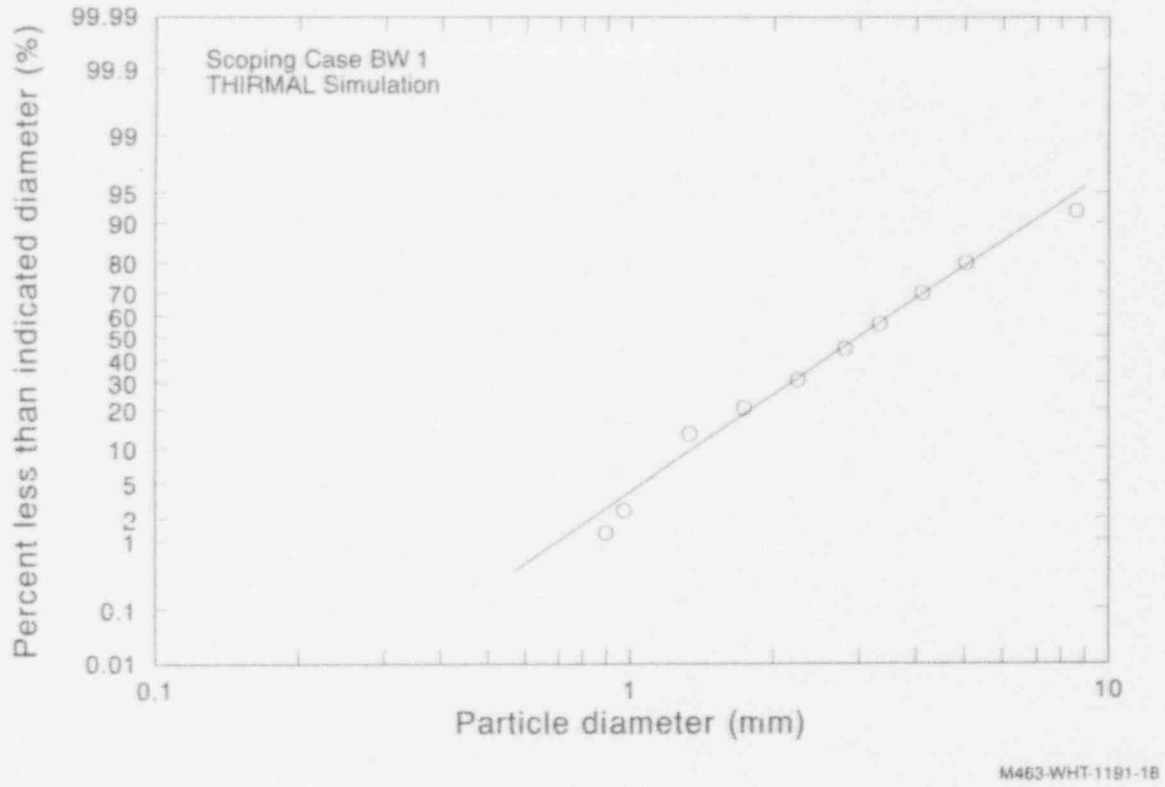

Figure 4-49. Dispersed particle size distribution for Scoping Case BW1.

Table 4-9. Melt release conditions of General Electric reference system cases.

Case no.	Initial and boundary conditions different from scoping Case GE 1
GE2	Melt composition = eutectic; water depth = 4.0 m
GE3	Melt composition = metallic; water depth = 4.0 m
GE4	Melt superheat = 400 K; water depth = 4.0 m
GE5	Jet diameter = 5 cm; water depth = 4.0 m
GE6	Peripheral relocation (i.e., water depth = 4.0 m)
GE7	Total melt mass = 50% of total mass; water depth = 4.0 m
GE8	Total melt mass = 10% of total mass; water depth = 4.0 m
GE9	Water subcooling = 70 K; water depth = 4.0 m
GE10	System pressure = atmospheric; water depth = 4.0 m
GE11	Melt composition = eutectic
GE12	Melt composition = metallic
GE13	Melt superheat = 400 K; water depth = 4.0 m; system pressure = atmospheric

Table 4-10. Melt release conditions of Babcock & Wilcox reference system cases

Case no.	Initial and boundary conditions different from scoping Case BW1
BW2	Melt composition = eutectic; water depth = 1.7 m
BW3	Melt composition = metallic; water depth = 1.7 m
BW4	Melt superheat = 400 K; water depth = 1.7 m
BW5	Jet diameter = 5 cm; water depth = 1.7 m
BW6	Peripheral relocation (i.e., water depth = 1.7 m)
BW7	Total melt mass = 50% of total mass; water depth = 1.7 m
BW8	Total melt mass = 10% of total mass; water depth = 1.7 m
BW9	Water subcooling = 50 K; water depth = 1.7 m
BW10	System pressure = atmospheric; water depth = 1.7 m
BW11	Melt composition = eutectic
BW12	Melt composition = metallic
BW13	Melt superheat = 400 K; water depth = 1.7 m

as a purely metallic mixture. The melt is assumed to consist of 20% UO2 and 80% stainless steel. For Case GE2, jet impingement is predicted to occur with a maximum heat flux of 40 MW/m^2. Compared to Case GE6, the metal-oxide melt material suffers less erosion during melt/water interaction and results in a higher impinging heat flux than a purely ceramic melt jet.

Metallic Melt Composition (Case GE3)

In Case GE3, a purely metallic melt is assumed in order to represent a low temperature melt with a high thermal conductivity. The melt is assumed to be composed of 100% stainless steel. The thermophysical properties assumed for this material were obtained from Appendix F.

For Case GE3, jet impingement is predicted to occur with a maximum heat flux of 38 MW/m^2, which is slightly lower than predicted for the metal-oxide melt jet (i.e., Case GE2). However, the maximum heat flux is still considerably higher than predicted for purely oxidic melt jet (i.e., Case GE6). Compared to Case GE2, less solid particle formation is predicted for Case GE3 because the heat of fusion of stainless steel is higher than for the metal-oxide melt. A lower average temperature of the collected solid particles (i.e., 850 K) reflects the effects of the lower initial relocation temperature.

Increased Melt Superheat (Case GE4)

In Case GE4, the melt superheat is increased to 400 K. The effect of the melt superheat is to increase the impinging heat flux when jet impingement occurs. For Case GE4, a maximum heat flux of 45 MW/m^2 is predicted which is 70% higher than predicted for Case GE6 due to the higher superheat of the impinging jet. However, the state of the accumulated melt is similar to Case GE6.

Table 4-11. Results of THIRMAL/0 calculations for General Electric cases.

	Extent of jet breakup		Aspects of heat transfer if jet impingement occurs on lower head							
Case no.	Jet impingement	Breakup length (L/D)	Number of jets	Maximum impinging jet diameter (m)	Maximum impinging jet superheat (K)	Maximum impinging jet velocity (m/s)	Duration of impingement (sec)	Max. heat transfer coefficient (MW/m^2K)	Maximum heat flux (MW/m^2)	Integrated heat flux[a] (MJ/m^2)
GE1	No	44.6	—	—	—	—	—	—	—	—
GE2	Yes	—	1	0.031	235	4.29	870	0.17	40	3.48×10^4
GE3	Yes	—	1	0.028	241	3.88	870	0.156	38.0	3.31×10^4
GE4	Yes	—	1	0.033	372	4.45	700	0.118	45.0	3.15×10^4
GE5	No	62	—	—	—	—	—	—	—	—
GE6	Yes	—	1	0.023	226	4.45	700	0.119	26.9	1.88×10^4
GE7	No	26	—	—	—	—	—	—	—	—
GE8	No	17	—	—	—	—	—	—	—	—
GE9	No	35	—	—	—	—	—	—	—	—
GE10	Yes	—	1	0.043	218	4.52	700	0.124	27.1	1.9×10^4
GE11	No	42	—	—	—	—	—	—	—	—
GE12	No	39	—	—	—	—	—	—	—	—
GE13	Yes	—	1	0.06	362	4.49	700	0.127	46.1	3.2×10^4

a. Maximum heat flux from impinging jet (MW/m^2) integrated over duration of impingement (s).

Table 4-11. (continued).

Case no.	Melt accumulation state upon lower head			Temperature of accumulated melt			Debris size distribution	
	Impinging jet (%)	Molten droplets (%)	Solid particles (%)	Impinging jet (K)	Molten droplets (K)	Solid particles (K)	Count median particle diameter (mm)	Number standard deviation
GE1	0	0	100	—	—	1598	3.5	2.0
GE2	6.8	23.3	69.9	2635	2460	2250	2.5	1.7
GE3	4.9	56.8	38.3	1911	1670	850	2.8	2.0
GE4	7.8	82.0	10.2	3232	2860	1330	3.0	2.0
GE5	0	41.4	58.6	—	2860	1350	3.7	2.5
GE6	3.8	83.4	12.8	3086	2860	1320	3.0	2.0
GE7	0	0	100	—	—	2000	3.5	2.0
GE8	0	0	100	—	—	1600	3.5	2.2
GE9	0	26.3	73.7	—	2860	1150	2.5	2.0
GE10	3.7	96.3	0	3078	2980	—	2.2	1.7
GE11	0	0	100	—	—	1500	2.5	2.0
GE12	0	19	81	—	1670	1450	3.0	2.0
GE13	26.1	64.5	9.4	3222	3090	2850	1.5	2.0

Table 4-12. Results of THIRMAL/0 calculations for Babcock and Wilcox cases.

Case no.	Extent of jet breakup: Jet impingement	Extent of jet breakup: Breakup length (L/D)	Aspects of heat transfer if jet impingement occurs on lower head: Number of jets	Maximum impinging jet diameter (m)	Maximum impinging jet superheat (K)	Maximum impinging jet velocity (m/s)	Duration of impingement (sec)	Maximum heat transfer coefficient (MW/m^2K)	Maximum heat flux (MW/m^2)	Integrated heat flux[a] (MJ/m^2)
BW1	Yes	—	4	0.026	176	2.28	380	0.077	13.6	5.17×10^3
BW2	No	4.3	—	—	—	—	—	—	—	—
BW3	No	3.8	—	—	—	—	—	—	—	—
BW4	Yes	—	4	0.027	332	2.28	380	0.077	25.0	9.50×10^3
BW5	No	2.6	—	—	—	—	—	—	—	—
BW6	Yes	—	4	0.036	197	2.23	380	0.075	14.8	5.62×10^3
BW7	No	4.2	—	—	—	—	—	—	—	—
BW8	No	2.6	—	—	—	—	—	—	—	—
BW9	No	3.9	—	—	—	—	—	—	—	—
BW10	No	3.3	—	—	—	—	—	—	—	—
BW11	No	3.5	—	—	—	—	—	—	—	—
BW12	No	3.8	—	—	—	—	—	—	—	—
BW13	Yes	—	4	0.027	332	2.28	380	0.077	25.0	9.50×10^3

a. Maximum heat flux from impinging jet (MW/m^2) integrated over duration of impingement (s).

Table 4-12. (continued).

Case no.	Melt accumulation state upon lower head			Temperature of accumulated melt			Debris size distribution	
	Impinging jet (%)	Molten droplets (%)	Solid particles (%)	Impinging jet (K)	Molten droplets (K)	Solid particles (K)	Count median particle diameter (mm)	Number standard deviation
BW1	10	4.7	85.3	3036	3000	1700	3.2	2.0
BW2	0	0	100	—	—	852	3.5	2.2
BW3	0	5.2	94.8	—	1670	750	3.5	2.2
BW4	10.9	5.5	83.6	3192	3170	1600	3.7	2.5
BW5	0	0	100	—	—	1100	4.5	1.8
BW6	18.9	3.8	77.3	3057	3030	1780	3.2	2.0
BW7	0	0	100	—	—	1490	3.7	1.8
BW8	0	0	100	—	—	1050	4.7	2.0
BW9	0	0	100	—	—	700	3.2	2.0
BW10	0	41	59	—	2900	2860	2.0	1.5
BW11	0	0	100	—	—	840[a]	3.4[a]	2.5
BW12	0	7.8	92.2	—	1670[a]	910[a]	3.0[a]	2.0
BW13	10.9	5.5	83.6	3192	3170	1600	3.7	2.5

a. Accumulation on elliptical flow distributor.

Decreased Initial Jet Diameter (Case GE5)

In Case GE5, the initial jet diameter is assumed to be 5 cm. It is predicted that complete jet breakup occurs after the jet has penetrated a distance of 62 jet diameters in water. Compared to Case GE6, the reduction of the jet diameter eliminates the occurrence of jet impingement.

Reduced Water Depth (Case GE6)

In Case GE6, melt is assumed to relocate through the peripheral region of the core. A peripheral relocation path differs from a central relocation path (i.e., Cases GE1 and GE2) because there is a reduced water depth on the vessel periphery and because the peripheral surface upon which the jet impinges is angled. However, the angle at which a jet from the core would impinge upon the vessel surface is expected to be less than 45 degrees from the horizontal; and data from several references[4-31,4-32] indicate that the differences in impinging jet heat transfer resulting from surface angle are less significant for a surface angle less than 45 degrees. Hence, these THIRMAL/0 calculations have focused on the impact of reduced water depth on impinging jet heat transfer. As discussed in Section 4.2.1.2.1, the jet breakup length is ~45 initial jet diameters (i.e., 4.5 m) for Case GE1 and therefore, jet impingement occurs in Case GE6. The maximum impinging heat flux is predicted to be 26.9 MW/m^2.

Fifty Percent Melt Mass (Case GE7)

In Case GE7, only 50% of the total core mass is assumed to melt and relocate to the lower head. Since the cross-sectional area of the molten pool is still assumed to be the whole cross-sectional area of the core, the effect of the reduction of the melt mass is to decrease the height of the molten pool. As a result, the initial jet velocity is reduced. In Case GE7, an initial jet velocity of 4.33 m/s is estimated. The jet is predicted to break up completely within a distance of 26 jet diameters (i.e., 2.6 m). The accumulated melt is predicted to completely consist of solid particles with an average temperature of 2000 K. The effect of the jet velocity on jet breakup is further discussed in Section 4.2.1.4.

Ten Percent Melt Mass (Case GE8)

In Case GE8, the relocated melt is further reduced to 10% of the total core mass and the corresponding initial jet velocity is reduced to 1.94 m/s. Similar to Case GE7, the jet is predicted to break up, and the jet breakup length is 17 jet diameters (i.e., 1.7 m). By comparing the breakup lengths of Cases GE1, GE7, and GE8, the jet breakup length found is roughly proportional to the jet initial velocity. A non-dimensional analysis of the jet breakup length is given in Section 4.2.1.4. The accumulated melt is predicted to consist of 100% solid particles with an average temperature of 1600 K. Compared to Case GE7, the lower debris temperature predicted for Case GE8 is simply due to a longer settling time for the droplets and particles to reach the lower head.

Increased Water Subcooling (Case GE9)

In Case GE9, the water temperature is assumed to be the same as the cold leg inlet temperature corresponding to a water subcooling of 70 K. The effects of the water subcooling on the melt/water interaction are: (a) enhancement of heat transfer and quench of the melt, (b) reduction of the steam generation, and (c) reduction of the void fraction in the mixing zone. It is predicted that the jet is more likely to break up completely in subcooled water because in subcooled water, flow dispersion is less likely to occur in the mixing zone, at least at the lower

portion of the jet column. As a result, more surface on the jet volume would be covered by a thin vapor film in which the steam velocity could be much higher than that occurring in the surrounding mixing zone.[4-25] Therefore, the jet volume experiences more erosion in the region where a thin vapor film exists at the melt/water interface and a shorter jet breakup length is predicted. For Case GE9, the jet is predicted to break up with a breakup length of 35 jet diameters (i.e., 3.5 m), which is considerably shorter than predicted for saturated water (i.e., Case GE1). Compared to Case GE6, more solid particles with a lower average temperature are predicted for Case GE9 with subcooled water.

Reduced System Pressure (Case GE10)

In Case GE10, the system pressure is assumed to be atmospheric during the melt/water interaction. It is recognized that the most important effect of the reduced system pressure is to cause the specific volume of the steam to be more than at the elevated pressure conditions increasing the vapor volume flux flowing through the fuel/coolant mixture. However, the steam density increases roughly linearly with the pressure. As discussed in References 4-25 and 4-26, the driving force of the melt surface erosion is the steam inertia, ρU^2, and the effects of the system pressure are thus dependent upon the variation of ρU^2 versus pressure.

For Case GE10 at atmospheric pressure, jet impingement is predicted to occur as for Case GE6. The maximum impinging jet diameter is predicted to be 0.043 m, which is greater than predicted for the full system pressure, indicating a lower extent of breakup at lower system pressure. However, since the jet is predicted to impinge on the lower head with a lower temperature than predicted for Case GE6, the resulting impinging heat flux is roughly the same as predicted for Case GE6.

Mixed Oxide Melt with Increased Water Depth (Case GE11)

Case GE11 is similar to Case GE1 except for the melt composition. In Case GE11, the melt is assumed to consist of 20% UO_2 and 80% stainless steel, and the water depth is the same as Case GE1. The breakup and quench behavior of Case GE11 is similar to Case GE1. No jet impingement is predicted to occur.

Metallic Melt with Increased Water Depth (Case GE12)

Case GE12 is similar to Case GE1 except that the melt is completely composed of stainless steel. Similar to Case GE1, no jet impingement is predicted to occur. However, unlike Case GE1, some molten droplets are predicted to accumulate on the lower head mainly due to a relatively greater heat of fusion for stainless steel.

Conservative Estimate for Jet Impingement (Case GE13)

Based on the calculational results of Cases GE1 to GE12, Case GE13 was defined so that the boundary and initial conditions would be expected to yield a conservative estimate of the impinging heat flux over the range of the calculational matrix.

In Case GE13, an impinging jet 0.06 m in diameter with 362 K superheat is predicted. The resulting heat flux is 46.1 MW/m^2, which is not much higher than predicted for Case GE4 because the only difference between Case GE4 and Case GE13 is the system pressure. This result further indicates that the impinging heat flux is not sensitive to the system pressure.

4.2.1.3.2 Results for B&W Cases—The results of the cases run for the B&W reference system are listed in Table 4-12. In general, the effects of the melt release conditions on jet breakup, quench, and impingement are similar to those predicted for the GE reference system cases. However, noticeable differences include the following:

1. The jet breakup lengths predicted for the B&W cases in which jet breakup occurs are much shorter than predicted for the GE cases. This is because when the jets break up in Region IV (Region III for BW11 and BW12), the initial jet velocities for the jets formed from the elliptical plate (grid forging for BW11 and BW12) are too low (i.e., ~1 m/s) for the jets to penetrate a considerable distance before breakup occurs.

2. The maximum impinging jet velocities are lower for the B&W cases also because of a slower initial jet velocity for the jets formed from the elliptical plate.

3. The maximum melt superheat for the impinging jet is lower for the B&W cases. This results from a longer travel time for the jets before they impinge on the lower head even though the water depth in the BW lower plenum is shallower than that for a GE lower plenum.

4. The resulting impinging heat flux is lower than that predicted for the GE cases. This shows that the core structure plates have an important effect in mitigating the heat flux on the lower head when jet impingement occurs.

5. Comparing Cases BW6 and BW10, the extent of breakup is less significant for a higher system pressure (i.e., 14.7 MPa), contrary to what was predicted for the GE cases. This indicates that the THIRMAL/0 model predicts a non-monotonic relation between the steam inertia, ρU^2, and the pressure.

4.2.1.3.3 Results for Westinghouse Cases—For the Westinghouse reference plant design, the major lower plenum structures are the lower core plate, core support, upper tie plate, lower tie plate, and secondary core support, as shown in Figure 4-50. If molten material from a fuel element is assumed to drain through the lower core plate, it is likely that the melt could accumulate on the horizontal plates (i.e., core support, upper tie plate, lower tie plate, and secondary core support). The core support has a 0.40-m diameter hole in the center, 92 holes 0.24 m in diameter, and 16 holes 0.18 m in diameter. The upper tie plate and the lower tie plate both have roughly a ring shape with some irregularly shaped holes. The secondary core support has a square shape with a square hole 0.57 x 0.57 m. As shown in Figure 4-51, a "straight-shot" jet relocation is possible if the melt is relocated from the central region of the core. For peripheral relocation, the melt can either penetrate one of the 0.24-m diameter holes on the core support or accumulate on the core support and drain from the adjacent holes. The jet (or jets) from the core support may not be intercepted by any of the horizontal plates below the core support for peripheral relocation (see Figure 4-50).

Based on the configuration of the horizontal plates in the lower plenum, it is assumed that a 0.1 m diameter jet interacts only with water in the lower plenum for both central relocation and peripheral relocation because a "straight-shot" jet can exist in both the central and peripheral regions. The dimensions of the lower plenum configuration used in this work are listed in Appendix F.

Based on the calculational results of the B&W cases, jet impingement is predicted to occur in Cases BW1, BW4, and BW6. Therefore, three corresponding cases (i.e., W1, W4, and W6)

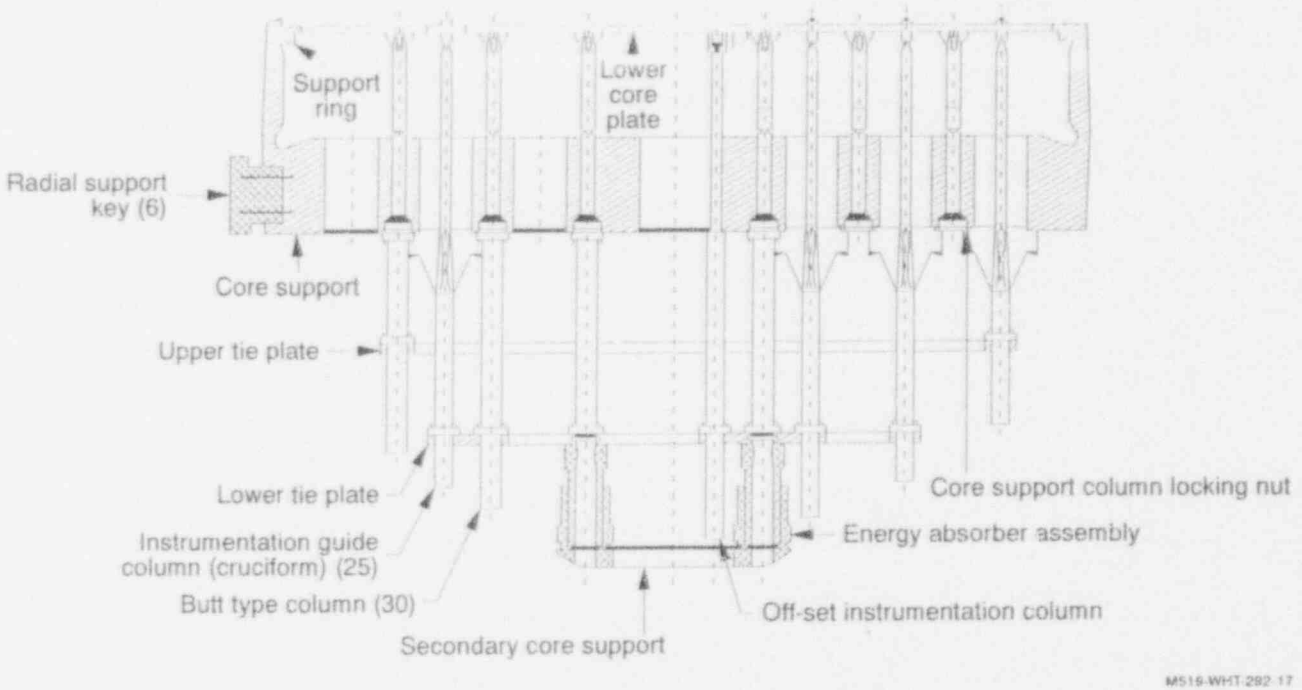

Figure 4-50. Lower plenum structures of Westinghouse vessel.[4-33]

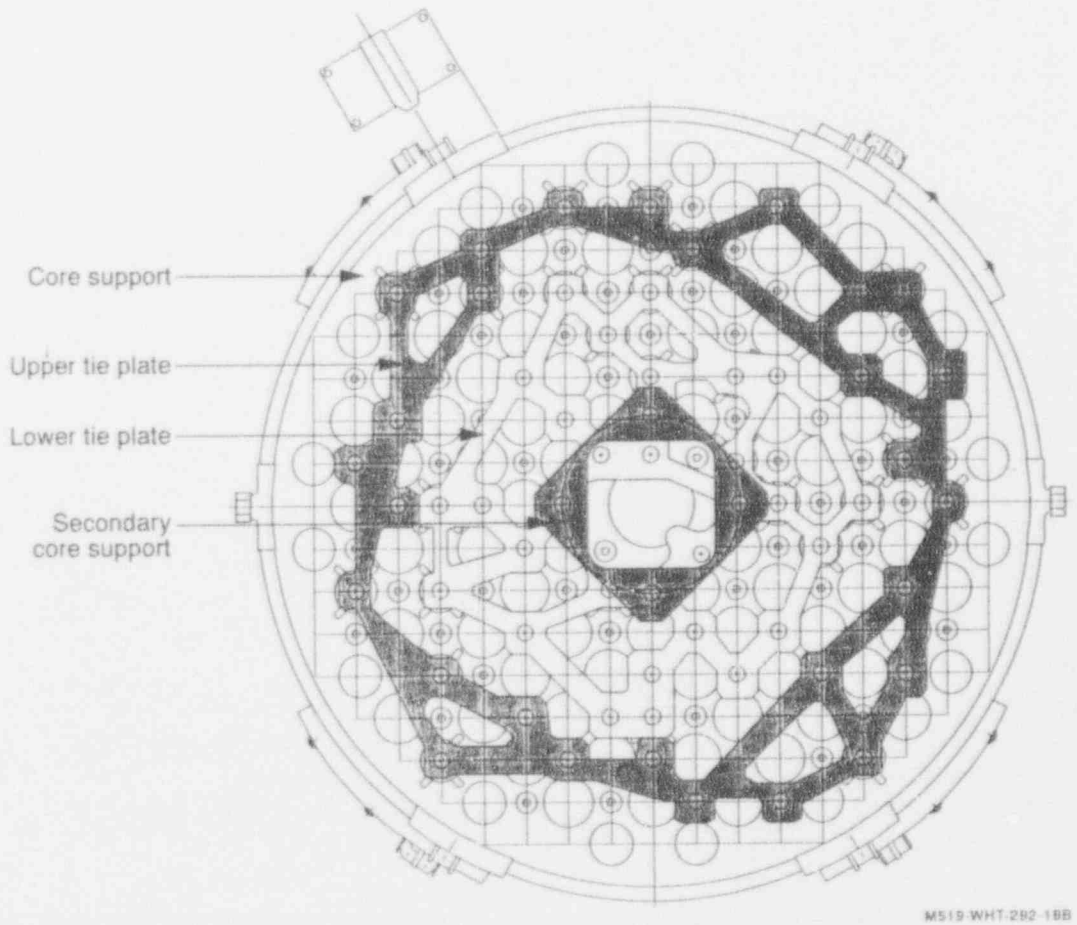

Figure 4-51. Cross-sectional-view of lower plenum structures.[4-33]

were carried out for the Westinghouse reference system. In order to evaluate the effects of the accumulation of the melt and the formation of multiple jets due to a non-straight through relocation, an additional case, W4a, in which four jets were assumed to form from the core support was also carried out. The melt release conditions for these cases are listed in Table 4-13.

The results of the Westinghouse cases are shown in Table 4-14. Jet impingement is predicted for all of the Westinghouse cases except for Case W4a in which credit is taken for accumulation of the melt and formation of the multiple jets with lower superheat and lower jet velocity. In general, the impinging jets predicted for the Westinghouse cases have larger diameters than predicted for the B&W cases, in spite of a deeper overall water pool residing in the Westinghouse lower plenum. This is because the multiple jets formed from various flow plates in the B&W lower plenum have much smaller initial jet velocities (resulting in relatively longer travel times for the jet column to shrink and break up). Also, the predicted impinging jet diameters in the Westinghouse cases are larger than those in the GE cases because of the smaller water depths in the Westinghouse plant lower plenum. However, for Case GE6, a larger integrated heat flux is predicted than for Case W6 despite the smaller impingement jet diameter. This is because the larger BWR core mass results in a longer time for melt relocation and impingement.

4.2.1.3.4 Results of CE Cases—For the CE reference system, the major lower plenum structure is the core support assembly as shown in Figure 4-52. The core support assembly is composed of two horizontal plates (i.e., the core support plate and bottom plate of

Table 4-13. Melt release conditions of Westinghouse cases.

	W1	W4/W4a	W6
Melt composition	Ceramic	Ceramic	Ceramic
Melt superheat, K	250	400	250
Melt mass, kg	1.84×10^5 (100% of total mass)	1.84×10^5	1.84×10^5
Jet diameter, m	0.1	0.1	0.1
Initial jet velocity, m/s	5.98	5.98	5.98
Relocation path	Central	Peripheral	Peripheral
Water depth, m	3.09	2.53	2.53
System pressure, MPa	15.3 (Full system pressure)	15.3	15.3
Water subcooling, K	0	0	0

Table 4-14. Results of THIRMAL/0 calculations for Westinghouse cases.

Case no.	Extent of jet breakup		Aspects of heat transfer if jet impingement occurs on lower head							
	Jet impingement	Breakup length (L/D)	No. of jet	Maximum impinging jet diameter (m)	Maximum impinging superheat (K)	Maximum impinging jet velocity (m/s)	Duration of impingement (s)	Maximum heat transfer coefficient (MW/m^2K)	Maximum heat flux (MW/m^2)	Integrated heat flux[a] (MJ/m^2)
W1	Yes	—	1	0.046	220	4.46	425	0.129	28.3	1.2×10^4
W4	Yes	—	1	0.072	373	4.58	425	0.128	47.6	2.02×10^4
W4a	No	5.6	—	—	—	—	—	—	—	—
W6	Yes	—	1	0.064	227	4.58	425	0.126	28.5	1.2×10^4

a. Maximum heat flux from impinging jet (MW/m^2) integrated over duration of impingement (s).

Case no.	Melt accumulation state on lower head			Temperature of accumulated melt			Debris size distribution	
	Impinging jet (%)	Molten droplets (%)	Solid particles (%)	Impinging jet (K)	Molten droplets (K)	Solid particles (K)	Count median particle diameter (mm)	Number standard deviation
W1	15.8	1.2	83.0	3080	3078	1200	2.5	1.5
W4	39.7	6.8	53.5	3233	3150	1800	2.4	1.6
W4a	0	0	100	—	—	—	3.5	2.0
W6	31.4	4.6	64.0	3087	3080	1400	2.5	1.5

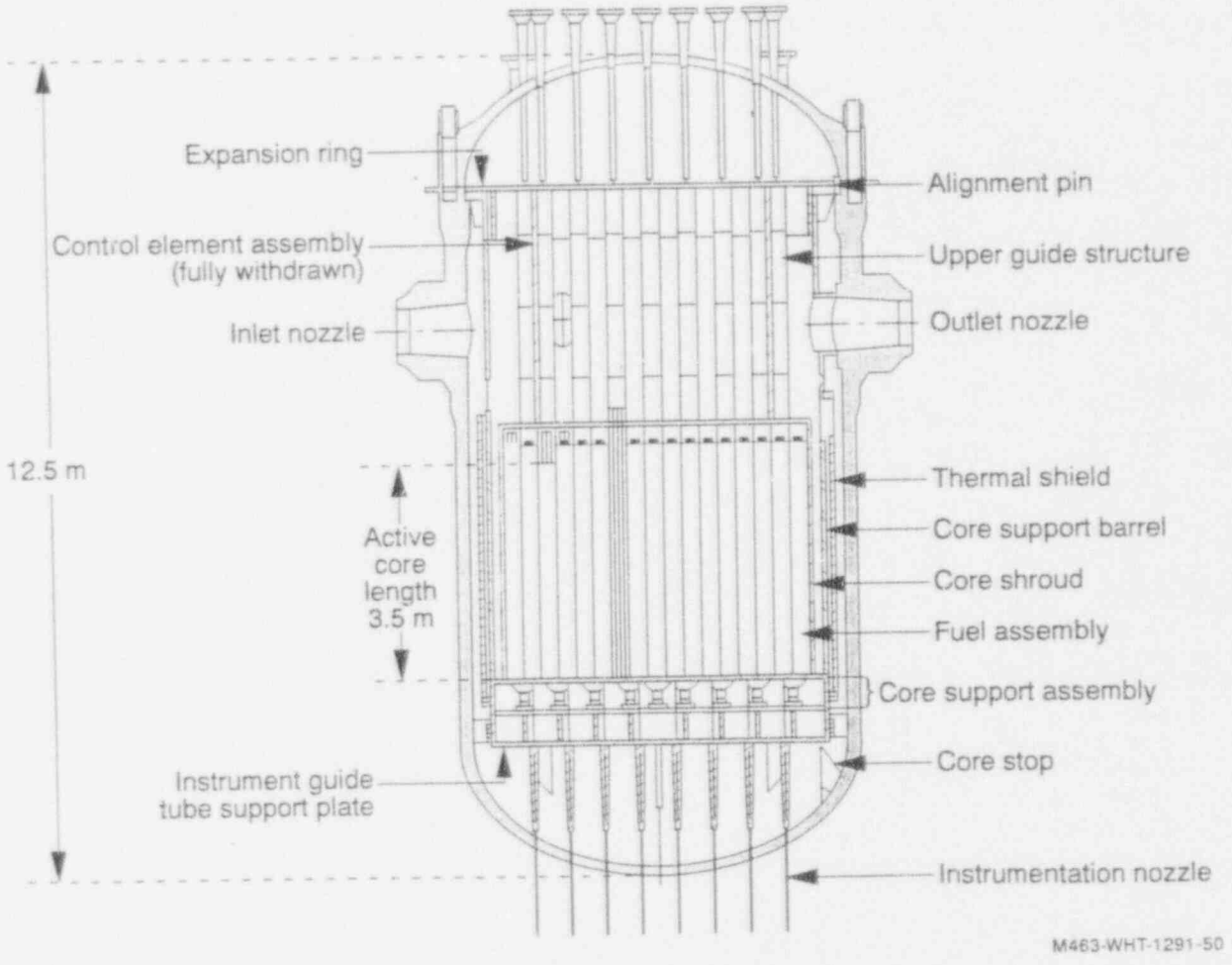

Figure 4-52. Lower plenum structures of reference CE vessel jet impingement calculations.[4-33]

the core support assembly). Beneath the core support assembly of this particular CE plant, the Maine Yankee plant, is the instrumentation guide tube support plate. Although most operating CE plants have no lower head penetrations, the Maine Yankee plant was analyzed because of design information availability. The dimensions of the core lower plenum structures used in this work are listed in Appendix F. Based on the calculational results of the B&W cases, three corresponding cases (i.e., CE1, CE4, and CE6) were carried out for the CE reference design. The melt release conditions for these cases are listed in Table 4-15.

If the melt is assumed to relocate from the bottom of the core (i.e., from the core support plate), the bottom plate of the core support assembly and the instrumentation guide tube support are the only plates where the melt can possibly accumulate. However, because the flow holes on the bottom plate of the core support assembly are closely spaced and densely packed (e.g., 25 0.076 diameter holes are located on a 0.49 x 0.49-m area near the center region of the bottom plate), a much larger fraction of the plate cross section corresponds to openings than in the other plant configuration. Thus a 0.1-m diameter jet relocating from the bottom of the molten core region would be expected to penetrate the bottom plate without undergoing significant dispersion by the plate structures. Therefore, corium emerging from the bottom plate is modeled in a different manner than in the previous calculations. In particular, the melt is not assumed to

Table 4-15. Melt release conditions of Combustion Engineering cases

	CE1	CE4	CE6
Melt composition	Ceramic	Ceramic	Ceramic
Melt superheat, K	250	400	250
Melt mass, kg	1.86×10^5	1.86×10^5	1.86×10^5
Jet diameter, m	0.1	0.1	0.1
Initial jet velocity, m/s	6.50	6.50	6.50
Relocation path	Central	Peripheral	Peripheral
Water depth, m	2.81	2.02	2.02
System pressure, MPa	15.3	15.3	15.3
Water subcooling, K	0	0	0

spread along the upper surface of the bottom plate, but to penetrate directly through those openings in the path of the jet. Since the 0.076-m hole diameter is less than the 0.1-m jet diameter, it is assumed that the plate transforms the melt into one 0.076-m diameter jet surrounded by four smaller jets corresponding to the melt passing through the four nearest adjacent holes.

The next horizontal plate below the bottom plate is the instrumentation guide tube support plate. On this plate, 82 flow holes 0.254-m in diameter are also closely spaced. Therefore, it is reasonable and conservative to assume that the multiple jets formed from the bottom plate would make a "straight-shot" penetration without being significantly impeded on the instrumentation guide tube support plate.

The THIRMAL/0 calculation results for the CE cases are listed in Table 4-16. Jet impingement is predicted for all cases. Only the middle jet of Case CE1 impinges on the lower head, while all five jets of Cases CE4 and CE6 impinge on the peripheral region of the lower head.

4.2.1.4 Non-dimensional Analysis of Jet Breakup and Jet Impingement. In this section the important combinations of variables that characterize the behavior of jet breakup and jet impingement are investigated using dimensionless groups in order to enhance the utility of the calculational results.

4.2.1.4.1 Jet Breakup Length—A liquid mass moving in a different ambient fluid will break up into drops. The jet breakup length is the distance the jet can penetrate before complete fragmentation occurs and can be expressed as

Table 4-16. Results of THIRMAL/0 calculations for Combustion Engineering cases.

Case no.	Extent of jet breakup: Jet impingement	Extent of jet breakup: Breakup length (L/D)	Aspects of heat transfer if jet impingement occurs on lower head: No. of jets	Maximum impinging jet diameter (m)	Maximum impinging superheat (K)	Maximum impinging jet velocity (m/s)	Duration of impingement (s)	Maximum heat transfer coefficient (MW/m^2K)	Maximum heat flux (MW/m^2)	Integrated heat flux[a] (MJ/m^2)
CE1	Yes	—	1	0.059	218	3.72	390	0.107	23.4	9.12×10^3
CE4	Yes	—	5[b]	0.068	377	3.81	390	0.106	39.8	1.55×10^4
CE6	Yes	—	5[b]	0.064	228	3.81	390	0.106	24.4	9.52×10^3

a. Maximum heat flux from impinging jet (MW/m^2) integrated over duration of impingement (s).

b. Impingement conditions apply to large centrally located jet in cluster of five jets.

Case no.	Melt accumulation state on lower head: Impinging jet (%)	Melt accumulation state on lower head: Molten droplets (%)	Melt accumulation state on lower head: Solid particles (%)	Temperature of accumulated melt: Impinging jet (K)	Temperature of accumulated melt: Molten droplets (K)	Temperature of accumulated melt: Solid particles (K)	Debris size distribution: Count median particle diameter (mm)	Debris size distribution: Number standard deviation
CE1	46.9	4.7	48.4	3078	3026	1867	3.2	2.2
CE4	63.8	20.5	15.7	3237	3118	2855	3.0	2.0
CE6	56.5	5.4	38.1	3088	3083	2067	3.2	2.2

$$L \sim U_J \tau \tag{4-40}$$

where

L = jet breakup length

U_J = jet velocity

τ = breakup time.

The breakup time, τ, is approximated by

$$\tau \sim \frac{D_J}{U_E} \tag{4-41}$$

where

D_J = jet diameter

U_E = erosion velocity on jet surface.

As discussed in References 4-25 and 4-26, the erosion velocity is the perpendicular component of the velocity of the eroded material with respect to the jet surface. For a high-temperature melt surface in a film boiling regime, the erosion velocity has been shown to be a function of the jet density, ρ_J, jet velocity, U_J , coolant vapor density, ρ_{cg}, and coolant vapor velocity, U_v, as given below.[4-26]

$$U_E = \frac{\left[K_1 \rho_{cg} \rho_J \left(U_v - U_J\right)^2 - \sigma_J k_p \left(K_1 \rho_{cg} + \rho_J\right)\right]^{1/2}}{K \rho_{cg} + \rho_J} \tag{4-42}$$

where $K_1 = (1 + \cosh k_p \delta_v)/\sinh k_p \delta_v$; and the most probable wave number, k_p, is

$$k_p = \frac{2\rho_{cg} U_v^2 K_1}{3\sigma_J} \tag{4-43}$$

where

σ_J = surface tension of jet material

δ_v = vapor film thickness.

When the void fraction is high enough for a dispersed flow regime to occur, the thin vapor film would not exist and the jet surface would be subjected to a global steam flow in the vicinity of the jet. The erosion velocity, as express in Equation (4-42), is obtained simply by setting the vapor film thickness to a large number under this condition.

Thus, Equation (4-42) becomes

$$U_E = \left(\frac{\rho_{cg} U_v^2 - \sigma_J k_p}{\rho_J} \right)^{1/2} \quad (4\text{-}44)$$

and

$$k_p = \frac{2\rho_{cg} U_v^2}{3\sigma_J} \quad . \quad (4\text{-}45)$$

It is interesting to note that Equations (4-44) and (4-45) are the same as obtained by Levich[4-34] for the erosion at the boundary between the media with nonzero relative velocity.

Combining Equations (4-40), (4-43), (4-46), and (4-47), the jet breakup length expressed in terms of the jet diameter, D_J, can be approximated by

$$\frac{L}{D_J} \sim C \sqrt{\frac{We_J}{k_p D_J}} \quad (4\text{-}46)$$

where

We_d = $U^2_J \rho_J D_J/\sigma_J$, the jet Weber number

C = a constant.

Based on Equation (4-46), the jet breakup lengths predicted by THIRMAL/0 in the present investigation are plotted in Figure 4-53. As shown in Figure 4-53, the predicted breakup lengths are very roughly correlated by the Weber number. The value of the constant, C, is very roughly equal to unity.

The correlations of jet breakup length predicted by some of the previous investigators are also shown in Figure 4-53 for comparison. These previous correlations will also be briefly discussed. Taylor[4-35] predicted that the breakup length of a low-melting-point metal jet (implicitly assumed to be atomizing) in water obtained using a linear analysis of the Kelvin-Helmholtz instability should depend on the jet-ambient fluid density ratio,

$$\frac{L}{D_J} \sim 5 \sqrt{\frac{\rho_J}{\rho_a}} \quad , \quad (4\text{-}47)$$

where a denotes the ambient fluid (i.e., water). This relation was later derived by Levich.[4-34] In general, Equation (4-47) agrees well with experiment data for liquid jets in immiscible liquids without significant vapor generation.

Another extreme breakup mechanism results from the capillary stresses on the jet column. The capillary instability of an inviscid liquid thread was first analyzed by Rayleigh and the jet breakup due to capillarity is often called "Rayleigh breakup." It has been shown[4-36] that the drops generated by capillary breakup will have a diameter of 1.89 D_J (i.e., nearly twice that of the

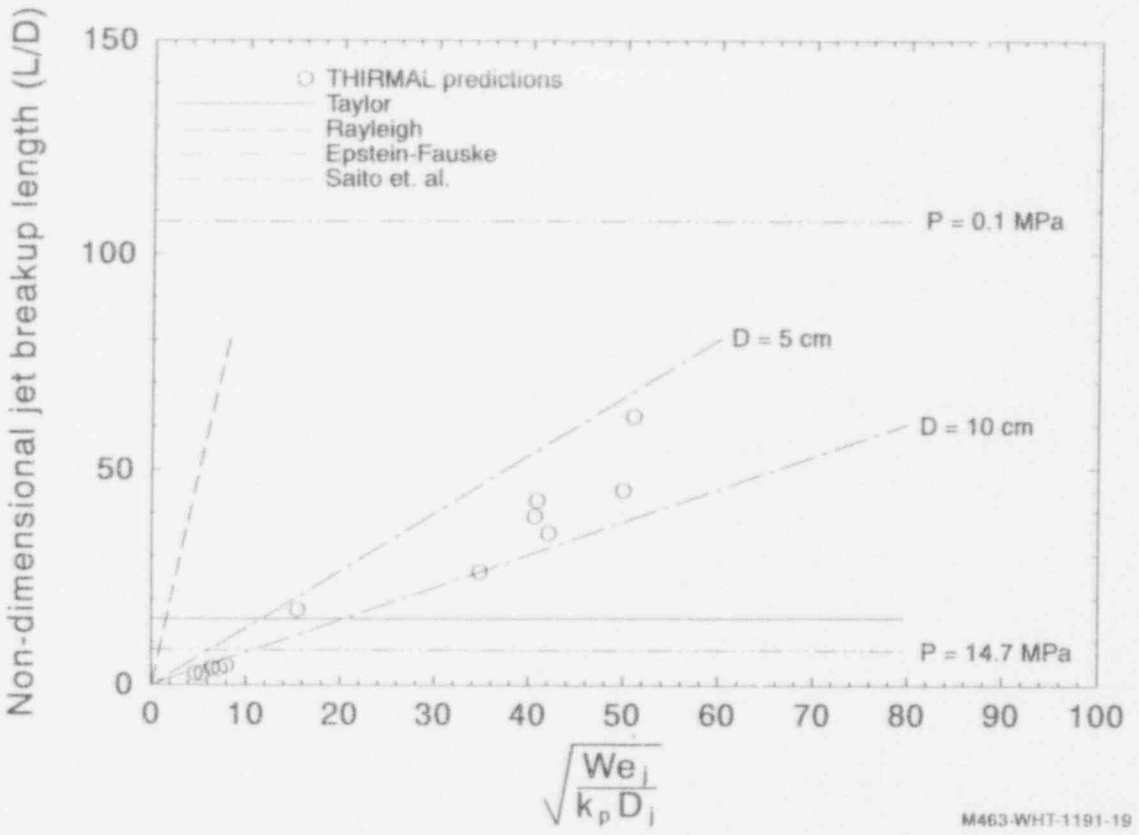

Figure 4-53. Non-dimensional jet breakup lengths calculated in current investigation versus various simple correlations.

undisturbed jet). According to Weber's analysis,[4-37] the breakup length of a viscous liquid jet in a gas atmosphere can be expressed as

$$\frac{L}{D_J} \sim 13\left[\sqrt{We_J} + \frac{3We_J}{Re_J}\right] \tag{4-48}$$

where

We_J = jet Weber number

Re_J = jet Reynolds number.

Epstein and Fauske[4-38] analyzed the Kelvin-Helmholtz instability on two parallel interfaces of the vapor film between a melt jet and the ambient water. By ignoring the steam velocity in the vapor film, they suggested that the jet breakup length is given by

$$\frac{L}{D_J} = \frac{\sqrt{3}}{2}\left(1 + \frac{\rho_{cg}}{\rho_J}\right)\left(\frac{\rho_J}{\rho_{cg}}\right)^{1/2} \tag{4-49}$$

where the subscript, g, denotes steam in the vapor film.

Although not compared in Figure 4-53, it should be noted that Epstein and Fauske[4-39] also suggest that data for water jets in air or water can be correlated using

$$\frac{L}{D_J} = 6.25 \left(\frac{\rho_J}{\rho_l}\right)^{1/2}$$

where the subscripts J and l denote the jet and the continuous phase (air or water), respectively.

From experiments with water jets penetrating Freon-11 and liquid nitrogen, Saito et al.,[4-40] obtained the following correlation for the steady state jet penetration length:

$$\frac{L}{D_J} = (2.1)\ Fr^{1/2} \sqrt{\frac{\rho_J}{\rho_l}} \qquad (4\text{-}50)$$

where the Froude number, $Fr = U_J^2/g\ D_J$, and the subscripts J and l denote jet and continuous phase (i.e., liquid), respectively.

Based upon THIRMAL/0 predictions, many factors can affect the jet breakup length, such as the initial jet velocity, melt temperature, water subcooling, system pressure, and vessel configuration. Equation (4-46) only suggests a qualitative estimate of the jet breakup length. An accurate estimate can be obtained only when all the factors mentioned above are considered.

4.2.1.4.2 Impinging Heat Flux and Energy Deposition—In order to evaluate the effects of the coolant and the lower plenum structures on mitigating the thermal loading from the impinging jets, the extent of reduction of the impinging heat flux and the local energy deposition on the impinging zone are expressed in terms of Q/Q_o and E_l/E_{lo}, respectively. Q/Q_o is the ratio of the impinging heat flux to that which would be calculated for the initial coherent jet without any melt/water and melt/structure interactions. E_l/E_{lo} is the ratio of the total energy deposited on the impinging zone by any of the impinging jets to that which would be deposited by the initial coherent jet without any melt/water and melt/structure interactions. Therefore, the ratio E_l/E_{lo} would give an estimate of how the local thermal load is reduced by the coolant and the lower plenum structures. Specifically, the ratio of the impinging heat flux is defined as

$$\frac{Q}{Q_o} = \frac{h_l\ \Delta T}{h_{lo}\ \Delta T_o} \qquad (4\text{-}51)$$

where the subscript o denotes the impingement without the effects of coolant and structures. The acceleration of a free fall jet is considered in evaluating h_o when the coolant and structures are assumed to be absent in the lower plenum. Similarly, the ratio of the energy deposited by a single impinging jet to the total energy which would be deposited by the initial jet impinging on the lower head without the melt-water and melt-structure interactions can be expressed as

$$\frac{E_l}{E_{lo}} = \frac{h\ \Delta T\ A\ \Delta t}{h_o\ \Delta T\ A_o\ \Delta t} = \frac{Q}{Q_o}\left(\frac{D_J}{D_{Jo}}\right)^2 \qquad (4\text{-}52)$$

where A and D are the impinging area and impinging jet diameter, respectively, and Δt is the duration of the jet impingement.

Table 4-17 lists the predicted values of Q/Q_o and E_l/E_{lo} for those cases with the occurrence of jet impingement. This prediction is further illustrated in Figure 4-54. In general, the impinging heat flux is reduced by a factor of two for Cases GE4 and GE6 and by approximately a factor of four for cases BW4 and BW6. However, the total energy deposited by any one of the impinging jets accounts for only a small fraction (i.e., 3 to 5% for Cases BW4 and BW6, and 4 to 11% for Cases GE4 and GE6) of the total energy that would be deposited by the initial jet if it were to impinge on the lower head without the obstacles imposed by coolant and structures. This also indicates that the formation of multiple jets resulting from various horizontal flow plates in the B&W vessel has a significant effect in reducing the thermal loading on the lower head. However, this effect is less significant for the Westinghouse and CE reference systems because of the specific configuration of the flow holes in the horizontal plates incorporated in these two designs.

Table 4-17. Non-dimensional thermal loading on lower head for cases with prediction of jet impingement.

Case number	Ratio of impinging heat flux (Q/Q_o)	Ratio of local energy deposition (E_l/E_{lo})
GE2	0.56	0.09
GE3	0.53	0.07
GE4	0.57	0.11
GE6	0.44	0.04
GE10	0.54	0.17
GE13	0.53	0.33
BW1	0.22	0.02
BW4	0.28	0.03
BW6	0.25	0.05
W1	0.44	0.15
W4	0.49	0.40
W6	0.47	0.30
CE1	0.38	0.20
CE4	0.43	0.33
CE6	0.43	0.24

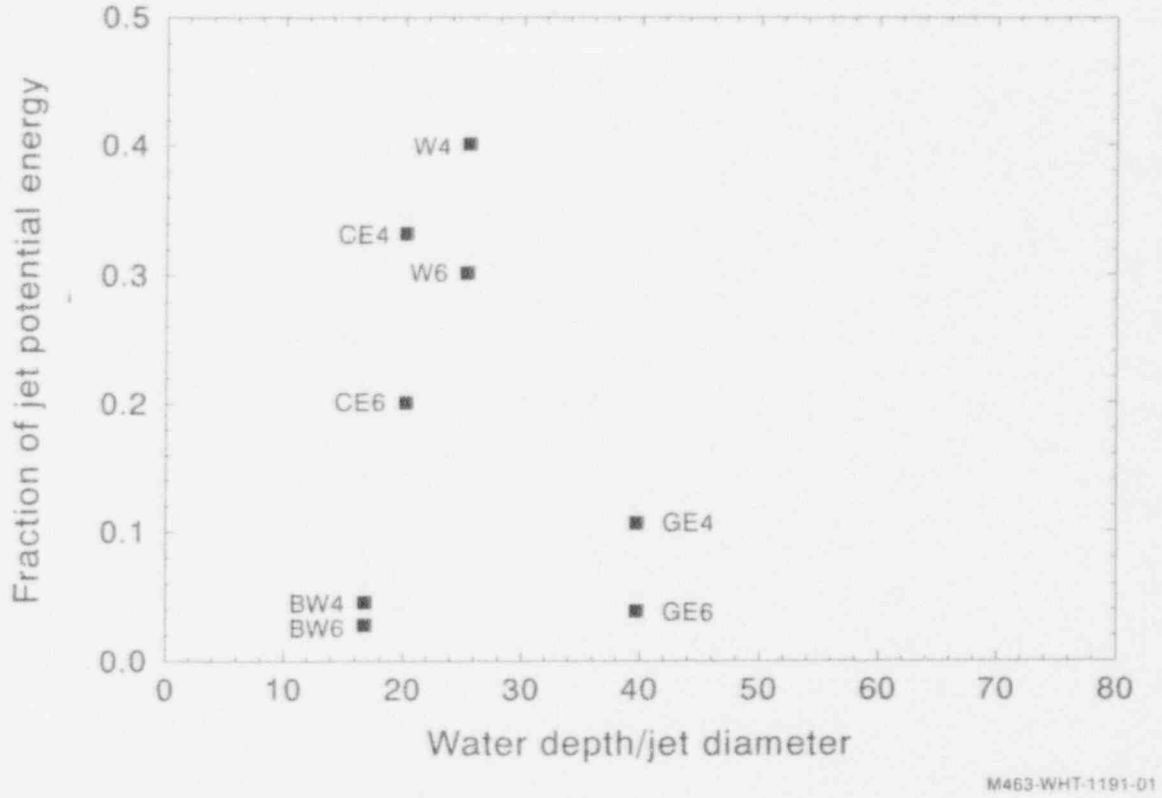

Figure 4-54. Non-dimensional impinging energy for deposition cases with impingement.

4.2.1.5 Summary and Conclusions. The following conclusions may be drawn from the results of the various THIRMAL/0 calculations of melt/water interactions and the conditions of arriving melt in the four reference LWR systems:

1. The occurrence of jet breakup and jet impingement on the lower head are calculated to be sensitive to many factors. The behavior of jet breakup depends on the conditions of the melt (i.e., material composition, initial melt temperatures, and initial jet geometry), water subcooling, water depth, and system pressure.

2. The presence of flow plates in the lower plena and the hole configuration within these flow plates strongly affect jet impingement for PWR plants. For B&W plants, the flow plates accumulate the melt and form multiple jets, reducing the velocity of the jets and the fraction of initial jet energy that can impinge on the vessel lower head. Unlike the flow plates in a B&W plant, the flow plates in Westinghouse and CE plants generally do not accumulate the melt. Rather, "straight shot" jets are more likely to occur in Westinghouse and CE lower plena, resulting in more significant jet impingement.

3. In the GE reference BWR system, the released melt jet is unimpeded by any horizontal structural plates. However, the GE lower head is protected by the water pool, which is deeper than the water pool present within PWR lower plena.

In the B&W reference plant, melt collection upon and drainage from the various flow distribution and support plates located inside the lower plenum are calculated to promote

additional melt breakup and quenching. However, the effects are strongly dependent upon the number of participating plates, the flow hole size, and the relative orientation of holes in successive plates. In particular for other LWR reference plants, the presence of nearly concentric openings enabling relocation through part of the lower plenum in a straight-shot manner is important. The state of the arriving melt is also strongly dependent upon the water depths, which differ among the PWR reference plants.

In the B&W reference system, melt jet impingement was calculated for only four of the thirteen cases calculated. For the assumed peripheral release of the total core mass of oxide composition with 250 K of initial molten superheat and a 10-cm initial diameter, 77% of the melt is calculated to arrive on the lower head as frozen particles, 4% as molten droplets, and 19% in the form of four impinging jets 3.6 cm in diameter. Any of the following conditions was found to eliminate the prediction of jet impingement: decreasing the jet diameter from 10 to 5 cm; decreasing the core pool height and corresponding gravity driving head from a value representative of 100% of the total core mass to 50%; increasing the water subcooling from zero to 50 K; decreasing the primary system pressure from the nominal operating pressure to atmospheric; or increasing the proportion of metal in the melt composition from 0 to 80% or greater.

For the GE reference system, melt impingement was predicted for less than half of the cases considered. For a case involving a peripheral release of 100% of the core mass as 80 wt% UO_2 - 20 wt% ZrO_2 oxide having initially 250 K of molten superheat and a diameter of 10 cm, 83% of the melt would arrive as molten droplets, 13% as particles, and only 4% as a 2.3-cm diameter impinging jet. Any of the following conditions were calculated to completely eliminate jet impingement: increasing the water depth from that representative of a release at the core periphery to one at the core center; decreasing the jet diameter from 10 to 5 cm; decreasing the core pool height and corresponding gravity driving head from a value representative of 100% of the core mass to 50% of the mass; increasing the water subcooling from zero to 70 K; or increasing the proportion of metal in the released melt from zero to 80% or greater.

For those cases in which jet impingement is calculated, the heat flux on the lower head is less than that which would be predicted if the jet released from the core were imagined to unrealistically relocate and impinge as a single coherent jet contracting under gravity without any melt/water or melt/structure interactions. The ratio of the heat flux for each individual jet and the heat flux corresponding to the idealized noninteracting jet were compared for two cases in which coherent jet impingement was predicted in all of the four reference plants. For the particular impingement heat transfer correlation assumed, this ratio is calculated to vary from 0.44 to 0.57 for Cases GE4 and GE6; 0.25 to 0.28 for Cases BW4 and BW6; 0.47 to 0.49 for Cases W4 and W6; and 0.43 for Cases CE4 and CE6.

Another measure of the impingement thermal loading on the lower head wall is the ratio of the energy deposited into the lower head inside the impingement zone of an individual jet to that from impingement of an idealized noninteracting single coherent jet. This ratio was also compared for two cases in which coherent jet impingement was predicted in all four reference plants: Case 4 and Case 6. The local energy deposition ratio is calculated to vary from 0.04 to 0.11 for the GE reference system, 0.03 to 0.05 for the B&W reference system; 0.3 to 0.4 for the Westinghouse reference system, and 0.24 to 0.33 for the CE reference system. Hence, the Westinghouse and CE plants are predicted to be subjected to higher thermal loading because of the potential for "straight-shot" relocation in conjunction with the shallower water depths that exist in PWR lower plena (compared to BWR lower plena).

In most cases, a significant portion of the released melt is calculated to collect on the lower head as frozen particles. In specific instances, the entire melt mass is predicted to accumulate as a solid debris bed. For example, this is calculated for the GE reference system when a 10-cm diameter jet of oxide having 250 K of initial molten superheat is released at the center of the core plate. In the B&W reference system, complete freezing is predicted in six out of the nine cases involving complete jet breakup. Less solidification was obtained for the Westinghouse and CE reference systems. In particular, no more than 48% of the melt collected as particles in the CE calculations. For the present investigation, predicted median particle sizes range from 1.5 to 4.5 mm median diameter. Because a distribution of sizes is obtained for each case, individual particles could be smaller or larger than this range.

For all of the cases in which jet breakup is calculated prior to jet impingement upon any structural plates or the lower head, the predicted jet breakup distance was found to be roughly proportional to the square root of the jet Weber number divided by the product of the jet diameter and the most probable wave number for Kelvin-Helmholtz disturbances. The resulting expression shows better agreement with simulant data on the breakup of a jet of one liquid penetrating into a second volatile liquid than the expressions of Taylor,[4-35] Weber,[4-37] as well as Epstein and Fauske.[4-38] However, a correlation based solely upon this relation still exhibits significant scatter because effects of variables, such as system pressure or water subcooling, are not included. Thus, detailed calculations are still required to obtain more precise predictions of the breakup length.

4.2.2 Localized Creep Rupture

This section focuses on the potential for a localized vessel failure to occur. As discussed in Section 2, no previous analyses of this vessel failure mode were found in the literature. Furthermore, this phenomenon was considered too complex to consider using a closed-form solution technique. Hence, a finite difference model was developed for analyzing this phenomenon. The model was applied to several types of thermal conditions having the potential to cause a localized vessel failure. These thermal conditions are discussed in Section 4.2.2.1. A description of the model is provided in Section 4.2.2.2. Additional details about the model development are provided in Appendix D, and results from verification calculations performed to compare results from this new model and a finite element structural analysis code are provided in Appendix E. The criteria used to predict failure are described in Section 4.2.2.3. Model results for thermal conditions discussed in Section 4.2.2.1 are presented in Section 4.2.2.4, and conclusions are summarized in Section 4.2.2.5.

4.2.2.1 Temperature Distributions for Localized Analyses. Calculations consider two types or sets of thermal conditions. The first set of conditions involve contrived, steady-state temperature profiles, simulating physical loads and illustrating features of an analytical structural method developed for examining vessel behavior under severe local loads. The second set of loads are time-dependent temperature distributions generated from finite element solutions to the vessel conduction problem using boundary conditions based on various debris characteristics.

Two different contrived temperature profiles are considered. The first is designated a "line source" profile, and simulates particulate or molten corium in an instrumentation tube. The presence of such material creates a localized preferential path for heat transfer out of the vessel. This is most significant in that the line source creates elevated temperatures through the thickness of the vessel around the tube. Previous analyses indicated that the consequences of highly elevated temperatures on the inside of the vessel are mitigated by the presence of cooler material on the outside; the lower temperature material absorbs the load from weakened material on the

inside. With elevated temperatures through the thickness, there is no material to provide strength and stiffness locally, which suggests the possibility of a failure around the tube. Local failure may also be precipitated by hot spots at certain discrete locations. The relocated core consists of a mixture of highly dissimilar materials and is not necessarily a homogeneous composition. Although there would be a pronounced radial temperature gradient underneath such a hot spot, the magnitude of the temperatures through thickness might again be high enough to weaken the material to the point where local failure is possible.

Steady-state temperature distributions simulating these local effects are superimposed on a background temperature distribution. The background distribution is assumed to vary linearly between an inner temperature, T_{in}, and an outer temperature, T_{out}, through the thickness of the vessel and not to vary along the meridian. The local temperature distributions are characterized by a peak temperature, ΔT, and angular spread, $\Delta\varphi_o$, about the bottom of the vessel. The distributions are contrived in that they are not obtained from solutions to a conduction equation with physical boundary conditions. Instead, they are intended to simulate peak temperature profiles and illustrate features of the analytical method described in Section 4.2.2.2. The following functional dependencies of the "line source" and "hot spot" temperature distributions are expressed in terms of variables ξ and ζ used to describe material points in the vessel:

Line source

$$T_1(\zeta,\xi) = \frac{1}{2}(T_{in} + T_{out}) - \frac{\zeta}{t_v}(T_{in} - T_{out}) + \left[\Delta T + \frac{1}{2}(T_{in} - T_{out}) + \frac{\zeta}{t_v}(T_{in} - T_{out})\right] e^{-\xi^m/\Delta\varphi_o} \quad (4\text{-}53)$$

Hot spot

$$T_2(\zeta,\xi) = \frac{1}{2}(T_{in} + T_{out}) - \frac{\zeta}{t_v}(T_{in} - T_{out}) + \Delta T\, e^{-(\xi^m/\Delta\varphi_o)^2 - 1/2 - \zeta/t_v} \quad (4\text{-}54)$$

Here, ΔT and $\Delta\varphi_o$ are parameters associated with the peak temperature profile, and T_{in} and T_{out} are the nominal inner and outer temperatures of a vessel with thickness, t_v. The variable ξ^m is used to describe the meridian of the lower head parametrically, varying from 0 to 1 between the bottom of the lower head and the junction with the cylindrical pressure vessel. The length ζ measures distance normal to the meridian; $\zeta = \pm t_v/2$ corresponds to the outer/inner surface of the vessel. Representative temperature distributions are illustrated in Figure 4-55 for T_{in} = 900 K, T_{out} = 700 K, and ΔT = 200 K for φ_o = 0.1, 0.2, and 0.3 radians. Results illustrate that a range of vessel deformations are possible, depending on the relative creep rates of the hot spot and the background portions of the vessel.

The second set of thermal conditions is based on transient heat conduction through the vessel. The pressure vessel is initially assumed to experience a benign temperature profile representative of operating conditions. The inner surface temperature is assumed uniform and equal to 600 K. The outer surface temperature is assumed uniform and equal to 550 K. For a vessel 12.7 cm thick with thermal conductivity 40 W/mK, the heat flux through the vessel is approximately 15 kW/m^2. The heat transfer coefficient to the ambient containment atmosphere is 100 W/m^{2}K, and the ambient temperature is assumed to be 400 K. Therefore, the initial

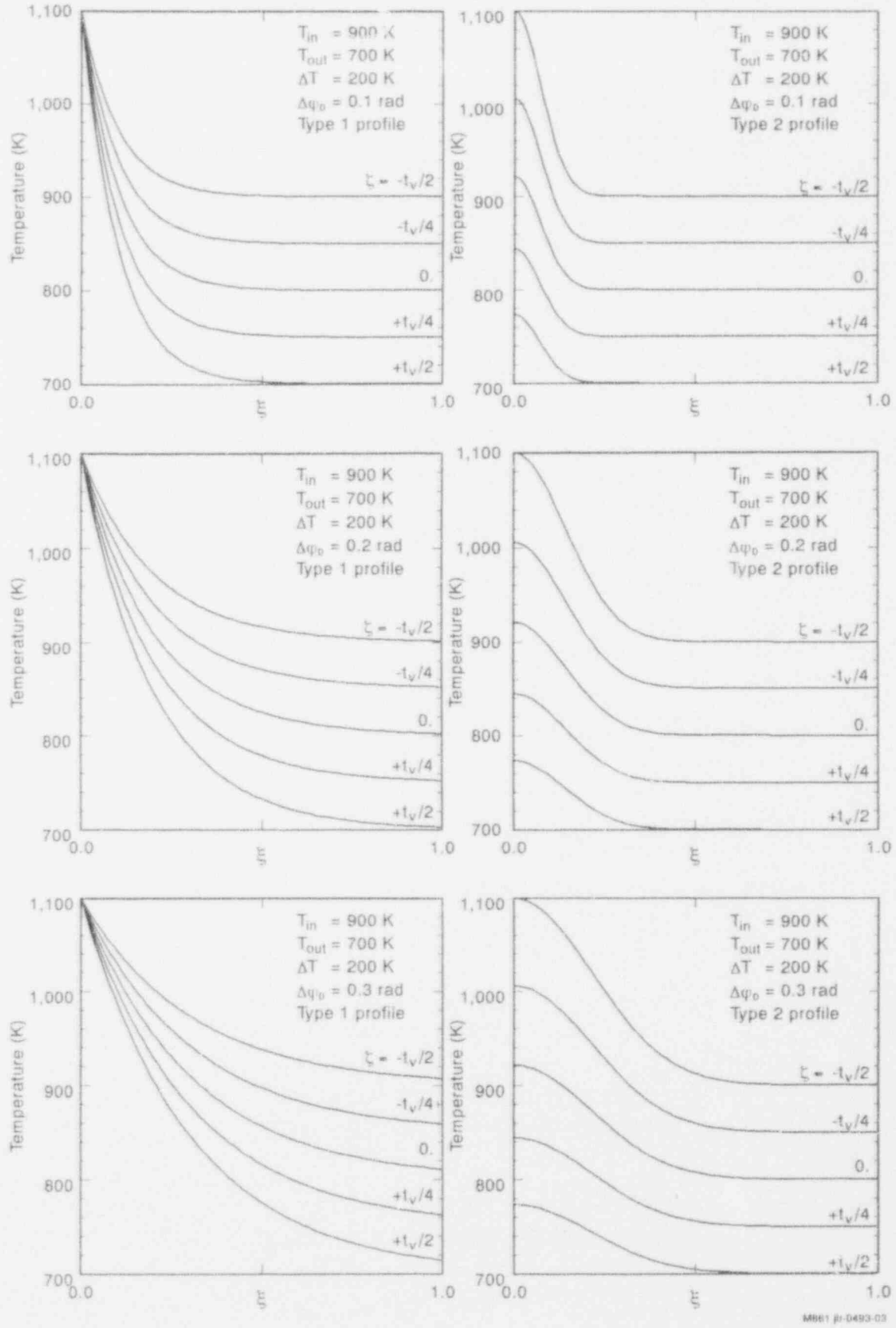

Figure 4-55. Representative peaked temperature distributions superimposed on a background temperature distribution.

conduction heat flux through the vessel is equal to the flux removed by convection on the vessel's outer surface.

The characteristic heat fluxes used in Section 4.1.1, which represent three different debris compositions: $q''_{metallic} = 15\ kW/m^2$, $q''_{ceramic\ slurry} = 50\ kW/m^2$, and $q''_{molten\ pool} = 200\ kW/m^2$, were also applied. The metallic heat flux is approximately equal to the steady-state heat flux associated with the initial temperature distribution. At t = 0, a peak heat flux q''_{peak} in excess of $q''_{metallic}$ is applied to a segment of the lower head, while the balance of the inner surface of the lower head experiences $q''_{metallic}$. These boundary conditions are illustrated in Figure 4-56. The vessel temperature distribution therefore rises from its initial state to an asymptotic distribution

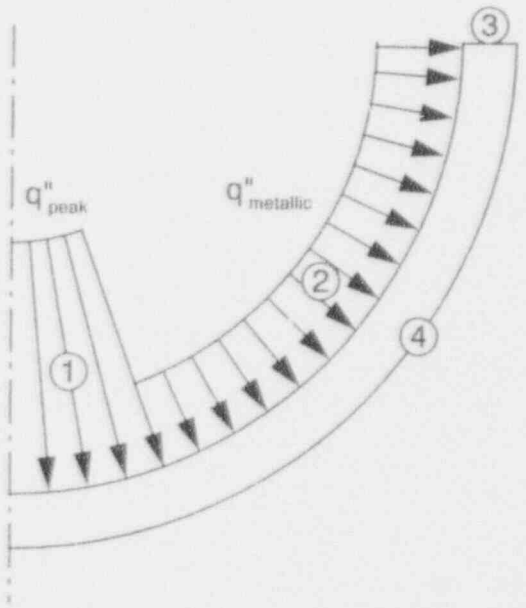

① Shell inner surface, peak heat flux applied in hot spot region

② Shell inner surface, background heat flux applied outside hot spot region

③ Nodes at junction with cylindrical pressure vessel; temperature fixed at 600 K

④ Shell outer surface, heat transfer coeffcient to ambient air at 400 K

M939-WHT-893-30

Figure 4-56. Boundary conditions used to obtain transient temperature distributions.

determined by $q"_{peak}$. Vessel response as $q"_{peak}/q"_{metallic}$ varied between 1 (background) and 10 (approaching $q"_{molten\ pool}$) is investigated for a range of pressures to determine how the vessel responds to a hot spot generated from a range of physically plausible boundary conditions.

The commercial finite element code PAFEC[4-41] was used to calculate the time-dependent temperature distributions in the vessel. Representative properties of the SA533B steel were used as inputs to the thermal analysis; a density of 7,800 kg/m^3, ad heat capacity of 700 J/kgK and a thermal conductivity of 40 W/mK were used. Contour plots are shown in Figure 4-57 for temperature distributions in the vessel at 1,000 seconds, 1 hour, and 2 hours into the transient using the boundary conditions of Figure 4-56 with $q"_{peak}/q"_{metallic} = 10$. An elapsed time of 4 hours is required before there is negligible change in the temperature distribution and the vessel has reached its asymptotic state.

4.2.2.2 Structural Model. Because of the short time and fine length scales associated with local failure modes, and the desire to generate failure maps over a range of plausible conditions, it is desirable to select an analytical method that minimizes the number of degrees-of-freedom modeled per time step. The algorithm used to study this problem is an extension of Reissner's theory of shells with finite deformations and inelastic strains, as used, for instance, in the problem of a corrugated tube at elevated temperature subjected to a constant axial load.[4-42] To cast the stress resultant form of the equilibrium equations in displacement-based form, the stresses in the resultants are written in terms of the elastic components of strain are represented through Hooke's Law and then the elastic strains are represented as the difference between the total and the sum of the thermal and inelastic strains, $\epsilon_e = \epsilon - \epsilon_{th} - \epsilon_{pl} - \epsilon_{cr}$. The displacement-based form results from writing the terms containing the total strains as the product of a linearized stiffness matrix and a displacement vector, while incorporating the thermal and inelastic components into a load vector. The through-thickness integration inherent in the resultant-based form leads to system of equations in which only the degrees-of-freedom along the midplane of the shell are modeled directly. The parametric representation of the midplane is also easily changed to provide a more dense distribution of nodes near the hot spot without adding additional degrees-of-freedom.

A second advantage of the shell theory is that it permits a natural definition of a local failure mode. Strain measures are written in terms of principal radii of curvature in the meridian, R_φ, and hoop, R_θ, directions. An initially hemispherical shell of radius, b, has initial principal radii of curvature $R_{\varphi_0} = R_{\theta_0} = b$. As the shell geometry changes under load, R_φ and R_θ evolve; a local failure is defined to have occurred when the failure geometry exhibits a change in sign of R_φ along the meridian. This is illustrated in Figure 4-58a, and is distinctly different from a failure geometry in which local thinning occurs around the hot spot, but the shell maintains positive R_φ along the whole meridian as in Figure 4-58b. The latter is described as a locally assisted global failure, whereas the former, involving the formation of a bulge or cusp, is defined as a local failure.

Modifications to the method provided in Reference 4-42 are needed to treat the present problem. Conventional shell theory treatments incorporate "thin shell" assumptions; a shell is assumed to be thin if the ratios of its thickness to its principal radii of curvature are much less than one. Although the initial configuration of the lower head may be described as a thin shell, the configuration late in the transient may contain local regions where t_v/R_φ and t_v/R_θ are not small. The cusped region in Figure 4-58a is such a region. Terms of the order of t_v/R_φ and t_v/R_θ are ordinarily discarded, but have been retained in this analysis. Conventional shell theory treatments also constrain material away for the shell midplane not to rotate relative to the

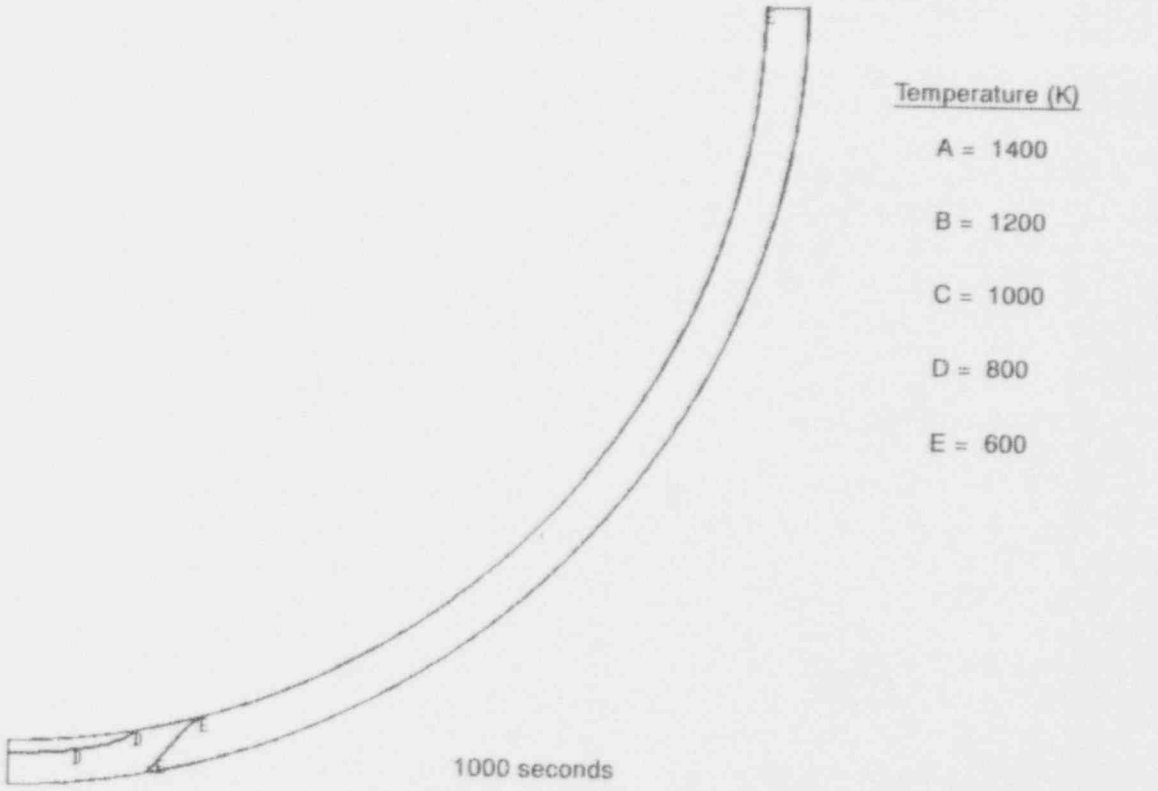

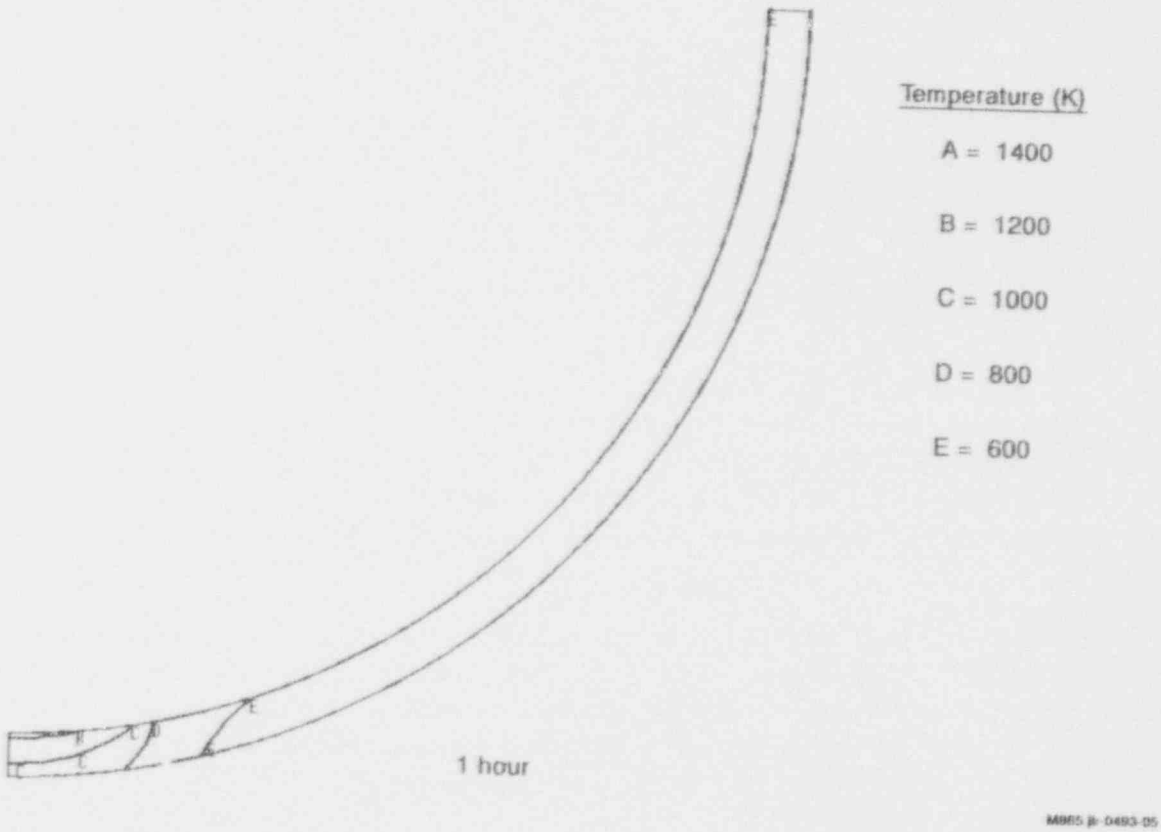

Figure 4-57. Temperature profile in vessel at 1,000 seconds, 1 hour, and 2 hours for $q''_{peak} = 10 \times q''_{metallic}$

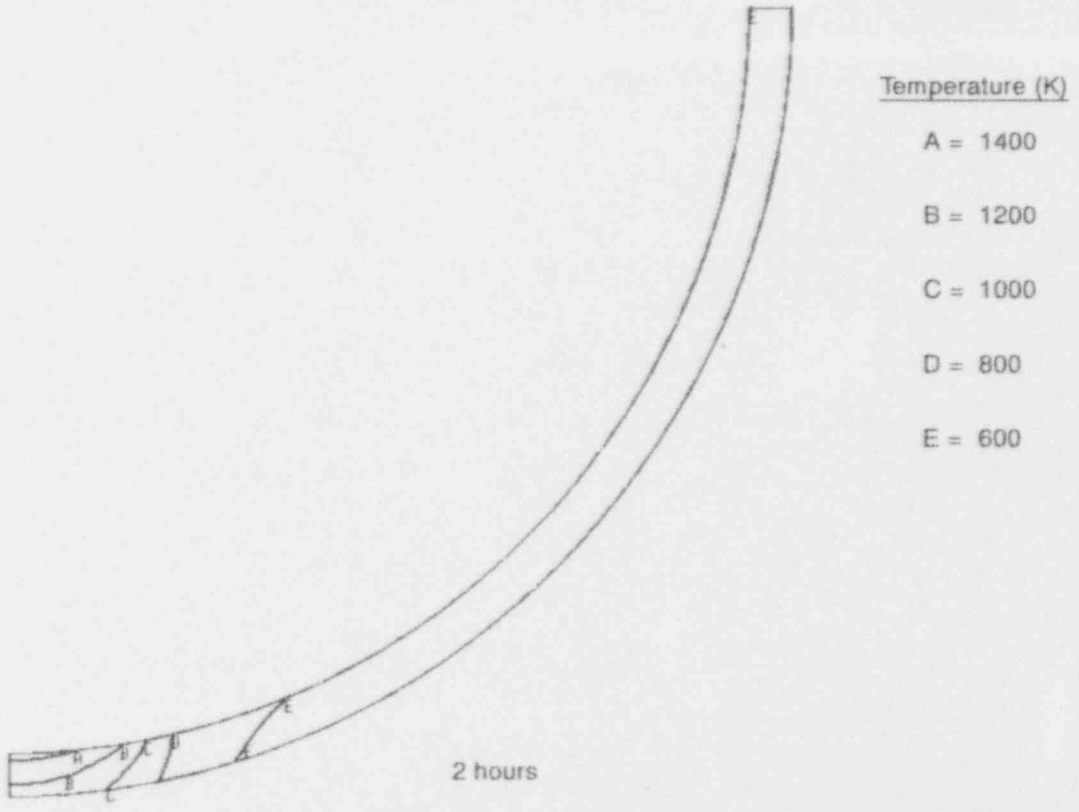

Figure 4-57. (continued).

midplane; this is embodied in the assumption that normals to undeformed middle surfaces remain normal to deformed middle surfaces. The shell material tends to resist the formation of a cusp, and it does so by sliding or shearing relative to the normal to the deformed middle surface. Finite material rotations from the deformed normal, denoted γ, are included in the model and permit the investigation of this behavior.

4.2.2.2.1 Model Formulation—Displacement-based horizontal, moment, and vertical equilibrium equations are written in terms of u/r_o, the hoop strain along the middle surface; β, the rotation of the meridian; and γ, the rotation of material away from the deformed normal:

$$A_1\left(\frac{u}{r_o}\right)'' + A_2\left(\frac{u}{r_o}\right)' + A_3\left(\frac{u}{r_o}\right) + A_4\beta'' + A_5\beta' + A_6\beta + A_7\gamma'' + A_8\gamma' + A_9\gamma = G_1 \qquad (4\text{-}55)$$

$$B_1\left(\frac{u}{r_o}\right)'' + B_2\left(\frac{u}{R_o}\right)' + B_3\left(\frac{u}{r_o}\right) + B_4\beta'' + B_5\beta' + B_6\beta + B_7\gamma'' + B_8\gamma' + B_9\gamma = G_2 \qquad (4\text{-}56)$$

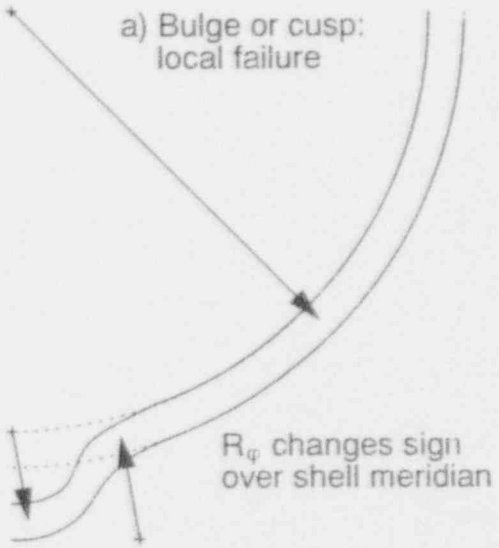

(a) Local or cusp failure geometry

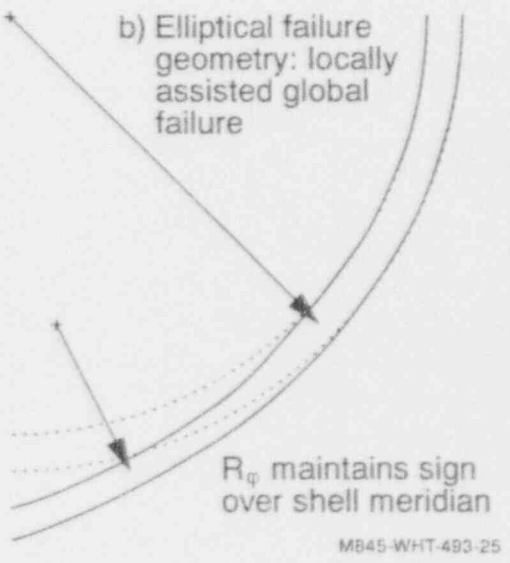

(b) Locally assisted global or elliptical failure geometry

Figure 4-58. Differences between a localized, cusped failure and a locally assisted global failure.

$$C_1\left(\frac{u}{r_o}\right)' + C_2\left(\frac{u}{r_o}\right) + C_3\beta' + C_4\beta + C_5\gamma + C_6\gamma = G_3 \quad . \tag{4-57}$$

Coefficients A_1 through A_9, B_1 through B_9, and C_1 through C_6 are dependent on the shell geometry, resulting in a non-linear stiffness matrix and necessitating an iterative solution to

Equations (4-55) through (4-57) within a load increment. The coefficients G_1 through G_3 contain both geometric terms and inelastic resultants driving the deformation.

These equations are solved subject to the boundary conditions $\left(\frac{u}{r_o}\right) = \beta = \gamma = 0$ at $\xi = 0,1$. The conditions at $\xi = 0$ are exact for an axisymmetric shell and are appropriate for hot spot profiles imposed on a shell without penetrations. The conditions are approximate for the line source profiles because the presence of an instrumentation tube does not provide infinite resistance to rotation of the shell. The conditions at $\xi = 1$ correspond to a roller boundary condition imposed at the junction of the hemispherical and cylindrical parts of the pressure vessel. Negligible rotations β and γ at $\xi = 1$ are consistent with the lower head's attachment to a much stiffer body.

Converting resultant-based equilibrium equations into the displacement-based equations in Equations (4-55) through (4-57) is discussed in Appendix D; explicit expressions for the coefficients are given there as well. The salient features of the approach are described here. The shell is described by $r(\xi)$, $z(\xi)$, where ξ is a parametric variable lying in the interval $0 \le \xi \le 1$. The shell is initially hemispherical, with inner radius $b = 2.2$ m and uniform thickness $t_{vo} = 12.7$ cm (dimensions are based on the reference B&W TMI-2 plant in Appendix F). The initial distribution of nodes on the meridian is described by

$$\frac{r_o(\xi)}{b} = \xi^m \tag{4-58}$$

$$z_o(\xi) = -b\sqrt{1 - \left(\frac{r_o}{b}\right)^2} \tag{4-59}$$

The parameter, m, can be varied to nest nodes near the hot spot; typically, $1 \le m \le 2$, with larger values of m producing a more dense distribution of nodes in the elevated temperature region. Results presented here have been obtained using 100, 200, or 300 nodes with a nesting parameter m of 1, 1.5, or 2, depending on the severity of the local temperature distribution. Ten Gauss points are used to capture the through-thickness behavior. The outermost Gauss point samples temperatures 97.4% of the way through the half-thickness, ensuring that extreme temperatures are adequately incorporated in simulations with steep radial gradients. An indication of the modeling detail is shown in Figure 4-59, where solid triangles represent locations on the meridian where degrees-of-freedom are defined, and open triangles normal to the midplane represent Gauss points used to evaluate through-thickness behavior.

At each iteration within a load increment, the displacements and rotations are used to update the coordinates through

$$r = r_o + u \tag{4-60}$$

$$\varphi = \varphi_o + \beta \tag{4-61}$$

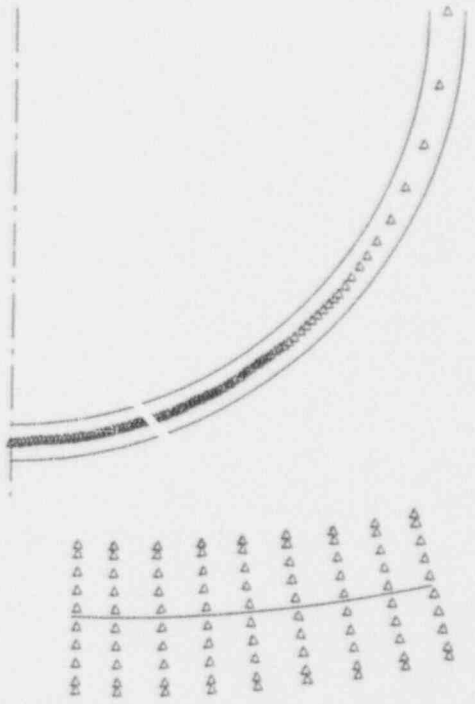

M845-WHT-493-29

Figure 4-59. Mesh detail associated with parametric representation of shell.

$$z = z_o + w \quad . \tag{4-62}$$

where the subscript, o, denotes the initial, undeformed surface. Figure 4-60 illustrates the notation associated with this method. The vertical deflections are calculated from other quantities through

$$w = \int_{\xi}^{1} (\alpha_o \sin \varphi_o - \alpha \sin \varphi) d\xi \tag{4-63}$$

where $\alpha = \dfrac{dS}{d\xi} = \sqrt{(r')^2 + (z')^2}$. The angular variable, φ is related to α through $r'/\alpha = \cos \varphi$. The normal strains at the middle surface are given by:

$$\epsilon_{\varphi_m} = \frac{dS}{dS_o} - 1 = \frac{\alpha}{\alpha_o} - 1 \tag{4-64}$$

$$\epsilon_{\theta_m} = \frac{u}{r_o} \quad . \tag{4-65}$$

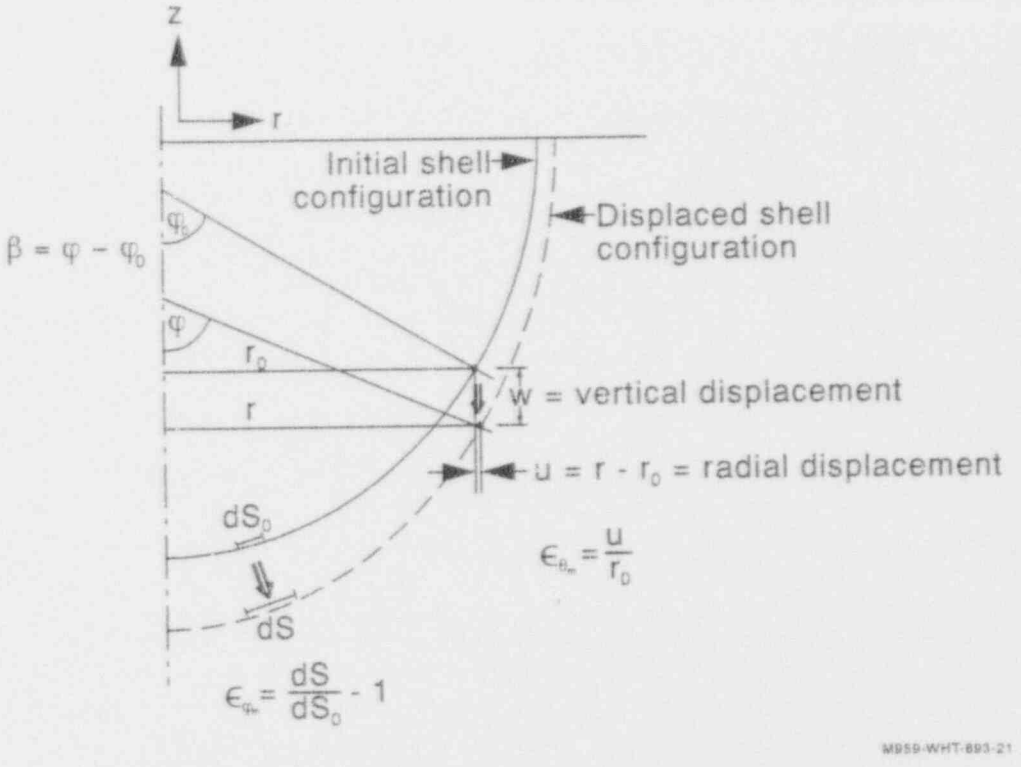

Figure 4-60. Notation associated with shell theory.

It is possible to obtain a compatibility equation between these strains that takes the form

$$\alpha_o \epsilon_{\varphi_m} \cos\varphi - (r_o \epsilon_{\theta_m})' = \alpha_o(\cos\varphi_o - \cos\varphi) \quad . \tag{4-66}$$

Within a load increment, the solution proceeds as follows:

1. Displacements and rotations $\frac{u}{r_o}$, β, and γ are found by solving the simultaneous system Equations (4-55) through (4-57). The radial coordinate, r, and meridian angle, φ, are updated from Equations (4-60) and (4-61).

2. Because ϵ_{θ_m} is defined as $\frac{u}{r_o}$, the middle surface hoop strain in known; the middle surface, meridian strain, ϵ_{θ_m}, is then found from the compatibility equation, Equation (4-66).

3. With ϵ_{θ_m} known, α is updated from Equation (4-64) through $\alpha = \alpha_o (1 + \epsilon_{\theta_m})$.

4. The vertical displacement is then calculated from Equation (4-63) and the vertical coordinate updated from Equation (4-62).

5. Principal radii of curvature are updated:

$$R_\varphi = \frac{\alpha}{\varphi'} = \frac{\alpha_o}{\varphi_o'} = \frac{\alpha_o}{\varphi_o'} \frac{1 + \epsilon_{\varphi_m}}{1 + \beta'/\varphi_o'} = R_{\varphi_o} \frac{1 + \epsilon_{\varphi_m}}{1 + \beta'/\varphi_o'} \tag{4-67}$$

$$R_\theta = \frac{r}{\sin\varphi} = \frac{r_o}{\sin\varphi_o} \frac{1 + u/r_o}{\cos\beta + \cot\varphi_o \sin\beta} = R_{\theta_o} \frac{1 + \epsilon_{\theta_m}}{\cos\beta + \cot\varphi_o \sin\beta} \tag{4-68}$$

6. The strain normal to the shell surface is evaluated from the elastic and inelastic components of the hoop and meridian strain:

$$\epsilon_\theta = \epsilon_{\theta_e} + \epsilon_{\theta_{in}} = -\frac{\upsilon}{1 - \nu}(\epsilon_{\varphi_e} + \epsilon_{\theta_e}) - (\epsilon_{\varphi_{in}} + \epsilon_{\theta_{in}}) \tag{4-69}$$

and the thickness is then updated from $t_v(\xi)/t_{vo} = e^{\epsilon\zeta}$.

7. If the convergence criterion is not satisfied, the information generated in Steps 2 through 6 is used to evaluate new coefficients A_1 through A_9, B_1 through B_9, C_1 through C_6, and G_1 through G_3 in Equations (4-55) through (4-57), and the process is repeated.

   When convergence is reached, a self-consistent determination of geometry, equilibrium, and inelastic deformation has been obtained for the current load increment. The convergence criteria for each degree-of-freedom is

$$\left| \frac{\beta_i^{n+1} - \beta_{i_n}}{\beta_{max}} \right| \le \text{tol}$$

   where the tolerance is 10^{-4} and normalization is with respect to the maximum value of the degree-of-freedom over the interval. Normalization has been taken with respect to the maximum value because normalization based on the local value, β_i^n, results in unnecessary iterations spent reaching convergence for degrees-of-freedom two or more orders of magnitude smaller than peak values in the field.

8. Having reached convergence in the current load increment, equivalent strains are evaluated at every Gauss point. If one of the failure criteria discussed in the next section is not met, creep strains are updated at all Gauss points according to the local temperature and stress state. A new time increment is selected based on the highest creep strain rate, and creep strain increments are evaluated and added to the accumulated creep strain. New values of creep resultants, appearing in G_1 through G_3 on the right hand sides of Equations (4-55) through (4-57) and defined as

$$N_{\varphi_{cr}} = \int_{-t_v/2}^{t_v/2} \frac{E(\zeta,\xi)}{1 - \upsilon^2} (\epsilon_{\varphi_{cr}} + \upsilon\epsilon_{\theta_{cr}}) \left(1 + \frac{\zeta}{R_\theta}\right) d\zeta \tag{4-70}$$

$$M_{\phi_{cr}} = \int_{-t_v/2}^{t_v/2} \frac{E(\zeta,\xi)}{1-\upsilon^2} \left(\epsilon_{\phi_{cr}} + \upsilon\epsilon_{\theta_{cr}}\right) \zeta \left(1 + \frac{\zeta}{R_\theta}\right) d\zeta \tag{4-71}$$

with analogous definitions for $N_{\theta_{cr}}$, $M_{\theta_{cr}}$, and $Q_{\phi\zeta_{cr}}$, are evaluated. Coefficients A_1 through A_9, B1 through B_9, and C_1 through C_6 are similarly updated. The algorithm returns to Step 1 and begins the iterative procedure for the new increment.

4.2.2.2.2 Evaluation of Thermal and Inelastic Strains—Although the creep resultants, defined by Equations (4-70) and (4-71), play the dominant role in advancing the deformation of the shell, there also exist plastic and thermal resultants, defined in an analogous fashion to the creep resultants. The thermal strains play an important role in establishing the stress state distribution in the shell, while the plastic strains keep the shell on the yield locus during deformation. This section describes how these strain components are obtained and used to advance the algorithm.

In the contrived, steady-state problems, it is assumed that the nominal dimensions of the vessel (b = 2.2 m; t_{vo} = 0.127 m) apply at 300 K, and that the vessel is free of stress at these conditions. The vessel response is first calculated at $t_v = 0$ by bringing the vessel up to temperature and pressure proportionally. Thermal strains are calculated at each Gauss point in Figure 4-59 by integrating $\alpha(T)$ over the appropriate temperature range as specified by either Equation (4-53) and (4-54). The mean $\alpha(T)$ for medium carbon steels rises initially from room temperature, reaches a peak of about 14.5 x 10^{-6} K^{-1} at 900 K, and then decreases smoothly to about 13 x 10^{-6} K^{-1} at 1200 K (see Appendix F). It is modeled as a piecewise linear fit to the data, and is taken as constant above 1200 K. A similar procedure is used in the transient hot spot problems, but the thermal strain distribution is updated throughout the transient as the temperature profile evolves.

During the simulation, the equivalent stress is compared at each point with the proportional limit, also taken from information in Appendix F, and also modeled in a piecewise linear fashion. If the equivalent stress exceeds the proportional limit, a variation of a radial return algorithm[4-42] is used to bring the stresses back to the yield locus. Equivalent strains and stresses, designated $\bar{\epsilon}$ and $\bar{\sigma}$, are evaluated using a Mises criterion. The SA533B steel is assumed to experience isotropic hardening of the form

$$\frac{\bar{\sigma}}{\sigma_p(T)} = \left(\frac{\bar{\epsilon}}{\epsilon_p(T)}\right)^{1/n} \tag{4-72}$$

where n varies weakly with temperature, but has been assumed constant with n = 6 in this study, again based on the data appearing in Appendix F. A typical value of the hardening exponent is n = 10. In this expression, σ_p and ϵ_p are the proportional limit and its corresponding strain. Once the radial return algorithm produces updated stresses, the elastic strains are calculated, and the plastic strain is calculated from the difference between total and (thermal + elastic + creep) strain. The plastic resultants are then updated, and the algorithm proceeds to the next iteration.

The creep strains and their associated resultants drive the deformation and are evaluated from data listed in Appendix F. Creep strain rates are cast in the power law form:

$$\dot{\bar{\epsilon}}_{cr} = A(T)\bar{\sigma}^{n(T)} \tag{4-73}$$

where $\dot{\bar{\epsilon}}_{cr}$ and $\bar{\sigma}$ are equivalent creep strain rates and stresses. The parameters A(T) and n(T) vary strongly with temperature and are provided in roughly 100 K increments between 900 and 1473 K. Below 900 K, the creep strains are evaluated using the relations of Reddy and Ayres.[4-44] A ferritic-to-austenitic transition at 1000 K results in especially high creep strain rates at this temperature, so that $\dot{\bar{\epsilon}}_{cr}$ is not necessarily a monotonically increasing function of temperature at a given stress level. Above 1473 K, the creep strain rate is assumed to have the same form as that at 1473 K. At temperatures between those for which data exists, the creep strain rate is linearly interpolated from the existing data.

Individual creep strain components are calculated by assuming that components are proportional to the corresponding deviatoric stress components, as commonly assumed in association flow rules:

$$\frac{\Delta\epsilon_{\varphi_{cr}}}{\sigma_\varphi - \frac{1}{3}(\sigma_\varphi + \sigma_\theta)} = \frac{\Delta\epsilon_{\theta_{cr}}}{\sigma_\varphi - \frac{1}{3}(\sigma_\varphi + \sigma_\theta)} = \frac{\Delta\gamma_{\varphi\zeta_{cr}}}{\tau_{\varphi\zeta}} \quad . \tag{4-74}$$

Here σ_ζ does not appear in the hydrostatic stress because it is assumed to be negligible compared with membrane stresses σ_φ and σ_θ. Using $\epsilon_{\zeta_{cr}} = -\epsilon_{\varphi_{cr}} - \epsilon_{\theta_{cr}}$ in Equation (4-73) and representing each creep strain component in the current time step as the sum of the total creep strain from the previous time step plus the increment in the current time step, $\epsilon^{n+1}_{\varphi_{cr}} = \epsilon^{n}_{\varphi_{cr}} + \Delta\epsilon_{\varphi_{cr}}$, Equation (4-74) can be used to obtain a quadratic equation in one of the componehts.

4.2.2.3 Failure Criteria. As the simulations proceed, the vessel experiences increasingly large strains and accumulates damage. The question arises as to what kind of failure criterion to use to halt the simulation and declare that the vessel has failed. Failure criteria can be either strain-based, stress-based, or some hybrid of the two. Two different kinds of failure criteria are used in the results that follow.

A strain-based criterion is used for the contrived, steady-state temperature profiles. The vessel is declared to have failed when the equivalent strain exceeds 20% at every Gauss point at a particular through-thickness location. For some combinations of elevated temperature and pressure, failure occurs as the initial temperature profile is established. This occurs because vessel stiffness falls dramatically for temperatures approaching the vessel melting temperature, and it is possible to achieve the required 20% through-thickness strains without undergoing creep.

A damage-based failure criterion is used for the transient hot spot calculations. Damage is defined on the basis of rupture time calculated using a Larson-Miller Parameter (LMP). At a particular Gauss point, the LMP is defined by the stress state, and the rupture time t_r is calculated from the LMP and temperature. As the transient proceeds in a series of small time steps, the damage accumulated during the time step is defined as $d_i = \Delta t_i/t_r$. The total accumulated damage from the start of the transient is then

$$D = \sum_i d_i \quad . \tag{4-75}$$

Failure at an individual Gauss point is defined to have occurred when the damage exceeds unity. The load carrying capacity of that Gauss point is then eliminated by shrinking the yield locus to zero, forcing load redistribution to other, intact Gauss points. This procedure is referred to as "ligament clipping." Structural failure is defined to have occurred when all Gauss points have been clipped at a particular through-thickness location. Unlike the contrived steady-state problems using a strain-based failure criterion, there are no immediate failures when this criterion is invoked, because time intervals at elevated temperature and stress are required to accumulate damage.

4.2.2.4 Results. One of the goals of this research is to understand the influence of different variables in precipitating local failure. Because depressurization may play an important role in accident management strategies,[4-45] primary system pressure is used as one of the parametric variables in this study. The size and severity of the peak temperature may also vary, so a normalized temperature difference or heat flux constitutes a second important variable. In the contrived steady-state profiles, the peak temperature ΔT is normalized to the difference between the steel melting temperature and the background inner surface temperature, $\Delta T/(T_{mp} - T_{in})$. In the transient simulations with physically plausible boundary conditions, the peak heat flux is normalized to the heat flux associated with metallic debris, $q"_{peak}/q"_{metallic}$. With pressure normalized to the initial system pressure (p_{io} = 15 MPa), p_i/p_{io} and $\Delta T/(T_{mp} - T_{in})$ or $q"_{peak}/q"_{metallic}$ provide dimensionless mechanical and thermal load variables for parametric studies.

4.2.2.4.1 Contrived, Steady-State Profiles.—Results are presented for an initially hemispherical lower head at a uniform background temperature ($T_{in} = T_{out}$ = 900 K) with a peak temperature distribution characterized by angular spread $\Delta\varphi_o$ = 0.2 rad. At a temperature of 900 K, the steel creeps under stress, so it is possible to discern a transition in failure geometry as the severity of the hot spot is increased. Under severe local loads, the failure mode can be understood in terms of meridional variations in p_i/E_o and creep strain. There is some similarity between this limit and a punch problem, the latter referring to the perforation of a plate by a blunt tool. In such a problem, the plate has a uniform initial stiffness, and a sharp variation in applied load along the plate arises from application of the punch. Finite deflections and rotations arise near the punch, while deformation far from the application is quite modest. In the present problem, the pressure is uniform along the shell's meridian, but the local stiffness falls and the creep strain increases dramatically around the hot spot. At the other extreme, a local temperature perturbation produces negligible meridional gradients in stiffness and creep strain, and the lower head expands nearly uniformly like a balloon under pressure.

The distributions of degrees-of-freedom and meridional radius of curvature at failure are shown in Figure 4-61 for two cases: ΔT = 100 K versus ΔT = 800 K at p_i = 2.5 MPa for line source profiles. These simulations were conducted with m = 2 and 200 nodes, so values of $\xi \le 0.5$ tend to be nested within or around the hot spot. In comparing plots of degrees-of-freedom, note the difference in relative magnitude of hoop strain and meridian rotation at failure. Peak rotations exceed peak hoop strains under the severe hot spot. A second distinction between the two plots is in the rate of change of quantities with respect to ξ. Peak strains and rotations are concentrated much more heavily in the hot spot for the case ΔT = 800 K. A third significant difference is in the size of the shear distribution γ relative to meridian rotation β. When the deformed shell geometry is elliptical (ΔT = 100 K), there is relatively little shear. Not that the γ distribution for the case ΔT = 100 K is amplified by a factor of 100 in Figure 4-61a to permit a comparison with the other distributions. When the hot region is punched out of the bottom of

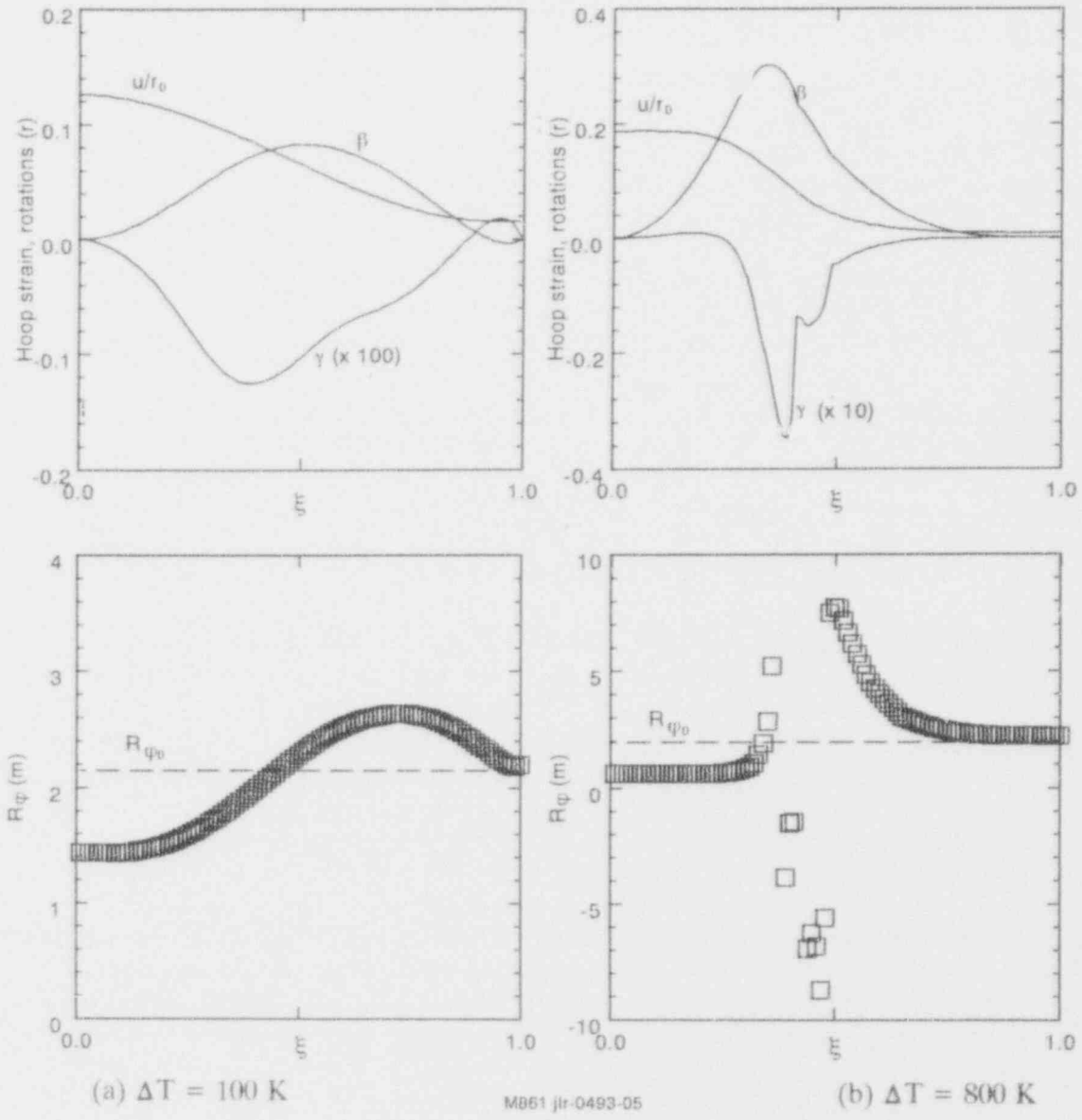

Figure 4-61. Distribution of degrees-of-freedom, R_φ at failure: $\Delta T = 100$ K versus $\Delta T = 800$ K, $p_i = 2.5$ MPa, line source profile.

the shell ($\Delta T = 800$ K), the material resists the motion by sliding against the attempted rotation of the meridian. Peak material shears for the case $\Delta T = 800$ K are 10 times the peak values associated with $\Delta T = 100$ K. Finally, note from Equation (4-67) that a change in sign in the R_φ distribution is possible only when β' is large and negative, which is only possible after the peak in the β-distribution has been reached. The plot of R_φ for the case $\Delta T = 800$ K illustrates the characteristic behavior associated with formation of a bulge.

The transition between locally assisted global failure and cusped failure is shown in Figure 4-62, which illustrates details of deformation around the hot spot as ΔT is increased from 100 K to 800 K in increments of 100 K. At the lowest peak temperature, $\Delta T = 100$ K, the creep strain rate at the bottom of the shell is only slightly higher than that associated with steel outside the hot spot. The lower head takes on a slightly elliptical shape at failure with very gradual gradients in thinning at the bottom of the shell. As ΔT is increased from 200 to 400 K, the

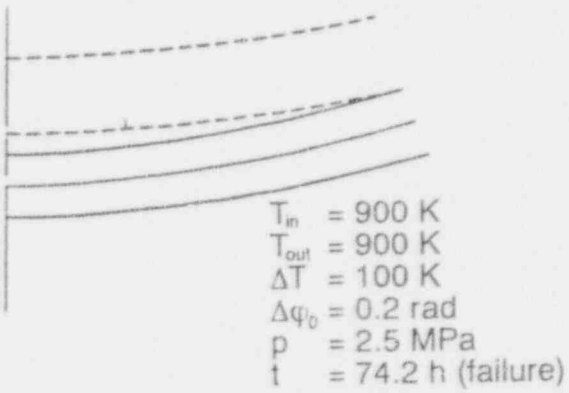

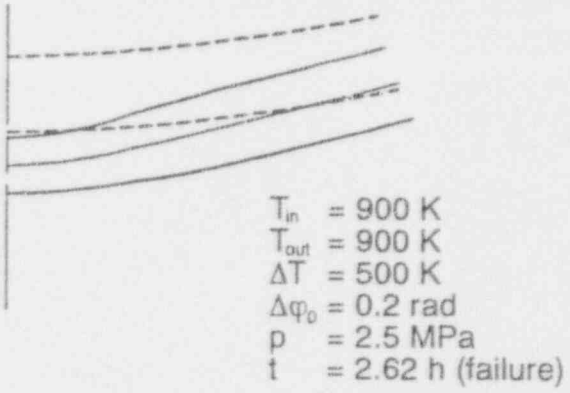

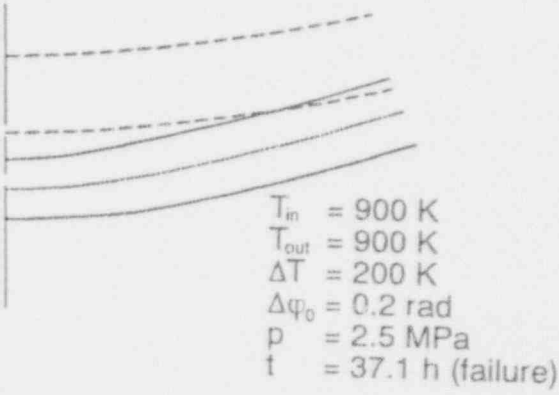

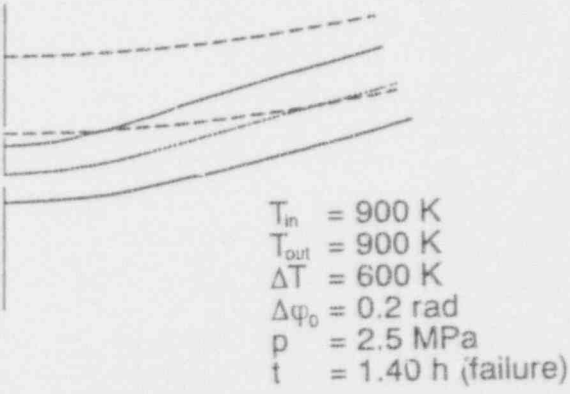

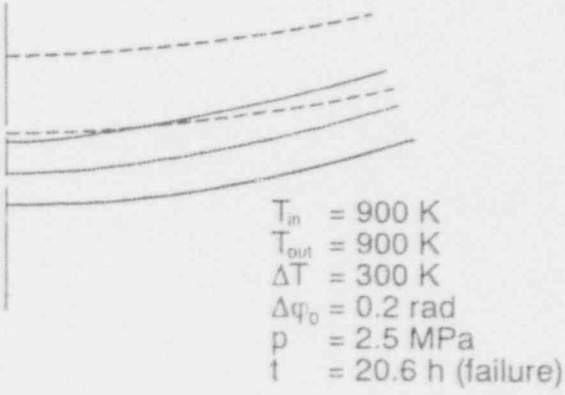

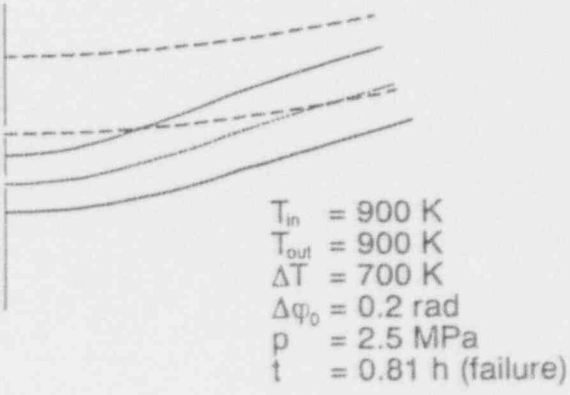

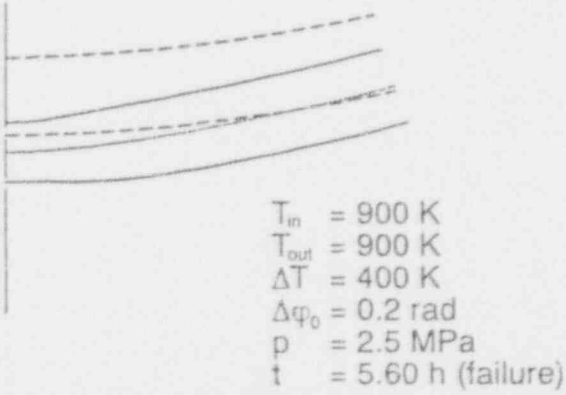

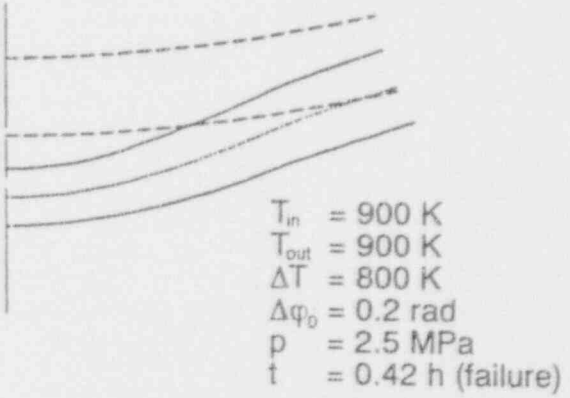

Figure 4-62. Transition from elliptical to cusped failure at p_i = 2.5 MPa as ΔT is raised from 100 K to 800 K in 100 K increments.

bottom of the shell deforms at a much faster rate than the balance of the lower head. The shell does not sag as dramatically before the bottom fails, so that the axial deflection at failure actually decreases with increasing temperature over this range of Δt. The gradient in thinning along the meridian also becomes more dramatic. Beginning at about 500 K, however, the trend in maximum axial deflection reverses direction, with the bottom of the shell experiencing increasingly greater deflections as ΔT rises from 400 K to 800 K. At the same time, the balance of the shell outside the hot spot does not have the opportunity to experience large deflections, forcing the formation of a bulge or cusp.

Repeating these calculations for other combinations of pressure and peak temperature results in the failure map for line source profiles shown in Figure 4-63. The contour plot is rough, created from results obtained in coarse increments of 2.5 MPa up to 15 MPa and peak temperatures in increments of 100 K up to 800 K; the plot is best used to illustrate trends in time-to-failure and failure geometry. Times to failure are given in hours. The region in the upper right corner denotes the locus of peak temperatures and system pressures resulting in failure without creep. The dashed region in the domain indicates the subspace of temperature and pressure where cusp formation is observed to occur. There is a slight pressure dependence to the cusped domain, indicating that lower peak temperatures may precipitate local failure at elevated pressure. Times to failure are monotonically decreasing functions of increasing pressure and temperature.

The failure map for the contrived hot spot profiles differs from that associated with the line source profiles. The cusped failure geometry is not observed over as large a subdomain of the

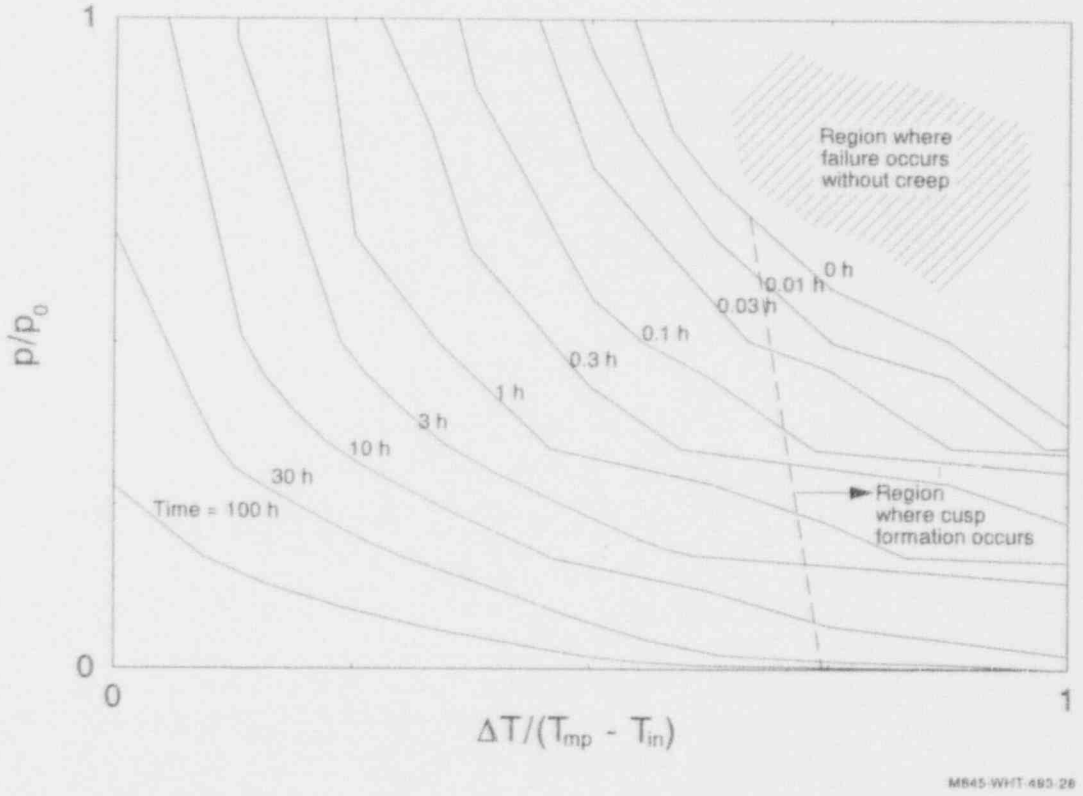

Figure 4-63. Failure map associated with line source profiles.

pressure and thermal load variables. Figure 4-64 compares the degrees-of-freedom and R_φ distribution at failure for hot spot profiles with $\Delta T = 100$ K and $\Delta T = 800$ K for $p_i = 2.5$ MPa. These are to be compared with the corresponding plots in Figure 4-61. The β-distribution in the $\Delta T = 800$ K hot spot profile has a peak value of comparable to the size of that for the line source profile, but the distribution has a more gradual dependence on ξ. Even though there is a region of very large R_φ in the failure geometry, the radius doesn't change sign anywhere along the meridian and hence is not designated a local failure. The large radial temperature gradient underneath the hot spot also results in greater retention of stiffness and lower creep strain for the same ΔT, so that times to failure are considerably longer for the hot spot profiles than for the line source profiles. The case shown on the right in Figure 4-64 failed in 20 hours; that on the right of Figure 4-61 reached failure in less than one hour.

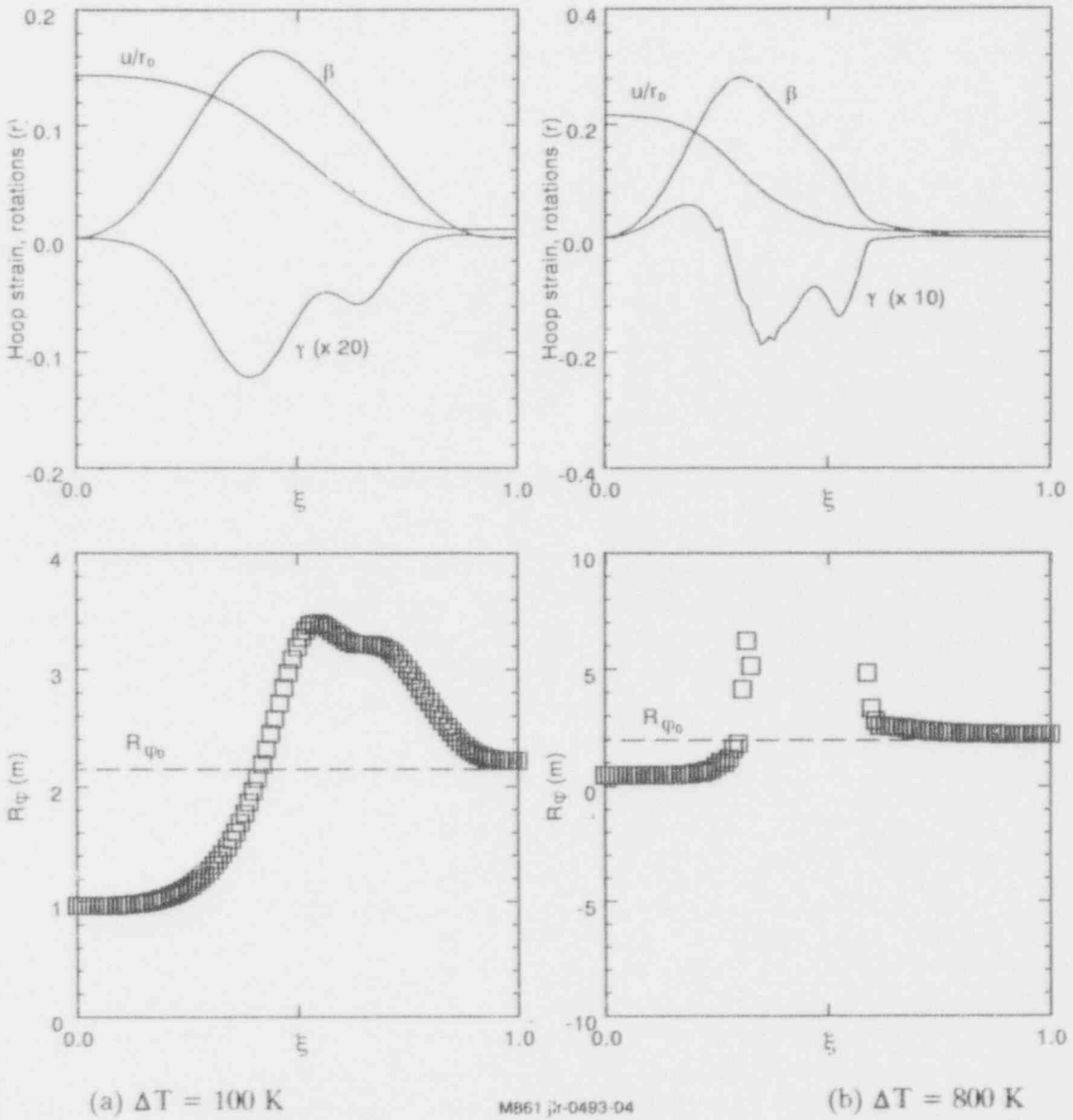

Figure 4-64. Distribution of degrees-of-freedom, R_φ at failure: $\Delta T = 100$ K versus $\Delta T = 800$ K, $p_i = 2.5$ MPa, hot spot profile.

Figure 4-65 illustrates a dimensionless failure map of times to failure for the hot spot profiles to be compared with Figure 4-63 for the line source profiles. The first significant difference is the absence of a region under the most severe conditions that results in immediate failure without creep. This absence can be attributed to the retention of stiffness under the largest peak temperatures because of the radial gradient beneath the hot spot. Cusped failure geometries now appear under the most severe combinations of pressure and peak temperature, and times to failure are both longer and less sensitive to p_i and ΔT than in the line source case, as evidenced by the wider spacing between contours in Figure 4-65. Implications of Figures 4-64 and 4-65 are that vessel failure can be significantly delayed and perhaps prevented by lowering system pressure and keeping the outer surface of the vessel cool.

4.2.2.4.2 Transient Hot Spot Profiles—Results are presented here for lower head subjected to the sudden application of a peak heat flux characterized by $q''_{peak}/q''_{metallic}$ = 2, 4, 6, 8, or 10 at pressures of 5, 10, and 15 MPa. The angular range of the peak heat flux corresponds to $\Delta\varphi_o$ = 0.2 rad. Table 4-18 lists the times to failure observed using the damage-based failure criterion described in Section 4.2.3. Figure 4-66 shows a typical plot of damage distribution and Figure 4-67 shows representative vessel deformation and damage distribution at failure.

Raising the heat flux suddenly results in a rapid increase in temperature, but does not produce a thermal shock and a resulting temperature spike hundreds of degrees C above the initial temperature when the applied heat flux is less than 150 kW/m^2. Given the density, heat capacity, and thermal conductivity of the SA533B, sudden heat fluxes of several thousand kW/m^2 are needed to produce a dramatic thermal shock. For this reason, damage does not become

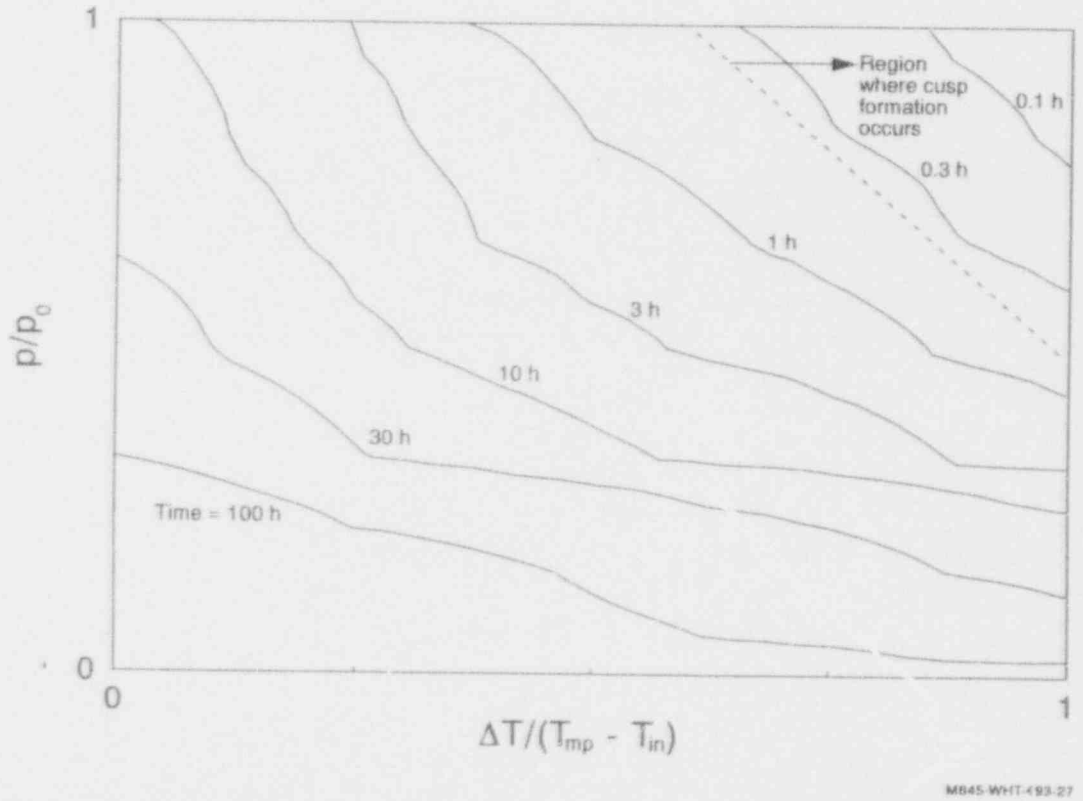

Figure 4-65. Failure map associated with hot spot profiles.

Table 4-18. Times to failure for transient hot spot simulations.

	Time to failure (hours)					
	$q''_{peak}/q''_{metallic}$					
p_i/p_{io}	1	2	4	6	8	10
1.00	no failure	no failure	>10000	16.8	5.4	2.2
0.67	no failure	no failure	>10000	46.7	12.1	3.6
0.33	no failure	no failure	>10000	345.0	59.3	9.2

significant until the thermal front propagates all the way through the vessel, which takes 20 to 30 minutes. The damage plotted in Figure 4-66 is a simple, unweighted average of all the individual damage values at Gauss points throughout the vessel. The damage does not become important until this propagation time is reached. As the vessel creeps under load, the stress states in the most severely loaded regions are relieved, and the damage drops. As the hot spot is punched out of the vessel, however, the severity of the damage again increases, and is rising dramatically at the point of vessel failure.

Figure 4-67 illustrates the evolution of vessel deformation and damage distribution for the case $q''_{peak}/q''_{metallic} = 6$ and $p_i = 10$ MPa. Each "x" indicates a point which has exceeded 100% damage. The figure indicates that the hot spot is being sheared off from the remainder of the vessel. The failure geometry is cusped or local. In this series of simulations, all failure geometries are local. This distribution occurs because of the relatively stiff nature of the vessel outside the hot spot region. The contour plots in Figure 4-57 show that the peak temperature drops rapidly away from the hot spot back to the benign levels representative of operating conditions. Achieving the elliptical failure geometries would require substantially higher background heat fluxes.

Finally, Table 4-18 shows the sensitivity of failure times to pressure and peak heat flux. Unlike the contrived cases, there are no immediate failures, because failure is based on damage and requires the vessel to exist at elevated temperature and stress for finite time intervals. As before, failure times are strong functions of both the pressure and thermal loading.

4.2.2.5 Conclusions. This section has described a method for examining local failures and presented results for two different types of thermal loads. The first loads were contrived, steady-state temperature profiles intended to demonstrate the range of behaviors possible under local hot spots. This section has demonstrated that a local hot spot does not always produce a bulge or cusp as it fails. The failure geometry depends on the creep rate of the balance of the shell relative to the hot spot. If the magnitude of the peak temperature is small, the failure geometry is elliptical, and the hot spot assists or accelerates failure that looks like global failure. If the magnitude of the peak temperature is large, the peak temperature is punched out of a comparatively stiff vessel, and the failure geometry is cusped.

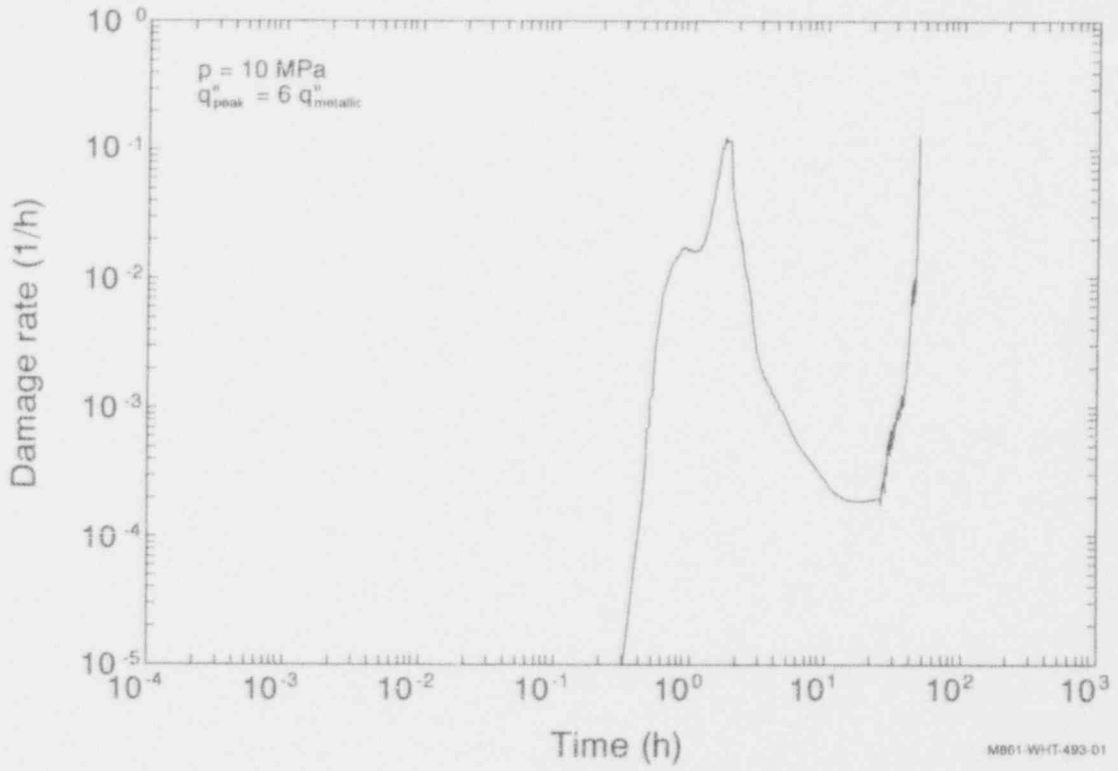

(a) Damage rate

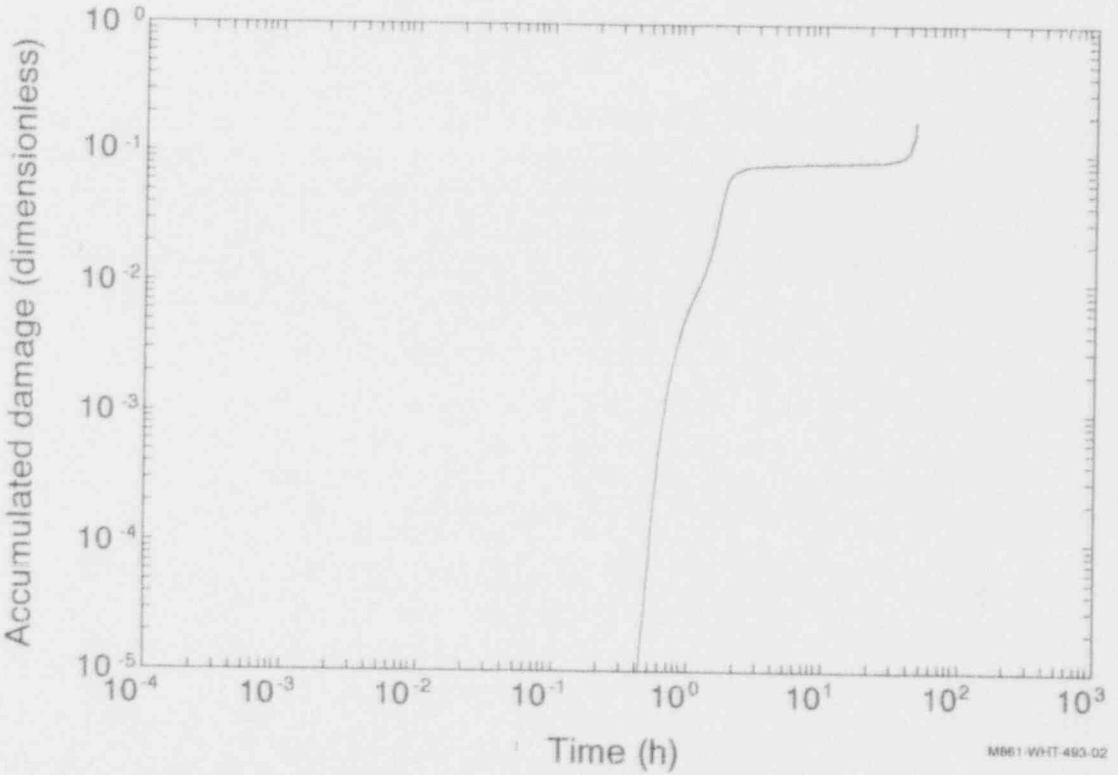

(b) Accumulated damage

Figure 4-66. Representative damage rate and accumulation in transient hot spot problem.

Figure 4-67. Representative vessel deformation and damage distribution in transient hot spot problem.

A second set of problems was examined based on transient thermal loads from applied heat fluxes associated with different debris characteristics. All failure geometries in these problems were local because the background heat flux was benign and the balance of the vessel remained cool. As with the contrived problems, times to failure were very strong functions of applied pressure and peak heat flux.

4.3 Summary

Models with closed form or simplified numerical solutions were applied to predict phenomena pertaining to vessel lower head and penetration failure. All of the failure mechanisms identified in Section 1 have been considered. Analytical models for performing thermal analyses, which provide boundary conditions for failure analyses, are also described in this section. Results from these analyses provide insight into which failure mechanisms are possible during different accident scenarios and in different reactor designs. Major points learned from these analyses are summarized below.

- *Event Timing.* Simple energy balances were performed to predict the time for core relocation, assuming an adiabatic heatup with coolant below the bottom of the core; and the time for coolant boiloff, assuming an isothermal and isobaric process.

  Relocation times for corium (fuel and core structures) varied from ~0.6 to 3.0 hours, depending on assumed corium composition and reactor design. Coolant boiloff times varied from ~1 to 6 hours, depending on assumed RCS pressure and reactor design. In general, longer relocation times and coolant boiloff times are predicted for BWR designs because of their larger initial coolant inventory, higher ratio of corium structural mass to initial power level, and lower operating temperature and pressure.

- *Vessel Thermal Response Time.* The one-dimensional form of the transient heat conduction equation was applied to predict vessel thermal response times. Resulting equations were written in terms of dimensionless groups that could be plotted as single curves.

  Although thermal response times are dependent upon parameters, such as debris to vessel heat flux, vessel thickness, and debris thermal properties, results were obtained for a B&W PWR and a GE BWR, assuming a range of severe accident condition parameters. Results indicated that BWR vessel response time is nearly twice as long as PWR response time because the BWR vessel is thicker.

- *In-vessel Tube Thermal Response Time.* An order-of-magnitude estimate for in-vessel tube heatup times was obtained by applying expressions for thermal relaxation times to debris in contact with the outer surface of penetrations. The time required for the thermal front from the hot debris to penetrate any lower head penetrations is estimated to be less than ~20 seconds. Tube melting times for thinner tubes, such as GE instrument tubes, are estimated as ~3 minutes. Thicker tubes, such as the thick section of a B&W instrument guide tube, a GE control rod guide tube, or a Westinghouse guide tube, are predicted to have longer thermal response times (as much as ~25 minutes for tube melting).

- *Jet Impingement.* The maximum amount of heat that can be transferred to the lower head from a coherent jet of debris was estimated by using the THIRMAL/0 code. A

wide range of debris and vessel system conditions were considered for each of the four reference U.S. LWR vessel designs.

In PWR designs, the presence of flow plates in the lower plena and the hole configuration within these flow plates strongly affect jet impingement. For B&W plants, the flow plates accumulate the melt and form multiple jets, reducing the jet velocity and the fraction of initial jet energy that can impinge on the vessel lower head. Unlike the flow plates in a B&W plant, flow plates in Westinghouse and CE plants do not generally accumulate melt, allowing "straight shot" jets to occur in any horizontal structural plates. The GE BWR lower head is protected by a water pool, which is deeper than the water pool present within PWR lower plena.

- *In-vessel Tube Melting.* An order-of-magnitude estimate of the debris thermal requirements to induce tube melting was obtained by applying a heat balance to a penetration tube in contact with corium debris. Results indicate that the ratio of the tube-to-debris mass ratio in the lower head governs the potential for in-vessel tube melting to occur. Because BWR vessels have a larger number of penetrations, higher temperature debris is needed to cause in-vessel tube melting. For example, in cases where no coolant is present in the reactor vessel lower head, ceramic debris temperatures greater than 1700 K are required to induce tube melting in a PWR, where only instrumentation tubes penetrate the lower head; whereas ceramic debris temperatures in excess of 2000 K are required to induce tube melting in a BWR lower head.

- *Melt Velocity Through Failed Tubes.* Order-of-magnitude estimates for the velocity of viscous melt through failed tubes were obtained by applying the energy equation for steady, adiabatic flow. The magnitude of the melt's velocity is dependent upon the differential pressure across the melt, melt composition, tube effective diameter for melt flow, and in-vessel tube length.

  Results indicate that the differential pressure across the melt has the most influence on melt velocity predictions. For cases in which only gravity forces act on melt in a penetration tube, melt velocities between 1 and 3 m/s are predicted, with higher velocity melts being predicted for a BWR drain line penetration tube because of its larger effective diameter available for melt flow. For cases where a pressure gradient exists between the inside and outside of the vessel, such as in the air-filled channel at atmospheric pressure within a BWR instrument tube, velocities of nearly 45 m/s are predicted to occur.

- *Melt Penetration Distance.* Two models were used to predict melt penetration distance: a modified bulk freezing model, which assumes that melt flow is sufficiently turbulent to preclude crust formation so that convection heat transfer dominates; and a conduction model, which assumes crust formation occurs along the tube outer wall so that conduction heat transfer dominates. Penetration distances predicted with the conduction model were longer than those predicted with the modified bulk freezing model. For cases where melt velocities are affected only by gravity, the conduction model predicts that melt will travel below the lower head for all LWR lower head penetrations; whereas the modified bulk freezing model predicts that melt will not travel below the lower head unless the tube has a fairly large effective diameter for melt flow and/or the tube has been ablated within the vessel at the point near the vessel inner surface. However, both models predict that melt will travel below the

lower head for the GE drain line penetration, which has a fairly large effective diameter for melt flow and no in-vessel structures. Furthermore, both models may predict that melt travels below the lower head through other penetrations if the tubes are ablated near the vessel and/or if the melt is driven by a large pressure gradient, such as the pressure difference between RCS operating pressure and the inner channel within instrument tubes.

- *Ex-vessel Tube Failure at Low Pressure.* For depresssurized conditions, thermal equilibrium calculations were used to provide lower bounds for conditions, such as debris relocation temperatures and debris heat flux, necessary to induce ex-vessel tube failure. Results indicate that tube geometry and material are important parameters in predicting tube failure. For example, thin-walled penetrations with larger effective diameters for melt flow are more susceptible to failure after melt penetrates below the lower head. Higher debris temperatures are required to induce tube failure if the debris is metallic rather than ceramic. Although additional data are needed to quantify ultimate strength behavior of the SA105/106 material used in BWR drain lines, longer term steady-state temperature estimates indicate that this lower head penetration is more susceptible to ex-vessel tube rupture than other LWR penetrations. Results indicate that heat fluxes characteristic of primarily ceramic debris (i.e., in excess of 0.05 MW/m^2) are needed to induce failure in a BWR drain line tube, which is composed of SA105/SA106 steel and has a relatively large cross-sectional area for melt flow. Heat fluxes characteristic of molten ceramic debris (i.e., as high as 0.2 MW/m^2) were not predicted to fail any of the other LWR penetrations.

- *Tube Failure and Global Vessel Failure at High Pressure.* For higher pressures (between ~0.1 and 16 MPa), analytical models with closed-form solutions were applied to compare the potential for tube ejection, tube rupture, and global vessel rupture. Failure maps were generated that indicate relative pressure bearing capacities of vessel heads and their penetration based on ultimate strength. Failure maps considered three types of debris beds: a primarily metallic debris, a primarily ceramic slurry, and primarily ceramic molten pool. Failure curves for tube ejection and tube rupture were found to form at the same location, in the vicinity of the tube material's melting temperature. For the case of a molten ceramic pool in a BWR vessel, model results indicate that tube failures will occur at lower temperatures than vessel failures for any system pressure. Except for the BWR case with a molten ceramic pool, model results indicate that global rupture is the controlling failure mode in BWRs or PWRs with system pressure above approximately 2 MPa. Although model results indicate that penetration tube failures control below 2 MPa, uncertainties in penetration material ultimate strength data at high temperatures do not allow a clear distinction of the controlling failure mode in this pressure range.

- *Localized Vessel Failure.* A new model, based on Reissner's theory of shells with finite deformation, was applied to the problem of local creep rupture on a corium-loaded lower head. This new model was applied to determine how local debris heat sources impact vessel failure times and what conditions are necessary for the formation and failure of a local bulge or cusp to occur. Two types of thermal loads were investigated.

  The first loads were contrived, steady-state temperature profiles intended to demonstrate the range of behaviors possible under local hot spots. It was found that a local hot spot does not always produce a bulge or cusp as it fails. The failure geometry depends on the creep rate of the balance of the shell relative to the hot spot. If the

magnitude of the peak temperature is small, the failure geometry is elliptical, and the hot spot assists or accelerates a failure that looks like global vessel failure. If the magnitude of the peak temperature is large, the hot spot is punched out of a comparatively stiff vessel, and the failure geometry is cusped.

A second set of problems was examined based on transient thermal loads for applied heat fluxes associated with different debris characteristics. All failure geometries in these problems were local because it was assumed that the background heat flux was benign and that the balance of the vessel remained cool. As with the contrived problems, times to failure were very strong functions of applied pressure and peak heat flux.

The thermal and failure analyses documented in this section were performed using analytical or simplified numerical techniques to look at a particular phenomenon. Results are generally presented as failure maps that have been developed in terms of dimensionless groups so that they can be applied to a broad range of reactor designs and severe accident conditions. More detailed calculations, such as the ones documented in Section 5, are needed to verify the simplifying assumptions made in developing these failure maps. However, once the governing relationships used to develop these maps are confirmed, these maps are useful for considering a broad range of reactor designs and severe accident conditions.

4.4 References

4-1. N. Todreas and M. Kazimi, *Nuclear Systems in Thermal Hydraulic Fundamentals*, New York: Hemisphere Publishing, 1990.

4-2. J. R. Larson, *System Analysis Handbook*, NUREG/CR-4041, EGG-2354, 1984.

4-3. D. Brownson, *Extension of Surry Late Depressurization Strategy Results to Commercially Operating Pressurized Water Reactors*, EGG-EAST-9717, EG&G Idaho, Inc., October 1991.

4-4. V. S. Arpaci, *Conduction Heat Transfer*, Reading, MA: Addison-Wesley Publishing Company, 1966.

4-5. F. B. Hildebrand, *Advanced Calculus for Applications*, Englewood Cliffs, NJ: Prentice-Hall, Inc., 1976.

4-6. J. E. O'Brien and G. L. Hawkes, "Thermal Analysis of a Reactor Lower Head with Core Relocation and External Boiling Heat Transfer," *Transactions from the 27th ANS/ASME/AIChE National Heat Transfer Conference, AIChE Symposium Series, 87*, 1991, p. 159.

4-7. H. S. Carslaw and J. C. Jaeger, *Conduction of Heat in Solids*, London: Oxford University Press, 1959, p. 288.

4-8. M. Epstein, "Heat Conduction in the UO_2-Cladding Composite Body with Simultaneous Solidification and Melting," *Nuclear Science and Engineering, 51*, 1973, pp. 84–87.

4-9. L. F. Moody, *Transactions of the American Society of Mechanical Engineers, 66*, 1944, p. 671.

4-10. Kays, W. M., *Convective Heat and Mass Transfer*, 2nd edition, New York: McGraw-Hill, 1964.

4-11. R. W. Ostensen and J. F. Jackson, *Extended Fuel Motion Study*, ANL-RDP-18, Argonne National Laboratory, July 1973.

4-12. R. W. Ostensen et al., "Fuel Flow and Freezing in the Upper Subassembly Structure Following an LMFBR Disassembly," *Transactions of the American Nuclear Society, 18*, 1974, p. 214.

4-13. M. Epstein et al., "Transient Freezing of Flowing Ceramic Fuel in a Steel Channel," *Nuclear Science and Engineering, 61*, 1976, pp. 310–323.

4-14. M. Epstein et al., "Analytical and Experimental Studies of Transient Fuel Freezing," *Proceedings of the International Meeting on Fast Reactor Safety and Related Physics, Volume IV, USERDA Conference No. 761001, Chicago, IL, October 1976*, pp. 1788–1798.

4-15. S. Glasstone and A. Sesonske, *Nuclear Reactor Engineering*, New York: Van Nostrand Reinhold Company, 1967.

4-16. M. El-Genk and A. W. Cronenberg, "An Assessment of Fuel Freezing and Drainage Phenomena in a Reactor Shield Plug Following a Core Disruptive Accident," *Nuclear Engineering and Design, 47*, 1978, pp. 195–225.

4-17. *ASME Boiler and Pressure Vessel Code, Section III*, American Society of Mechanical Engineers, 1989.

4-18. W. C. Young, *Roark's Formulas for Stress and Strain*, 6th Edition, New York: McGraw-Hill, 1989.

4-19. R. D. Cook and W. C. Young, *Advanced Mechanics of Materials*, New York: Macmillan, 1985.

4-20. T. Baumeister et al., *Marks' Standard Handbook for Mechanical Engineers*, 8th Edition, New York: McGraw-Hill, 1978.

4-21. R. S. Chambers, *A Finite Element Analysis of a Pressurized Containment Vessel During Core Melt Down*, SAND87-2183, Sandia National Laboratory, 1987.

4-22. L. E. Anderson et al., *Effects of a Hypothetical Core Melt Accident on a PWR Vessel with Top-Entry Instruments*, IDCOR Program Technical Report 15.2A, Electric Power Research Institute, June 1983.

4-23. G. V. Smith, *Evaluations of the Elevated Temperature Tensile and Creep-rupture Properties of C-Mo, Mo-Mo and Mn-Mo-Ni Steels*, Metal Properties Council, American Society for Testing and Materials, ASTM Data Series Publication DS47, 1971.

4-24. S. K. Wang, J. J. Sienicki and B. W. Spencer, "Assessment of the Integrity of TMI-2 Lower Head During Core Relocation," *Fifth Proceedings of Thermal Hydraulics, 1989 ANS Winter Meeting, San Francisco, CA*, 1989, p. 36.

4-25. S. K. Wang, C. A. Blomquist and B. W. Spencer, "Modeling of Thermal and Hydrodynamic Aspects of Molten Jet/Water Interactions," *ANS Proceedings of 1989 ANS/ASME/AIChE National Heat Transfer Conference, August 6-9, Philadelphia, PA*, 1989, p. 225.

4-26. S. K. Wang, C. A. Blomquist and B. W. Spencer, "Interfacial Instability Leading to Bubble Departure and Surface Erosion During Molten Jet/Water Interaction," *ANS Proceedings of the 1989 ANS/ASME/AIChE National Heat Transfer Conference, August 6-9, Philadelphia, PA*, 1989, p. 31.

4-27. S. A. Hodge, "BWR Reactor Vessel Bottom Head Failure Modes," *Proceedings on Fission Product Transport Processes in Reactor Accidents, Dubrovnik, Yugoslavia, May 22–26, 1989*. CONF-890546-3, December 1989.

4-28. K. Sato, A. Furutani, M. Saito and M. Isozaki, "Melting Attack of Solid Plates by a High Temperature Liquid Jet [II]-Erosion Behavior by a Molten Metal Jet," *27th ANS/ASME/AIChE National Heat Transfer Conference, Minneapolis, MN, July 28–31, 1991*.

4-29. R. D. Blevins, *Applied Fluid Dynamics Handbook*, New York: Van Nostrand Reinhold Co., 1984, p. 208.

4-30. S. K. Wang and J. J. Sienicki, *THIRMAL Calculations of Lower Plenum Melt/Water Interactions and Conditions of Melt Arrival on the Lower Head in U.S. LWR Designs*, ANL/RE/LWR 91-4, Argonne National Laboratory, July 1991.

4-31. D. Magellon, R. Zeyen, and H. Hohmann, "Pouring of 100 kg-Scale Molten UO_2 Out-of-Pile Interactions with LMFBR Structures: Plate Erosion and Fuel Freezing in Channels," *International Conference on Fast Reactor Core and Fuel Structural Behaviour, Inverness, Scotland, June 4–6, 1990*.

4-32. J. A. Pessanha and M. Z. Podowski, "Ablation of Solid Walls Subjected to Impinging Inclined Jets," *ANS Proceedings of the 1989 ANS/ASME/AIChE National Heat Transfer Conference, Philadelphia, PA*, August 1989.

4-33. G. Jaross, J. Maneke, and T. Stoodt, *A Study on the Configuration and Safety Features of U.S. Nuclear Power Plants*, ANL/LWR/SAF 82-2, Argonne National Laboratory, July 1982.

4-34. V. C. Levich, *Physiochemical Hydrodynamics*, Englewood Cliffs, NJ: Prentice-Hall, Inc., 1962.

4-35. G. I. Taylor, "The Dispersion of Jets of Metals at Low Melting Point in Water," *The Scientific Papers of G. I. Taylor*, Vol. 3, G. K. Batchlor (ed.), Reading, MA: 1942.

4-36. R. S. Brodkey, *The Phenomena of Fluid Motions*, Reading, MA: Addison-Wesley Publishing Co., 1967.

4-37. C. Weber, "On the Breakdown of a Fluid Jet," *Zeitschrift fur ange wanate Mathematik and Mechanik, 11*, 1931, p. 136.

4-38. M. Epstein and H. K. Fauske, *The TMI-2 Core Relocation Heat Transfer and Mechanism*, EGG-TMI-7956, EG&G Idaho, Inc., July 1987.

4-39. M. Epstein and H. K. Fauske, "The Three Mile Island Unit 2 Core Relocation-Heat Transfer and Mechanism," *Nuclear Technology, 87*, 1989, p. 1021.

4-40. M. Saito et al., "Melting Attack of Solid Plates by a High Temperature Liquid Jet-Effect of Crust Formation," *Nuclear Engineering and Design, 121*, 1990, p. 11.

4-41. PAFEC, Version 6.1, Nottingham, England: PAFEC Ltd., 1984.

4-42. S. Lin, T. Lin, and B. Mazelsky, "Large Deflection of Axisymmetric Shell with Creep Strain," *ASCE Journal of Engineering Mechanics, 100*, 1974, pp. 79–94.

4-43. R. D. Krieg and D. B. Krieg, "Accuracies of Numerical Solution Methods for the Elastic-Perfectly Plastic Model," *ASME Journal of Pressure Vessel Technology, 99*, 1977, pp. 510–514.

4-44. G. G. Reddy, and D. J. Ayres, *High-Temperature Elastic-Plastic and Creep Properties for SA 533 Grade B Class 1 and SA 508 Materials*, EPRI NP-2763, Electric Power Research Institute, 1982.

4-45. D. J. Hanson et al., *Depressurization as an Accident Management Strategy to Minimize the Consequences of Direct Containment Heating*, NUREG/CR-5447, EGG-2574, 1990.

5. FINITE-ELEMENT ANALYSES OF PENETRATION AND VESSEL THERMAL AND STRUCTURAL RESPONSE

As discussed in Section 1.3, a final aspect of this research program is to apply more detailed numerical methods to gain insight into the importance of two-dimensional effects and into special geometries where analytical techniques may be insufficient. This section documents the results from a study that assessed the two-dimensional thermal and structural response of a BWR penetration and vessel. Numerical results from this study are compared with results obtained using the simpler models documented in Section 4. Then, failure maps are used to consider the response of penetrations in other LWR geometries.

As discussed in Section 2.3, finite-element analyses of a lower head vessel subjected to accident conditions have been performed previously. This study differs from previous studies in that it evaluates an accident scenario where creep plays a dominant role in the vessel behavior. Several of the previous studies either did not include creep[5-1,5-2] or did not include thermal or pressure conditions where creep would dominate the behavior. In the case of the EPRI study,[5-3] the vessel was heated rapidly and subjected to relatively high pressures, so that creep and ultimate strength failures should have been very closely timed; the GRS analysis[5-4] also had a short creep failure time (less than 1 hour), indicating that the material was probably close to its ultimate strength. The ORNL study[5-5] used very low pressures, so that creep failure and melt should have been closely timed. The previous INEL study on the TMI-2 accident[5-6] used a constant average through-wall temperature and a constant pressure to predict creep failure. Predicted creep failure times were very short (less than 10 minutes) or very long (100 hours), indicating that ultimate strength or melt failures are eminent. A key contribution of the structural finite-element analysis performed here is the use of full thermal-hydraulic analysis of accident scenarios in a two-dimensional elastic-plastic-creep structural analysis where creep behavior plays an important role.

5.1 Introduction

5.1.1 Problem Description

Detailed calculations described in this section center on a BWR vessel and its drain line penetration. A schematic of the BWR/4 vessel and drain line is shown in Figure 5-1. Dimensions for the analysis, which are primarily based on Peach Bottom plant drawings,[a] are summarized in Appendix F. The vessel is composed of SA533, Grade B, Class I steel.[5-7] The lower head is somewhat thicker than the sidewalls so that it can be penetrated by 185 control rod guide tubes, 55 instrument tubes, and the drain line tube. A support skirt, composed of SA302 Grade B steel, is attached to the lower head. Surrounding the lower head and support shirt is reflective insulation, which is composed of layered stainless steel.

Analyses in the first part of this section focus on the drain line because initial studies indicate that this penetration will fail earlier than other locations in BWR vessels. The drain line penetration is located in the bottom of the reactor vessel, 15.24 cm (6 in.) off the centerline. It directs flow to the reactor water cleanup system to aid in the removal of suspended solids, to

---

a. Most dimensions were obtained from plant drawings for the Peach Bottom Unit 2, Peach Bottom Unit 3, and Dresden Unit 3 reactors. The drawings were provided by the Philadelphia Electric Company, Diamond Power Specialty Corporation, and Impell Corporation.

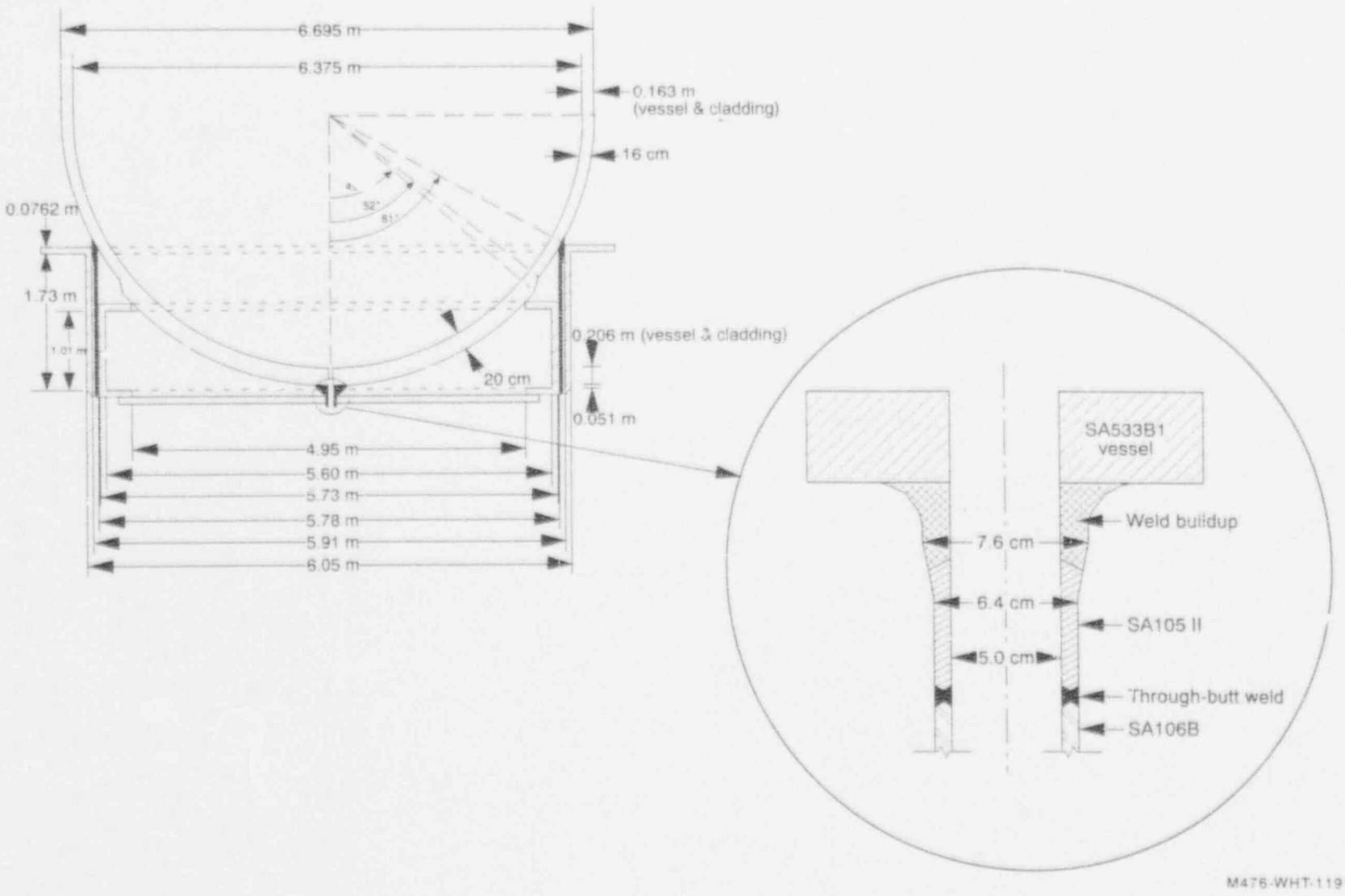

Figure 5-1. Typical BWR vessel and drain line configuration.

provide a temperature measurement of water in the bottom head area, and to minimize cold water stratification in the bottom head area.[5-8] The portion of the drain line analyzed in this study consists of a SA105 Class II carbon steel nozzle and SA106 Grade B mating pipe. A schematic of the drain line penetration is shown in Figure 5-1.[5-9] The pipe extends 0.61 m (2 ft) vertically below the vessel before connecting to an elbow joint.

Preliminary study indicated that drain line penetration failure will occur earlier than other locations in a BWR for the following reasons:

- System pressures considered in this analysis produce very low (below 60 MPa, 8,700 psi) primary stresses in the vessel and drain line. Therefore, failure is likely to occur from the reduction in strength at elevated temperatures.

- Drain line thickness (0.7 cm) is much less than the vessel lower head thickness (20.0 cm). Thus, if debris relocates onto the lower head and into the drain line, the drain line may be susceptible to reaching failure temperatures more rapidly than the vessel.

- Once high temperatures are reached, drain line material is more susceptible to high-temperature failure than the vessel or other BWR penetration material. The drain pipe material, SA106 Grade B, is not recommended for use above 811 K.[5-10] The ultimate strength of SA106 is 238 MPa at 811 K;[5-11] whereas, the ultimate strength of the vessel material, SA533B, is over 350 MPa at the same temperature (see Appendix F).

- Although BWR instrument tube walls are thinner than the drain line, the drain line has a larger effective diameter for melt flow. Furthermore, the drain nozzle is directly open to corium melt (thus, no in-vessel structure melting is required for melt penetration).

Results from closed-form solution models in Section 4.1.3 indicate that if several types of debris enter a penetration at pressures below approximately 2 MPa, failure will occur by tube ejection or tube rupture before the vessel ruptures. Two assumptions are inherent in analytical model predictions that the penetration will fail first at lower pressures: (a) debris must enter the penetration and (b) failure must be governed by instantaneous plastic deformation from pressure loads (thermal stresses and creep are negligible). For higher pressure cases and in the event that debris does not enter a penetration, it becomes important to assess the vessel structural response with thermal stresses and creep included. Analyses in the latter portion of this section assess time-dependent elastic-plastic-creep response of the vessel lower head to severe accident temperature histories for a range of constant system pressures.

5.1.2 Objectives

Detailed calculations described in this section were performed to accomplish the following objectives:

- Assess the relative timing of BWR vessel and penetration failure for a wide range of accident conditions

- Estimate the fraction of corium that is molten at the time of vessel failure

- Interface a commercially available two-dimensional, finite-element structural code with the thermal-hydraulic code, SCDAP/RELAP5, to perform the detailed structural analysis

- Investigate the roles of thermal stresses and creep (neglected in the simplified Section 4.1.4 analysis) in vessel failure

- Confirm simpler analytical model predictions with numerical model results.

Although these objectives require more detailed numerical techniques than discussed in Section 4, results from a limited number of numerical calculations can be used in conjunction with Section 4 analytical results to obtain general conclusions related to the nature of lower head failure.

5.1.3 Approach

This section describes the investigation of the thermal and structural response of a BWR vessel and drain line penetration. The impact of debris composition, porosity, vessel coolant pressure, heat removal conditions, and debris-to-vessel and debris-to-drain line thermal contact is assessed using the SCDAP/RELAP5 code.[5-12] In addition, results are applied to other LWR geometries using failure maps, based on the methodology described in Section 4. The roles of thermal stresses, plasticity, and creep in these accident scenarios are investigated using the ABAQUS code.[5-13]

Models used in this analysis are described in Section 5.2. Results from the thermal and structural analyses are presented in Sections 5.3 and 5.4. Section 5.5 summarizes major results and conclusions from these calculations.

5.2 Methodology

5.2.1 SCDAP/RELAP5 Thermal Analysis Model

A two-dimensional finite-element analysis was performed using the COUPLE thermal analysis model in Version 3.0 of the SCDAP/RELAP5/MOD2 code.[5-12] Primary objectives of this thermal analysis were (a) to assess the relative importance of thermal fronts created by the debris in the drain line and on the vessel lower head; (b) to assess the sensitivity of thermal response to debris composition, porosity, and heat removal from the lower head and drain line; (c) to provide input to the mechanical response analyses; and (d) to provide input to subsequent consequence analysis codes by specifying the fraction of the debris that is molten at the time of vessel failure. Section 5.2.1.1 describes the SCDAP/RELAP5 model. Input assumptions and bases for these assumptions are summarized in Section 5.2.1.2.

5.2.1.1 Model Description. Although analytical closed-form solutions are available to evaluate heat transfer from debris to the penetration tube and the vessel separately, a two-dimensional numerical solution is needed to simultaneously evaluate the relative importance of the thermal fronts transmitted from the debris through the drain line and through the vessel lower head. SCDAP/RELAP5 offers a number of advantages over most two-dimensional heat-transfer codes because it simulates reactor thermal-hydraulic conditions, fuel liquefaction and relocation, time- and composition-dependent debris pool formation, and natural convection from a pool of molten debris.

Because a primary objective of this analysis was to determine vessel and penetration thermal response, a simplified RELAP hydrodynamic model was used with a detailed COUPLE model (the finite-element conduction heat-transfer model in SCDAP/RELAP5) of the debris, vessel, and drain line configuration. As shown in Figure 5-2, two representative RELAP circuits were used to represent the hydrodynamic conditions through the vessel and through the reactor building cavity. The first loop includes an eight subvolume "pipe" component (volumes 70-01 through 70-08) to model the heat removal from the debris to coolant in the vessel. Liquid in the first subvolume (volume 70-01) is in contact with the debris, which was assumed in base case calculations to relocate to the lower head and into the penetration at the beginning of the transient. As vapor is generated in this volume, it travels upward (from volume 70-01 to volume 70-08) and eventually exits to a time-dependent "sink" component (volume 10). The second loop is included to model the heat removal from the vessel to the reactor building cavity (volume 250).

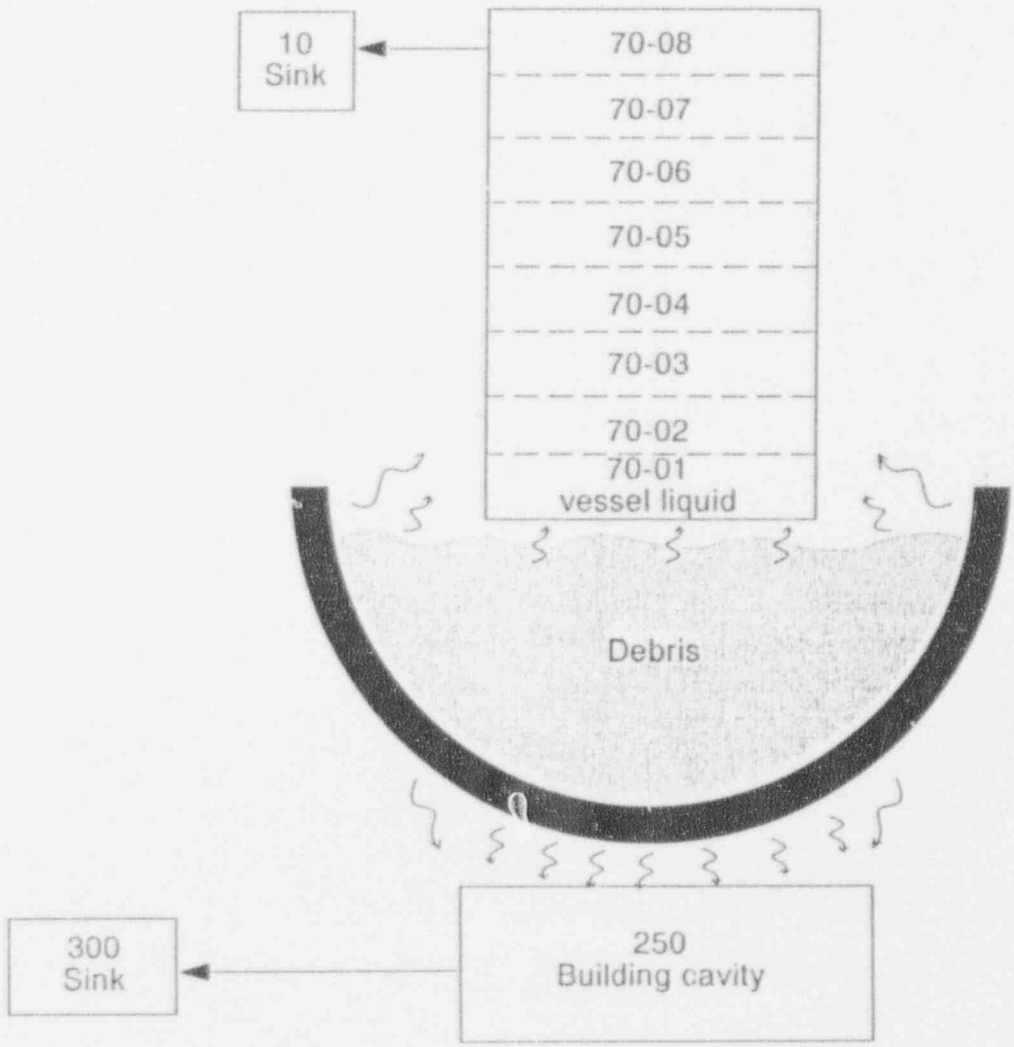

Figure 5-2. RELAP hydrodynamic model used for modeling BWR vessel and drain line penetration.

Finite-Element Analysis

Figures 5-3 and 5-4 illustrate the COUPLE models for the debris/vessel and debris/vessel/drain line configurations. Meshes were generated using the PATRAN[5-14] code, which has recently been interfaced to output mesh nodal locations for SCDAP/RELAP5 input and to read COUPLE temperature output for two-dimensional display. Models were constructed in r-z geometries that are axisymmetric with respect to the center of the vessel or with respect to the penetration tube. Only a portion of the vessel was modeled in the drain line mesh (Figure 5-4). The maximum radial width of this mesh was selected to correspond to half the distance between the center of the drain line and the center of the nearest penetration in a BWR lower head (7.62 cm). The axial length was based on the distance traveled by the melt before it solidified within the drain line pipe (see Section 5.2.1.2) and the maximum expected debris height.

Up to four types of materials are included in the models. Both meshes contain carbon steel for the vessel and drain line; a null material for the debris-to-vessel and debris-to-drain line gaps; and a mixture consisting of UO_2, stainless steel, zircaloy or zirconium oxide, and B_4C for the slumped corium. In addition, the mesh for the drain line contains Inconel for the vessel liner. Accuracy requirements for mesh nodalization precluded the inclusion of this thin liner in the global vessel mesh.

Sensitivity studies were used to confirm that the nodalization scheme and the time steps chosen for calculations performed with both of these meshes were adequate. Note that self-leveling debris models in the COUPLE model of SCDAP/RELAP5 require that quadrilateral elements with two horizontal sides be used in the vessel debris bed (three nodes are co-linear). Hence, it was necessary to include triangular-shaped quadrilateral elements in the debris bed. The large aspect ratio of angles in such quadrilaterals can cause numerical errors, and slight temperature variations in these triangular quadrilateral debris elements were noted. However, these elements were placed in the center of the debris bed to minimize their impact on vessel temperatures predicted in these calculations.

Boundary conditions for each of the COUPLE meshes are also illustrated in Figures 5-3 and 5-4. Heat is convected away from the top surface of the debris to the coolant in vessel subvolume 70-01. For the vessel calculations, heat is convected along the vessel outer surface (along the surface with nodes 17 through 32) and the vessel support skirt surfaces (surfaces with nodes 1 through 16) to the containment building. An adiabatic boundary condition is assumed at the center of the axisymmetric mesh. For the drain line calculations, heat is also convected from the drain line and vessel outer surface (along the surfaces with nodes 7, 21, 35, 61 and 87 through 93) to the containment building. Adiabatic boundary conditions are assumed at the outer surface of the mesh, the lower edge of the drain pipe, and at the center of the axisymmetric mesh.

Sensitivity studies were performed to consider different containment heat removal conditions (e.g., for dry and flooded containment buildings). Radiative and convective heat transfer from the vessel or drain line to structures in a dry containment was modeled by using an effective conductivity for the steam/air containment atmosphere. As discussed in Reference 5-15, the insulation present around the outside of the vessel will not impede water from contacting the vessel if the containment is flooded. Hence, flooded outer boundary conditions for the vessel and drain line were simulated by applying the appropriate convective heat transfer coefficient.

The rate of heat transfer from the debris region to the vessel and drain line is a strong function of the conditions at the interface between the debris and structure. The modeling of this heat transfer was simulated by including a gap between these materials. The gap heat-transfer coefficient was divided into two regimes for solidified and liquefied debris. For the solidified debris regime, the heat-transfer coefficient was based on a user-specified value derived from

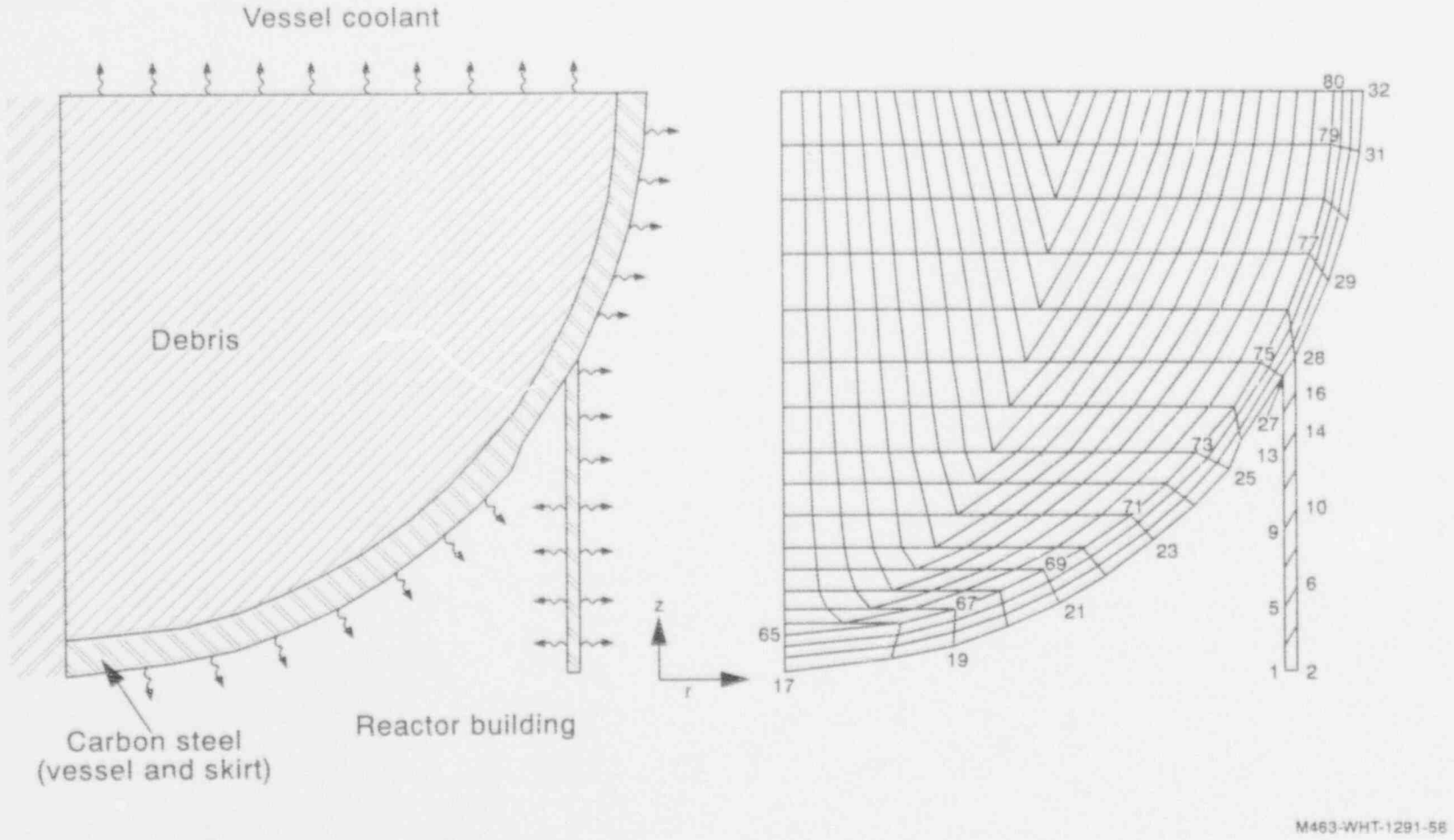

Figure 5-3. COUPLE mesh nodalization scheme and boundary conditions for BWR vessel thermal analysis.

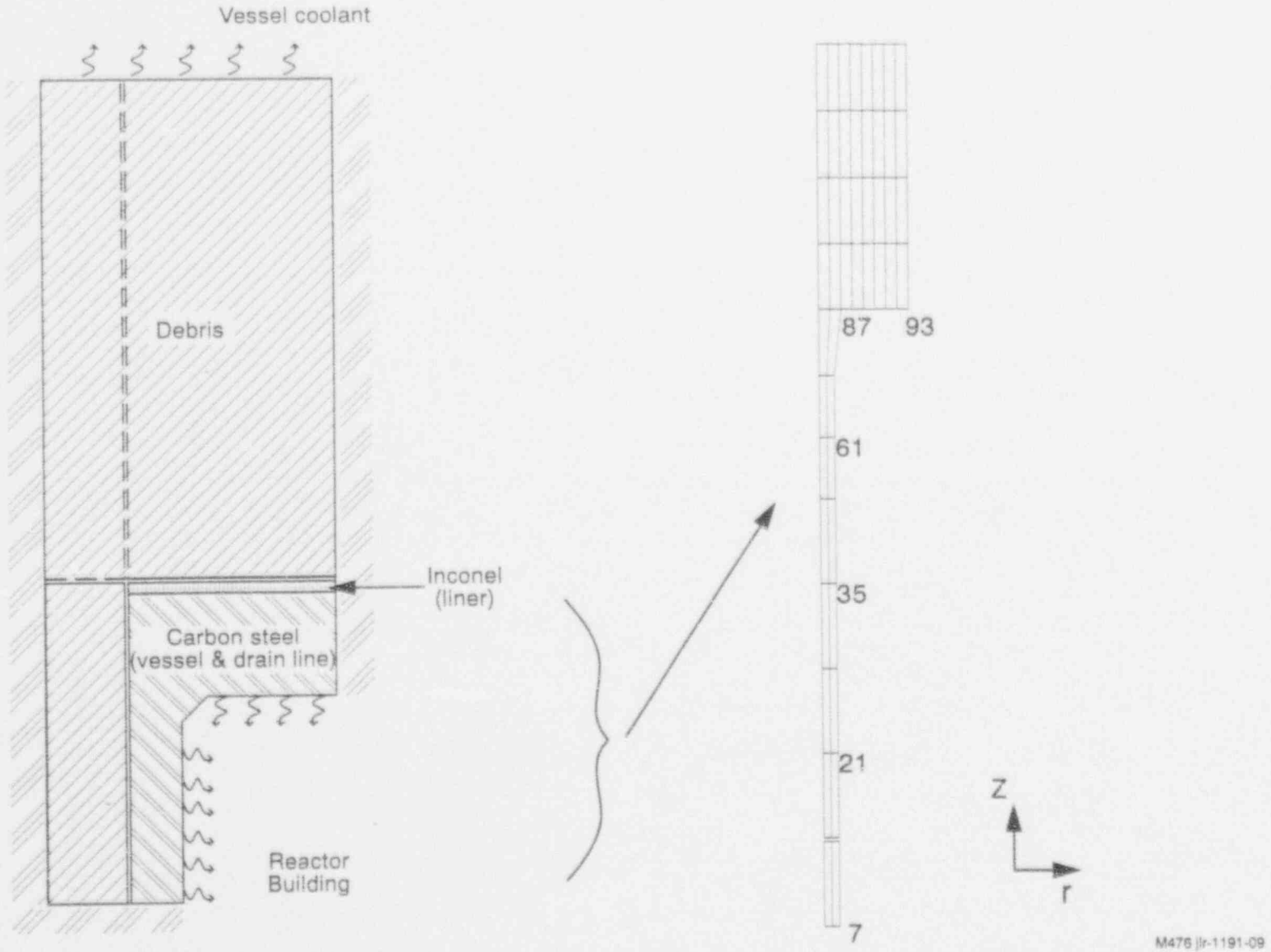

Figure 5-4. COUPLE mesh nodalization scheme and boundary conditions for BWR drain line thermal analysis.

parameters such as the debris and structure surface roughness.[5-16] In the liquefied debris regime, a gap heat-transfer coefficient was based on the rate of heat transfer through the thermal boundary layer between the liquefied debris and the structure in contact with the liquefied debris.[5-17]

Because the COUPLE model in SCDAP/RELAP5 is strictly a heat-conduction code, convective heat transfer was modeled at the liquid-solid debris interface using an effective conductivity that includes an empirical convective heat-transfer coefficient, which is calculated based on data from Mayinger[5-17] and Jahn and Reineke.[5-18] Although these data were obtained for molten pools with Rayleigh numbers, Ra, with values of $10^4 \leq Ra \leq 10^9$, recently obtained data[5-19] from a small scale experiment with higher Ray numbers (10^{12} to 10^{13}) indicate that the data by obtained Mayinger and Jahn and Reineke are appropriate for nuclear reactor accident analysis (where Ra numbers as high as 10^{17} are postulated to occur). A detailed description of the manner in which this effective conductivity was calculated is provided in Reference 5-20.

5.2.1.2 Input Assumptions. Table 5-1 summarizes input assumptions and parameters used in these calculations. Three types of debris beds are considered: a uniform debris bed that is primarily metallic (Case I); a uniform debris bed that is primarily ceramic (Case II); and a layered debris bed with metallic debris near the vessel and ceramic debris on top (Case III). These debris bed compositions were selected to envelop possible BWR debris bed compositions during severe accidents. Sensitivity studies were performed to consider the effects of parameters, such as debris decay heat, debris porosity, debris particle size, debris-to-surface gap resistance, reactor coolant pressure, and heat-transfer conditions, on the outer surface of the drain line and vessel.

In Case I calculations, it was assumed that 10% of the core and structural materials would relocate to the lower head. The debris was assumed to contain a relatively large fraction of control rod and structural materials and to have a relatively low power density.

In Case II calculations, it was assumed that 50% of the corium mass would relocate to the lower head. Although all the control rods and structural materials were assumed to be included in the core debris, they represent a small fraction of the total corium mixture, which consists primarily of UO_2. Case II's debris composition is more similar to the debris found in the TMI-2 vessel and corresponds to the type of relocation scenario postulated for a long-term SBO event. During this event, loss of control air or dc power normally precludes the opening of the safety relief valves, so that coolant within the vessel causes molten material to form blockages above the core plate. When the core plate fails, the corium relocates as a fully molten mass into the lower plenum.

In Case III calculations, it was assumed that over 50% of the corium mass would relocate to the lower head. However, the composition of the relocating debris would vary with time. Case III debris bed assumptions were selected to represent BWR severe accident relocation scenarios predicted by Hodge et al. using the BWRSAR code[b] for a short-term SBO sequence. In this event, the automatic depressurization system (ADS) has actuated to depressurize the reactor vessel so that the water level is below the core prior to the onset of relocation. Although the debris was postulated to relocate to a dry core plate, no blockages were assumed to occur so that the debris would be quenched when it relocated to the lower plenum after core plate failure, which was assumed to occur relatively early. Thus, the debris was either solid or at a very low

b. S. A. Hodge, J. C. Cleveland, and T. S. Kress, unpublished research on the external flooding of a BWR reactor vessel as a late accident mitigation strategy, Oak Ridge National Laboratory, August 1991.

Table 5-1. Input assumptions for thermal analysis.

Parameter	Case I	Case II	Case III	
			Layer 1	Layer 2
Corium Mass, kg				
UO_2	1,200	108,000	1,200	108,000
Zircaloy	17,804	—	17,804	—
Zircaloy in ZrO_2	—	9,370	—	9,370
B_4C	330	174	330	174
Stainless steel	4,666	2,456	4,666	2,456
Total, kg	24,000	120,000	24,000	120,000
Relocation time period, s	5,000	5,000	5,000	5,000
Corium temperature, K	2100	2700	2100	2700
Power density, MW/m^3	0.1	0.4	0.1	0.4
Corium relocated (%)	10	50	60	
Water inventory, kg	88,000	260,000	88,000	
Water temperature (saturated), K	433	559	433	
System pressure, MPa	0.62	7.0	0.62	
Drain line/vessel temperature, K	433	559	433	
Reactor building temperature, K	373	373	373	

superheat at the time it relocated to the lower head. However, decay heat within the ceramic debris would cause a molten pool to form in the center of this debris bed.

Other assumptions used in these calculations are summarized below:

- *Material Thermal Properties.* Corium thermal properties, such as specific heat, density, thermal conductivity, latent heat of fusion, fusion temperature, and viscosity of the corium, are calculated in SCDAP/RELAP5 based on the debris composition.

  Structural material thermal properties were also calculated in SCDAP/RELAP5 using temperature-dependent functions. Before these calculations were performed, carbon steel thermal properties (enthalpy, conductivity, and density) in SCDAP/RELAP5 were updated using data from the references indicated on these curves in Appendix F. However, note that these updated thermal properties of carbon steel were extrapolated for temperatures above approximately 900 K.

- *Corium Porosity and Particle Size.* This study investigated the sensitivity of results to corium porosity. As a lower bound, a porosity of 0.0 was assumed to simulate cases where the debris is liquid. An upper bound porosity of 0.7 was chosen based on the upper values observed in debris from the TMI-2 vessel. A particle size of 1 cm was used in simulations with porosities of 0.7.

- *Debris Relocation Time.* The debris was assumed to relocate during the first 5,000 seconds of the transients simulated in Cases I and II. The relocation time for the multilayer debris simulated in Cases I and II was based on calculations performed by Hodge.[c]

- *Melt Plug Distance within the Penetration Tube.* In selecting a proper length that the melt could travel in the drain pipe before solidification, or the melt "plug" distance, it must first be established that the melt could enter the drain pipe, which is filled with reactor coolant. Applying the Taylor wavelength criteria for two fluids with unequal densities,[5-21] it was established that molten debris will penetrate any tube with a diameter larger than 0.5 cm.

  Although detailed numerical calculations may provide an exact distance that the melt could penetrate a tube filled with water, it was decided to bound possible distances by neglecting the resistance and cooling from water within the tube. The melt plug distance selected was 0.66 m. This plug distance was calculated using analytical expressions for a condition where conduction heat transfer dominated (using the model proposed by Epstein in Reference 5-22) and for a condition where turbulent heat transfer dominated (using a modified version of the model proposed by Ostensen and Jackson in Reference 5-23).[d] Although plug distances for both methods were greater than 1.0 m, preliminary analyses indicated that hot spots within the drain line occurred

---

c. S. A. Hodge, J. C. Cleveland, and T. S. Kress, unpublished research concerning external flooding of a BWR reactor vessel as a late accident mitigation strategy, Oak Ridge National Laboratory, August 1991.

d. Conduction-dominated and turbulent-dominated heat-transfer models for predicting melt penetration distance are discussed in Section 4.1.2.

nearer to the vessel/drain line interface. Hence, the mesh was truncated at 0.66 m; and an adiabatic boundary condition was applied to the lower edge of the tube and debris.

- *Debris to Vessel Thermal Contact.* When debris relocates to the lower head, the thermal contact between the debris and the structural material is reduced because of surface roughness and gas trapped between the debris and the surface of the vessel or drain line. A debris-to-vessel heat-transfer coefficient of 500 W/m^2K was assumed for all of the base cases considered. Values for this heat transfer coefficient, h_{gap}, were estimated using the equation below from Reference 5-16:

$$h_{gap} = \frac{k_g}{3.6\left(R_1 + R_2\right) + \left(g_1 + g_2\right)}$$

where

k_g = thermal conductivity of steam in vessel/debris gap (W/m^2K)

R_1, R_2 = surface roughness of material on each side of gap; typical debris roughness is 2×10^{-6} (m)

g_1, g_2 = temperature jump distance terms to account for temperature discontinuity caused by incomplete thermal accommodation of gas molecules to surface temperatures and to account for the inability of gas molecules leaving the surface to completely exchange their energy with neighboring gas molecules (m), defined by the following:

$$g_1 + g_2 = \frac{0.0247\ k_g\ T_{gas}^{0.5}}{P_{gas}\ \frac{a_{gas}}{M_{gas}}}$$

where

T_{gas} = gap steam temperature (K)

P_{gas} = gap steam pressure (Pa)

a_{gas} = gap steam accommodation coefficient (typically between 0.4 and 0.8)

M_{gas} = steam molecular weight (18 kg/kg-moles).

Upper and lower bounds for variables were used to estimate an appropriate range of values for h_{gap}. For these calculations, a value of 500 W/m^2K was selected as a lower bound and a value of 10,000 W/m^2K was selected as an upper bound for h_{gap}.

- *Heat Removal from Vessel Outer Surface.* Heat was assumed to be transferred from the vessel to the containment cavity via convection and radiation. In base case calculations,

it was assumed that the cavity contains a steam and air environment at atmospheric pressure. A sensitivity study was performed in which the vessel outer surface was exposed to water to study the effects of flooding in the reactor building cavity on vessel temperatures.

- *Debris to Coolant Heat Transfer.* Heat transfer from the debris to the coolant is dependent on the debris porosity and the heat-transfer regime of the reactor vessel coolant. For zero porosity debris, a boiling curve in SCDAP/RELAP5 was used to govern the selection of heat-transfer correlations. The various heat-transfer correlations used in SCDAP/RELAP5 are discussed in Reference 5-12. For porous debris beds, models within SCDAP/RELAP5 assume that decay heat from the debris is transferred to RCS coolant as long as there is liquid present in the vessel. If the liquid has been vaporized, heat is transferred via conduction and radiation to the reactor vessel.

5.2.1.3 Application of Numerical Results to Analytically Developed Models. Although a numerical analysis can provide answers to questions that cannot be answered by Section 4 models with closed-form solutions, it is not cost effective to perform detailed calculations for each type of reactor design. However, several key questions related to the response of other LWR penetrations can be answered by applying failure maps, similar to those developed in Section 4. Using the debris conditions input for the BWR drain line and vessel calculations, failure maps were applied to answer the following questions, which are identified in the lower right hand corner of Figure 1-2:

- Is the temperature and mass of the debris sufficient to induce in-vessel tube melting?
- Will the melt penetrate below the vessel?
- Will the tube fail ex-vessel?

Numerical calculation results can be used to verify that the governing relationships used in failure map development are sufficient for predicting penetration response. Furthermore, this application allows penetrations with geometries significantly different than the BWR drain line to be considered.

The application of Section 4 methods required that the debris conditions and reactor geometries be viewed in terms of key parameters and dimensionless groups. Table 5-2 summarizes some key geometrical dimensionless parameters, and Table 5-3 summarizes some scenario-dependent dimensionless parameters for base Cases I and II that will be used in determining the potential for vessel and penetration failure. As discussed in Section 4, the Table 5-2 groups emphasize some key geometrical differences between LWR vessel and penetration designs. For example, values for the ratio of the vessel radius to the vessel thickness indicate that the BWR lower head is relatively thicker than PWR lower heads. Dimensionless groups comparing the tube cross-section area to effective flow area and effective flow diameter to tube outer diameter indicate that Westinghouse and GE control rod guide tubes are relatively thick-walled tubes with small effective flow areas and that the GE drain line has a relatively high flow area compared with other LWR penetrations. Table 5-3 parameters emphasize differences between the ceramic and metallic debris compositions considered, such as the higher ceramic melt temperature and heat flux to the tube from debris decay heat.

Table 5-2. Key geometrical LWR dimensionless groups.

Parameter	General Electric			Babcock & Wilcox	Combustion Engineering	Westinghouse Plant 1	Westinghouse Plant 2
Vessel							
Radius/thickness	13.13			17.48	19.73	15.71	15.00
Penetration[a]	DN	IT	CR	IT	NA[b]	IT	IT
Outer radius/inner radius	1.26	1.31	1.23	1.71	NA	4.13	2.25
Effective flow diameter/ outer diameter	0.79	0.67	0.22	0.52	NA	0.14	0.35
Tube cross-sectional area/effective flow area	0.59	0.93	7.33	2.47	NA	6.72	45.95

a. Penetration abbreviations designate
DN - drain line nozzle
IT - instrument tubes
CR - control rod guide tube.

b. Representative Combustion Engineering plant considered has no lower head penetrations.

5.2.2 Structural Analysis Model

The structural analysis in this study used the temperature history from SCDAP/RELAP5, with temperature-dependent material properties, loads, and boundary conditions, to evaluate the elastic, plastic, and creep behavior of the lower head vessel during a severe accident. A key contribution of this study is the use of time-dependent vessel temperature histories from full thermal-hydraulic studies of accident scenarios. The thermal history of the vessel plays a crucial role in this analysis because (a) material properties deteriorate dramatically at high temperatures, (b) thermal stresses are typically 5 to 6 times higher than stresses induced from pressure loads, and (c) creep behavior at accident temperatures can cause failure at stresses below the yield stress. The two cases analyzed for structural response, one with primarily metallic debris (Case I-1) and the other with primarily ceramic debris (Case II-1), encompassed the low- and high-temperature extremes of the vessel thermal history under accident conditions for this study.

The remainder of this section discusses the structural model and the input assumptions. Section 5.2.2.1 briefly describes application of the various commercially available and

Table 5-3. Key parameters and dimensionless groups for base cases.[a]

Parameter	Case I	Case II
In-vessel tube melting		
θ_d/θ_t[b]	0.88–0.93	1.17–1.32
Melt penetration		
Pe_d[c]	173,400	18,500
Ex-vessel tube failure		
θ_d/θ_t[d]	0.7–2.2	1.1–3.1
$\rho_t c_{pt}/\rho_d c_{pd}$	1.6	0.8
$(T_{t/f}^4 - T_a^4)/T_a^4$	400	94
$\dot{q}_d/\epsilon_t \sigma T_a^4$	11	36

a. Drain line geometry and material properties were used to estimate dimensionless parameters.

b. Ratio of effective debris temperature change to effective tube temperature change (see Section 4.1.2.2).

c. Debris Peclet number ($Pe = d_e v_d/\alpha_{td}$).

d. Ratio of effective debris temperature change to effective tube temperature change (see Section 4.1.2.5).

NRC-developed codes used in this analysis. Section 5.2.2.2 details the input assumptions used in this analysis. Of particular interest are the assumptions used to tabulate the material properties and to determine the creep failure criterion. Structural results are discussed in Section 5.4, following the thermal results.

5.2.2.1 Model Description. Figure 5-5 shows the various programs used to complete the structural analysis. In this diagram rectangles indicate NRC-developed codes, ellipses indicate commercially available codes, and octagons are files. As shown in Figure 5-5, SCDAP/RELAP5 first generates a file "thermal mesh" containing PATRAN-generated nodal locations and time-dependent temperatures. Independently, a finer structural mesh is created using PATRAN; and the file, "structural mesh," containing the structural node locations is written. Temperatures from the SCDAP/RELAP5 thermal mesh are interpolated to the ABAQUS[5-13] structural mesh through a FORTRAN program, CPL2ABQ, developed at the INEL. The interpolated time-dependent temperatures are input into ABAQUS, along with the PATRAN generated mesh and all other parameters needed for a well-defined problem. ABAQUS performs the actual structural analysis, evaluating elastic-plastic and creep behavior throughout the accident history, up to 24 hours after debris relocation onto the lower head. Results are used to calculate creep damage and as input to PATRAN for graphic display.

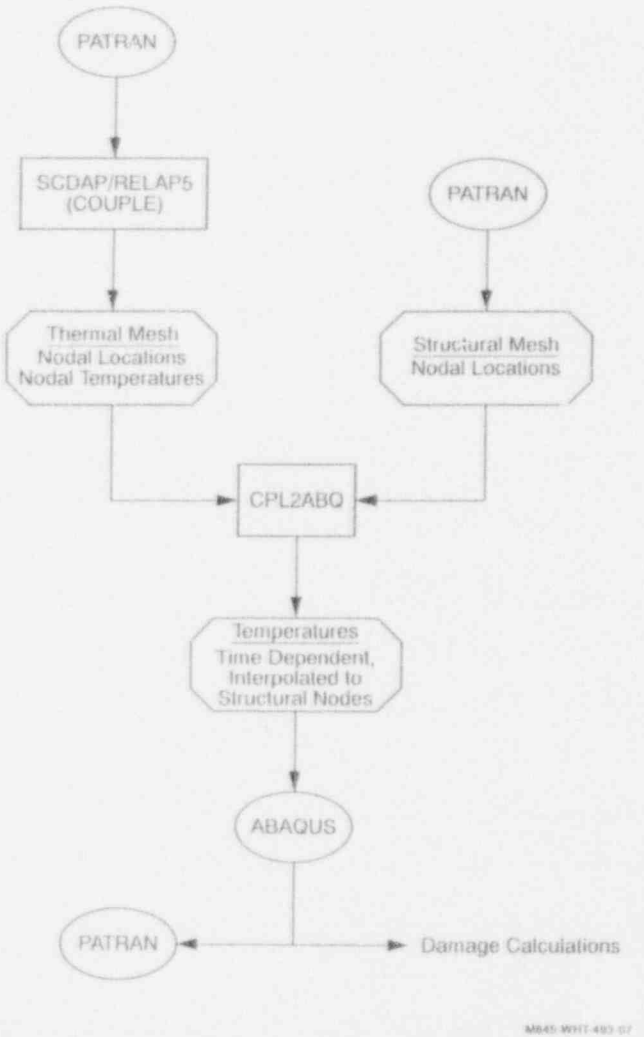

Figure 5-5. Flow chart of codes used in structural analysis.

Structural Mesh—PATRAN

PATRAN, a commercially available code for pre- and post-processing finite-element analyses, was used for mesh generation. The vessel mesh, symmetric about the y axis, is shown in Figure 5-6. Axisymmetric, four-noded isoparametric elements with reduced integration were used through most of the mesh. The mesh was biased to be finest where the largest through-thickness temperature gradients were expected; the aspect ratio in this region is 2:1. Aspect ratios overall were kept below 4:1, and abrupt changes in element size were avoided. Three-noded axisymmetric triangular elements were used in the transition region where the vessel thickens. One triangular element was used to connect the skirt and the vessel. As will be seen later, the change in element type did not cause inconsistencies in the results.

Mesh density was evaluated in a parametric study using a section of a sphere with the same thickness as the vessel bottom, axisymmetric elements with an aspect ratio of 2:1, and symmetric boundary conditions at the end sections (Figure 5-7). The most severe temperature gradient

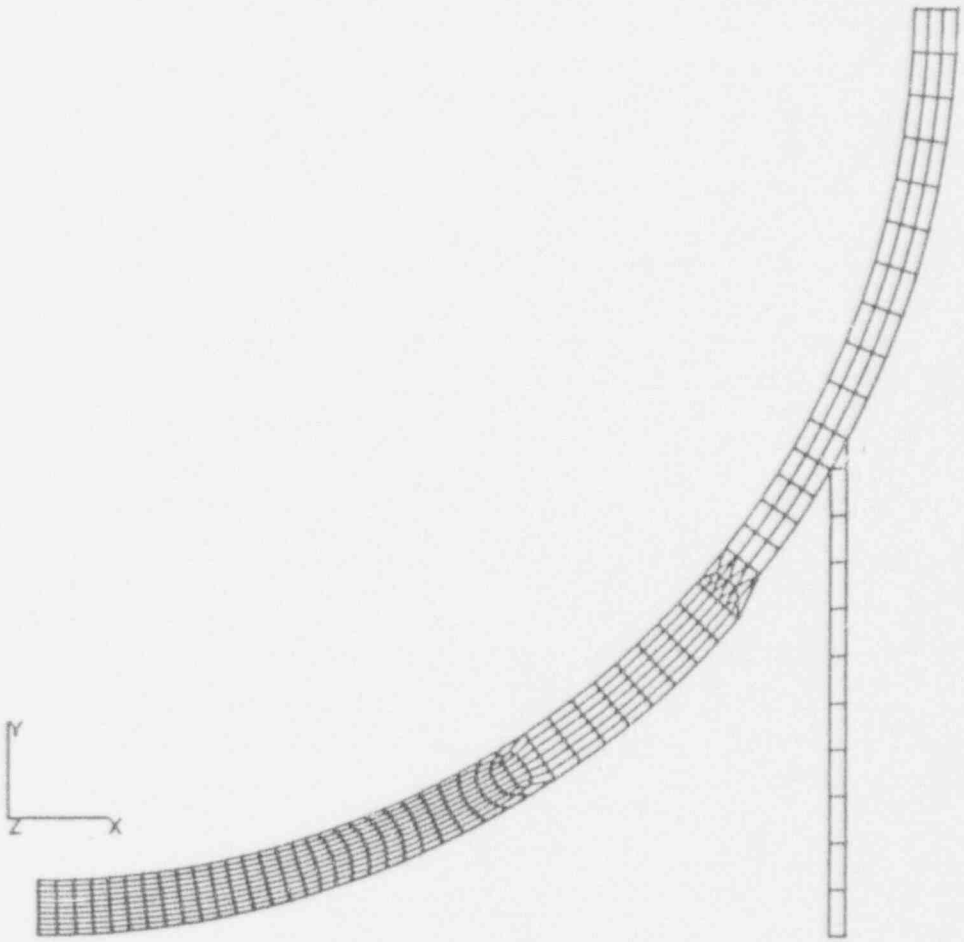

Figure 5-6. Structural vessel mesh (axisymmetric model).

observed in sample SCDAP/RELAP5 runs with metallic debris (1050 K inside, 850 K outside) and ceramic debris (1150 K inside, 950 K outside) were held constant with a 7-MPa constant pressure. Vessel response was evaluated after 2 hours (a time that is 50% longer than that predicted by thermal analyses for peak temperatures to be sustained in severe cases). The number of elements through the thickness was doubled until the change in hoop strain was less than 5%. This occurred between 10 and 20 elements through the thickness. On this basis, it was determined that with an aspect ratio of 2:1, 10 elements through the vessel thickness were adequate for analysis of problems similar to the metallic and ceramic debris cases.

Temperature Interpolator—CPL2ABQ

A FORTRAN program, CPL2ABQ, interpolated temperatures from the COUPLE mesh used in SCDAP/RELAP5 to the structural mesh (Figure 5-5). Generally, the structural mesh was specified to be finer than the COUPLE mesh. The interpolator CPL2ABQ took a structural node location and identified which COUPLE element it lay in when the two meshes were superposed. Using the COUPLE nodal locations and temperatures associated with this element, CPL2ABQ performed a bilinear interpolation of the temperature to the structural node location. In this study, only quadrilateral COUPLE elements were used; however, the interpolator also

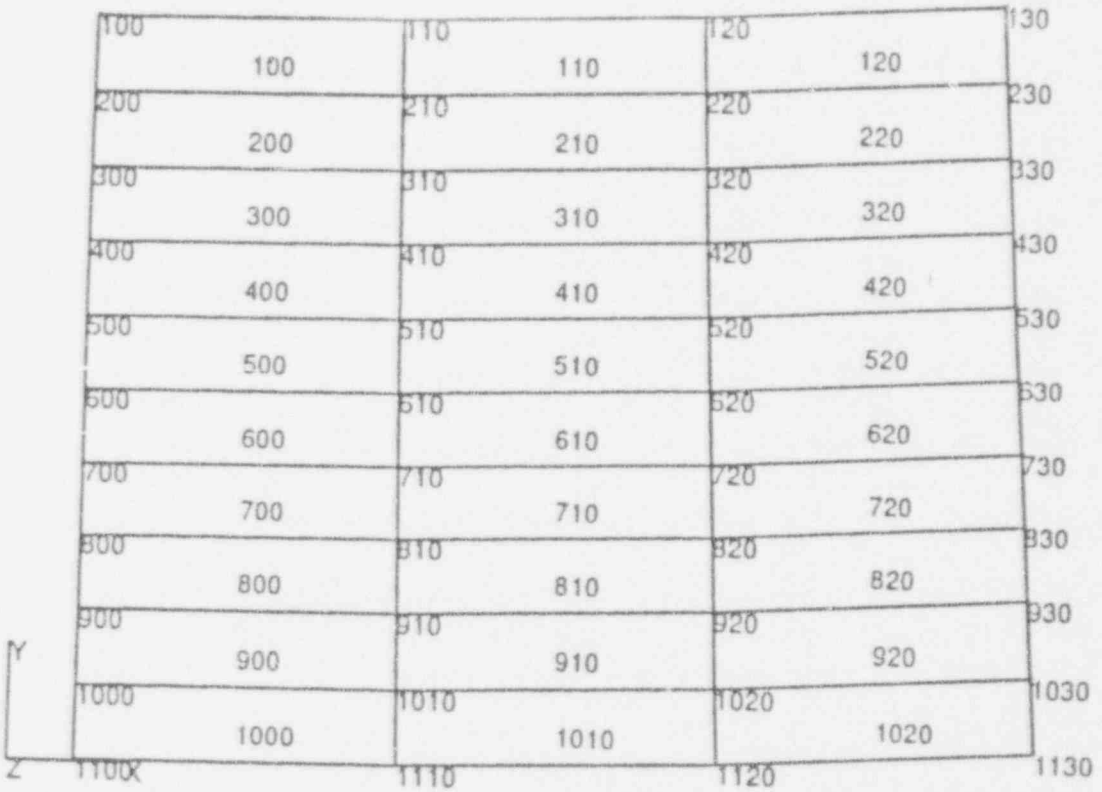

Figure 5-7. Mesh to check element density (axisymmetric model).

accepts triangular elements. Because only structural nodal locations were used, structural elements may be of any shape.

It was necessary for the structural vessel mesh to fit inside the boundaries of the COUPLE vessel mesh to transfer temperatures accurately. Currently, the interpolator cannot accommodate structural nodes that lie outside the COUPLE mesh; an error message results. Near the inside vessel wall, the interpolator cannot distinguish between COUPLE vessel and debris elements. A structural vessel node located slightly inside the debris was interpolated to debris temperatures without an error message. Structural node locations along the inner and outer vessel walls were adjusted to fit the structural mesh inside COUPLE for use with the interpolator. However, the original, geometrically correct mesh was used in the stress analysis.

Structural Analysis—ABAQUS

Elastic-plastic and creep structural analysis was performed by inputting the above parameters to ABAQUS, a commercially available, finite-element code. First, the vessel was assumed to be stress free at the 7-MPa saturation temperature (559 K), and elastic-plastic response to pressure loads was evaluated. In fact, there is no plasticity under these conditions. Subsequent time steps for analysis were selected by dividing the temperature history of the hottest region in the vessel into piecewise linear segments. Elastic-plastic and creep analyses were performed at each time step following debris relocation. Temperatures were linearly ramped between time steps. Solution convergence was verified by decreasing the force tolerance and the maximum allowable difference in creep strain increment over each increment by a factor of 10.

Results Post-Processing—Damage Calculations

ABAQUS does not contain any failure criteria. Intuitively, one might think that failure could be specified through the material properties; however, this is not the case. For example, creep properties have no provision for inputting creep rupture data, such as the Larson-Miller parameter (see Appendix B, Section B-5.1). Therefore, ABAQUS continues to calculate vessel behavior, using the time hardening creep relations, even after the vessel should have failed.

To predict vessel failure by creep rupture, damage calculations of the critical region were performed using a spread sheet. Damage calculations incorporate a creep damage model based on the life-fraction rule. First, effective stresses and temperatures (from ABAQUS) averaged over each time step were calculated and stored for each element of interest. Time to rupture for these stress and temperature combinations were calculated using the Larson-Miller parameter. The actual time spent at a given effective stress and temperature divided by the time to rupture at that stress and temperature is the damage. When the sum of all damage for different stress-temperature conditions equals 100%, the element was assumed to fail.

5.2.2.2 Input Assumptions. Input assumptions for the structural analysis are listed below.

Structural Mesh

In the structural analysis, the vessel was modeled using an axisymmetric geometry with no penetrations. This choice was made to be consistent with the thermal analysis, which did not include penetrations because of meshing considerations. This analysis, then, assumes that the penetration holes do not create a significant stress concentration in the vessel.

Several assumptions are inherent in using an axisymmetric geometry. Even when a hole is modeled in the bottom of the vessel, the axisymmetric modeling inherently assumes that the stress fields around the penetration holes do not interact and that the intersection angle for penetrations away from the vessel bottom does not have a significant effect. Hot spots must be modeled at the bottom of the vessel, using an axisymmetric geometry, which provides an adequate model of hot spots anywhere in the vessel as long as the structural constraints (vessel skirt and the intersection of the hemisphere and cylinder) are far field and the hot spot is more or less round.

The two-dimensional axisymmetric geometry cannot model cracks in the vessel, with the exception of circumferentially oriented cracks that close on themselves (e.g., a crack running completely around a penetration). Cracks initiating at a hole and emanating radially from the centerline of a penetration cannot be modeled with an axisymmetric geometry. A three-dimensional analysis may be required for cases where the stress fields of penetration holes interact, such as where structural constraints are not far field; where hot spots are not round; or where stress concentrations such as notches and cracks (with the one noted exception) play an important role.

Finally, the finite element mesh did not include the 3-mm Inconel vessel cladding because of meshing considerations.

Material Properties

Properties of SA533B1 vessel steel used in this analysis are documented in Appendix F. These data were obtained from References 5-24 and 5-25, and new high-temperature data were

obtained as part of this research program (see Appendix B). Temperature-dependent properties include thermal coefficient of expansion, elastic modulus, yield strength, plastic stress-strain behavior, time and stress dependent creep, and creep rupture. Poisson's ratio was approximated to be constant at 0.3. Properties (with the exception of creep rupture) were input to ABAQUS in tabular form with linear interpolation between specified temperatures. At temperatures above and below the tabulated temperatures, ABAQUS assumes that properties remain constant at the highest or lowest given temperature. Creep rupture properties were used in damage calculations, separate from ABAQUS.

For elastic behavior, the elastic modulus and yield stress were linearly interpolated with temperature. Poisson's ratio was assumed to remain constant because high-temperature data were not available and the temperature dependence was not expected to have a significant impact on results. For plastic behavior, the stress-versus-plastic-strain linearly interpolated the stress between given strains and temperatures.

There is a slight discontinuity between the new INEL SA533B data at 900 K and published SA533B data[5-24,5-25] at 922 K for elastic modulus, yield strength, and plastic behavior observed in the ultimate strength. The INEL data at 900 K are not as consistent as the EPRI and ASTM data at 922 K, so they are omitted in the analysis.

The time hardening law was used to fit the creep data, primarily because of its simplicity; additionally, not enough high-temperature creep data existed to justify a more complicated model. Using a least-squares best-fit on the data, the creep coefficients listed in Appendix B were obtained. ABAQUS interpolated the creep constants linearly between given temperatures. Unfortunately, when this interpolation scheme was used with these data, the creep strain did not increase monotonically between some temperatures. Such was the case around 672 K, 922 K, and 1150 K. This non-monotonic behavior was not physically realistic and causes difficulty in convergence. For these reasons, creep data at 922 K and 1150 K were omitted in this analysis. Instead, the linear interpolation between the nearest data points was used. Note that the INEL creep data at 900 K were continuous with the rest of the data and were included. The creep data at 672 K are the lowest temperature data and have a very low strain rate for the stresses of interest. Nonetheless, rather than assume no creep at 672 K, the creep behavior at 755 K was also used at 672 K. The creep damage model used one linear fit for Larson-Miller parameter versus effective stress, combining the high- and low-temperature SA533B data shown in Appendix B.

Because this model used an effective stress, no distinction was made between compression and tension. For the cases studied, the inside portion of the vessel undergoes a stress reversal, initial compressive thermal stresses going into tension as a result of reduced temperature gradients combined with the pressure load. When a specimen undergoes stress reversal, it is expected to exhibit primary and secondary creep, similar to virgin material.[5-26] Ordinarily, applying a simple time hardening rule to a stress reversal produces erroneous results because it continues secondary behavior from the point of the stress reversal, omitting primary creep. In this case, high-temperature creep testing has shown that SA533B vessel steel is dominated by secondary creep, with negligible primary behavior, so the simple time hardening model was applicable.

All property data at the transition temperature (1000 K) were also omitted. Because behavior at this temperature was erratic and a limited number of tests were run at this temperature, the uncertainty in the data was considered too high to include them in this analysis. This may result in a non-conservative analysis if at a given time a significant portion of the vessel

experiences the transition temperature and the properties at the transition temperature are significantly degraded.

Loads and Boundary Conditions

In the structural analysis, a constant pressure load of 7 MPa was applied to the inside vessel wall for both cases. Although the metallic case was assumed to have an internal pressure of only 0.62 MPa for the thermal analysis, a higher pressure was assumed in the structural analysis. However, if the vessel holds a 7-MPa pressure without failing, the same will be true for low pressures. Stresses from the weight of the vessel, water, and debris were less than 2% of the pressure-induced stress and were ignored.

Roller (symmetric) boundary conditions were used at the top of the hemisphere where the vessel would join a cylindrical section and at the vessel bottom plane of symmetry. Chambers[5-2] reported that the actual behavior of a hemisphere attached to a cylindrical section was closely bounded by a model using fixed conditions at the joining point and one using symmetric conditions. The vessel modeled in Chamber's study had a thin bottom section and a thicker section at the hemisphere/cylinder joint; whereas, the vessel modeled in this study was reversed (thick at the bottom and thin at the top). Because the hemisphere/cylinder joint modeled in this study was more flexible than Chamber's, the symmetric boundary was chosen. Boundary conditions for the base of the skirt constrained vertical motion. Horizontal motion should probably be constrained as well. However, because the area of interest in both cases was at the bottom of the vessel, the difference was not detectable.

Applied Temperatures

The initial stress-free temperature was assumed to be the saturation temperature of steam at 7 MPa, 559 K. Temperatures for specified time steps were applied at the structural nodes by using the linearly interpolated temperatures from the thermal mesh nodes, as discussed earlier. Time steps were chosen based on the temperature history of a cross section in the hottest section and a sampling of locations on the inside vessel surface. This may have been non-conservative in that local temperature maximums at other locations, which do not coincide with the chosen time steps, would be smoothed out. Temperatures were ramped linearly between time steps.

Creep Failure Criterion

A creep damage model based on the life-fraction rule was used to predict vessel failure by creep rupture. Effective stress and temperature for each element of interest were averaged over the time step. Time to rupture was calculated from the combined high- and low-temperature Larson-Miller parameter data. The actual time spent at a given effective stress and temperature divided by the time to rupture at that stress and temperature was the element damage.

Because ABAQUS calculates element stresses for all time steps specified, regardless of the amount of damage, some of the elements may have damage greater than 100%. Modifying ABAQUS to account for creep damage was beyond the scope of this project; therefore, a simple failure criterion was used. Creep rupture was predicted to occur when the average damage for the vessel cross section is 100%.

5.3 Thermal Analysis Results

Detailed results for each of the base cases described in Section 5.2.1 are presented in Section 5.3.1. In addition, sensitivity analyses were performed to evaluate the effects of debris porosity, containment heat removal, debris-to-surface gap resistance, and debris penetration distance. Table 5-4 lists the matrix of cases analyzed. Base case results are compared with results from these sensitivity studies in Section 5.3.2. Calculational results were then applied to Section 4 failure maps to predict the response of other LWR designs. Results from this application are discussed in Section 5.3.3. Conclusions from these calculations are summarized in Section 5.3.4.

5.3.1 Base Case Results

As discussed in Section 5.2, three types of debris beds were considered for base case analyses in these calculations. The debris beds considered include a uniform debris bed that is primarily metallic (Case I), a uniform debris bed that is primarily ceramic (Case II), and a layered debris bed with metallic debris near the vessel and ceramic debris on top (Case III). Results for each base case are discussed in this section.

In discussing thermal analysis results, it is of interest to compare the integrity of the drain line with the vessel. Because structures fail before they melt, it would be desirable to compare results by considering the time until the structure reaches temperatures where its ultimate strength is less than the average stress from system pressure. This is not necessarily the failure time because stresses tend to redistribute to the cooler portions of the vessel. However, it is a helpful parameter for comparison purposes. Unfortunately, the data for SA105/SA106 drain line steel and for SA533 vessel steel at high temperatures are limited. In fact, before the NRC Lower Head Failure Program, the data base for SA105/SA105 steel was limited to temperatures below 800 K, and the data base for SA533B steel was limited to temperatures below 1000 K. Figure 5-8 compares ultimate strength data for these materials.

Table 5-4. Cases for analysis.

Case	Composition	Porosity	Vessel pressure (MPa)	Debris-to-vessel/drain line gap heat-transfer coefficient (W/m^2K)	Building humidity
I-1	Metallic	0.0	0.62	500	Dry
II-1	Ceramic	0.0	7.0	500	Dry
II-2	Ceramic	0.0	1.0	500	Dry
II-3	Ceramic	0.7	7.0	500	Dry
II-4	Ceramic	0.0	7.0	500	Wet
II-5	Ceramic	0.0	7.0	10000	Dry
III-1	Layered	0.0	0.62	500	Dry

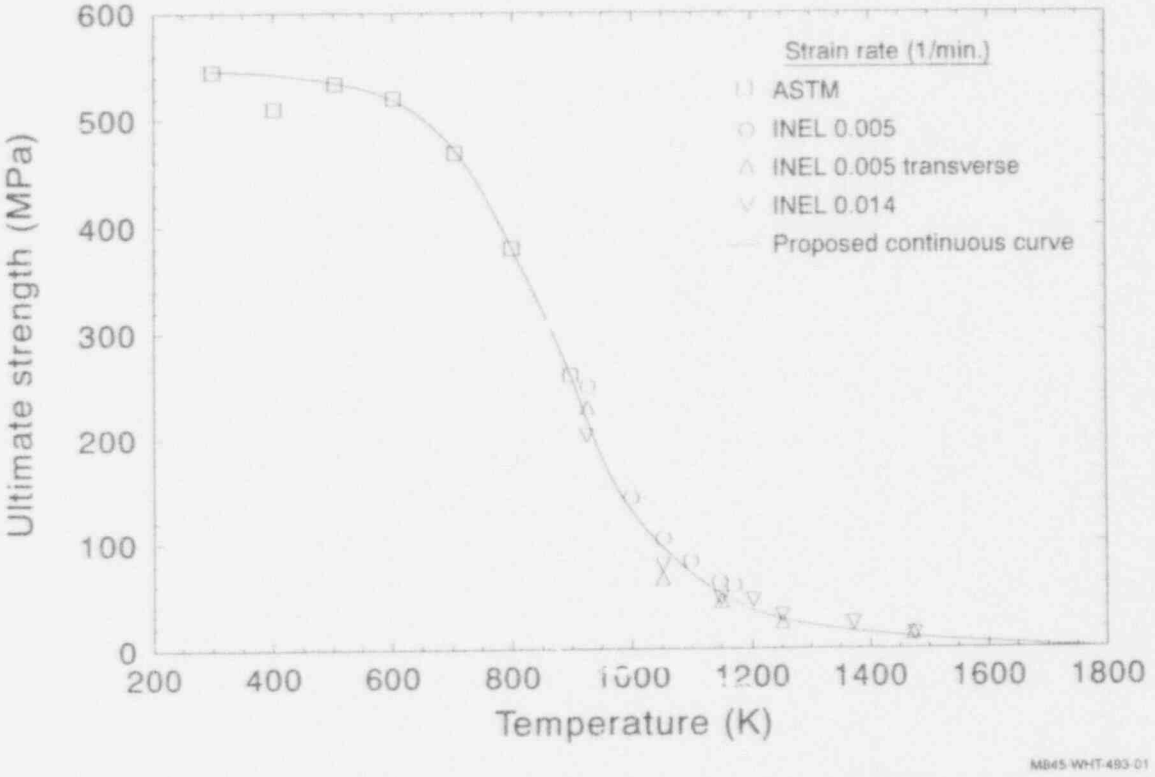

(a) SA533B Ultimate Strength

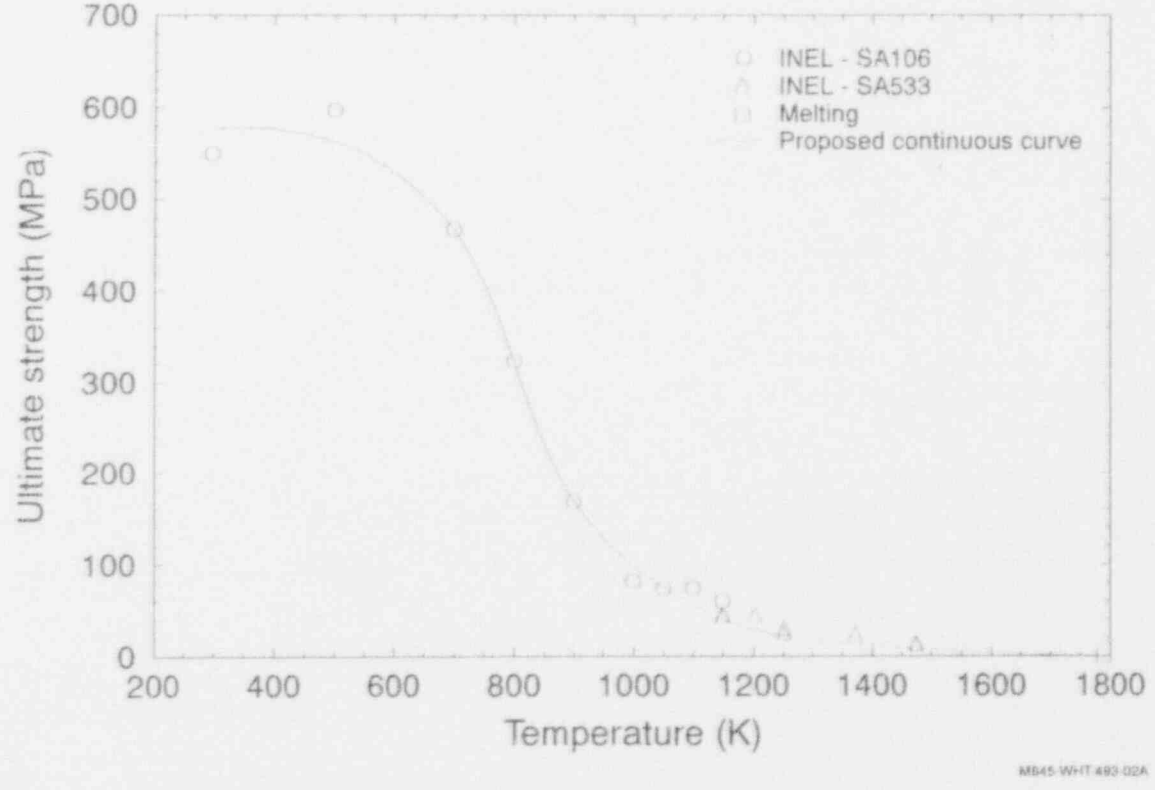

(b) SA105/SA106 Ultimate Strength

Figure 5-8. Comparison of ultimate strength for vessel material (SA533B) and drain line material (SA105/SA106).

The average stress in a BWR vessel with a 7-MPa internal pressure is 46 MPa, and the average stress in a BWR vessel with a 0.62-MPa internal pressure is 4 MPa. As illustrated in Figure 5-8(a), results from INEL SA533B tests indicates that at 1150 K, its ultimate strength is less than 46 MPa; and at 1450 K, its ultimate strength is less than 4 MPa.

For the drain line geometry, the tube material's ultimate strength must be greater than 25 MPa in a tube with a 7-MPa internal pressure and greater than 3 MPa in a tube with a 0.62 MPa internal pressure. As illustrated in Figure 5-8(b), INEL SA106 tests were not performed for temperatures above 1150 K. This temperature was well above the 1000 K value where previous data indicated that the ultimate strength for this material becomes negligible. However, test results indicate that the ultimate strength of SA105/SA106 material is 60 MPa at 1150 K. Although there are no SA105/SA106 data for higher temperatures, the SA105/SA106 material would not be any stronger than the SA533 material at higher temperatures. Furthermore, the strength of the SA105/SA106 material is zero at its melting temperature of 1789 K. Using this information, the drain line material data were extrapolated to obtain the continuous curve shown in Figure 5-8(b). Using this continuous curve, it is predicted that the drain line material's ultimate strength will be less than the stress in a tube with a 7-MPa internal pressure at approximately 1200 K, and that the ultimate strength will be less than the stress in a tube subjected to a 0.62-MPa internal pressure at approximately 1700 K. However, there is considerable uncertainty associated with this method of extrapolation because of the lack of SA105/SA106 data at higher temperatures.

5.3.1.1 Base Metallic Debris Case (Case I-1). In Case I-1, approximately 24,000 kg of metallic debris was assumed to relocate as a liquid within 5,000 seconds to the lower head. Temperatures in the vessel and drain line are shown in Figures 5-9 and 5-10, respectively. As shown in Figure 5-9, temperatures in the debris bed remain below ~1250 K and are decreasing after 2 hours. Thus, the debris rapidly cools below its solidus temperature of ~2100 K after relocation.

Heat is primarily transferred from the debris bed to the coolant (volume 70 in Figure 5-2), although some heat is initially transferred to the cooler vessel steel below the debris bed. For example at 2 hours, 87% of the heat is transferred to the vessel coolant; whereas after 4 hours, nearly 100% of the heat is transferred to the vessel coolant.

Vessel temperatures remain below 1000 K, and drain line temperatures remain below 1200 K throughout the transient. Peak vessel temperatures are predicted to occur near the bottom of the vessel at the debris/vessel interface, and peak drain line temperatures are predicted to occur at a location ($\leq$10 cm) below the lower head. Because drain line temperetures are decreasing after 125 seconds and vessel temperatures are decreasing after 5,000 seconds, neither drain line nor vessel melting is predicted to occur during the transient. Using the ultimate strength data discussed in Section 5.3.1, neither drain line nor vessel failure temperatures are predicted to occur for this low-pressure scenario.

5.3.1.2 Base Ceramic Debris Case (Case II-1). In Case II-1, approximately 120,000 kg of ceramic debris was assumed to relocate as a liquid within 5,000 seconds to the lower head. Temperatures within the vessel and drain line are shown in Figures 5-11 and 5-12, respectively. As shown in Figure 5-11, temperatures in the debris bed have cooled to approximately 2000 K during this relatively slow relocation. However, peak debris temperatures exceed 3100 K after 7 hours and continue to rise because of decay heat.

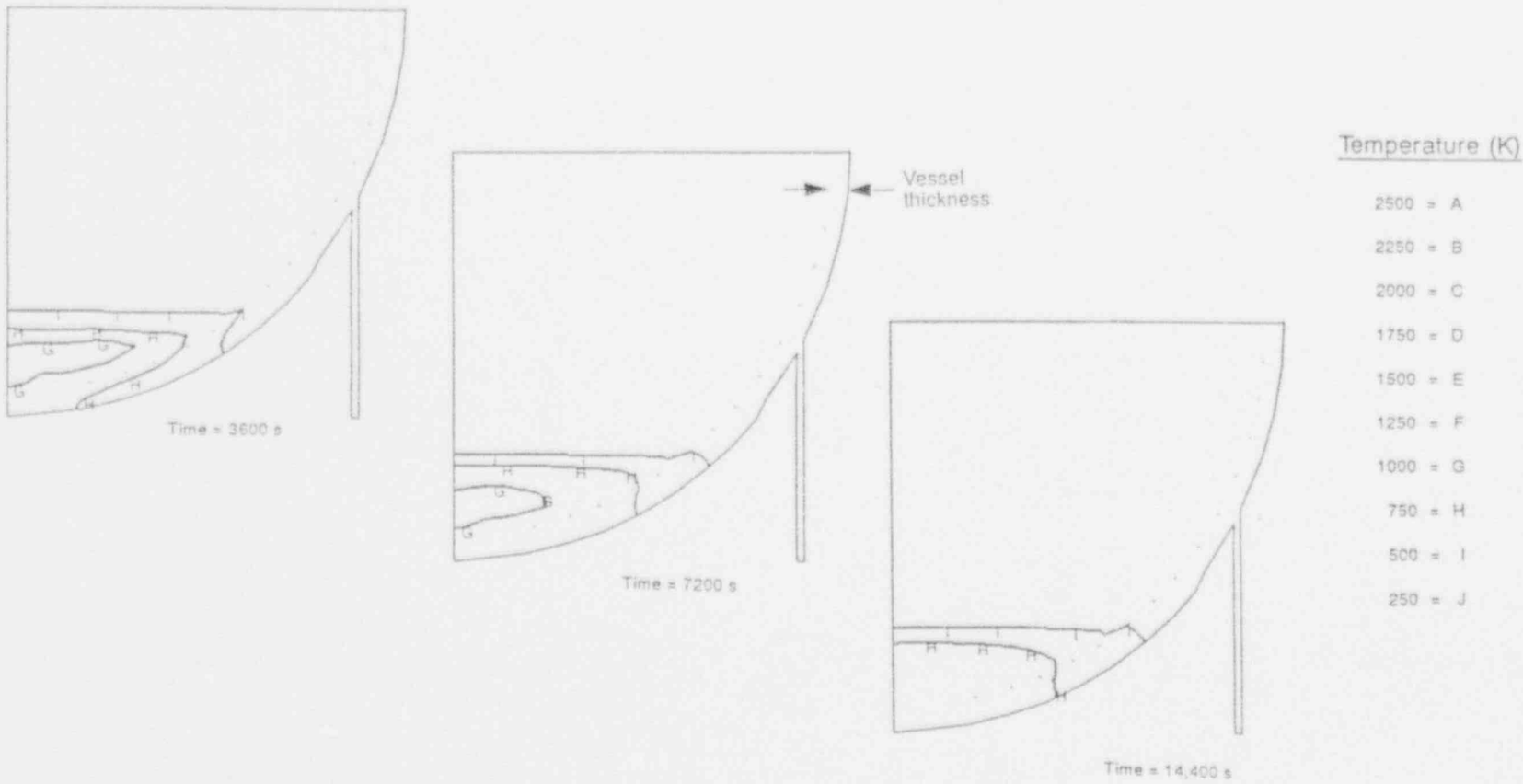

Figure 5-9. Vessel and debris thermal response for Case I-1.

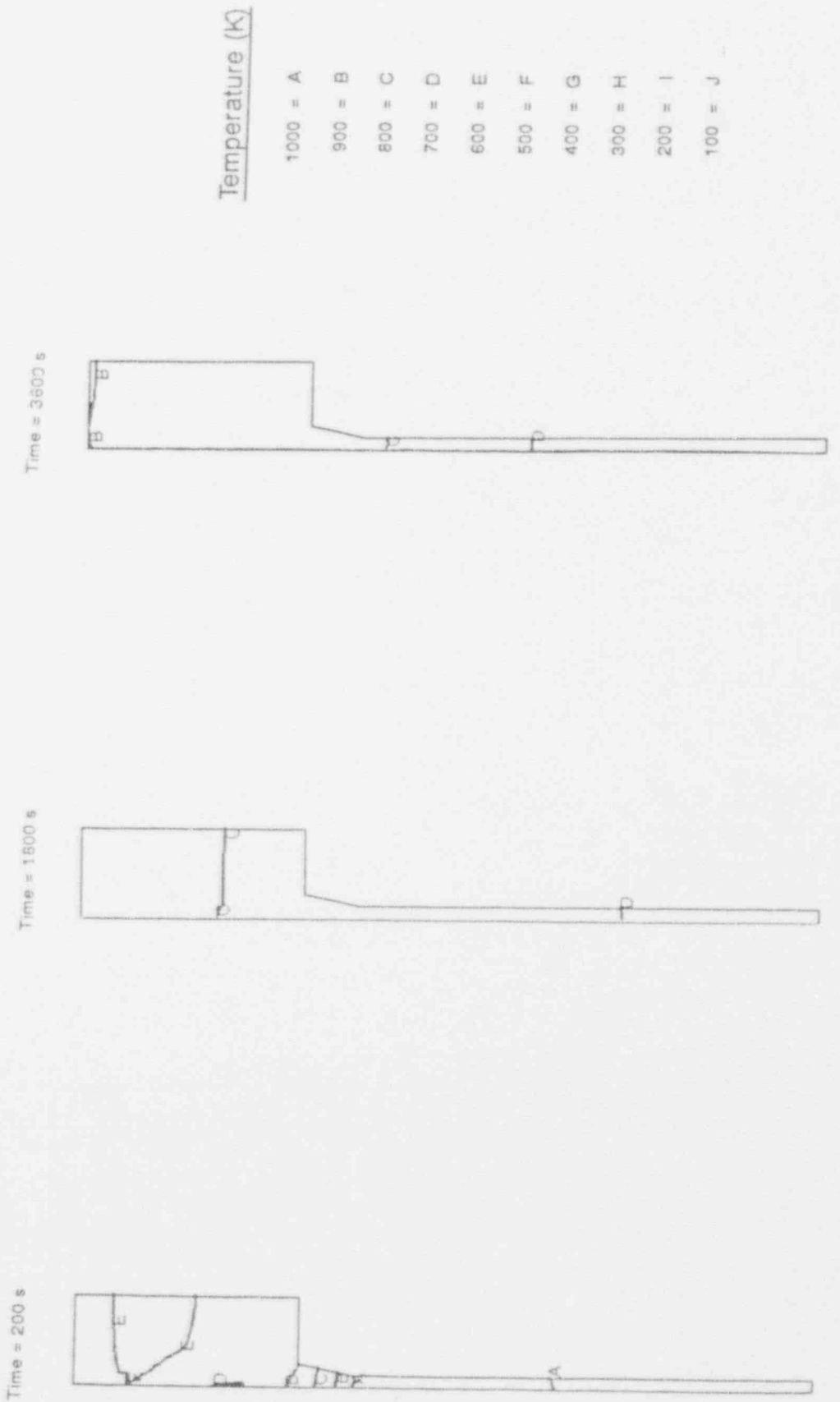

Figure 5-10. Drain line thermal response for Case I-1.

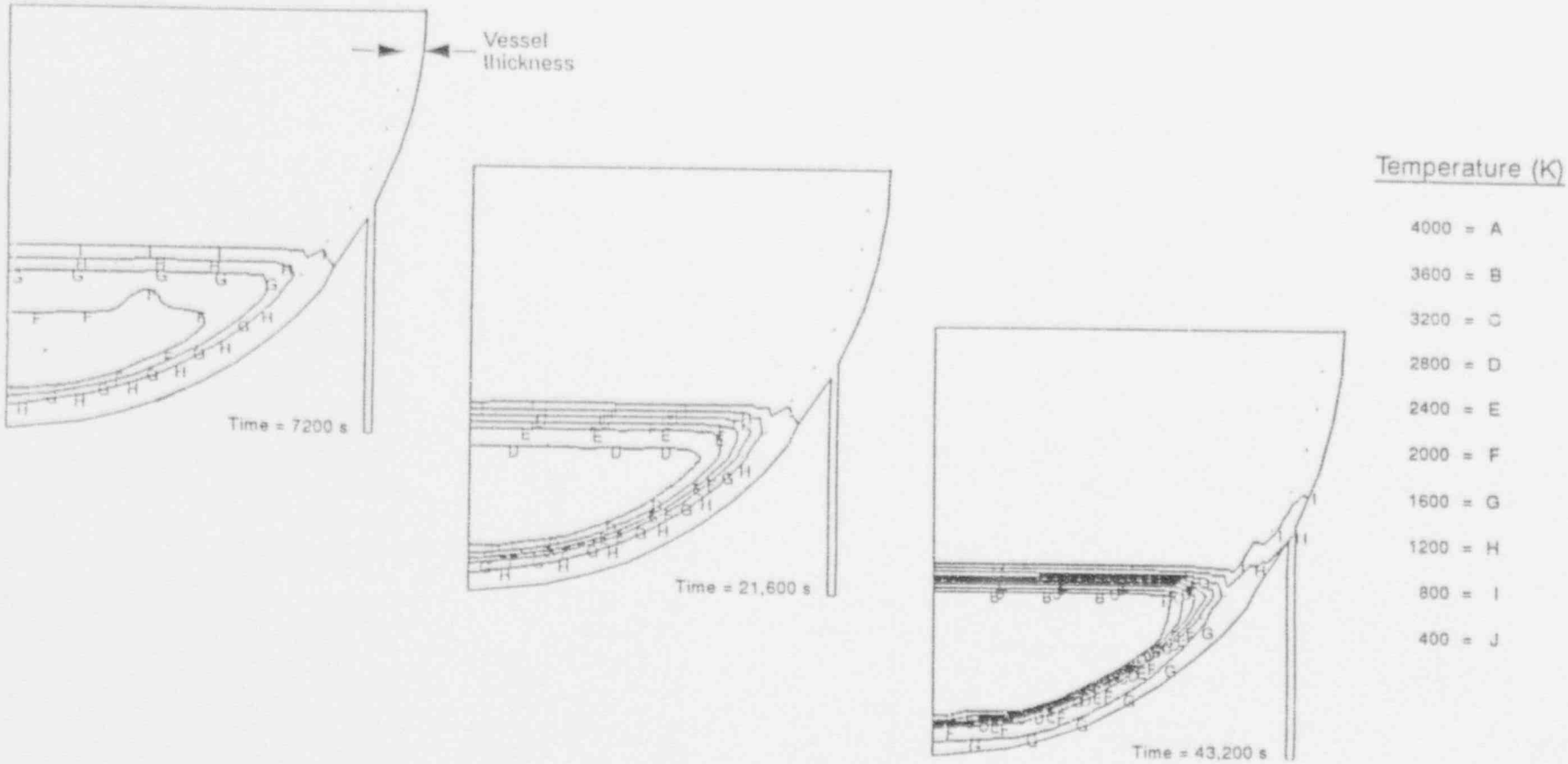

Figure 5-11. Vessel and debris thermal response for Case II-1.

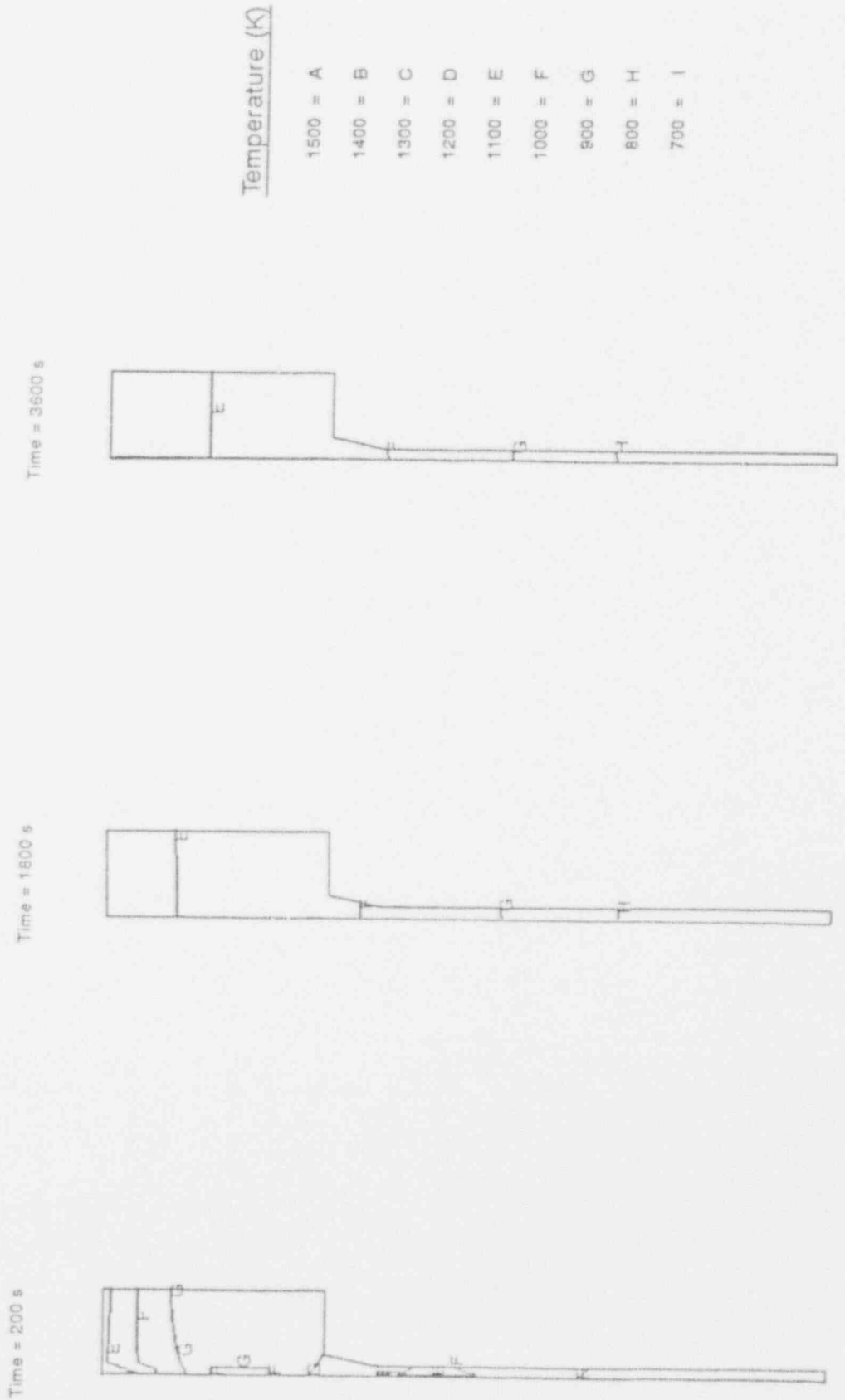

Figure 5-12. Drain line thermal response for Case II-1.

The fraction of debris heat transported to the vessel coolant (volume 70 in Figure 5-2) and the reactor building cavity (volume 250 in Figure 5-2) varied during the time the transient was evaluated. During earlier stages (from 2 to 6 hours), equal amounts of heat are predicted to be transferred from the debris bed to the coolant and from the vessel steel to the reactor building cavity. For example at 2 hours, 20% of the debris decay heat is transferred to the vessel coolant and 16% of the debris decay heat is transferred to the reactor building cavity. After 6 hours, the amount of heat transported to the reactor building becomes negligible. After this time, any moisture in the cavity has become vapor and a marked increase in the reactor building air/vapor temperature occurs, decreasing the temperature difference between the building and the vessel and reducing the heat transferred from the vessel.

Within 2 hours, the inner surface of the vessel reaches temperatures above 1150 K, the temperature where the ultimate strength of SA533B1 steel is less than the stress from the applied system pressure of 7 MPa; and within 11 hours, vessel melting temperatures occur. Peak vessel temperatures are predicted to occur near the bottom of the vessel at the debris/vessel interface. Peak drain line temperatures occur at a location (~10 cm) below the lower head. Drain line temperatures are predicted to peak at 1175 K and then decrease after 200 seconds. Although drain line temperatures are below 1200 K, the temperature where SA105/SA106 steel's ultimate strength is predicted to be less than the stress in a tube subjected to a 7-MPa pressure load, there is considerable uncertainty associated with SA105/SA106 ultimate strength data (see Section 5.3.1). Hence, additional high-temperature SA105/SA106 data are needed to determine whether drain line failure temperatures occur in this scenario.

5.3.1.3 Base Layered Debris Case (Case III-1). In Case III-1, approximately 24,000 kg of metallic debris was assumed to relocate as a liquid within the first 5,000 seconds of the transient and approximately 120,000 kg of ceramic debris was assumed to relocate as liquid on top of the solidified metallic debris during the second 5,000 seconds of the transient. Temperatures within the vessel and debris bed are shown in Figure 5-13. Debris bed temperatures are below 1200 K in the vessel while metallic debris is relocating. However, debris temperatures increase after 2 hours (when ceramic debris is relocating) and continue to rise because of debris decay heat. Because metallic debris is the first material that relocates to the lower head, it is assumed that metallic debris fills the drain line and that drain line thermal response is similar to that predicted for Case I-1 in Figure 5-10.

The fraction of heat transferred from the debris bed to the reactor vessel coolant and the reactor building cavity varied over the time that this transient was evaluated. During initial stages of the transient, a larger fraction of heat is transferred from the debris bed to the reactor vessel coolant; for example at 2 hours, 30% of the debris decay heat is transferred to the vessel coolant and 12% of the debris decay heat is transferred from the vessel steel to the reactor building cavity. During later stages, equal amounts of heat are predicted to be transferred from the debris bed coolant and from the vessel steel to the reactor building cavity. For example at 4 hours, when vessel temperatures have significantly increased, 19% of the debris heat is predicted to be transferred to the reactor building cavity and 16% of the debris decay heat is predicted to be transferred to the reactor vessel coolant. After 6 hours, the amount of heat transported to the reactor building becomes negligible. After this time, any moisture in the cavity has become vapor and a marked increase in the reactor building air/vapor temperature occurs, decreasing the temperature difference between the building and the vessel and reducing the heat transferred from the vessel.

Vessel temperatures exceed 1450 K, the temperature where the ultimate strength of SA533B1 steel is less than the stress from the applied system pressure of 0.62 MPa, within

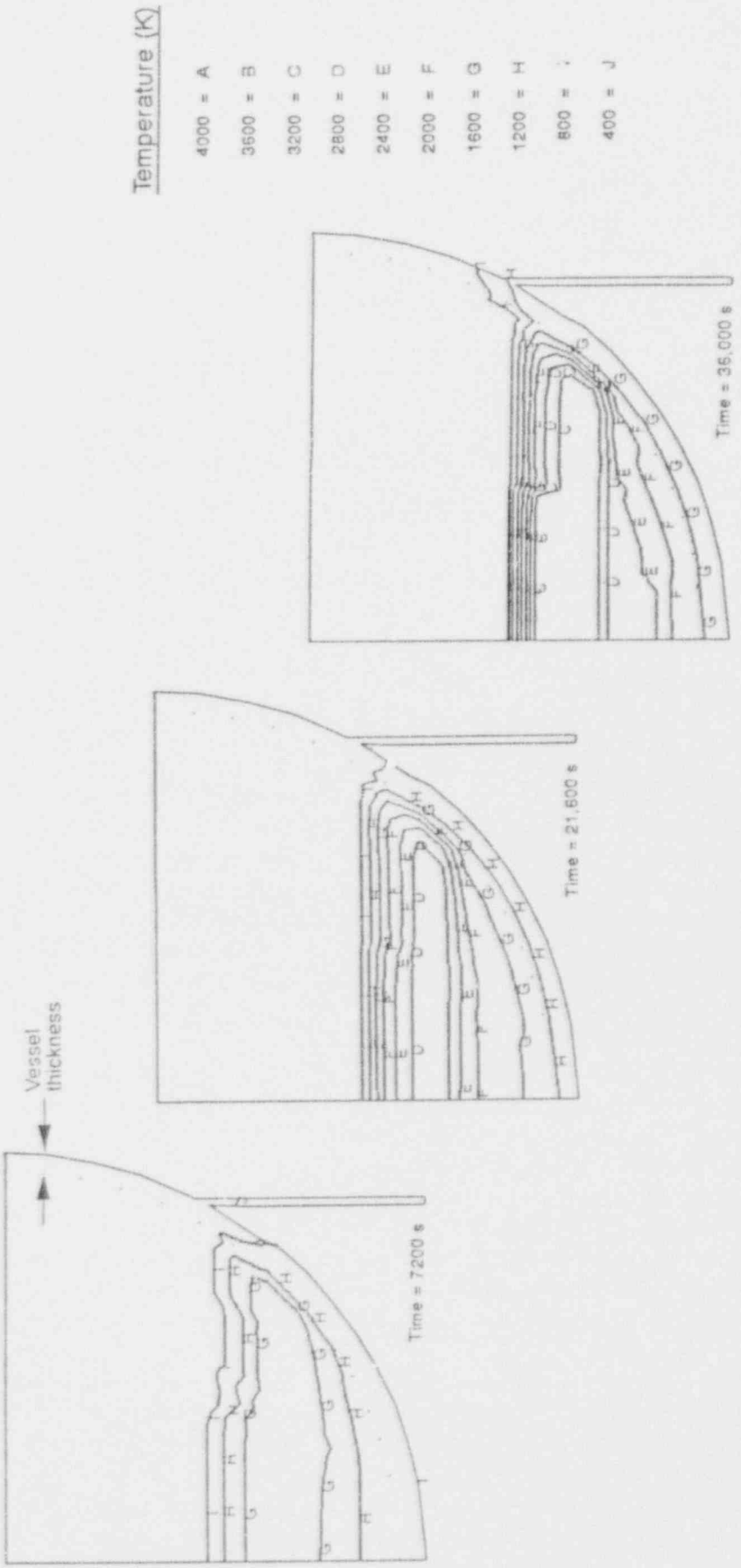

Figure 5-13. Vessel and debris thermal response for Case III-1.

7 hours. Peak vessel temperatures during the 10 hours that the transient was evaluated remained below 1600 K, which is well below the SA533B melting temperature of 1789 K. Peak vessel temperature location varies during the transient. While metallic melt is relocating to the lower head (the first 5,000 seconds), peak vessel temperatures are predicted to occur near the bottom of the vessel at the debris/vessel interface. As shown in Figure 5-13, peak vessel temperatures are predicted to shift from the bottom of the vessel after ceramic debris begins relocating onto this metallic debris bed (after 6,000 seconds). In fact, after around 3 hours, peak vessel temperatures are predicted to occur near node 70 (refer to Figure 5-3 for vessel nodalization). As discussed in Section 5.3.1.1, a metallic-filled drain line does not reach temperatures where the SA105/SA106 steel ultimate strength is less than the stress from the 0.62-MPa applied system pressure. Hence, drain line failure temperatures are not predicted to occur during this scenario.

5.3.2 Sensitivity Analyses Results

As discussed above, sensitivity runs were performed to investigate the relative importance of debris porosity, containment heat removal, reactor coolant system pressure, and debris-to-vessel thermal contact. Sensitivity studies primarily focused on base Case II parameters and were generally analyzed for only the first 2 hours of the transient. Results for these studies, which are summarized in Table 5-5, are discussed below:

5.3.2.1 Reactor System Pressure. Reactor system pressure impacts vessel and drain line thermal response primarily through the initial conditions and thermal properties of the coolant within the vessel and drain line. Calculations were performed in which pressure assumptions varied from a relatively high value (7.0 MPa for Case II-1) to a much lower value (1.0 MPa for Case II-2). As shown in Table 5-5, initial system pressure has a relatively minor impact on vessel and drain line thermal response. However, the stress within the drain line and the vessel is considerably reduced at the lower 1-MPa pressure. Hence, vessel and drain line temperatures remain well below values where their ultimate strength is less than the stress due to a 1-MPa system pressure during the 2 hours that this transient was simulated.

5.3.2.2 Debris Porosity. If the debris quenches during relocation and forms a rubble bed in the lower head, the rate at which heat is transferred from the debris to the vessel and drain line material is reduced because of the reduced debris power density and thermal conductivity. Calculations were performed to bound the range of debris porosities, from zero porosity (Case II-1) to 0.7 porosity debris beds with 1-cm particles (Case II-3).

As shown in Table 5-5, the large increase in porosity reduces the volumetric debris decay heat and precludes the drain line from reaching failure temperatures. The debris is predicted to quench during relocation, and sufficient coolant remains in the reactor vessel to maintain both the vessel and the drain line below failure temperatures.

5.3.2.3 Heat Removal from Vessel Outer Surface. Base case analyses were performed assuming that the vessel outer surface was in contact with a steam and air environment. Heat was removed from the vessel primarily through natural convection and radiation. Because of recent interest in the potential for flooding the reactor building cavity to prevent vessel failure, a sensitivity run was performed in which it was assumed that the vessel outer surface was exposed to water.

As shown by results for Case II-4 in Table 5-5, heat-removal assumptions from the vessel and drain line outer surface significantly impact thermal response. Peak temperatures of the

Table 5-5. Sensitivity analysis results.

					Thermal response characteristics					
					Drain line			Vessel		
Case	Debris porosity	Debris-to-vessel/drain line gap heat-transfer coefficient (W/m^2K)	Building humidity	RCS pressure (MPa)	Time for $T_{peak} > T_{fail}$ (s)	Peak temperature node location	Peak temperature during first 2 hours (K)	Time for $T_{peak} > T_{f.\ l}$ (s)	Peak temperature node location	Peak temperature during first 2 hours (K)
I-1	0.0	500	Dry	0.62	NA[a]	46	1160	NA[a]	65	910
II-1	0.0	500	Dry	7.0	NA[b]	5-59	1175	7,000	65-69	1160
II-2	0.0	500	Dry	1.0	NA[a]	5-72	1160	>7,200	65	1150
II-3	0.7	500	Dry	7.0	NA[c]	NA[c]	NA[c]	NA[c]	NA[c]	NA[c]
II-4	0.0	500	Wet	7.0	NA[a]	59-111	1050	>7,200	65	1040
II-5	0.0	10,000	Dry	7.0	10	5-85	1300	2,000	65	1270
III-1	0.0	500	Dry	0.62	NA[a]	46	1160	26,000	65-70	950

a. Structure temperatures are well below failure temperatures throughout the transient.

b. Drain line temperatures are slightly below the temperature where its ultimate strength is exceeded by the stress from the applied system pressure of 7 MPa.

c. Debris quenches to coolant saturation temperatures during relocation, and decay heat is insufficient to boil off coolant.

drain line and vessel remain below 1050 K throughout the time that the transient was evaluated (2 hours). Hence, neither drain line nor vessel failure is predicted for this scenario.

5.3.2.4 Debris to Vessel/Drain Line Thermal Contact. When debris relocates to the lower head, the thermal contact between the debris and the structural material is reduced because of surface roughness and gas trapped between the debris and vessel or drain line surfaces. Base case analyses were performed assuming a debris-to-drain line and a debris-to-vessel gap heat-transfer coefficient of 500 W/m^2K. As discussed in Section 5.2.1.2, this value represents a lower bound for heat-transfer coefficients calculated using information in Reference 5-16. A sensitivity case (Case II-5) was performed in which it was assumed that the thermal contact between the vessel was increased. In Case II-5, a debris-to-drain line and a debris-to-vessel gap heat-transfer coefficient of 10,000 W/m^2K was assumed. This value represents an upper bound for the gap heat-transfer coefficient.

Results in Table 5-5 indicate that heat-transfer coefficient assumptions significantly increase peak temperature predictions for the vessel and drain line. For Case II-5, the vessel and drain line thermal response times were also significantly shorter than response times for Case II-1.

5.3.2.5 Summary. Table 5-6 compares the sensitivity of vessel and drain line thermal response to the parameters tested using sensitivity factors, which were evaluated for the first 2 hours of each transient using:

$$\text{Drain Line Sensitivity Parameter} = \frac{\text{Peak drain line temperature}}{\text{Case II-1 peak drain line temperature}} \quad (5\text{-}1)$$

$$\text{Vessel Sensitivity Parameter} = \frac{\text{Peak vessel temperature}}{\text{Case II-1 peak vessel temperature}} \quad (5\text{-}2)$$

Results indicate that the potential for water to quench the debris during relocation and form a porous debris has the most impact on peak vessel and drain line temperatures, reducing peak values by over 50%. Increased heat removal from the vessel and drain line outer surface, which may occur if the reactor building cavity were flooded, also reduces peak structure temperatures significantly. Values selected in both the Case II-3 and II-4 sensitivity analyses are sufficient to preclude the drain line and vessel from reaching failure temperatures.

Debris composition effects are noticeable, although less important than debris porosity effects. Sensitivity parameters in Table 5-6 indicate that peak temperature predictions were impacted less by changes in debris composition (Cases I-1, II-1, and III-1) than by changes in debris porosity (Cases II-1 and II-3). However, results in Table 5-5 indicate that vessel and drain line thermal responses are slower in the layered case than in the base case ceramic debris (Case II-1).

Thermal contact between the debris and structural surfaces is also important in predicting thermal response. As indicated in Table 5-6, peak temperatures are about 10% higher in Case II-5 than in Case II-1.

5.3.3 Application to Analytical Model Predictions

As discussed in Section 5.2.1.3, a final objective of the thermal analysis is to consider other LWR penetrations using Section 4 failure maps. Results are presented as responses to the key

Table 5-6. Comparison of sensitivity parameters tested.

Parameter	Cases	Sensitivity factor[a] Drain line	Vessel
Debris composition	I-1	0.99	0.78
	II-1	1.00	1.00
	III-1	0.99	0.82
RCS pressure	II-2	0.99	0.99
Debris porosity	II-3	0.48	0.48
Vessel outer surface heat-transfer coefficient	II-4	0.89	0.90
Debris-to-structure gap heat-transfer coefficient	II-5	1.11	1.09

a. Drain line and vessel sensitivity factors calculated using Equations (5-1) and (5-2).

questions discussed in Section 5.2.1.3. Although each failure map development is summarized when it is applied in this section, more detailed descriptions of failure map development are found in Section 4.1.2.

Is the temperature and mass of the debris sufficient to induce in-vessel tube melting?

The drain line does not contain any in-vessel structure that must be attacked by the debris before the melt exits the vessel. However, in-vessel tube melting is of interest when considering the potential for melt to enter instrument tube and control rod penetrations found in LWR lower heads.

Figure 5-14 is a failure map (similar to the one shown in Section 4.1.2) for predicting the potential for debris heat capacitance to induce tube failure. The abscissa for points in this failure map is the mass ratio of the tube material to the debris material that relocates to the lower head (M_t/M_d) and the ordinate for points is the ratio of the effective debris to tube temperature, θ_d/θ_t, which is defined by the following equations:

$$\theta_d = T_d(0) - T_{mp/t} \quad \text{for solid debris with } T_{mp/t} \le T_d(0) < T_{mp/d} \text{ ; or}$$

$$\theta_d = T_d(0) - T_{mp/t} + \frac{L_d}{c_{pd}} \quad \text{for molten debris with } T_d(0) \ge T_{mp/t} \text{ ; and}$$

$$\theta_t = T_{mp/t} - T_t(0) + \frac{L_t}{c_{pt}}$$

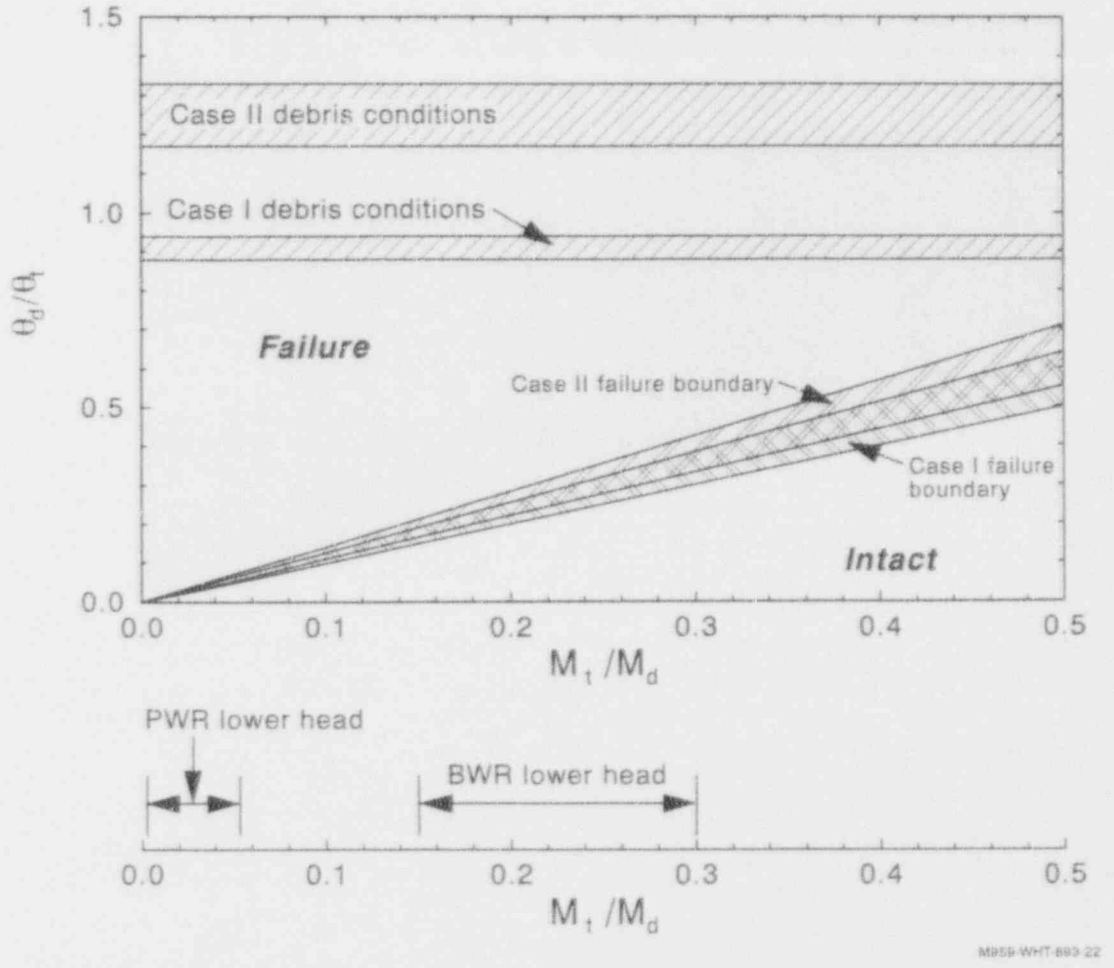

Figure 5-14. Failure map for determining requirements for Case I and Case II debris conditions to induce in-vessel tube melting.

where $T_{mp/t}$ represents the tube melting point, T(0) represents the initial temperature, c_p represents the specific heat capacity, and L represents the latent heat of fusion for the debris or tube material (denoted by the subscripts d or t).

The failure region is separated from the intact region by lines that are dependent upon the debris composition and the tube material (note that only Inconel and stainless steel are considered on this map because there are no drain line in-vessel structures). These lines were obtained by applying the energy conservation equation to the debris that relocates around vessel penetrations, which simplifies to

$$\frac{\theta_d}{\theta_t} = \frac{c_{pt} M_t}{c_{pd} M_d} \quad . \tag{5-3}$$

Two types of debris are considered in this map: the base Case I metallic debris and the base Case II ceramic debris.

The lower axis in Figure 5-14 illustrates the range of tube-to-debris-mass ratios that occur in PWR and BWR lower heads. Ranges are presented in this figure because the ratios are highly dependent on the location in the lower head penetration configuration (i.e., whether along the periphery or the central region of the reactor vessel).

Figure 5-14 contains cross-hatched horizontal bars that correspond to the ratios of debris-bed-to-tube effective temperatures. As indicated in Figure 5-14, tube melting is predicted to occur in both BWR and PWR lower heads for the highly metallic base Case I and highly ceramic base Case II debris bed compositions considered. In-vessel tube melting is also predicted for base Case III, in which the lower portion of the debris bed is metallic and the upper portion of the debris bed is ceramic.

Will the melt travel through the penetration to a distance below the lower head?

Section 4.1.2 describes the methodology used to predict the distance that the melt will travel in a penetration until it solidifies. As discussed in Section 4.1.2, melt penetration distances are highly dependent on whether conduction or turbulent heat transfer dominates between the melt and the tube. Some of the more important parameters identified in Section 4.1.2 for predicting penetration distance, X_p, are shown in Figure 5-15 and include the distance required for the melt to travel until it has gone beyond the lower head, l_t; the effective diameter for melt flow within a tube, d_e; and the Peclet number for the debris, Pe, which is a function of the melt velocity, v_d, melt thermal diffusivity, α_{td}, and d_e.

Figure 5-16 contains a map for predicting melt penetration distance. This map is developed in terms of the dimensionless Peclet number and the ratio of the predicted melt penetration distance, X_p, to the difference in the tube and instrument string diameters, $d_i - d_{so}$. The large horizontal bar contains bounding values for the ratio of the distance that the melt must travel through different LWR

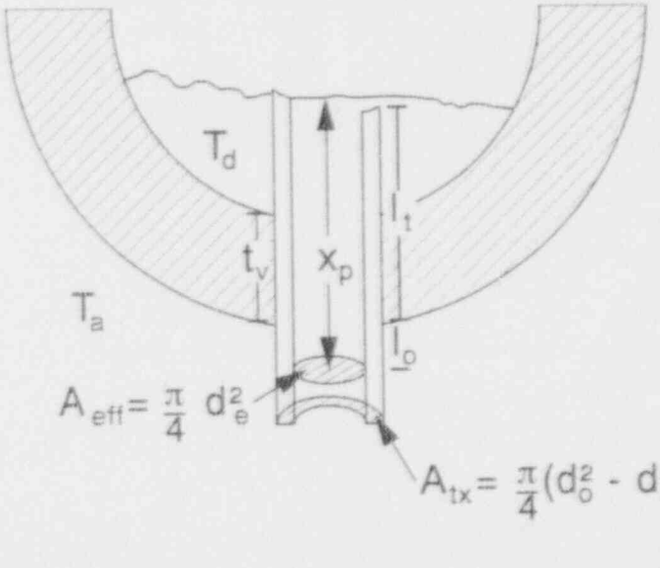

Figure 5-15. Geometry of tube and vessel configuration for developing melt penetration and ex-vessel tube failure maps.

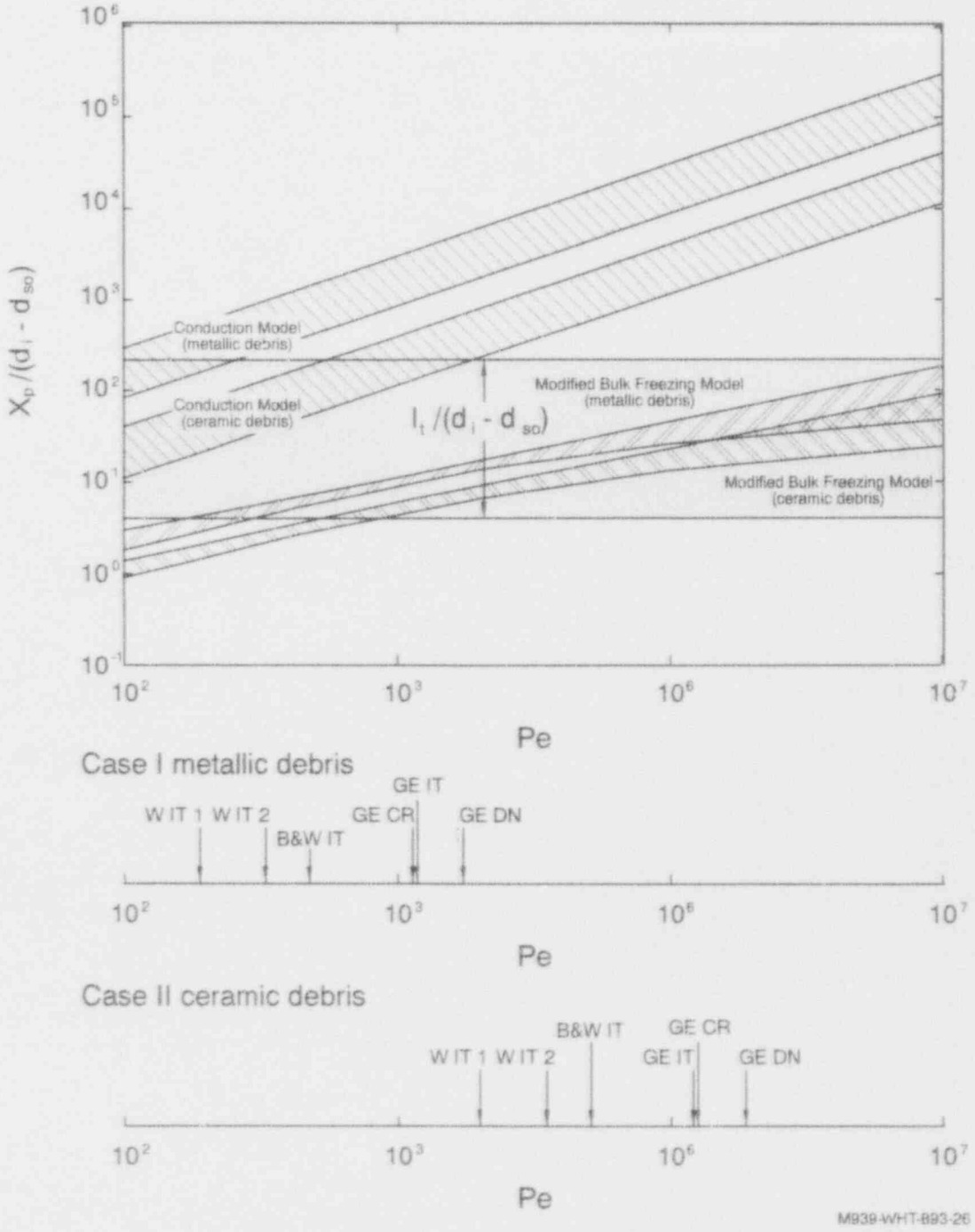

Figure 5-16. Comparison of melt penetration distances.

penetrations so that it is below the lower head, l_t, to the gap available for melt flow in the tube, $d_i - d_{so}$. The lower bound represents the distance that melt must travel through a GE drain line nozzle and is simply the vessel thickness divided by the drain line inner diameter. The upper bound represents an upper estimate for the distance that melt must travel through a Westinghouse instrument tube and is an estimated upper in-vessel ablation height for this tube divided by the gap available for melt flow in the tube. The four regions in Figure 5-16 represent penetration distance ranges predicted for metallic and ceramic flows using the bulk freezing model

(in which turbulent heat transfer is assumed to dominate) and the conduction model (in which conduction heat transfer is assumed to dominate). As discussed in Section 4.1.2, molten debris is predicted to travel much longer distances if conduction heat transfer dominates because the crust that is assumed to form along the wall retards heat transfer between the tube and the molten debris.

Lower axes in Figure 5-16 are marked to indicate Peclet numbers calculated for Case I and Case II debris conditions and various penetrations found in LWR lower heads: a GE BWR instrument tube (GE IT), a BWR drain line nozzle (GE DN), a GE BWR control rod guide tube (GE CR), two Westinghouse PWR instrument tubes (W IT 1 and W IT 2), and a B&W PWR instrument tube (B&W IT). As indicated on these axes, higher Peclet numbers (and thus longer melt distance predictions) occur for penetrations with larger effective diameters (e.g., a GE drain line).

As shown in Figure 5-16, the melt is predicted to travel distances significantly longer than the bottom of the lower head if the melt follows conduction model predictions. If the melt behaves according to modified bulk freezing model predictions, the melt is predicted to remain within the lower head for either type of melt composition in the two Westinghouse instrument tubes, the B&W instrument tube, and the GE control rod guide tube. Ceramic and metallic melts will flow through GE instrument tubes and drain lines to locations below the lower head according to modified bulk freezing model predictions.

Will ex-vessel tube failure occur?

Figure 5-17 is a failure map for predicting tube equilibrium temperature using a heat balance. The abscissa for points in this map is the ratio of the tube cross sectional area, A_{tx}, to the tube effective area for melt flow, A_{eff}, as defined in Figure 5-15. The ordinate for points in this map is the ratio of the effective debris to tube temperature ratio, θ_d/θ_t, with θ_d and θ_t defined by the following equations:

$\theta_d = T_d(0) - T_{t/f}$ for solid debris with $T_{t/f} \le T_d(0) < T_{mp/d}$; or

$$\theta_d = T_d(0) - T_{t/f} + \frac{L_d}{c_{pd}} \quad \text{for molten debris with } T_d \ge T_{mp/d} \quad \text{and} \quad \theta_t = T_{t/f} - T_t(0) \qquad (5\text{-}4)$$

where $T_{t/f}$ represents the tube failure temperature, which is the temperature where the tube material's ultimate strength decreases to zero. In this map, the failure region is separated from the intact region by lines that are dependent on the debris composition and the tube material. These lines were obtained by applying the energy conservation equation to debris that relocates into the penetrations, which simplifies to

$$\frac{\theta_d}{\theta_t} = \frac{A_{tx}}{A_{eff}} \frac{\rho_t c_{pt}}{\rho_d c_{pd}} \qquad (5\text{-}5)$$

Differences in slope between Case I and Case II lines result from differences in debris composition.

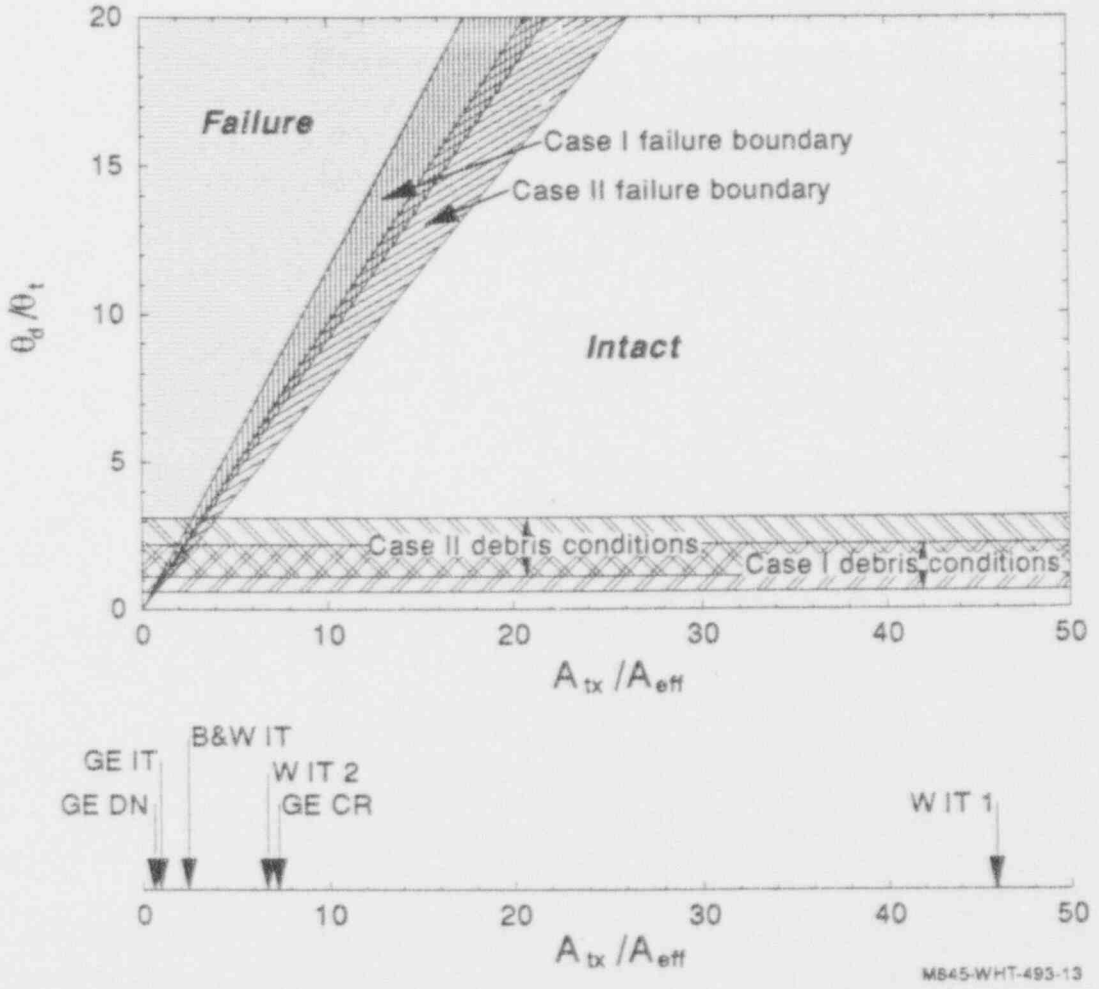

Figure 5-17. Failure map obtained from heat balance between tube and debris.

The lower axis in Figure 5-17 illustrates the range of area ratios that exist in LWR penetrations. The axis emphasizes the point that PWR instrument tubes and BWR control rod guide tubes are relatively thick-walled and have relatively low areas available for melt flow.

This failure map indicates that all other LWR lower head penetrations are less susceptible to failure than the BWR drain line. The failure map indicates that penetrations with relatively thick walls and small areas available for melt flow, such as the Westinghouse instrument tubes and the GE control rod guide tube, will not experience failure temperatures when subjected to either Case I or Case II debris conditions for extended time periods. Although failure temperatures are predicted to occur in the GE drain line and the GE and B&W instrument tubes, it must be noted that this failure map was developed assuming that a tube is exposed to a constant temperature debris for extended time periods. Hence, heat losses via radiation and convection from the tube's outer surface are neglected.

Figure 5-18 is a failure map for predicting tube failure by considering debris decay heat and radiation heat transfer to the reactor containment building. The abscissa for points in this map is the ratio of the tube effective diameter for melt flow to the tube outside diameter (see Figure 5-15). The ordinate for points in this map is the ratio of the debris heat flux ($\tilde{q}_d$) to the

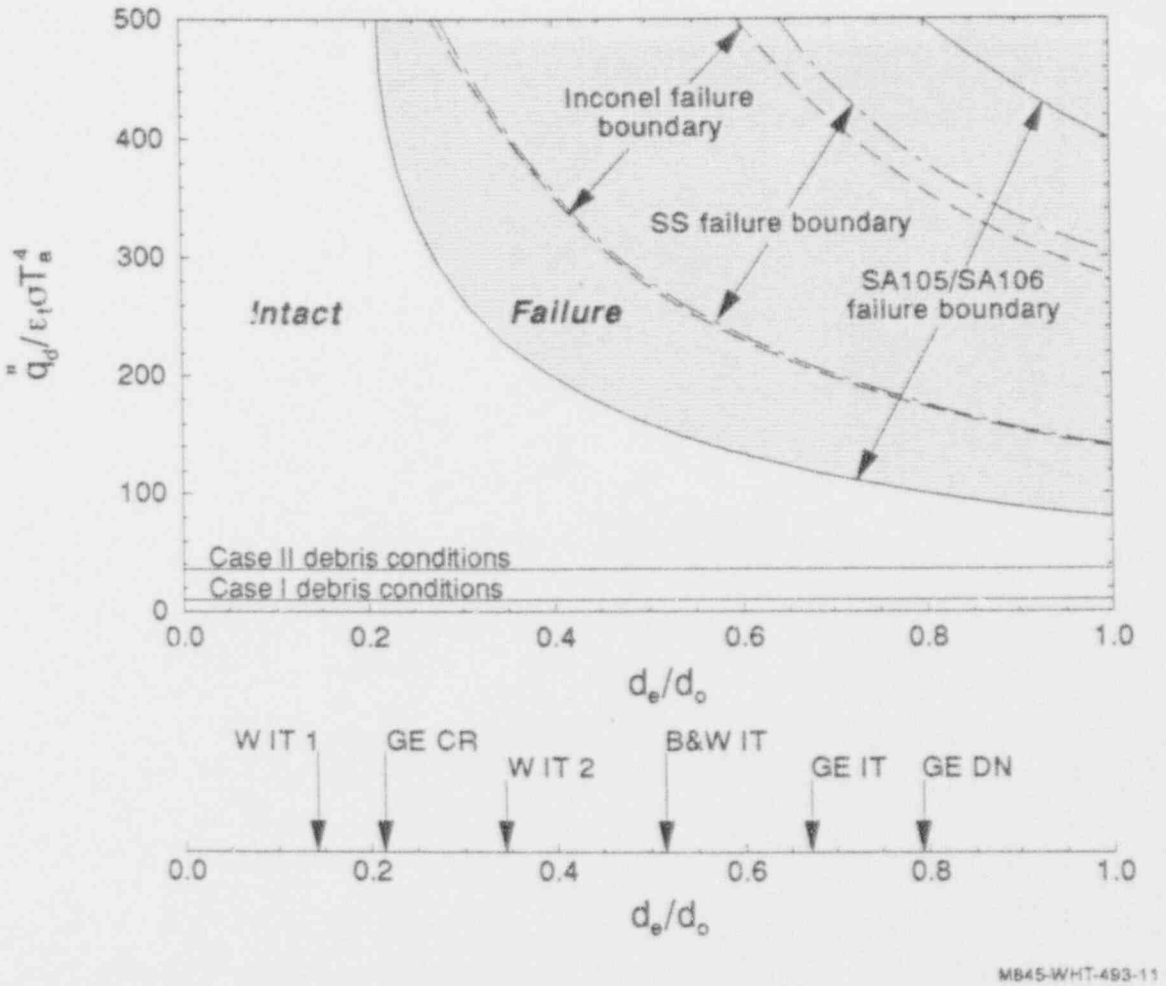

Figure 5-18. Failure map obtained considering debris decay heat and radiation to containment.

tube emissivity (ϵ_t), the Stefan-Boltzmann constant (σ), and the containment temperature (T_a). The failure region is separated from the intact region in Figure 5-18 by boundaries that are dependent upon tube material composition. As previously discussed, there are limited data for predicting tube material ultimate strength at high temperatures. Hence, subregions in Figure 5-18 indicate possible lower and upper boundaries for each tube material's failure region. Note that uncertainty related to the boundary for SA105/SA106 is largest in this figure because there are no data for this material above 1150 K.[e] Hence, there is more uncertainty in predicting the ultimate strength of this material at high temperatures than for stainless steel and Inconel, for which tests at 1373 K were performed. Upper bounds for estimating failure boundaries are based upon tube material melting temperatures.

e. INEL SA106 tests were not performed for temperatures above 1150 K. This temperature was well above the 1000 K value where previous data indicated that the ultimate strength of this material becomes negligible. However, test results (see Appendix B) indicate that the ultimate strength of SA105/SA106 material is 60 MPa at 1150 K. Although there were no other higher temperature data available for the SA105/SA106 steel, its ultimate strength was extrapolated based upon data for SA533B steel.

On the lower x-axis, the ratio, d_e/d_o, has been evaluated assuming that the debris fills the entire cross section of area available for melt flow in the different penetration geometries described in Appendix F. This axis emphasizes the point that drain line penetrations have a considerably larger effective diameter for melt flow and relatively thinner walls than other LWR penetrations.

Consistent with results from the numerical calculation, this failure map indicates that none of the LWR lower head penetrations will experience failure temperatures if subjected to either Case I or Case II debris conditions. However, it should be noted that there is more uncertainty in predicting high-temperature ultimate strength behavior for drain line SA105/SA106 carbon steel and that additional high-temperature SA105/SA106 data are needed to determine whether drain line failure occurs. Hence, the most important result in this map is the fact that other penetrations, for which there are more data available for high-temperature material properties, are predicted to be less susceptible to failure than the BWR drain line.

5.3.4 Summary

A study was performed to assess the two-dimensional thermal response of a BWR drain line penetration and vessel when subjected to relocated debris from a severe accident. Sensitivity analyses were performed to consider the effect of debris composition, debris porosity, debris-to-surface gap resistance, reactor system pressure, and building heat removal. Results indicate that drain line failure will not occur in cases where metallic debris relocates to the lower head. In cases where ceramic debris relocates to the lower head, drain line temperatures peak near values where failure may occur within several minutes; whereas vessel failure temperatures do not occur until several hours into the transient. Sensitivity results indicate that high porosity debris or the high heat removal rates from the vessel or drain line outer surface that may occur if the containment cavity were flooded will preclude both penetration and vessel failure.

Peak vessel temperatures are predicted to occur at the bottom of the vessel near the debris/surface interface for base case ceramic and metallic debris. However, the peak vessel temperature location varies during the transient in which it is assumed that ceramic debris relocates on top of a metallic debris bed. Although peak temperatures always occur along the debris/vessel interface, the second layer of ceramic debris causes peak vessel temperatures to shift away from the bottom of the vessel toward the point where the skirt is attached to the vessel.

Both the metallic and ceramic debris are predicted to initially solidify after relocation onto the lower head. For base case analyses, primarily metallic debris temperatures remain below the eutectic's solidus temperature ($\leq$2100 K) throughout the transient. Peak temperatures of the primarily ceramic debris begin to exceed the eutectic's solidus temperatures ($\leq$2700 K) within 4 hours, and within 6 hours the debris bed is primarily molten. However, only a small fraction of the debris bed is molten at the time the vessel is predicted to structurally fail (between 3.5 and 4 hours).

Failure maps, which were developed using analytical, closed-form solution techniques, were applied to predict other LWR penetration responses. Results from the two-dimensional calculations were compared with analytical failure map predictions to determine (a) if governing relationships used to develop failure maps were adequate for predicting drain line response, (b) the response of other LWR penetrations when subjected to similar debris conditions, and (c) general conclusions related to the parameters focused on for the two-dimensional analysis with respect to other LWR penetrations and debris conditions.

Two-dimensional results confirm failure map predictions for the base case metallic (Case I-1) and base case ceramic (Case II-1) debris conditions. Application of failure maps to other LWR geometries indicate that in-vessel tube melting will occur following either debris condition in any of the BWR and PWR vessel designs considered. Melt is predicted to travel distances well below the lower head for base case debris conditions in any of the reference LWR penetrations if heat transfer from the melt to the tube is conduction-dominated. However, if turbulent heat transfer dominates, melt is predicted to travel only to ex-vessel locations through tubes with larger areas available for melt flow, such as the BWR drain line and instrument tubes. Failure maps indicate that ex-vessel tube-temperature peaking near values where failure may occur is specific to the BWR drain line because of its relatively large effective diameter for melt flow and its material composition. For example, failure maps indicate that most other LWR penetrations will remain intact if subjected to either base case metallic or ceramic debris conditions.

In conclusion, two-dimensional results indicate that governing relationships used in analytically developed failure maps are adequate for predicting penetration thermal response. Furthermore, failure maps indicate that the response predicted for the BWR drain line subjected to ceramic debris may be unique to that LWR penetration because of its geometry and material composition.

5.4 Structural Analysis Results

Structural analysis was performed using time-dependent vessel temperature data from the SCDAP/RELAP5 analysis of the metallic debris (Case I-1) and ceramic debris (Case II-1). These two cases represented the lower and upper bound thermal challenges to the vessel from the base case debris relocation scenarios considered. The following section discusses the vessel structural response to these conditions, with detailed discussions on the stress, strain, and damage incurred in the ceramic debris case.

5.4.1 Structural Response to Metallic Debris Case (Case I-1)

The metallic debris case represents the least severe challenge to vessel structural integrity in this study, with peak vessel temperatures of less than 950 K and very low primary stresses (approximately 5 MPa) in the vessel wall. (For reference, the ultimate strength of vessel steel at 950 K is about 150 MPa). With these relatively low temperatures and stresses, significant plastic or creep behavior is not expected. Recognizing the limited challenge that this case represented to vessel integrity, the system pressure for the structural analysis was raised from 0.62 MPa specified in Case I-1 to the operating pressure of 7 MPa. This increased the primary stresses in the vessel from approximately 5 MPa to 54 MPa. Failure was still not expected, although increased creep deformation under these conditions was expected (but ultimately not realized).

Results from the structural finite-element analysis of the metallic debris case subjected to operating pressures for 24 hours predict maximum combined creep and plastic strains of less than 1%. Failure at these temperatures typically occurs at creep strains greater than 20%. Because thermal analysis results indicate that vessel temperatures decline within the first 2 hours, a vessel subjected to metallic debris with system pressures up to (and probably well over) 7 MPa is not predicted to sustain significant damage. Creep damage calculated by the life-fraction rule is less than 1% after 24 hours.

5.4.2 Structural Response to Ceramic Debris Case (Case II-1)

Of the three base cases analyzed, the ceramic debris case with its high vessel temperatures and operating pressure represents the most severe challenge to vessel integrity. The first question in this analysis was whether the vessel starts to melt before creep mechanisms have enough time to play a significant role. Naturally, because plastic behavior is considered static (instantaneous), one would expect the vessel to fail by exceeding the ultimate strength before melt. However, at these relatively low primary stresses, melt and static failure were expected to be fairly closely timed.

Before the discussion of results from the ceramic debris analysis, a short review of primary and secondary stresses may be in order. Primary stresses are generally defined as stresses that are not relieved by deformation. For this analysis the only primary stress is caused by the system pressure. Had the dead weight of the vessel, debris, and water been significant, these also would be considered primary stresses. Even if the vessel deforms under these stresses, they each continue to exert force on the vessel wall until failure. Secondary stresses, on the other hand, are relieved by deformation; thermal stress being the most common type. If allowed to deform, a body will relieve thermal stresses through elastic, plastic, or creep deformation until the stresses are zero.

Figure 5-19 shows the predicted deformed shape of the vessel 3.4 hours after ceramic debris relocation using an axisymmetric model. The vessel is shown to sag significantly with extensive wall thinning at the lowest elevation. Failure is predicted to occur in this region from localized creep deformation, which causes the observed thinning of the vessel wall.

Figures 5-20 and 5-21 show the tangential stress and strain contours in the vessel wall. At first glance, Figure 5-20 may seem contradictory to the evidence presented in Figure 5-19. Bending stresses near the vessel skirt are created as the vessel tries to expand, but is prevented from doing so by the skirt. It is in this region that maximum tension and compression are occurring. The region where thinning is observed is under very modest tension (less than 80 MPa). Figure 5-21 plots the strain contours of the vessel at the same point in time. Here, it is clear that maximum strain deformation is taking place in the area of thinning, with a local maximum in the outside wall. The low stress in the thinning region results from the deformation observed in the strain contour plot; stresses are being relieved. The material in this region readily deforms because of high temperatures. Average through-wall stresses will not go below the primary stress (approximately 54 MPa) caused by system pressure. Near the skirt, the vessel is constrained from deforming by the skirt. Additionally, temperatures in this region are low; because little plastic or creep deformation is taking place to relieve the stresses, higher stresses are maintained.

Figures 5-22, 5-23, and 5-24 illustrate why maximum strain in the thinning region takes place on the cooler outer wall, rather than on the hot inner wall. Figure 5-22 shows the temperature history of four through-wall locations in the region of thinning; Figure 5-23 shows the tangential stress history of the same through-wall points; and Figure 5-24 shows the equivalent creep strain history. Points slightly interior to the inside and outside wall surfaces are used because they are free from surface effects, such as very localized hot spots.

Referring first to Figures 5-23 and 5-24, the initial condition for the vessel is 559 K with an average primary stress 54 MPa through the wall. At 0.03 hours, the temperature difference between the point 31-mm from the inside surface and the point 193-mm from the inside surface is a maximum of 200 K. Because the material near the inside surface is hotter, the 31 mm location

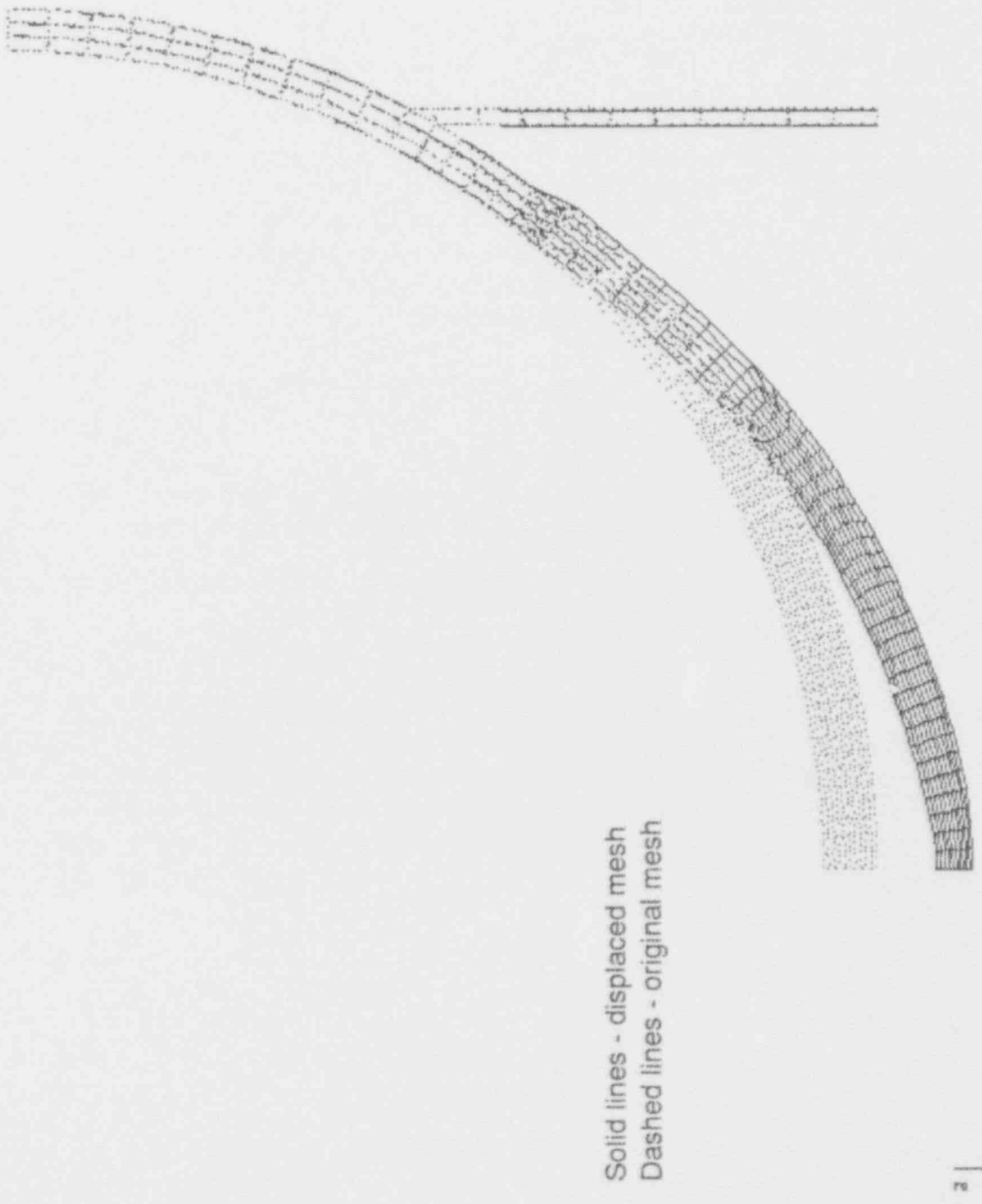

Figure 5-19. Deformed vessel (Ceramic Case II-1).

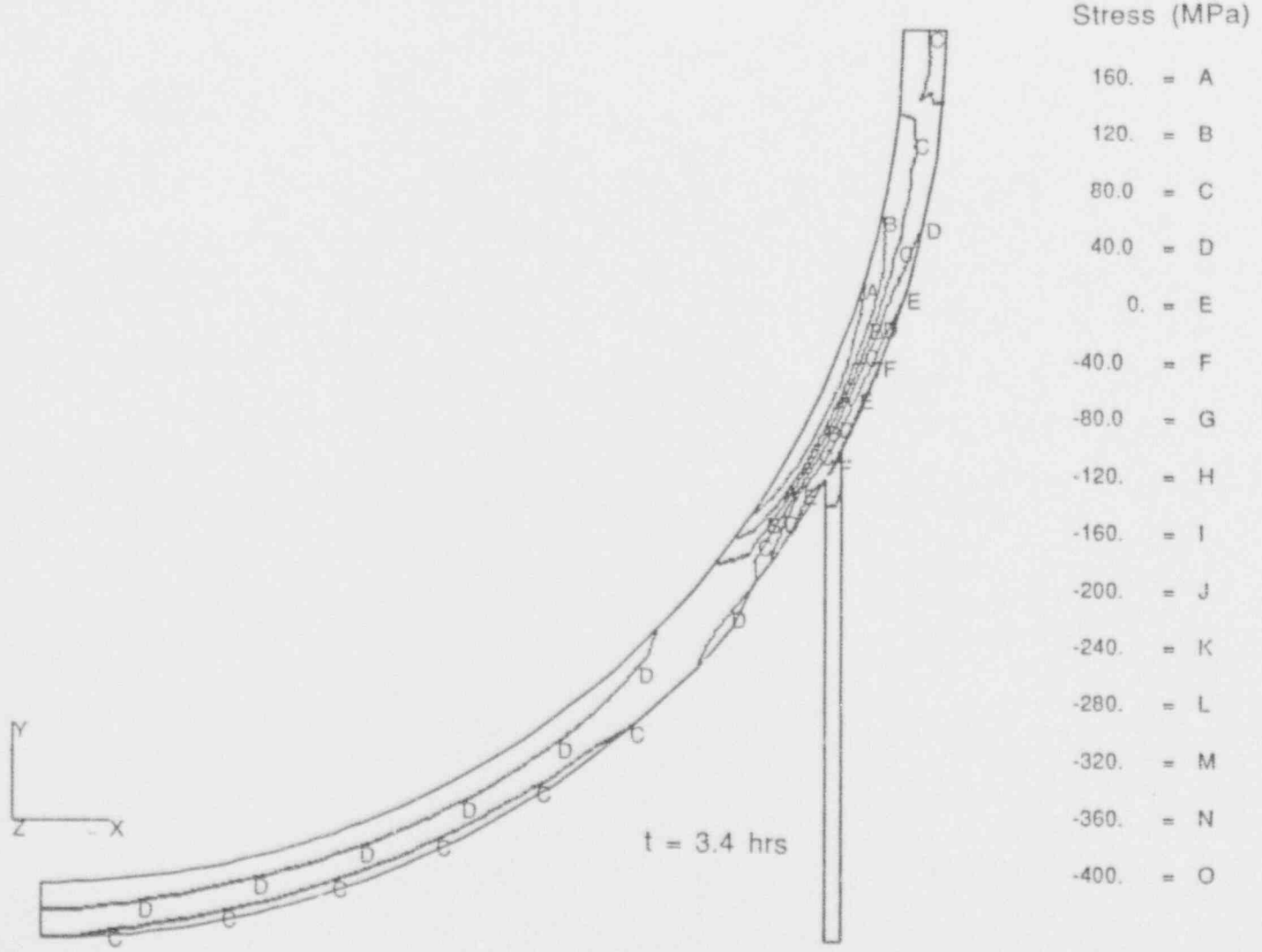

Figure 5-20. Tangential stress contours in MPa (Ceramic Case II-1).

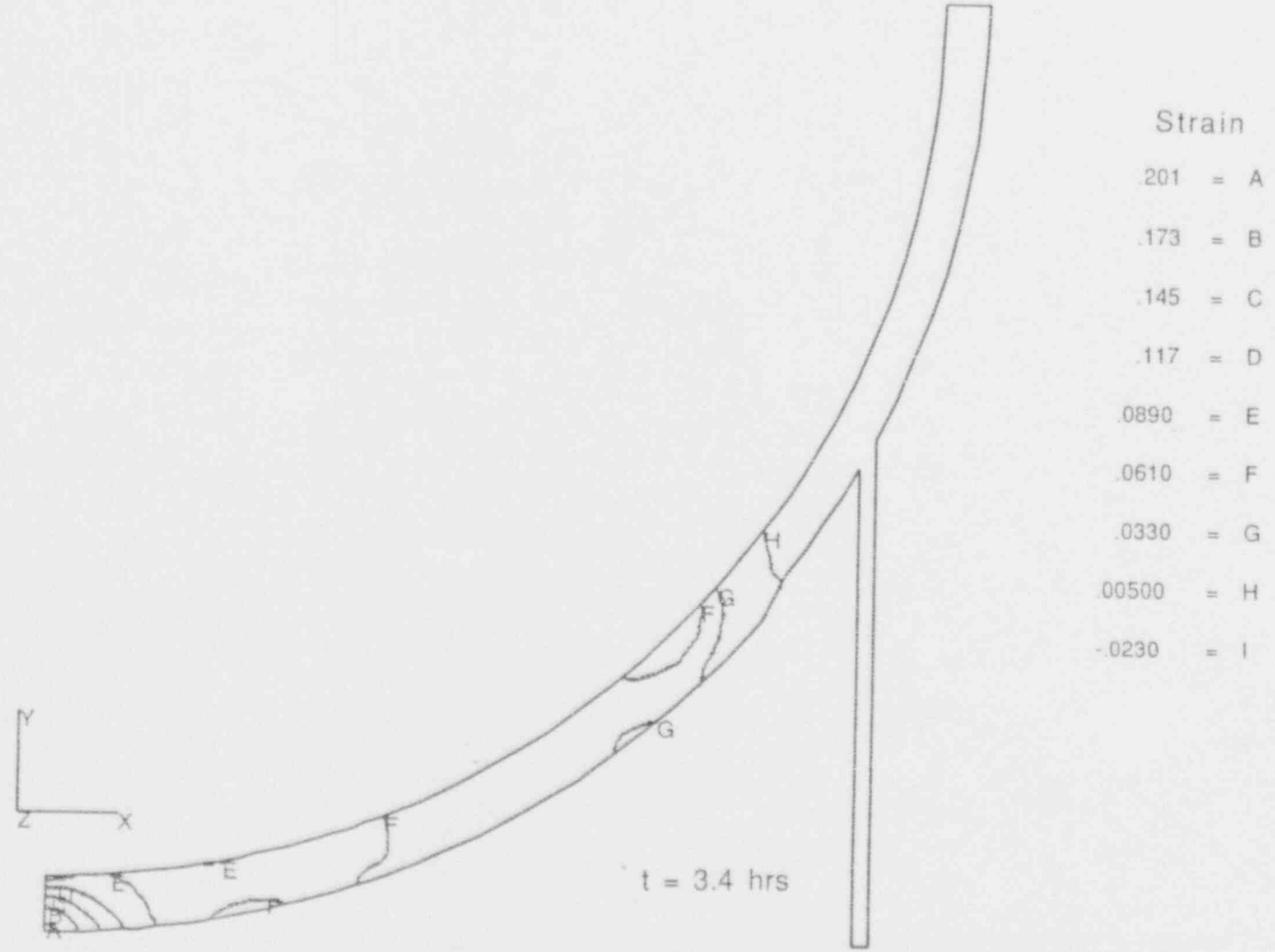

Figure 5-21. Tangential strain contours (Ceramic Case II-1).

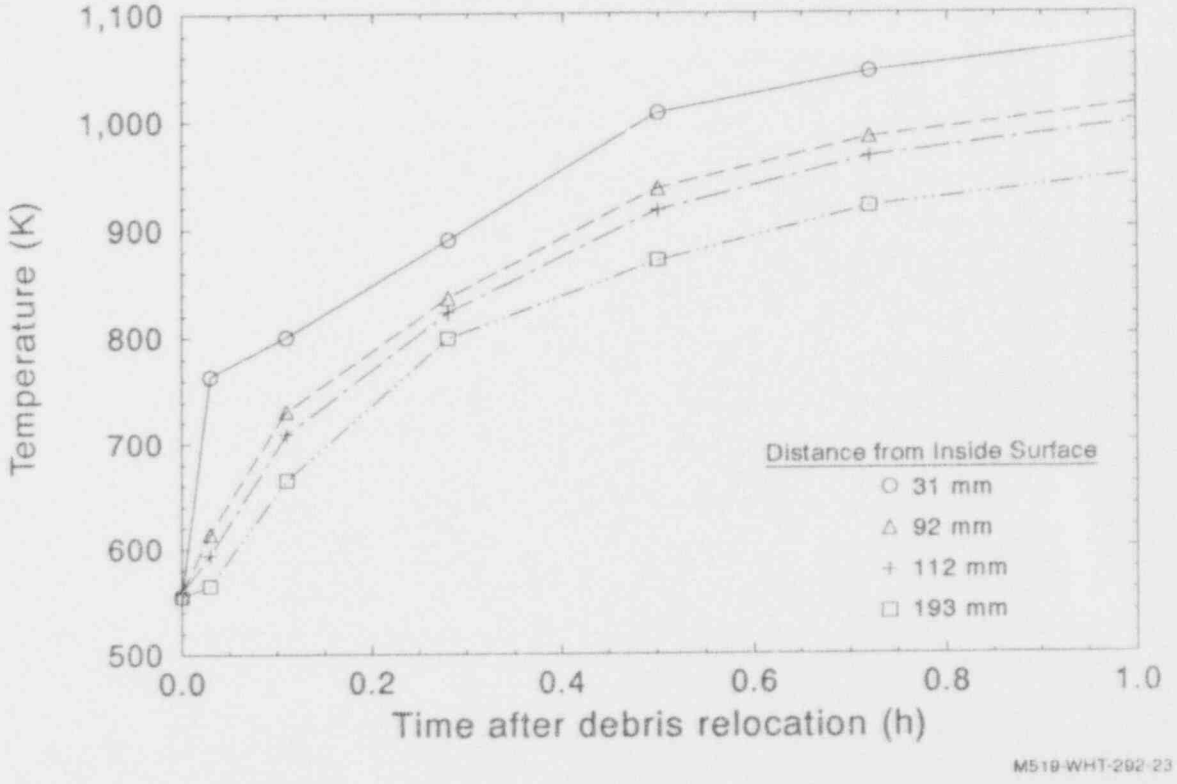

Figure 5-22. Temperature data points input to ABAQUS (Ceramic Case II-1).

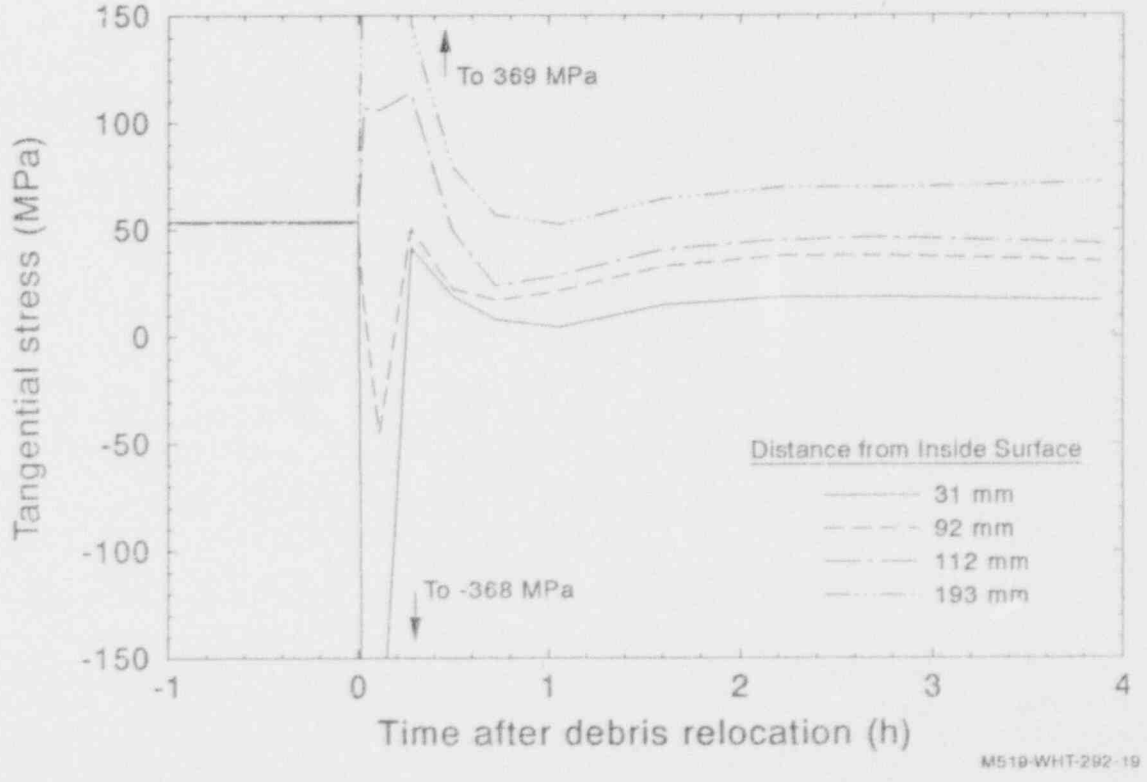

Figure 5-23. Stress history of vessel (Ceramic Case II-1).

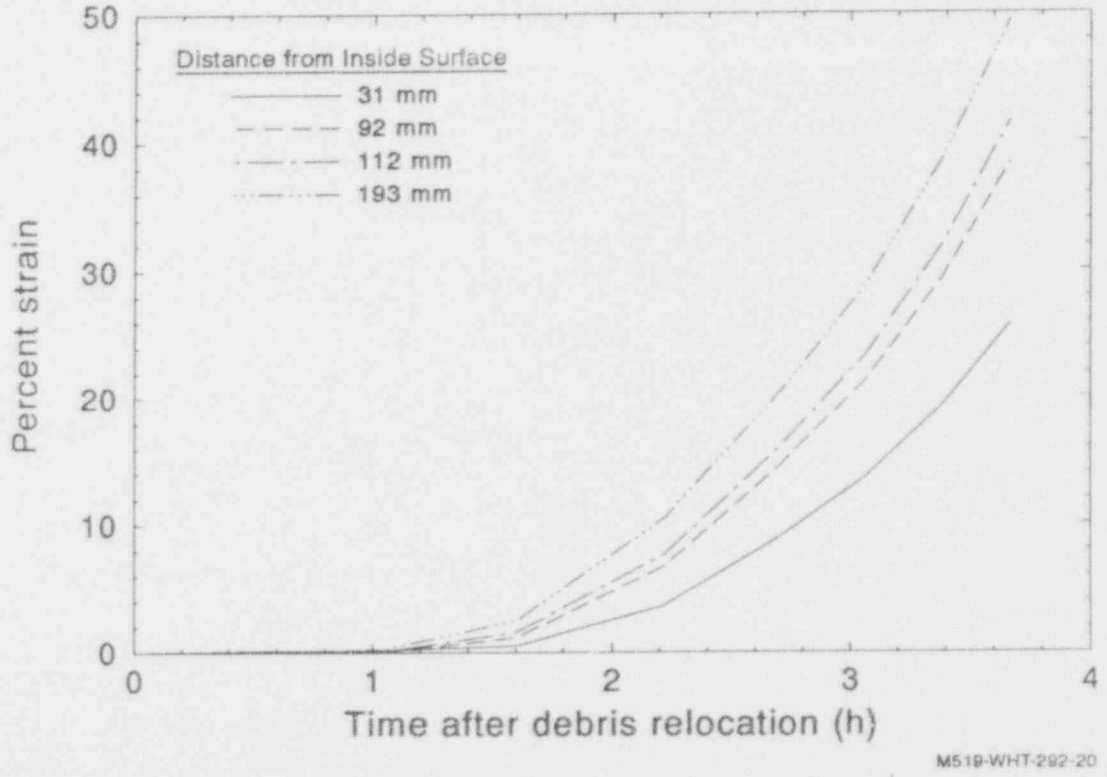

Figure 5-24. Equivalent creep strain (Ceramic Case II-1).

is in compression, while the 193 mm location is in tension. At this time, material to a depth of about 50 mm from the inside surface yields slightly from high stresses and reduced ultimate strength at these temperatures. The cooler outside wall does not yield. At 0.3 hours, the temperature difference between these same two points is reduced to 91 K, and the corresponding stress difference is greatly reduced, bringing the entire vessel wall into tension. Between 1 and 4 hours, the temperature increases very slowly, and a fairly constant stress gradient is established with the 31-mm location at about 23 MPa and the 193-mm location at about 70 MPa.

Throughout this accident history plastic strains are minimal (less than 0.3%). However, as the accident progresses, creep strains become quite large. The equivalent creep strains plotted in Figure 5-24 result from taking the three-dimensional creep strains and equating them to strains in a one-dimensional state. Although the inside locations are hotter than the outside locations, the outside locations strain more because they are under higher stresses. This implies that for these conditions, creep strain is more sensitive to stress differences than temperature differences. A similar progression will also be observed in the creep damage of the vessel.

Recall that creep damage is calculated using the life-fraction rule. Effective (or equivalent) stress and temperature for each element of interest are averaged over the time step. Time to rupture is calculated from the Larson-Miller parameter data (the method for applying the Larson-Miller parameter is described in Section B-5.1). The actual time spent at a given effective stress and temperature divided by the time to rupture at that stress and temperature is the element damage. Since ABAQUS does not have a means of determining failure, it continues to assume that every element has load bearing capability, even after some of the elements may have failed.

Therefore, some of the elements will exhibit damage greater than 100%. To account for this, simple averaging of the damage through the wall thickness is used. Failure is predicted when the average through-wall damage is 100%.

The time history of creep damage for these same four locations is shown in Figure 5-25. A small amount of damage is sustained during the first 0.2 hours at the 31-mm location from the high compression excursion caused by thermal stresses. For the most part, however, the vessel does not sustain much damage until after 1.5 hours. The damage that occurs after 1.5 hours is greatest in the outer portions of the vessel, indicating that failure starts in the outside wall and proceeds inward. Figure 5-26 shows the average through-thickness damage as a function of time. From this plot, failure is predicted to occur between 3.5 and 4 hours after debris relocation.

Note that both creep damage and equivalent creep strain histories have the same general shape. Both creep strain and damage are very low for the first 1.5 hours, after which they exponentially. The creep strain and creep damage relations are separate, independent functions of stress, time and temperature fit to data from material property testing. Creep strain uses the time hardening relations to describe deformation history (with no specification of failure) and damage uses the Larson-Miller parameter to specify failure (with no mention of past strain history). That they follow each other in form is, of course, expected from a physical standpoint. However, only the consistency of the material property data and the proper application of structural analysis compels these two parameters to do so. These two plots qualitatively verify the creep material properties and the finite-element analysis performed in this study.

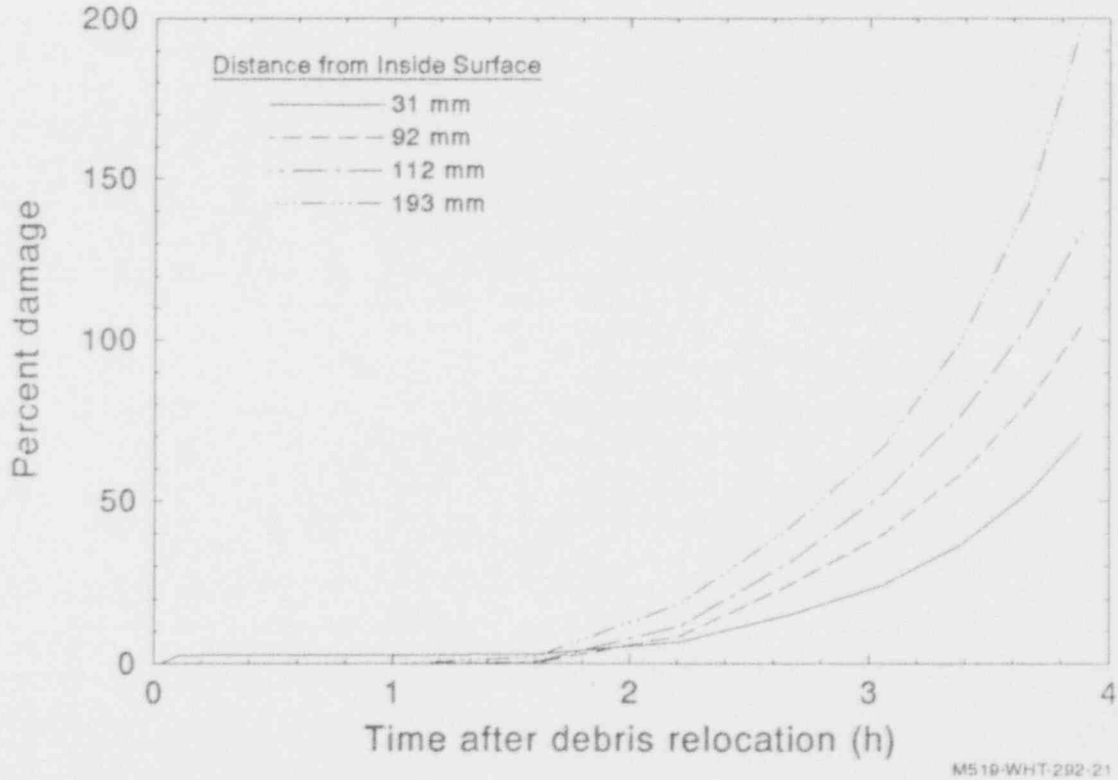

Figure 5-25. Damage history (Ceramic Case II-1).

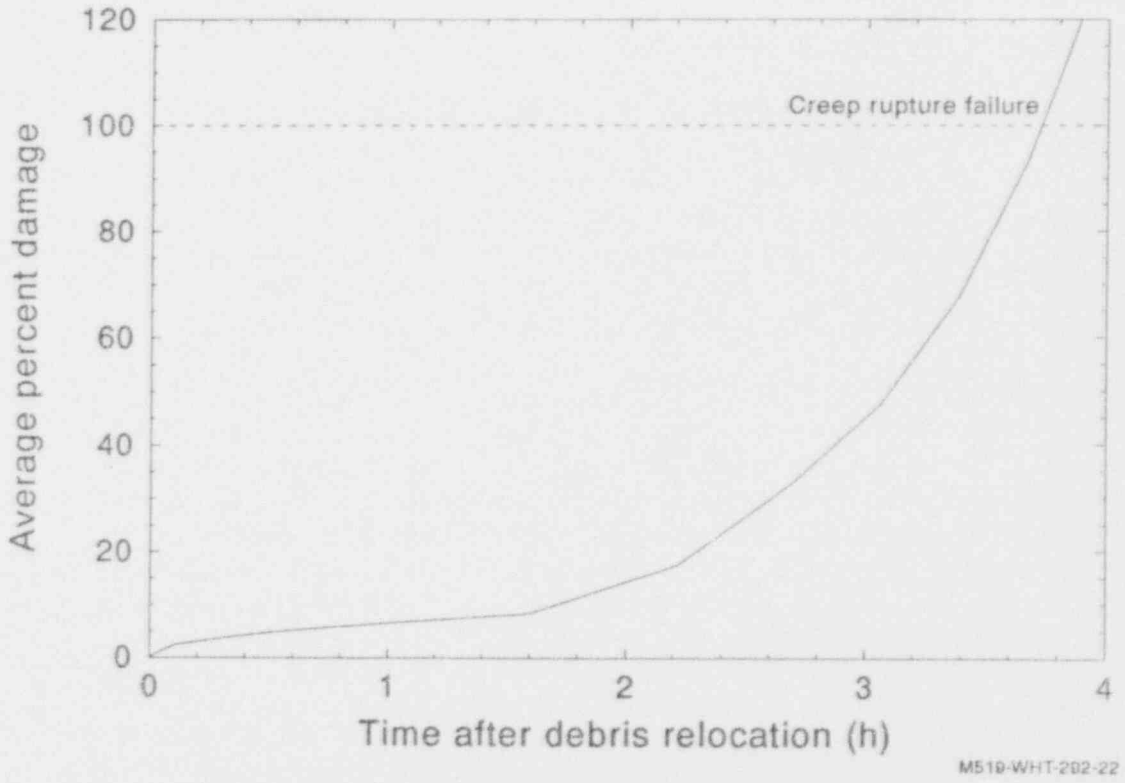

Figure 5-26. Average through-wall damage history (Ceramic Case II-1).

5.4.3 Summary

Structural finite-element analyses were performed for the metallic and ceramic debris cases. These two cases represent the lower and upper bounds, respectively, of thermal challenge to the vessel from debris relocation. The metallic case exhibits very little plastic or creep deformation after 24 hours. Because temperatures are dropping at 24 hours, the vessel is predicted to remain intact, sustaining very little damage. The ceramic case exhibits high creep strains and is predicted to fail less than 4 hours after debris relocation. Neither case exhibits significant plastic deformation.

The ceramic case fails by localized thinning from creep deformation in the bottom (lowest elevation) of the vessel. Examination of this region reveals that from 1.5 to 4 hours, creep strains are highest in the outer, cooler regions of the vessel wall, from thermal stresses. This is because compressive thermal stresses on the inside portion of the vessel superposed on the tensile primary stresses from system pressures result in low total stresses on the inside surface. Near the outside vessel wall, tensile thermal stresses are added to tensile primary stresses, causing the greater creep deformation in this region. Creep damage also proceeds from the outside to the inside wall. Therefore, failure initiates on the outside portion of the wall and moves inward.

Both creep strain and creep damage remain very low for the first 1.5 hours after debris relocation. Thereafter, they both rise exponentially with time. The concurrence of these two independent parameters is a qualitative verification of the material properties and finite-element method used in this analysis.

5.5 Conclusions

Detailed numerical calculations were performed to predict BWR vessel and drain line penetration thermal and structural response following debris relocation during a range of severe accident conditions. Detailed numerical models were applied for these analyses because Section 4 models with closed-form or simplified numerical solution techniques could not provide insight into the following areas:

- The relative likelihood of BWR vessel and penetration failure for a wide range of accident conditions
- The roles of thermal stresses and creep in vessel failure.

Furthermore, numerical model results were used to confirm analytical model predictions.

Thermal analyses considered three types of debris conditions: (a) a uniform debris bed that is primarily metallic (Case I), (b) a uniform debris bed that is primarily ceramic (Case II), and (c) a layered debris bed with metallic debris near the vessel and ceramic debris on top (Case III). These debris bed compositions were selected to envelop possible BWR debris bed compositions during severe accidents. Sensitivity studies were performed to consider the effects of parameters, such as debris porosity, debris-to-surface gap resistance, reactor coolant pressure, and heat-transfer conditions on the outer surface of the drain line and vessel.

Thermal analysis results indicate that drain line failure will not occur in cases where metallic debris relocates to the lower head. In cases where ceramic debris relocates to the lower head, drain line temperatures peak near values where failure may occur within several minutes; whereas vessel failure temperatures do not occur until several hours into the transient. Sensitivity study results indicate that large-porosity debris or high heat removal rates from the vessel and drain line outer surfaces can preclude drain line and vessel failure temperatures from occurring.

Peak vessel temperatures are predicted to occur at the bottom of the vessel near the debris/surface interface for base case ceramic and metallic debris. However, peak vessel temperature locations vary during the transient in which it is assumed that ceramic debris relocates on to the top of a metallic debris bed. Although peak temperatures always occur along the debris/vessel interface, the second layer of ceramic debris causes peak vessel temperatures to shift away from the bottom of the vessel toward the point where the skirt is attached to the vessel.

Both the metallic and ceramic debris are predicted to solidify initially after relocation onto the lower head. For base case analyses, primarily metallic debris temperatures remain below the eutectic's solidus temperature ($\leq$2100 K) throughout the transient. Peak temperatures of the primarily ceramic debris begin to exceed the eutectic's solidus temperatures ($\leq$2700 K) within 4 hours, and within 6 hours the debris bed is primarily molten. However, only a small fraction of the debris bed is molten at the time the vessel is predicted to structurally fail (between 3.5 and 4 hours).

Two-dimensional thermal analysis results confirm failure map predictions for the base case metallic (Case I-1) and base case ceramic (Case II-1) debris conditions. Failure maps were applied to compare the response of representative plants designed by each U.S. vendor (GE, Westinghouse, B&W, and CE). Results indicate that in-vessel tube melting will occur following

either debris condition in any of the BWR and PWR vessel designs with lower head penetrations (the reference CE plant does not have any lower head penetrations). Melt is predicted to travel distances well below the lower head for base case debris conditions in any of the reference LWR penetrations if heat transfer from the melt to the tube is conduction-dominated. However, if turbulent heat transfer dominates, melt is predicted to travel only to ex-vessel locations through tubes with larger areas available for melt flow, such as the BWR drain line and instrument tubes. Failure maps indicate that ex-vessel tube temperature peaking near values where failure may occur is specific to the BWR drain line because of its relatively large effective diameter for melt flow and its material composition. For example, failure maps indicate that most other LWR penetrations will remain intact if subjected to base case metallic or ceramic debris conditions.

Structural analyses were performed to ascertain time-dependent (up to 24 hour) vessel response, assuming debris is unable to enter a penetration for two types of accident conditions. The primarily metallic (Case I-1) and ceramic (Case II-1) debris represented the lower and upper bound thermal challenges to the vessel from relocation of base case debris scenarios considered in this study. Results from these analyses indicate that if accident conditions include a primarily metallic debris, vessel failure will not occur, with less than 1% creep damage predicted after 24 hrs. If primarily ceramic debris is unable to enter a penetration, vessel failure is predicted in less than 4 hours after debris relocation, initiating on the outside wall of the vessel and progressing inward. Plastic deformation for both cases is negligible.

The ceramic case fails by localized thinning from creep deformation in the bottom (lowest elevation) of the vessel. Examination of this region reveals that creep strains for the first 1.5 hours after debris relocation are quite low. However, between 1.5 and 4 hours, creep strains grow exponentially with the largest strains in the outer, cooler regions of the vessel wall. The stress history of several locations through the wall thickness shows that, though system pressures create a relatively uniform tensile stress through the wall, superposed compressive thermal stresses on the inside portions and tensile thermal stresses on the outside result in a stress gradient that is larger in the outer portions of the vessel wall. Evidently under these conditions, creep deformation is more sensitive to the difference in stress than to difference in temperature. Creep damage is also higher on the outside, leading to the conclusion that failure initiates on the outside and progresses inward.

Both creep strain and creep damage remain very low for the first 1.5 hours after ceramic debris relocation. Thereafter, they both rise exponentially with time. The creep strain and creep damage relations are separate, independent functions of stress, time, and temperature fit to data from material property testing. Therefore, concurrence of these two independent parameters is a qualitative verification of the material properties and finite-element method used in this analysis.

5.6 References

5-1. *Reactor Safety Research Semiannual Report July–December 1987*, NUREG/CR-5039, SAND87-2411 (Vol. 2 of 2), 1988.

5-2. R. S. Chambers, *A Finite Element Analysis of a Pressurized Containment Vessel During Core Melt Down*, SAND87-2183, Sandia National Laboratory, 1987.

5-3. L. E. Anderson et al., *Effects of a Hypothetical Core Melt Accident on a PWR Vessel with Top-Entry Instruments*, EPRI, IDCOR Program Technical Report 15.2A, Electric Power Research Institute, June 1983.

5-4. P. Gruner and H. Schulz, "Investigations on the Primary Pressure Boundary within Risk Analyses of German PWRs," Transactions of the 10th International Conference on Structural Mechanics in Reactor Technology, SMIRT-10/M, 1989.

5-5. S. A. Hodge and L. J. Ott, *Failure Modes of the BWR Reactor Vessel Bottom Head*, Boiling Water Reactor Severe Accident Technology Program, ORNL/M-1019, Oak Ridge National Laboratory, May 10, 1989.

5-6. G. L. Thinnes and R. L. Moore, "Comparison of Thermal and Mechanical Responses at the Three Mile Island Unit-2 Reactor Vessel," *Nuclear Technology, 87*, 4, December 1989.

5-7. Tennessee Valley Authority, *Brown's Ferry Nuclear Plant Final Safety Analysis Report*, Unit 1, Docket No. 50-259, September 1970.

5-8. Yankee Atomic Power Company, *Maine Yankee Atomic Power Station Final Safety Analysis Report*, (through Amendment 66), Docket Number 50-309, August 1972.

5-9. Philadelphia Electric Company, *Peach Bottom Units 2 and 3 Final Safety Analysis Report*, (through Amendment 68), Docket No. 50-277, November 1972.

5-10. United States Steel, *Steels for Elevated Temperature Service*, ADUSS 43-1089-05, December 1974.

5-11. *Boiler and Pressure Vessel Code*, Section III, Division I, Appendix I, Table I-3.1, American Society of Mechanical Engineers, 1989.

5-12. C. M. Allison and E. M. Johnson (eds.), *SCDAP/RELAP5/MOD2 Code Manual, Volumes 1, 2, 3 and 4*, NUREG/CR-5273, EGG-2555, 1989.

5-13. *ABAQUS User's Manual*, Version 4.8, Providence, RI: Hibbitt, Karlsson, & Sorensen, Inc., 1989.

5-14. PDA Engineering, *PATRAN Plus User Manual*, Release 2.5, Costa Mesa, CA, 1990.

5-15. R. E. Henry et al., "Cooling of Core Debris within the Reactor Vessel Lower Head," *Annual Meeting of the American Nuclear Society, Orlando, FL, June 2-6, 1991.*

5-16. J. Garnier, *Ex-Reactor Determination of Thermal and Contact Conductance*, NUREG/CR-0330, 1979.

5-17. F. Mayinger et al., *Examination of Thermal-Hydraulic Processes and Heat Transfer in a Core Melt*, BMFT RS 48/1, Institute für Verfahrenstechnik der T.U. Hanover, 1976.

5-18. M. Jahn and H. H. Reineke, "Free Convection Heat Transfer with Internal Heat Source Calculations and Measurements," *Proceedings of the 5th International Heat Transfer Conference*, Tokyo, Japan, September 1974, pp. 74–78.

5-19. B. Frantz and V. K. Dhir, "Experimental Investigation of Natural Convection in Spherical Segments of Volumetrically Heated Pools," *ASME Proceedings of the 28th*

AIChE/ANS/ASME National Heat Transfer Conference, San Diego, July 1992 (HTD-Vol. 192, Thermal Hydraulics of Severe Accidents, ASME 1992).

5-20. E. W. Coryell et al., *Theory and Model Descriptions Made for Savannah River Site Severe Accident Analysis*, EGG-EAST-9282, EG&G Idaho, Inc., September 1990.

5-21. F. J. Moody, *Introduction to Unsteady Thermofluid Mechanics*, New York: John Wiley & Sons, 1990.

5-22. M. Epstein, "Heat Conduction in the UO_2-Cladding Composite Body with Simultaneous Solidification and Melting," *Nuclear Science and Engineering, 51*, 1976, pp. 310-323.

5-23. R. W. Ostensen and J. F. Jackson, *Extended Fuel Motion Study*, ANL-RDP-18, Argonne National Laboratory, July 1973.

5-24. G. B. Reddy and D. J. Ayers, *High-Temperature Elastic-Plastic and Creep Properties for SA533 Grade B Class 1 and SA508 Materials*, NP-2763, Electric Power Research Institute, 1982.

5-25. G. V. Smith, *Evaluation of the Elevated Temperatures Tensile and Creep-Rupture Properties for C-Mo, Mn-Mo, and Mn-Mo-Ni Steels*, Metal Properties Council, American Society for Testing and Materials, ASTM Data Series Publication DS47, 1971.

5-26. H. Kraus, *Creep Analysis*, New York: John Wiley & Sons, 1980.

6. DISCUSSION AND CONCLUSIONS

This section summarizes work that was performed to accomplish the lower head research program objectives outlined in Section 1. Section 6.1 describes major accomplishments and insights gained from failure analyses. Section 6.2 presents the examples that illustrate how models developed from various tasks can be applied to determine which failure mechanism will occur first in a particular reactor design. Finally, Section 6.3 lists areas that have been identified where additional research could reduce uncertainties related to lower head failure predictions.

6.1 Major Accomplishments and Insights from Lower Head Failure Analyses

A wide range of tasks have been completed as part of this research program. This section describes the tasks and summarizes major insights gained from performing the tasks.

6.1.1 High-Temperature Creep and Tensile Data for Vessel and Penetration Materials

The lower heads of commercial power reactor pressure vessels are generally fabricated from the plate material SA533B1 or its predecessor, SA302B, which has very similar structural properties. Lower head penetrations, such as instrument tubes, control rod guide tubes, and the drain nozzle are constructed of Inconel 600, 304 stainless steel, or SA105/SA106B carbon steel. High-temperature creep and tensile tests were performed for these materials so that structural analyses can be made in much higher temperature regimes than previously possible.

Before these tests, no creep and tensile data existed for the SA533B1 material at temperatures above 922 K. Because this material undergoes a ferritic to austenitic phase change at temperatures near 1000 K, it was recognized that higher temperature data were needed to accurately predict vessel response. Creep tests were completed up to 1373 K, and tensile tests were completed up to 1473 K. Relationships were developed for using these data in simple analytical models and in finite element structural analysis codes.

Creep tests were performed on Inconel 600 and stainless steel at temperatures up to 1366 and 1350 K, respectively. Tensile tests were performed on these materials at temperatures up to 1373 K. For the SA106B material, creep tests were completed up to 1050 K, and tensile tests were completed up to 1150 K. Relationships were developed for using these data in simple analytical models and in finite element structural analysis codes.

Although the new data are beneficial because they extend into temperature regions where data were previously unavailable, the data are limited, and additional tests are needed to reduce the range of uncertainty associated with these data. In particular, data were not previously available for the SA106 material at temperatures above 811 K, and extrapolation of previously available data indicated that the ultimate strength of this material became negligible at 1000 K. However, test results indicate that the ultimate strength of SA106B material is considerably stronger than indicated by previous data. Hence, additional SA106B tests are needed so that the ultimate strength of this material can be predicted at temperatures above 1150 K.

6.1.2 Review of Previous Failure Analyses

A literature search was conducted to review previous experimental and analytical studies of mechanisms that have the potential to cause lower head failure. Previous analyses for predicting in-vessel and ex-vessel tube failure were limited. No previous analyses for predicting localized vessel failure were found in the literature. Limited, if any, model validation was found that was applicable to LWR severe accidents.

The literature review was useful for identifying existing methods or selecting new approaches for predicting vessel and penetration failure. For example, two methods that were previously employed to predict melt penetration distance in channels were used to predict melt penetration distance in lower head penetrations (although one of the methods was modified to include heat losses to coolant present in the tubes). Furthermore, the review suggested that previous analyses of penetration failure were deficient because they did not simultaneously consider the competing failure mechanisms of tube ejection, tube rupture, and global vessel rupture.

6.1.3 Review of Accident Thermodynamic and Vessel Geometric Conditions

A literature search was conducted to determine appropriate ranges for thermal-hydraulic conditions and vessel geometrical parameters that are input to failure calculations. Previous accident analyses concentrated on a limited number of plants and accident scenarios. Furthermore, results for a particular reactor and event varied significantly because of differences in the phenomena modeled and assumptions related to the event's progression. Hence, it was decided to look at bounding conditions (for example, high pressure versus low pressure events and flooded versus dry containment cavities). A review of plant-specific features affecting vessel failure, such as vessel and penetration geometry, internal structure geometry, and vessel cavity configuration, identified dramatic differences between vendor designs. Hence, it was decided to use dimensionless groups to characterize appropriate ranges for plant-specific features so that a broader range of conditions could be considered simultaneously.

6.1.4 Analytical and Simplified Numerical Lower Head Failure Calculations

Because a wide range of reactor designs and severe accident conditions must be considered, this research program relied heavily on models with closed-form or simplified numerical solution techniques. Results are typically presented as failure maps, developed in dimensionless groups so that a broader range of conditions could be considered simultaneously. Models with closed-form solution techniques were developed for predicting vessel and penetration thermal response, timing for key severe accident phenomena (such as melt relocation and coolant boiloff), in-vessel tube melting, gravity- and pressure-driven melt velocity through a failed tube, and ex-vessel tube failure at low pressure. An existing model and a modified version of an existing model were applied to bound the distance that melt would penetrate through a failed tube or a tube with no internal structures. For high-pressure analysis, a simple model was developed that simultaneously predicts the potential for tube ejection, tube rupture, and global vessel rupture. An existing model was applied for predicting the potential for corium melt to impinge coherently upon the lower head. A finite-difference model was developed for predicting a localized creep rupture.

Thermal analyses were performed to obtain order-of-magnitude estimates for PWR and BWR responses using values typical of depressurized severe accident conditions. Results from these models indicate that a PWR transient will proceed more rapidly (by as much as a factor of two) than a BWR transient. These results were attributed to higher ratios of BWR structural

mass per heat generation rate, larger initial BWR water inventories, and thicker BWR lower heads.

The maximum amount of heat that can be transferred to the lower head from a coherent jet of debris was estimated by using the THIRMAL/0 code. A variety of debris and vessel system conditions were considered for four reference reactor designs that are representative of U.S. LWR vendors (CE, GE, B&W, and Westinghouse). In PWR designs, the presence of flow plates in the lower plena and the hole configuration within these flow plates strongly affect jet impingement. For B&W plants, the flow plates accumulate the melt and form multiple jets, reducing the jet velocity and the fraction of initial jet energy that can impinge on the vessel lower head. Unlike the flow plates in a B&W plant, flow plates in Westinghouse and CE plants do not generally accumulate melt, allowing "straight shot" jets to occur in any horizontal structural plates. The GE BWR lower head is protected by a water pool, which is deeper than water pools in PWR lower plena.

An order-of-magnitude estimate of the thermal requirements for debris to induce tube melting was obtained by applying a heat balance to a penetration tube in contact with corium debris. Results indicate that the ratio of the tube-to-debris mass in the lower head governs the potential for in-vessel tube melting to occur. Since BWR vessels have a larger number of penetrations, higher temperature debris is needed to cause in-vessel tube melting in this reactor vessel. For example, in cases where no coolant is present in the reactor vessel lower head, ceramic debris temperatures greater than 1700 K are required to induce tube melting in a PWR, where only instrumentation tubes penetrate the lower head; whereas ceramic debris temperatures in excess of 2000 K are required to induce tube melting in a BWR lower head.

Order-of-magnitude estimates for the velocity of viscous melt through failed tubes were obtained by applying the energy equation for steady, adiabatic flow. The magnitude of the melt's velocity is dependent on the differential pressure across the melt, melt composition, tube effective diameter for melt flow, and in-vessel tube length. Tube geometry and melt composition effects were each found to affect melt velocity predictions by 10%. The differential pressure across the melt was found to have the most influence on melt velocity predictions. For higher differential pressures (8.6 to 17 MPa), velocity predictions ranged from 35 to 63 m/s. For depressurized reactor conditions, velocity predictions ranged between 1.8 to 2.6 m/s. Hence, gravity-driven melt velocity predictions are relatively low for all of the melt material properties and penetration geometries considered.

Melt penetration distances through failed tubes or tubes with no in-vessel structures were estimated by applying two models: (a) the conduction model, where a crust is assumed to form along the tube surface, so that conduction heat transfer through this crust dominates melt behavior; and (b) a modified bulk freezing model, where turbulence within the melt is assumed to preclude crust formation, so that turbulent heat transfer dominates melt behavior. The bulk freezing model applied in these calculations was modified to consider the effects of coolant that are present in some lower head penetration flow paths. Results for a case with gravity-driven melt flow indicate that melt penetration distances predicted by the conduction model are considerably longer than those predicted by the modified bulk freezing model. In fact, melt is predicted to travel below the lower head through all LWR penetrations if the conduction model is applied; whereas melt is only predicted to travel below the lower head through penetrations having larger effective areas for melt flow and/or penetrations that are ablated near the vessel inner surface if the modified bulk freezing model is applied. Experimental data are needed to determine which of these models is appropriate for severe accident analysis.

For depressurized reactor vessels, thermal equilibrium calculations were used to provide order-of-magnitude estimates for minimum debris requirements, such as the debris relocation temperature and the debris heat flux, necessary to induce ex-vessel tube failure. Results indicate that tube geometry and material are important parameters in predicting tube failure. Although additional data are needed to quantify ultimate strength behavior for the SA105/SA106 material used in BWR drain lines, results indicate that this lower head penetration is more susceptible to ex-vessel tube rupture than other LWR penetrations. Results indicate that heat fluxes characteristic of a mostly ceramic slurry (i.e., in excess of 0.05 MW/m^2) may induce failure in a BWR drain line tube, which is composed of SA105/SA106 steel and has a relatively large cross-sectional area for melt flow. However, higher heat fluxes characteristic of molten ceramic debris (i.e., as high as 0.2 MW/m^2) were not predicted to fail any of the other LWR penetrations.

For higher pressures (between ~0.1 and 16 MPa), analytical models with closed-form solutions were applied to compare the potential for the following failure mechanisms: tube ejection, tube rupture, and global vessel rupture. Failure maps were generated that indicate relative pressure-bearing capacities of vessel heads and their penetrations based on ultimate strength. Failure maps considered three types of debris beds: a primarily metallic debris, a primarily ceramic slurry, and a primarily ceramic molten pool. Failure curves for tube ejection and tube rupture were found to form at the same location near the tube material's melting temperature. For the case of a molten ceramic pool in a BWR vessel, model results indicate that tube failures will occur at lower temperatures than vessel failures for any system pressure. Except for the BWR case with a molten ceramic pool, model results indicate that global rupture is the controlling failure mode in BWRs or PWRs with system pressure above approximately 2 MPa. Although model results indicate that penetration tube failures control below 2 MPa, uncertainties in penetration material ultimate strength data at high-temperatures do not allow a clear distinction of the controlling failure mode in this pressure range.

A new model, based on Reissner's theory of shells with finite deformation, was applied to the problem of local creep rupture on a corium-loaded lower head. This new model was applied to determine how local debris heat sources impact vessel failure times and what conditions are necessary for the formation and failure of a local bulge or cusp to occur. Two types of thermal loads were investigated. The first set of loads used contrived, steady-state temperature profiles to demonstrate the range of behaviors possible under local hot spots. It was found that a local hot spot does not always produce a bulge or cusp as it fails. The failure geometry depends on the creep rate of the balance of the shell relative to the hot spot. If the magnitude of the peak temperature is small, the failure geometry is elliptical, and the hot spot assists or accelerates a failure that looks like global failure. If the magnitude of the peak temperature is large, the hot spot is punched out of a comparatively stiff vessel, and the failure geometry is cusped. The second set of problems examined used transient thermal loads from applied heat fluxes associated with different debris characteristics. All failure geometries in these problems were local because it was assumed that the background heat flux was benign and that the balance of the vessel remained cool. As with the contrived problems, times to failure were very strong functions of applied pressure and peak heat flux. Results indicate that failure times were lengthened for cases with lower system pressure or lower hot spot peak heat fluxes.

6.1.5 Thermal and Structural Finite Element Analyses

More detailed numerical methods were applied to gain insight into the importance of two-dimensional effects in special geometries where models with closed-form solution techniques may be insufficient to investigate the roles of thermal stress and creep in vessel failure. To complete this analysis, an interface was created so that temperatures from the COUPLE model of

SCDAP/RELAP5 could be entered into the structural analysis code, ABAQUS. Analyses considered the effects of debris composition, debris porosity, debris-to-surface gap resistance, reactor coolant pressure, and heat transfer conditions on the outer surface of the drain line and vessel. If melt travels through the drain line to locations below the vessel outer surface, thermal analysis results indicate that drain line failure will not occur in cases where metallic debris relocates to the lower head. In cases where ceramic debris relocates to the lower head, drain line temperatures peak near values where failure may occur within the first few minutes of the transient; whereas vessel failure temperatures do not occur until several hours into the transient. Sensitivity study results indicate that high porosity in a debris bed or high heat removal rates from the vessel and drain line outer surface, such as might occur in a flooded containment cavity, can significantly affect predictions for peak drain line and vessel temperatures. In fact, neither drain line nor vessel failure temperatures are predicted to occur in the ceramic debris cases that assume high porosity debris or high removal rates for exterior drain line and vessel surface heat.

In the event that drain line failure does not occur, structural analysis results indicate that vessel creep rupture can occur as early as 4 hours after debris relocation. For ceramic debris with a 7-MPa pressure, failure occurs from excessive creep deformation that results in thinning at the bottom of the vessel. Failure starts at the outer wall and moves inward, despite the fact that the inside wall is hotter than the outside wall. This pattern results from thermal stresses (compressive on the inside and tensile on the outside) superposed on relatively uniform pressure-induced tensile stresses. Apparently, under these conditions, creep is more sensitive to stress than to temperature. Creep strain and accumulated creep damage in the bottom of the vessel remain relatively low for the first 2 hours, after which both increase quite dramatically until failure is predicted between 3.5 and 4 hours. In the case of metallic debris at low pressures, failure was not predicted because effective creep strains were less than 0.5%. In both the ceramic and the metallic debris cases, plasticity did not play a significant role (strains were less than 0.5%).

6.1.6 Comparison of Closed-Form and Finite Element Structural Analyses

In this document, lower head vessel failure is predicted using models with closed-form and finite element solution techniques. The model with a closed-form solution technique uses a simplified mechanics of materials stress analysis with a tensile (ultimate) strength failure criterion; the finite element model incorporates creep stress analysis with a Larson-Miller/time damage creep failure criterion. Because creep is a time-dependent failure that can occur at stresses below the ultimate strength of a material, the creep analysis will always predict an earlier failure than the tensile strength analysis. This is illustrated by comparing results from the closed-form and finite element models for the primarily ceramic debris case (Case II-1) considered in Section 5.

Figure 6-1 plots the temperature history of the inside and outside vessel walls near the bottom of the vessel. Creep failure is noted on the plot, as well as the finite element ultimate strength failure predicted by the closed-form model, both for a 7-MPa system pressure. Table 6-1 lists the specific values for failure times and temperatures. It is interesting to note that the finite element plastic analysis (no creep behavior) predicts failure at the same time, and hence the same inside and outside wall temperatures, as the closed-form solution model. This indicates that the unconstrained boundary conditions assumed in the simplified analysis are very close to the boundary conditions in the plastic analysis, which included the vessel skirt. It also verifies that thermal stresses (which are accounted for in the finite element analysis, but not in the simplified analysis) do not play a significant role in the timing of ultimate strength failure, as discussed in Section 2.3.

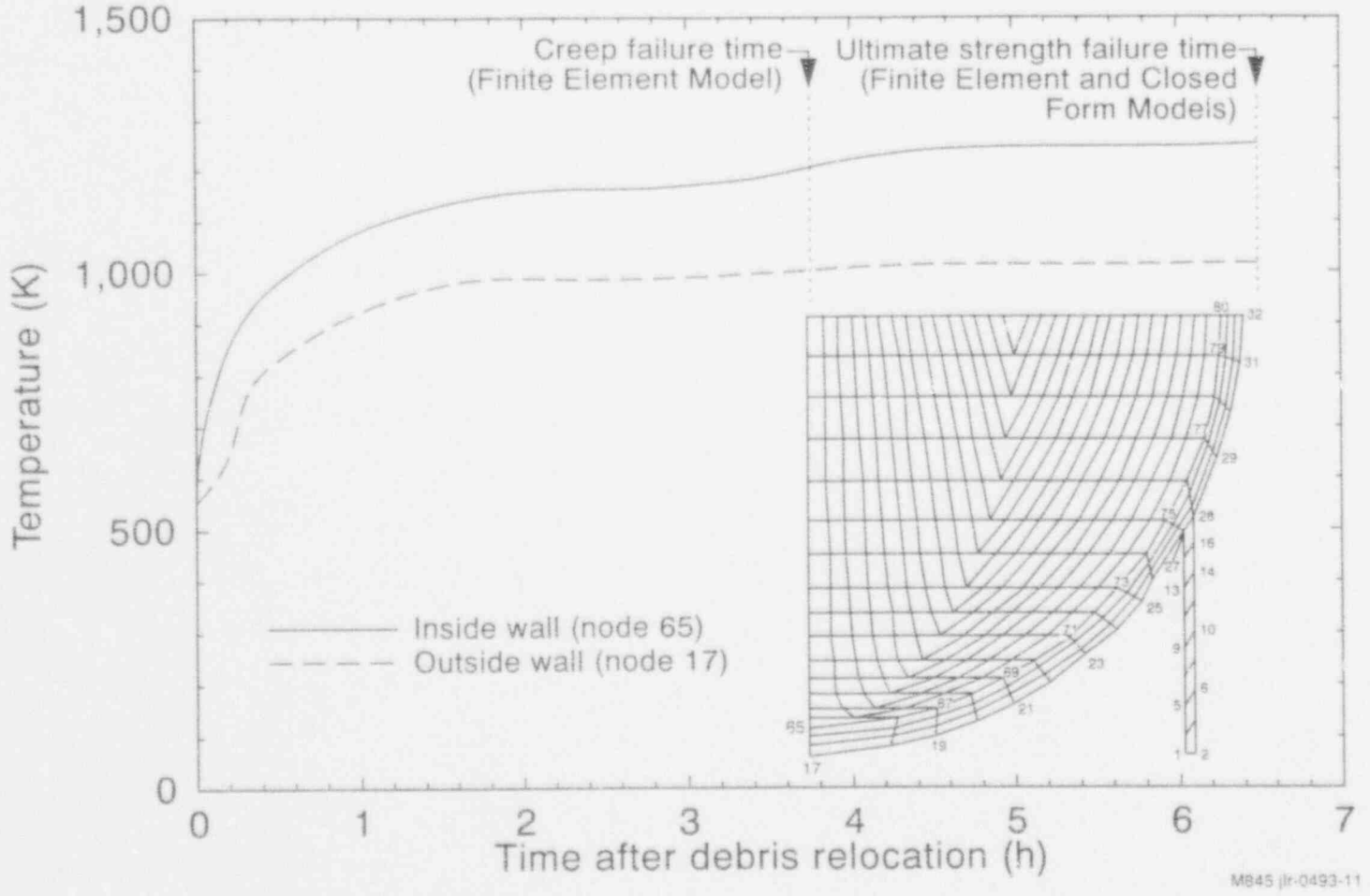

Figure 6-1. Section 5 Case II-1 vessel temperature history.

Table 6-1. Comparison of results from closed-form and finite element solution models.

	Ultimate strength failure analysis		Creep failure analysis
Parameter	Closed-form	Finite element	Finite element
Failure time, h	5.7	5.7	3.7
Inside wall temperature, K	1266	1266	1210
Outside wall temperature, K	1076	1076	1001

Creep failure is predicted at about 3.7 hours, whereas an ultimate strength failure is predicted 2 hours later. The large discrepancy in failure times is a result of the temperature history shown in Figure 6-1. Here, through-wall temperatures exceed half the melting temperature within one hour. The vessel is held at very high-temperatures, but below the point where ultimate strength would be exceeded, for more than 4 hours. Although the temperatures are not high enough to cause an instantaneous (ultimate strength) failure, over time the vessel is degraded, resulting in an early creep rupture failure. Clearly, temperature histories of this type require a creep analysis.

The following general rules of thumb can be used to determine when a creep analysis is necessary:

- Creep analysis is needed when the ultimate strength predicts a long failure time and temperatures are fairly constant, with respect to time, before the predicted failure. This occurs when the vessel approaches thermal steady state at temperatures greater than half the melting point, such as in the ceramic debris case discussed above.

- Creep analysis is not needed if the failure time is short and temperatures are rising rapidly with respect to time, before ultimate strength predicted failure. This corresponds to a case in which relatively high debris heat fluxes are imposed on a vessel with a nearly adiabatic condition on the outer surface. Although technically, creep failure precedes ultimate strength failure, the two events are very closely timed.

- Creep analysis is not needed if ultimate strength failure is not predicted and the peak temperature produces to a creep failure time, predicted by the Larson-Miller parameter, that is longer than the time period of interest. For example, a creep failure time well over 100 hours was predicted in Section 5.3.1.1 for a peak vessel temperature of 950 K (based on temperatures predicted for a vessel subjected to Case I metallic debris in Section 5) and a system pressure of 7 MPa.

A more detailed approach to determining when creep analysis is needed is outlined in Appendix B, Section B-5.1.1

6.2 Application of Models for Predicting Failure

Although a detailed analysis is required to obtain quantitative answers related to event progression, results documented in this report were used to make qualitative judgements about which failure mechanisms are possible and which failure mechanism will occur first during various severe accident scenarios. Using the flow diagram in Figure 1-2, significant questions related to melt relocation and vessel failure were answered to determine which failure mechanisms are possible for three debris configurations: a metallic slurry, a primarily ceramic slurry, and a high-temperature, molten ceramic material that relocates to form a molten pool. Results in Sections 4 and 5 were used to answer questions related to debris relocation and vessel/penetration failure. Results for four representative plant designs are summarized in Table 6-2. Failure analysis results are presented as a function of vessel inner surface temperature and system pressure. *However, it is emphasized that these temperatures and pressures should only be considered as approximate values because there is considerable uncertainty associated with these values.*

The potential for melt to relocate as a coherent jet or for melt to arrive in a coolable configuration was evaluated based on results in Section 4.2.1. Where possible, actual percentages for the fraction of melt arriving as a coherent jet are cited using values in Section 4.2.1. In the case of CE and Westinghouse plants, qualitative judgements were made using the limited results for these plants and results for the B&W and GE plants. The presence of flow plates in the lower plena and the hole configuration within these flow plates strongly affect jet impingement in PWR plants. Lower fractions of melt are predicted to arrive as a coherent jet in a B&W plant because of flow plates that accumulate the melt and form multiple jets. In CE and Westinghouse plants, "straight shot" paths for relocating material are possible. Hence, higher fractions of melt are estimated to arrive as a coherent jet in these plants. Although relocating melt is not impeded by any horizontal plates, the GE BWR lower head is protected by coolant in the lower head, which is deeper than the coolant level in PWR lower plena.

Although small fractions of the metallic slurry may arrive as a coherent jet on the lower head, this debris is predicted to be coolable because most of the melt arrives as solid particles. Results in Section 4.1.2 indicate that molten metallic material will cause in-vessel tube melting. Irrespective of whether conduction or turbulent heat transfer dominates, metallic melt will travel to locations below the lower head through penetrations with larger effective diameters for melt flow, such as the GE drain line nozzle or instrument tube penetrations. However, if turbulent heat transfer dominates, melt will be predicted to migrate below the lower head only if penetrations have larger areas available for melt flow or if penetrations are ablated within the lower head near the vessel inner surface. However, thermal analysis results in Sections 4.1.1.2 and 5.3 indicate that peak vessel and penetration temperatures following relocation of a metallic slurry remain below values where vessel or penetration failure occurs. Hence, neither vessel nor penetration failure is predicted to occur following relocation of a primarily metallic slurry in any of the LWRs considered.

Plant design affects whether a ceramic slurry is predicted to arrive incoherently or coherently upon the lower head. However, thermal analysis results in Section 5.3 indicate that decay heat causes a molten pool to form within debris that relocates to the lower head. Because a high percentage of the melt may arrive as a coherent jet in the CE plant, which has no lower head penetrations, results in Sections 4.1 and 4.2 indicate that both localized and global vessel failures are possible, depending on conditions such as the accident's pressure history, heat removal from the vessel, and heat transfer from the debris to the vessel. To determine if a localized failure occurs before a global vessel failure, one must determine if there are factors such as non-uniform

Table 6-2. Dominant failure modes for various debris conditions and reactor designs.

Reactor type	Debris composition	Debris arrival state	Failure mode
PWR			
B&W	Metallic	Incoherent, coolable	None
	Ceramic Slurry	Incoherent	Localized or global failure for pressures above ~1.5 MPa and vessel inner surface temperatures above ~1000 K; tube failure for pressures less than ~1.5 MPa and vessel inner surface temperatures above ~1600 K.[a]
	Ceramic Pool	Coherent (10-20%)[b]	Localized or global failure for pressures above 2.5 MPa and vessel inner surface temperatures above 1200 K; tube failure for pressures less than 2.5 MPa and vessel inner surface temperatures above 1600 K.
Westinghouse	Metallic	Coherent	None
	Ceramic Slurry	Coherent	Localized or global failure for pressures above 1 MPa and vessel inner surface temperatures above 1000 K; tube failure for pressures less than 1 MPa and vessel inner surface temperatures above 1600 K.
	Ceramic Pool	Coherent (15-40%)	Localized or global vessel failure for pressures above 2.5 MPa and vessel inner surface temperatures above 1200;[c] tube failure for pressures less than 2.5 MPa and vessel inner surface temperatures above 1600 K.
CE	Metallic	Coherent	None
	Ceramic Slurry	Coherent	Localized or global vessel failure
	Ceramic Pool	Coherent (45-60%)	Localized or global vessel failure
BWR			
GE	Metallic	Coherent (<5%)	None
	Ceramic Slurry	Coherent (<7%)	Localized or global failures for pressures above 2 MPa and vessel inner surface temperatures above 1100 K; tube failure for pressures less than 2 MPa and vessel inner surface temperatures above 1600 K.[d]
	Ceramic Pool	Coherent (<10%)[e]	Tube failure (via ejection and/or rupture) for all pressure ranges and vessel inner surface temperatures above ~1200 K.

a. Temperature and pressure values are approximate because temperature distributions depend on assumptions related to accident pressure history, exterior surface heat transfer to the containment, debris-to-vessel heat transfer, etc.

b. Approximately 10% of the material arrives as a coherent jet if a central relocation path is assumed, and less than 20% of the material arrives as a coherent jet if a peripheral relocation path is assumed.

c. Vessel inner surface temperatures are higher in the ceramic pool case because failure is predicted to occur during the initial transient heatup stages of the accident.

d. Because there is considerable uncertainty in the ultimate strength of drain line SA106, analyses suggest that it may be possible for drain line tube failure to occur earlier than global or localized vessel failures at high pressures.

e. No coherent jet reaches the lower head if a central relocation path is assumed; less than 20% of the material relocates as a coherent jet if a peripheral relocation path is assumed.

heat sources in the debris or locations with enhanced debris-to-vessel contact in the debris bed. For plants with lower head penetrations, results in Section 4.1.2 indicate that ceramic melt will cause in-vessel tube melting. Irrespective of whether conduction or turbulent heat transfer dominates, melt will travel to locations below the lower head through penetrations with larger effective diameters for melt flow, such as the GE drain line nozzle or instrument tube penetrations. However, if turbulent heat transfer dominates, melt is predicted to migrate below the lower head only if penetrations have larger areas available for melt flow or if penetrations are ablated within the lower head near the vessel inner surface. For higher pressures (above 1 or 2 MPa) and vessel inner surface temperatures above ~1000 K, results in Sections 4.1.3 and 4.2.2 indicate that global or localized vessel failure generally occurs before tube failure. Because there is considerable uncertainty in the ultimate strength data at high temperature, analyses indicate that it may be possible for drain line failure to occur prior to vessel failure in some cases. However, the exact temperatures and pressures where failure occurs are dependent on factors such as vessel and penetration geometry, material composition, and heat removal conditions from the vessel to the containment. For low pressures, results in Section 4.1.3 indicate that tube failures may dominate in plants with lower head penetrations if vessel inner surface temperatures exceed ~1600 K. However, uncertainties in high-temperature ultimate strength behavior for tube materials make it difficult to determine which failure will occur first at these low-pressure/high-temperature conditions.

Coherent jet impingement of high-temperature ceramic melt is predicted to occur, although the fraction arriving as a coherent jet depends on plant lower plena design. Because a high percentage of the melt arrives as a coherent jet in the CE plant, which has no lower head penetrations, results in Sections 4.1 and 4.2 indicate that both localized and global vessel failure are possible, depending on conditions, such as the accident's pressure history and heat removal from the vessel. For plants with lower head penetrations, results in Section 4.1.2 indicate that ceramic melt causes in-vessel tube melting. Irrespective of whether conduction or turbulent heat transfer dominates, melt is predicted to travel through penetrations to locations below the lower head through penetrations with larger effective diameters for melt flow, such as the GE drain line nozzle or instrument tube penetrations. However, if turbulent heat transfer dominates, melt will be predicted to migrate below the lower head only if penetrations have larger areas available for melt flow or if penetrations are ablated within the lower head near the vessel inner surface. For higher pressures (above around 2.5 MPa), results in Sections 4.1.3 and 4.2.2 for PWRs indicate that global or localized vessel failure occurs before tube failure if vessel inner surface temperatures are above ~1200 K. However, the exact temperatures and pressures where failure occurs are dependent upon factors, such as vessel and penetration geometry, material composition, and heat removal conditions from the vessel to the containment. For low pressures, results in Section 4.1.3 indicate that tube failures may dominate in PWRs with lower head penetrations, once vessel inner surface temperatures exceed ~1600 K. However, uncertainties in high-temperature ultimate strength behavior for tube materials make it difficult to determine which failure will occur first in these PWRs at low pressure. In BWRs with relatively high vessel inner surface temperatures (greater than ~1200 K), tube failures are predicted to occur before vessel failures for all pressure ranges.

6.3 Areas for Additional Work

Several areas have been identified where additional work could reduce uncertainties in predicting vessel failure. Major areas are listed below:

- *Additional High-Temperature Penetration Material Creep and Tensile Data.* As discussed in Section 6.1.1, the ultimate strength behavior of penetration tube material (Inconel, stainless steel, and SA106B carbon steel) is not well defined at high-temperatures. In fact, before the NRC Lower Head Failure Program, high-temperature data for these materials were limited, if nonexistent, for temperatures above 1000 K. As discussed in Appendix B, a limited number of high-temperature tests for penetration tube materials have been completed. Although the new data are beneficial because they extend into temperature regions where data were previously unavailable, the data are limited, and additional tests are needed to reduce the range of uncertainty associated with these data. In particular, data were not previously available for the SA106 material at temperatures above 811 K, and extrapolation of available data indicated that the ultimate strength of this material became negligible at 1000 K. However, test results indicate that the ultimate strength of SA106B material is considerably stronger than indicated by previous data. Hence, additional SA106B tests are needed to reduce the uncertainty in predicting the ultimate strength of this material at temperatures above 1150 K.

- *Model Validation.* As noted in Section 6.1, a limited amount of the validation for failure analysis models is applicable to LWR severe accident conditions. Several organizations are performing experiments that are applicable to LWR vessel failure analyses. Additional work should be performed to validate models used for lower head failure calculations.

- *Additional Application to a Broader Range of Conditions.* Although an extensive effort has been made to apply failure models for a wide range of severe accident conditions, additional applications could reduce failure analysis uncertainties. For example, it is desirable to apply the newly-developed localized creep rupture model to cases where a larger angle of the vessel is exposed to a peak temperature distribution.

- *Structural Analysis of PWR Vessel.* PWR vessel plastic and creep response have not been addressed in this study. Given the thinner vessel wall and higher operating pressure, it is possible that both creep and plasticity will play a role in PWR vessel failure.

Appendix A

Nomenclature

Appendix A

Nomenclature

Lower Case

a_{gas} - Gap steam accommodation coefficient

b - Midwall radius of hemispherical shell (m)

c_{pl} - Liquid coolant specific heat capacity (J/kgK)

c_{pg} - Vapor coolant specific heat capacity (J/kgK)

c_{pd} - Debris specific heat capacity [may be further designated with the subscript (m) for molten debris, or (s) for solid debris] (J/kgK)

c_{pt} - Tube material specific heat capacity (J/kgK)

c_{pv} - Vessel specific heat capacity (J/kgK)

d_e - Effective diameter of melt (length - mm, cm, or m)

d_h - Vessel penetration hole diameter (length - cm or m)

d_{hole} - Lower plenum structure hole diameter (length - mm, cm, or m)

d_i - Tube inner diameter (length - cm or m)

d_i - Damage accumulated during a time interval, Δt_i

d_o - Tube outer diameter (length - cm or m)

d_{so} - Penetration tube internal structure outer diameter (cm)

f_f - Dimensionless friction factor

g - Gravitational acceleration (980 cm/s^2 or 9.8 m/s^2)

g_1, g_2 - Temperature jump distances (m)

h_c - Critical thickness of accumulated melt (m)

h_{fg} - Coolant heat of vaporization (J/kg)

h_{gap} - Debris to structure gap convective heat transfer coefficient (W/m^2K)

h_{in} - Inlet enthalpy (J/kg)

h_L - Head loss due to friction (m^2/s^2)

h_{out} - Exit enthalpy (J/kg)

h_t - Convective heat transfer coefficient from molten debris to structure [may be further designated with the subscript (o) to signify cases without melt/water or melt/structure interactions during melt relocation] (W/m^2K)

h_{tv} - Convective heat transfer coefficient from the vessel to the building atmosphere (W/m^2K)

k_d - Debris thermal conductivity [may be further designated with the subscript (m) for molten debris or (s) for solid debris] (W/mK)

k_g - Thermal conductivity of steam in vessel/debris gap (W/mK)

k_p - Most probable wave number

k_t - Tube material thermal conductivity (W/mK)

k_v - Vessel thermal conductivity (W/mK)

l_t - In-vessel length of penetration tube containing debris (length - mm, cm, or m)

l_o - Ex-vessel length of penetration tube containing debris (length - mm, cm, or m)

m - Dimensionless parameter used to nest nodes (degrees-of-freedom) in or around a hot spot (Section 4.2.2)

$\dot{m}$ - Melt relocation rate (kg/s)

$\dot{m}_{in}$ - Inlet coolant mass flow rate (kg/s)

$\dot{m}_{out}$ - Exit coolant mass flow rate (kg/s)

p_i - Internal pressure (MPa)

q'' - heat flux from the debris to the vessel [may be further designated by the subscripts (ceramic slurry), (metallic), or (molten pool) to describe different debris conditions or (peak) to describe hot spot heat flux] (MW/m^2)

$\tilde{q}_d(0)$ - Initial debris heat flux (MW/m^2)

$\bar{q}_d(0)$ - Initial debris volumetric heat source (MW/m^3)

r - Radial location [may be further designated by the subscript (o) to denote the original (undeformed) value] (length - mm, cm, or m)

r_h - Radius of penetration hole in pressure vessel lower head (length - mm, cm, or m)

r_i - Inside radius of penetration tube (length - mm, cm, or m)

r_o - Outside radius of penetration tube [may be further designated by the subscripts (T) or (P) to describe a change in outside radius due to temperature or pressure changes] (length - mm, cm or m)

t - Time (time - s or hours)

t_1^* - Dimensionless time $[6t\alpha_{tv}/t_v^2]$

t_2^* - Dimensionless time $[(t-t_{vp})/\tau_v]$

t_{bo} - Boiloff time (s)

t_d - Debris height (m)

t_r - Time to creep rupture (hours)

t_{rel} - Relocation time (time - s or hours)

t_t - Penetration tube wall thickness (length - mm, cm, or m)

t_{tm} - Thermal relaxation time for tube melting (s)

t_{tol} - Tolerance limit for failure time (s or hours)

t_{tp} - Thermal relaxation time required for transmittal of a thermal front through a penetration tube wall (s)

t_u - Time to ultimate strength failure (s or hours)

t_v - Reactor pressure vessel lower head thickness [may be further designated with the subscript (o) to denote original (undeformed) value] (length - cm or m)

t_{vp} - Thermal relaxation time required for transmittal through the vessel wall (s)

u - Radial displacement (m)

u_c - Coolant internal energy [may be further designated by the superscript (b) for beginning state or (e) for end state] (J/kg)

u_d - Debris internal energy [may be further designated by the superscript (b) for beginning state or (e) for end state] (J/kg)

v - Differential shear force (N/m)

v_d - Melt velocity [may be further designated by the subscript (1) for tube entrance, (2) for tube exit, or (avg) for average tube velocity] (m/s)

w - Axial displacement (m)

x - Distance through vessel wall (Section 4.1.1) (m)

x - Dimensionless fraction of the available effective flow area for melt in a penetration in (Section 4.1.2)

y - Vertical location of debris within a tube [may be further designated by the subscript (1) to denote the tube entrance or (2) to denote the tube exit] (m)

z - Axial location [may be further designated by the subscript (o) to denote original (undeformed) value] (m)

Upper Case

A - Area of impingement zone [may be further designated by the subscript (o) to denote cases without any melt/water or melt/structure interactions during melt relocation] (m^2)

A_{eff} - Effective flow area for melt within a vessel penetration (m^2)

A_d - Cross-sectional area of debris surrounding a penetration in a lower head unit cell (m^2)

A_t - Cross-sectional area encompassed by a penetration in a lower head unit cell (m^2)

A_{tx} - Tube cross-sectional area (m^2)

Bi_v - Vessel Biot number ($h_{tv}t_v/k_v$)

D - Total accumulated damage

D_J - Jet diameter [may be further designated by the subscript (o) to denote cases without any melt/water or melt/structure interactions during melt relocation] (length - cm or m)

E - Young's Modulus [may be further designated with the subscript (o) to denote value at midplane] (MPa)

E_t - Total energy deposited [may be further designated with the subscript (o) for cases without melt/water or melt/structure interactions during melt relocation] (J)

Fr - Dimensionless Froude number

F_p - Pressure force acting on a penetration (N)

G - Shear modulus (N/m^2)

K - Entrance loss coefficient

L - Jet breakup length (m)

L_d - Debris latent heat of fusion (J/kg)

L_t - Tube material latent heat of fusion (J/kg)

L_w - Weld length (m)

LMP - Dimensionless Larson-Miller parameter

M - Moment resultant [may be further designated by the subscript (φ) for values along the meridian, (θ) for values in the hoop direction, (cr) for creep component, (pl) for plastic component, (th) for thermal component, (fr) for finite rotation correction term, or (ym) for Young's Modulus correction term] (N-m/m)

M_c - Coolant mass [may be further designated by the superscript (b) for beginning state or (e) for end state] (kg)

M_d - Debris Mass [may be further designated by the superscript (b) for beginning state or (e) for end state] (kg)

M_{gas} - Steam molecular weight (kg/kg-mole)

M_t - Tube mass (kg)

N - Force resultant [may be further designated by the subscript (φ) for values along the meridian, (θ) for values in the hoop direction, (cr) for creep component, (pl) for plastic component, (th) for thermal component, (fr) for finite rotation correction term, or (ym) for Young's Modulus correction term] (N/m)

Nu - Dimensionless Nusselt number

N_c - Ultimate membrane capacity of vessel wall (MPa•m)

N_{hole} - Dimensionless number of holes in a lower plenum structure

N_p - Membrane load on vessel wall due to pressure (MPa•m)

Pe - Dimensionless Peclet number

Pr - Dimensionless Prandtl number

P - Pressure [may be further designated by the subscript (1) for tube entrance, (2) for tube exit, (gas) for gap steam, (init) for initial, (f) for final, (relief) for relief valve, (th) for tube-hole interface] (pressure - Pa or MPa)

Q - Impinging heat flux [may be further designated with the subscript (o) for cases without melt/water or melt/structure interactions (during melt relocation)] (W/m^2)

$Q_{\varphi\zeta}$ - Shear resultant along normal to deformed middle surface [may be further designated by the subscript (cr) for creep component, (pl) for plastic component, (fr) for finite rotation correction term, or (ym) for Young's Modulus correction term] (N/m)

$\dot{Q}_d$ - Power produced by debris decay heat (J/s)

$\dot{Q}_o$ - Initial power level (J/s)

$\dot{Q}_{ox}$ - Energy production from oxidation (J/s)

$\dot{Q}_s$ - Energy loss rate from the vessel (J/s)

R - Surface roughness of material [may be further designated with a subscript (1) or (2) to denote a particular side of a gap] (m)

R - Principal radius of curvature [may be further designated by the subscript (φ) for deformed principal radius of curvature along the meridian, (φ_o) for undeformed principal radius of curvature along the meridian, (θ) for deformed principal radius of curvature in the hoop direction, or (θ_o) for undeformed principal radius of curvature in the hoop direction] (m)

R - Radius of reactor pressure vessel of the lower head [may be further designated by the subscript (in) for inner, (out) for outer, or (m) for mean or midwall] (length - mm, cm, or m)

R_h - Horizontal distance from the vertical axis/centerline of the spherical head for calculating ξ (m)

Re - Dimensionless Reynolds number [may be further designated by the subscript (J) for a jet]

S - Arc length [may be further designated with the subscript (o) to denote original (undeformed) value] (m)

T - Temperature [may be further designated by the subscript (in) to denote the vessel inner surface temperature, (out) to denote the vessel outer surface temperature, (mp) to denote the vessel liquidus temperature, or (1) or (2) to denote a particular type of temperature distribution (Section 4.2.2)] (K or when used to determine the Larson-Miller parameter, degrees R)

ΔT - Difference between debris and tube temperature (Section 4.1) (K)

ΔT - Difference between jet and vessel temperature [may be further designated by the subscript (o) for cases without melt/water or melt/structure interactions (during melt relocation)] (K)

ΔT - Amplitude of peak temperature distribution (Section 4.2.2) (K)

T_a - Reactor building temperature (K)

T_d - Debris temperature (K)

T_g - Coolant vapor temperature [may be further designated by the subscript (sat) for saturated or (sup) for superheated (K)]

T_{gas} - Gap steam temperature (K)

T_h - Local penetration hole temperature [may be further designated by a subscript to indicate (i) inner or (o) outer vessel wall location] (K)

T_l - Bulk coolant temperature [may be further designated by the subscript (i) for initial, (f) for final, (sub) for subcooled, or (sat) for saturated] (K)

$T_{mp/d}$ - Liquidus temperature for debris material (K)

$T_{mp/t}$ - Liquidus temperature for tube material (K)

T_p - Particle temperature (K)

T_{ref} - Reference temperature (K)

T_t - Local tube mean wall temperature [may be further designated by a subscript to indicate tube position at inner (i) or outer (o) vessel wall] (K)

$T_{t/f}$ - Tube failure temperature (K)

T_v - Vessel temperature [may be further designated by the subscript (i) for inner surface temperature, (o) for outer surface temperature, or (avg) for average through-thickness values] (K)

T_v - Coolant vapor temperature (K)

T_{v1}^* - Dimensionless vessel temperature $[2k_v(T_v-T_{vi})/(q''_d(0)t_v)]$

T_{v2}^* - Dimensionless vessel temperature $[h_{tv}(T_v-T_a)/q''_d(0)]$

U - Velocity [may be further designated by the subscript (E) for erosion velocity, (J) for jet velocity, (c) for critical melt velocity, (l) for coolant liquid velocity, or (v) for coolant vapor velocity] (m/s)

X_p - Axial distance melt penetrates through instrumentation tube prior to plugging (m)

V_c - Coolant volume (m^3)

V_f - Frictional shear force (N)

We_J - Dimensionless Jet Weber number

Greek

α - Mean coefficient of thermal expansion [may be further designated by the subscript (h) for vessel hole, (t) for tube, (vi) for vessel inner surface, or (vo) for vessel outer surface; assumes a reference temperature of 294 K] (m/m/K)

α - Change in arc length with respect to the parametric variable ξ [may be further designated by the subscript (o) to denote the initial (undeformed) value]

α_{td} - Debris thermal diffusivity [may be further designated by the subscript (m) for molten debris or (s) for solid debris] (mm^2, cm^2/s, or m^2/s)

α_{tt} - Tube thermal diffusivity (mm^2/s, cm^2/s, or m^2/s)

α_{tv} - Vessel thermal diffusivity (mm^2/s, cm^2/s, or m^2/s)

β - Rotation of shell midplane from its initial location ($\varphi - \varphi_o$)

γ - Material rotations from normal to the deformed middle surface [may be further designated by the subscript (o) to denote value at midplane]

$\gamma_{\varphi\zeta}$ - Shear strain along the normal to the deformed middle surface [may be further designated by the subscript (cr) for creep component or (pl) for plastic component]

δ - Penetration distance of temperature front through vessel wall (in Section 4.1) (m)

δ_v - Vapor film thickness (Section 4.2.1 and Appendix C) (m)

δ_l - Liquid film thickness (Section 4.2.1 and Appendix C) (m)

δ_i - Difference between the penetration tube outer radius and the vessel hole radius (length - mm, cm, or m)

ϵ - Strain measure [may be further designated by the subscript (e) for elastic strain, (th) for thermal strain, (pl) for plastic strain, (cr) for creep strain, (ΔT) for strain due to temperature change, (φ) for values along the meridian, (θ) for values in the hoop direction, or (ζ) for strains normal to the shell] (m/m)

ζ - Distance between shell material and midplane, measured normal to the deformed middle surface (m)

ε_t - Tube emissivity

θ_d - Dimensionless effective debris temperature

θ_t - Dimensionless effective tube temperature

λ_c - Dimensionless debris solidification constant

λ_t - Dimensionless penetration melting constant

ν - Poisson's ratio [may be further designated by the subscript (t) for tube material]

υ_f - Coolant liquid specific volume (m^3/kg)

υ_g - Coolant vapor specific volume (m^3/kg)

ξ - Parametric variable used to define shell meridian, $0 \leq \xi \leq 1$

ρ_a - Ambient fluid density (kg/m^3)

ρ_c - Coolant density [may be further designated by the subscript (g) for vapor phase or (f) for liquid phase] (kg/m^3)

ρ_d - Debris density (kg/m^3)

ρ_l - Continuous phase density (kg/m^3)

ρ_J - Melt density (kg/m^3)

ρ_t - Tube density (kg/m^3)

ρ_v - Vessel density (kg/m^3)

σ - Stefan-Boltzmann constant (5.672×10^{-8} W/m^2K^4)

σ - Stress [may be further designated by the subscript (a) to denote applied, (u) to denote ultimate, (y) to denote yield, (e) to denote effective, or i (r,φ,θ, or ζ) to denote components in the radial, meridional, hoop, and surface normal directions] (N/m^2)

σ_c - Crust thickness (length - mm, cm, or m)

σ_J - Surface tension (N/m)

σ_u - Ultimate stress (MPa)

τ - Timescale for jet breakup (Section 4.2.1) (s)

$\tau_{\varphi\zeta}$ - Shear stress measure (N/m^2)

τ_v - Time constant in calculating time required for vessel to reach steady-state temperature profile (s)

τ_w - Shear stress in a weld (Section 4.1) (N/m^2)

φ - Angle between the normal to the middle surface and the vertical axis [may be further designated by the subscript (o) to denote original (undeformed) value]

$\Delta\varphi_o$ - Angular spread characteristic of peak temperature distribution

Appendix B

High-Temperature Creep and Tensile Data for Pressure Vessel Steel and Penetration Materials

Appendix B

High-Temperature Creep and Tensile Data for Pressure Vessel Steel and Penetration Materials

B-1. INTRODUCTION

The lower heads of commercial power reactor pressure vessels are generally fabricated from the plate material SA533B1 or its predecessor, SA302B, which has very similar structural properties. Where forgings are required, such as in skirt junctions in the lower head, SA508-CL2 material is used. Lower head penetrations, such as instrument tubes, control rod guide tubes, and the drain nozzle are constructed of Inconel 600, 304 stainless steel, or SA106B carbon steel. This appendix discusses material creep and tensile test data for SA533B1, Inconel 600, 304 stainless steel, and SA106B that have been developed at the Idaho National Engineering Laboratory (INEL) for the U.S. Nuclear Regulatory Commission (USNRC) Lower Head Failure Analysis Program and material creep data for SA508-CL2 developed in a previous USNRC task. With the data supplied in this appendix, structural analyses, both simplified analytical solutions and detailed finite element calculations, can be made in much higher temperature regimes for these vessel materials than previously possible. Section B-2 discusses the SA533B1 tests; Section B-3 covers those for the SA508-CL2 material; Section B-4 covers testing of the penetration materials; Section B-5 discusses the possible use of the data; and Section B-6 offers concluding remarks.

B-2. SA533B1 MATERIAL CREEP RUPTURE AND TENSILE DATA FROM TESTS AT INEL

Previous stress calculations[B-1] to assess creep failure of the reactor pressure vessel lower head during the Three Mile Island (TMI)-2 accident indicated the need for creep and stress-strain curves for the vessel material at very high temperatures. Previously, such data were only available up to 922 K for SA533B1,[B-2, B-3] the plate material in the TMI-2 lower head and the one most common material in all commercial reactor vessel lower heads. A gap in the data remained for these structural properties between 922 K and the melting temperature, 1789 K. At temperatures near 1000 K, SA533B1 undergoes a ferrite-to-austenite phase transformation that can alter material properties considerably. For this reason, the INEL has performed tensile tests up to 1473 K and creep tests up to 1373 K to extend the structural property data base and to aid future structural calculations.

B-2.1 Test Setup

High-temperature behavior of the SA533B1 material presented special problems that caused some difficulty in performing the creep tests. High surface oxidation rates on test coupons at these elevated temperatures required that the creep tests be performed in an inert atmosphere. Therefore, an environmental chamber filled with argon gas was installed around the test coupon to counteract this oxidation effect. Additionally, high ductility of the material at these temperatures required the use of large-ranging extensometers installed inside the environmental chamber to measure the entire time-dependent creep response. Figure B-1 illustrates the creep test setup.

The test coupons for this series of creep and tensile tests were fabricated from archived material obtained from the Midland reactor vessel. Coupons were fabricated from samples having either a meridional orientation with respect to the vessel lower head or a radial, or through-wall, orientation in the vessel plate material (see Figure B-1). Orientation effects were evaluated because of expected variations in strength resulting from the plate rolling process. As a baseline reference, tensile test results for a room temperature test conducted at the INEL have been compared to results of room temperature tensile tests conducted on this same material at other institutions. The INEL results generally lie at the upper end of the tensile test data ranges. They are also within the permissible range of the ASTM material specification for SA533B1.

B-2.2 Tensile Tests

The tensile tests considered variations in material orientation and load strain rate. Initially, tensile tests were conducted by American Society of Testing and Materials (ASTM) Standards E8[B-4] and E21[B-5] that allow a higher loading rate in the plastic range (0.05 m/m/min) than in the elastic range (0.005 m/m/min) for loading rate insensitive material. However, SA533B1 material has some load rate sensitivity, as indicated by the plots of yield and ultimate tensile strength data in Figures B-2 and B-3 when different loading rates are used. In these plots the coupon material is oriented in the meridional direction unless the legend indicates a strain rate accompanied with a "radial" designation. Strain rate variation has some effect on yield strength below temperatures of 1050 K, while the 0.05 m/m/min strain rate increases the ultimate strength by 20% in the 1100 K to 1200 K range. A linear trend is inferred from this curve into the higher temperature ranges up to the melting temperature of 1789 K. The corresponding ductility plots of Figures B-4 and B-5 also indicate the load rate sensitivity of the material. These ductility plots indicate a trend of reducing ductility with some data scatter between 900 and 1250 K. The data scatter is most likely

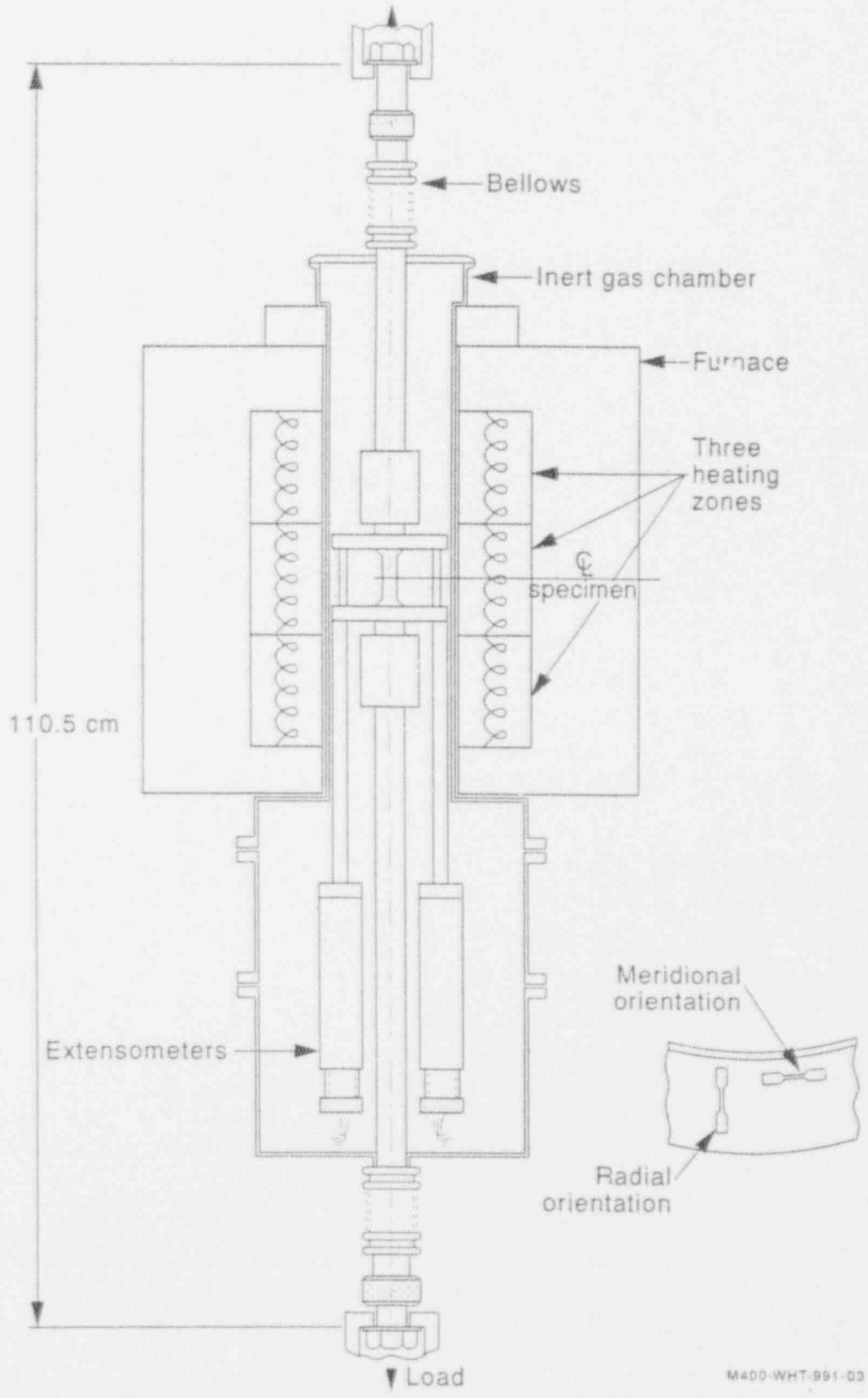

Figure B-1. Schematic of the creep test setup.

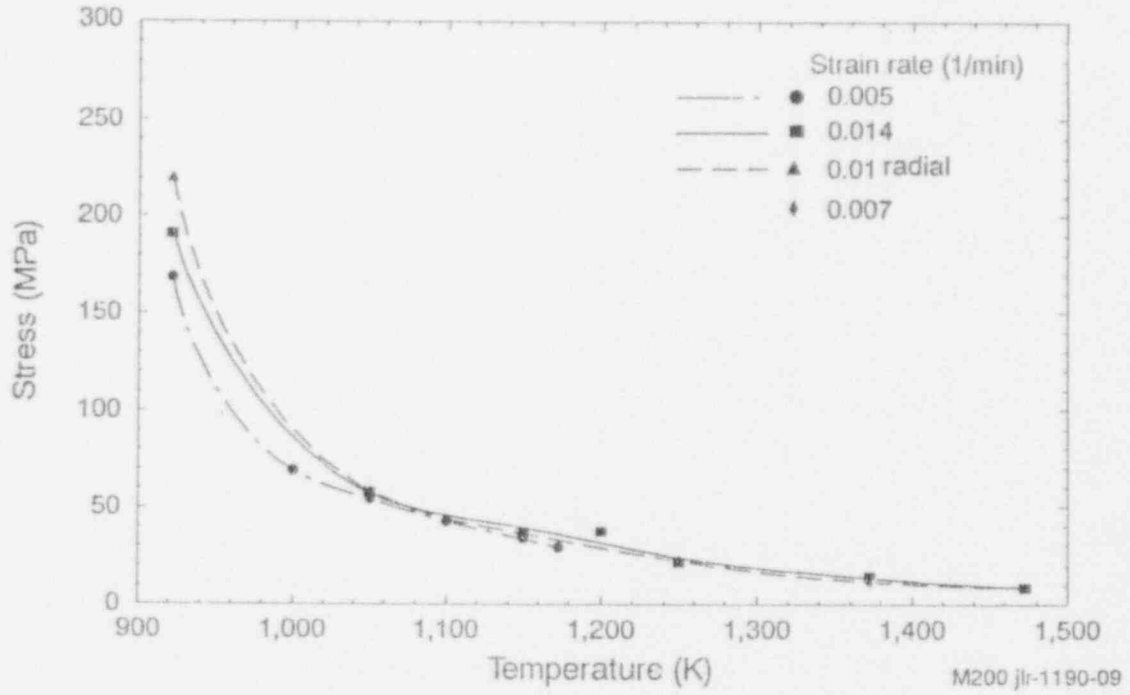

Figure B-2. INEL SA533B1 tensile test results for yield strength.

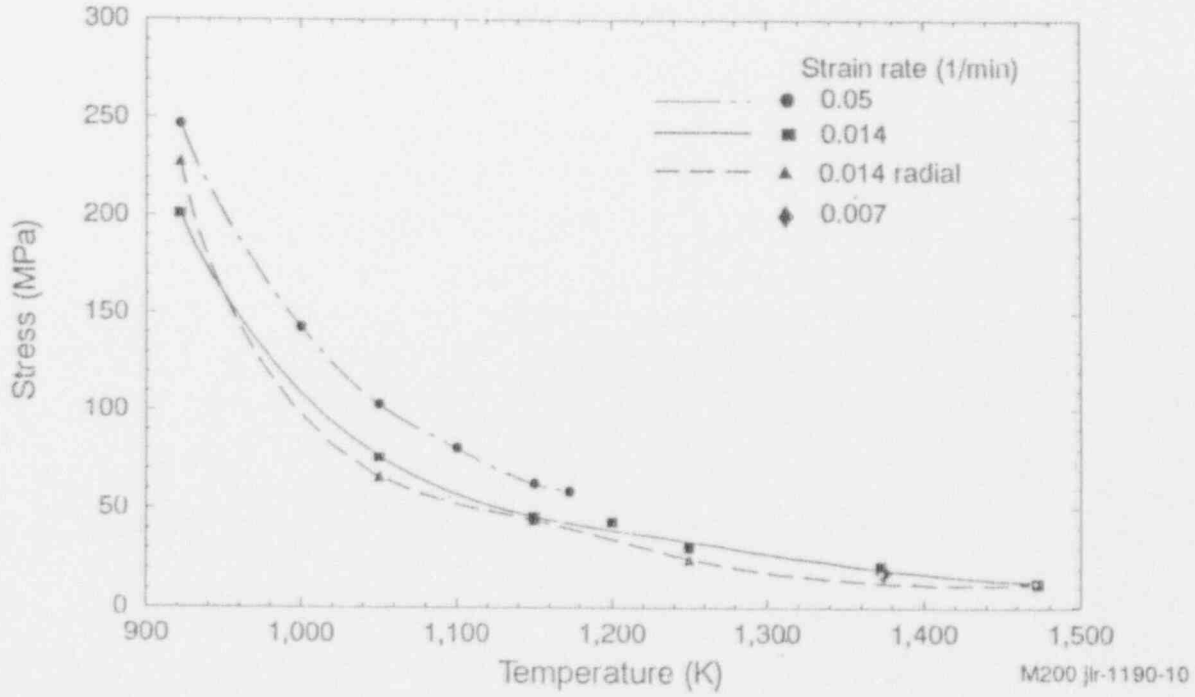

Figure B-3. INEL SA533B1 tensile test results for ultimate strength.

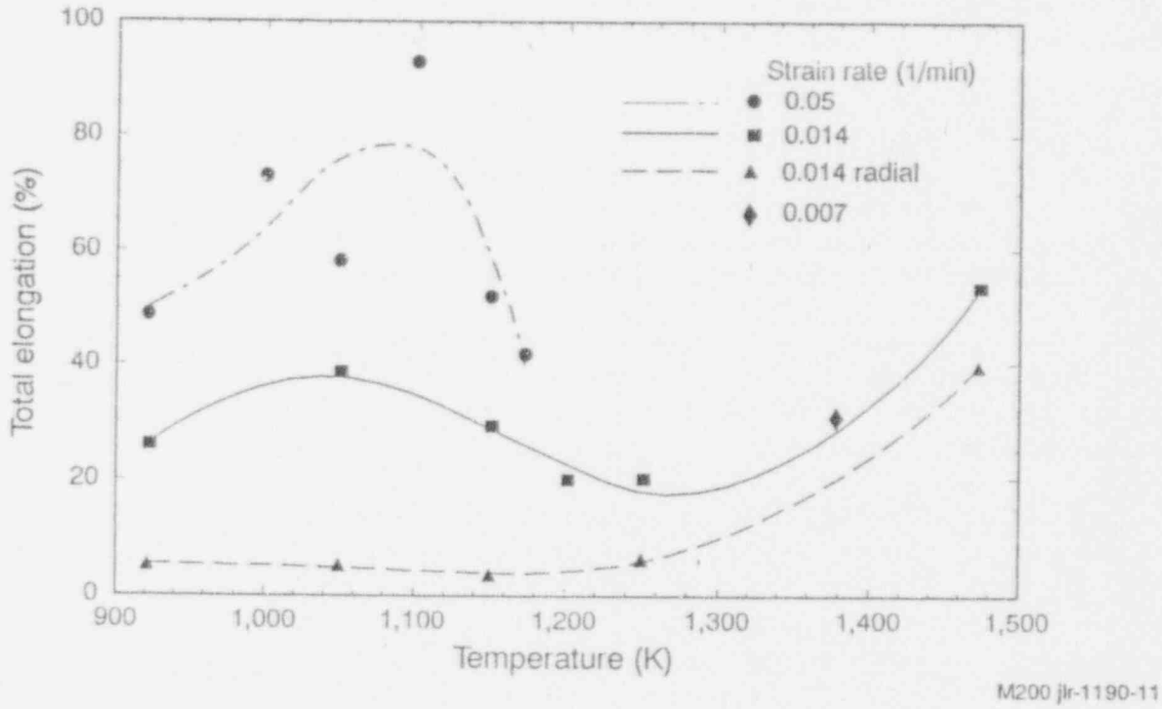

Figure B-4. INEL SA533B1 tensile test results for ductility (elongation).

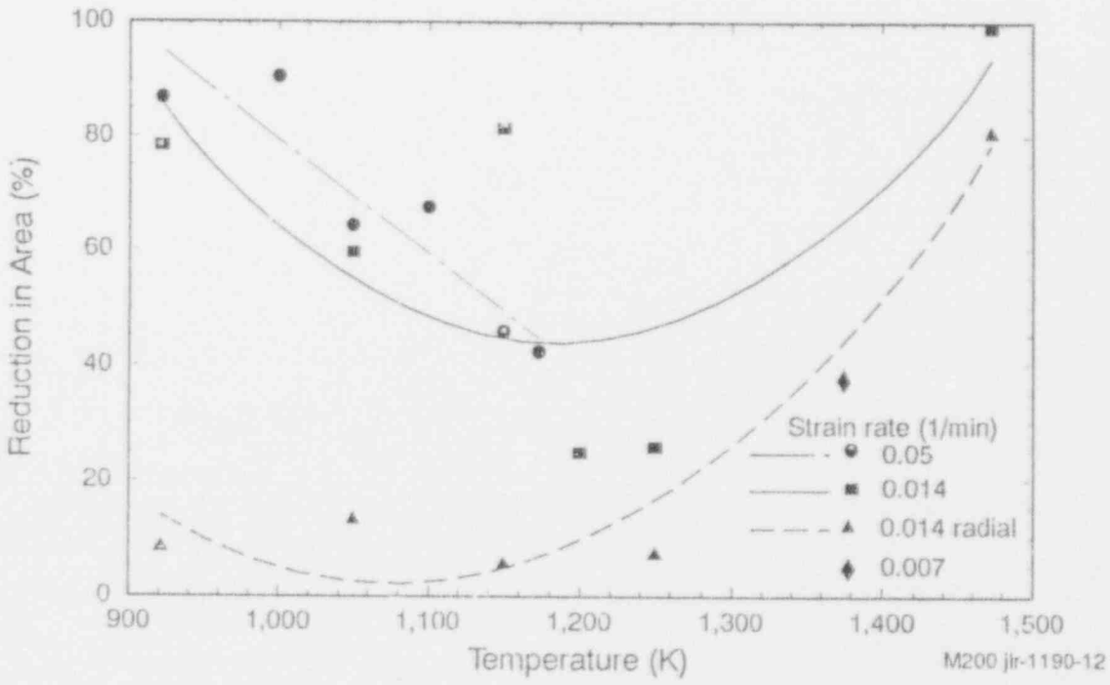

Figure B-5. INEL SA533B1 tensile strength results for ductility (area reduction).

the result of the ferrite-to-austenite phase transformation at about 1000 K. The increasing trend in ductility above 1250 K is probably the result of the austenitic form of this material.

High-temperature ultimate strength and yield strength data obtained from these tests are plotted in Figures B-6 and B-7 with previously published ASTM[B-3] data obtained at lower temperatures. Ultimate strength was the peak stress recorded during the test. Yield strength was determined using a 0.2% strain offset from the linear elastic portion of the curve. Ultimate strength data show excellent continuity between the two studies. Yield strength is continuous except at 922 K, where yield strengths obtained in this study lie above the ASTM data.

INEL strain measurements were intended to capture relatively large deformations. They were not sensitive enough to measure elastic moduli accurately. For this reason, use of published values for elastic moduli, such as EPRI[B-2] or Takeuti,[B-6] is recommended. Figure B-8 shows EPRI and INEL elastic moduli data.

To offer some reference for the tensile test strain rates, a simple calculation[B-7] of the elastic compressive strain $\epsilon_{\Delta T}$ induced in the surface layer of a solid body, such as the vessel lower head wall, when subjected to a surface temperature change, ΔT, is given by

$$\epsilon_{\Delta T} = \frac{\alpha \Delta T}{1 - \nu}$$

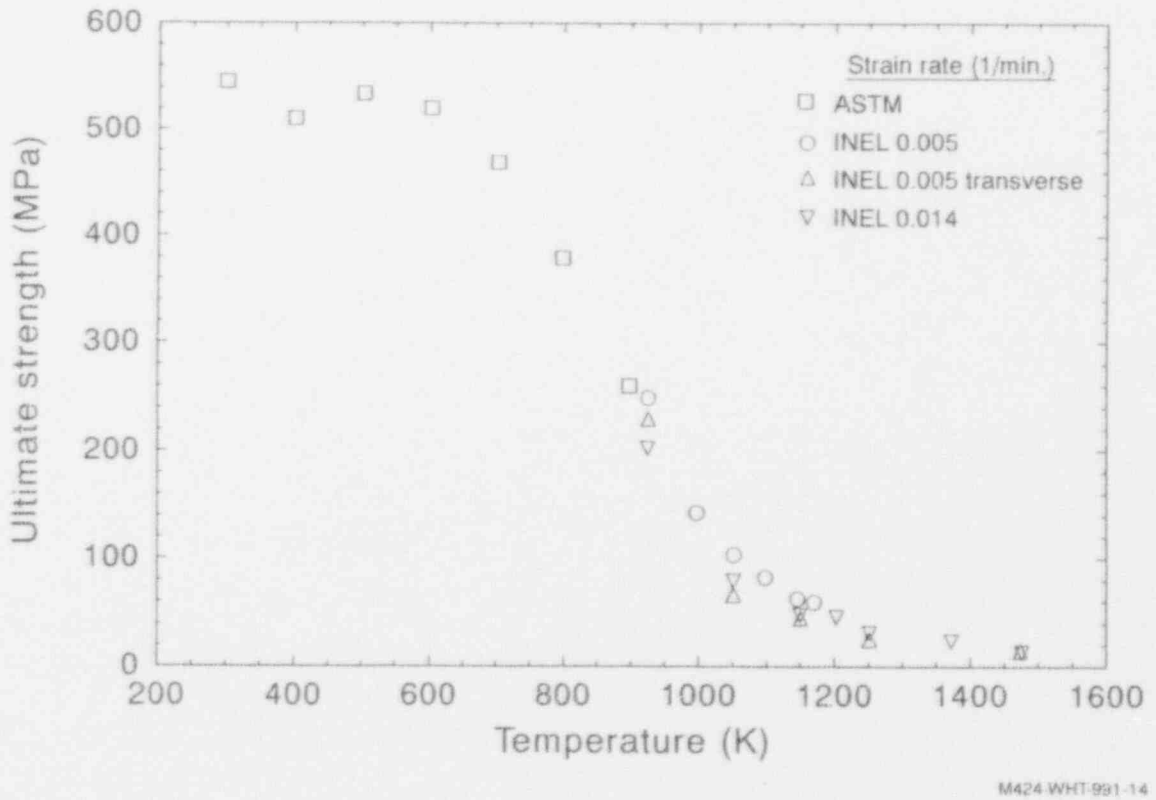

Figure B-6. INEL and ASTM tensile test results for ultimate strength.

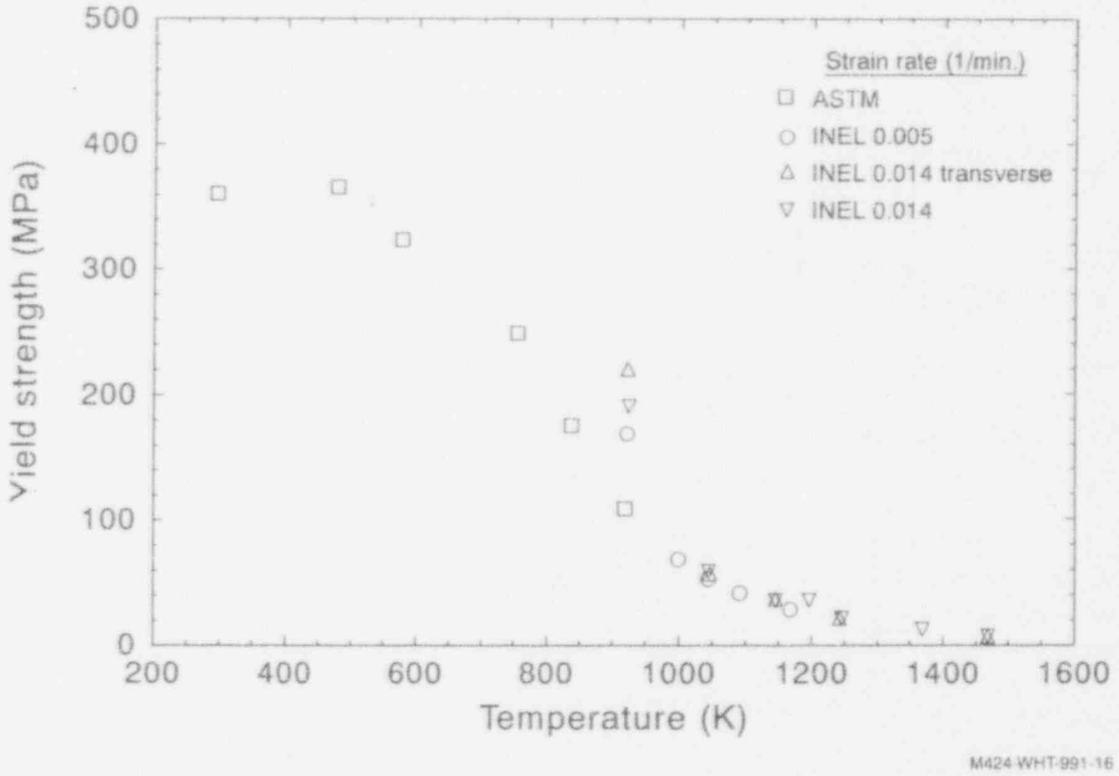

Figure B-7. INEL and ASTM tensile test results for yield strength.

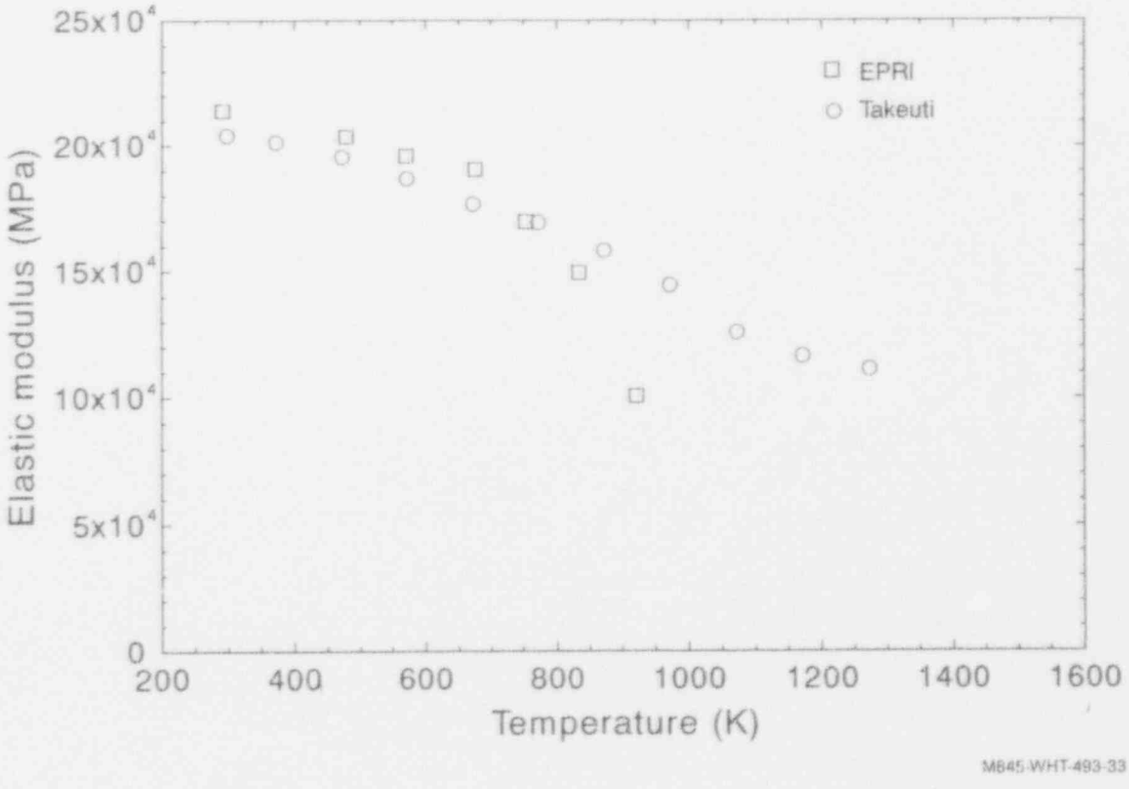

Figure B-8. Published test results for elastic modulus.[B-2,B-6]

where

α = mean coefficient of thermal expansion

ν = Poisson's ratio.

Thus, the strain rate for this condition is directly related to the rate of temperature change. For this material at high temperatures, a temperature change rate of 100 K/min produces a strain rate of approximately 0.003 m/m/min.

Stress-strain curves for meridional specimens have been generated for tensile tests run at a strain rate of 0.014 m/m/min and temperatures ranging from 922 to 1473 K. Results for these tests are shown in Figure B-9.

B-2.3 Creep Tests

The creep tests performed at the INEL are summarized in Table B-1. Thirteen creep tests were performed with temperatures ranging from 900 to 1373 K and times to rupture ranging from 2 minutes to 264 hours. Time dependent creep measurements were recorded as well as the times to rupture for the material. Figures B-10 through B-15 plot these measurements at temperature for the tests summarized in Table B-1. For example, Figure B-10 plots total strain versus time with an applied stresses of 69.71 MPa and 140.1 Mpa for a material temperature of 900 K. This curve shows the primary, secondary, and tertiary phases of creep in the specimen. The secondary, or minimum strain rate, phase of the creep curve is estimated by a linear regression shown on the

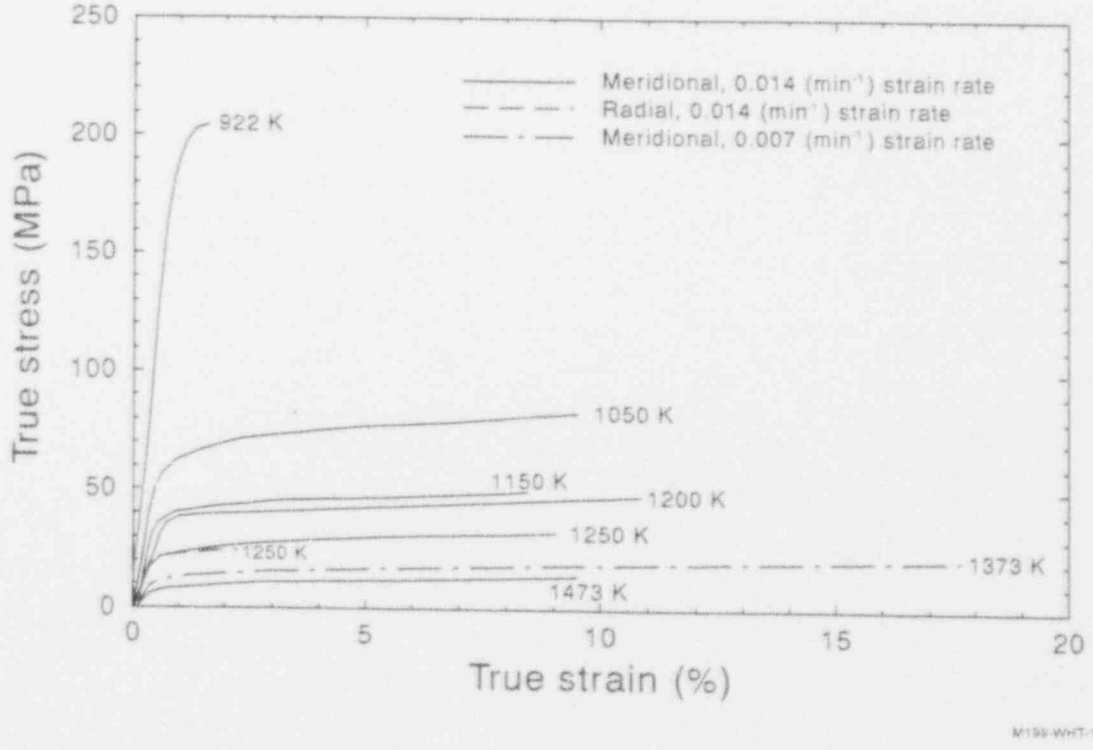

Figure B-9. Stress-strain curve for SA533B1 at various temperatures (strain rate of 0.014 m/m/min).

Table B-1. Summary of SA533B1 material creep tests performed at the INEL.

	Creep rupture		Creep rupture		Creep rupture	
Temperature K (°C)	Stress MPa (ksi)	Time (h)	Stress MPa (ksi)	Time (h)	Stress MPa (ksi)	Time (h)
900 (627)	140.1 (20.3)	11.3	69.6 (10.1)	190.1	—	—
1000 (727)	55.6 (8.1)	4.6	39.0 (5.7)	8.9	—	—
1050 (777)	26.3 (3.8)	18.9	13.9 (2.0)	264.4	—	—
1150 (877)	26.5 (3.8)	4.1	12.5 (1.8)	54.7	—	—
1250 (977)	26.5 (3.8)	0.05	12.6 (1.8)	2.2	8.0 (1.2)	61.2
1373 (1100)	7.0 (1.0)	0.7	3.5 (0.5)	46.9	—	—

plot with the resulting slope indicated. A parallel line offset 0.2% up the strain axis offers an estimate of the onset of tertiary creep, where that offset line intersects the creep curve. These plots provide data for further development of material-dependent creep laws that can be incorporated into structural finite element models of reactor vessel lower heads. Such laws typically estimate creep strain rate as a power function involving variables of applied stress and time and temperature-dependent parameters.

Other, more standard, representations of this creep data are shown in Figures B-16 and B-17. Figure B-16 plots the times to rupture for the applied stresses given in Table B-1, while Figure B-17 plots the minimum creep strain rates for the tests.

B-2.4 Summary of SA533B1 Tests

Creep and tensile tests of SA533B1 pressure vessel steel were performed at temperatures higher than any previous tests. Because of the high oxidation rates at these higher temperatures, the tests had to be performed in an inert atmosphere. Results from the tensile data indicated a rapid reduction in yield and ultimate strengths up to the phase transformation temperature of 1000 K for this material with a much more moderate decline in strength beyond that temperature. Some sensitivity to loading rate was seen in the ultimate strength and material ductility. Ductility also exhibited a marked increase in temperature ranges above the phase transition temperature. Creep data, such as stress at rupture time (Figure B-16) and stress versus minimum creep rate (Figure B-17), like the yield and ultimate strength data, also exhibited fairly rapid declines just below the phase transition temperature with more moderate declining rates in stress at higher temperatures.

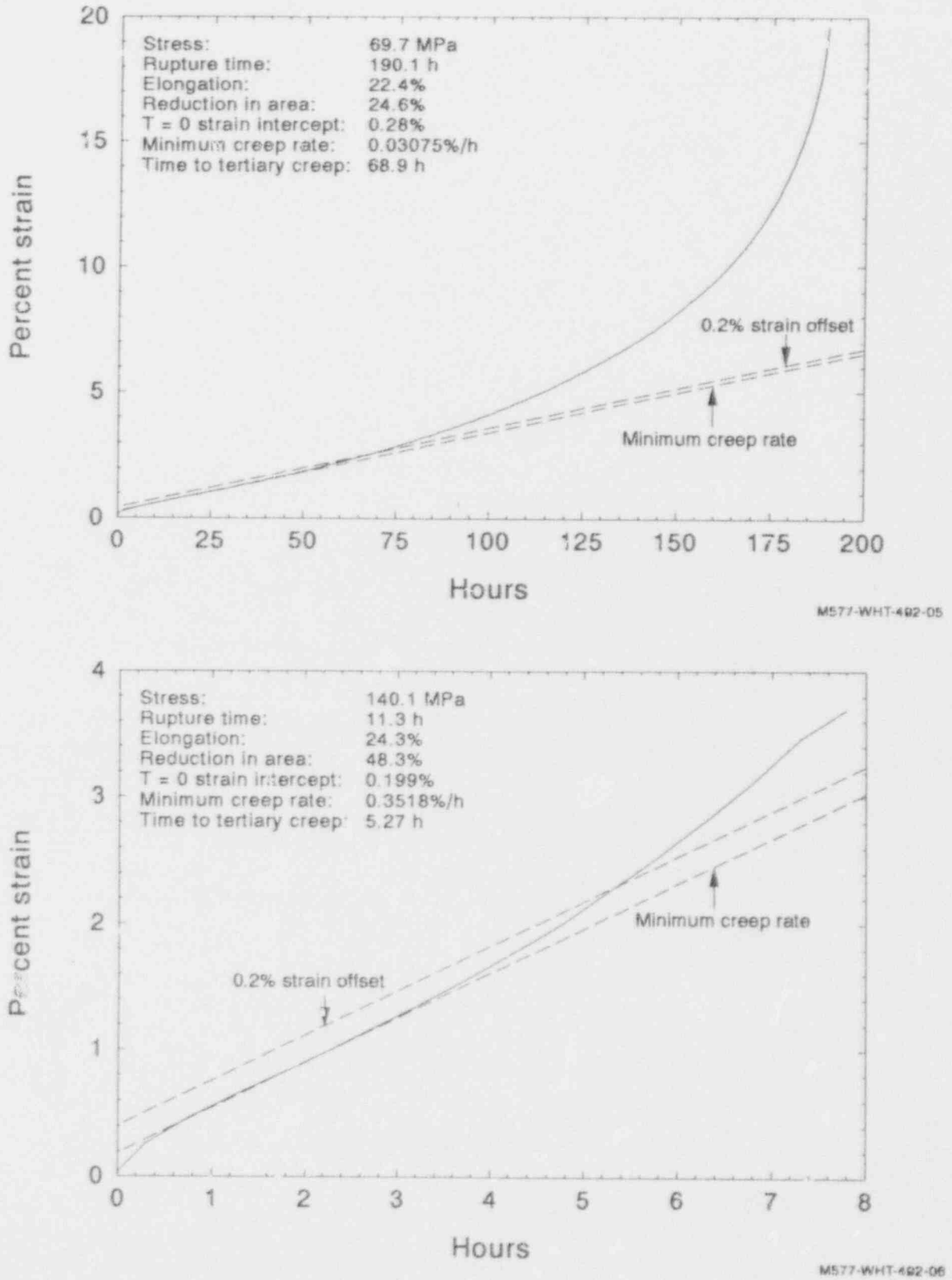

Figure B-10. Creep curves for SA533B1 at 900 K.

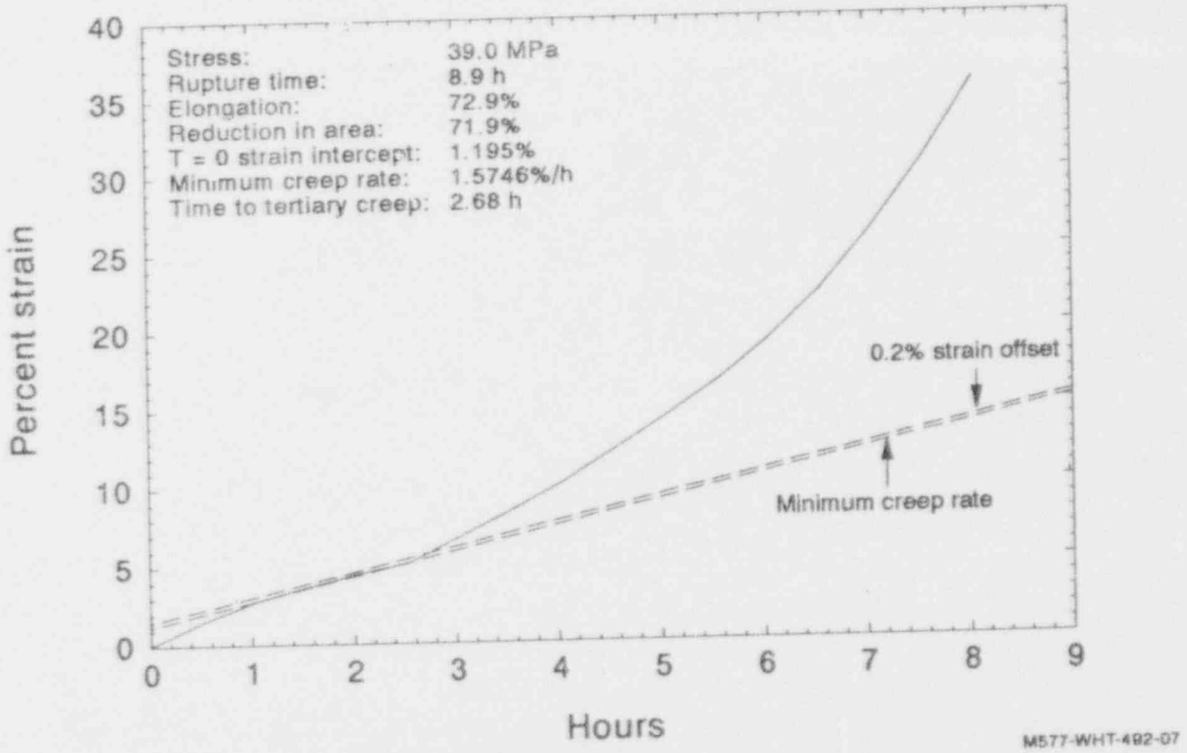

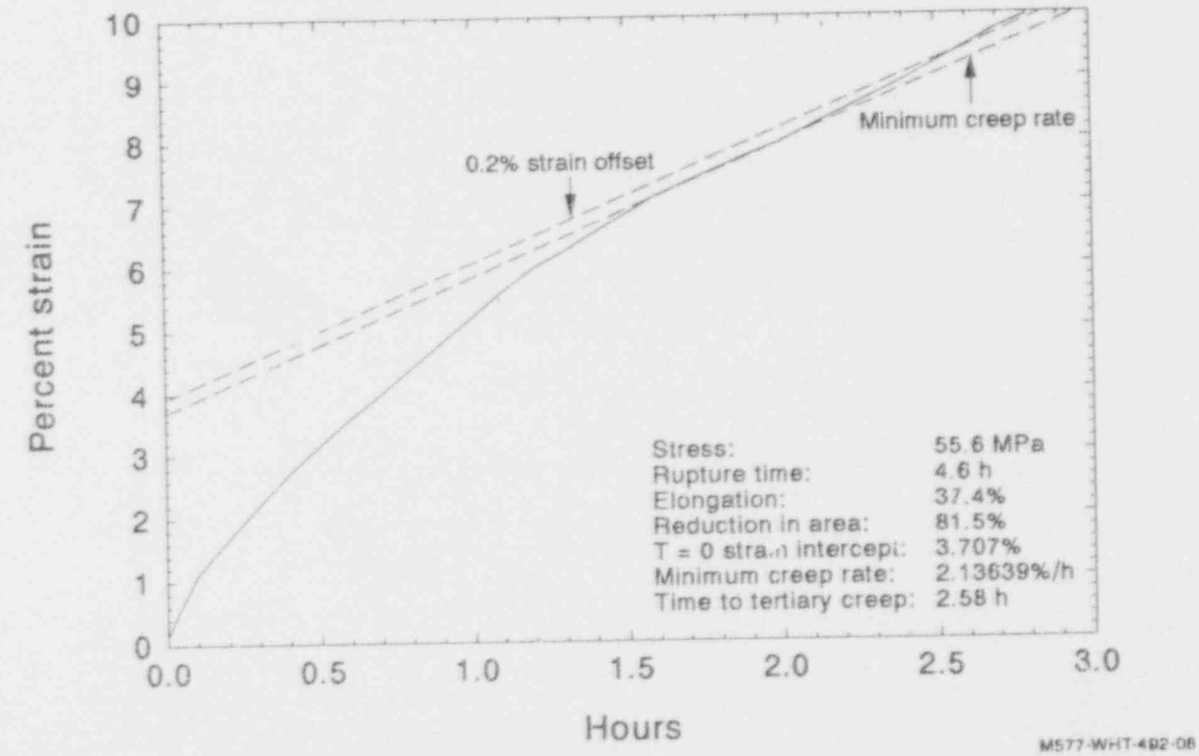

Figure B-11. Creep curves for SA533B1 at 1000 K.

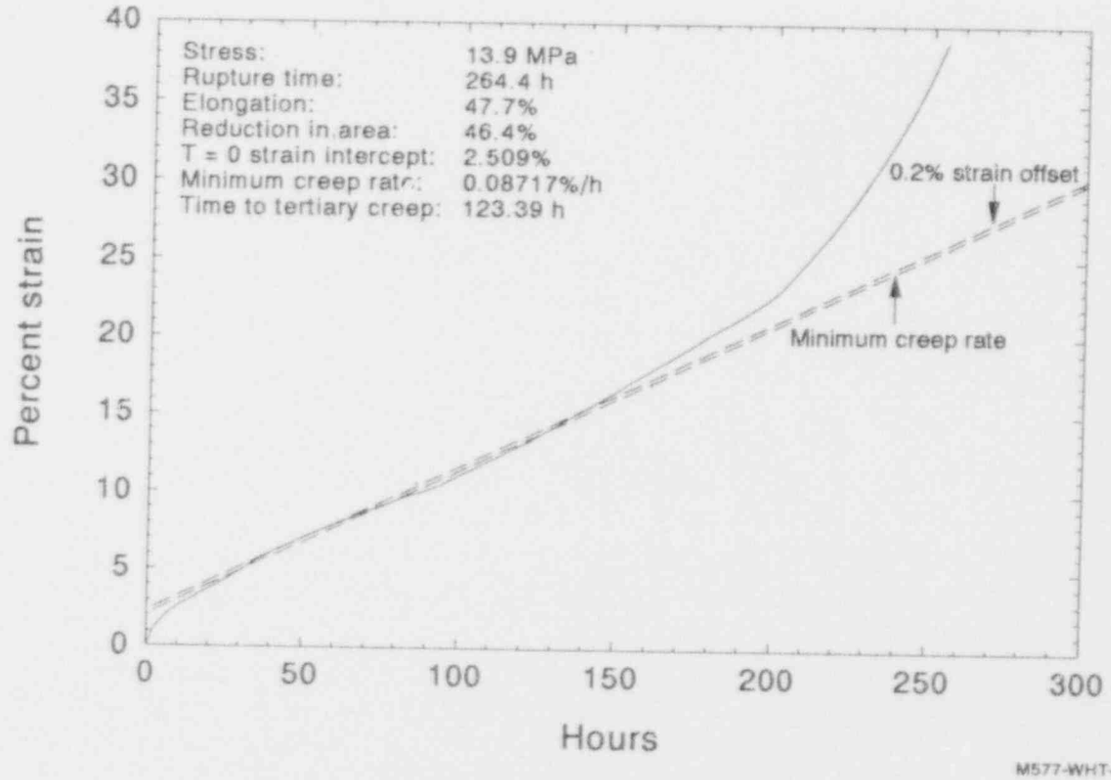

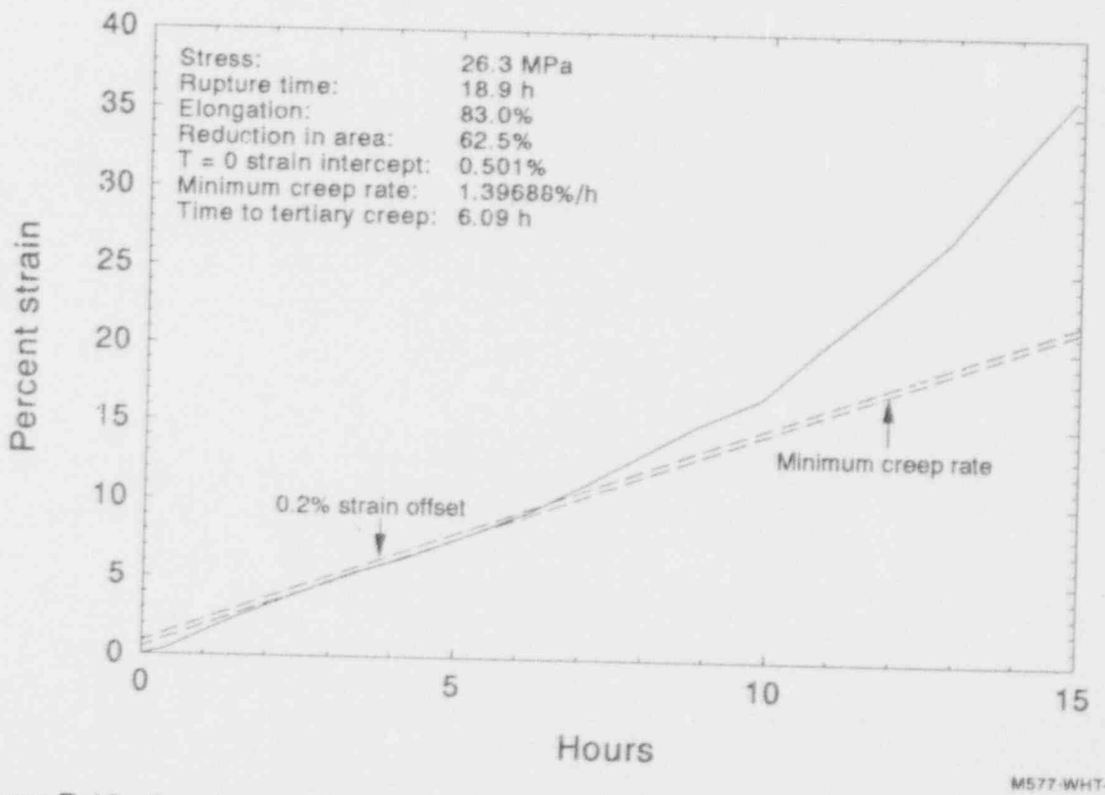

Figure B-12. Creep curves for SA533B1 at 1050 K.

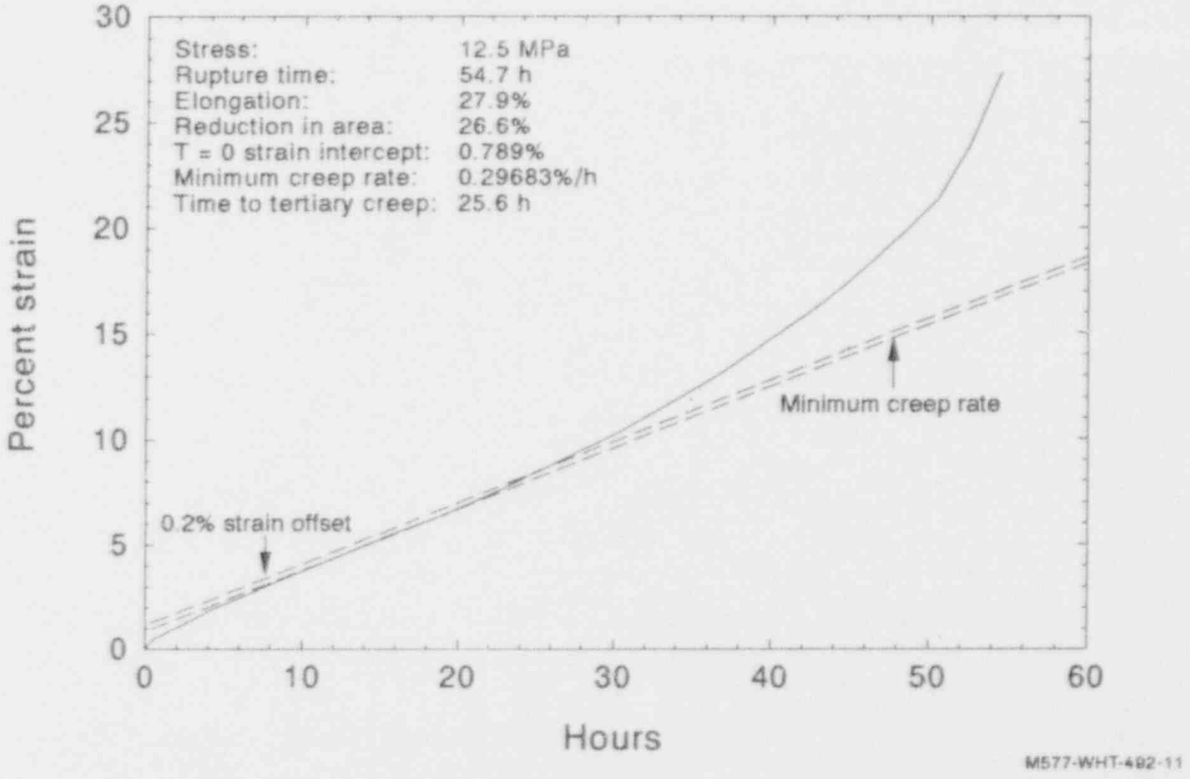

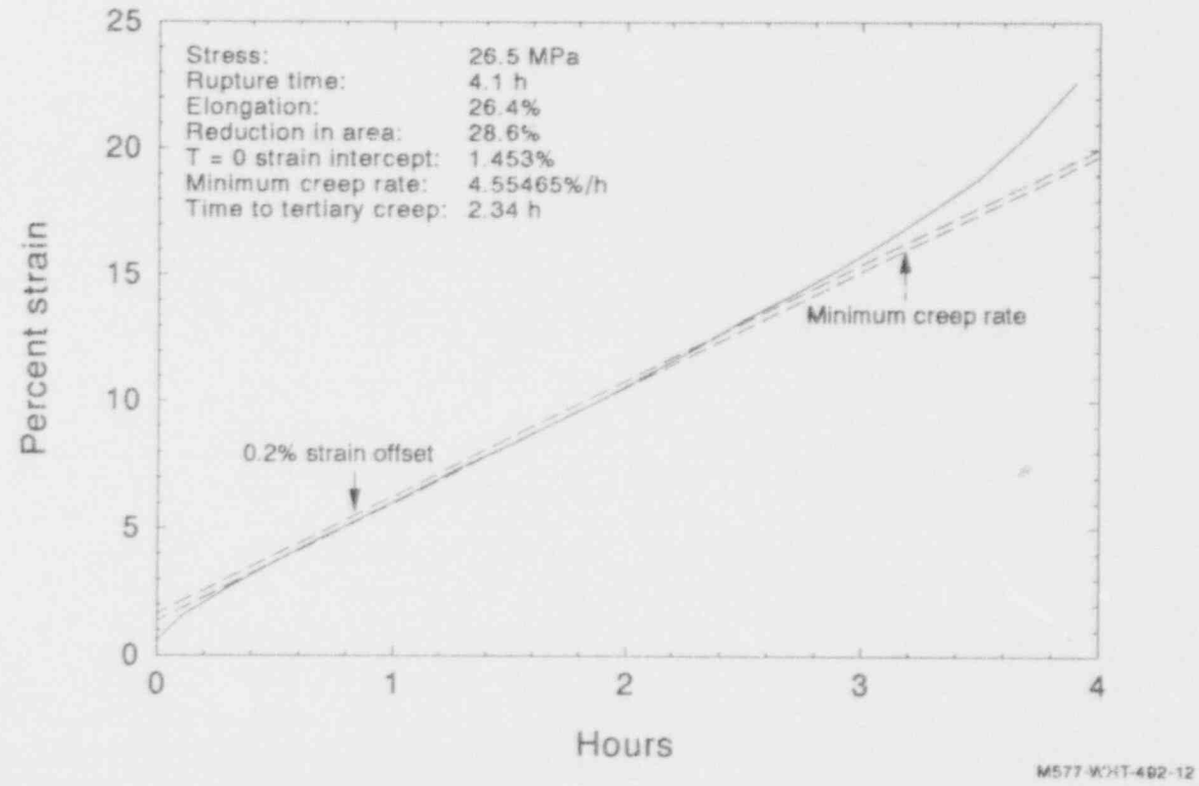

Figure B-13. Creep curves for SA533B1 at 1150 K.

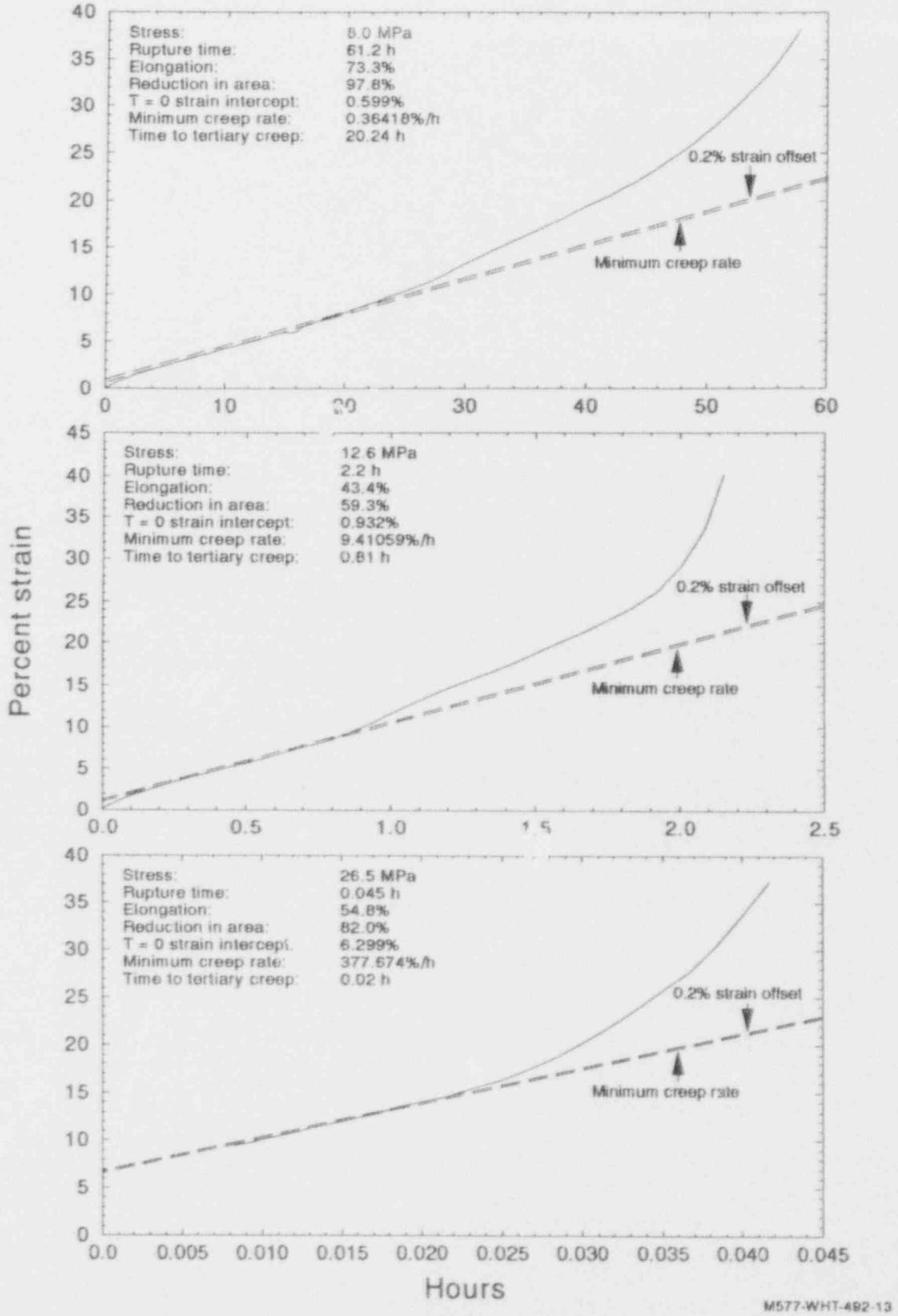

Figure B-14. Creep curves for SA533B1 at 1250 K.

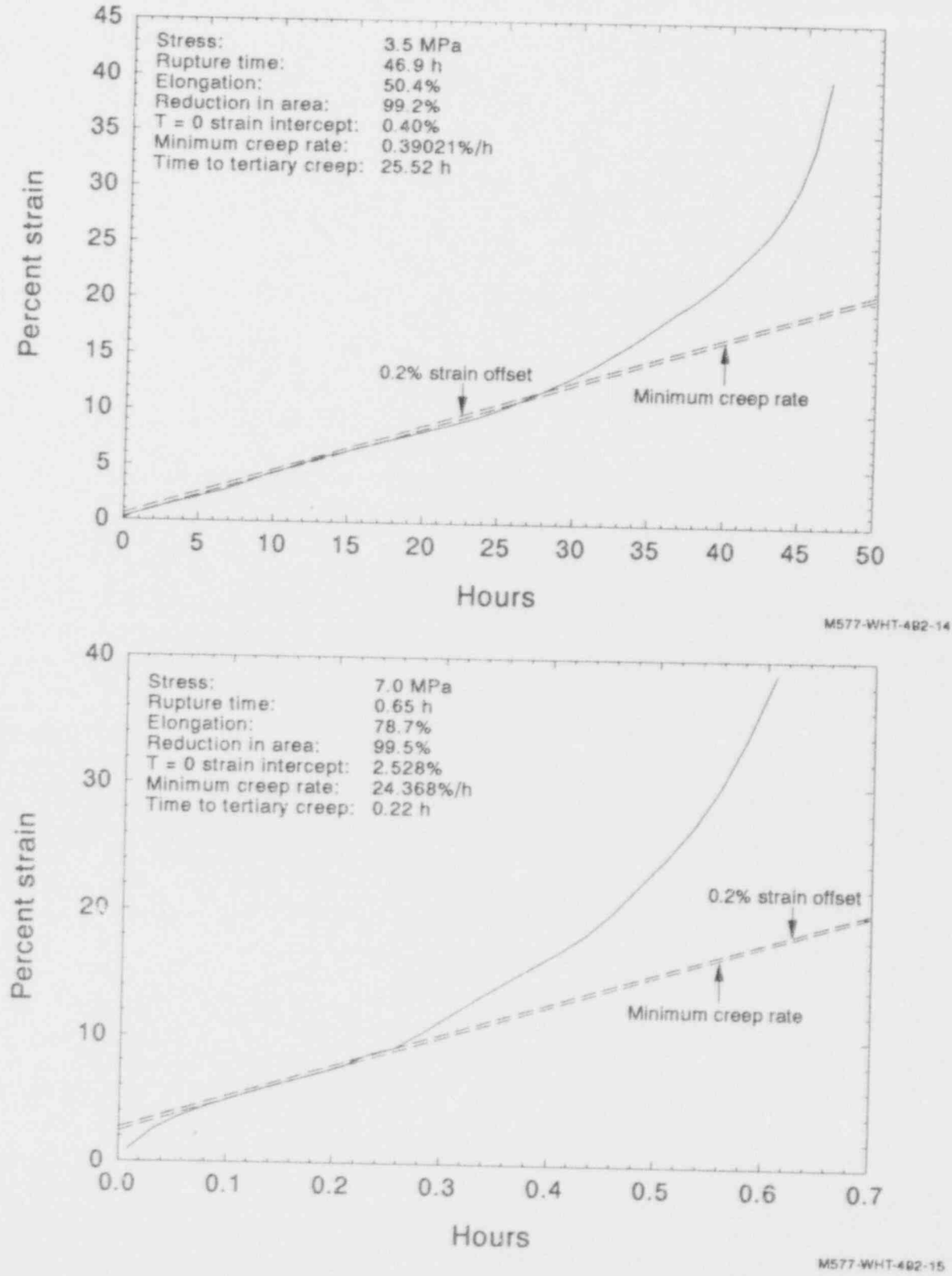

Figure B-15. Creep curves for SA533B1 at 1373 K.

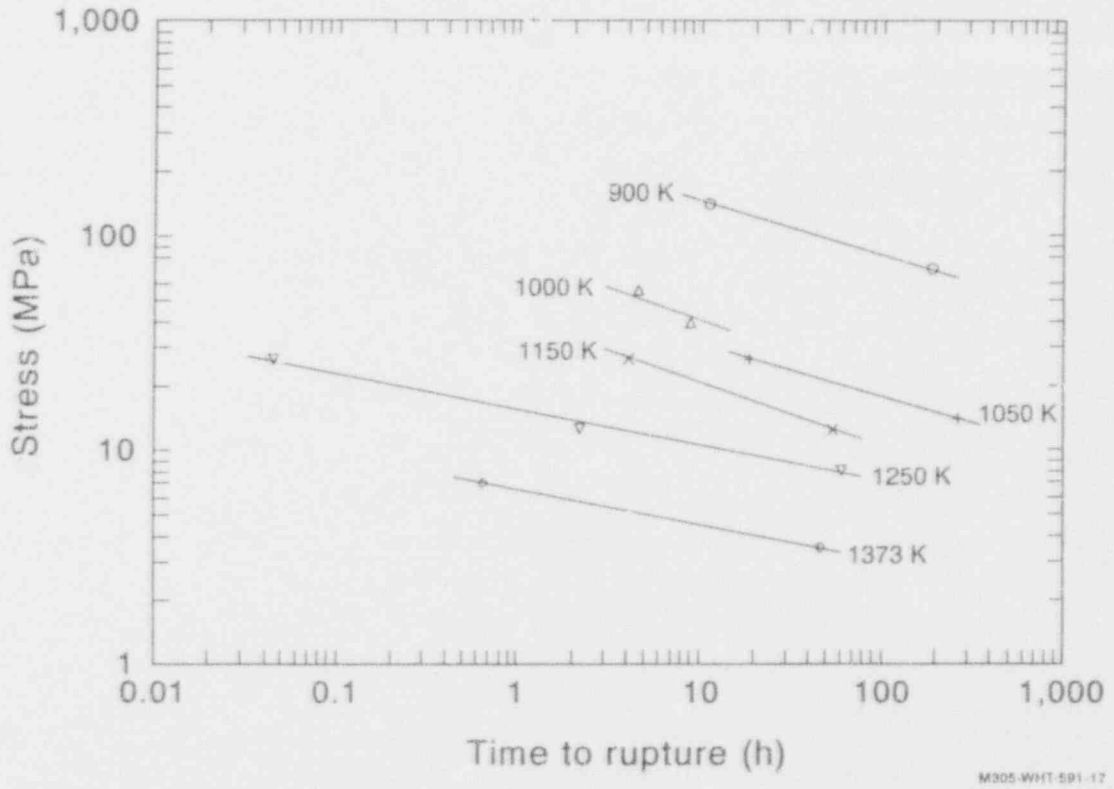

Figure B-16. Creep rupture stress versus time to rupture for SA533B1.

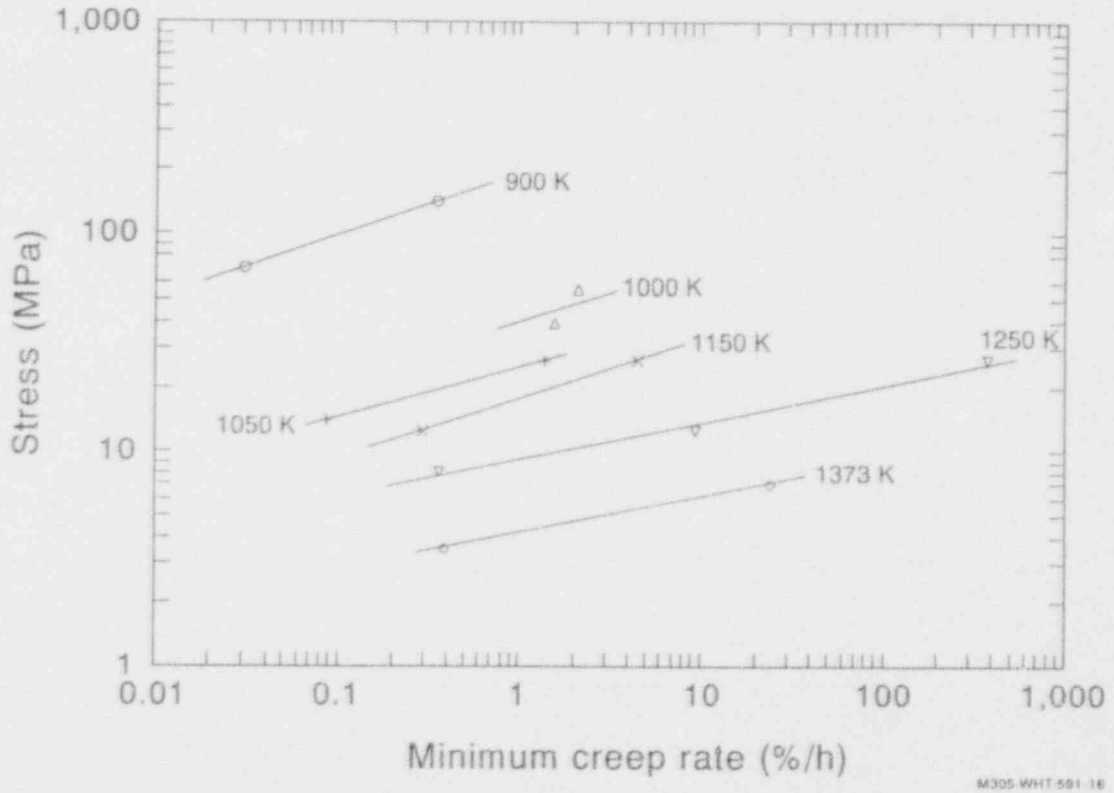

Figure B-17. Creep rupture stress versus minimum creep rate for SA533B1.

B-3. SA508-CL2 CREEP TEST DATA FROM TESTS AT THE INEL

The INEL[B-8] also conducted creep testing of SA508-CL2 material, used for lower head vessel forgings, under a previous USNRC task. These data are included in this section to provide known creep curves that might be used to formulate material creep laws in detailed structural analyses of reactor vessel lower heads.

B-3.1 Test Description

The coupons for this series of creep tests were fabricated from a section taken from the Intermediate Test Vessel V-3, documented in the Heavy-Section Steel Technology Program at Oak Ridge National Laboratory.[B-9] Twenty-one coupons were cut from the section, each having a meridional orientation with respect to the 6-inch wall of the vessel.

The creep tests were conducted in air using a constant load testing machine equipped with an auto-leveling lever arm and an electric furnace. Oxidation rates for this material at the creep test temperatures were not significant enough to warrant inert atmosphere testing. The coupon dimensions and the testing procedure complied with testing standard ASTM E139.[B-10]

B-3.2 Creep Tests

As indicated in Table B-2, the creep tests were performed at temperatures ranging from 900 to 1025 K, with rupture times varying from 6 minutes to 13.7 hours. It should be noted that SA508 material undergoes a phase transition near 1000 K similar to that of SA533B1. Figures B-18 through B-23 plot the creep curves from the test conditions summarized in Table B-2. These tests are also summarized in a plot of rupture stress versus time to rupture (Figure B-24) and stress versus minimum creep rate (Figure B-25).

Table B-2. Summary of SA508-CL2 material creep tests performed at the INEL.

	Creep rupture		Creep rupture		Creep rupture	
Temperature K (°C)	Stress MPa (ksi)	Time (h)	Stress MPa (ksi)	Time (h)	Stress MPa (ksi)	Time (h)
900 (627)	140.7 (20.4)	13.7	111.7 (16.2)	43.7	—	—
925 (652)	112.4 (16.3)	9.4	97.9 (14.2)	23.7	84.1 (12.2)	42.5
950 (677)	111.7 (16.2)	2.4	98.6 (14.3)	4.6	84.1 (12.2)	10.1
975 (702)	111.7 (16.2)	0.4	97.9 (14.2)	1.1	84.1 (12.2)	2.7
1000 (727)	111.7 (16.2)	0.1	83.4 (12.1)	1.0	55.8 (8.1)	6.9
1025 (752)	56.5 (8.2)	0.4	55.8 (8.1)	2.6	—	—

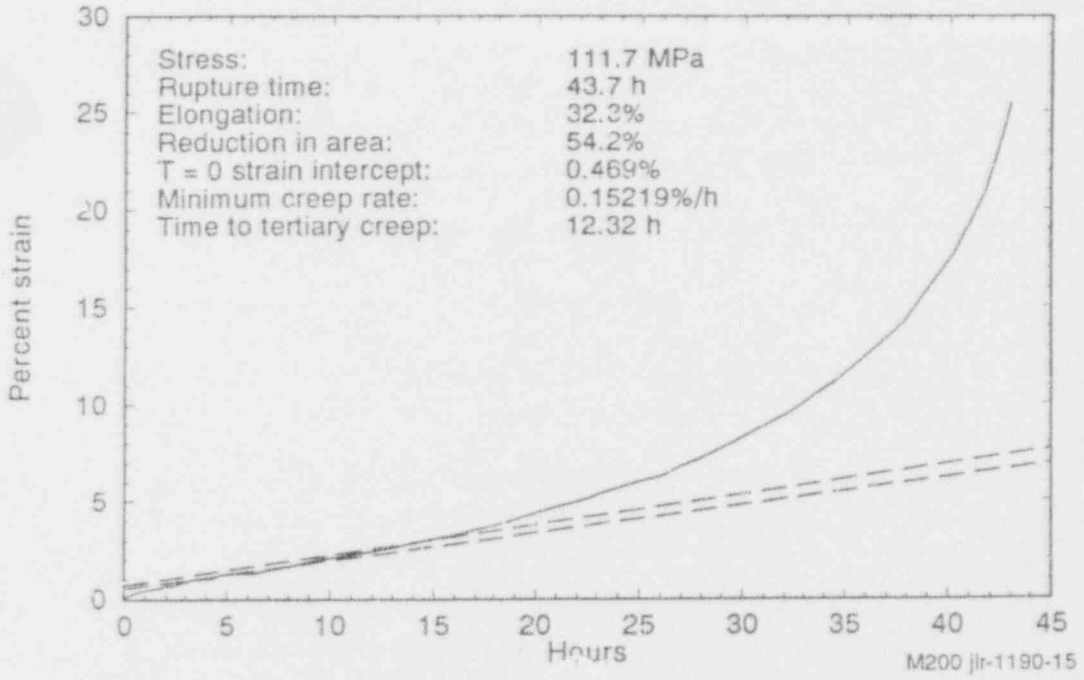

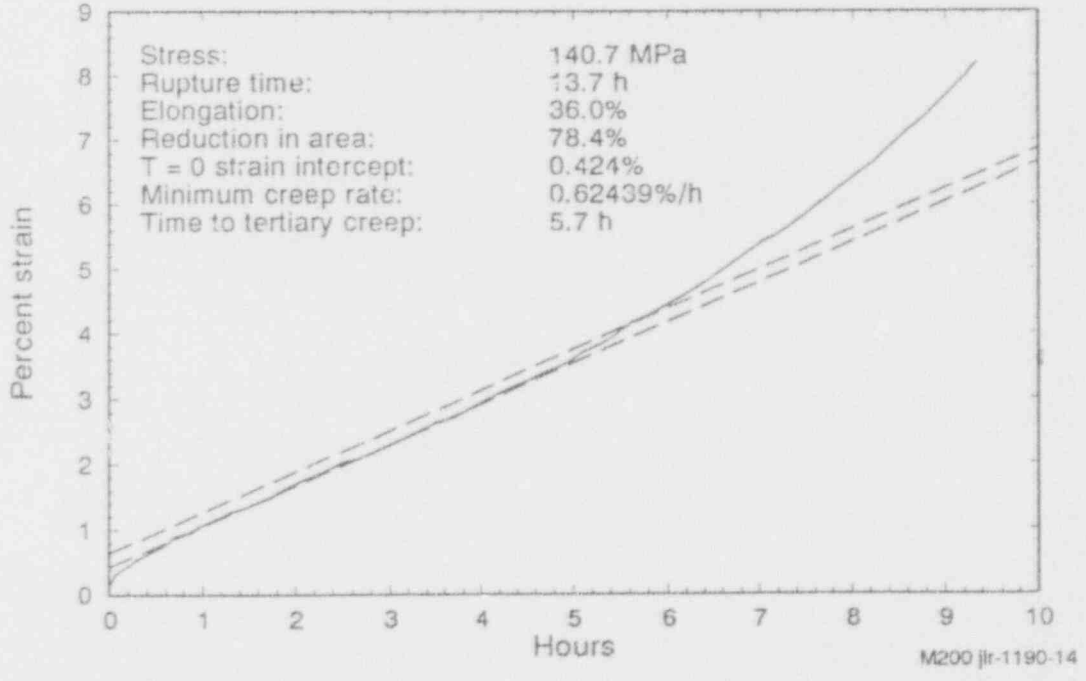

Figure B-18. SA508-CL2 creep test curve at 900 K.

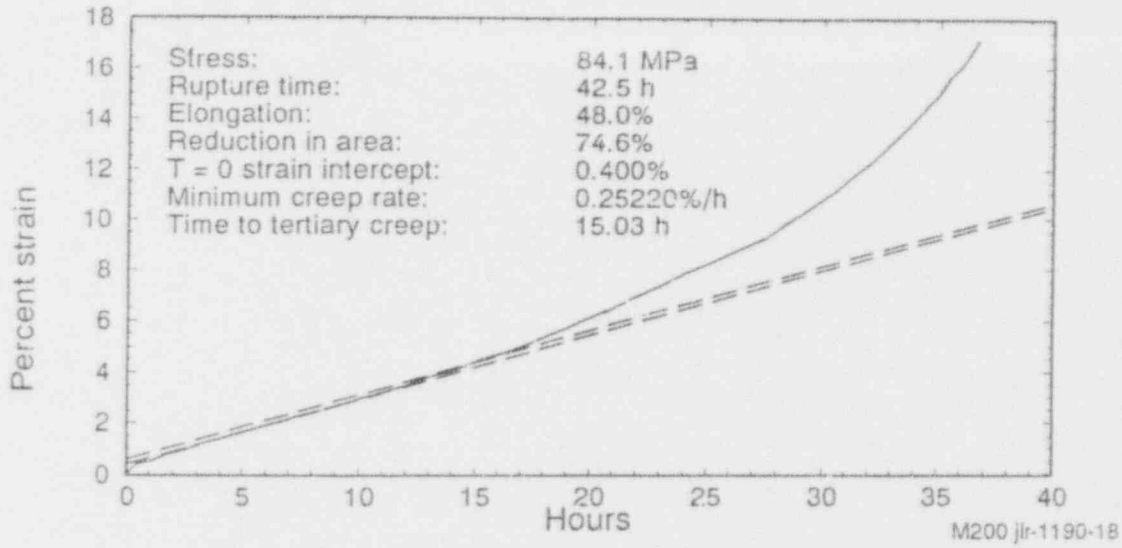

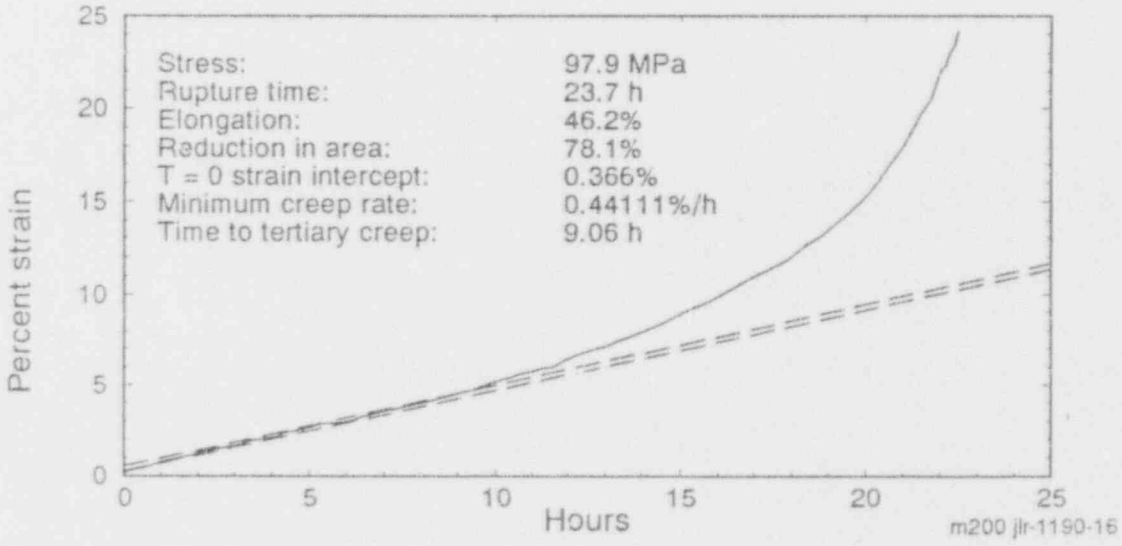

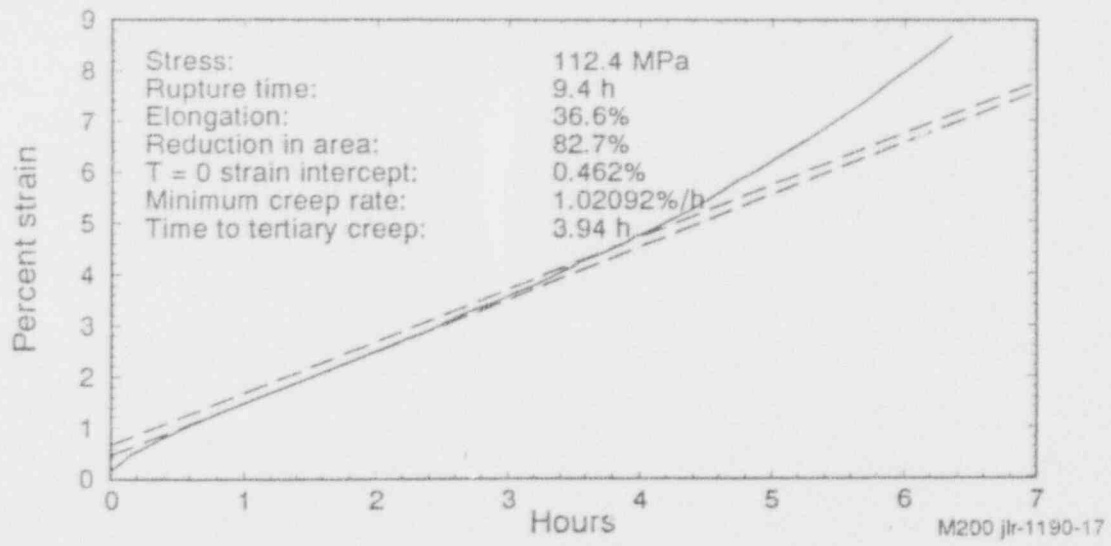

Figure B-19. SA508-CL2 creep test curve at 925 K.

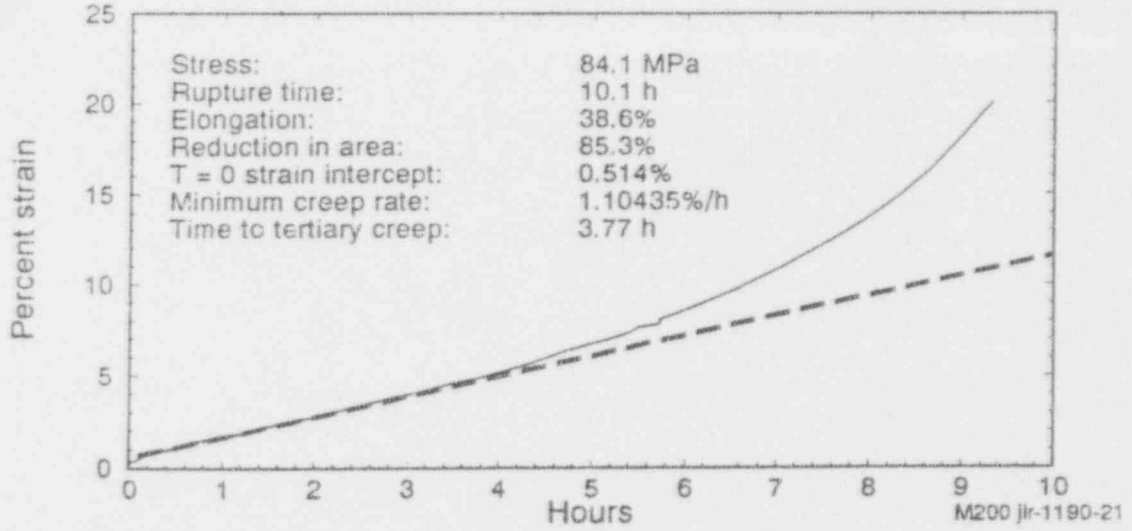

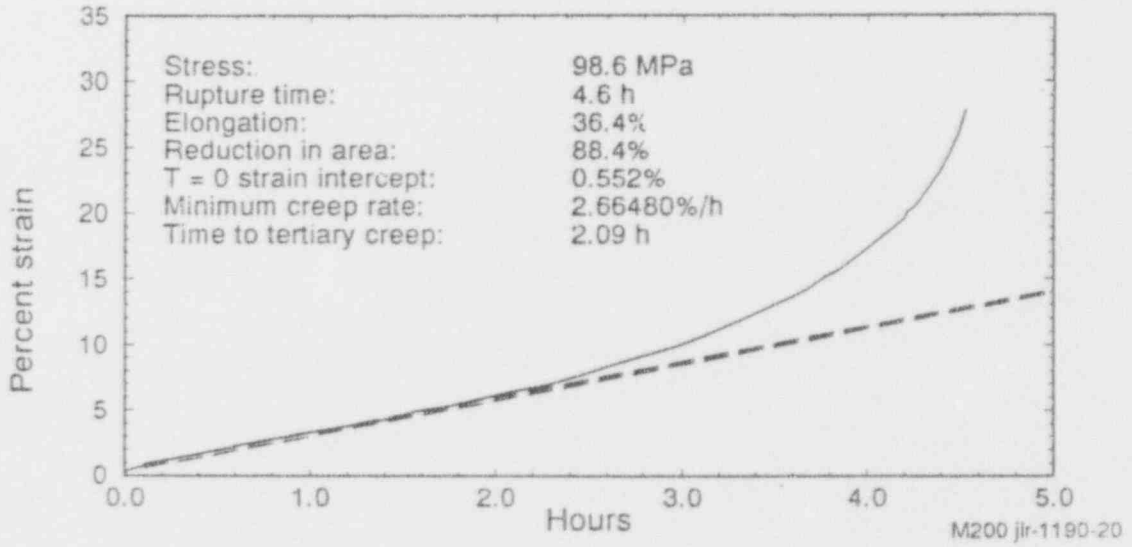

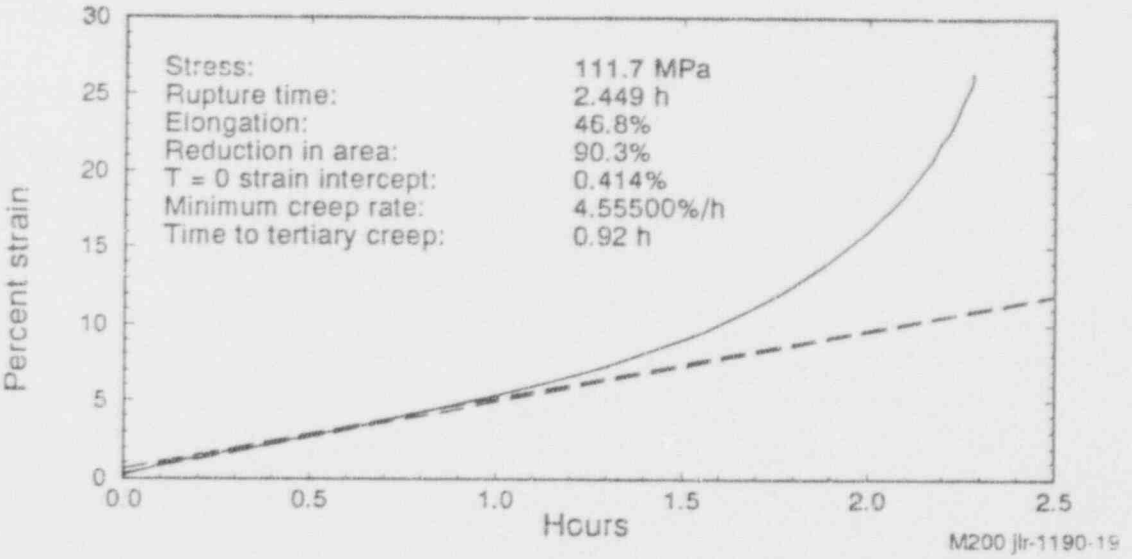

Figure B-20. SA508-CL2 creep test curve at 950 K.

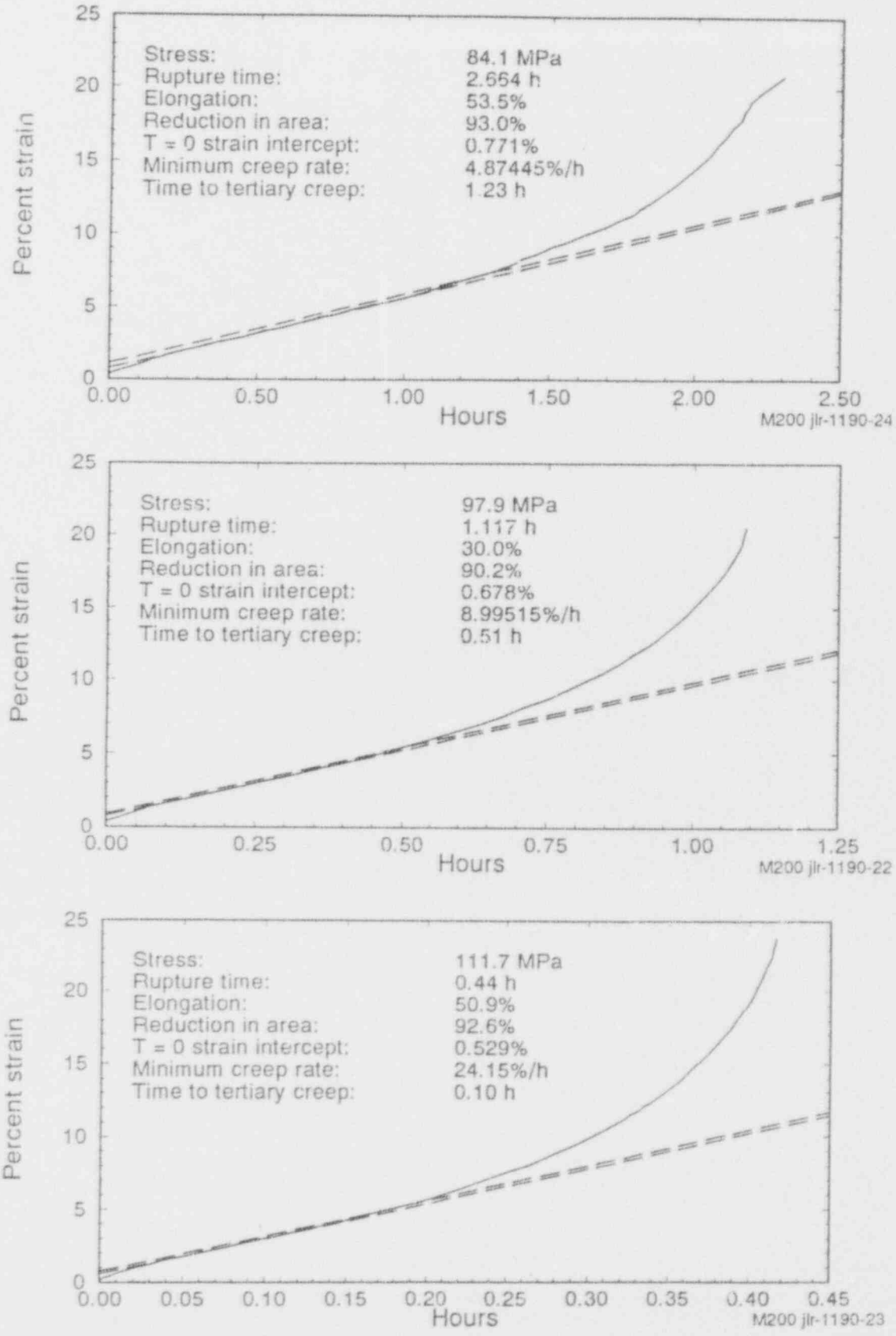

Figure B-21. SA508-CL2 creep test curve at 975 K.

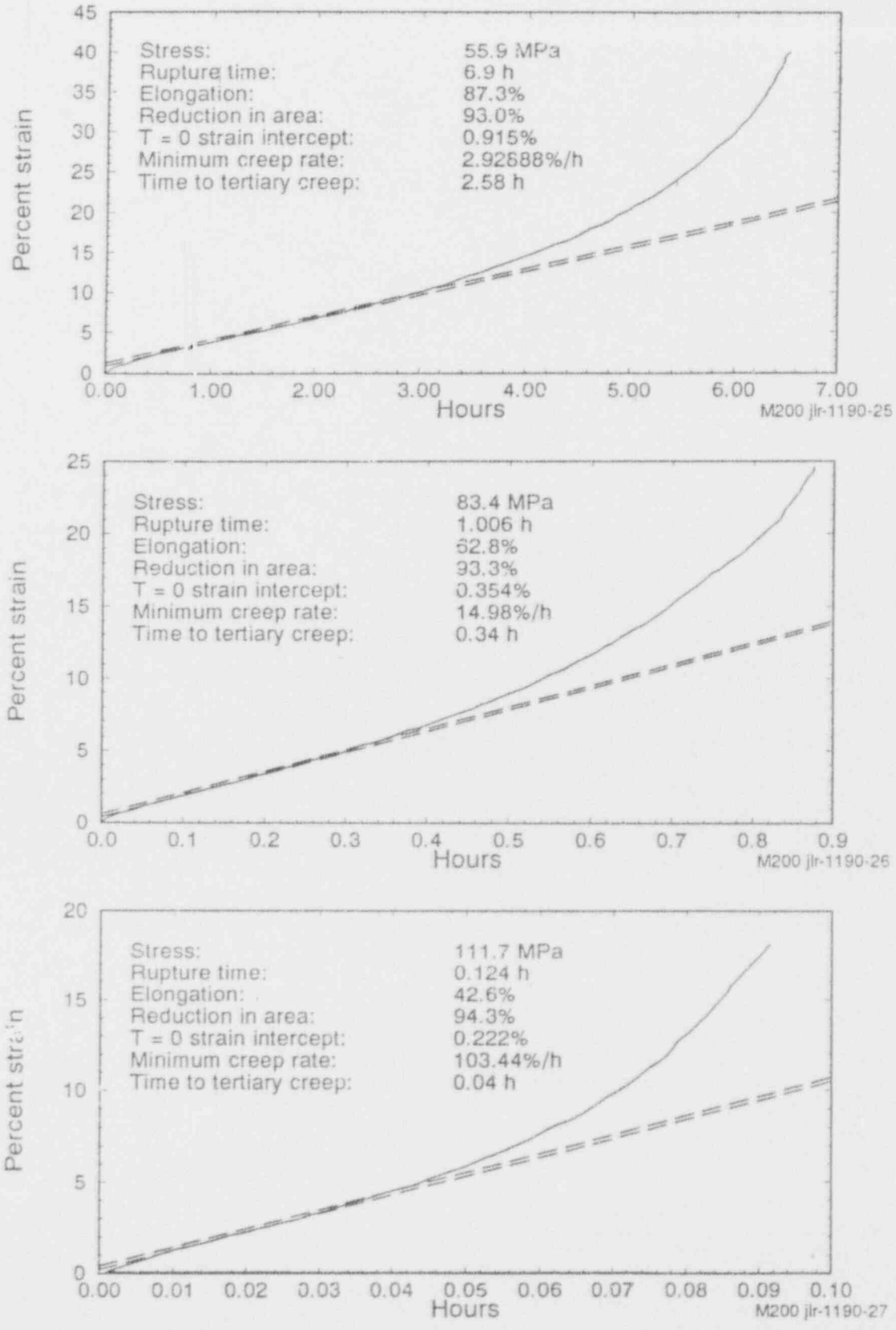

Figure B-22. SA508-CL2 creep test curve at 1000 K.

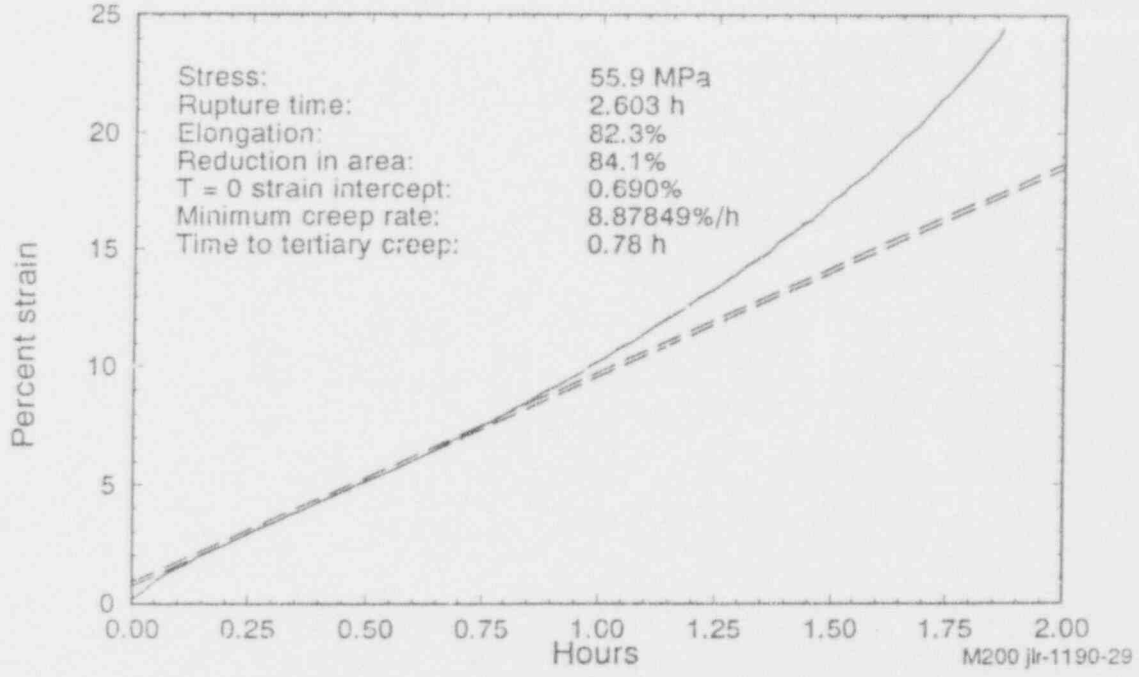

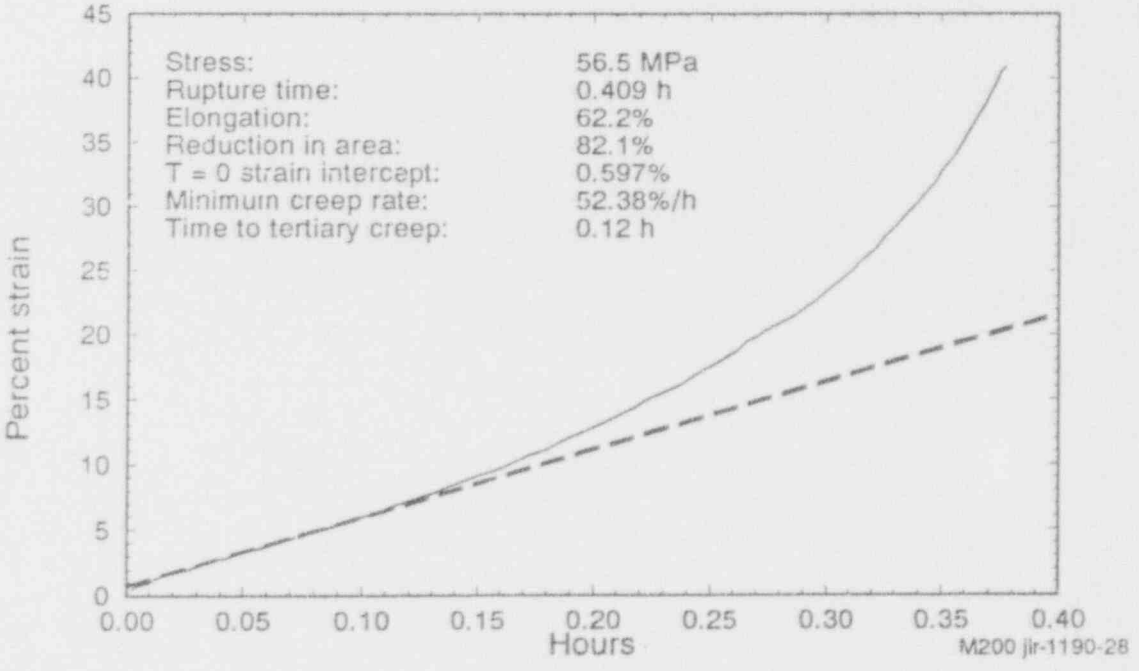

Figure B-23. SA508-CL2 creep test curve at 1025 K.

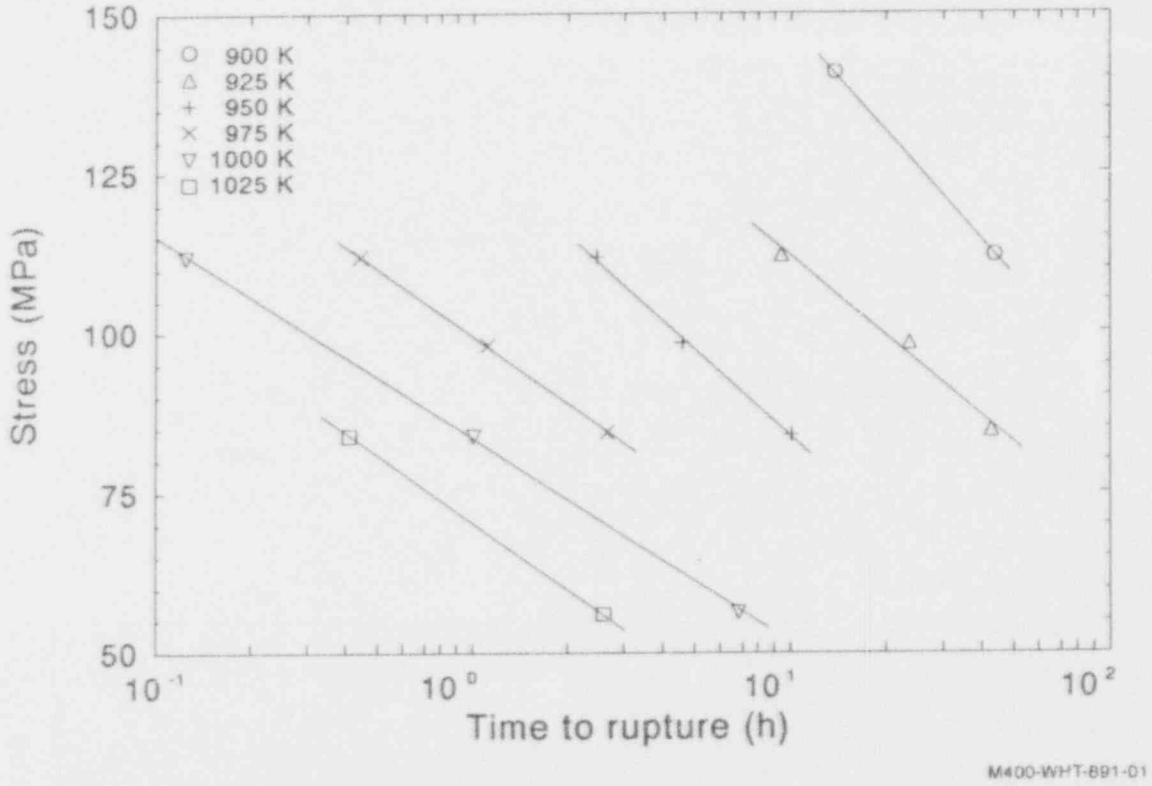

Figure B-24. Creep rupture stress versus time to rupture for SA508-CL2.

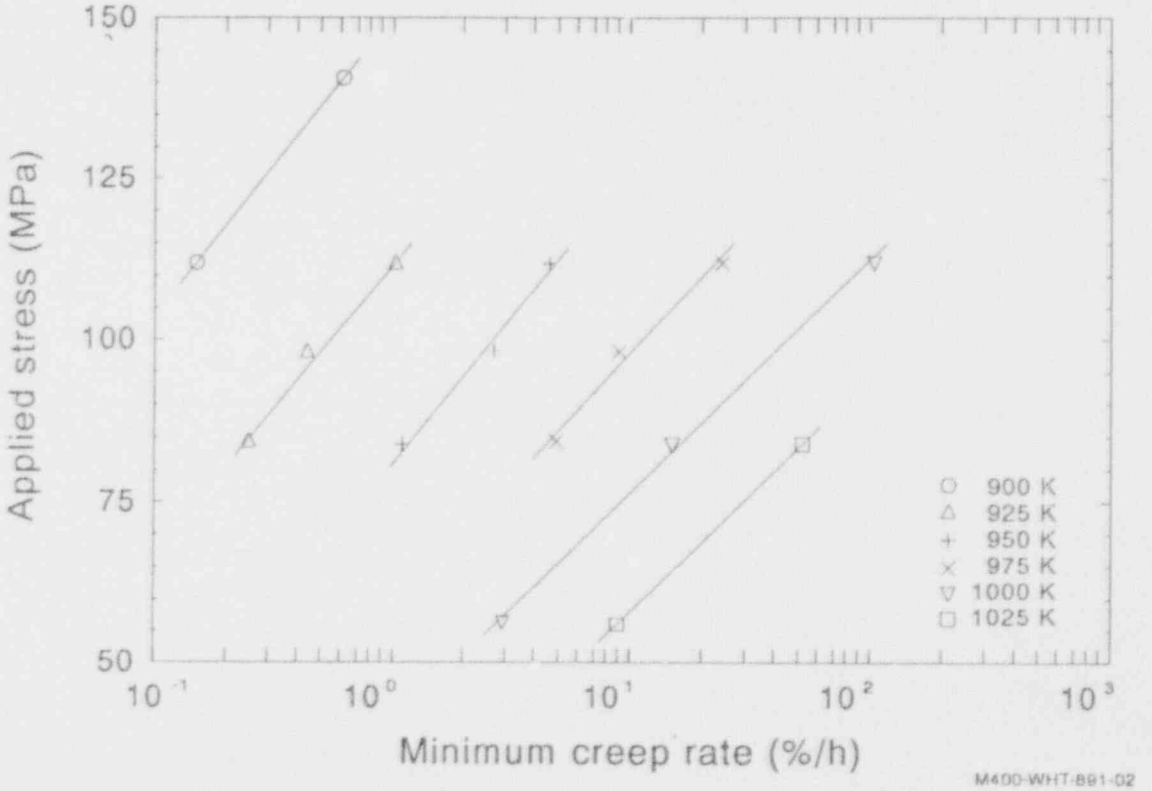

Figure B-25. Creep rupture stress versus minimum creep rate for SA508-CL2.

B-4. PENETRATION MATERIALS CREEP RUPTURE AND TENSILE DATA FROM TESTS AT THE INEL

High temperature creep and tensile data are needed to assess the likelihood of a structural penetration failure in the lower head during a severe accident, particularly if finite element analysis is used. Penetrations targeted by this study include instrument tubes (Inconel 600 or 304 stainless steel), control rod guide tubes (304 stainless steel), and drain lines (SA106B) (see Appendix F). Table B-3 lists data for penetration materials found in published reports with maximum test temperatures and INEL data with maximum temperatures. It should be noted that in creep testing, stress, as well as the temperature, determines material response. For example, although the maximum INEL test temperature for creep rupture of Inconel 600 is the same as those discussed in the published results, those tests were performed at much lower stresses than the INEL tests. Typical creep rupture times for published data are over 100 hours; whereas, in the INEL tests, rupture occurred near 10 hours, the time frame of interest in severe accidents.

B-4.1 Test Setup and Procedures

High temperature tensile and creep tests were performed on Inconel 600, 304 stainless steel, and SA106B carbon steel using the same test setup described in Section B.2.1. Tensile and creep tests were performed using ASTM testing standards[B-4,B-5,B-10]. Tensile tests were conducted in air; creep tests were conducted in an argon purge environment.

Table B-3. Maximum tensile and creep test temperatures in published data and in this study.

	Maximum temperature in published data (K)	Maximum temperature in this study (K)
Inconel 600		
Yield strength (σ_y)	1255[B-11]	1373
Ultimate strength (σ_u)	1255[B-11]	1373
Stress-strain curves	none found	1373
Creep rupture data	1366[B-11]	1366
Creep strain history	none found	1366
304 Stainless steel		
Yield strength (σ_y)	923[B-12]	1373
Ultimate strength (σ_u)	1000[B-12]	1373
Stress-strain curves	977[B-13]	1373
Creep rupture data	1144[B-12]	1350
Creep strain history	1089[B-14]	1350
SA106B Carbon steel		
Yield strength (σ_y)	811[B-15]	1150
Ultimate strength (σ_u)	811[B-15]	1150
Stress-strain curves	none found	1150
Creep rupture data	811[B-15]	1050
Creep strain history	none found	1050

B-4.2 Data Reduction

Tensile data are presented primarily in the form of stress-strain curves, with specific points of interest (e.g., yield and ultimate strengths) in tables and plots. For all tensile tests discussed here, strain measurement was intended to capture relatively large deformation behavior and was not sensitive enough to measure elastic moduli accurately. For this reason, published values of elastic moduli and their extrapolations to high temperatures were used to construct the elastic portions of the stress-strain curves. Tensile data include both true and engineering ultimate strength because true ultimate strength is used in finite element analysis and engineering ultimate strength is used in mechanics of materials analysis. Because of small strains, the difference between true and ultimate yield is negligible. Percent elongations and area reductions are referenced to the initial state.

Creep behavior is presented in plots of creep strain history and creep rupture data. In the creep strain history plots, minimum creep rate was estimated by a linear regression on the secondary phase of the creep curve. The intersection of the creep curve and a line parallel to the minimum creep rate line, with 0.2% strain offset, was used to estimate the onset of tertiary creep. The Larson-Miller parameter (LMP)[B-16] is often used to predict creep rupture for combinations of stress and temperature different from those tested (see Section B-5). Creep rupture data are presented using the LMP, as well as in plots and tables.

B-4.3 Inconel 600

B-4.3.1 Inconel 600 Tensile Tests

Results from Inconel 600 tensile tests at temperatures up to 1373 K are summarized in Table B-4 and plotted in Figures B-26 through B-29. Current tests were conducted using 12.7-mm round bar stock as the stock material. The material was annealed at 1143 K for one hour. The published values of elastic moduli[B-11] used to construct the elastic portion of the stress-strain curve are listed in Table B-4. Elastic moduli were extrapolated from temperatures above 1273 K, using a second order polynomial fit. All other values listed in Table B-4 were obtained from tests performed at the INEL.

Figure B-26 shows stress-strain curves for various temperatures. The stress-strain curve at 1150 K shows a slight jump at approximately 0.12 strain; also, the curve for 1200 K is not consistent with other curves. These anomalies resulted from problems with temperature control. Nonetheless, yield and ultimate strength values obtained for 1150 and 1200 K appear to be consistent with tests at other temperatures, as shown in Figures B-27 and B-28. Figure B-27 plots temperature-dependent yield strength, and Figure B-28 plots temperature-dependent ultimate strengths, both engineering and true. Figure B-29 compares the INEL ultimate strength (engineering) data to data published in Reference B-11, the INEL data are very consistent with the published data.

B-4.3.2 Inconel 600 Creep Tests

Table B-5 summarizes creep data obtained for 11 tests run from 1005 to 1366 K. Stresses varied from approximately 14 to 173 MPa; times to rupture ranged from half an hour to 38.5 hours.

Figure B-30 plots stresses versus logarithmic times to rupture for the temperatures tested. The INEL data tend to have shorter times to rupture than the published data. This difference is

Table B-4. Inconel 600 tensile data.[a]

Temperature (K)	E[b] (GPa)	Proportional limit (MPa)	σ_y[c] (MPa)	True σ_u[d] (MPa)	Engineering σ_u[d] (MPa)	Uniform elongation (%)	Total elongation (%)	Area reduction (%)
297	213.26	307.00	374.00	942.35	733.00	30	43	68
600	198.18	314.00	315.00	900.71	689.00	30	39	61
800	185.05	256.00	280.00	789.27	617.00	26	39	65
900	177.53	221.00	266.00	567.25	468.00	16	45	73
1000	169.38	165.00	237.00	304.74	273.00	4	76	94
1050	165.07	121.00	187.00	231.83	212.00	6	76	95
1100	160.60	73.00	132.00	171.30	154.00	6	76	93
1150	155.97	60.00	98.00	131.31	113.00	5	88	91
1200	151.19	55.00	74.00	85.28	79.00	7	62	83
1300	141.14	31.00	45.00	56.00	50.00	3	66	91
1373	133.41	18.00	21.00	28.65	27.00	7	55	97

a. Product information: 1/2 in. rod, heat no. NX678714, annealed 1 hour at 1143 K, forced-air cooled.

Chemistry: 0.060 C, 0.250 Mn, 0.001 S, 0.250 Si, 76.10 Ni, 14.890 Cr, 0.140 Cu, 8.310 Fe.

b. Young's modulus.

c. Yield stress.

d. Ultimate stress.

probably due to grain size or heat-to-heat effects. However, both data sets are too small to say if the difference is significant. Figure B-31 plots the LMP against logarithmic stress (ksi). The LMP was calculated from the following equation:

$$LMP = T[13 + \log(t_r)] \ (10^{-3})$$

where T is temperature (°R) and t_r is time to rupture (h). English units were used to be consistent with historical data.

Strain versus time data, often used in finite element creep analysis, are shown in Figures B-32 through B-35. The creep strain versus time data appear very consistent. It is interesting to note that none of these high temperature curves exhibits much, if any, primary creep.

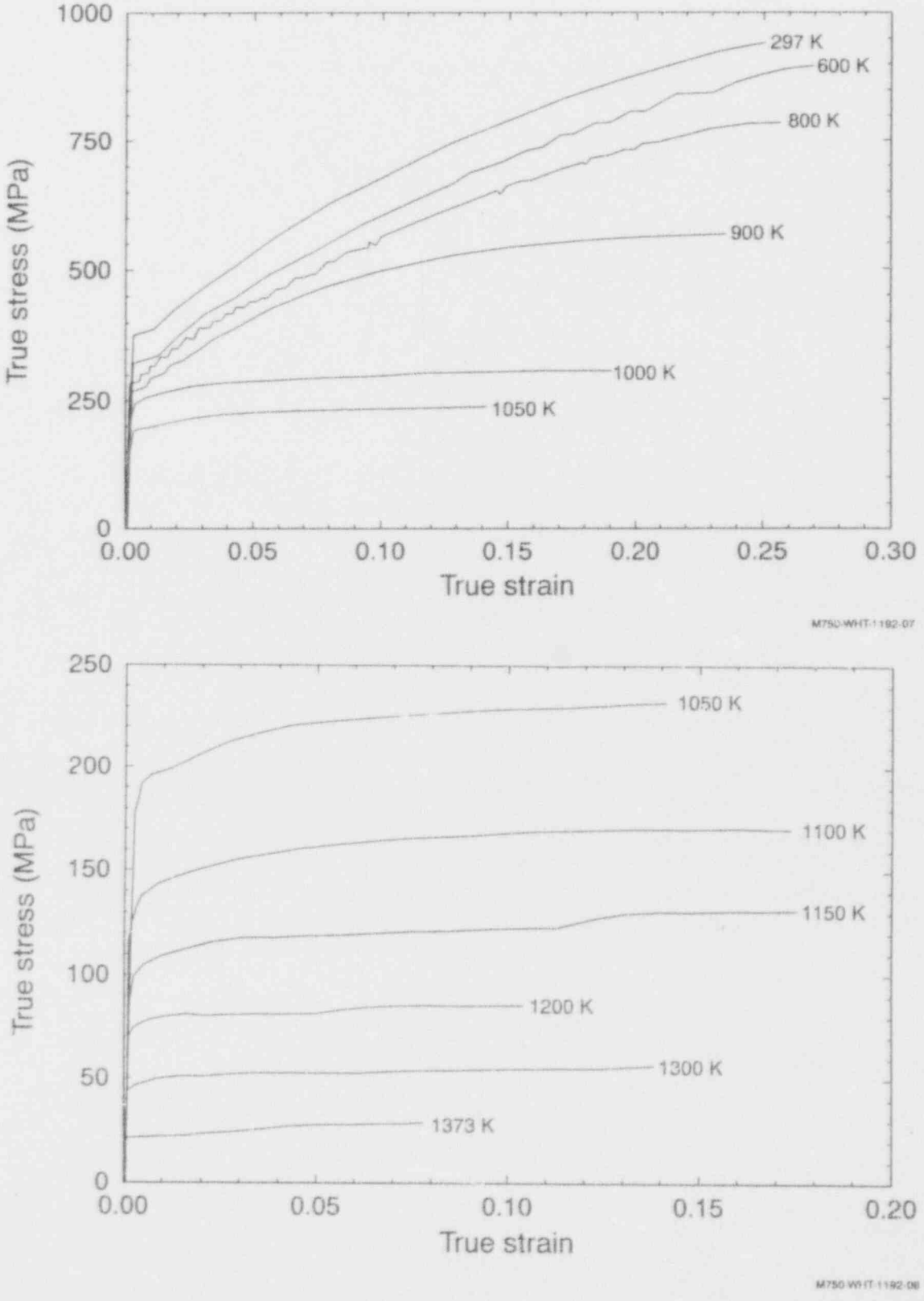

Figure B-26. Stress-strain curves for Inconel 600 at various temperatures— INEL tensile test results.

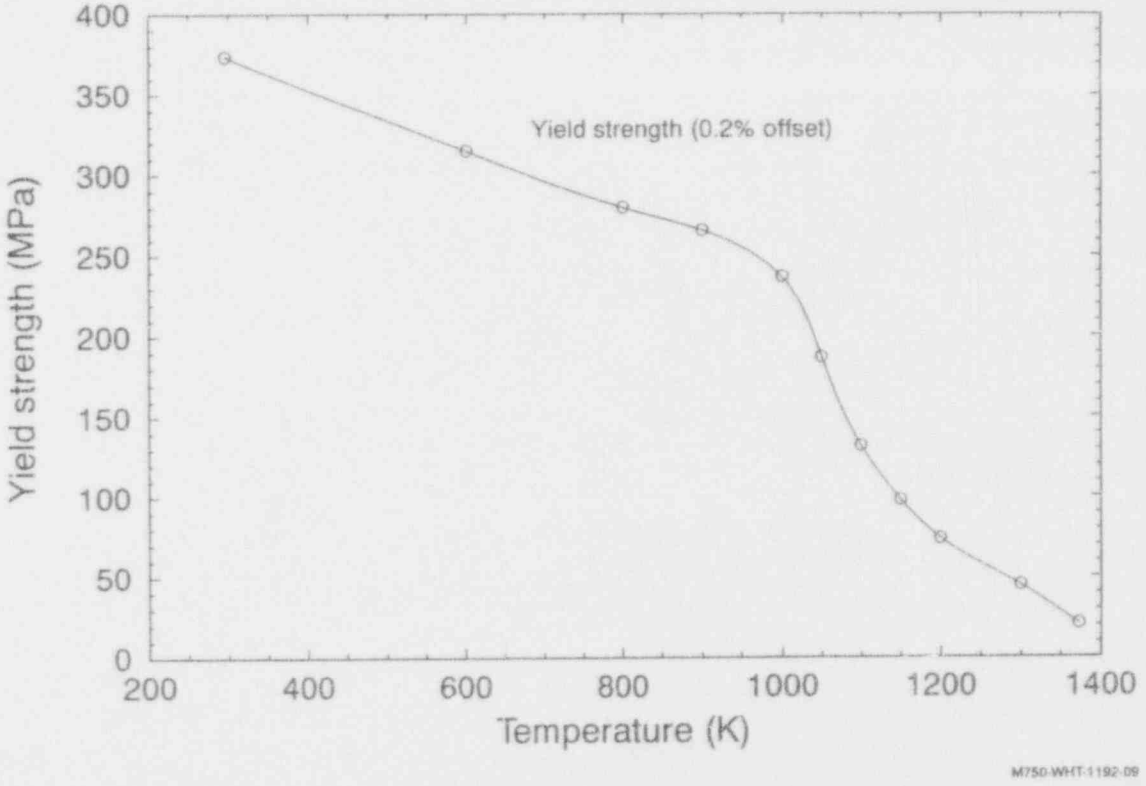

Figure B-27. Inconel 600 yield strength (0.2% offset)—INEL tensile test results.

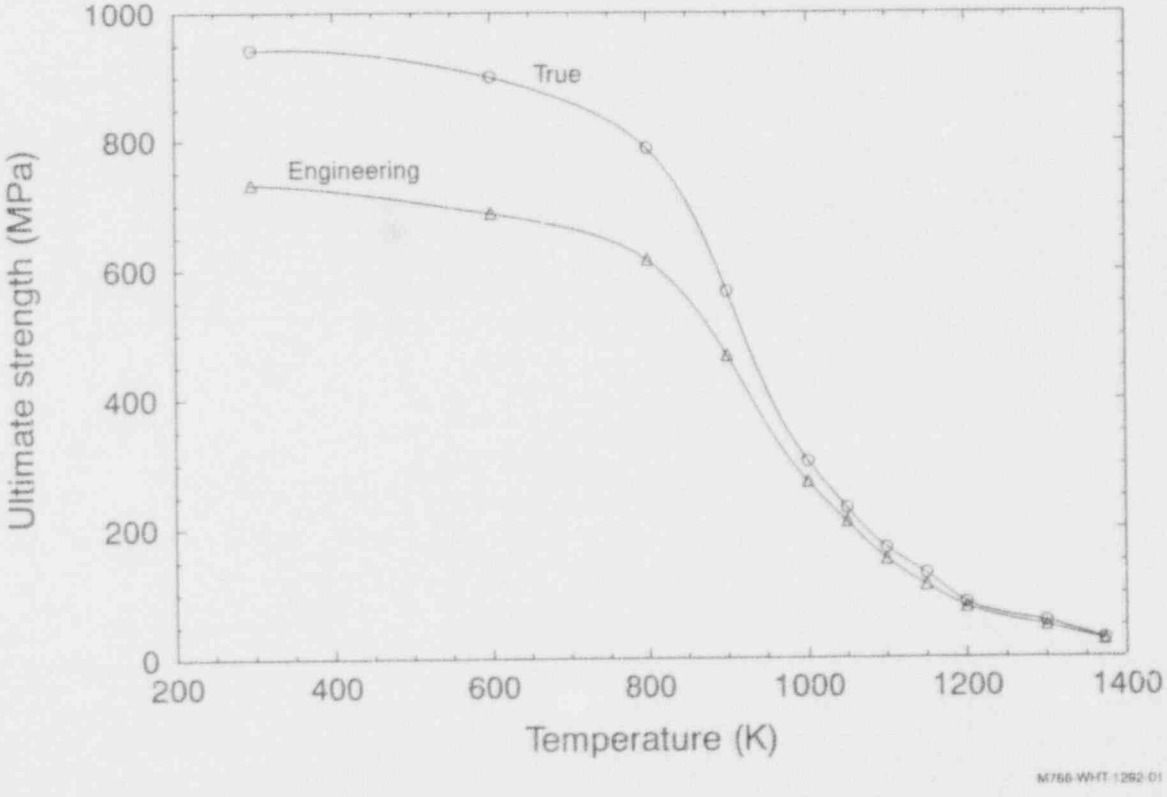

Figure B-28. Inconel 600 ultimate strength, true and engineering—INEL tensile test results.

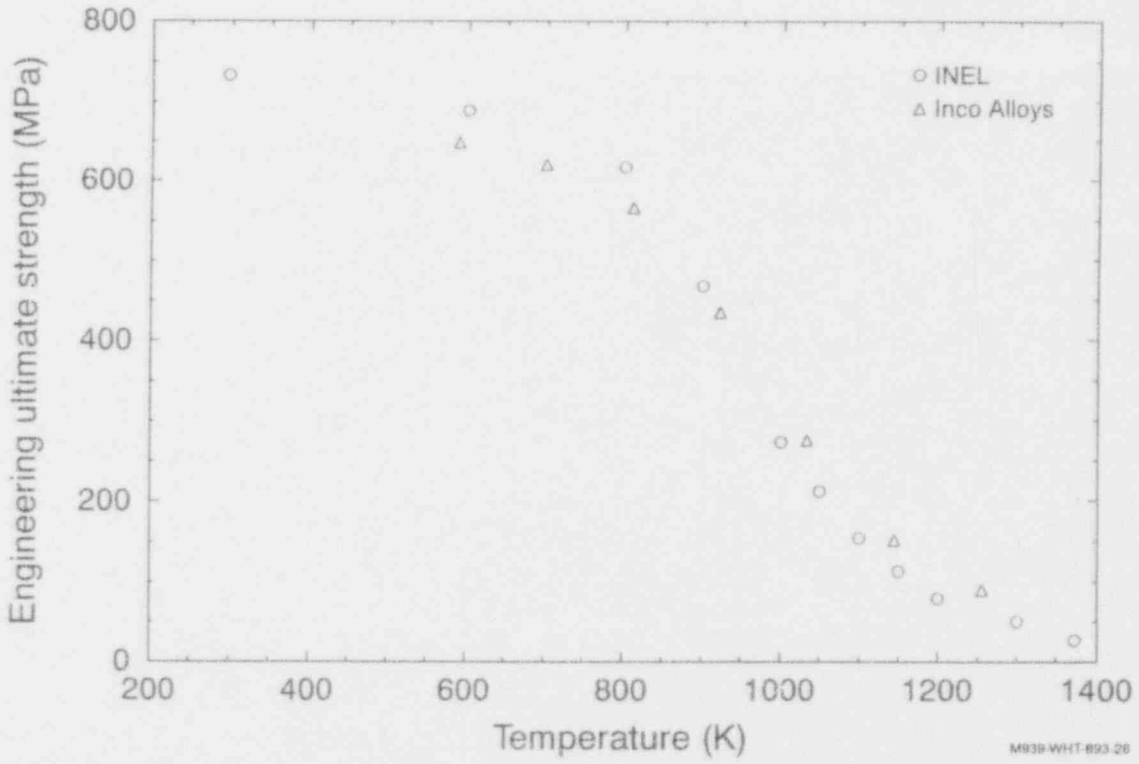

Figure B-29. Inconel 600, ultimate strength--INEL and Inco Alloys, International Inc., tensile test results.[B-11]

Table B-5. Inconel 600 creep data.

Temperature (K)	Stress (MPa)	Time to rupture (h)	Minimum creep rate (%/h)	Time to tertiary creep (h)	Total elongation (%)	Area reduction (%)
1005	173.20	1.30	22.034	0.60	64.0	77.1
1005	137.80	5.00	5.505	2.20	65.4	88.7
1005	93.60	38.50	0.517	10.60	67.9	84.4
1144	71.10	1.20	17.066	0.30	67.9	87.7
1144	55.60	3.00	4.528	0.80	68.3	79.4
1144	36.10	11.50	1.312	2.90	76.4	67.6
1255	44.40	0.50	60.332	0.17	88.6	88.6
1255	40.60	1.80	16.407	1.00	55.7	63.2
1255	29.50	3.20	9.738	2.20	46.6	57.5
1366	22.20	0.75	24.854	0.25	79.0	96.1
1366	14.10	5.90	3.987	2.90	58.1	64.4

Product information: 1/2 in. rod, heat no. NX678714, annealed 1 hour at 1143 K, forced-air cooled.

Chemistry: 0.060 C, 0.250 Mn, 0.001 S, 0.250 Si, 76.10 Ni, 14.890 Cr, 0.140 Cu, 8.310 Fe.

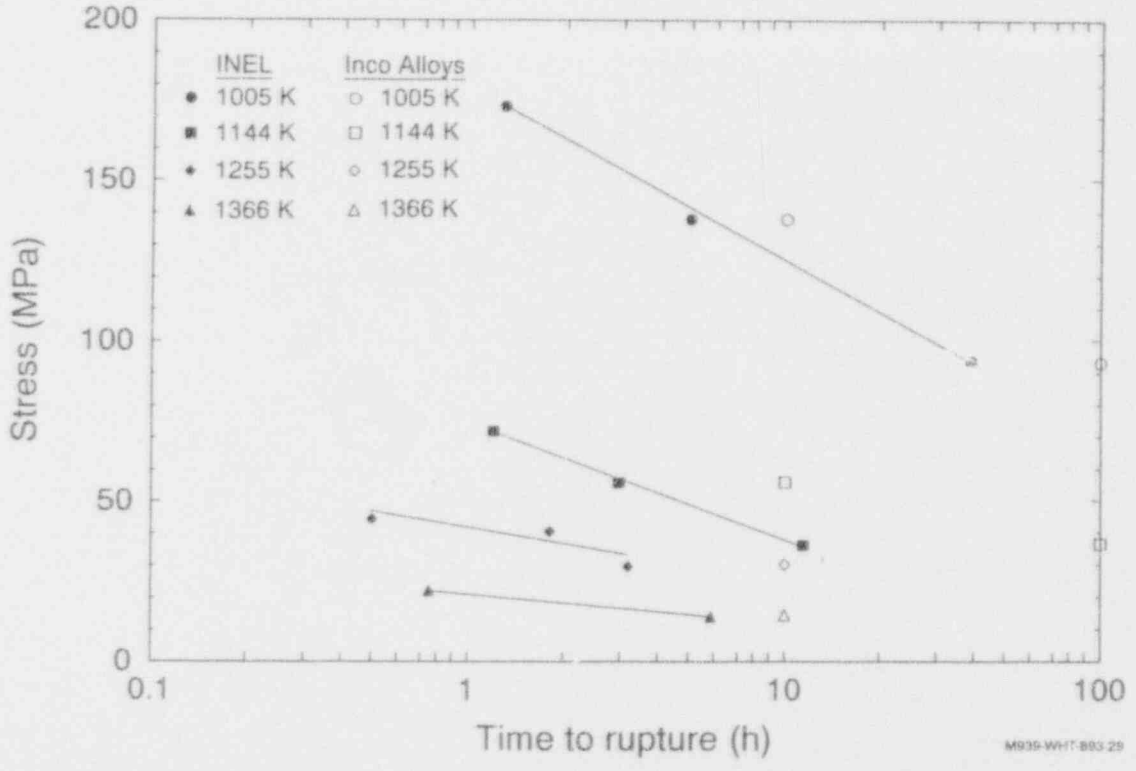

Figure B-30. Inconel 600, stress versus time to rupture—INEL and International Nickel Company, Inc. creep test results.[B-11]

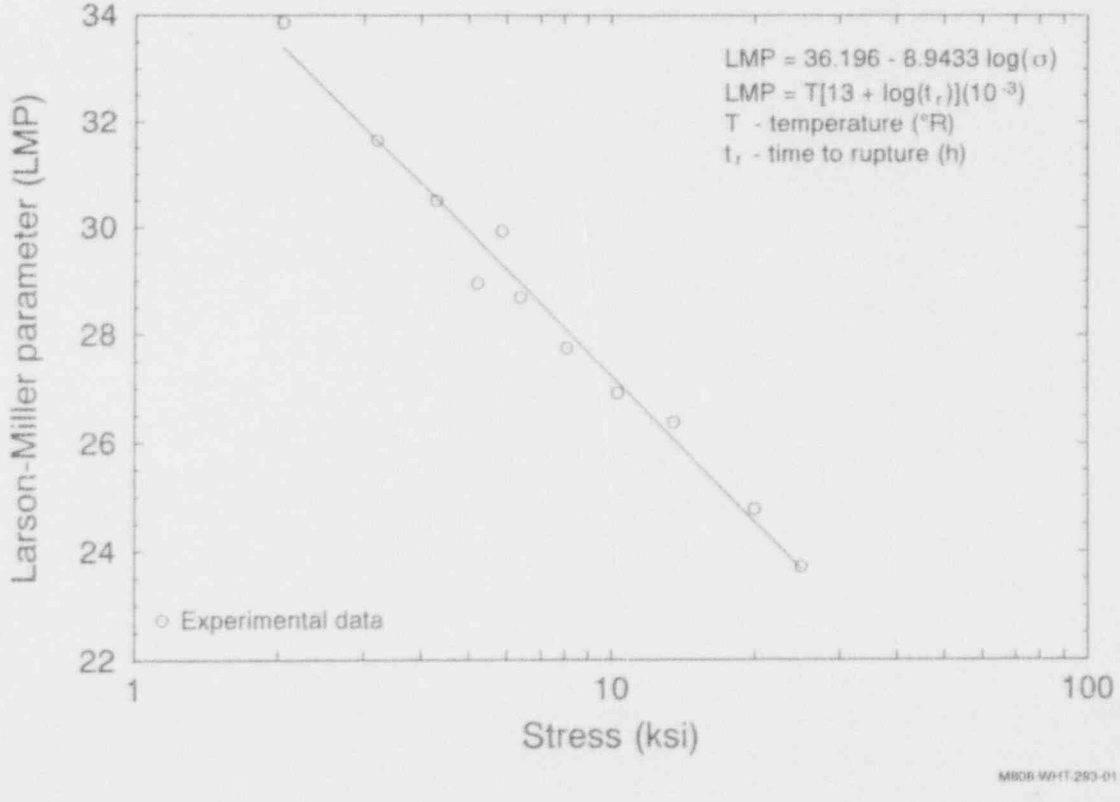

Figure B-31. Inconel 600 Larson-Miller parameter versus stress—INEL creep test results.

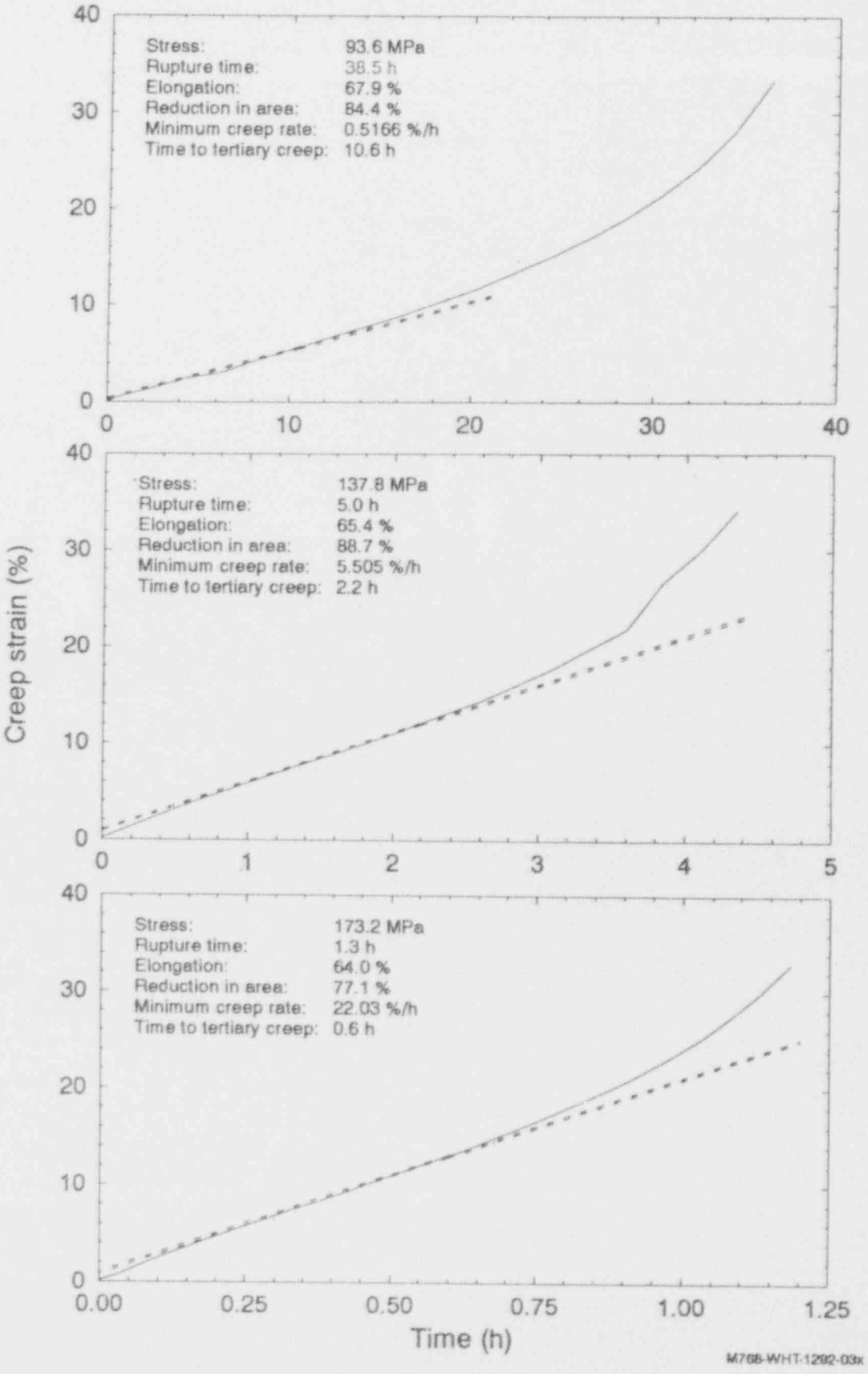

Figure B-32. Inconel 600 creep strain versus time at 1005 K—INEL results.

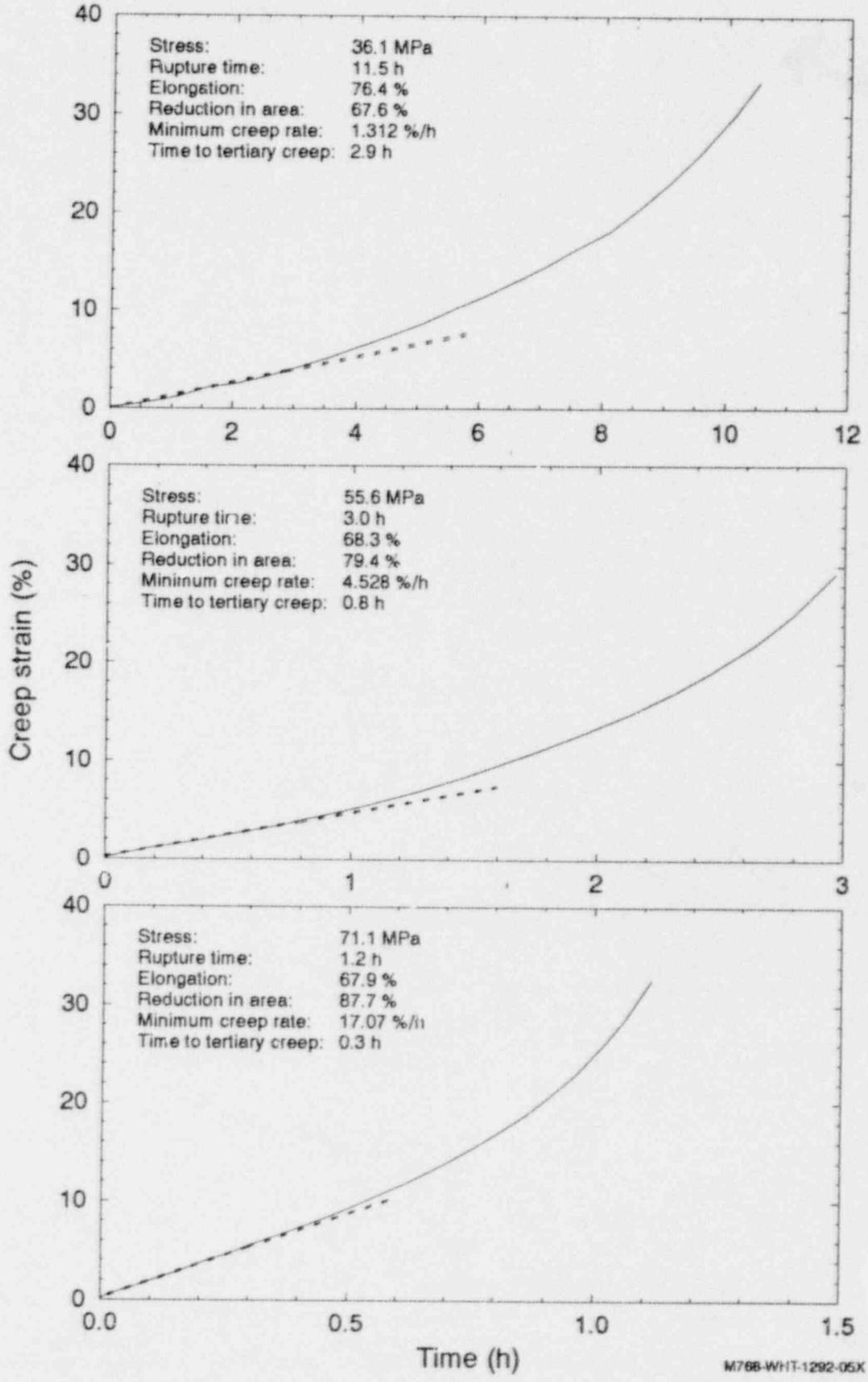

Figure B-33. Inconel 600 creep strain versus time at 1144 K—INEL creep test results.

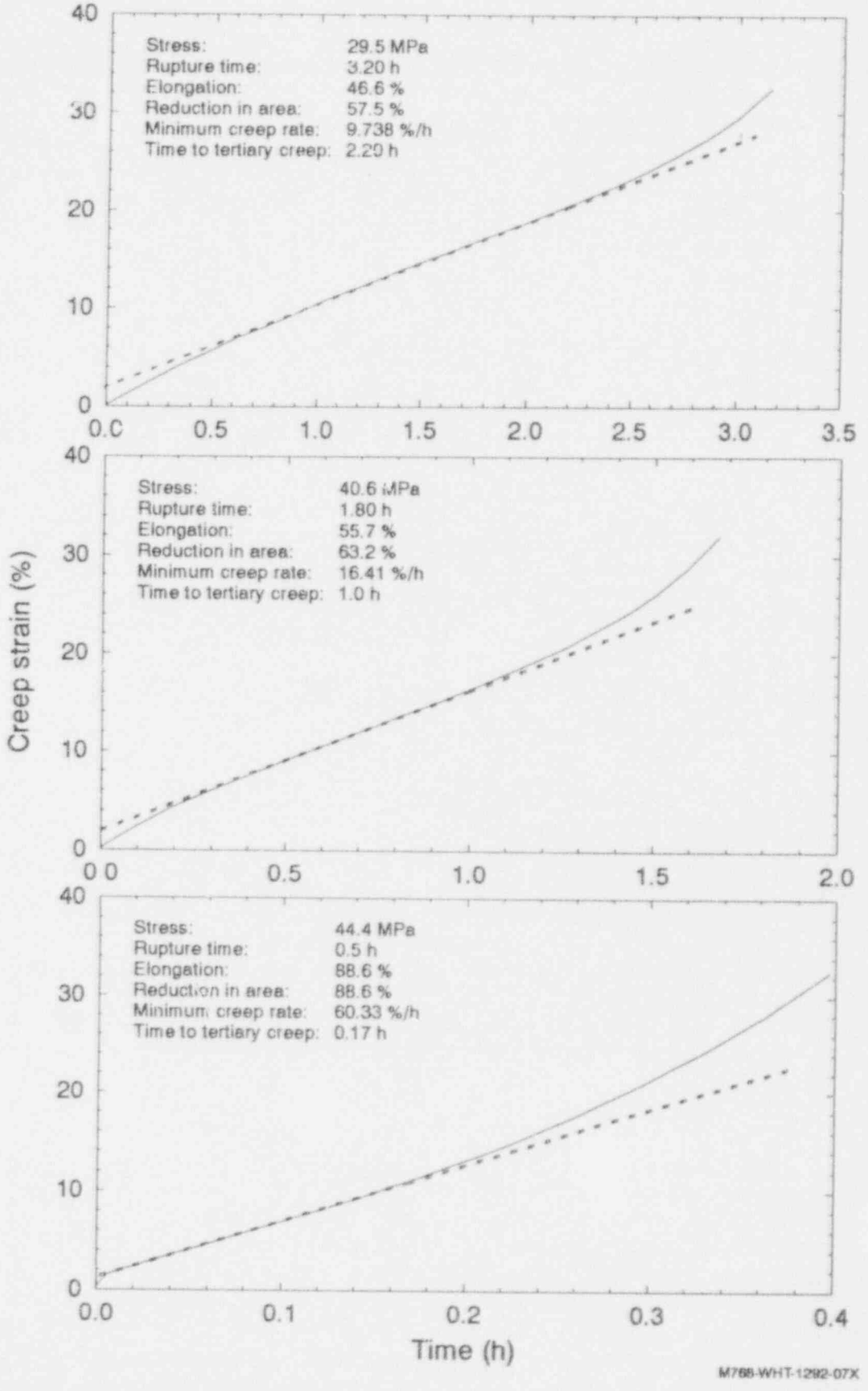

Figure B-34. Inconel 600 creep strain versus time at 1255 K—INEL creep test results.

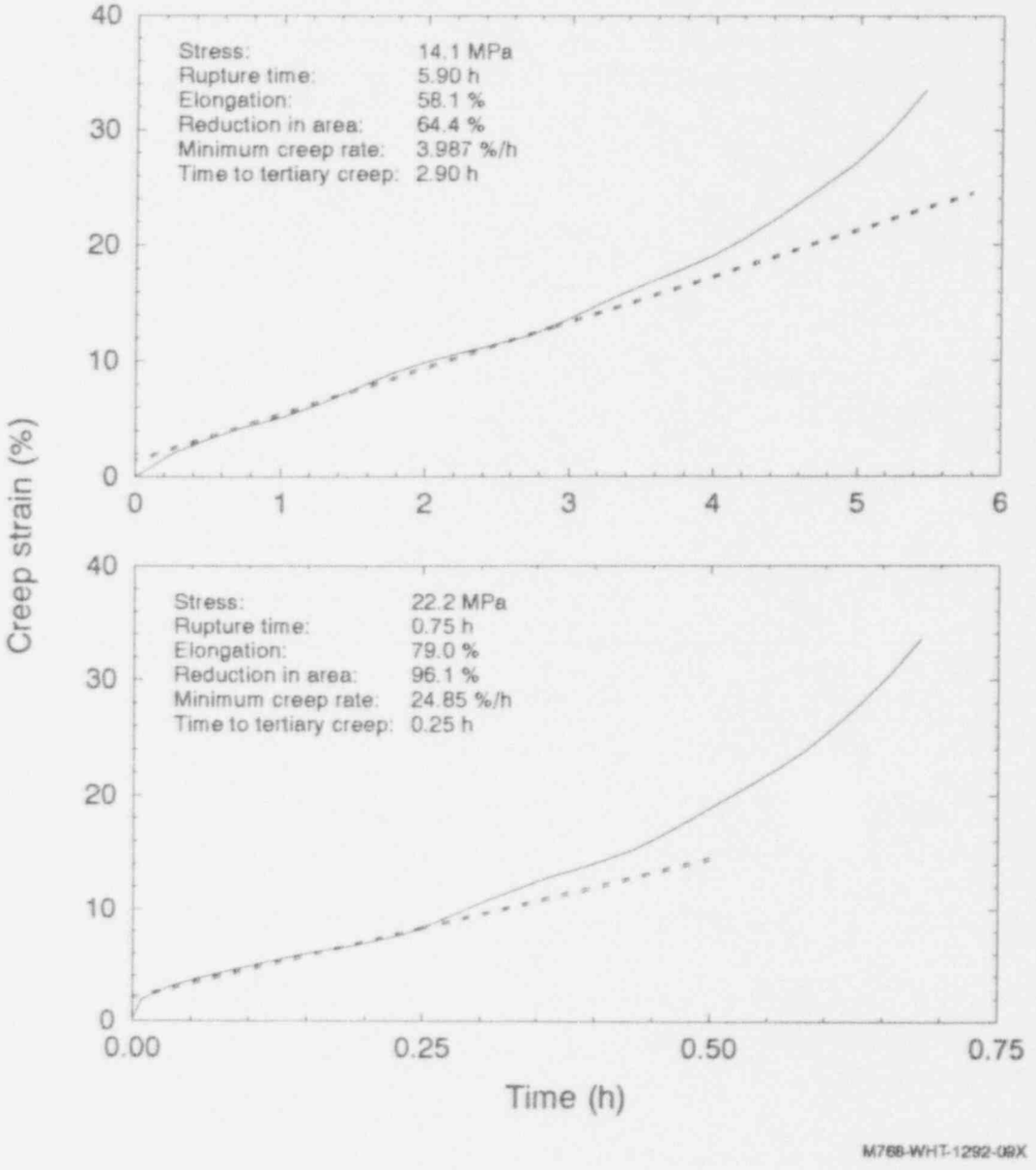

Figure B-35. Inconel 600 creep strain versus time at 1366 K—INEL creep test results.

B-4.4 304 Stainless Steel

B-4.4.1 304 Stainless Steel Tensile Tests

The stainless steel specimens, fabricated from 12.7-mm round bar, were annealed for 1 hour at 1323 K and forced-air cooled prior to testing. Figure B-36 plots stress-strain curves from 304 stainless steel tensile tests for temperatures up to 1373 K. The published values of elastic modulus[B-17] are listed in Table B-6, which summarizes the results from tensile testing. Elastic moduli were extrapolated for temperatures above 1048 K using a second order polynomial fit. All other values listed in Table B-6 were obtained from tests performed at the INEL. In Figure B-36, the stress-strain curve at 1150 K shows a slight jump at approximately 0.23 strain;

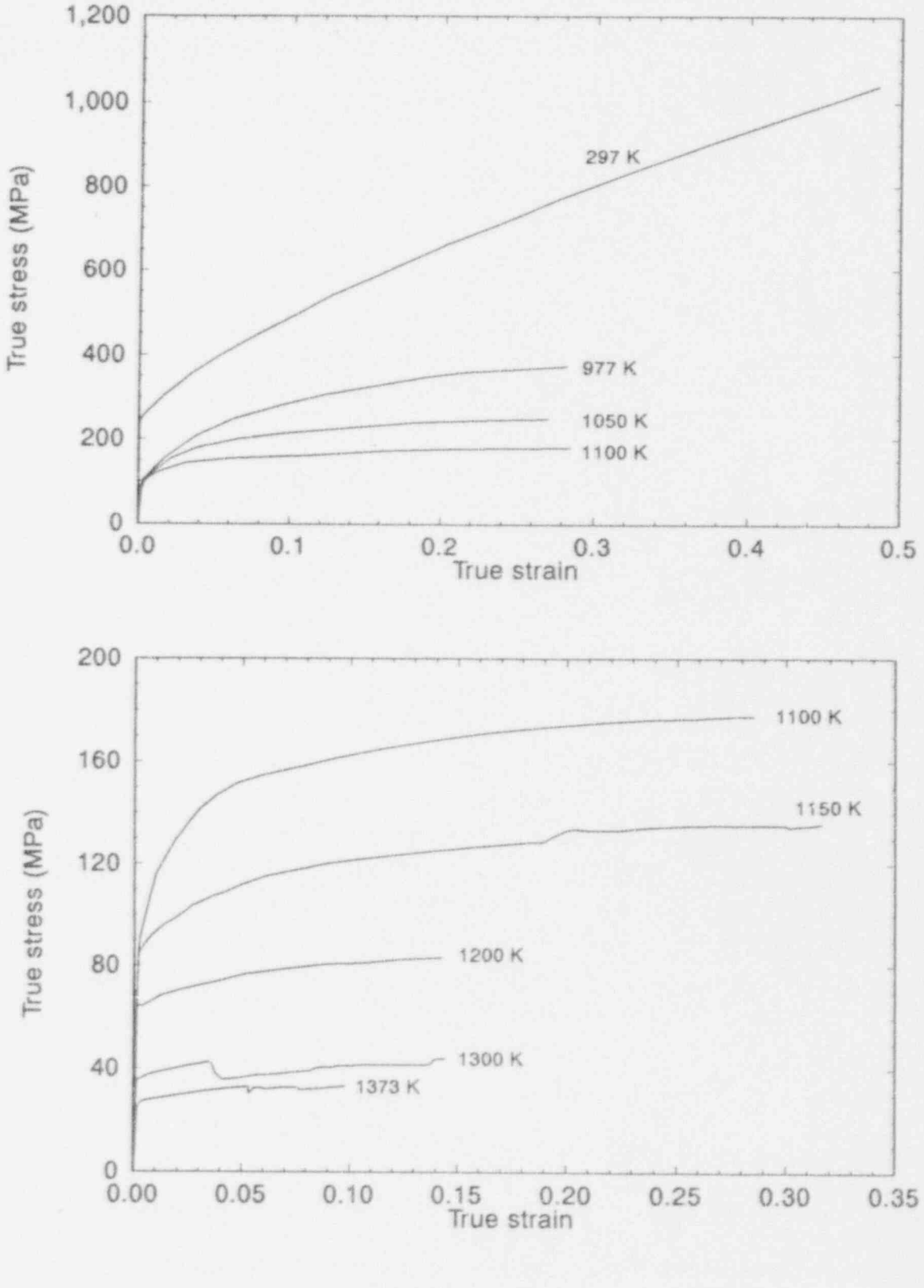

Figure B-36. Stress-strain curves for 304 stainless steel at various temperatures—INEL tensile test results.

Table B-6. 304 stainless steel tensile data.[a]

Temperature (K)	E[b] (GPa)	Proportional limit (MPa)	σ_y[c] (MPa)	True σ_u[d] (MPa)	Engineering σ_u[d] (MPa)	Uniform elongation (%)	Total elongation (%)	Area reduction (%)
297	194.77	208.00	252.00	1044.7	642.00	66	81	80
977	138.17	77.00	98.00	372.46	285.00	24	54	68
1050	129.81	61.00	93.00	245.45	197.00	17	64	78
1100	123.83	66.00	91.00	177.46	147.00	11	74	73
1150	117.64	60.00	85.00	135.58	109.00	25	71	68
1200	111.24	46.00	64.00	82.45	73.00	8	52	75
1300	97.83	26.00	35.00	43.47	40.00	4	29	59
1300	97.83	27.00	36.00	40.68	39.00	1	25	58
1373	87.51	17.00	26.00	32.64	30.00	5	50	64

a. Product information: 1/2 in. rod, heat no. 602151, annealed 1 hour at 1323 K, forced-air cooled.

Chemistry: 0.06 C, 1.25 Mn, 0.031 P, 0.023 S, 0.610 Si, 8.180 Ni, 18.410 Cr, 0.380 Mo, 0.130 Co, 0.063 N.

b. Young's modulus.

c. Yield stress.

d. Ultimate stress.

additionally, the curve for 1300 K is not consistent with other curves. Both the nontypical flow curves at 1150 and 1300 K resulted from temperature control problems. These anomalies do not appear to affect the yield and ultimate strength values. These values are consistent with tests at other temperatures, as shown in Figures B-37 and B-38, which plot temperature-dependent yield and ultimate strengths, both true and engineering. Figure B-39 compares INEL ultimate strength (engineering) data and published data.[B-14,B-15,B-18,B-19] The two data sets compare very well.

B-4.4.2 304 Stainless Steel Creep Tests

Table B-7 summarizes creep data obtained for six tests run from 1089 to 1350 K. Stresses varied from approximately 8 to 85 MPa; times to rupture ranged from about one hour to 85.3 hours. These data and previously published data[B-20] are plotted in Figure B-40. The INEL data at 1089 K fit reasonably well with the published data and are consistent with tests at different temperatures.

Figure B-41 plots the LMP against logarithmic stress (ksi). The LMP was calculated from the following equation:

$$LMP = T[16 + \log(t_r)]\ (10^{-3})$$

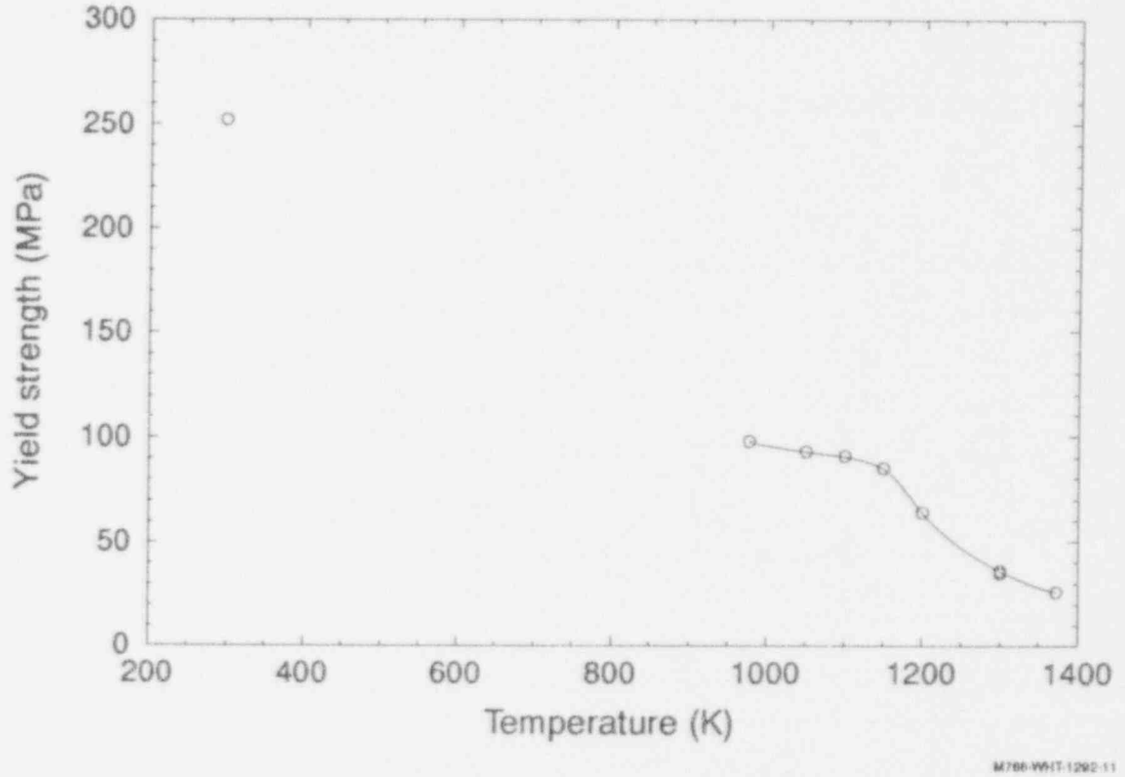

Figure B-37. 304 stainless steel yield strength (0.2% offset)—INEL tensile test results.

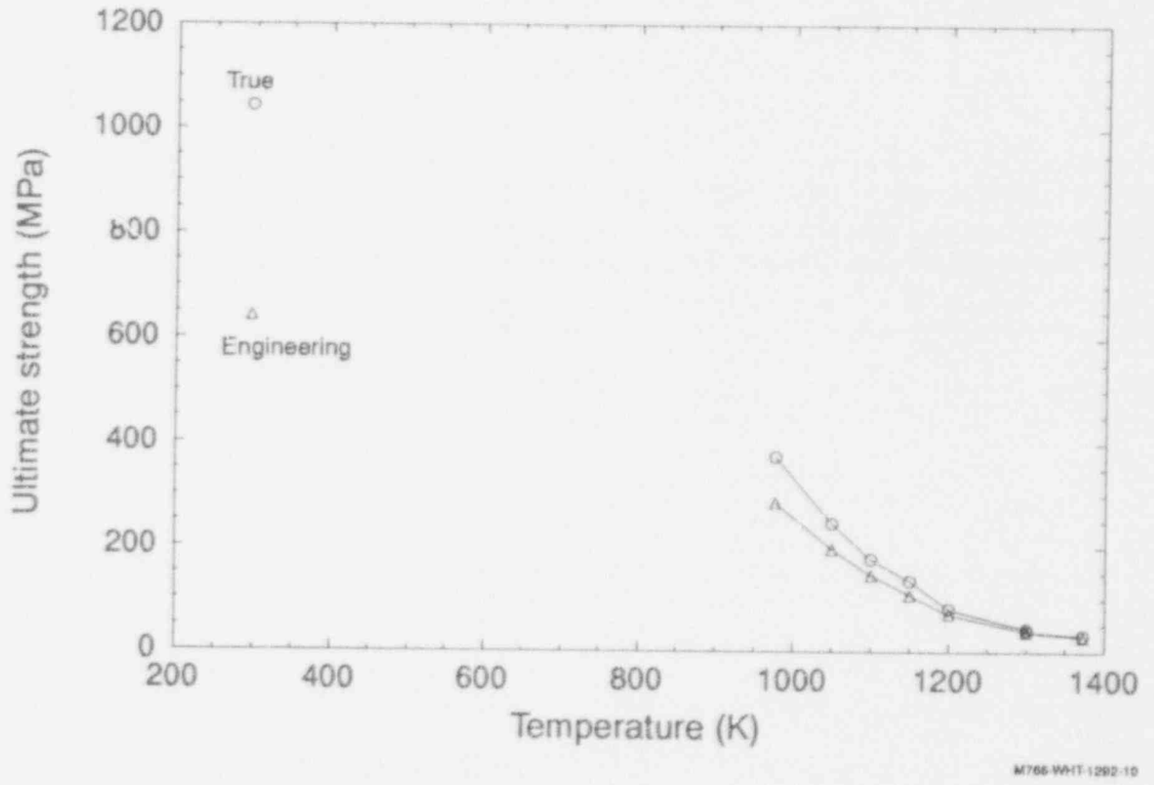

Figure B-38. 304 stainless steel ultimate strength, true and engineering—INEL tensile test results.

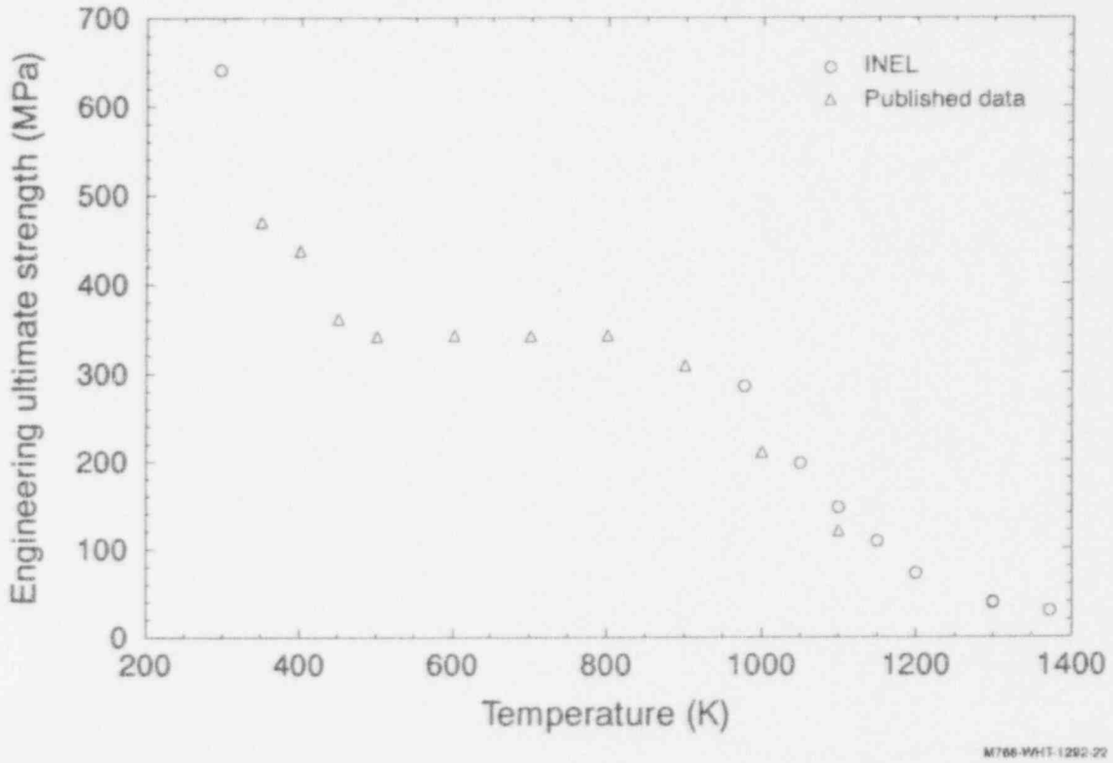

Figure B-39. 304 stainless steel, ultimate strength—INEL and published tensile test results.[B-14,B-15,B-18,B-19]

Table B-7. 304 Stainless steel creep data.

Temperature (K)	Stress (MPa)	Time to rupture (h)	Minimum creep rate (%/h)	Time to tertiary creep (h)	Total elongation (%)	Area reduction (%)
1089	85.30	8.00	4.086	4.24	54	57
1200	40.50	5.90	4.174	3.08	46	41
1200	54.60	1.30	23.604	0.64	57	55
1350	8.40	21.80	0.940	12.36	32	25
1350	9.80	17.20	1.560	5.79	41	31
1350	16.90	2.35	11.102	1.07	54	42

Product information: 1/2 in. rod, heat no. 602151, annealed 1 hour at 1323 K, forced-air cooled.

Chemistry: 0.06 C, 1.25 Mn, 0.031 P, 0.023 S, 0.610 Si, 8.180 Ni, 18.410 Cr, 0.380 Mo, 0.130 Co, 0.063 N

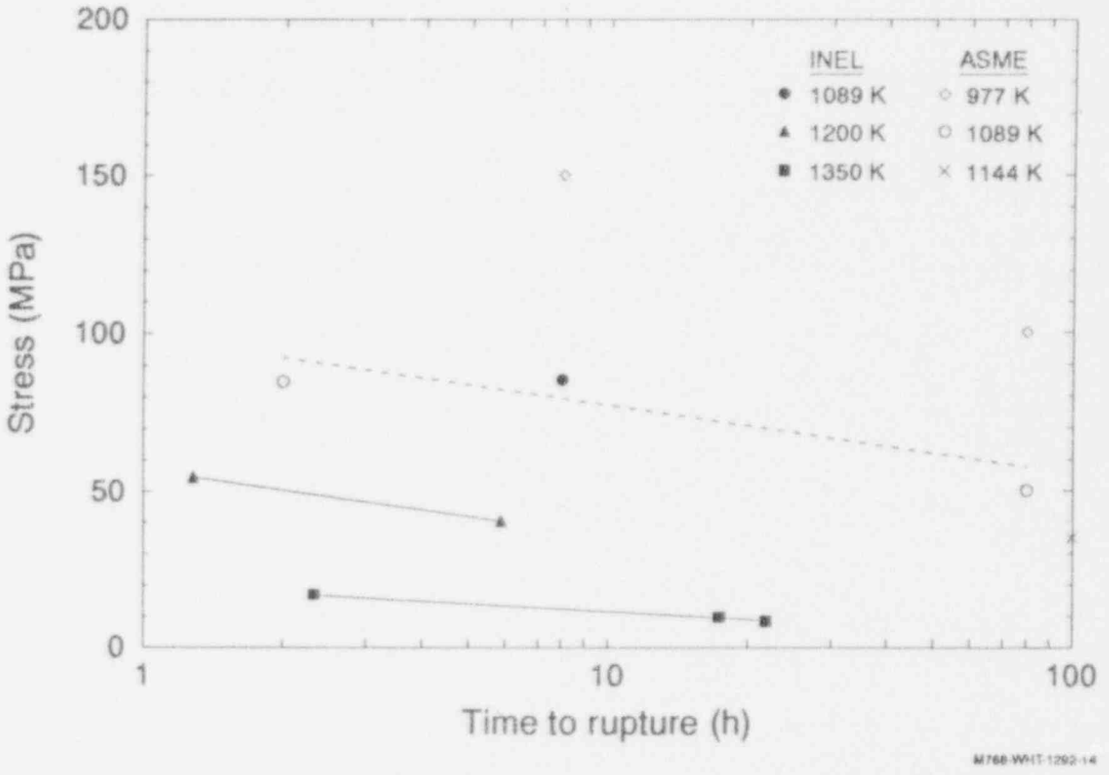

Figure B-40. 304 stainless steel, stress versus time to rupture—INEL and ASME creep test results.[B-20]

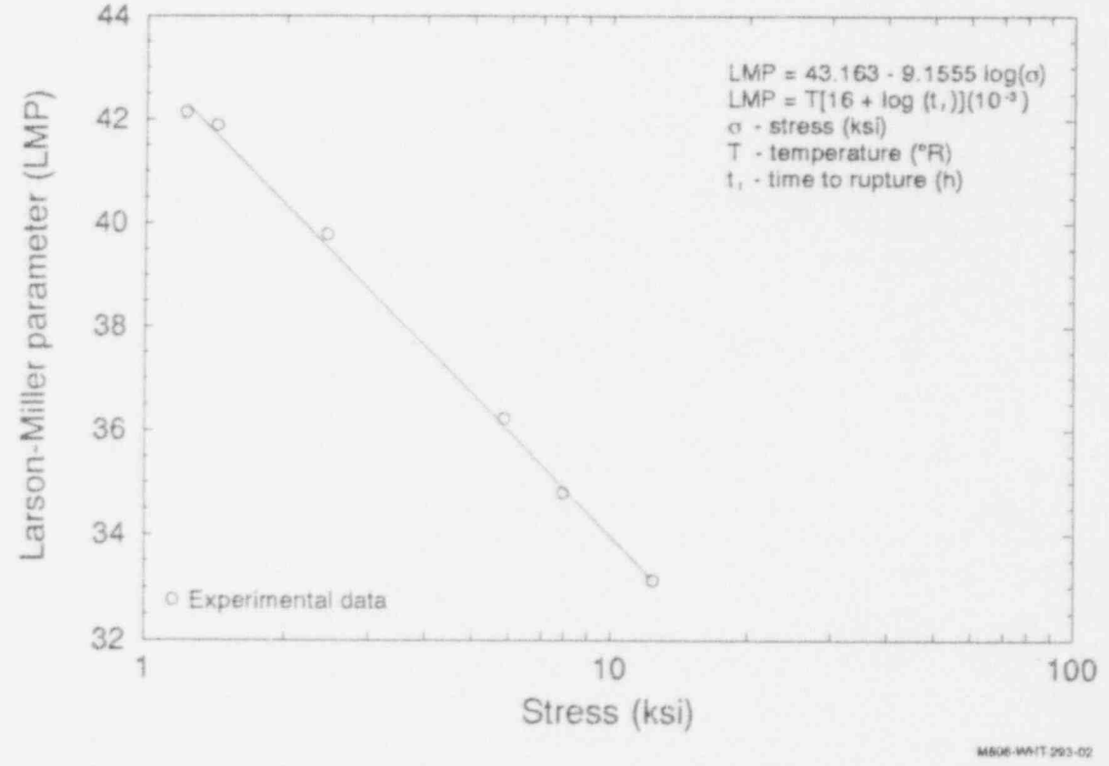

Figure B-41. 304 stainless steel Larson-Miller parameter versus stress—INEL creep test results.

where T is temperature (°R) and t_r is time to rupture (h). English units were used to be consistent with historical data. Though data are limited, the linear fit is quite good.

Strain versus time data, often used in finite element creep analysis, are shown in Figures B-42 through B-44.

B-4.5 SA106B Carbon Steel

B-4.5.1 SA106B Carbon Steel Tensile Tests

Results from SA106B carbon steel tensile tests for temperatures up to 1150 K are plotted in Figures B-45 through B-48 and summarized in Table B-8. Specimens were fabricated from 6-in. Schedule 120 pipe and tested in the as-received condition. Published values of elastic modulus tested between room temperature and 1273 K[B-6] were used to construct the stress-strain curves, as listed in Table B-8. All other values listed in Table B-8 were obtained from tests performed at the INEL.

Figure B-45 shows stress-strain curves for various temperatures. Curves at 500 and 1100 K show ultimate strengths higher than those measured at the next lower temperature. The causes of this phenomenon are unknown. The material changes from ferrite to austenite in the 1000-1100 K regime, which may partially explain the unusual results at 1100 K. Figures B-46 and B-47 plot temperature-dependent yield and ultimate strengths, true and engineering. Figure B-48 shows INEL and published data[B-21] for ultimate strength (engineering). The INEL data are considerably higher than the published data for temperatures below 800 K; however, the high

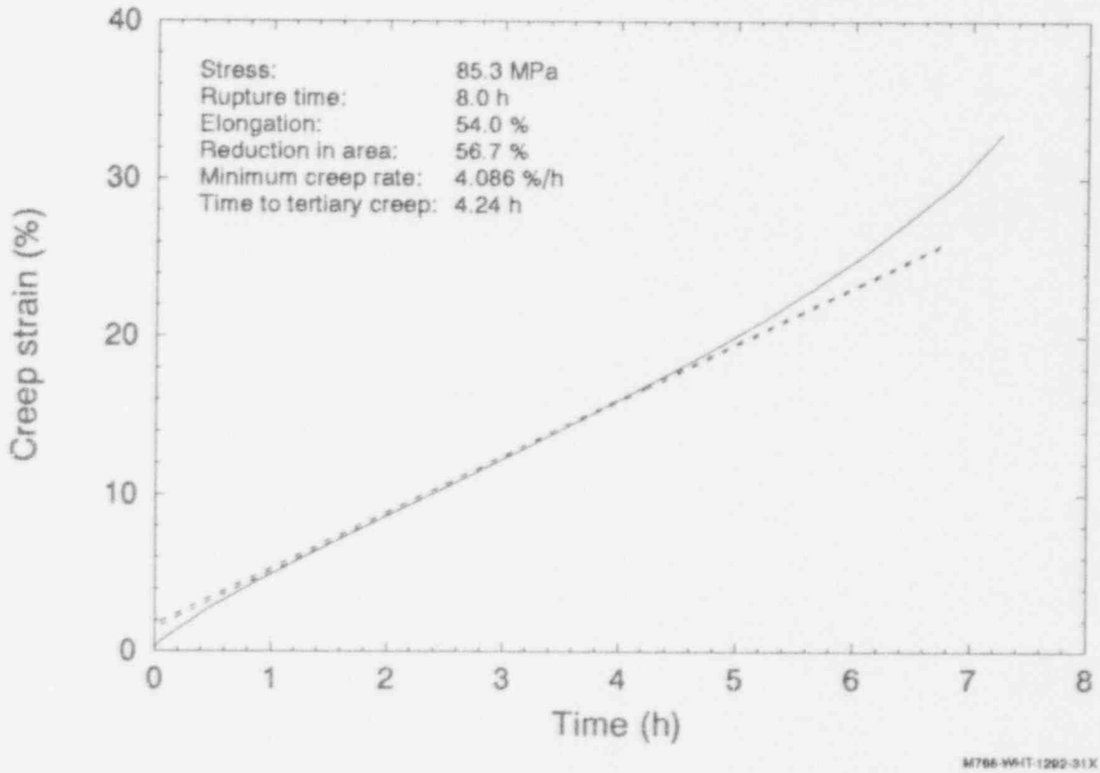

Figure B-42. 304 stainless steel creep strain versus time at 1089 K—INEL creep test results.

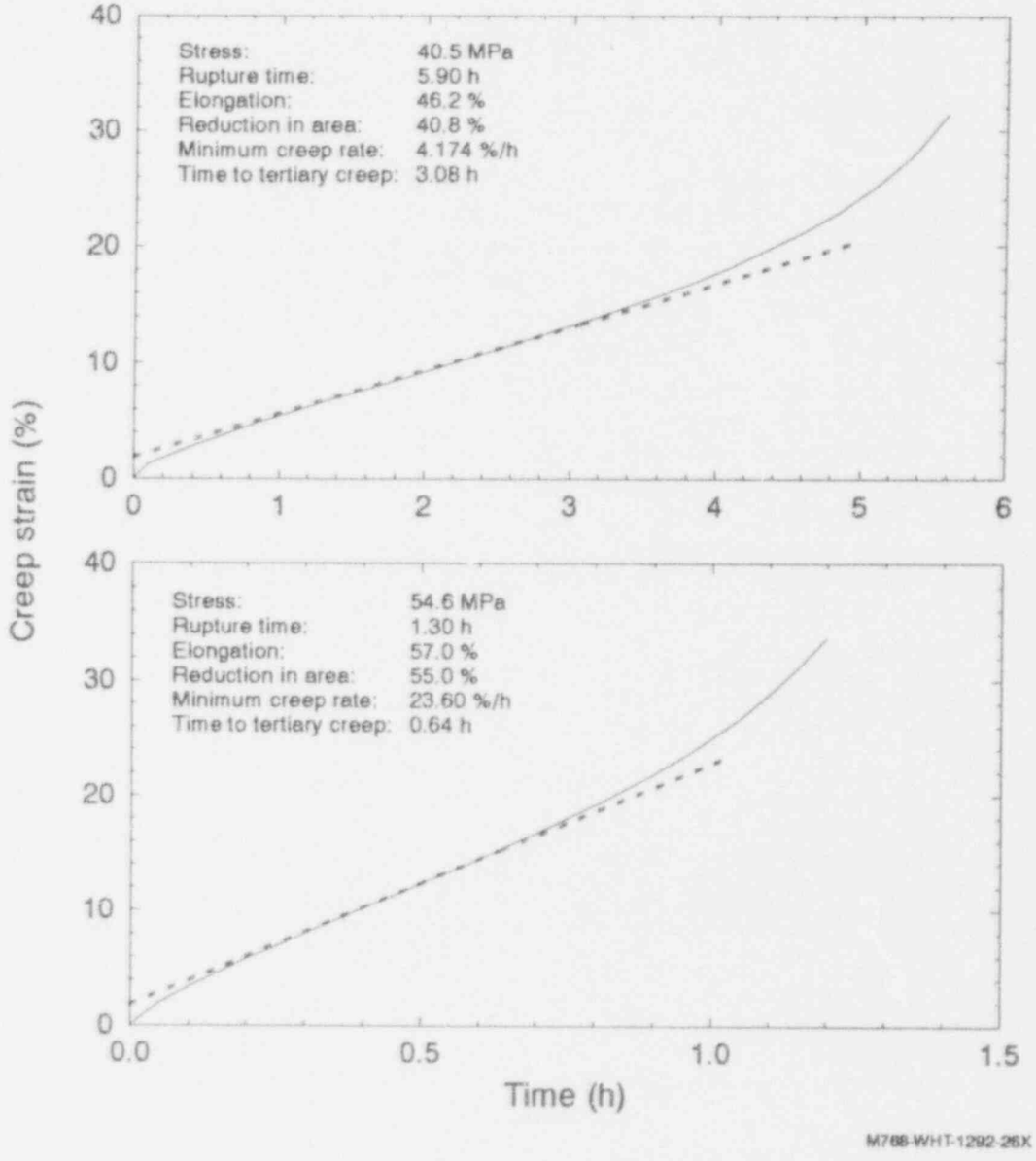

Figure B-43. 304 stainless steel creep strain versus time at 1200 K—INEL creep test results.

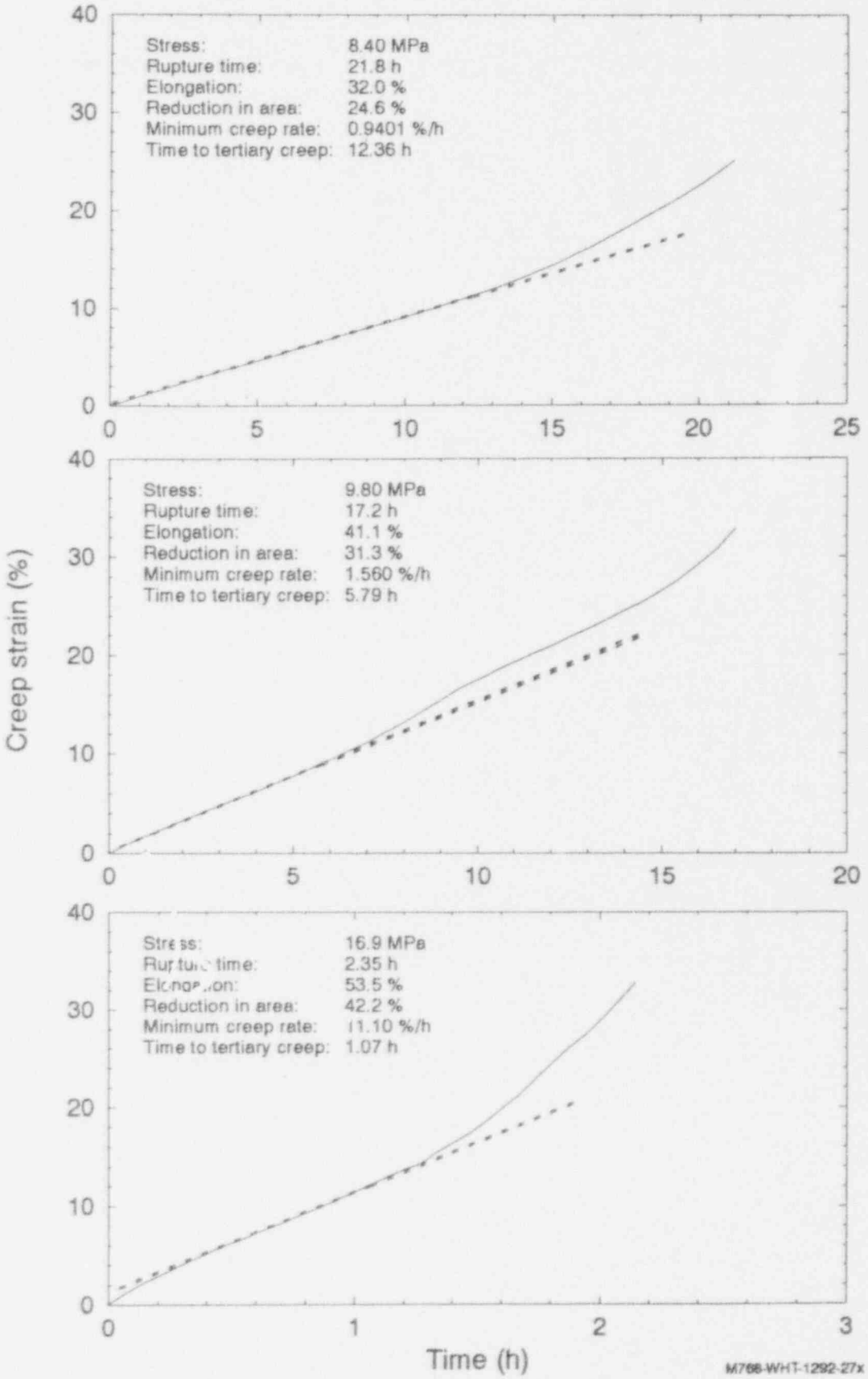

Figure B-44. 304 stainless steel creep strain versus time at 1350 K—INEL creep test results.

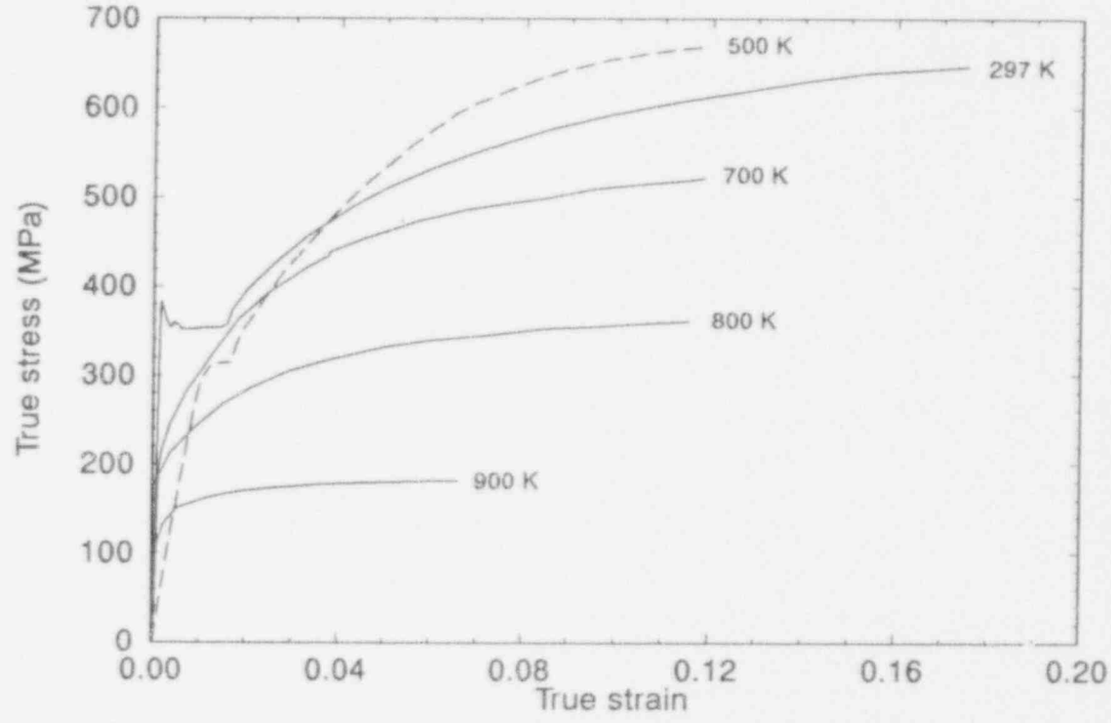

M786 sac-1292-18

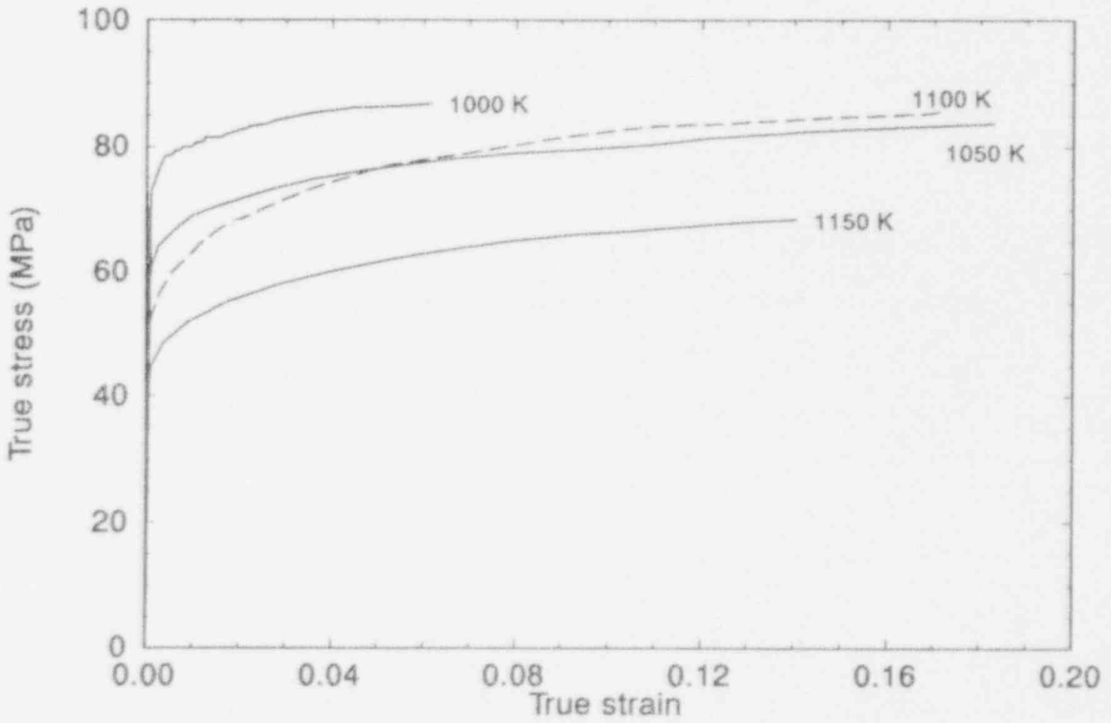

M786 sac-1292-19

Figure B-45. Stress-strain curves for SA106B carbon steel at various temperatures—INEL tensile test results.

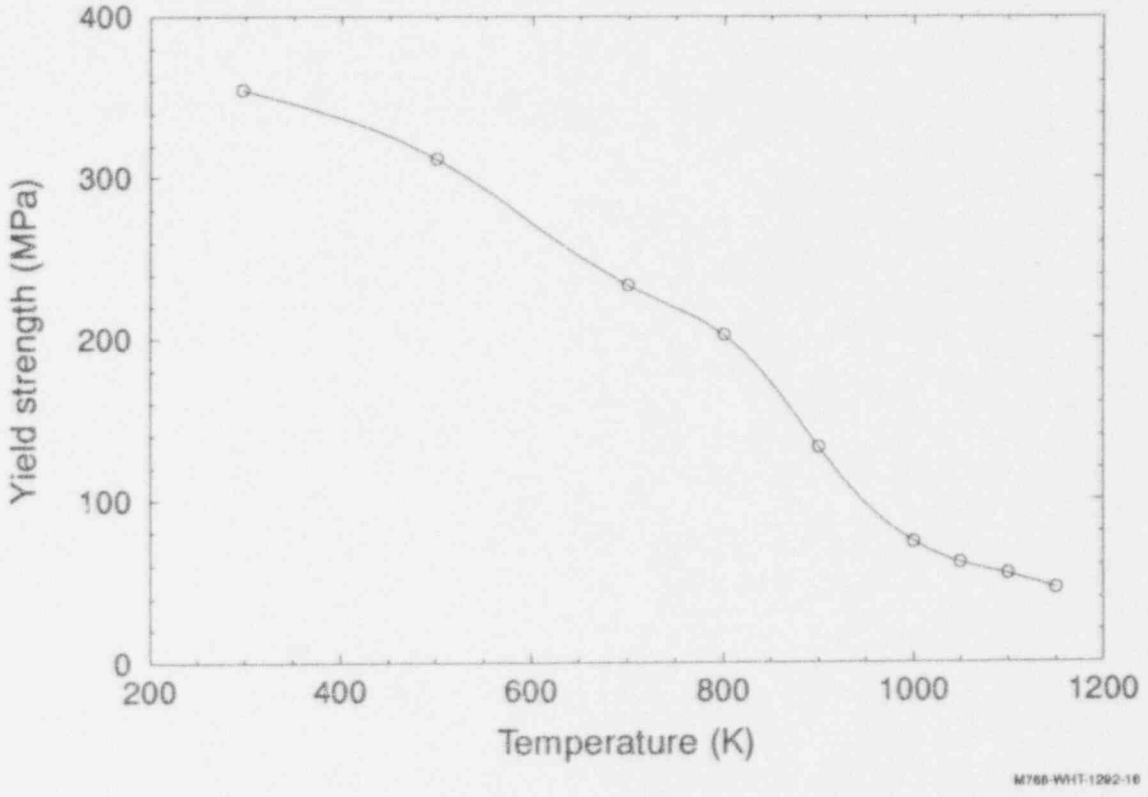

Figure B-46. SA106B carbon steel yield strength (0.2% offset)—INEL tensile test results.

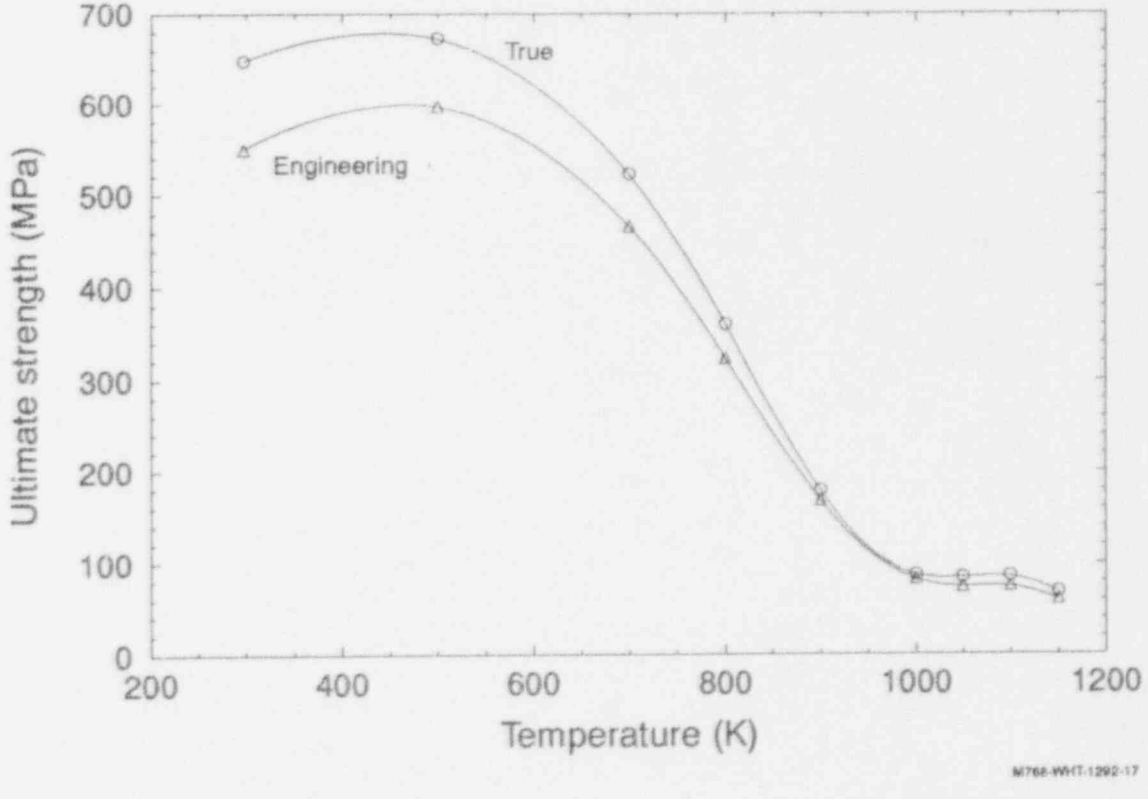

Figure B-47. SA106B carbon steel ultimate strength, true and engineering—INEL tensile test results.

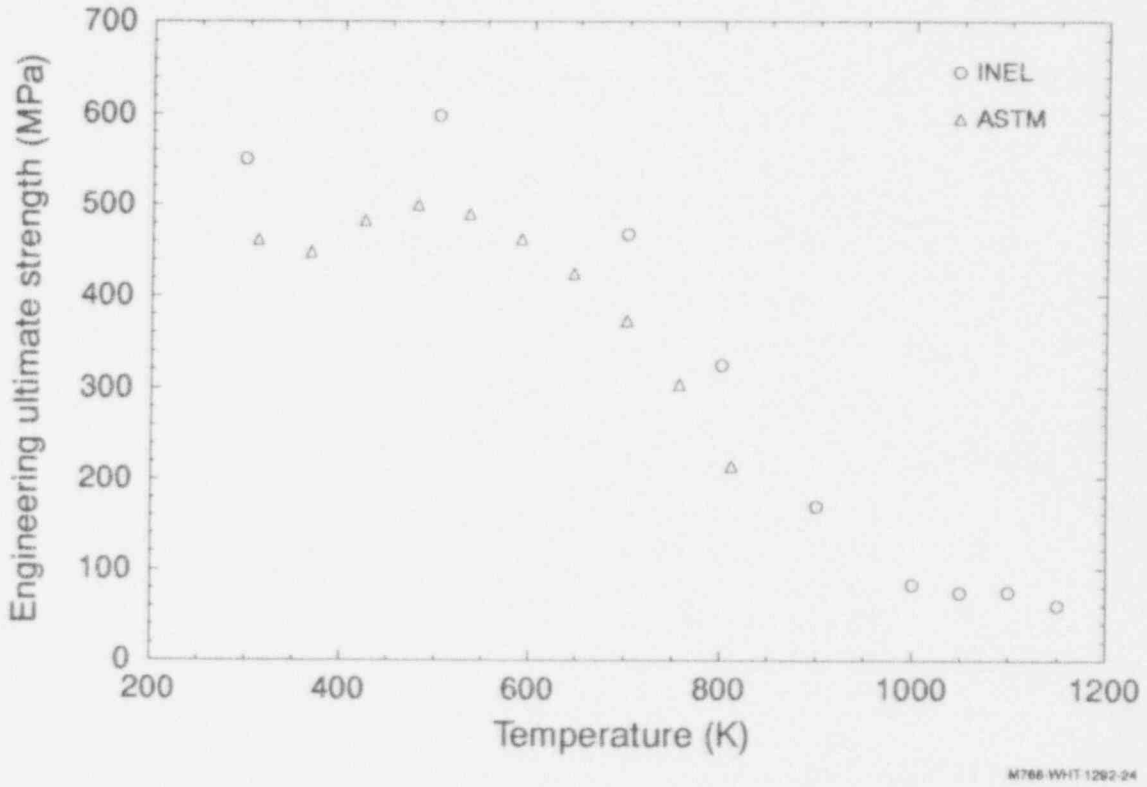

Figure B-48. SA106B carbon steel ultimate strength—INEL and ASTM tensile test results.[B-21]

Table B-8. SA106B carbon steel tensile data.[a]

Temperature (K)	E[b] (GPa)	Proportional limit (MPa)	σ_y[c] (MPa)	True σ_u[d] (MPa)	Engineering σ_u[d] (MPa)	Uniform elongation (%)	Total elongation (%)	Area reduction (%)
297	204.37	374.00	355.00	648.47	550.00	16	33	66
500	193.31	281.00	312.00	673.78	598.00	10	21	46
700	175.00	143.00	234.00	523.50	467.00	11	31	68
800	166.54	127.00	203.00	360.70	324.00	8	37	76
900	154.65	76.00	133.00	179.57	169.00	5	55	81
1000	139.47	42.00	74.00	87.51	83.00	4	65	89
1050	130.05	41.00	62.00	84.02	74.00	6	58	59
1100	123.20	41.00	55.00	85.89	75.00	11	49	52
1150	118.54	25.00	46.00	68.63	60.00	10	44	45

a. Product information: 6-in. Schedule 120 pipe, heat no. A84239, as received.

Chemistry: 0.25 C, 0.94 Mn, 0.014 P, 0.010 S, 0.25 Si, 0.02 Cu, 0.02 Ni, 0.06 Cr, 0.01 Mo.

b. Young's modulus.

c. Yield stress.

d. Ultimate stress.

temperature INEL data appear to be consistent with published data if they are extrapolated beyond their temperature range. The low temperature discrepancy may result from differences in heat treatment or heat-to-heat variations, which would become inconsequential at high temperatures.

B-4.5.2 SA106B Carbon Steel Creep Tests

Table B-9 summarizes creep data obtained for seven tests run from 811 to 1050 K. Stresses varied from approximately 20 to 125 MPa, with times to rupture from less than one hour to about 87 hours, as plotted in Figure B-49. INEL data, tested at 124 MPa and 811 K, indicated failure at 85 hours. This was within the range of stress values given for a failure time of 85 hours in the published data.[B-21]

Figure B-50 plots the LMP against logarithmic stress (ksi). The LMP was calculated from the following equation:

$$LMP = T[13 + \log(t_r)] \ (10^{-3})$$

where T is temperature (°R) and t_r is time to rupture (h). English units were used to be consistent with historical data.

Strain versus time data, often used in finite element creep analysis, are shown in Figures B-51 through B-53.

Table B-9. SA106B carbon steel creep data.

Temperature (K)	Stress (MPa)	Time to rupture (h)	Minimum creep rate (%/h)	Time to tertiary creep (h)	Total elongation (%)	Area reduction (%)
811	124.60	80.90	0.0876	14.90	40.7	77.0
900	49.20	86.60	0.0676	16.47	62.3	87.6
900	79.70	7.20	1.629	2.12	55.3	88.5
900	103.70	1.70	7.698	0.64	53.6	85.3
1050	29.40	9.70	1.309	3.61	38.1	41.3
1050	19.80	23.05	0.391	8.58	37.5	54.6
1050	53.20	0.80	26.859	0.38	46.0	47.3

Product information: 6-in Schedule 120 pipe, heat no. A84239, as received.

Chemistry: 0.25 C, 0.94 Mn, 0.014 P, 0.010 S, 0.25 Si, 0.02 Cu, 0.02 Ni, 0.06 Cr, 0.01 Mo.

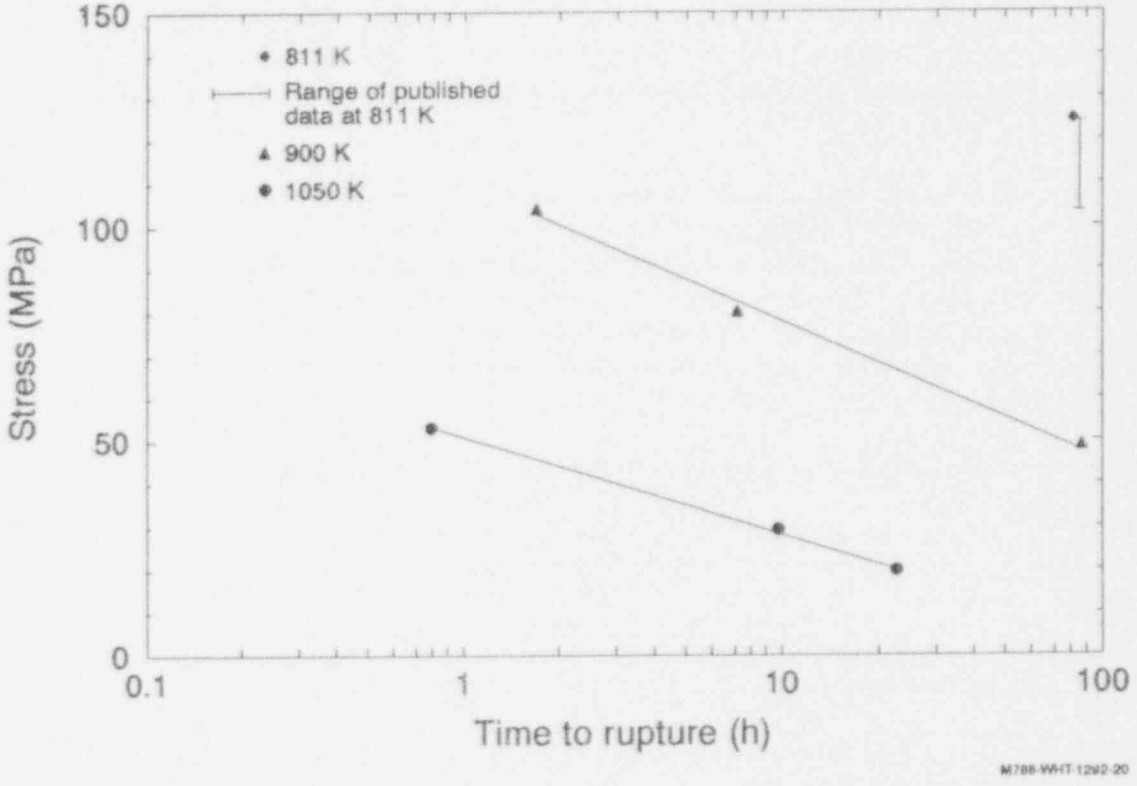

Figure B-49. SA106B carbon steel versus time to rupture—INEL and ASTM creep test results.[B-21]

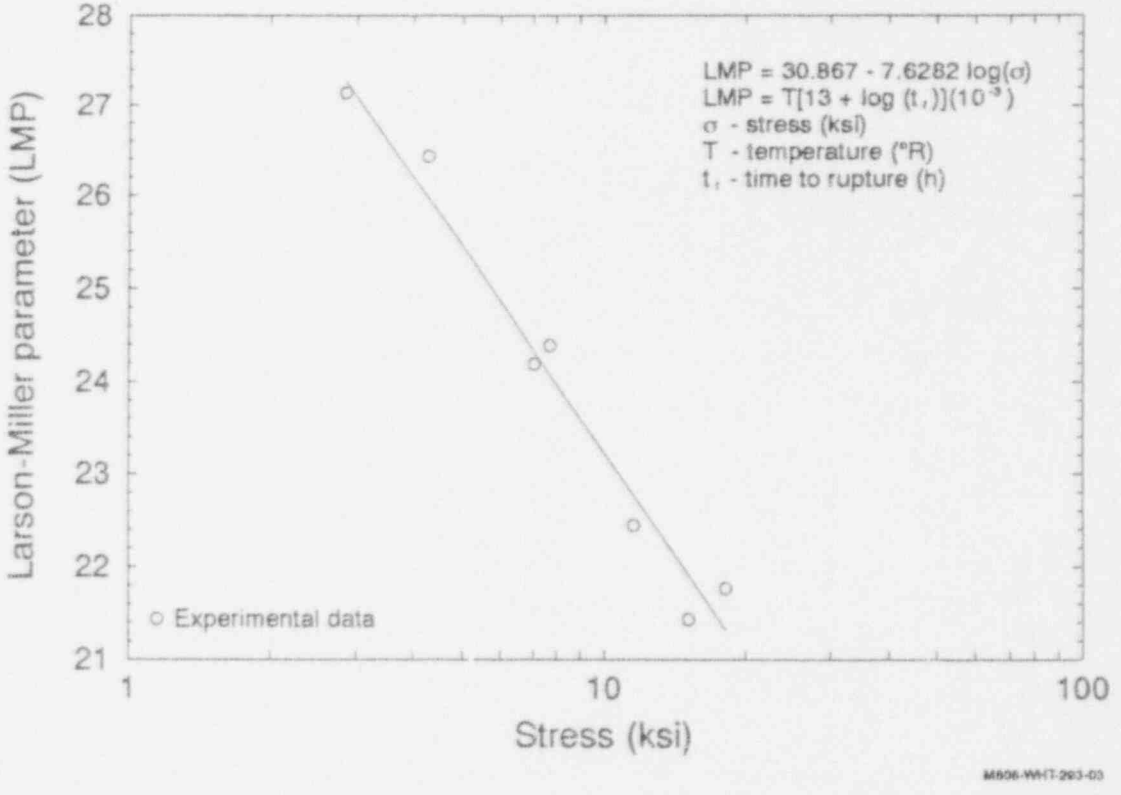

Figure B-50. SA106B carbon steel Larson Miller parameter versus stress—INEL creep test results.

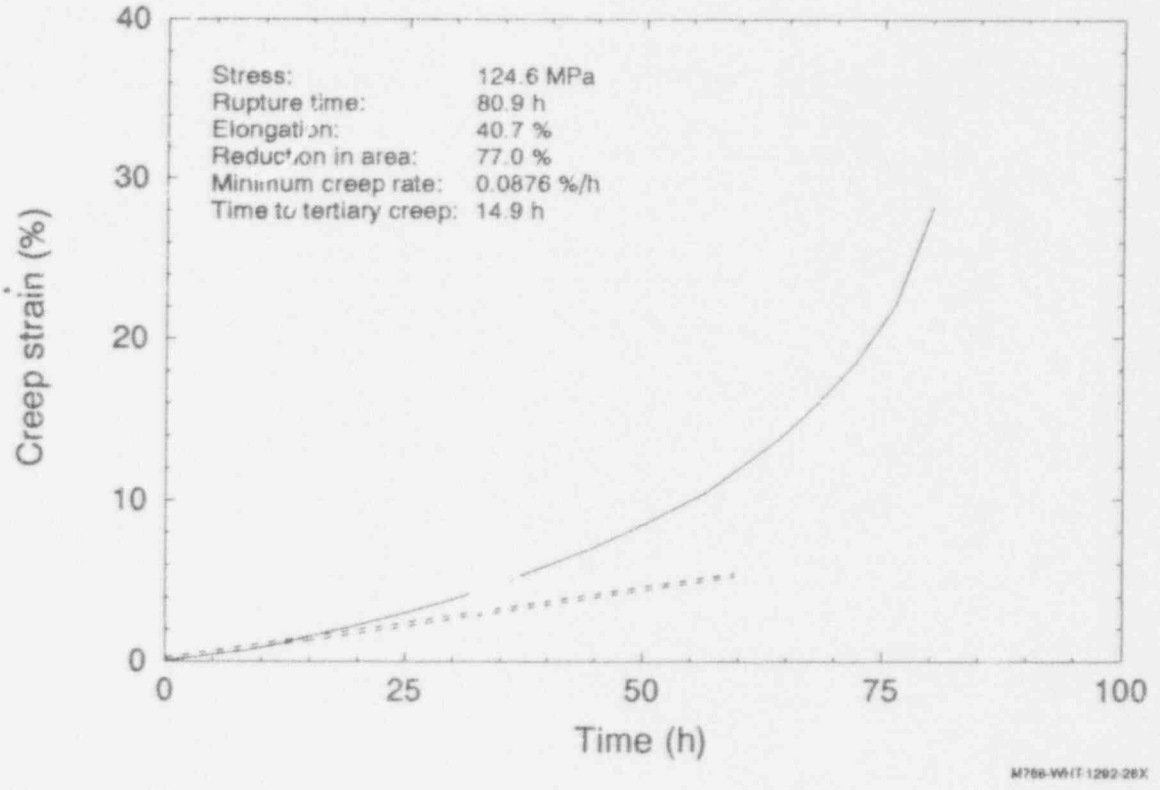

Figure B-51. SA106B carbon steel creep strain versus time at 811 K—INEL creep test results.

B-4.6 Summary of Penetration Materials Tests

Creep and tensile tests of penetrations materials, Inconel 600, 304 stainless steel, and SA106B carbon steel, were performed at temperatures higher than any previous tests, or in the case of some creep testing, at stresses higher than previous tests. Inconel 600 tensile data show a rapid loss in ultimate strength for temperatures above 800 K; creep data indicate failure times of less than 10 hours for temperatures greater than 1000 K and stresses greater than approximately 130 MPa. The 304 stainless steel tensile data show good consistency with published data, extending the maximum tested temperature to 1366 K. In this material, ultimate strength remains above 300 MPa until temperatures reach approximately 800 K, where the strength drops rapidly. Creep data for stainless steel predict failure times less than 10 hours for temperatures above 1089 K and stresses greater than 80 MPa. SA106B carbon steel, used in drain lines of BWRs, is not intended for high temperature applications; this material loses ultimate strength rapidly for temperatures above approximately 600 K. Tensile testing of this material extends the tested temperature range from 800 to 1150 K. Creep data indicate failure in less than 10 hours for temperatures greater than 900 K and stresses greater than approximately 75 MPa.

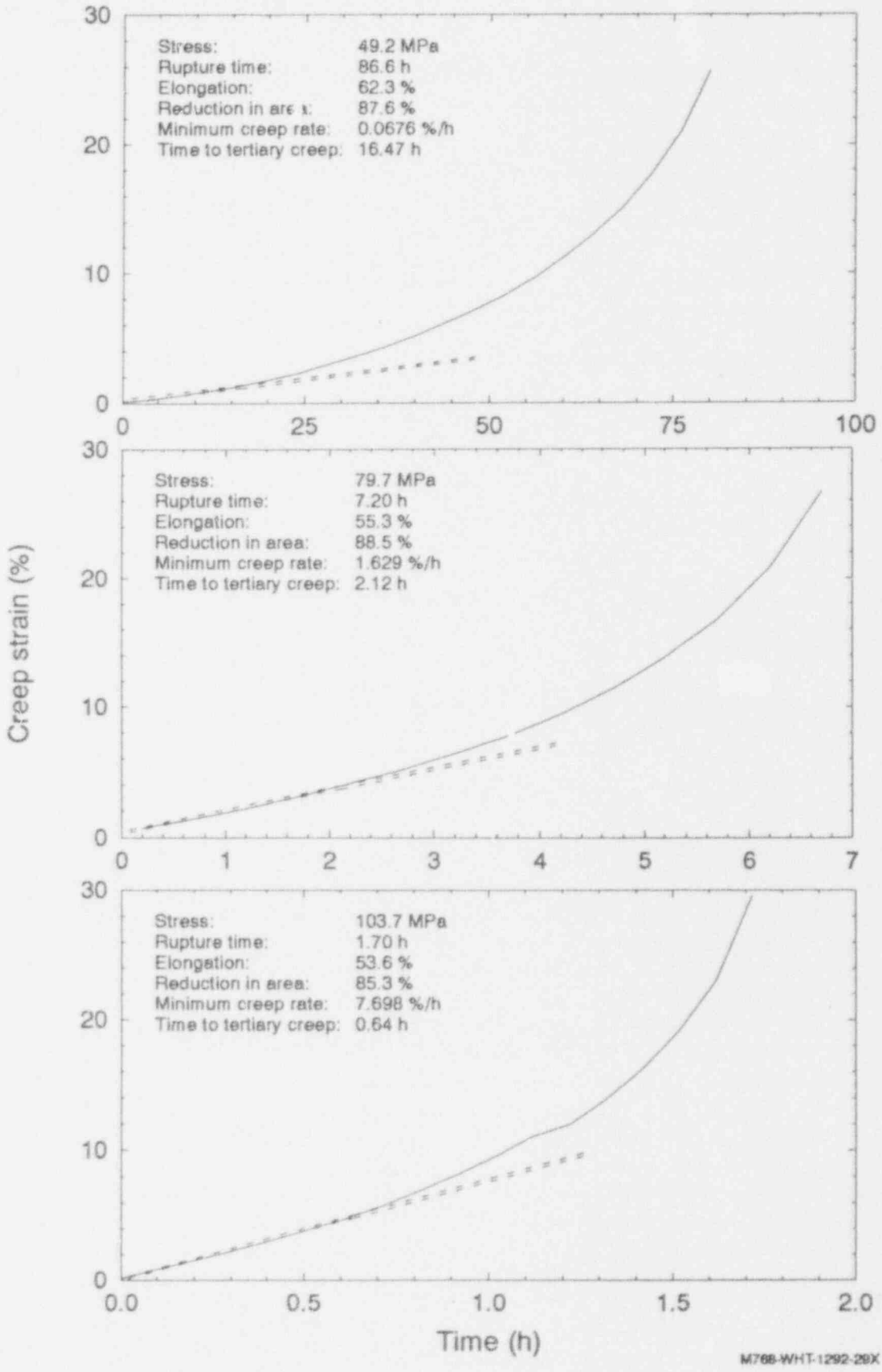

Figure B-52. SA106B carbon steel creep strain versus time at 900 K—INEL creep test results.

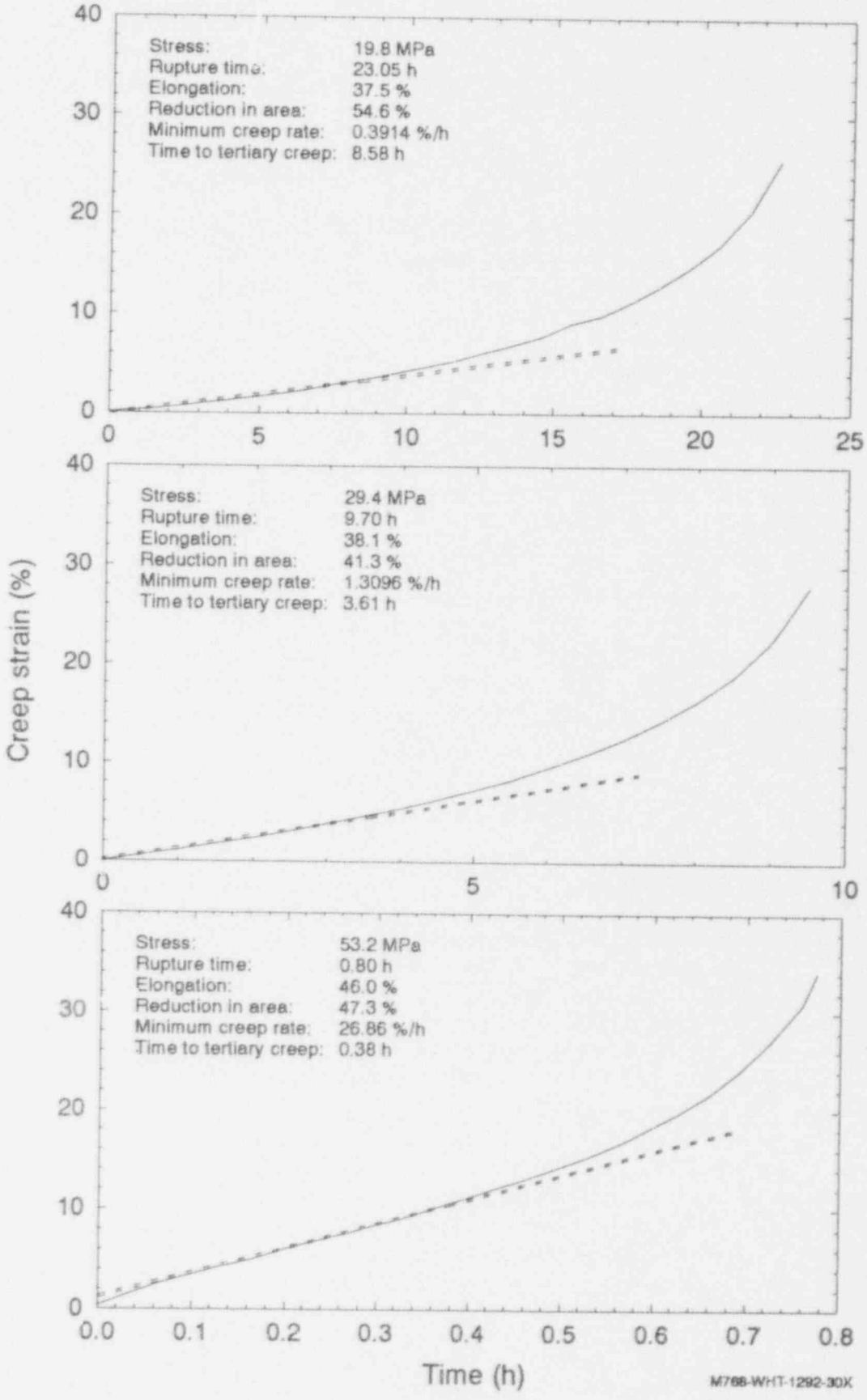

Figure B-53. SA106B carbon steel creep strain versus time at 1050 K—INEL creep test results.

B-5. TOOLS FOR APPLYING CREEP DATA

Results from these creep tests can be used in both simple analytical calculations and in detailed finite element analyses of these materials at elevated temperatures.

B-5.1 Larson-Miller Curves

In creep rupture evaluations the method proposed by Larson and Miller[B-16] is used with calculations of the primary stress in a structure to estimate failure times, assuming various constant stresses and temperatures. The LMP can be derived assuming that creep rate is governed by the Arrhenius equation

$$LMP = 0.001*T[C + \log(t_r)]$$

where

T = test temperature, Rankine

t_r = time to rupture, hours

C = material dependent constant, often set equal to 20.

Time, temperature, and stress data are fit to this equation by creep testing several constant stress levels to rupture at various constant temperatures. The LMP is calculated for each test from the temperature and time to rupture. It is plotted against the corresponding test stress, as shown in Figure B-54.

Given an arbitrary constant temperature and constant stress within the tested range, the time to rupture can be predicted by finding the LMP corresponding to the stress and calculating the time to rupture from the above equation using the given temperature.

If the stress or temperature is not constant, time to failure must be predicted with a damage model. Creep damage is often calculated using the life-fraction rule. Effective stress and temperature for each element of interest are applied over a time step. Time to rupture is calculated from the LMP. Element damage for a given time step is the actual time at given effective stress and temperature divided by the time to rupture at that effective stress and temperature. Failure is predicted when the sum of the damage over the time steps is 1.0 (or 100%).

Previous, lower temperature creep test data[B-3] for SA533B1 material, which are summarized in Table B-10, are included in the Larson-Miller curve fit of Figure B-54. This figure also includes the creep rupture test data for SA508-CL2 for comparison. Considering that the data transcend a phase transformation temperature for SA533B1, there appears to be little effect on the resulting curves. The Larson-Miller curve fitting the previous data, which are all from tests at temperatures below the phase transformation temperature, compare very well with the new INEL data, which span the phase transformation temperature. Their slopes are almost equal, and a slight offset reduction in applied stress for the higher temperature data is evident. Note that, as rupture times become very short, the extrapolation of the curve shows that the creep rupture stress agrees well with the ultimate tensile strength data.

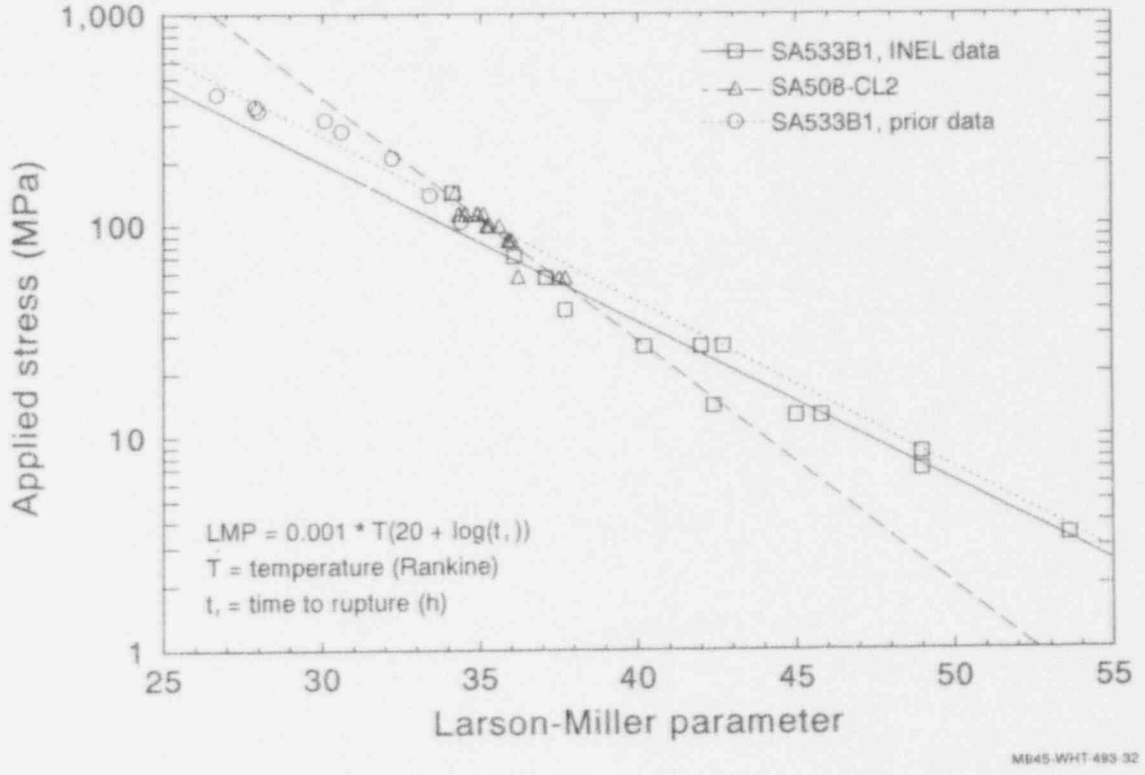

Figure B-54. Larson-Miller curve fit for SA533B1 and SA508-CL2 creep data.

Table B-10. Summary of low temperature SA533B1 material creep tests from Reference B-9.

	Creep rupture		Creep rupture		Creep rupture	
Temperature K (°C)	Stress MPa (ksi)	Time (h)	Stress MPa (ksi)	Time (h)	Stress MPa (ksi)	Time (h)
728 (455)	413.7 (60.0)	2.3	361.3 (52.4)	21.0	310.3 (45.0)	907.0
783 (510)	344.8 (50.0)	0.7	275.8 (40.0)	54.0	206.9 (30.0)	657.0
867 (594)	137.2 (19.9)	23.3	102.7 (14.9)	103.0	102.7 (14.9)	106.0

The SA508-CL2 curve is characterized by a steeper slope, which indicates more sensitivity in the creep rupture stress to increasing temperature than the SA533B1 material.

B-5.1.1 Approximating Creep Failure Time Using LMP

The Larson-Miller parameter can be used to approximate creep failure time relative to failure predicted by ultimate strength. A comparison of the two times may help determine if a finite element creep analysis is needed. The following procedure can be used to roughly approximate creep failure time.

1. Plot the peak or average through-wall history. Peak temperature, obviously, gives a more conservative estimate of the time to failure.

2. Define a tolerance limit, t_{tol}, for the failure time. This is the time before the predicted ultimate strength failure, within which the user would not be concerned if creep failure occurred.

3. Divide the temperature history between $t = 0$ and $t = t_u - t_{tol}$ into n approximately linear segments, where t_u is the time to ultimate strength failure.

4. Calculate the time to failure for each segment using the Larson-Miller parameter.

5. Calculate the damage for each time segment up to $t = t_u - t_{tol}$. Sum the damage over the time steps.

Creep analysis is recommended if the damage summation for times between $t = 0$ and $t = t_u - t_{tol}$ is 100% or greater.

B-5.2 Constitutive Creep Law

Structural finite element analyses consider creep effects by calculating the creep strain at each solution increment and including that effect in the total component strain of the element for that solution increment. These test data can be fit to an analytical creep law just for this purpose.

The SA533B1 creep curves show little or no primary creep, as exemplified in Figure B-13. Tertiary creep, defined here by a 0.2% strain offset from the minimum creep rate, occurs at strains that are close to, or exceed, the strain at which necking occurs in tensile tests of the same temperature. Since these tests are conducted at a constant load, rather than constant stress, the increase in strain rate in the later stages of the test is probably a result of reduction in cross-sectional area. If tertiary creep is assumed to be caused by changes in geometry, rather than metallurgy, secondary creep, where the creep strain rate is constant, dominates the overall creep response.

A creep relationship that describes primary and secondary creep strain as a power function in stress and time can be fit by the least squares method to the experimental data:

$$\epsilon_{cr} = \frac{A}{m + 1} \sigma_a^n t^{m+1} + B$$

where

ϵ_{cr} = creep strain

σ_a = applied stress (MPa)

t = time (h)

A, m, n = temperature-dependent parameters

B = strain offset.

The final term, B, is likely a result of inaccurate calculation of elastic or plastic strain. If this term is set to zero, the equation reduces to the Bailey-Norton equation[B-22] with the parameter, m, equal to zero. The final term, B, does not affect the time hardening form of strain rate, which is often used in finite element analysis:

$$\frac{d(\epsilon_{cr})}{dt} = A\sigma_a^n t^m$$

With the parameter m equal to zero, the remaining parameters needed for the analytical creep law, A and n, are listed in Table B-11 for each curve at temperature.

The experimental data are well-described by a cubic function with an excellent fit for creep strain as a function of time at given stresses and temperatures:

$$\epsilon_{cr} = A + Bt - Ct^2 + Dt^3$$

where

ϵ_{cr} = creep strain (including the tertiary portion)

t = time (h)

A, B, C, and D = constants.

The constants A, B, C, and D are listed in Table B-12 with the Index of Determination, R^2, for each curve at temperature.

Table B-11. Power fit to SA533B1 primary and secondary creep strain data.

Temperature (K)	Equation parameters	
	A	n
900	8.0080E-11	3.5821
1000	2.7564E-5	1.7627
1050	1.5003E-8	4.1983
1150	3.5934E-7	3.5747
1250	3.3895E-8	5.7124
1373	1.4911E-6	6.2967

Table B-12. Cubic fit for SA533B1 creep data.

Temperature (K)	Stress (MPa)	A	B	C	D	R^2
900	140.1	5.1104E-4	3.5517E-3	-4.4140E-5	2.1078E-5	0.9998
900	69.7	1.3453E-3	4.4070E-4	-6.6319E-6	9.9982E-8	0.9998
1000	55.6	2.9054E-3	6.3494E-2	-1.9444E-2	2.9983E-3	0.9980
1000	39.0	5.4870E-3	1.8416E-2	-6.2405E-4	3.6381E-4	0.9997
1050	26.5 & 26.3[a]	7.2408E-4	1.5835E-2	-9.0730E-4	8.3713E-5	0.9980
1050	13.9	8.8445E-3	1.4580E-3	-7.2792E-6	2.5053E-8	0.9994
1150	26.5	9.3271E-3	5.7503E-2	-1.0037E-2	2.0396E-3	0.9998
1150	12.5	9.7656E-4	4.3835E-3	-8.7818E-5	1.5647E-6	0.9991
1250	26.5	4.5920E-2	6.9991E-0	-2.5548E+2	5.8283E+3	0.9999
1250	12.6	-5.1739E-4	1.4677E-1	-7.3259E-2	3.3529E-2	0.9957
1250	8.0	3.0580E-3	4.0922E-3	-3.3795E-5	9.7726E-7	0.9995
1373	7.0	9.4656E-3	4.4365E-1	-9.2150E-1	1.7052E-0	0.9993
1373	3.5	-6.9919E-3	7.3030E-3	-2.6037E-4	5.2984E-6	0.9970

a. Data from 26.3 MPa and 26.5 MPa at 1050 K were combined.

B-6. CONCLUSIONS

The test data collected on SA533B1 and SA508-CL2 pressure vessel steels are meant to assist analysts in evaluating reactor vessel lower head failures during severe accidents. With this purpose in mind, several observations about the materials' temperature dependent response may be useful.

Evaluation of the test data for SA533B1 material would indicate that, while the phase transformation at 1000 K seems to affect yield strength and ductility, the plots of stress versus time to rupture indicate only a moderate sensitivity to that transformation and Larson-Miller curves show little sensitivity to that transformation. These SA533B1 data also indicate some strain rate dependency of the material's ultimate strength. However, as temperatures exceed 1400 K, the test data indicate a linear reduction in strength to zero at 1789 K.

The SA508-CL2 creep data exhibit more sensitivity to temperature in the Larson-Miller curve by having a greater slope to the curve than that of SA533B1. It is noted, however, that the temperature range of these data is not as large as that of the SA533B1 data and that several more creep test data points for this material should be generated to verify the current slope of the Larson-Miller curve.

Tensile and creep data collected on Inconel 600, 304 stainless steel, and SA106B carbon steel can be used to evaluate failure of reactor vessel penetrations, such as instrument tubes, control rod guide tubes, and the drain nozzle. For the most part, the INEL data are consistent with published data and with reasonable extrapolations of published data. Exceptions include Inconel 600 creep data, where INEL failure times tend to be shorter than published data, and SA106B tensile tests, where INEL ultimate strength data are higher at temperatures below 800 K. However, the INEL high temperature SA106B creep data (above 800 K) appear to be consistent with a reasonable extrapolation of published data. The data collected here, particularly in the creep tests, are limited. Testing was performed to assist in extrapolating property data where none existed to severe accident temperatures. More testing with repetition is needed to reduce the range of uncertainty.

B-7. REFERENCES

B-1. G. L. Thinnes, *TMI-2 Lower Head Creep Rupture Analysis*, EGG-TMI-8133, EG&G Idaho, Inc., August 1988.

B-2. G. B. Reddy and D. J. Ayres, *High-Temperature Elastic-Plastic and Creep Properties for SA 533 Grade B Class 1 and SA 508 Materials*, EPRI NP-2763, Electric Power Research Institute, 1982.

B-3. G. V. Smith, *Evaluations of the Elevated Temperature Tensile and Creep Rupture Properties of C-Mo, Mo-Mo, and Mn-Mo-Ni Steels*, Metal Properties Council, American Society for Testing and Materials, ASTM Data Series Publication DS47, 1971.

B-4. American Society of Testing and Materials, "Standard Methods of Tension Testing of Metallic Materials," ASTM Standard E8-82, *Annual Book of ASTM Standards*, Vol. 03.01, Section 3, Metals Test Methods and Analytical Procedures, 1983.

B-5. American Society of Testing and Materials, "Standard Recommended Practice for Elevated Temperature Tension Testing of Metallic Materials," ASTM Standard E21-82, *Annual Book of ASTM Standards*, Vol. 03.01, Section 3, Metals Test Methods and Analytical Procedures, 1983.

B-6. Y. Takeuti et al., "Thermal-Stress Problems in Industry. 3: Temperature Dependency of Elastic Moduli for Several Metals at Temperatures from -196°C to 1000°C," *Journal of Thermal Stresses 2*, pp. 233–250 (steel referenced: STBA12), 1979.

B-7. W. C. Young, *Roark's Formulas for Stress and Strain*, 6th edition, New York: McGraw-Hill Book Co., 1989.

B-8. B. L. Harris et al., *Creep Rupture Failure of Three Components of the Reactor Primary Coolant System During the TMLB' Accident*, EGG-EA-7431, EG&G Idaho, Inc., November 1986.

B-9. R. H. Bryan et al., *Test of 6-Inch Thick Pressure Vessels, Series 2: Intermediate Test Vessels V-3, V-4, and V-6*, ORNL-5059, Oak Ridge National Laboratory, November 1974.

B-10. American Society of Testing and Materials, Title, "Standard Practice for Conducting Creep, Creep Rupture, and Stress-Rupture Tests of Metallic Materials," ASTM Standard E139-83, *Annual Book of ASTM Standards*, Vol. 03.01, Section 3, Metals Test Methods and Analytical Procedures, 1983.

B-11. "Hunting Alloy, Inconel Alloy 600," Technical Bulletin of the International Nickel Company, Inc., now Inco Alloys International, Inc. Huntington Alloy Products Division, Seventh Edition, Huntington, WV, 1987.

B-12. G. V. Smith, *An Evaluation of the Yield Tensile Creep and Rupture Strengths of Wrought 304, 316, 321, and 347 Stainless Steels at Elevated Temperatures*, ASTM DS5-52, 1969.

B-13. D. R. Diercks and W. F. Burke, "Elevated-Temperature True Stress-True Strain Tensile Behavior of AISI Type 304 Stainless Steel," *Spring Meeting of the Pressure Vessel and Piping Division of ASME, Miami, Florida, June 24–28, 1974.*

B-14. W. F. Simmons and J. A. VanEcho, *The Elevated Temperature Properties of Stainless Steels*, ASTM, DS5-S1, 1965.

B-15. *Aerospace Structural Metals Handbook (ASMH)*, Code 1303 (Types 304 and 304L), extracts from Carpenter Steel (1962) and United States Steel (1956), March 1967.

B-16. F. R. Larson and J. Miller, "A Time-Temperature Relationship for Rupture and Creep Stress," *Transactions of the ASME*, July 1952, pp. 765-775.

B-17. American Society of Mechanical Engineers (ASME), Section III, *Nuclear Power Plant Components*, 1971.

B-18. W. F. Simmons and H. C. Cross, *The Elevated Temperature Properties of Stainless Steels*, ASTM STP-124, 1952.

B-19. United States Steel Corporation (USSC), *Mechanical and Physical Properties of Steels for Nuclear Applications*, ADUSS 92-1625, Section 3, 1967, pp. 20,43.

B-20. R. W. Swindeman, 1975, "Creep-Rupture Correlations for Type 304 Stainless Steel Heat 9T2796," *Symposium on Structural Materials for Service at Elevated Temperatures in Nuclear Power Generation, ASME Winter Annual Meeting, Houston, Texas, November 30-December 3, 1975.*

B-21. W. F. Simmons and H. C. Cross, *Elevated-Temperature Properties of Carbon Steels*, ASTM STP-180, 1955.

B-22. H. Kraus, *Creep Analysis*, New York: John Wiley and Sons, 1980.

Appendix C

Description of the THIRMAL/0 Code

Appendix C

Description of the THIRMAL/0 Code

C-1. INTRODUCTION

When a high temperature corium jet interacts with water, small particles are dispersed from the jet and the heat transfer rate is greatly enhanced by the increased corium/water interfacial area. Therefore, it is obvious that a successful interpretation of all thermal phenomena following the jet interaction will depend on an accurate, quantitative prediction of the jet behavior (e.g., jet breakup length and dispersed particle size distribution).

Based on observations from tests using simulant materials, a phenomenological model was developed to describe the jet breakup behavior. In this model the jet material is assumed to be dispersed from the coherent jet column, as well as from the vortex ball formed at the jet leading edge. Kelvin-Helmholtz instability is assumed to be the only surface erosion mechanism on the coherent column, with shearing by the ambient fluid accounting for most of the material eroded from the leading edge. The most probable sizes of particles dispersed from the column and the leading edge are thus predicted from different dispersion mechanisms. A detailed description of the interfacial instability and the jet breakup mechanisms are documented in References C-1 and C-2.

C-2. THIRMAL/0 COMPUTER CODE

The Thermal-Hydrodynamic Interaction and Reaction of Melt and Liquid, version 0, (THIRMAL/0) computer code was developed at Argonne National Laboratory (ANL) to provide a capability to calculate the breakup and quenching behavior of melt entering water as a jet. Given the diameter, velocity, and temperature of melt entering the water, THIRMAL/0 mechanistically calculates the time-dependent jet penetration distance, breakup of the jet into droplets, quenching of the jet column and individual droplets, void formation and boilup of the surrounding water, steam/hydrogen formation from melt-water interaction, steam condensation within subcooled water, and the resulting system pressurization. THIRMAL/0 calculates the erosion of the jet into droplets by shearing off the leading edge and interfacial instability along the vapor-covered jet column. The code considers heat transfer from the jet to surrounding water by film boiling. Local conditions of temperature and velocity within the jet are calculated using a multicell, Lagrangian numerical formulation. Temperatures and velocities of droplets formed from the breakup of the jet column are also obtained from Lagrangian calculations along the droplet/particle trajectories.

The assumption that a continuous vapor film exists between the melt jet and surrounding water during the interaction, as described in References C-1 and C-2, becomes inadequate when a continuous liquid phase no longer exists near the jet. Specifically, when the steam generation rate is high enough to globally levitate the liquid phase, water may be dispersed in the form of droplets while steam becomes the continuous phase. When this dispersed flow regime occurs, the jet surface erosion is no longer driven by the steam flow in the thin vapor film, but rather by the steam flow surrounding the jet. In general, the steam velocity is much higher for a thin vapor film than for a steam flow distributed over the vapor continuous region. As a result, erosion of the jet is typically reduced when dispersed flow occurs. In order to identify the flow regime of the multiphase (i.e., melt particles/water/steam mixture) region, the detailed local void fraction, phase temperature, and velocity in the mixing region become important. Furthermore, the characteristics of the jet debris depend strongly on the history of melt particulates in the multiphase mixing region. In simulating the flow conditions of the multiphase mixing region, previous investigators usually solved governing equations of mass, momentum, and energy for all the phases (i.e., water, steam, and melt particulates). The resulting numerical process generally involves solving nine conservation equations (for one dimension), one matching equation, and one equation of state. In the THIRMAL/0 code, a simple, one-dimensional, multiphase, flow model using drift-flux correlations is solved to calculate the local flow conditions, as described below.

In the THIRMAL/0 code, the two-dimensional effects resulting from flow inhomogeneity in lateral directions on the jet breakup, as described above, are estimated by using a "mixing zone" approximation. The mixing zone is the region containing the jet column, dispersed particulate, steam, and water. The geometry of the mixing zone can be considered as a cylinder, with diameter and length varying in space and time, as sketched in Figure C-1. The single-phase water region (i.e., region outside of the mixing zone) is not considered in the model equations. The one-dimensional mass equation for the steam is expressed in Eulerian form.

The cross-sectional area of the mixing zone, A, is defined as the area where the dispersed particles have migrated laterally. As analyzed in Reference C-2, the perpendicular component of the velocity of the eroded material with respect to the jet surface is the erosion velocity, U_E. The lateral distance that a particle can migrate is obtained by integrating the momentum equation containing U_E twice.

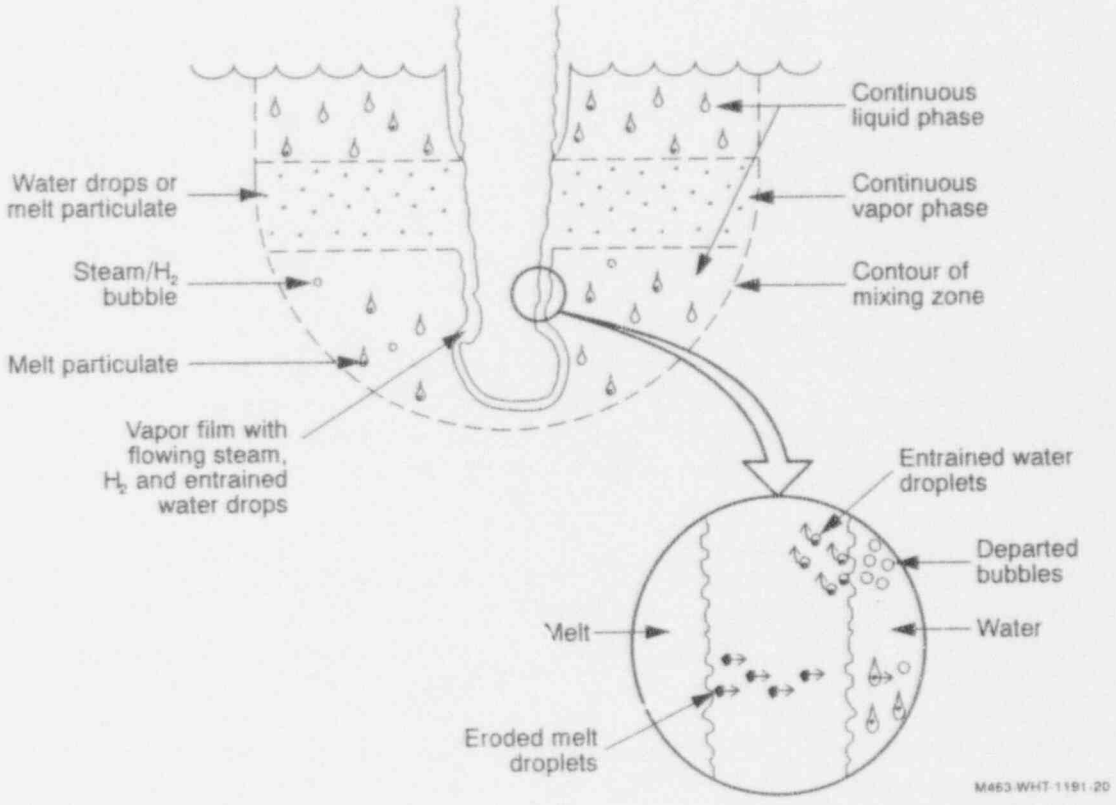

Figure C-1. Schematic illustration of THIRMAL/0 model.

In addition, the code also allows the mixing zone of the cell at (z_i, t_j) to be replaced by the cell at (z_{i-1}, t_j) at the time t_{j+k} if the mixing zone of the cell at (z_{i-1}, t_j) is greater than that of the cell at (z_i, t_j). This means that a cell can replace a smaller cell right above it after k time steps when all the vapor has risen into the new cell, with the time lag determined by $k = \delta z/(\delta t\ U_v)$. Note that the Courant condition for stability has been applied in selecting the time step (i.e., $U_v \delta t/\delta z < 1$).

The basic assumption of the model in solving for the flow conditions of the mixing zone is that the void fraction and vapor superficial velocity can be related by a single correlation, thus eliminating the vapor momentum equation. A further simplification is made by assuming that the liquid velocity is negligible compared to the vapor velocity. This means that the mixing zone is treated as a quasi-static bubbling pool with little net liquidflow. Kataoka and Ishii[C-3] correlated a large amount of experiment data for pool void fraction over wide ranges of gas flux, vessel diameter, system pressure, and liquid physical properties. They concluded that in bubbling or pool boiling systems, the void fraction can be represented by a drift flux correlation.

The vapor velocity, U_v, in the vapor mass equation is then replaced by an appropriate drift flux correlation that depends on the gas superficial velocity. The void fraction can thus be determined if the rates of liquid evaporation and vapor condensation are known.

The source term of the vapor mass equation (i.e., the liquid evaporation rate) depends on the number and temperature of melt particles that are either eroded from the jet or transported from elsewhere in the mixing zone. In order to obtain a temperature history of each group of particulates, their motion is traced in Lagrangian coordinates rather than in Eulerian coordinates. Based on the force balance of a single spherical particle in the axial direction, the velocities of droplets/particles can be obtained by solving the momentum equation for a single particle. At each numerical grid cell during one time step, steam generated from the particles (either just eroded from the jet or convected from the adjacent cells) is summed to yield the source term of the vapor mass equation. The energy (temperature) of each particle is expressed in terms of a Lagrangian formulation similar to the particle momentum equation.

For a liquid-continuous regime, the heat transferred from the particles to the vapor phase is set to zero because the energy transferred from the particles is predominantly absorbed by the liquid. If flow dispersion occurs, particles are suspended in a vapor-continuous phase and the forced convective heat transfer coefficient is given by the spherical particle correlation.[C-4] Under these conditions, heat transfer between suspended particulate and water droplets is assumed to be zero.

For a particle in a film boiling heat transfer regime, previous experimental and analytical studies on the heat transfer coefficients generally do not agree well, especially at high particle temperatures or high liquid subcooling. The THIRMAL/0 code incorporates an analytical model developed from observations of high-temperature melt/water interactions for film boiling heat transfer from a spherical particle. Usually, a descending particle is covered by a thin vapor blanket on its lower section and a stretched, roughly elliptically shaped vapor dome behind it. As the vapor dome grows from steam generation, buoyancy overcomes surface tension to cause a steam bubble to leave the vapor dome and rise to the water surface, as illustrated in Figure C-2. By assuming a linear temperature profile in the vapor film and a parabolic profile for both the liquid velocity and temperature in the liquid boundary layer, and by applying the integral momentum and energy equations, the vapor film thickness, vapor velocity, and liquid boundary layer thickness can be determined, as described in Reference C-1. The heat transfer is composed of heat conduction across the vapor film and radiation. Once the temperature of the particle has dropped below the minimum film boiling temperature, heat transfer will occur by nucleate boiling. A correlation suggested by Rohsenow[C-5] is used in THIRMAL/0. When nucleate boiling occurs, it is assumed that all of the heat transferred from the particle generates the steam because the liquid surrounding the particle is, at least locally, well saturated.

The energy equations of the coolant vapor and liquid phases can be formulated once the source terms generated by the melt droplets and particles are determined. Similar to the vapor mass equations, the energy equations for the coolant vapor and coolant liquid phases are described in a Eulerian formulation.

In the THIRMAL/0 model, pressure gradients other than the hydrostatic head of the water pool are neglected. This assumption is valid as long as an abrupt pressure variation, such as that occurring during a steam explosion, is absent.

The numerical scheme for solving the conservation equations uses a finite difference method with upwind/donor cell differencing of the convective terms.[C-6] The spatial nodalization is sketched in Figure C-3.

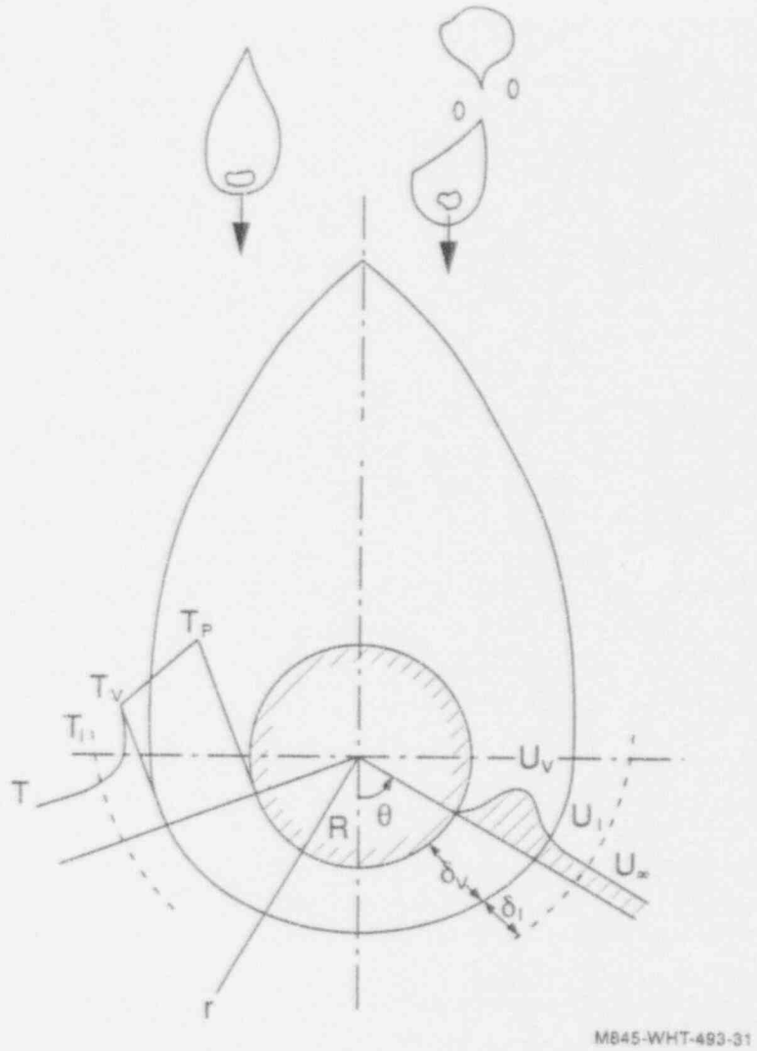

Figure C-2. Film boiling on a spherical particle.

The general procedure for obtaining the flow field solution is as follows:

1. Determine the erosion rate by assuming a zero void fraction inside the mixing zone.

2. Solve the momentum and energy equations of the particles in Lagrangian coordinates to yield the source and sink terms for the conservation equations.

3. Apply the drift flux correlation to yield a single unknown in the vapor mass equation and solve for the void fraction. Check for dispersed flow.

4. Determine the vapor and liquid temperatures using the energy conservation equations.

5. Determine the system pressure based on the vapor exit temperature and system geometry.

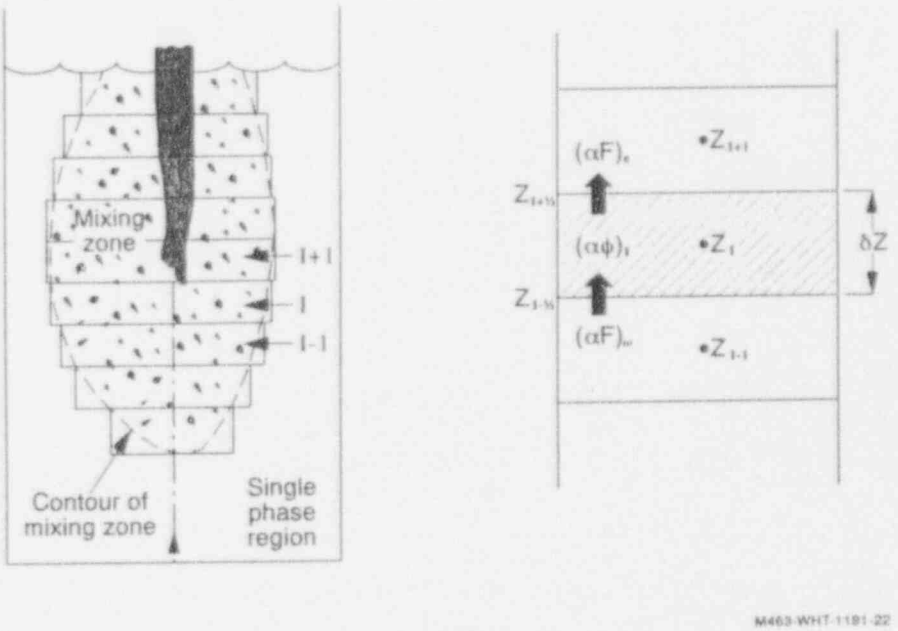

Figure C-3. Nodalization of mixing zone.

6. Iterate Steps 1 through 5 using the updated flow and system conditions.

The occurrence of dispersed flow is constantly checked when the vapor superficial velocity is determined. In THIRMAL/0, a dispersion criterion developed by Leung et al.[C-7] is used. When this criterion is met, the code switches the local mixing zone geometry from a vapor film to a dispersed flow channel. The erosion velocity under this condition is obtained simply by setting the vapor film thickness to a large number. It is interesting to note that under this condition, the erosion velocity and the most unstable wave number are the same as obtained by Levich[C-8] for the erosion at the boundary between two media with nonzero relative velocity.

C-3. REFERENCES

C-1. S. K. Wang, C. A. Blomquist, and B. W. Spencer, "Modeling of Thermal and Hydrodynamic Aspects of Molten Jet/Water Interactions," *ANS Proceedings of the 1989 ANS/ASME/AIChE National Heat Transfer Conference, Philadelphia, PA, August 6–9, 1989*, p. 225.

C-2. S. K. Wang, C. A. Blomquist, and B. W. Spencer, "Interfacial Instability Leading to Bubble Departure and Surface Erosion During Molten Jet/Water Interaction," *ANS Proceedings of the 1989 ANS/ASME/AIChE National Heat Transfer Conference, Philadelphia, PA, August 6–9, 1989*, p. 31.

C-3. I. Kataoka and M. Ishii, *Prediction of Pool Void Fraction by New Drift Flux Correlation*, NUREG/CR-4657, ANL-86-29, Argonne National Laboratory, 1986.

C-4. R. B. Bird, W. E. Stewart, and E. N. Lightfoot, *Transport Phenomena*, New York: John Wiley & Sons, 1960.

C-5. W. H. Rohsenow, "A Method of Correlating Heat Transfer Data for Surface Boiling of Liquid," *Transactions of the ASME, 74*, 37, 1952, p. 969.

C-6. S. V. Patankar, *Numerical Heat Transfer and Fluid Flow*, Bristol, PA: Hemisphere Publishing Corporation, McGraw-Hill Book Company, 1980.

C-7. J. C. M. Leung, G. A. Lambert, and L. J. Stachyra, "Transition to Dispersed Flows in a Stagnant Pool with Gas Injection," *ANS Transactions, 38*, 1981.

C-8. V. C. Levich, *Physiochemical Hydrodynamics*, Englewood Cliffs, NJ: Prentice-Hall, Inc., 1962.

Appendix D

Displacement Form of Equilibrium Equations

Appendix D

Displacement Form of Equilibrium Equations

This appendix introduces the resultant-based equilibrium equations and describes the process by which they are converted into the displacement-based equilibrium equations (Equations 4-55 through 4-57). Horizontal, moment and vertical equilibrium are written in terms of the force and moment resultants defined in Figure D-1 and take the form:

$$\left[N_\varphi r \cos \varphi\right]' - \left[Q_{\varphi c} r \sin \varphi\right]' - \alpha N_\theta + \alpha r \sin \varphi \, p_i = 0 \tag{D-1}$$

$$(M_\varphi r)' - \alpha \cos\varphi \, M_\theta - \alpha r Q_{\varphi c} = 0 \tag{D-2}$$

$$2\pi r(N_\varphi \sin\varphi + Q_{\varphi c} \cos \varphi) = \pi r^2 p_i \tag{D-3}$$

These resultants, which are defined from integrating stresses through the thickness, represent forces and moments per unit of circumferential length of the shell. The resultants are defined as

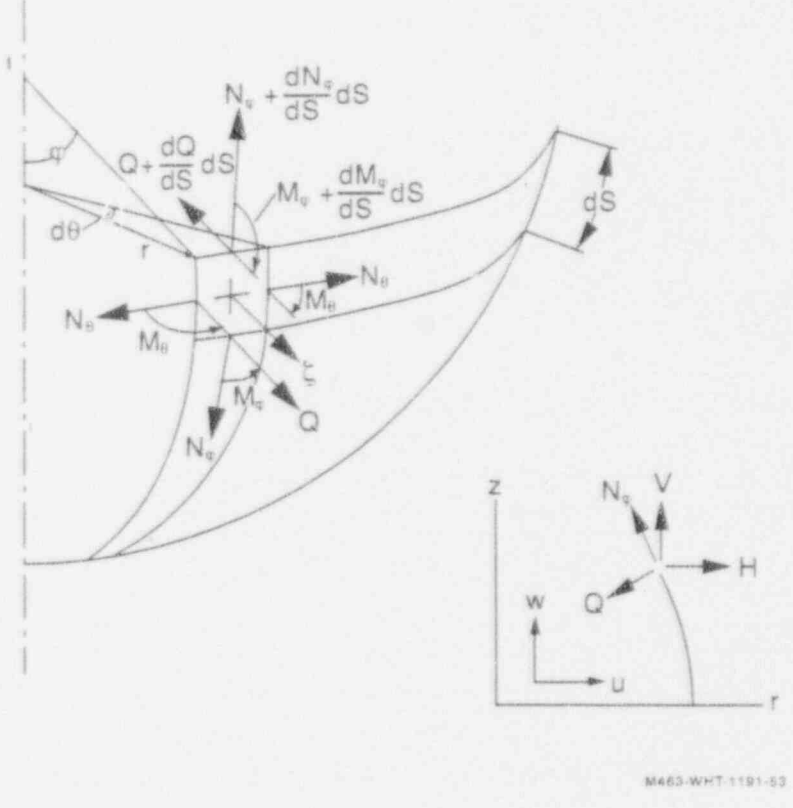

Figure D-1. Differential element for constructing equilibrium equations.

Equilibrium Equations

$$N_\varphi = \int_{-t_w/2}^{t_w/2} \sigma_\varphi\left(1+\frac{\zeta}{R_\theta}\right)d\zeta \tag{D-4}$$

$$N_\theta = \int_{-t_w/2}^{t_w/2} \sigma_\theta\left(1+\frac{\zeta}{R_\varphi}\right)d\zeta \tag{D-5}$$

$$M_\varphi = -\int_{-t_w/2}^{t_w/2} \sigma_\varphi\left(1+\frac{\zeta}{R_\theta}\right)\zeta d\zeta \tag{D-6}$$

$$M_\theta = -\int_{-t_w/2}^{t_w/2} \sigma_\theta\left(1+\frac{\zeta}{R_\varphi}\right)\zeta d\zeta \tag{D-7}$$

$$Q_{\varphi\zeta} = -\int_{-t_w/2}^{t_w/2} \tau_{\varphi\zeta}\left(1+\frac{\zeta}{R_\theta}\right)d\zeta \tag{D-8}$$

In order to derive Equations (4-55) through (4-57) and separate the displacements and rotations on the left-hand side from the inelastic components on the right-hand side, the stresses in the integrands are written in terms of the elastic strains through Hooke's Law relations:

$$\sigma_\varphi = \frac{E(\zeta,\xi)}{1-\nu^2}\left(\epsilon_\varphi + \nu\epsilon_\theta - \epsilon_{\varphi_{cr}} - \nu\epsilon_{\theta_{cr}}\ \epsilon_{\varphi_{pl}} - \nu\epsilon_{\theta_{pl}} - (1+\nu)\epsilon_{th}\right) \tag{D-9}$$

$$\sigma_\theta = \frac{E(\zeta,\xi)}{1-\nu^2}\left(\epsilon_\theta + \nu\epsilon_\varphi - \epsilon_{\theta_{cr}} - \nu\epsilon_{\varphi_{cr}} - \epsilon_{\theta_{pl}} - \nu\epsilon_{\varphi_{pl}} - (1+\nu)\epsilon_{th}\right) \tag{D-10}$$

where $\sigma_\zeta = 0$ has been incorporated into the relations, and

$$\tau_{\varphi\zeta} = G(\zeta,\xi)\gamma_{\varphi\zeta e} = G(\zeta,\xi)[\gamma_{\varphi\zeta} - (\gamma_{\varphi\zeta_{cr}} + \gamma_{\varphi\zeta_{pl}})]$$

$$\tau_{\varphi\zeta} = G(\zeta,\xi)\gamma + G(\zeta,\xi)(\gamma_{\varphi\zeta} - \gamma) - G(\zeta,\xi)(\gamma_{\varphi\zeta_{cr}} + \gamma_{\varphi\zeta_{pl}}) \tag{D-11}$$

where a distinction has been made between the shear along the normal to the deformed middle surface, $\gamma_{\varphi\zeta}$, and the shear along the material rotating away from the deformed normal, γ. A differential element of deformed shell shown in Figure D-2 illustrates this distinction. The properties of the strain tensor may be used to show

$$\gamma_{\varphi\zeta} - \gamma = \gamma(\sec(2\gamma) - 1) - (\epsilon_\zeta - \epsilon_\varphi)\tan(2\gamma) \quad . \tag{D-12}$$

The left-hand side of Equations (4-55) through (4-57) is derived from the leading terms involving total strains ϵ_φ, ϵ_θ, and γ in Equations (D-9), (D-10), and (D-11). The total strains at the location or any through-thickness are expressed in terms of the middle surface strains through

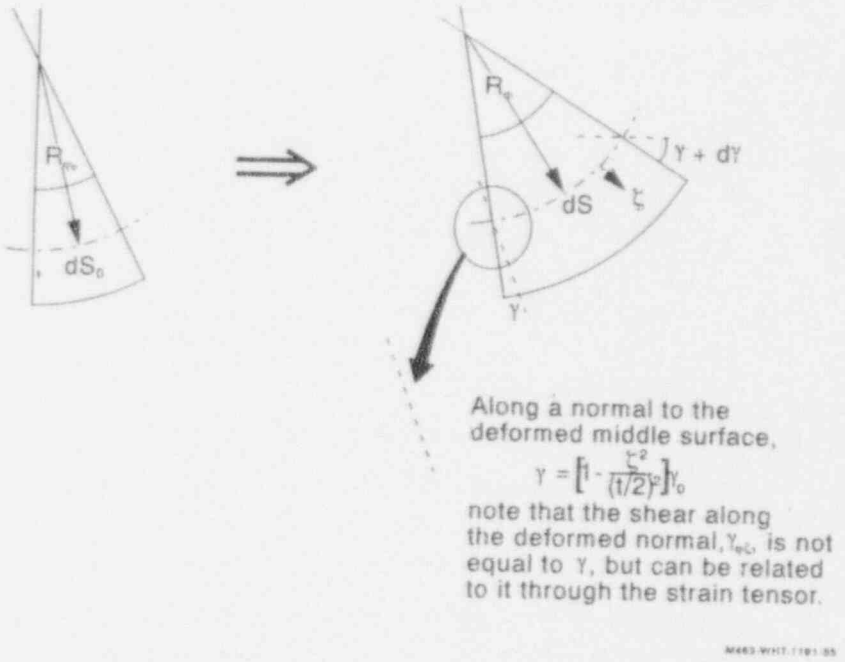

Figure D-2. Notation used to define strain measures.

$$\epsilon_\varphi = \epsilon_{\varphi m}\left(1 + \left[\frac{\zeta}{R_\varphi}\right]\right) + \zeta\left(\frac{1}{R_\varphi} - \frac{1}{R_{\varphi_o}} + \left[\frac{\gamma'}{\alpha_o}\sec^2\gamma\right]\right) \tag{D-13}$$

$$\epsilon_\theta = \epsilon_{\theta m}\left(1 + \left[\frac{\zeta}{R_\theta}\right]\right) + \zeta\left(\frac{1}{R_\theta} - \frac{1}{R_{\theta_o}}\right) \tag{D-14}$$

The term in $\gamma' \sec^2\gamma$ appearing in Equation (D-13) arises from the finite rotation of material away from the normal to the deformed middle surface; Figure D-2 also indicates how the presence of a gradient in γ provides a source of meridional strain. The terms in ζ/R_φ and ζ/R_θ multiplying the middle surface strains have been included because t_v/R_φ and t_v/R_θ are not generally small in the vicinity of the cusped regions. The conventional representation of the strain measures does not include terms enclosed in brackets []. Across the normal to the deformed meridian, the finite rotation is assumed to have the form

$$\gamma(\zeta,\xi) = \left[1 - \frac{\zeta^2}{(t_v(\xi)/2)^2}\right]\gamma_o(\xi) \quad . \tag{D-15}$$

Substituting Equations (D-13) through (D-15) into the leading terms in Equations (D-9) through (D-11), integrating those terms through-thickness in the resultant definitions, and eliminating the meridian midplane strain $\epsilon_{\varphi m}$ using the compatibility relationship, Equation (4-66), the stress resultants can be written

$$N_{\varphi} = \frac{E_o(\xi)t_{vo}}{1 - \nu^2} \left\{ a_1\left(\frac{u}{r_o}\right)' + a_2\left(\frac{u}{r_o}\right) + a_3\beta' + a_4\beta + a_5\gamma' \right.$$
$$+ b_1\left[\cos\varphi_o(1 - \cos\beta) + \sin\varphi_o(\sin\beta - \beta)\right]$$
$$+ b_2\left[\sin\varphi_o(1 - \cos\beta) + \cos\varphi_o(\beta - \sin\beta)\right]$$
$$\left. + N_{\varphi_{fr}} + N_{\varphi_{ym}} - N_{\varphi_{th}} - N_{\varphi_{pl}} - N_{\varphi} \right\} \qquad \text{(D-16)}$$

$$N_{\theta} = \frac{E_o(\xi)t_{vo}}{1 - \nu^2} \left\{ c_1\left(\frac{u}{r_o}\right)' + c_2\left(\frac{u}{r_o}\right) + c_3\beta' + c_4\beta + c_5\gamma' \right.$$
$$+ d_1\left[\cos\varphi_o(1 - \cos\beta) + \sin\varphi_o(\sin\beta - \beta)\right]$$
$$+ d_2\left[\sin\varphi_o(1 - \cos\beta) + \cos\varphi_o(\beta - \sin\beta)\right]$$
$$\left. + N_{\theta_{fr}} + N_{\theta_{ym}} - N_{\theta_{th}} - N_{\theta_{pl}} - N_{\theta_{cr}} \right\} \qquad \text{(D-17)}$$

$$M_{\varphi} = \frac{E_o(\xi)t_{vo}^2}{12(1 - \nu^2)} \left\{ f_1\left(\frac{u}{r_o}\right)' + f_2\left(\frac{u}{r_o}\right) + f_3\beta' + f_4\beta + f_5\gamma' \right.$$
$$+ g_1\left[\cos\varphi_o(1 - \cos\beta) + \sin\varphi_o(\sin\beta - \beta)\right]$$
$$+ g_2\left[\sin\varphi_o(1 - \cos\beta) + \cos\varphi_o(\beta - \sin\beta)\right]$$
$$\left. + M_{\varphi_{fr}} + M_{\varphi_{ym}} - M_{\varphi_{th}} - M_{\varphi_{pl}} - M_{\varphi_{cr}} \right\} \qquad \text{(D-18)}$$

$$M_{\theta} = -\frac{E_o(\xi)t_{vo}^2}{12(1 - \nu^2)} \left\{ h_1\left(\frac{u}{r_o}\right)' + h_2\left(\frac{u}{r_o}\right) + h_3\beta' + h_4\beta + h_5\gamma' \right.$$
$$+ k_1\left[\cos\varphi_o(1 - \cos\beta) + \sin\varphi_o(\sin\beta - \beta)\right]$$
$$+ k_2\left[\sin\varphi_o(1 - \cos\beta) + \cos\varphi_o(\beta - \sin\beta)\right]$$
$$\left. + M_{\theta_{fr}} + M_{\theta_{ym}} - M_{\theta_{th}} - M_{\theta_{pl}} - M_{\theta_{cr}} \right\} \qquad \text{(D-19)}$$

$$Q_{\varphi\zeta} = \frac{E_o(\xi)t_{vo}}{1-\nu^2}\, e_1\gamma + Q_{\varphi\zeta_{fr}} + Q_{\varphi\zeta_{ym}} - Q_{\varphi\zeta_{pl}} - Q_{\varphi\zeta_{cr}} \quad . \tag{D-20}$$

The resultants with subscripts "th," "cr," and "pl" are defined directly from Equations (D-9) through (D-11) and (D-4) through (D-8), as, for instance,

$$N_{\varphi_{cr}} = \int_{-t_v/2}^{t_v/2} \frac{E(\zeta,\xi)}{1-\nu^2}\left(\epsilon_{\varphi_{cr}} + \nu\epsilon_{\theta_{cr}}\right)\left(1+\frac{\zeta}{R_\theta}\right)d\zeta \quad . \tag{D-21}$$

The additional terms subscripted "fr" and "ym," for finite rotation and Young's modulus, require some explanation. In the definition of resultants N_φ, N_θ, M_φ, and M_θ, there are terms of the form $\sec^2\gamma\,\frac{\gamma'}{\alpha}$. Because of the form of Equation (D-15), these terms cannot be integrated in closed form. This term is therefore rewritten as

$$\sec^2\gamma\gamma' = \sec^2\gamma_o(\xi)\gamma_o'(\xi) + \left\{\sec^2\left[\left(1+\frac{\zeta^2}{(t_v(\xi)/2)^2}\right)\gamma_o(\xi)\right] - \sec^2\gamma_o(\xi)\right\}\gamma_o'(\xi)$$

$$+ \sec^2\left[\left(1+\frac{\zeta^2}{(t_v(\xi)/2)^2}\right)\gamma_o(\xi)\right]\left[\frac{\zeta^2}{(t_v(\xi)/2)^2}\,\gamma_o(\xi)\right]'$$

The first term is integrated through the thickness and defines a_5, c_5, f_5, and h_5 in the above equations. [The subscript "o" has been omitted from γ_o in Equations (4-55) through (4-57) and above, but it is understood to be the value of the finite rotation at the midplane]. The remaining term is defined as a finite rotation correction and is defined, for instance, as

$$N_{\varphi_{fr}} = \frac{E_o(\xi)}{1-\nu^2}\int_{-t_v/2}^{t_v/2}\left\{\left[\sec^2\left[\left(1+\frac{\zeta^2}{(t_v(\xi)/2)^2}\right)\gamma_o(\xi)\right] - \sec^2\gamma_o(\xi)\right]\gamma_o'(\xi)\right.$$

$$\left. + \sec^2\left[\left(1+\frac{\zeta^2}{(t_v(\xi)/2)^2}\right)\gamma_o(\xi)\right]\left[\frac{\zeta^2}{(t_v(\xi)/2)^2}\,\gamma_o(\xi)\right]'\right\}\left(1+\frac{\zeta}{R_\theta}\right)d\zeta \tag{D-22}$$

with analogous definitions for the resultants $N_{\theta_{fr}}$, $M_{\varphi_{fr}}$ and $M_{\theta_{fr}}$. The finite rotation correction to $Q_{\varphi\zeta}$ arises from the difference between the shear strains on the faces parallel to and rotated γ from the normal to deformed middle surface:

$$Q_{\varphi fr} = - \frac{E_o(\xi)}{2(1+\nu)} \int_{-t_v/2}^{t_v/2} (\gamma_{\varphi\zeta} - \gamma)\left(1 + \frac{\zeta}{R_\theta}\right) d\zeta \qquad \text{(D-23)}$$

where, from Equation (D-12), $\gamma_{\varphi\zeta} - \gamma = \gamma\,(\sec 2\gamma - 1) - (\epsilon_\zeta - \epsilon_\varphi)\tan 2\gamma$.

The corrections with subscript "ym" account for the variations in the Young's modulus through the thickness, which varies with the local temperature. The functional form of E(T), which is based on information in Appendix F, is also modelled in a piecewise linear fashion. Given a $T(\zeta,\xi)$ from Equations (4-53) or (4-54), the Young's modulus is represented as

$$E(\zeta,\xi) = E_o(\xi) + E_1(\zeta,\xi)$$

where $E_o(\xi)$ is a modulus based on a representative temperature at that location on the meridian and $E_1(\zeta,\xi)$ is a local correction accounting for the through-thickness variation in stiffness. Terms subscripted "ym" therefore take the form

$$N_{\varphi ym} = \int_{-t_v/2}^{t_v/2} \frac{E_1(\zeta,\xi)}{1-\nu^2}(\epsilon_\varphi + \nu\epsilon_\theta)\left(1 + \frac{\zeta}{R_\theta}\right) d\zeta \quad . \qquad \text{(D-24)}$$

Resultants with subscripts "fr" and "ym" are grouped into the load vector along with the thermal, creep, and plastic resultants. These terms are typically small compared with their inelastic counterparts, but are included to preserve the equilibrium equations. The terms that remain form the product of stiffness matrix and load vector.

Because of the way the resultants are defined, the resultants N_φ and N_θ have a certain symmetry when expressed in displacement-based form. Terms in which R_θ appears in the definition of N_φ have complementary forms in which R_φ appears in the definition of N_θ. Terms with and without Poisson's ratio in the definition of N_φ appear without and with Poisson's ratio in the definition of N_θ. The coefficients a_1 through a_5 and c_1 through c_5 can be written

$$a_1 = \frac{t_v}{t_{vo}}\left[\frac{r_o}{r_o'}\frac{\cos\varphi_o}{\cos\varphi} + \frac{1}{12}\frac{t_v^2}{\alpha\alpha_o}\frac{\beta'}{\cos\varphi}\frac{r_o}{R_\theta}\right] \qquad \text{(D-25)}$$

$$c_1 = \nu\frac{t_v}{t_{vo}}\left[\frac{r_o}{r_o'}\frac{\cos\varphi_o}{\cos\varphi} + \frac{1}{12}\frac{t_v^2}{\alpha\alpha_o}\frac{\beta'}{\cos\varphi}\frac{r_o}{R_\varphi}\right] \qquad \text{(D-26)}$$

$$a_2 = \frac{r_o'}{r_o}\, a_1 + \frac{t_v}{t_{vo}}\, \nu \tag{D-27}$$

$$c_2 = \frac{r_o'}{r_o}\, a_2 + \frac{t_v}{t_{vo}} \tag{D-28}$$

$$a_3 = \frac{1}{12}\, \frac{t_v}{t_{vo}}\, \frac{t_v^2}{\alpha R_\theta} \tag{D-29}$$

$$c_3 = \frac{\nu}{12}\, \frac{t_v}{t_{vo}}\, \frac{t_v^2}{\alpha R_\varphi} \tag{D-30}$$

$$a_4 = \frac{t_v}{t_{vo}}\, \frac{\sin\varphi_o}{\cos\varphi} + \frac{1}{12}\, \frac{t_v}{\alpha}\left[\frac{\sin\varphi_o}{\cos\varphi}\, \frac{t_v}{R_\theta}\, \beta' + \nu \frac{\alpha}{r} \cos\varphi_o \left(1 + \frac{u}{r_o}\right) \frac{t_v}{R_\theta}\right] \tag{D-31}$$

$$c_4 = \frac{t_v}{t_{vo}}\, \nu \frac{\sin\varphi_o}{\cos\varphi} + \frac{1}{12}\, \frac{t_v}{\alpha}\left[\nu \frac{\sin\varphi_o}{\cos\varphi}\, \frac{t_v}{R_\varphi}\, \beta' + \frac{\alpha}{r} \cos\varphi_o \left(1 + \frac{u}{r_o}\right) \frac{t_v}{R_\varphi}\right] \tag{D-32}$$

$$a_5 = \frac{1}{12}\, \frac{t_v}{t_{vo}}\, \frac{t_v^2}{\alpha_o R_\theta} \sec^2\gamma \tag{D-33}$$

$$c_5 = \frac{\nu}{12}\, \frac{t_v}{t_{vo}}\, \frac{t_v^2}{\alpha_o R_\varphi} \sec^2\gamma \tag{D-34}$$

while the coefficients b_1, d_1 and b_2, d_2 can be written

$$b_1 = \frac{t_v}{t_{vo}} \frac{1}{\cos\varphi}\left[1 + \frac{1}{12}\frac{t_v^2}{\alpha R_\theta}\beta'\right] \tag{D-35}$$

$$d_1 = \nu\frac{t_v}{t_{vo}} \frac{1}{\cos\varphi}\left[1 + \frac{1}{12}\frac{t_v^2}{\alpha R_\varphi}\beta'\right] \tag{D-36}$$

$$b_2 = -\frac{\nu}{12}\frac{t_v}{t_{vo}}\frac{t_v^2}{rR_\theta}\left(1 + \frac{u}{r_o}\right) \tag{D-37}$$

$$d_2 = -\frac{1}{12}\frac{t_v}{t_{vo}}\frac{t_v^2}{rR_\varphi}\left(1 + \frac{u}{r_o}\right) \tag{D-38}$$

Similarly, the resultants M_φ and M_θ have a certain symmetry; coefficients f_1 through f_5 and h_1 through h_5 take the form

$$f_1 = \left(\frac{t_v}{t_{vo}}\right)^2 \frac{r_o}{\alpha_o}\frac{1}{\cos\varphi}\left(\frac{t_v}{R_\theta} + \beta'\frac{t_v}{\alpha}\right) \tag{D-39}$$

$$h_1 = \left(\frac{t_v}{t_{vo}}\right)^2 \frac{r_o}{\alpha_o}\frac{\nu}{\cos\varphi}\left(\frac{t_v}{R_\varphi} + \beta'\frac{t_v}{\alpha}\right) \tag{D-40}$$

$$f_2 = \left(\frac{t_v}{t_{vo}}\right)^2\left[\frac{t_v}{R_\theta}\left(\frac{\cos\varphi_o}{\cos\varphi} + \nu\right) + \frac{t_v}{\alpha}\frac{\cos\varphi_o}{\cos\varphi}\beta'\right] \tag{D-41}$$

$$h_2 = \left(\frac{t_v}{t_{vo}}\right)^2\left[\frac{t_v}{R_\varphi}\left(\nu\frac{\cos\varphi_o}{\cos\varphi} + 1\right) + \nu\frac{t_v}{\alpha}\frac{\cos\varphi_o}{\cos\varphi}\beta'\right] \tag{D-42}$$

$$f_3 = \left(\frac{t_v}{t_{vo}}\right)^2 \frac{t_v}{\alpha} \tag{D-43}$$

$$h_3 = \nu\left(\frac{t_v}{t_{vo}}\right)^2 \frac{t_v}{\alpha} \tag{D-44}$$

$$f_4 = \left(\frac{t_v}{t_{vo}}\right)^2\left[\left(\frac{t_v}{R_\theta} + \frac{t_v}{\alpha}\beta'\right)\frac{\sin\varphi_o}{\cos\varphi} + \nu\frac{t_v}{r}\cos\varphi_o\left(1 + \frac{u}{r_o}\right)\right] \tag{D-45}$$

$$h_4 = \left(\frac{t_v}{t_{vo}}\right)^2\left[\nu\left(\frac{t_v}{R_\varphi} + \frac{t_v}{\alpha}\beta'\right)\frac{\sin\varphi_o}{\cos\varphi} + \frac{t_v}{r}\cos\varphi_o\left(1 + \frac{u}{r_o}\right)\right] \tag{D-46}$$

$$f_5 = \left(\frac{t_v}{t_{vo}}\right)^2 \frac{t_v}{\alpha_o}\sec^2\gamma \tag{D-47}$$

$$h_5 = \nu\left(\frac{t_v}{t_{vo}}\right)^2 \frac{t_v}{\alpha_o}\sec^2\gamma \tag{D-48}$$

while the coefficients g_1, k_1 and g_2, k_2 can be written

$$g_1 = \left(\frac{t_v}{t_{vo}}\right)^2 \frac{1}{\cos\varphi}\left(\frac{t_v}{R_\theta} + \frac{t_v}{\alpha}\beta'\right) \tag{D-49}$$

$$k_1 = \nu\left(\frac{t_v}{t_{vo}}\right)^2 \frac{1}{\cos\varphi}\left(\frac{t_v}{R_\varphi} + \frac{t_v}{\alpha}\beta'\right) \tag{D-50}$$

$$g_2 = -\nu\left(\frac{t_v}{t_{vo}}\right)^2 \frac{t_v}{r}\left(1 + \frac{u}{r_o}\right) \tag{D-51}$$

Equilibrium Equations

$$k_2 = -\left(\frac{t_v}{t_{vo}}\right)^2 \frac{t_v}{r}\left(1 + \frac{u}{r_o}\right) \quad . \tag{D-52}$$

A single coefficient is used to represent $Q_{\varphi\zeta}$ in terms of the displacement γ:

$$e_1 = -\frac{2}{3}\left(\frac{1-\nu}{2}\right)\frac{t_v}{t_{vo}} \quad . \tag{D-53}$$

With these definitions, the coefficients appearing in the horizontal equilibrium equation are

$$A_1 = a_1 \frac{r}{t_{vo}} \cos\varphi \tag{D-54}$$

$$A_2 = \left(a_1 \frac{r}{t_{vo}} \cos\varphi\right)' + a_1 \frac{E_o'}{E_o} \frac{r}{t_{vo}} \cos\varphi + a_2 \frac{r}{t_{vo}} \cos\varphi - \frac{\alpha}{t_{vo}} c_1 \tag{D-55}$$

$$A_3 = \left(a_2 \frac{r}{t_{vo}} \cos\varphi\right)' + a_2 \frac{E_o'}{E_o} \frac{r}{t_{vo}} \cos\varphi - \frac{\alpha}{t_{vo}} c_2 \tag{D-56}$$

$$A_4 = a_3 \frac{r}{t_{vo}} \cos\varphi \tag{D-57}$$

$$A_5 = \left(a_3 \frac{r}{t_{vo}} \cos\varphi\right)' + a_3 \frac{E_o'}{E_o} \frac{r}{t_{vo}} \cos\varphi - \frac{\alpha}{t_{vo}} c_3 \tag{D-58}$$

$$A_6 = \left(a_4 \frac{r}{t_{vo}} \cos\varphi\right)' + a_4 \frac{E_o'}{E_o} \frac{r}{t_{vo}} \cos\varphi - \frac{\alpha}{t_{vo}} c_4 \tag{D-59}$$

$$A_7 = a_5 \frac{r}{t_{vo}} \cos\varphi \tag{D-60}$$

$$A_8 = \left(a_5 \frac{r}{t_{vo}} \cos \varphi\right)' + a_5 \frac{E_o'}{E_o} \frac{r}{t_{vo}} \cos \varphi - e_1 \frac{r}{t_{vo}} \sin \varphi - \frac{\alpha}{t_{vo}} c_5 \tag{D-61}$$

$$A_9 = -\left(e_1 \frac{r}{t_{vo}} \sin \varphi\right)' - e_1 \frac{E_o'}{E_o} \frac{r}{t_{vo}} \sin \varphi \tag{D-62}$$

$$\begin{aligned}
G_1 = & -(1 - \nu^2) \sin \varphi \frac{\alpha r}{t_{vo}^2} \frac{p_i}{E_o} \\
& - \left[\left(b_1 \frac{r}{t_{vo}} \cos\varphi\right)' + b_1 \frac{E_o'}{E_o} \frac{r}{t_{vo}} \cos \varphi - \frac{\alpha}{t_{vo}} d_1 \right] \\
& \cdot \left[\cos \varphi_o (1 - \cos\beta) + \sin \varphi_o (\sin\beta - \beta) \right] \\
& - \left[\left(b_2 \frac{r}{t_{vo}} \cos\varphi\right)' + b_2 \frac{E_o'}{E_o} \frac{r}{t_{vo}} \cos \varphi - \frac{\alpha}{t_{vo}} d_2 \right] \\
& \cdot \left[\sin \varphi_o (1 - \cos\beta) + \cos \varphi_o (\beta - \sin \beta) \right] \\
& - b_1 \frac{r}{t_{vo}} \cos \varphi \left[\cos \varphi_o (1 - \cos \beta) + \sin \varphi_o (\sin \beta - \beta) \right]' \\
& - b_2 \frac{r}{t_{vo}} \cos \varphi \left[\sin \varphi_o (1 - \cos \beta) + \cos \varphi_o (\beta - \sin \beta) \right]' \\
& - (1 - \nu^2) \frac{1}{E_o t_{vo}} \left[\frac{r}{t_{vo}} \cos \varphi (N_{\varphi_{fr}} + N_{\varphi_{ym}} - N_{\varphi_{th}} - N_{\varphi_{pl}} - N_{\varphi_{cr}}) \right]' \\
& + (1 - \nu^2) \frac{1}{E_o t_{vo}} \left[\frac{r}{t_{vo}} \sin \varphi (Q_{\varphi\zeta_{fr}} + Q_{\varphi\zeta_{ym}} - Q_{\varphi\zeta_{pl}} - Q_{\varphi\zeta_{cr}}) \right]' \\
& - (1 - \nu^2) \frac{\alpha}{t_{vo}} \frac{1}{E_o t_{vo}} \left(N_{\theta_{fr}} + N_{\theta_{ym}} - N_{\theta_{th}} - N_{\theta_{pl}} - N_{\theta_{cr}} \right)
\end{aligned} \tag{D-63}$$

Those coefficients appearing in the moment equilibrium equation are

$$B_1 = f_1 \frac{r}{t_{vo}} \tag{D-64}$$

$$B_2 = \left(f_1 \frac{r}{t_{vo}}\right)' + f_1 \frac{E_o'}{E_o} \frac{r}{t_{vo}} + f_2 \frac{r}{t_{vo}} - h_1 \frac{\alpha}{t_{vo}} \cos \varphi \tag{D-65}$$

$$B_3 = \left(f_2 \frac{r}{t_{vo}}\right)' + f_2 \frac{E_o'}{E_o} \frac{r}{t_{vo}} - h_2 \frac{\alpha}{t_{vo}} \cos \varphi \tag{D-66}$$

$$B_4 = f_3 \frac{r}{t_{vo}} \tag{D-67}$$

$$B_5 = \left(f_3 \frac{r}{t_{vo}}\right)' + f_3 \frac{E_o'}{E_o} \frac{r}{t_{vo}} + f_4 \frac{r}{t_{vo}} - h_3 \frac{\alpha}{t_{vo}} \cos \varphi \tag{D-68}$$

$$B_6 = \left(f_4 \frac{r}{t_{vo}}\right)' + f_4 \frac{E_o'}{E_o} \frac{r}{t_{vo}} - h_4 \frac{\alpha}{t_{vo}} \cos \varphi \tag{D-69}$$

$$B_7 = f_5 \frac{r}{t_{vo}} \tag{D-70}$$

$$B_8 = \left(f_5 \frac{r}{t_{vo}}\right)' + f_5 \frac{E_o'}{E_o} \frac{r}{t_{vo}} - h_5 \frac{\alpha}{t_{vo}} \cos \varphi \tag{D-71}$$

$$B_9 = 12\frac{\alpha r}{t_{vo}^2}e_1 \tag{D-72}$$

$$G_2 = -\left[\left(g_1\frac{r}{t_{vo}}\right)' + g_1\frac{E_o'}{E_o}\frac{r}{t_{vo}} - \frac{\alpha}{t_{vo}}k_1\cos\varphi\right]\cdot\left[\cos\varphi_o\,(1-\cos\beta) + \sin\varphi_o\,(\sin\beta-\beta)\right]$$

$$-\left[\left(g_2\frac{r}{t_{vo}}\right)' + g_2\frac{E_o'}{E_o}\frac{r}{t_{vo}} - \frac{\alpha}{t_{vo}}k_2\cos\varphi\right]\cdot\left[\sin\varphi_o\,(1-\cos\beta) + \cos\varphi_o\,(\beta-\sin\beta)\right]$$

$$-g_1\frac{r}{t_{vo}}\left[\cos\varphi_o\,(1-\cos\beta) + \sin\varphi_o\,(\sin\beta-\beta)\right]' - g_2\frac{r}{t_{vo}}\left[\sin\varphi_o\,(1-\cos\beta) + \cos\varphi_o\,(\beta-\sin\beta)\right]'$$

$$+12(1-\nu^2)\frac{1}{E_o t_{vo}^2}\left[\frac{r}{t_{vo}}\left(M_{\varphi_{fr}} + M_{\varphi_{ym}} - M_{\varphi_{th}} - M_{\varphi_{pl}} - M_{\varphi_{cr}}\right)\right]'$$

$$-12(1-\nu^2)\frac{1}{E_o t_{vo}^2}\frac{\alpha}{t_{vo}}\cos\varphi\left(M_{\theta_{fr}} + M_{\theta_{ym}} - M_{\theta_{th}} - M_{\theta_{pl}} - M_{\theta_{cr}}\right)$$

$$-12(1-\nu^2)\frac{\alpha r}{t_{vo}^2}\frac{1}{E_o t_{vo}}\left(Q_{\varphi\zeta_{fr}} + Q_{\varphi\zeta_{ym}} - Q_{\varphi\zeta_{pl}} - Q_{\varphi\zeta_{cr}}\right). \tag{D-73}$$

Finally, the coefficients appearing in the vertical equilibrium equation are

$$C_1 = a_1 \sin\varphi \tag{D-74}$$

$$C_2 = a_2 \sin\varphi \tag{D-75}$$

$$C_3 = a_3 \sin\varphi \tag{D-76}$$

$$C_4 = a_4 \sin\varphi \tag{D-77}$$

$$C_5 = a_5 \sin\varphi \tag{D-78}$$

Equilibrium Equations

$$C_6 = e_1 \sin \varphi \tag{D-79}$$

$$G_3 = (1 - \nu^2)\frac{r}{2t_{vo}} \frac{p_i}{E_o} - b_1 \sin \varphi \left[\cos\varphi_o (1 - \cos \beta) + \sin\varphi_o(\sin\beta - \beta)\right]$$

$$- b_2 \sin \varphi \left[\sin \varphi_o (1 - \cos \beta) + \cos\varphi_o(\beta - \sin \beta)\right]$$

$$- (1 - \nu^2) \sin \varphi \frac{1}{E_o t_{vc}} \left(N_{\varphi_{fr}} + N_{\varphi_{ym}} - N_{\varphi_{th}} - N_{\varphi_{pl}} - N_{\varphi_{cr}}\right)$$

$$- (1 - \nu^2) \cos \varphi \frac{1}{E_o t_{vo}} \left(Q_{\varphi\varepsilon_{fr}} + Q_{\varphi\varepsilon_{ym}} - Q_{\varphi\varepsilon_{pl}} - Q_{\varphi\varepsilon_{cr}}\right) \tag{D-80}$$

Appendix E

Results from Verification Calculations for Localized Effects Model

Appendix E

Results from Verification Calculations for Localized Effects Model

E-1. SUMMARY

Verification calculations were performed to compare results from the shell model (TSM) used in Section 4.2.2 to predict localized creep rupture with results from a finite element model. Calculation results provide several insights into the applicability of TSM for use in analyses of lower head severe accident structural response. First of all, the purpose for developing this model was to provide a fast-running solution to predict the collapse of a localized portion of the vessel wall, resulting from hot spots in a debris bed resting on the lower head. Thus, the program would be appropriate for scoping parameter studies in various accident scenarios. Results of the benchmark problems used in this verification effort indicate that TSM performs well for its intended purpose.

TSM was benchmarked against an ABAQUS[E-1] axisymmetric solid finite element model using two hot spot load cases. One load case consisted of a moderate thermal gradient in the hot spot region and an internal pressure of 45 MPa. The second case represented a more severe temperature gradient in the hot spot region and an applied pressure of 55 MPa. These pressures, selected to enhance plastic deformation through the thickness of the wall, are several times greater than the 15.5 MPa expected in reactor operations. The choice of these pressures did help to identify a portion of the disagreement between ABAQUS and TSM.

In the cooler boundary areas of the hot spot and the cooler portion of the vessel wall under the hot spot, which was basically that portion outside the vessel midsurface, hoop and meridional stresses were within 4% of the ABAQUS model results. TSM generally underpredicted the strains in both of these benchmark hot spot cases. Because TSM is based on shell model assumptions, which neglect radial stresses through the vessel wall, it underpredicted stresses and strains in the hoop and meridional components in the very hottest areas of the model. This was because the vessel material was relatively soft in these areas at the load case temperatures, and the radial stresses, as calculated in the ABAQUS model, were of the same order as the hoop and meridional stresses. Thus, the Poisson effect from the radial stresses would significantly affect the hoop and meridional components. TSM underpredicted hoop and meridional stresses by as much as 60% in the hottest areas, where the stresses were typically two orders of magnitude lower than the peak values on the shell outer surface. Total strain comparisons ranged from underpredictions of 24% on the inside surface to 11% on the outside surface in the hot spot region for the severe thermal gradient load case. In the cooler boundary areas, strain comparisons ranged from underpredictions of 13% on the inner surface to 7% on the outer surface. Examinations of the plastic strains indicated that plasticity of the wall had propagated from the outside inward one Gauss point further in the ABAQUS model than in the TSM model for the two hot spot load cases.

It should be noted, however, that the cooler outer portions of the vessel wall carry the majority of the pressure load in these cases and that vessel wall material yielding eventually begins at the outer surface and propagates inward to final failure. Hoop and meridian stress levels are typically 35 times higher in the outer portions than the inner regions of the vessel wall. Thus,

model accuracy in these high stress areas is most crucial to accurate predictions of vessel failure margins.

The benchmark thermal load cases included a maximum internal pressure of 45 to 55 MPa, while an accident condition would result in maximum pressures no greater than around 15 MPa. Therefore, additional cases were examined where the thermal loadings of both hot spot load cases were applied to TSM and ABAQUS models with an internal pressure load of 15 MPa. For the moderate thermal load case, TSM calculated stresses in the inside third of the wall 13% lower than those of ABAQUS, while stress estimates for the remaining portion of the wall were within 3%. The severe thermal load case stresses were an average of 4% lower than the ABAQUS model results throughout the wall. Total meridian and hoop strains ranged from underpredictions of 16% on the inside to 2% on the outside portions of the vessel wall in the hot spot region and within 5% in areas away from the hot spot. These figures represent a substantially better agreement than the same thermal conditions at elevated pressures and indicate that the TSM assumption of negligible radial stress is acceptable for loading histories representative of accident conditions.

E-2. INTRODUCTION

Verification calculations were undertaken to compare results from the localized creep rupture model, described in Section 4.2.2 and Appendix D of this report, and a finite element model developed with the ABAQUS code.[E-1] As described in Section 4.2.2 and Appendix D, the localized creep rupture model, which was developed at the University of Wisconsin, Madison, is a finite difference shell theory model. Several benchmark problems have been performed to compare results from TSM (see Figure E-1) and the ABAQUS finite element code, which used an axisymmetric continuum model (see Figure E-2). The remainder of this appendix is divided into six sections: Section E-3 details the four benchmark problems, Section E-4 describes the TSM and ABAQUS models, Section E-5 discusses the results from the first two (spherically symmetric) benchmark problems, Section E-6 includes the results from the remaining two (localized thermal loading) benchmark problems, and Section E-7 gives conclusions.

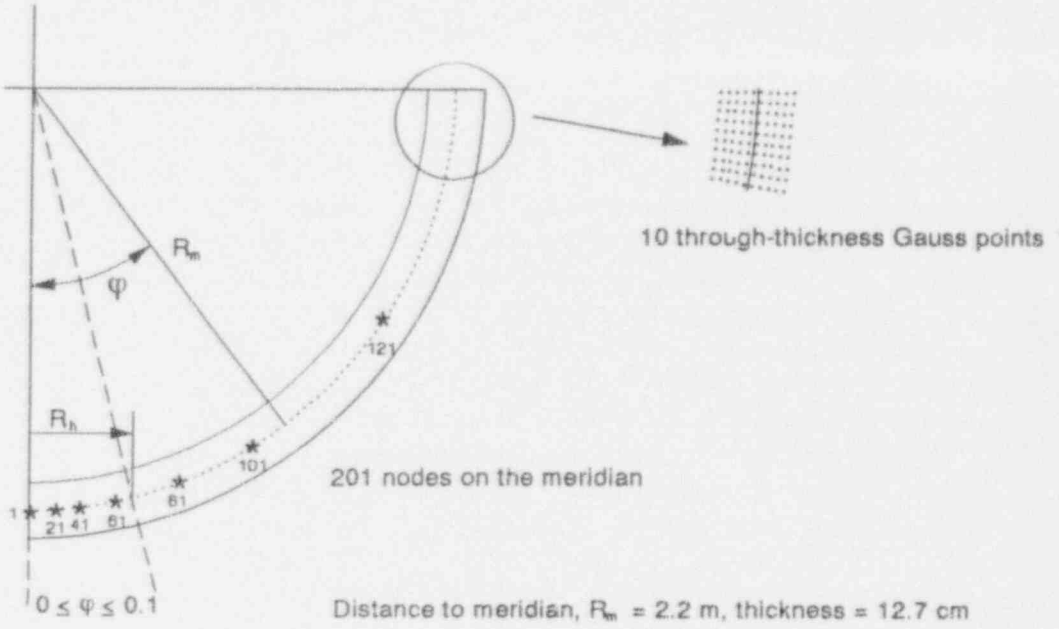

Figure E-1. The shell model (TSM).

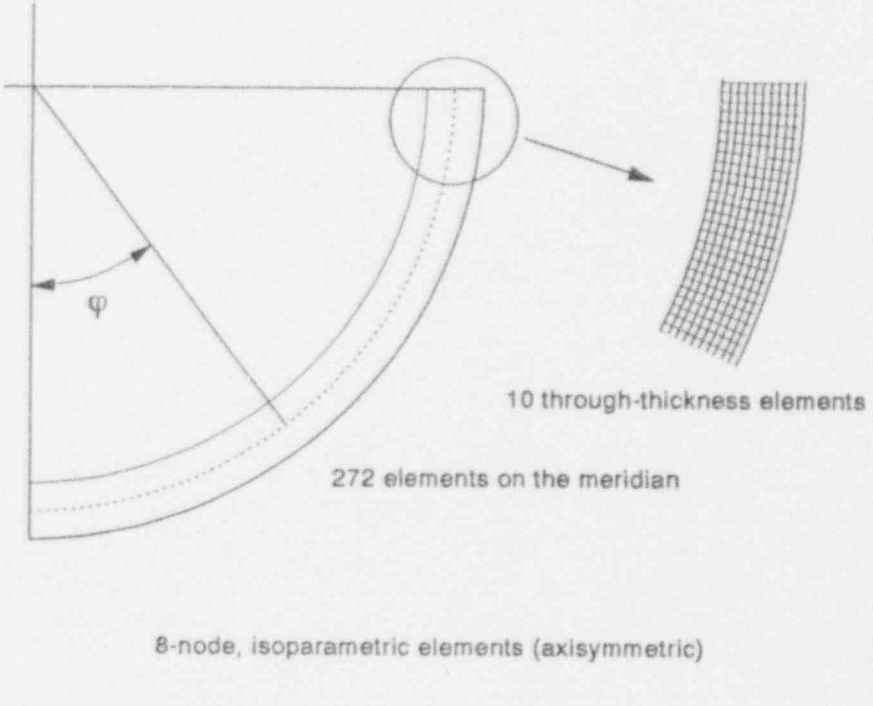

Figure E-2. ABAQUS model.

E-3. DESCRIPTION OF BENCHMARK PROBLEMS AND MATERIAL PROPERTIES

Four benchmark problems were suggested[a] as verification calculations for TSM. The suggested problems were refined during the analysis to reach required final states; specifically, the relative contributions of thermal and pressure loadings were modified to achieve plasticity one-quarter of the way through the thickness at some location along the shell. The purpose of the problems was to determine the ability of TSM to accurately resolve the spatial variation of displacement, stress, and strain fields near a localized thermal loading (hot spot). None of the problems included creep in the material response; creep introduces complexities in the material model and global solution algorithms but not in the ability to represent the spatial variation of the computed fields. The following four problems were considered:

1. *Internal Pressure Only*. This problem tested the elastic response of TSM by ramping an internal pressure load to 10 MPa while employing material properties at 300 K. The problem was essentially one-dimensional with no variation along the meridian. This problem is shown as Case I in Figure E-3.

2. *Internal Pressure, Background Temperature*. This problem tested the elastic-plastic response by employing an internal pressure and a background temperature profile. The response was one-dimensional. The desired final state had to show plasticity penetrating one-quarter of the wall. The problem was run by taking the initial state as 0 MPa internal pressure, and inside and outside surface temperatures (T_{in},T_{out}) at 300 K. The subsequent state of 10 MPa, T_{in} at 900 K and T_{out} at 700 K (and a linear temperature gradient through-thickness) was reached by linearly ramping both pressure and temperature. This second state corresponded to the background state for Problems 3 and 4. At this point, yielding initiated at the outer surface of the shell in TSM. Continued ramping of both temperatures and pressure to reach the desired final state was found to be unacceptable because of the progressive softening of the shell at elevated temperatures (above 1000 K). The desired final state was reached by ramping the pressure to 35 MPa while holding T_{in} and T_{out} at 900 and 700 K, respectively. This problem is shown as Case II in Figure E-3.

3. *Internal Pressure, Moderate Localized Thermal Loading*. This problem tested the elastic-plastic response by employing a moderate localized thermal loading onto a background internal pressure and temperature profile, producing a two-dimensional loading with modest gradients along the meridian directly underneath the hot spot. The desired final state had to show plasticity penetrating one-quarter of the wall. The problem first established the spherically symmetric state described in Problem 2 (10 MPa pressure, temperature field of T_{in} at 900 K and T_{out} at 700 K, linear through-thickness temperature gradient). At this point, a moderate localized thermal loading was applied. This loading consisted of ramping the temperature at the bottom inner surface to 1400 K (at $\varphi = 0$), with a linear gradient to the outside surface and to the background profile at $\varphi = 0.1$ (see Figure E-1). Then the internal pressure was

---

a. Professor R. H. Dodds, University of Illinois at Urbana-Champaign, letter to S. Chávez, INEL, regarding benchmarking calculations of Professor R. Witt model for predicting localized rupture (Consultant Agreement 92-160236-HRS-284-92), July 20, 1992.

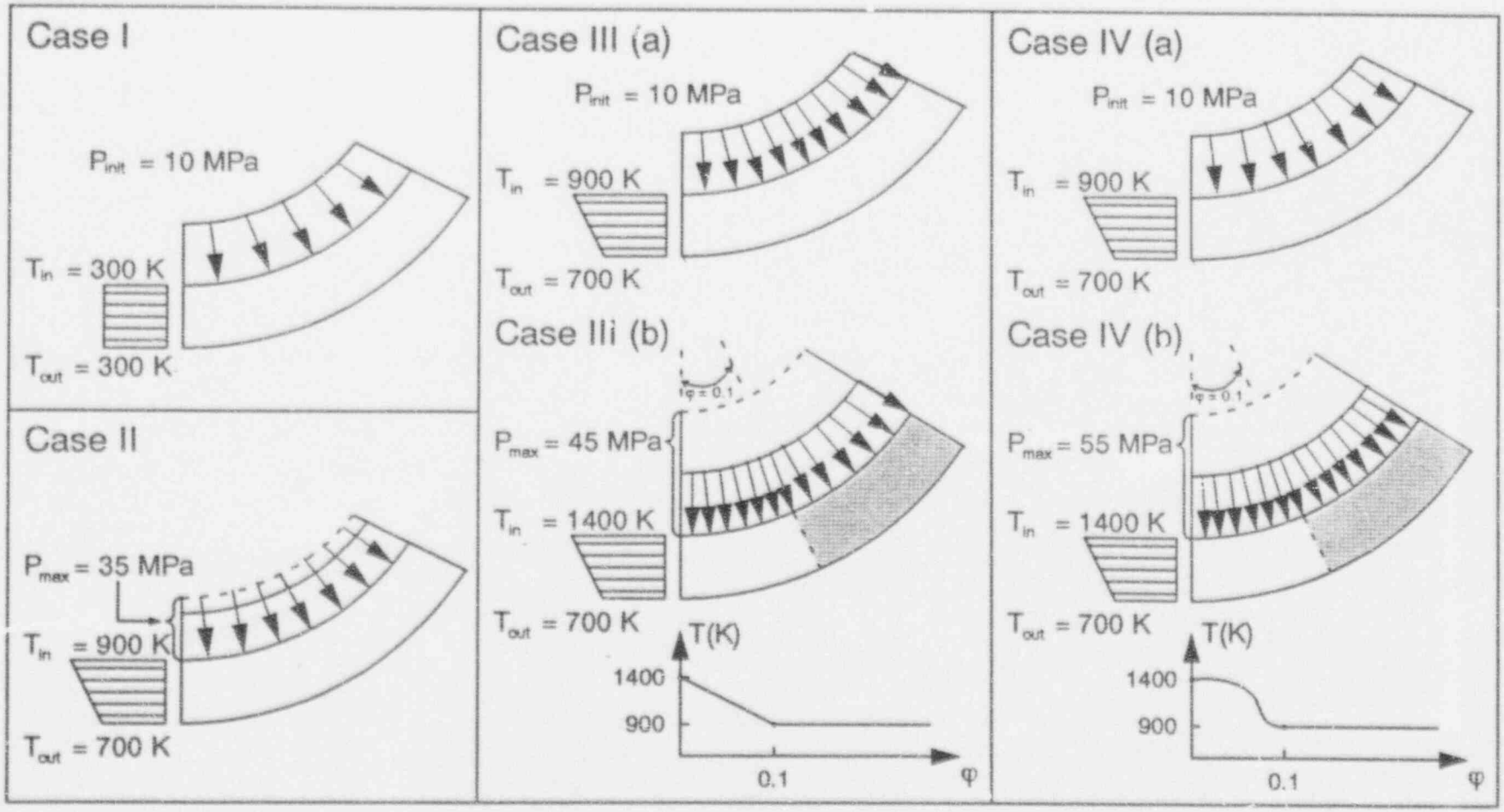

Figure E-3. Benchmark problem loadings.

increased to 45 MPa to reach the final state. This problem is shown as Case III in Figure E-3.

4. *Internal Pressure, Severe Localized Thermal Loading.* This problem tested the elastic-plastic response by employing a severe localized thermal loading onto a background internal pressure and temperature profile, representing a two-dimensional problem with pronounced gradients along the meridian. The desired final state had to show plasticity penetrating one-quarter of the wall directly underneath the hot spot. The problem first established the spherically symmetric state described in Problem 2 (10 MPa internal pressure, temperature field of T_{in} at 900 K and T_{out} at 700 K, linear through-thickness temperature gradient). At this point, a Type 2 [hot spot defined by Equation (4-54) in Section 4] temperature distribution was applied over $0 < \varphi < 0.1$, with a peak temperature of 1400 K. This temperature profile was more severe than that of Problem 3 because of the nonlinearity of the distribution. Then the internal pressure was increased to 55 MPa to reach the final state. This problem is shown as Case IV in Figure E-3.

The material properties required for these analyses included Young's modulus as a function of temperature, mean thermal expansion coefficient as a function of temperature, and yield strength and plastic deformation characteristics as independent of temperature. The material properties used were taken from Appendices B and F and Reference E-2. Poisson's ratio was taken as independent of temperature as $\nu = 0.29$.

E-4. TSM AND ABAQUS MODELS

The spatial model for TSM calculations was made using the axisymmetric representation $R_h/R_m = x^2$ with 201 nodes, where R_h is the horizontal distance from the vertical axis and R_m is the initial radius of the vessel middle surface (see Figure E-1). The model represented a spherical head with a mean radius, R_m, of 2.2 m and a uniform thickness of 12.7 cm.

The ABAQUS model consisted of a quarter sphere that used axisymmetric solid (eight-node, isoparametric with reduced integration) elements. The model was meshed with 10 elements through the thickness and 272 along the meridian (uniformly spaced), giving approximately square elements. The free ends of the quarter sphere were restrained for symmetry, the loading conditions and geometry being symmetric about the two global axes. A second ABAQUS model was prepared with 15 elements through the thickness and 408 along the meridian. Both ABAQUS models were evaluated using ABAQUS, a multipurpose finite element solution package, for all four benchmark problems. The output data (stress, strain, and displacement) for the two ABAQUS models were compared, and the results showed that the data varied by less than 1%. This indicated that the mesh refinement of the first ABAQUS model was sufficient to accurately describe the response for the benchmark problems. Only the results of the first ABAQUS model were compared to those of TSM in the following sections. Figure E-2 outlines the ABAQUS model.

Note that the ABAQUS model was developed so that nodes in both TSM and ABAQUS models overlapped at ξ = 0, 0.1, 0.2, 0.3, 0.4, 0.5 and 0.6, corresponding to TSM node numbers 1 (shell bottom), 21, 41, 61, 81, 101 and 121 (see Figure E-1). The through-thickness location of information differed in the two models, with TSM providing information at 10 Gauss points through the thickness, while ABAQUS calculated information at element integration points, then interpolated (and averaged) that information at the nodes. This latter difference required interpolation of results from the ABAQUS nodes to TSM Gauss points to allow comparison of the results. All comparisons using average data weighted each data point equally, unless specified differently in the discussion. In the spherically symmetric problems (benchmark Problems 1 and 2 only) the results were identical on all radial lines, and only one set of output information was given.

E-5. RESULTS OF BENCHMARK PROBLEMS 1 AND 2

Benchmark problems 1 and 2 were spherically symmetric problems. A separate means of evaluating TSM exists, in that closed-form solutions are available for infinitesimal deformation, constant elastic property problems with arbitrary temperature distributions through thickness. Since some insight into the shortcomings of TSM can be gained by obtaining closed-form solutions, the results are summarized below. In a spherically symmetric problem, the meridian and hoop strains and stresses become identical and the radial equilibrium equation is

$$\frac{d\sigma_r}{dr} + \frac{2(\sigma_r - \sigma_\varphi)}{r} = 0 \quad . \tag{E-1}$$

The Hooke's Law relationships are

$$\sigma_r = \frac{E(\epsilon_r - \epsilon_{th})}{1 + \nu} + \frac{\{\nu E[\epsilon_r - \epsilon_{th} + 2(\epsilon_\varphi - \epsilon_{th})]\}}{(1 + \nu)(1 - 2\nu)} \tag{E-2}$$

$$\sigma_\varphi = \frac{E(\epsilon_\varphi - \epsilon_{th})}{1 + \nu} + \frac{\{\nu E[\epsilon_r - \epsilon_{th} + 2(\epsilon_\varphi - \epsilon_{th})]\}}{(1+ \nu)(1 - 2\nu)} \quad . \tag{E-3}$$

Using the strain/displacement relationships

$$\epsilon_r = \frac{du}{dr} \quad \text{and} \quad \epsilon_\varphi = \frac{u}{r} \tag{E-4}$$

the Hooke's Law form of the stress/displacement relationship may be substituted into the equilibrium equation to obtain a second-order equation for u

$$\frac{d^2u}{dr^2} + \frac{2}{r}\left(\frac{du}{dr} - \frac{u}{r}\right) = \frac{1 + \nu}{1 - \nu}\frac{d\epsilon_{th}}{dr} \quad . \tag{E-5}$$

The complete solution of which is

$$u(r) = C_1 r - \frac{C_2}{r^2} + \frac{1 + \nu}{r^2(1 - \nu)}\int_{R_{in}}^{R_{out}} \epsilon_{th} r'^2 dr' \tag{E-6}$$

subject to the resolution of constants C_1 and C_2. If the requirements are that $\sigma_r = -p_i$ at $r = R_{in}$ and $\sigma_r = 0$ at $r = R_{out}$, then the strains can be shown to be

$$\epsilon_\varphi = \frac{1 - 2\nu}{1 - (R_{in}/R_{out})^3}\frac{p_i}{E}\left[(R_{in}/R_{out})^3 + \frac{(1 + \nu)(R_{in}/r)^3}{2(1 - 2\nu)}\right] + \frac{2(1 - 2\nu)\epsilon_{th_{avg}}}{3(1 - \nu)} \tag{E-7}$$

$$\left[1 + \frac{(1+\nu)(R_{in}/r)^3}{2(1-2\nu)}\right] + \frac{1+\nu}{(1-\nu)r^2}\int_a^b \epsilon_{th} r'^2 dr'$$

$$\epsilon_r = \frac{1-2\nu}{1-(R_{in}/R_{out})^3}\frac{p_i}{E}\left[(R_{in}/R_{out})^3 - \frac{(1+\nu)(R_{in}/r)^3}{2(1-2\nu)}\right] + \frac{2(1-2\nu)\epsilon_{th_{avg}}}{3(1-\nu)} \qquad \text{(E-8)}$$

$$\left[1 + \frac{(1+\nu)(R_{in}/r)^3}{2(1-2\nu)}\right] + \frac{(1+\nu)\epsilon_{th}}{(1-\nu)} - \frac{2(1+\nu)}{(1-\nu)r^2}\int_a^b \epsilon_{th} r'^2 dr'$$

where $\epsilon_{th_{avg}}$ is the average thermal strain, defined as

$$\epsilon_{th_{avg}} = \frac{3}{R_{out}^3 - R_{in}^2}\int_{R_{in}}^{R_{out}} \epsilon_{th} r^2 dr \quad . \qquad \text{(E-9)}$$

In Benchmark Problem 1 (see Figure E-3), a purely elastic response showed that stresses and strains varied through the thickness for the exact solution (from closed-form equations) and ABAQUS. The stress and strain results of the exact and ABAQUS solutions were within 1%. TSM stress and strain results were constant throughout the thickness at the calculated average for the shell.

For an internal pressure of 10 MPa with the inner surface temperature brought to 900 K and the outer surface temperature brought to 700 K (from initially 300 K), a purely elastic analysis produced TSM stresses that varied throughout the thickness. Those stresses were within 2% of the values for the exact solution. However, TSM strains were constant throughout the thickness at the calculated average for the shell. The most obvious shortcoming of TSM is in the isothermal problem. With the strains formulated as, for instance,

$$\epsilon_\varphi = \epsilon_{\varphi m}(1 + \xi/R_\varphi) + \xi[1/R_\varphi - 1/R_{\varphi 0} + (\gamma'/\alpha_0)\sec^2\gamma] \qquad \text{(E-10)}$$

and the deformed radius of curvature related to the initial radius of curvature through

$$R_\varphi = R_{\varphi 0}\left[\frac{1+\epsilon_{\varphi m})}{1+\frac{\beta'}{\varphi_0'}}\right] \quad . \qquad \text{(E-11)}$$

Then in spherically symmetric problems ($\beta = \varphi = 0$), substitution of $R_\varphi = R_{\varphi 0}(1 + \epsilon_{\varphi m})$ into the strain measure [see Equation (E-10)] yields

$$\epsilon_\varphi = \epsilon_{\varphi m} \quad . \qquad \text{(E-12)}$$

i.e., no through-thickness dependence. The exact result shows the strain measure has a constant component and a component that scales inversely to distance cubed. The shortcoming is of less consequence in the problem with a temperature gradient through the thickness because the

gradient in thermal strain provides a much larger bending component of stress than is obtained from the finite thickness of the shell.

In Benchmark Problem 2 (see Figure E-3), yielding occurred approximately one-quarter way through the thickness after ramping the internal pressure to 35 MPa. The ABAQUS data were interpolated to coincide with TSM Gauss point data. Because TSM results varied somewhat from ABAQUS, a comparison of the difference was in order. The comparison used the ABAQUS results as the baseline. TSM values for meridional stress were on average 1.0% below ABAQUS in the outer two-thirds of the wall. In the inner third of the wall, the meridional stress levels predicted by TSM were an average of 50% below those given by ABAQUS. That underprediction resulted from the radial stresses in the area, whose magnitudes were on the same order as those of the meridional stresses. TSM assumes that the radial component of stress was negligible throughout the model. That assumption was not true in the inner third of the wall, and TSM meridional stress levels reflected that error. Benchmark Problems 3 and 4 discuss that assumption in detail.

TSM values for total meridional strain averaged 1% below ABAQUS. The ABAQUS plastic strains began one Gauss point location closer to the inside surface than those of TSM. However, TSM meridional plastic strains were an average of 1% above those of ABAQUS.

E-6. RESULTS OF BENCHMARK PROBLEMS 3 AND 4

A far greater amount of output information was associated with Benchmark Problems 3 and 4 because the hoop and meridian stresses and strains were not generally identical and those states varied along the shell meridian. In Problem 3, the inner surface temperature was raised to 1400 K (over the defined local area), then the pressure was raised to 45 MPa to get yielding one-quarter of the way through the thickness near $\varphi = 0$. Yielding occurred to a greater extent under these conditions at positions away from the bottom (edge of shell at $\varphi = 0$) of the shell. In Problem 4, the inner surface temperature was raised to 1400 K (over the defined local area), then the pressure was raised to 55 MPa to get yielding one-quarter of the way through the thickness at the shell bottom. Again, yielding was more severe away from $\varphi = 0$ in this case.

E-6.1 Problem 3 Results

The moderate localized thermal loading applied in this problem is shown in Figure E-3. The pressure was raised to 45 MPa to get yielding one-quarter of the way through the thickness near $\varphi = 0$. It is of interest that yielding occurred to a greater extent under these conditions at positions away from the bottom (edge of shell at $\varphi = 0$) of the shell. Because of the volume of data and locations available in the models, the evaluation was limited to seven specific meridional points and their 10 associated through-thickness Gauss point locations. Four of the meridional points were within the hot spot, one on the inside edge (near $\varphi = 0$), two in the middle, and one near the outside edge. Points 5 through 7 were outside the hot spot, the fifth being near the outside edge of the spot, the sixth, and seventh being well away from it (see Figure E-1).

A graphical representation of the comparison between TSM and ABAQUS meridian and hoop stresses is given in Figures E-4 through E-10. Note that TSM meridian and hoop stresses inside the midplane in the hot spot underpredicted those calculated by ABAQUS. This portion of the wall was very soft because of the temperature profile and the material definition. A small percentage of the total load was carried by this half of the wall. Because of the softness of the wall, the radial component of stress up to the midplane maintained a magnitude higher than that of the hoop and meridian stresses. The underprediction of hoop and meridian stresses by TSM resulted largely from the absence of a radial stress component in TSM model. This was confirmed by comparing the ABAQUS and TSM results at the same thermal conditions at a lower pressure (discussed below). As discussed in Section 4.2.2 and Appendix D, the TSM solution scheme assumed that radial stresses were negligible. This was true beyond the midplane in the hot spot because the radial stresses quickly decreased to zero at the outside surface, and the hoop and meridian stresses increased by a factor of 50 to 100. TSM meridian and hoop stresses in this area underpredicted those calculated by ABAQUS by about 2%. This portion of the wall carried the majority of the load, and shell yielding propagated from the outer surface inward. Near the outside edge of the hot spot (point 61) and far-field (points 81 through 121), meridian and hoop stresses were about 18% lower in the inner 30% of the wall than predicted by ABAQUS, while the stresses over the outer 70% of the wall were within 3%.

The TSM solution scheme and model were prepared to predict a particular failure mechanism (a bulging/shear-through type resulting from a local hot spot) in a reactor vessel lower head during an accident scenario. It is important to note that Benchmark Problem 3 included a maximum internal pressure of 45 MPa; an accident condition would specify maximum pressures closer to 15 MPa. Therefore, the moderate localized thermal loading of Problem 3 was applied to

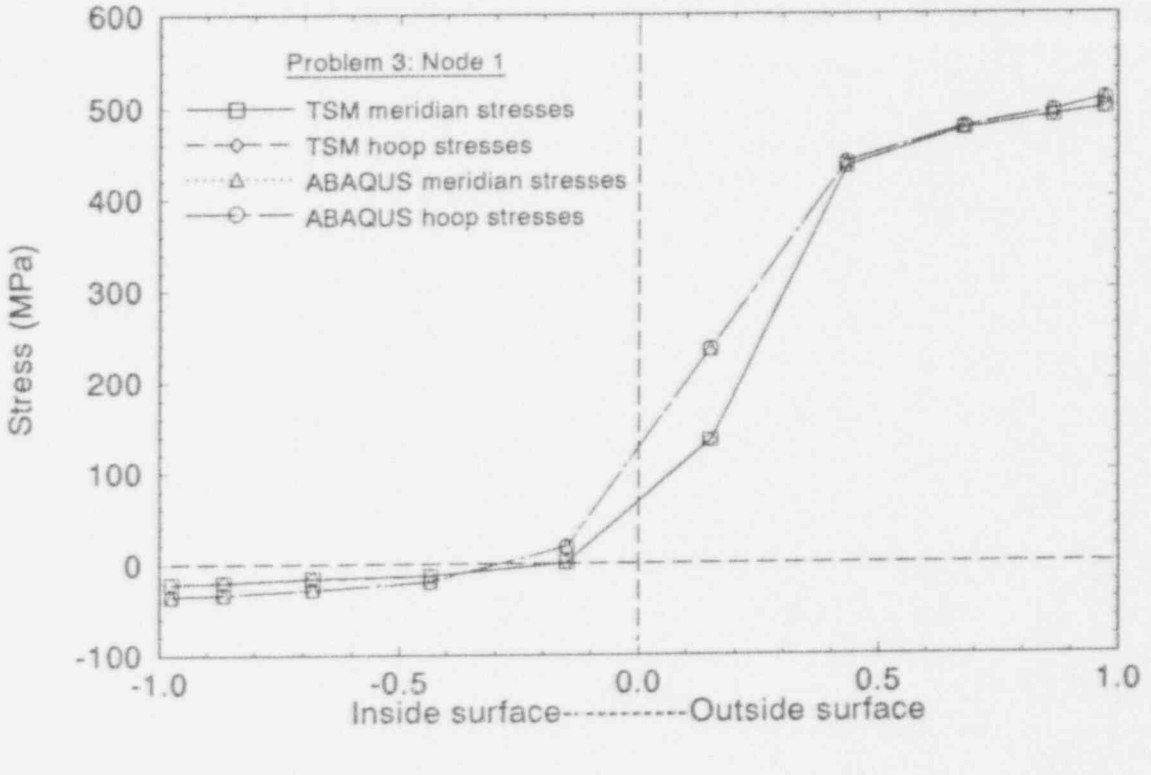

Figure E-4. Problem 3: Node 1 stresses.

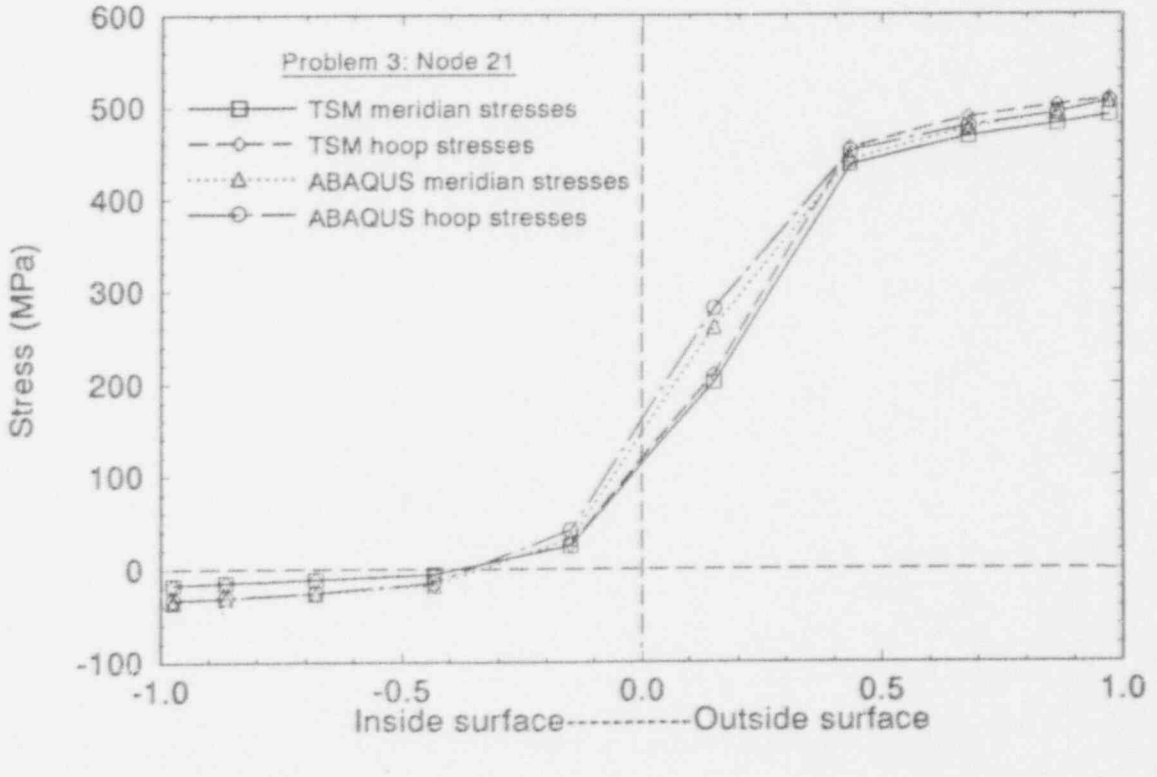

Figure E-5. Problem 3: Node 21 stresses.

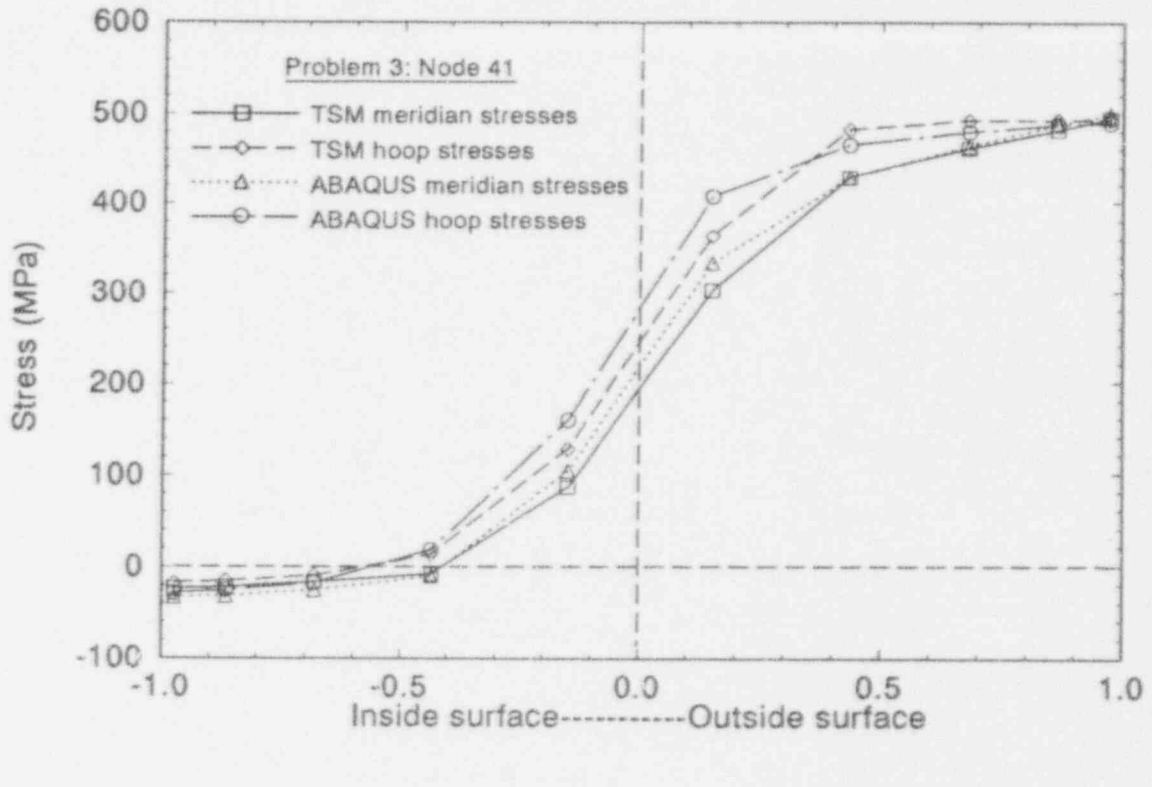

Figure E-6. Problem 3: Node 41 stresses.

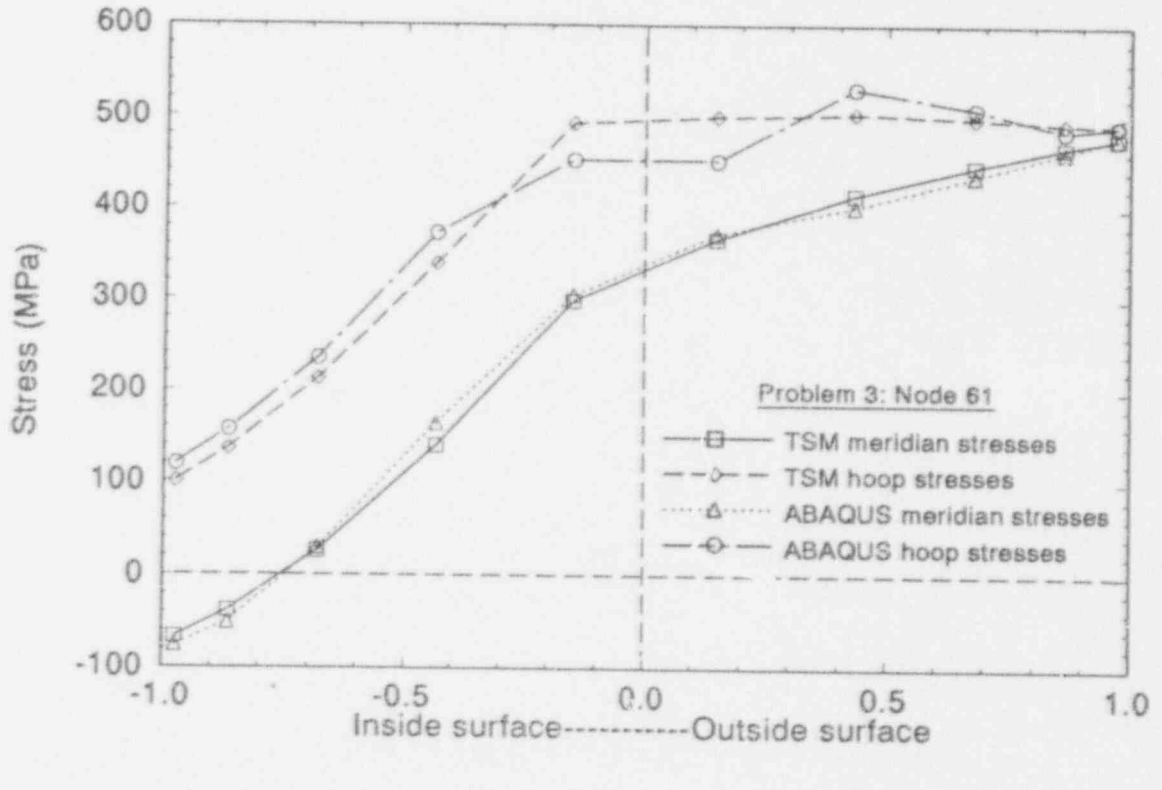

Figure E-7. Problem 3: Node 61 stresses.

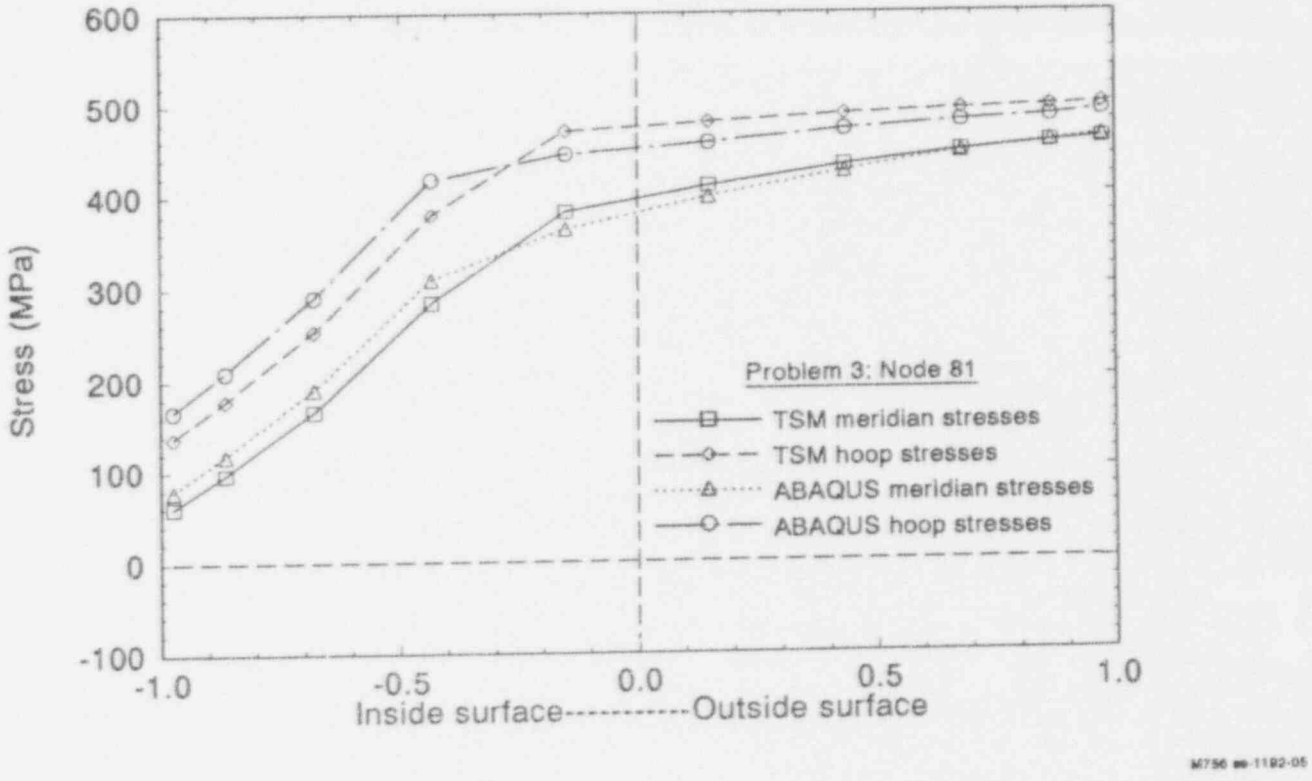

Figure E-8. Problem 3: Node 81 stresses.

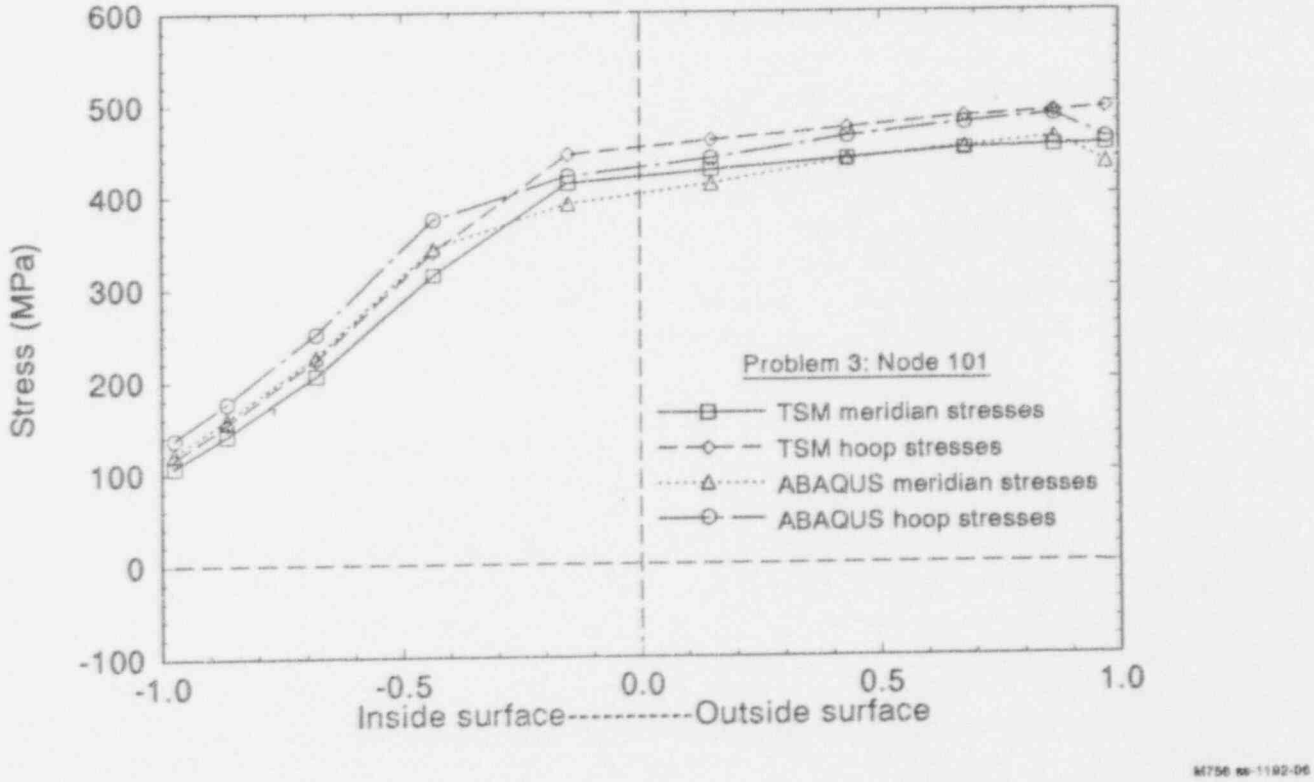

Figure E-9. Problem 3: Node 101 stresses.

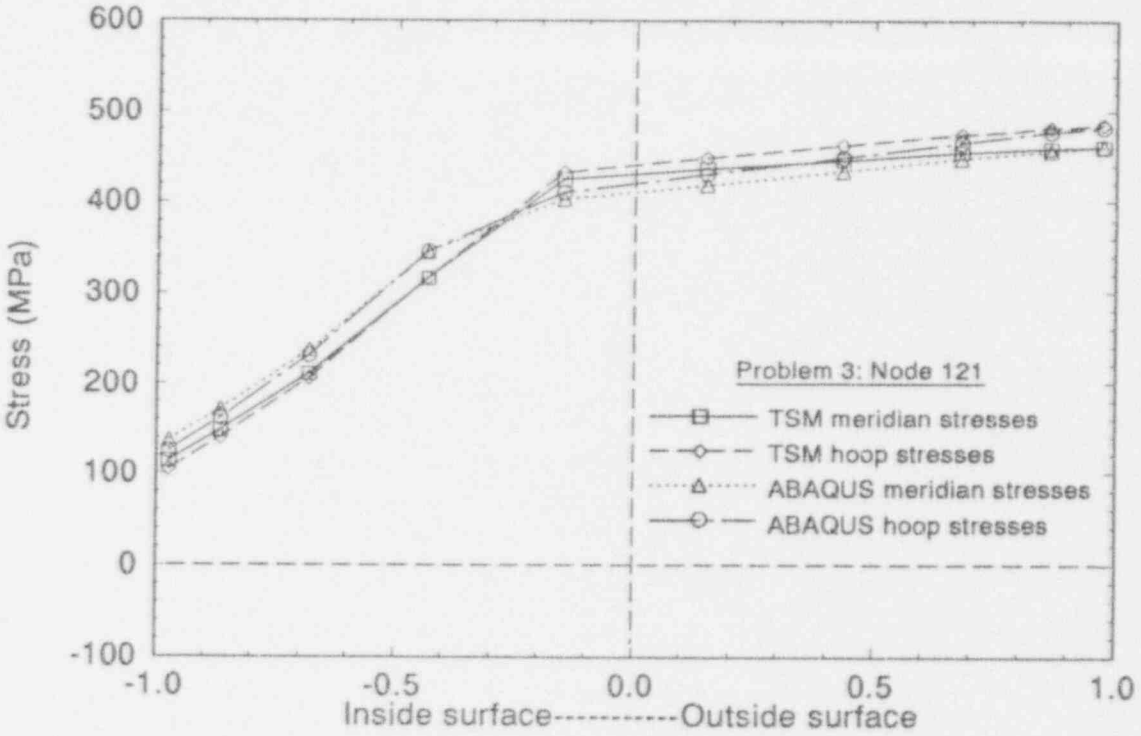

M756 ■■-1192-07

Figure E-10. Problem 3: Node 121 stresses.

TSM and ABAQUS models with a maximum internal pressure load of 15 MPa. Figures E-11 and E-12 compare the hoop and meridian stresses of the two models for node point 41 (located in the middle of the hot spot). TSM stresses in the inside third of the wall were 13% (or less) lower than those of ABAQUS and the remaining portion of the wall was within 3%. These levels of agreement are representative of all points examined along the meridian (1, 21,. . . 121) and indicate that the discrepancies in Figures E-4 through E-10 are rooted largely in the absence of a radial stress in TSM and not the severity of the temperature gradient.

The TSM total meridian and hoop strain results for Benchmark Problem 3 underpredicted the values calculated by ABAQUS an average of 3.6%. Figure E-12 gives the comparison of total hoop and meridian strains for Node 41, which is typical of all node locations.

TSM Benchmark Problem 3 results at the middle of the hot spot (Nodes 21 and 41) showed that plastic strains (meridian and hoop) began at Gauss point 7 location (of 10 total) from the inside surface and increased to the outer surface. ABAQUS results identified plastic strains beginning at Gauss point 6 and increasing to the outside surface. The difference was 100% for the point 7 (where plastic strains were smallest), then decreased for each successive location to an average of 8% at the outside surface (where plastic strains reached a maximum). Outside of the hot spot (Nodes 81 through 121), the plastic strain in both models began one Gauss point location closer to the inside surface. The difference in plastic strains was 100% for point 4 (where plasticity began in the ABAQUS model), but averaged 9% or less for the entire outer half of the wall.

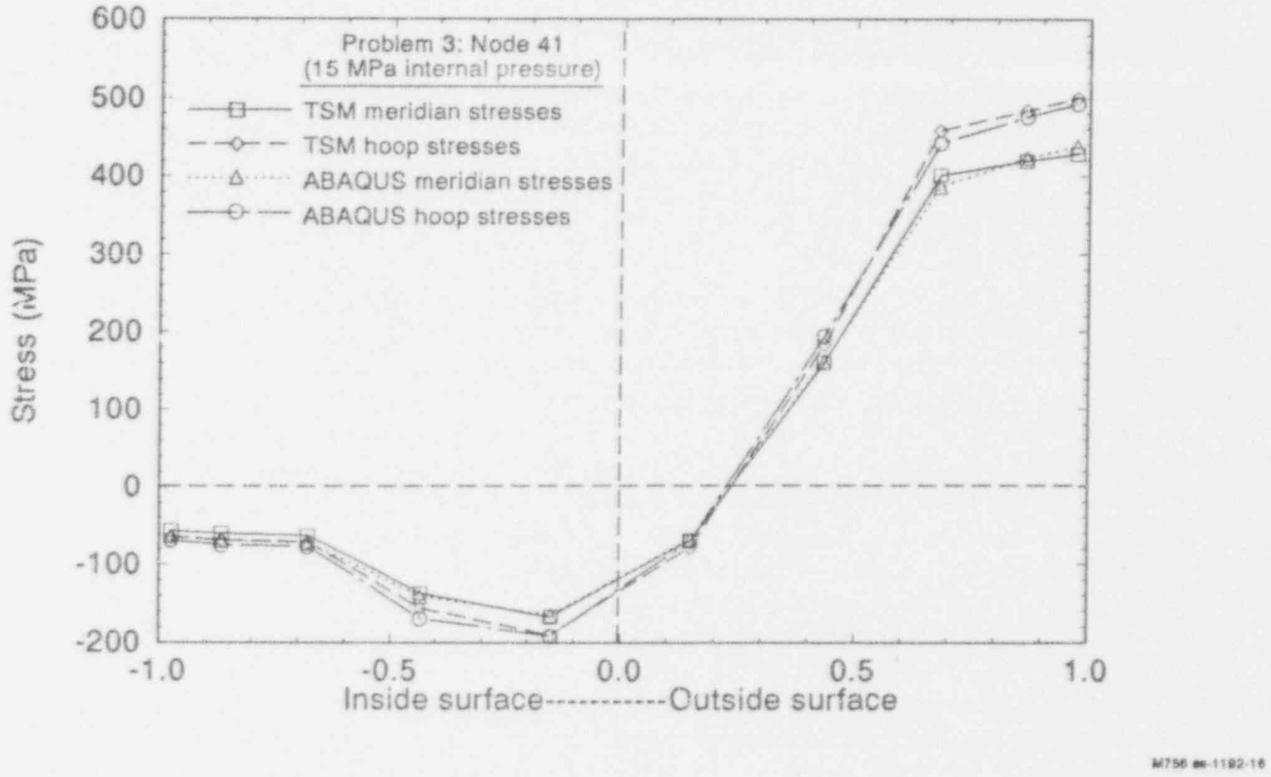

Figure E-11. Problem 3: Thermal loading with only 15 MPa internal pressure: Node 41 stresses.

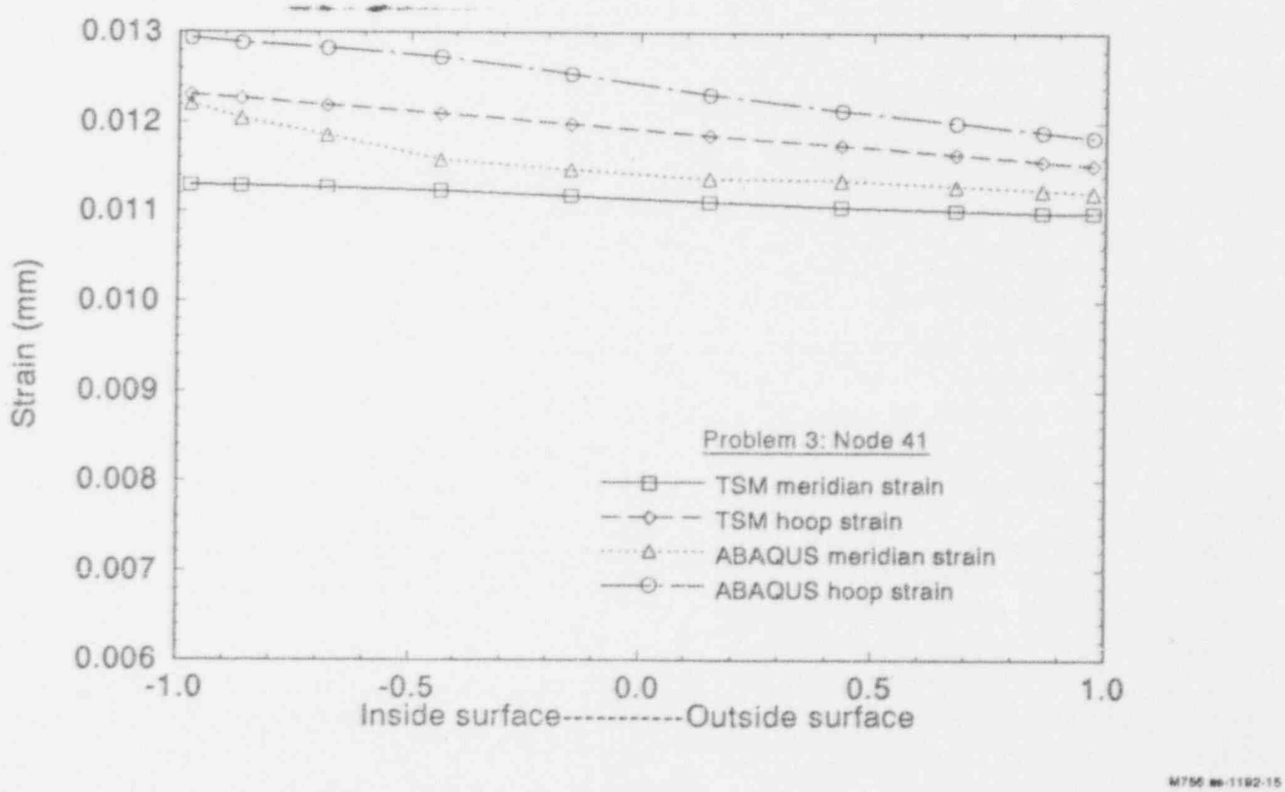

Figure E-12. Problem 3: Node 41 strains.

E-6.2 Problem 4 Results

The severe localized thermal loading for this problem involved a nonlinear temperature distribution (see Figure E-3). The pressure was raised to 55 MPa to get yielding one-quarter of the way through the thickness at the shell bottom. Again, yielding was more severe away from $\varphi = 0$. The same meridian points and their associated through-thickness Gauss point locations were evaluated as in Problem 3.

A graphical representation of the comparison between TSM and ABAQUS meridian and hoop stresses is given in Figures E-13 through E-19. Note that TSM meridian and hoop stresses up to the Gauss point 6 (just beyond the midplane) in the middle of the hot spot underpredicted those calculated by ABAQUS. This area of underprediction was larger than the underpredicted area in Problem 3. This portion of the wall was very soft because of the temperature profile and the material definition. A small percentage of the total load was carried by this portion of the wall. Because of the softness of the wall, the radial component of stress up to Gauss point 4 from the inside surface maintained a magnitude higher than that of the hoop and meridian stresses. As in Problem 3, the underprediction of hoop and meridian stresses by TSM was largely a result of neglecting the radial stress component in the calculations. As discussed in Section 4.2.2 and Appendix D, the TSM solution scheme assumes that radial stresses are negligible. This was true beyond the Gauss point 6 in the hot spot because the radial stresses quickly dropped off to zero at the outside surface while the hoop and meridian stresses rose by a factor of 50 to 100. TSM meridian and hoop stresses in this area underpredicted those calculated by ABAQUS by about 4%. This portion of the wall carried the majority of the load, and shell yielding propagated from the outer surface inward. The far-field (points 101 and 121) meridian and hoop stresses were within an average of 4% of ABAQUS values for the entire wall.

Next, TSM and ABAQUS models were evaluated with the severe localized thermal loading of Problem 4 applied with a maximum internal pressure of 15 MPa. Figure E-20 compares the hoop and meridian stresses of the two models for node point 41 (located in the middle of the hot spot). The TSM stresses throughout the wall were an average of 4% lower than those of ABAQUS. The agreement between ABAQUS and TSM in the more severe temperature gradient at 15 MPa pressure is comparable to the agreement between the two models in a moderate temperature gradient at 15 MPa pressure, indicating again that the absence of radial stress in TSM is primarily responsible for the differences between the two models at elevated pressures.

The TSM total meridian and hoop strains in Benchmark Problem 4 underpredicted the values calculated by ABAQUS by up to 24% on the inside surface to near 10% on the outside for locations within the hot spot at elevated pressures. Away from the hot spot those values were reduced to 12% on the inside and 7% on the outside surfaces. For the condition including the Problem 4 thermal loading with a maximum pressure of 15 MPa, the total meridian and hoop strains in the hot spot were, at most, 16% lower than ABAQUS on the inside surface and within 2% on the outside. Outside of the hot spot all TSM total strains were within 5% of ABAQUS values. Figure E-21 compares the total strains of the two models for the Problem 4 thermal loading with an internal pressure of 15 MPa.

TSM results for Problem 4 showed that all plastic strains (meridian and hoop) occurred one or two Gauss point locations closer to the outer surface than ABAQUS. Those plastic strains increased towards the outer surface. As in Problem 3, TSM plastic meridian and hoop strains started at 100% lower values (at the smallest plastic strains) and steadily increased to, at most, 1% lower values than ABAQUS (where the plastic strains reached maximum values).

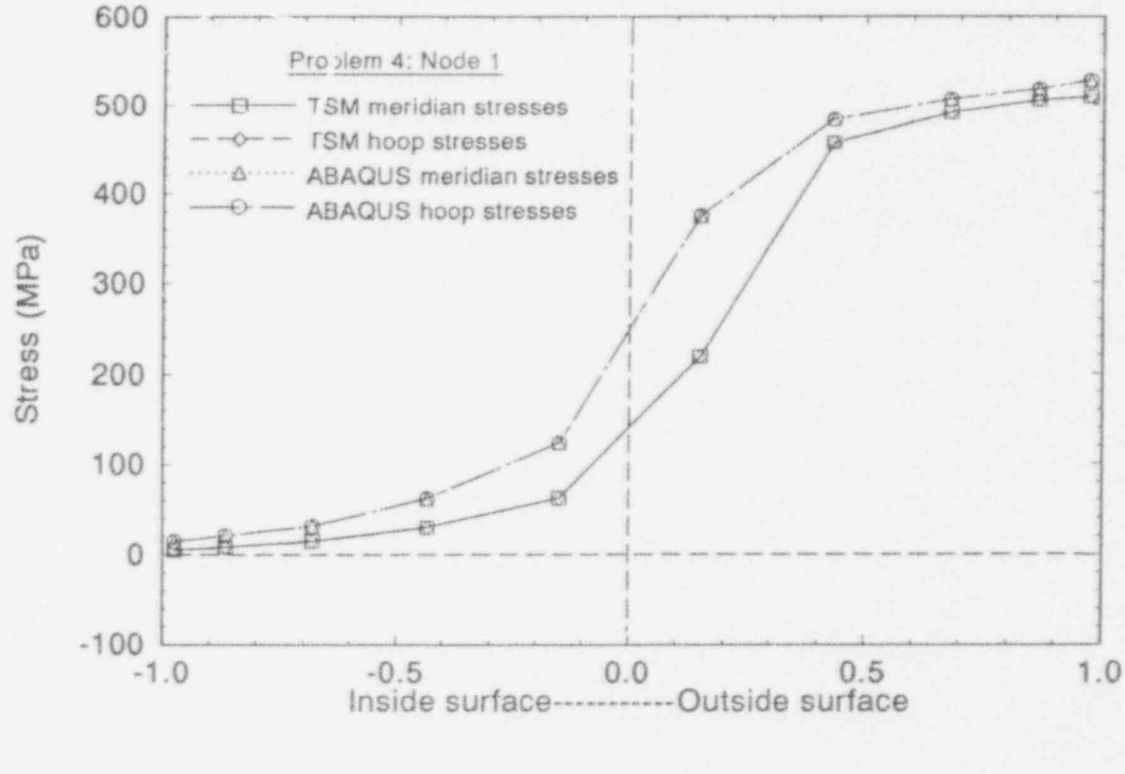

Figure E-13. Problem 4: Node 1 stresses.

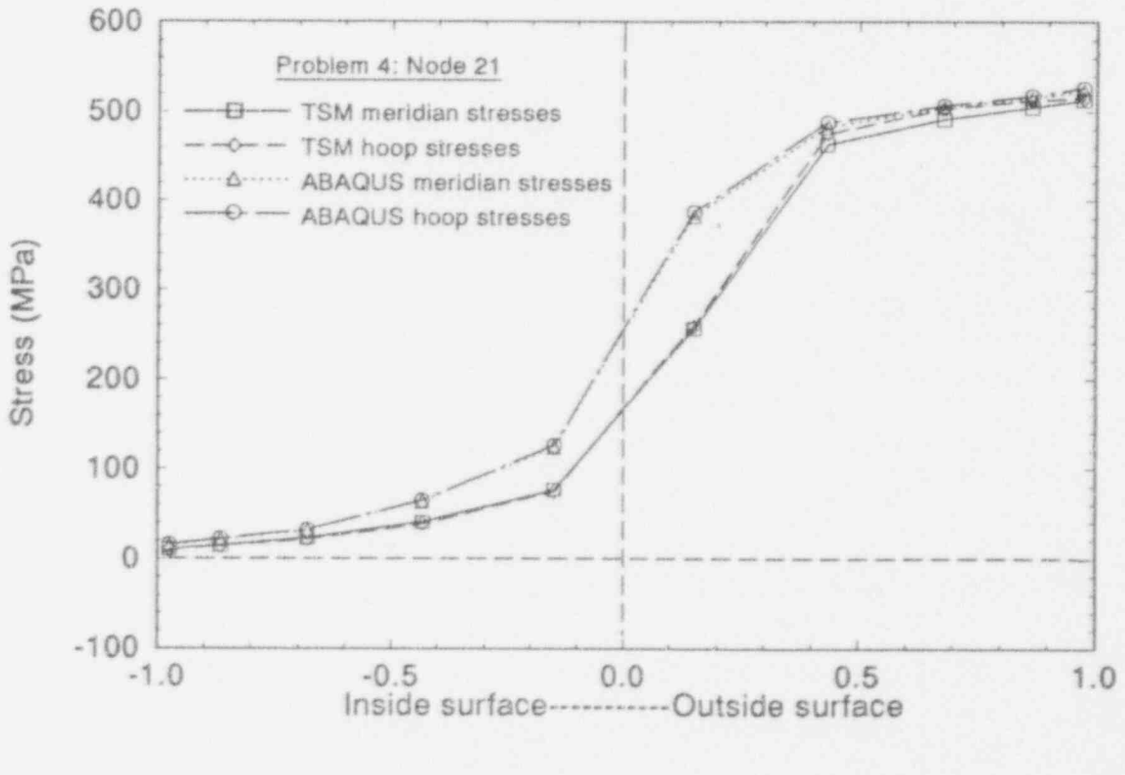

Figure E-14. Problem 4: Node 21 stresses.

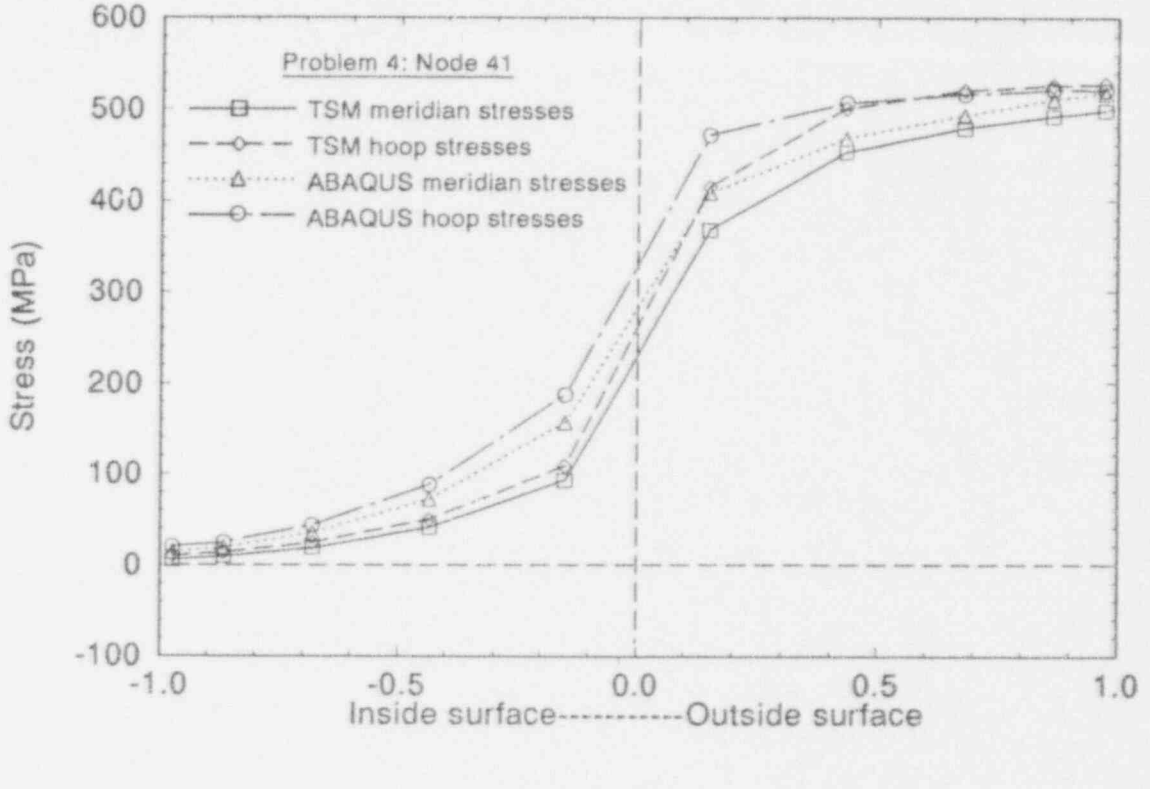

Figure E-15. Problem 4: Node 41 stresses.

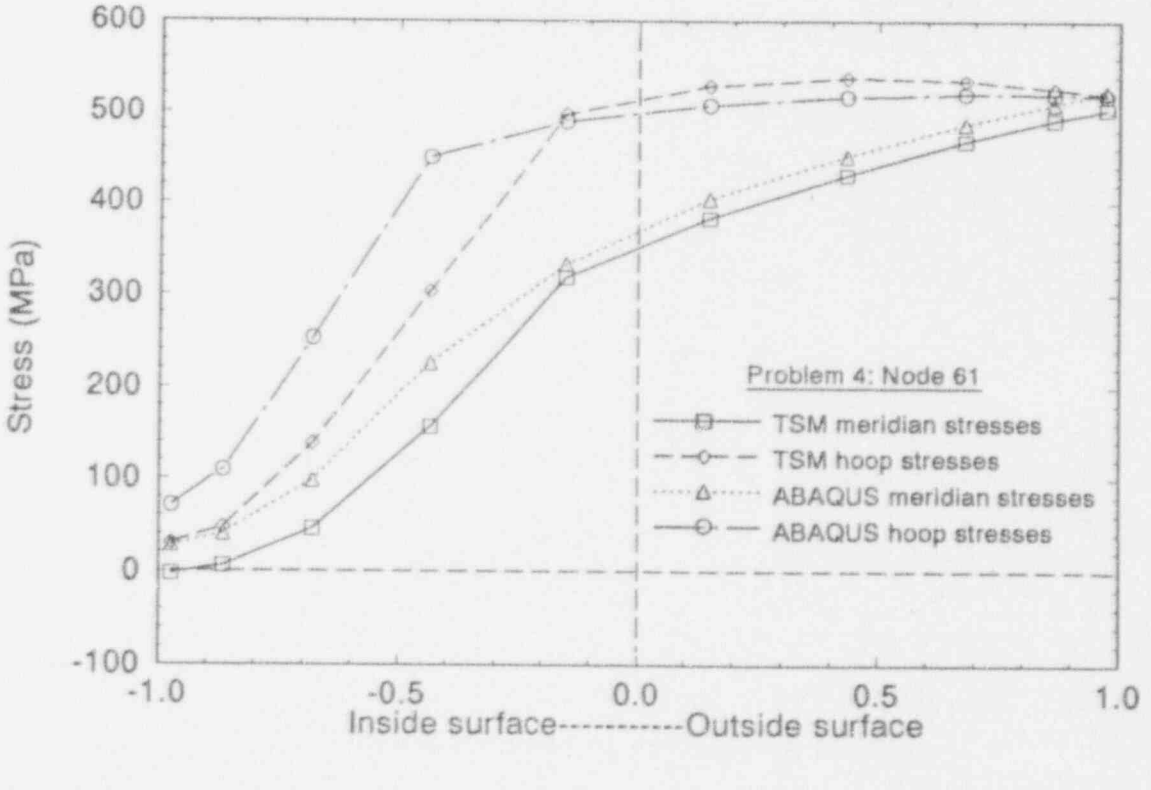

Figure E-16. Problem 4: Node 61 stresses.

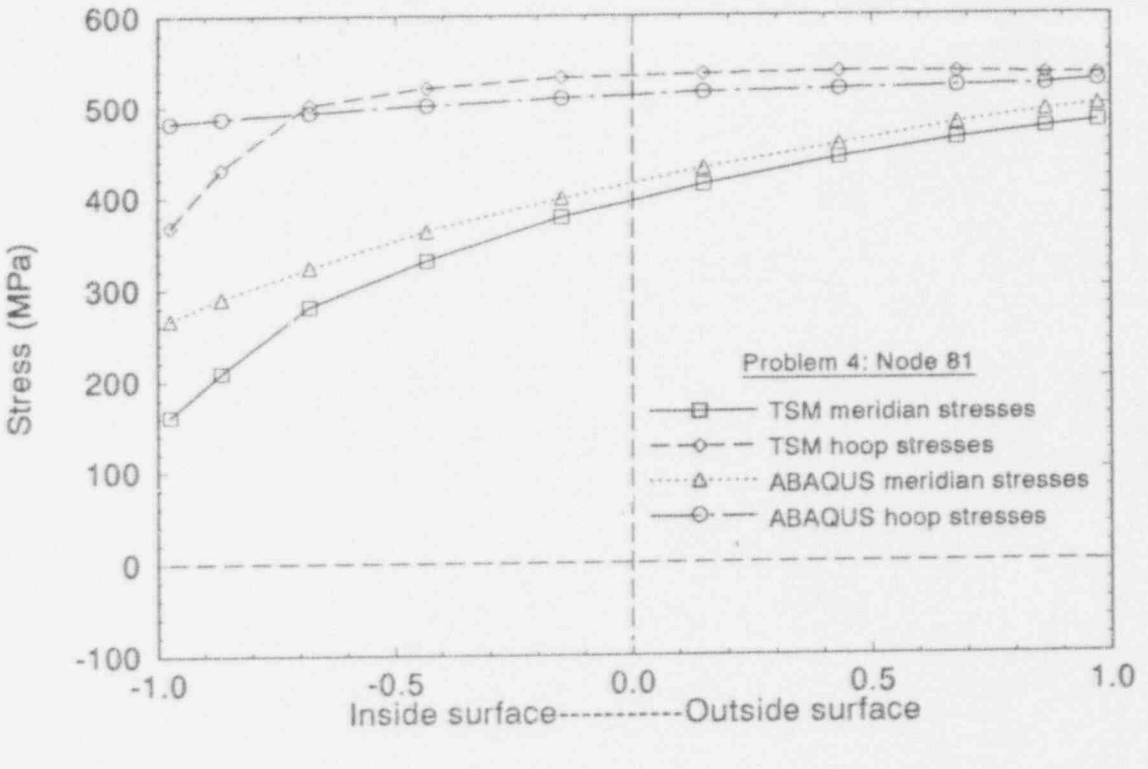

Figure E-17. Problem 4: Node 81 stresses.

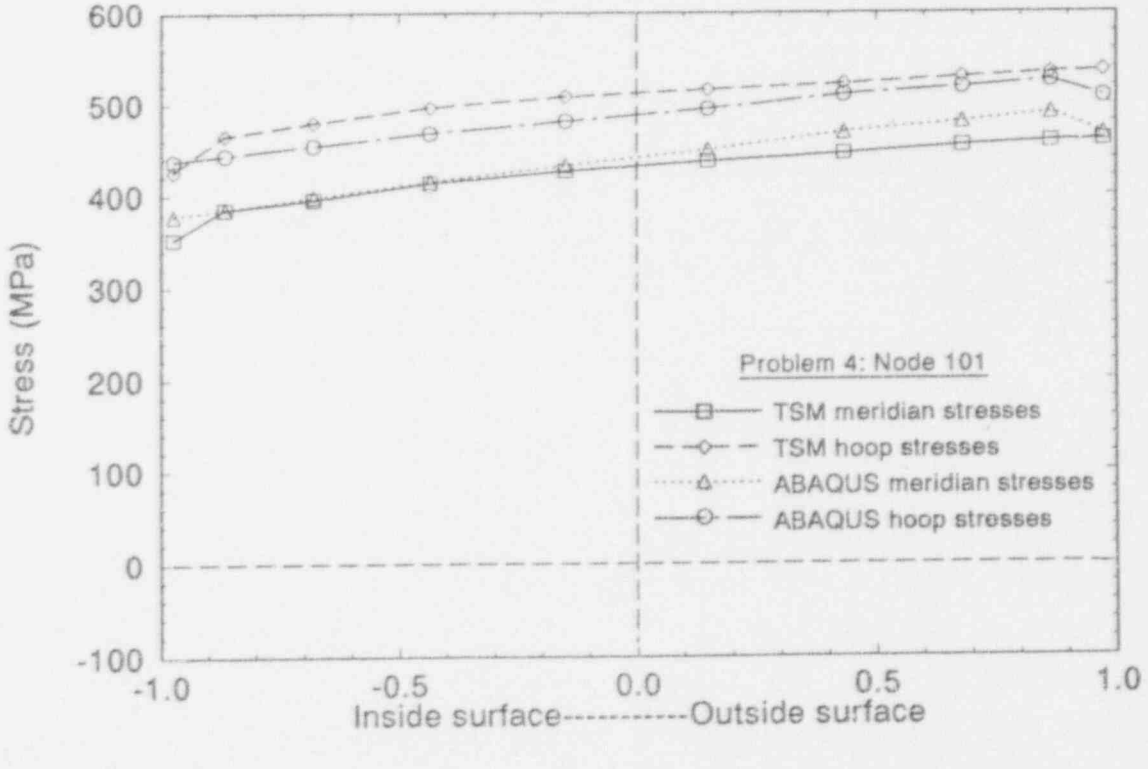

Figure E-18. Problem 4: Node 101 stresses.

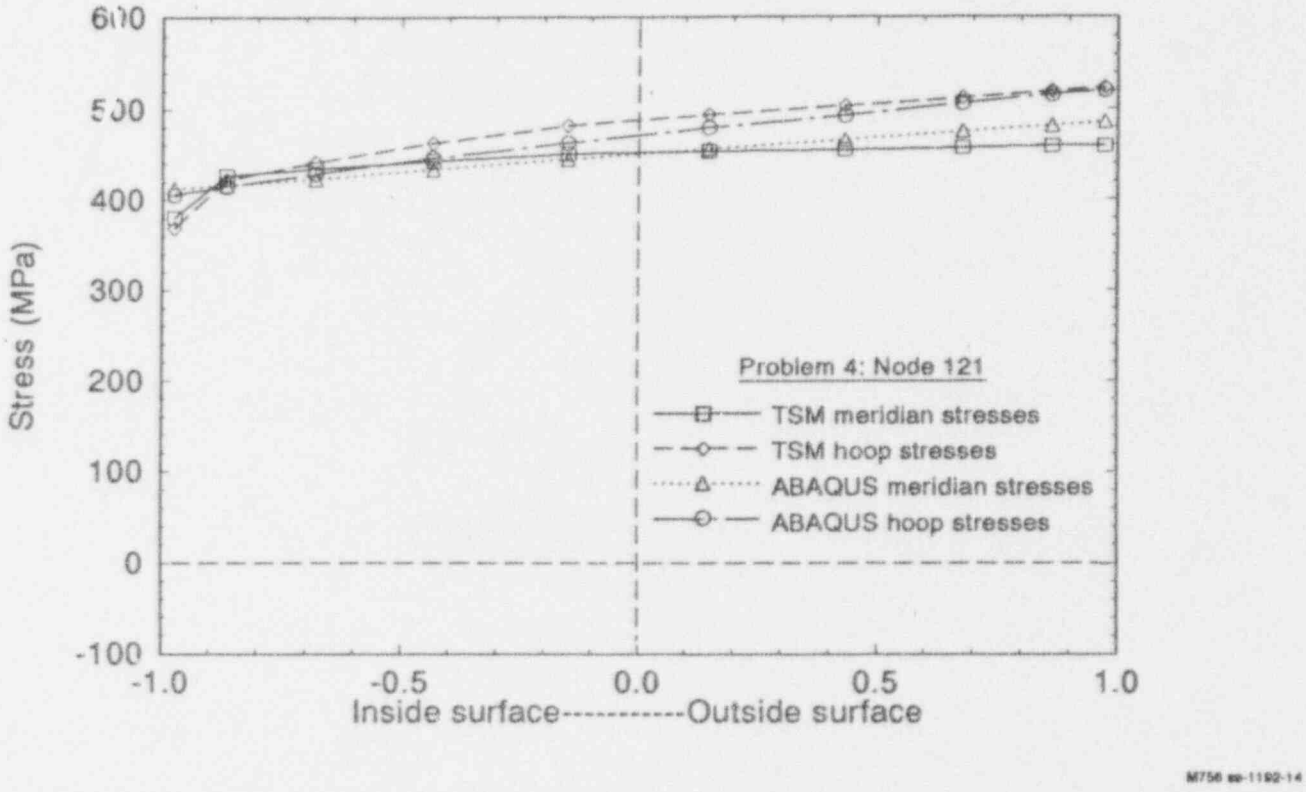

Figure E-19. Problem 4: Node 121 stresses.

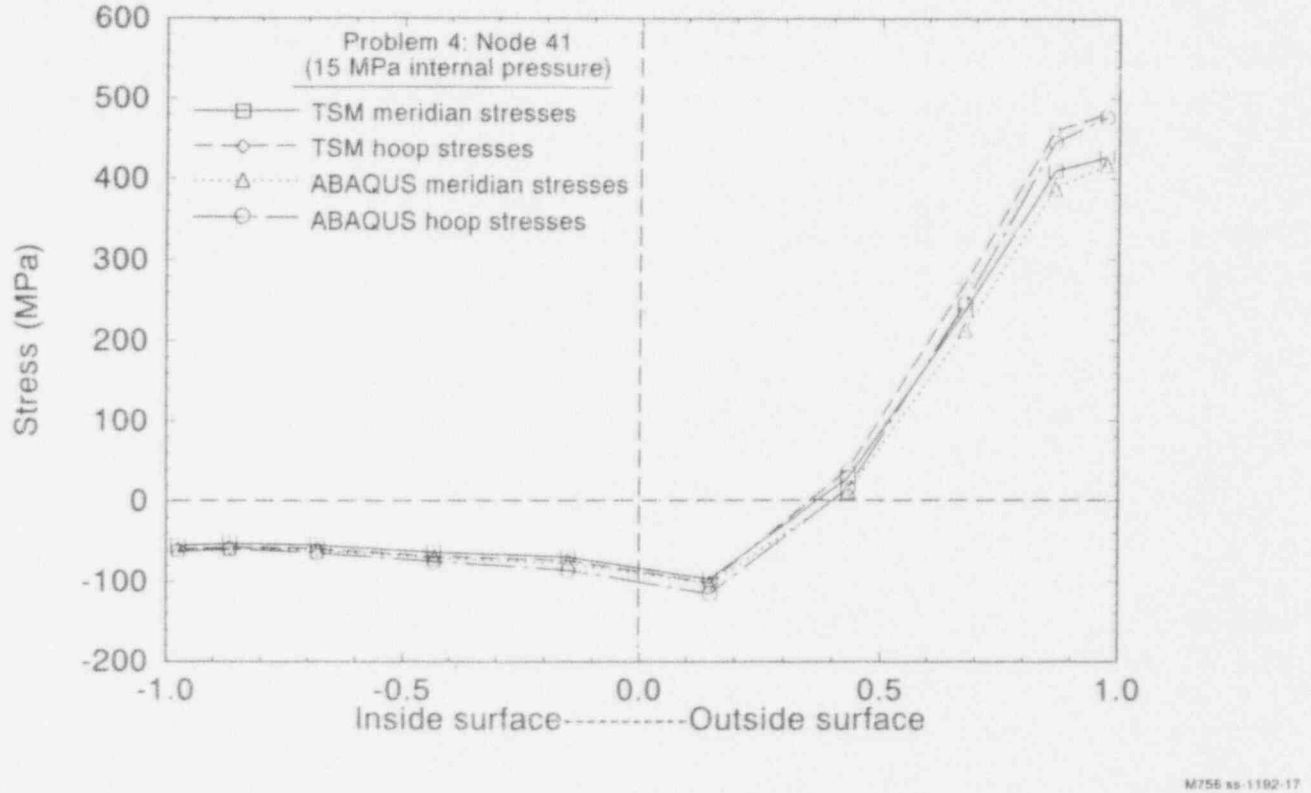

Figure E-20. Problem 4: Thermal loading with only 15 MPa internal pressure: Node 41 stresses.

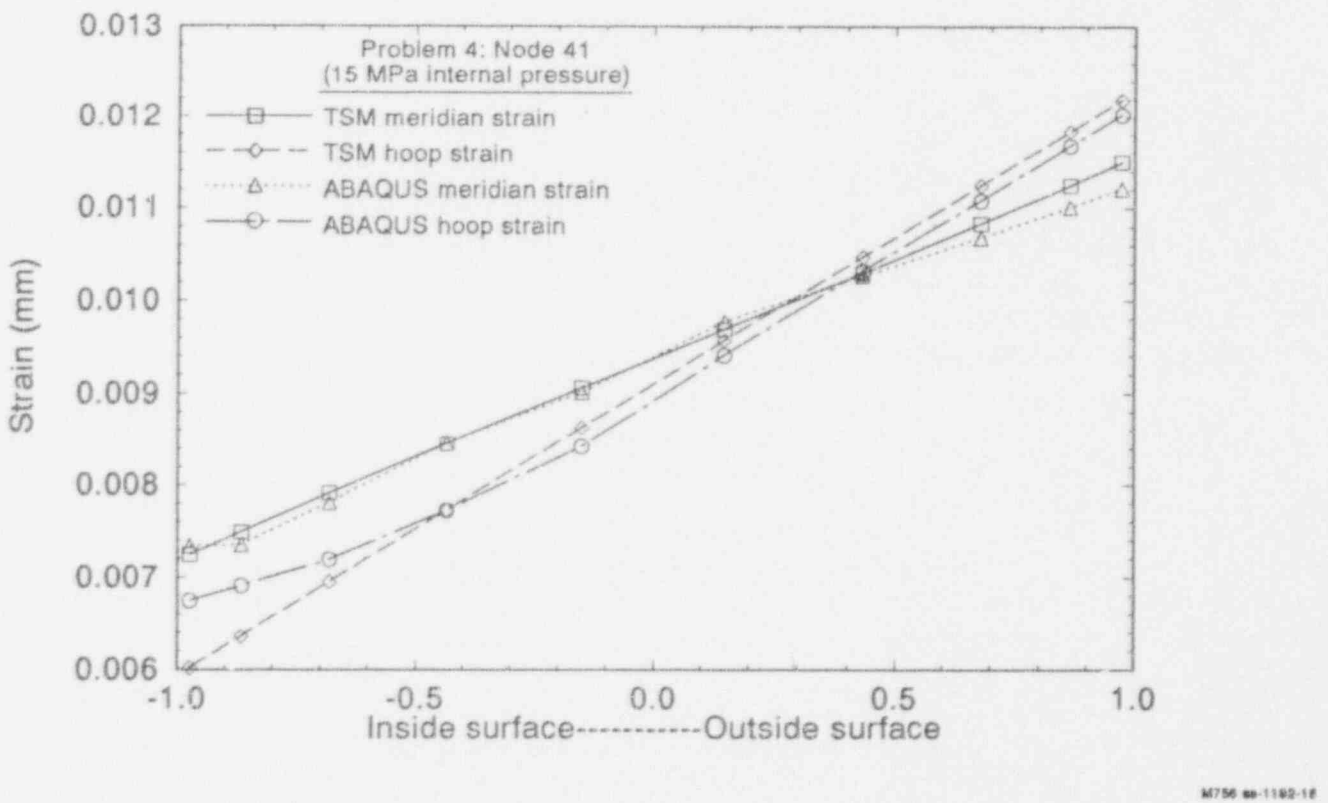

Figure E-21. Problem 4: Thermal loading with only 15 MPa internal pressure: Node 41 strains.

E-7. CONCLUSIONS

The verification of TSM has provided several insights into the applicability of this program for calculating lower head severe accident structural response. First of all, this program was developed to provide a fast-running solution to predict the collapse of a localized portion of the vessel wall resulting from hot spots in a debris bed resting on the lower head. Thus, the program would be appropriate for scoping parameter studies in various accident scenarios. Results of the benchmark problems used in this verification effort indicate that TSM performs well for its intended purpose.

The two benchmark problems that applied a localized hot spot (Problems 3 and 4) with an internal pressure of 45 to 55 MPa identified that TSM does not accurately predict the stresses in the hottest regions. This resulted from the TSM assumption that the radial component of stress was negligible. However, the hottest areas carry a very small percentage of the total pressure load. The assumption of negligible radial stresses was shown to be valid in the cooler regions under the hot spot, which is essentially the portion beyond the midplane and away from the hot spot. That portion of the wall carried the majority of the pressure load in these cases. Vessel wall material yielding eventually begins at the outer surface and propagates inward to final failure. Hoop and meridian stress levels are typically 35 times higher in the outer portions than the inner regions of the vessel wall. Thus, model accuracy in these areas is most crucial to accurate predictions of vessel failure margins.

Two additional load cases were evaluated that employed the thermal hot spot definitions from Problems 3 and 4 with a pressure of 15 MPa. This lower pressure was more representative of accident conditions on a reactor vessel. The evaluation of these two cases verified that the TSM assumption of negligible radial stresses was acceptable for the more representative accident conditions.

TSM total strain comparisons ranged from underpredictions of 24% on the inside surface to 11% on the outside surface in the hot spot region for the severe thermal gradient load case at elevated pressures. In the cooler boundary areas, strain comparisons ranged from underpredictions of 13% on the inner surface to 7% on the outer surface. Examinations of the plastic strains indicated that plasticity of the wall had propagated from the outside inward one Gauss point further in the ABAQUS model than in TSM model for the two hot spot load cases. The magnitude of plastic strains for Benchmark Problems 3 and 4 were 3 to 5 times lower than the total strain values. Use of TSM for predicting vessel response is considered acceptable for pressure levels at or below 15 MPa.

E-8. REFERENCES

E-1. ABAQUS, Version 4-8-5, Providence, Rhode Island: Hibbit, Karlsson, and Sorenson, Inc. 1990.

E-2. R. H. Bogaard et al., *Thermophysical Properties of Selected Manganese and Nickel Steels and High Nickel Iron*, CINDAS Special Report (Part VI), Center for Information and Numerical Data Analysis and Synthesis, Purdue University, January 1978.

Appendix F

Modeling Input

Appendix F

Modeling Input

F-1. MATERIAL PROPERTY DATA

Calculations performed for the lower head failure analysis used the materials property data summarized in this appendix. This appendix contains sections for properties of the following materials: UO_2, zircaloy, ZrO_2, Inconel-600, stainless steel (304SS), silver-indium-cadmium, boron carbide (B_4C), and carbon steel. Thermal properties for these materials include conductivity, density, enthalpy, specific heat, and viscosity. Solidus and liquidus temperatures for the materials are provided in Table F-1.1. Mechanical properties include ultimate strength, coefficient of thermal expansion, Young's modulus, and thermal expansion strain.

These data were extracted primarily from Reference F-1, although information from the other references and new data from the high-temperature testing described in Appendix B supplemented the database.

Table F-1.1. Solidus and liquidus temperatures[F-1,F-2,F-3]

Material	$T_{solidus}$ (K)	$T_{liquidus}$ (K)
UO_2	3113	3113
UO_2 Compounds:		
20% UO_2 - 80% SS[a]	2400	2400
80% UO_2 - 20% ZrO_2	2860	2860
Zircaloy	2175	2200
ZrO_2[b]	2960	2960
Inconel-600	1644	1700
304SS	1671	1727
Ag-In-Cd	1073	1123
B_4C	2743	2743
Carbon Steel	1789	1789

a. Although these materials are immiscible, this composition was used to represent materials containing melt with high melting temperatures.

b. For oxygen-to-metal ratio of 2.0.

F-1.1 UO_2 and UO_2 Compounds Data

This section contains data for properties of UO_2 and selected UO_2 compounds. Properties, such as thermal conductivity, theoretical density, enthalpy, specific heat capacity, and viscosity are summarized in Figures F-1.1-1 through F-1.1-13.

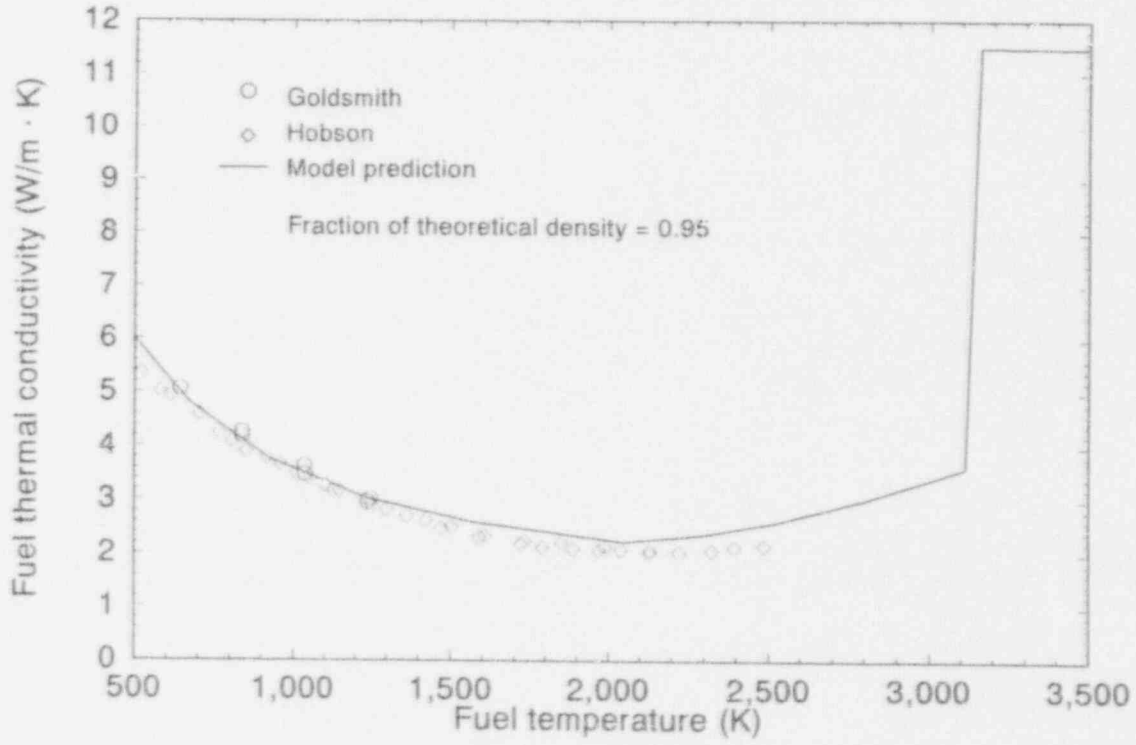

M619 jk-0692-07

Figure F-1.1-1. Model prediction for thermal conductivity of 0.95 TD UO_2 compared with data from specimens with densities in the range of 0.945 to 0.955 TD.[F-1]

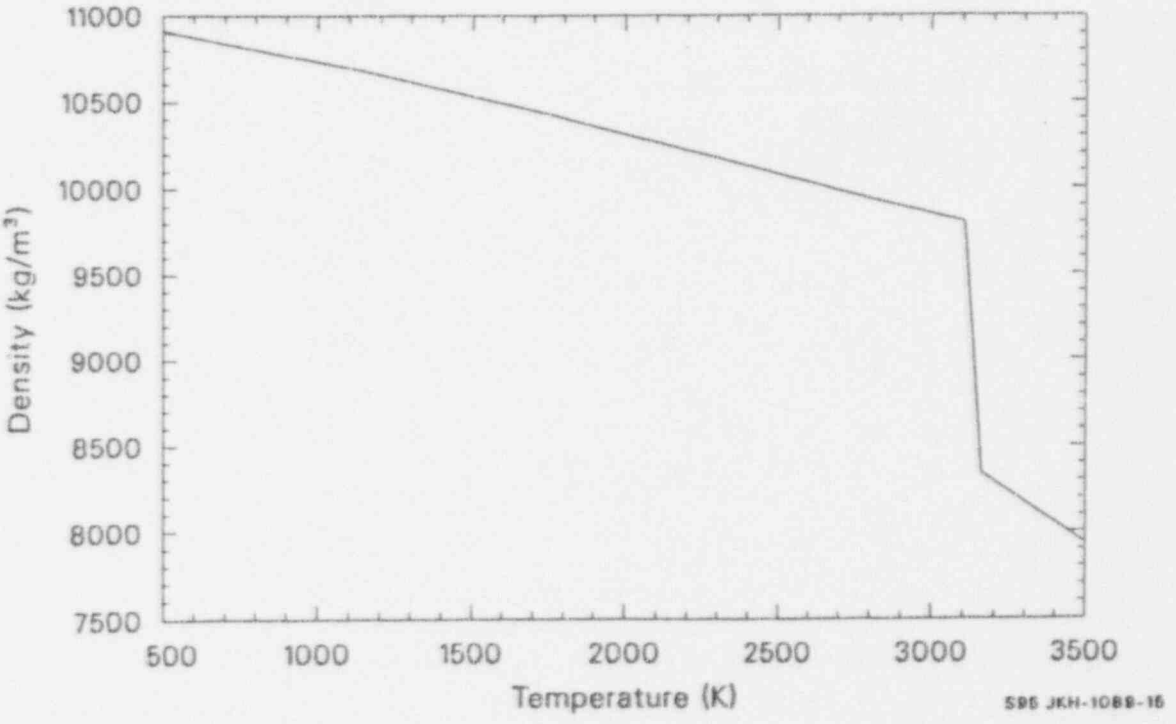

Figure F-1.1-2. Theoretical density of UO_2.[F-1]

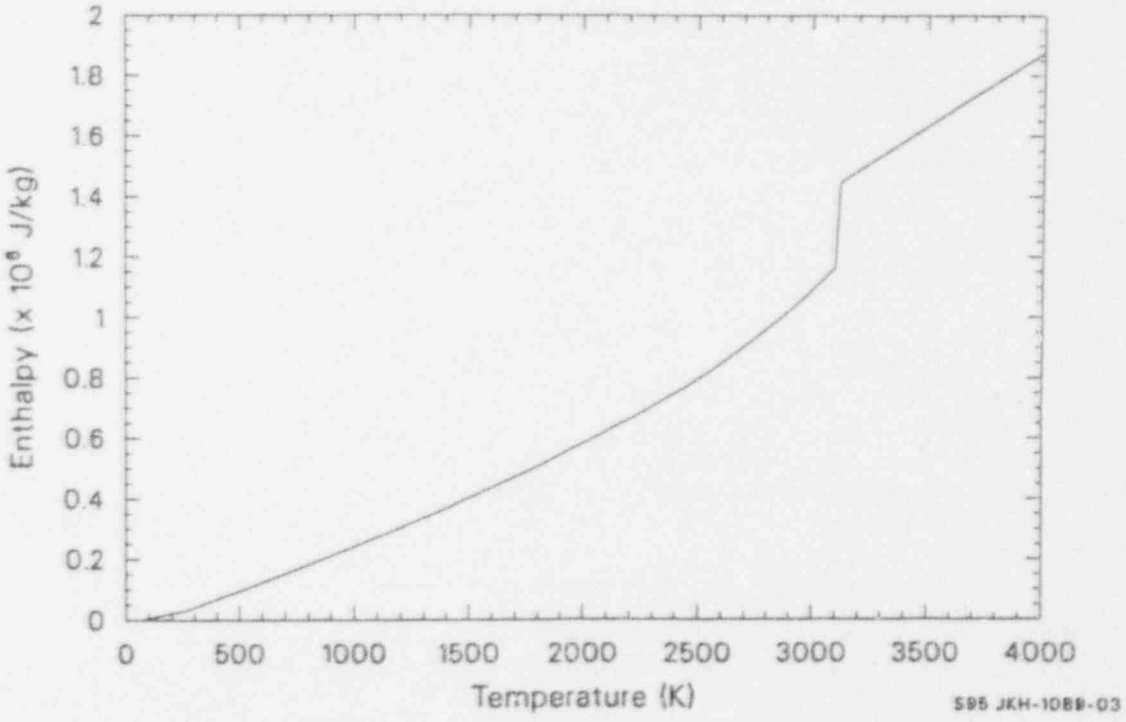

Figure F-1.1-3. Enthalpy of UO_2 as a function of temperature to 4000 K.[F-1]

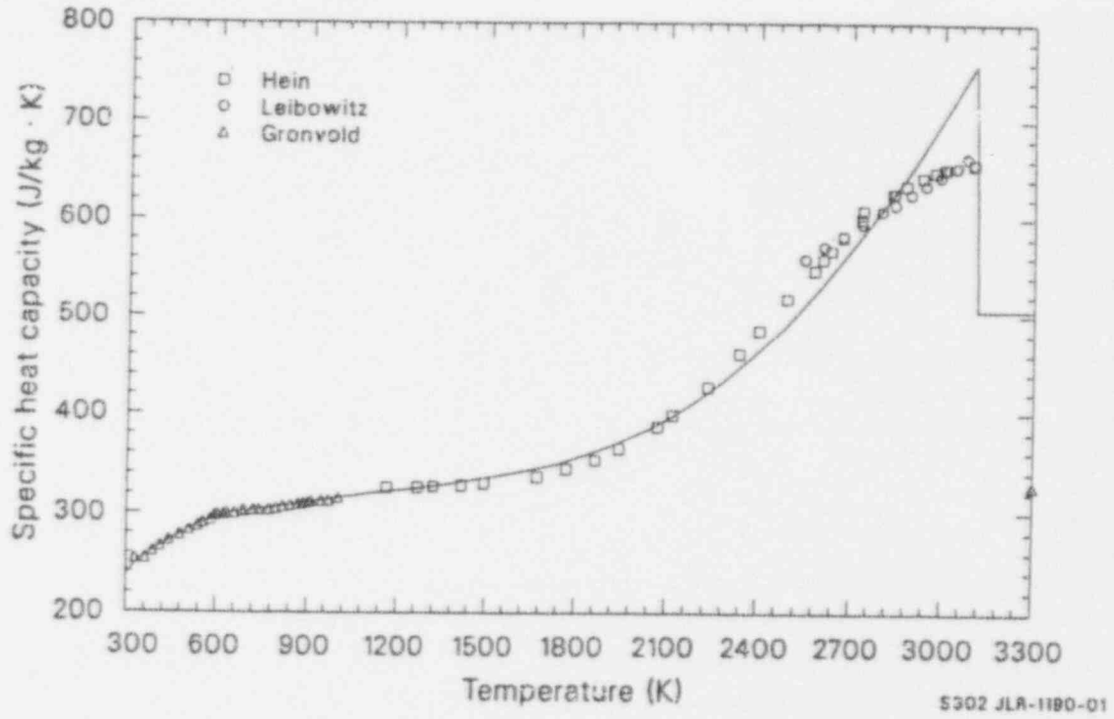

Figure F-1.1-4. Specific heat capacity of UO_2 from three experimenters compared with the specific heat capacity correlation (solid line) for UO_2.[F-1]

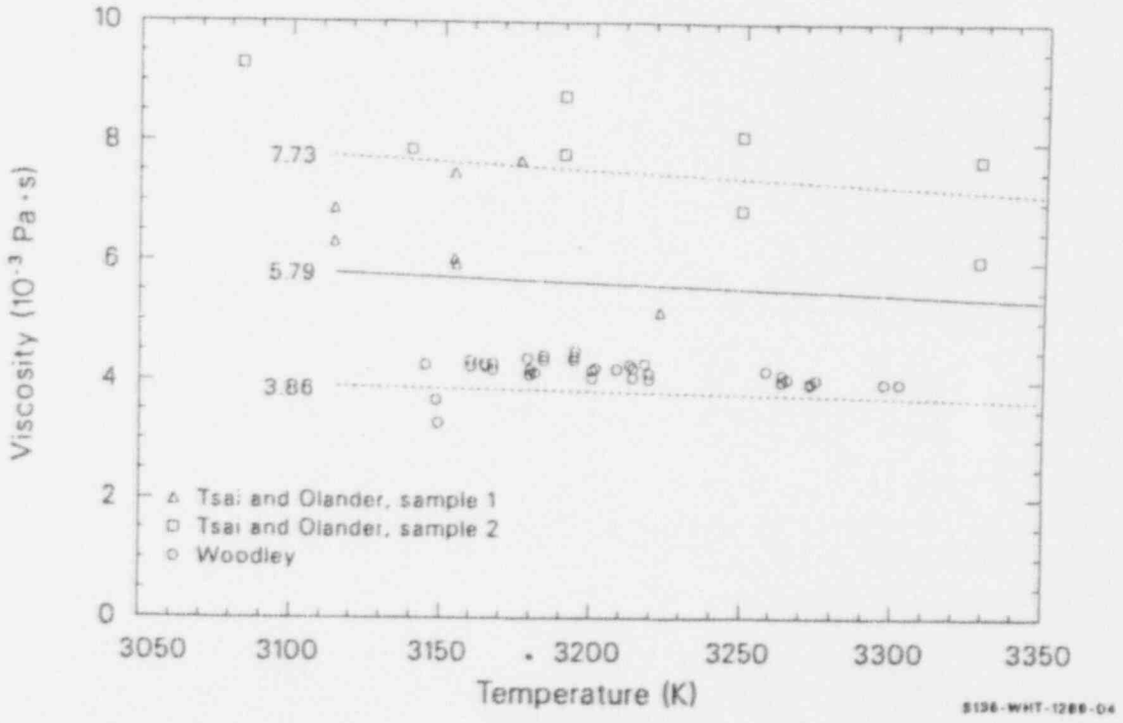

Figure F-1.1-5. Calculated UO_2 viscosity (solid line) with upper and lower uncertainty estimates (dashed lines) compared with data.[F-1]

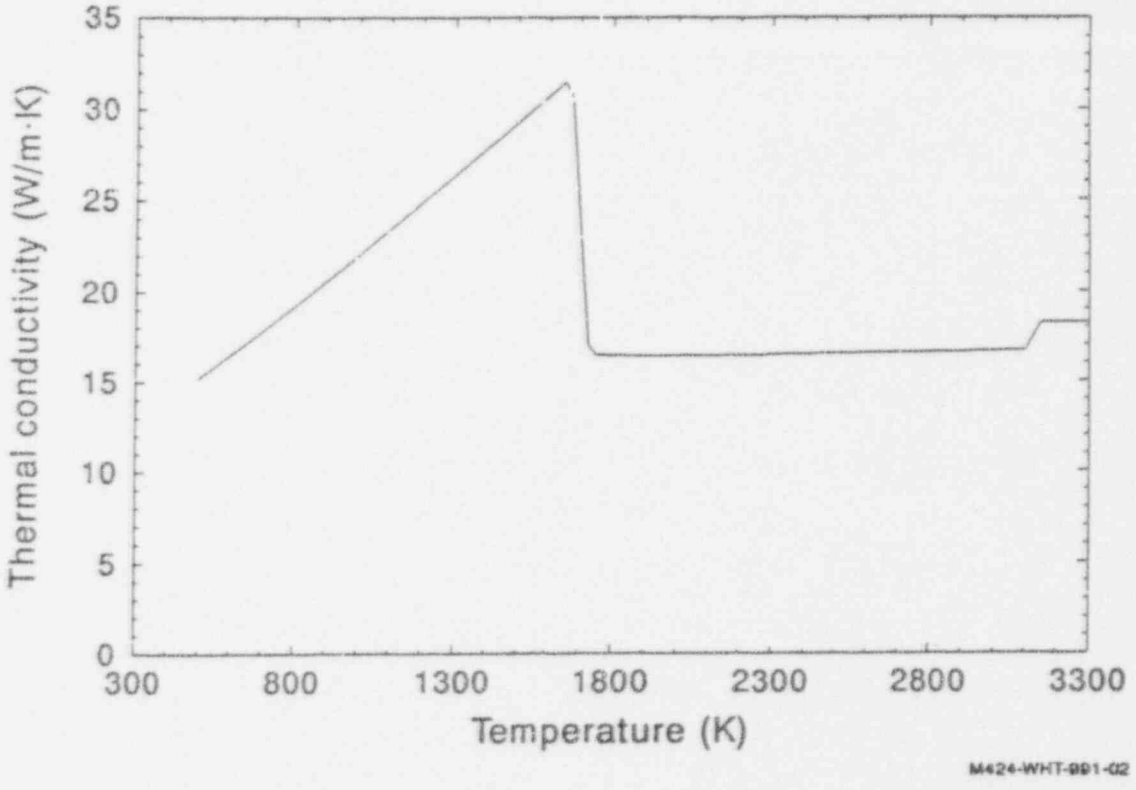

Figure F-1.1-6. Thermal conductivity for 20% UO_2 - 80% stainless steel weight fraction compound.[F-1]

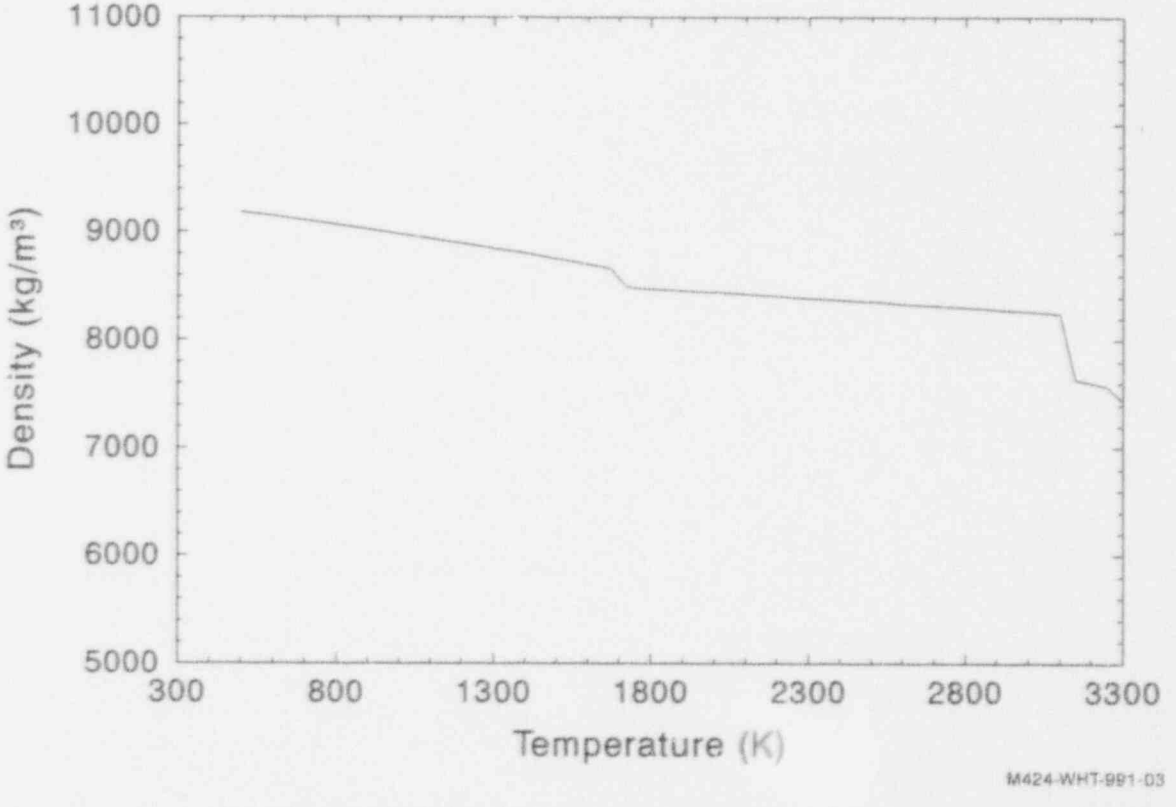

Figure F-1.1-7. Density of 20% UO_2 - 80% stainless steel weight fraction compound.[F-1]

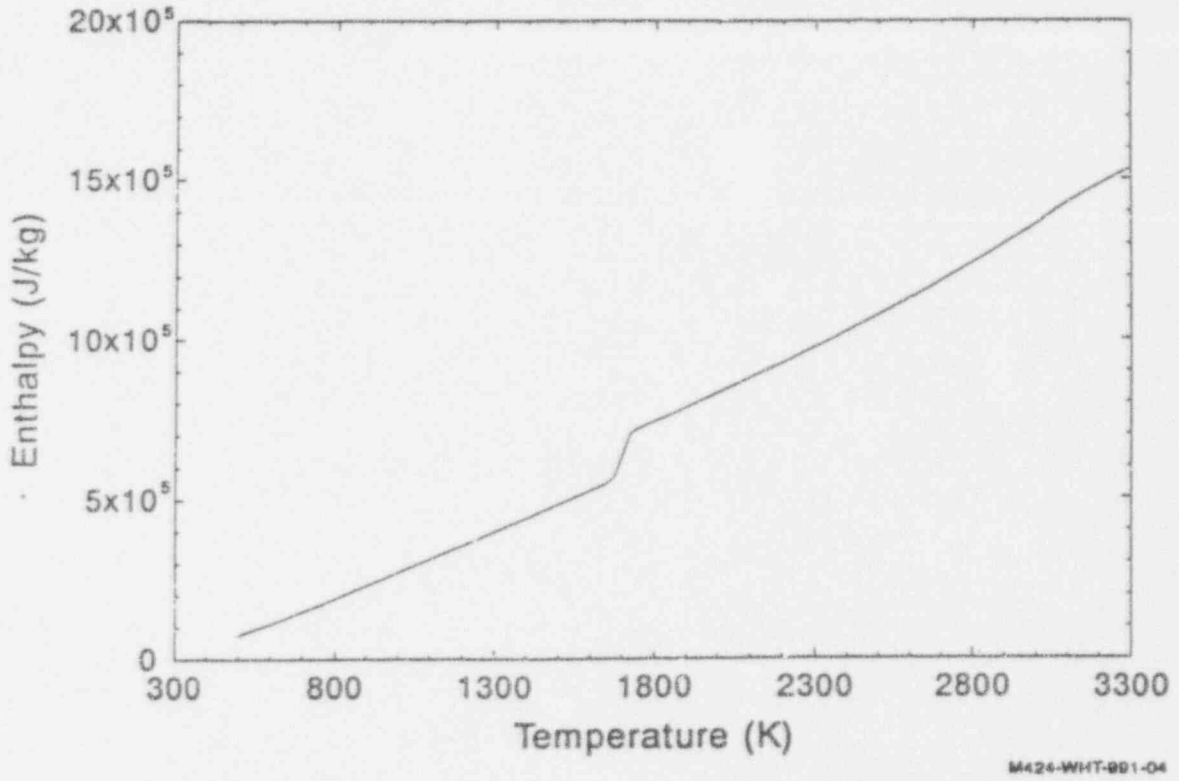

Figure F-1.1-8. Enthalpy of 20% UO_2 - 80% stainless steel weight fraction compound.[F-1]

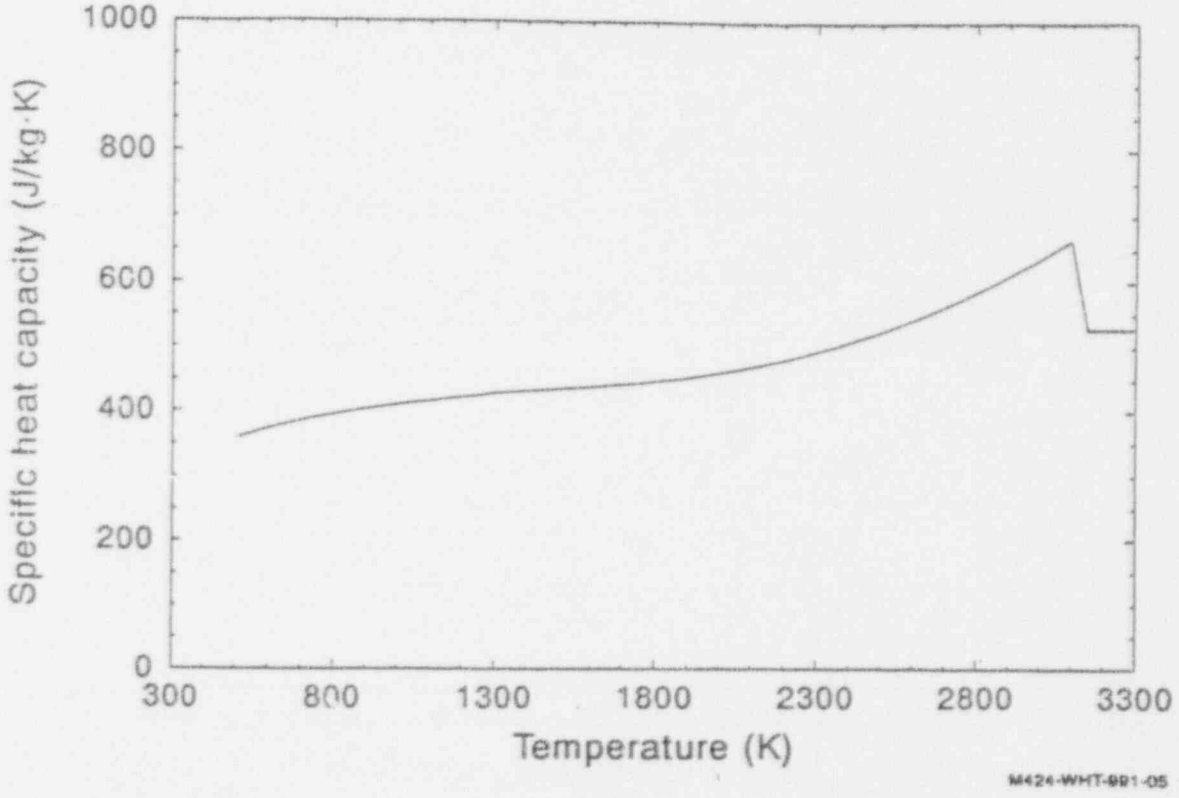

Figure F-1.1-9. Specific heat capacity for 20% UO_2 - 80% stainless steel weight fraction compound.[F-1]

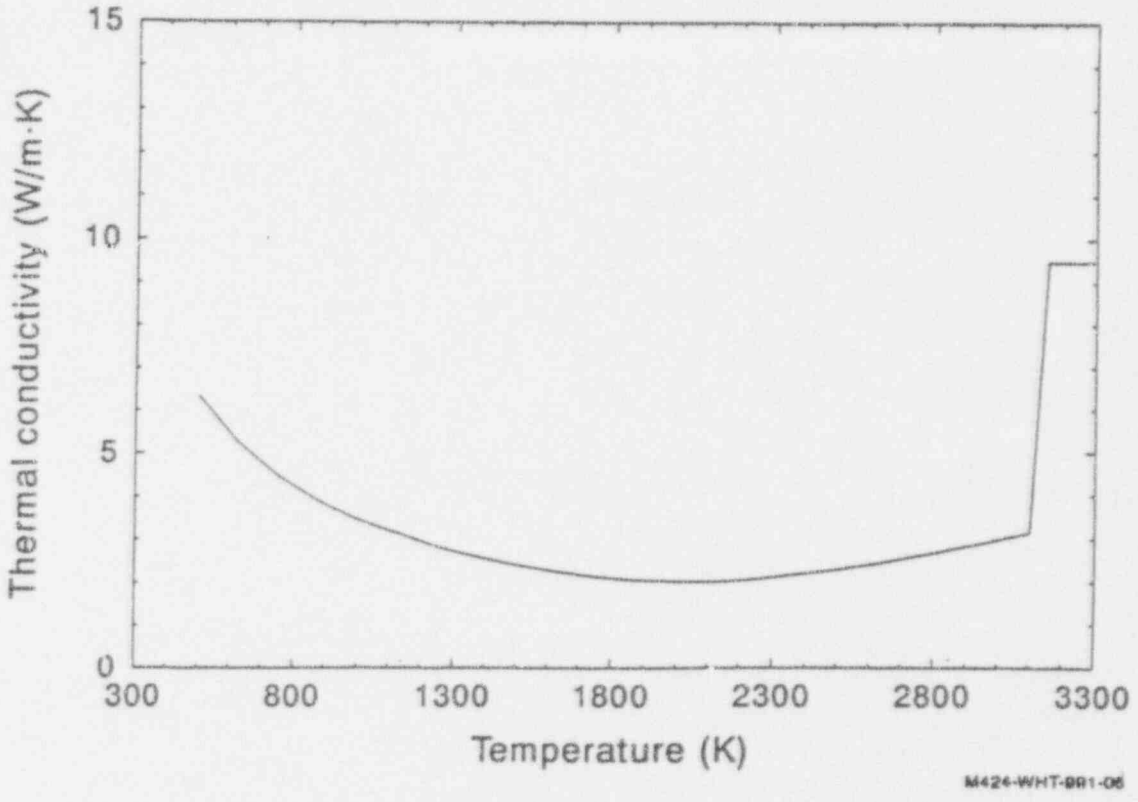

Figure F-1.1-10. Thermal conductivity for 80% UO_2 - 20% ZrO_2 weight fraction compound.[F-1]

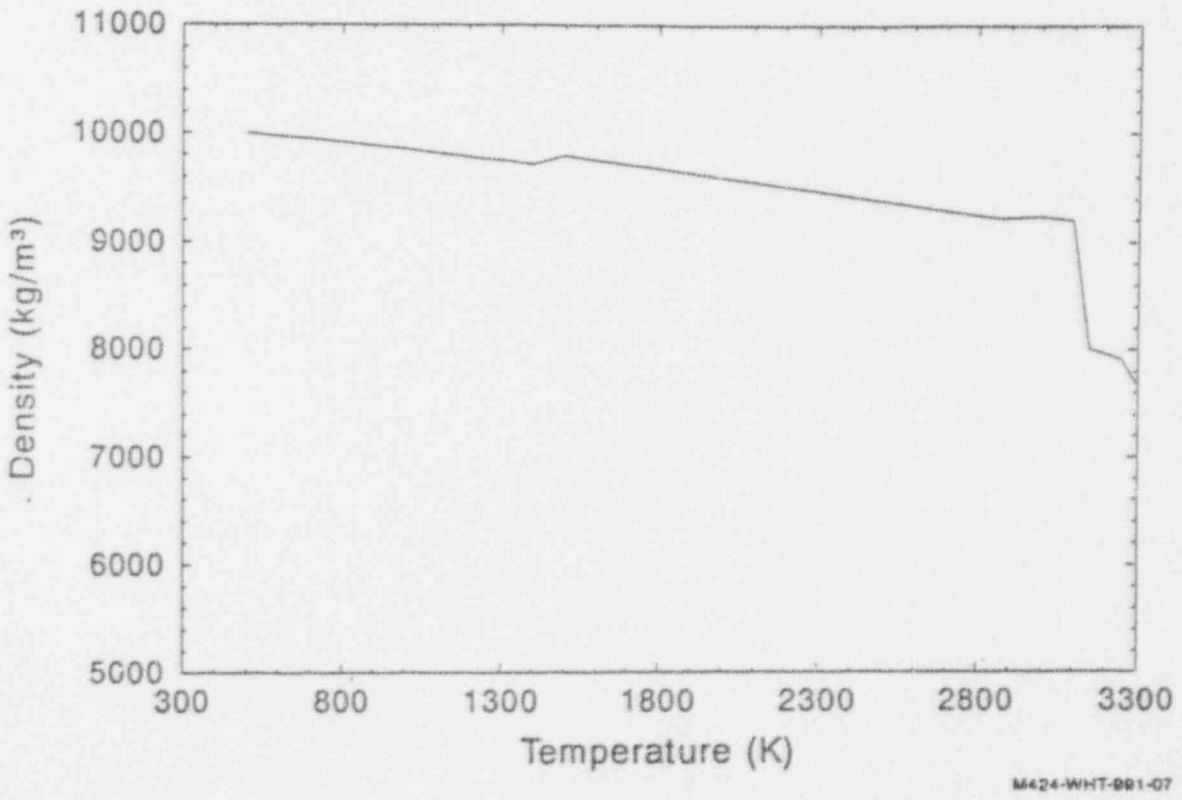

Figure F-1.1-11. Density of 80% UO_2 - 20% ZrO_2 weight fraction compound.[F-1]

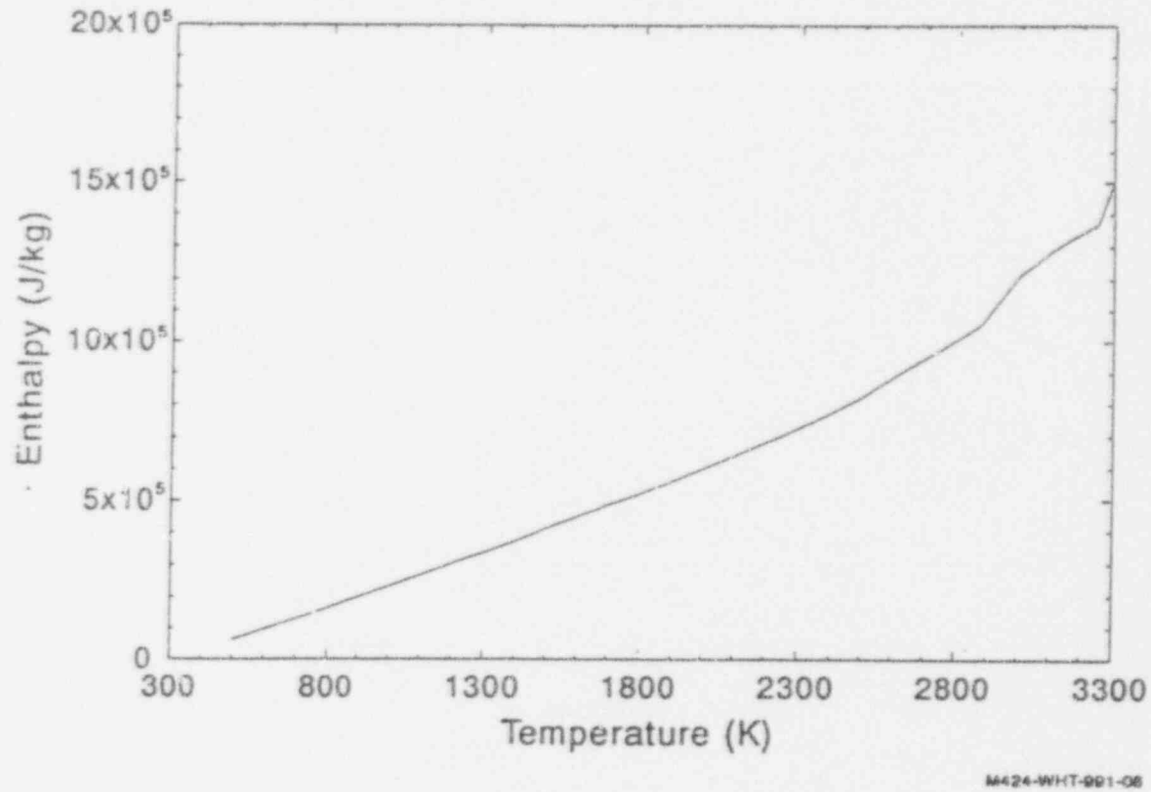

Figure F-1.1-12. Enthalpy of 80% UO_2 - 20% ZrO_2 weight fraction compound.[F-1]

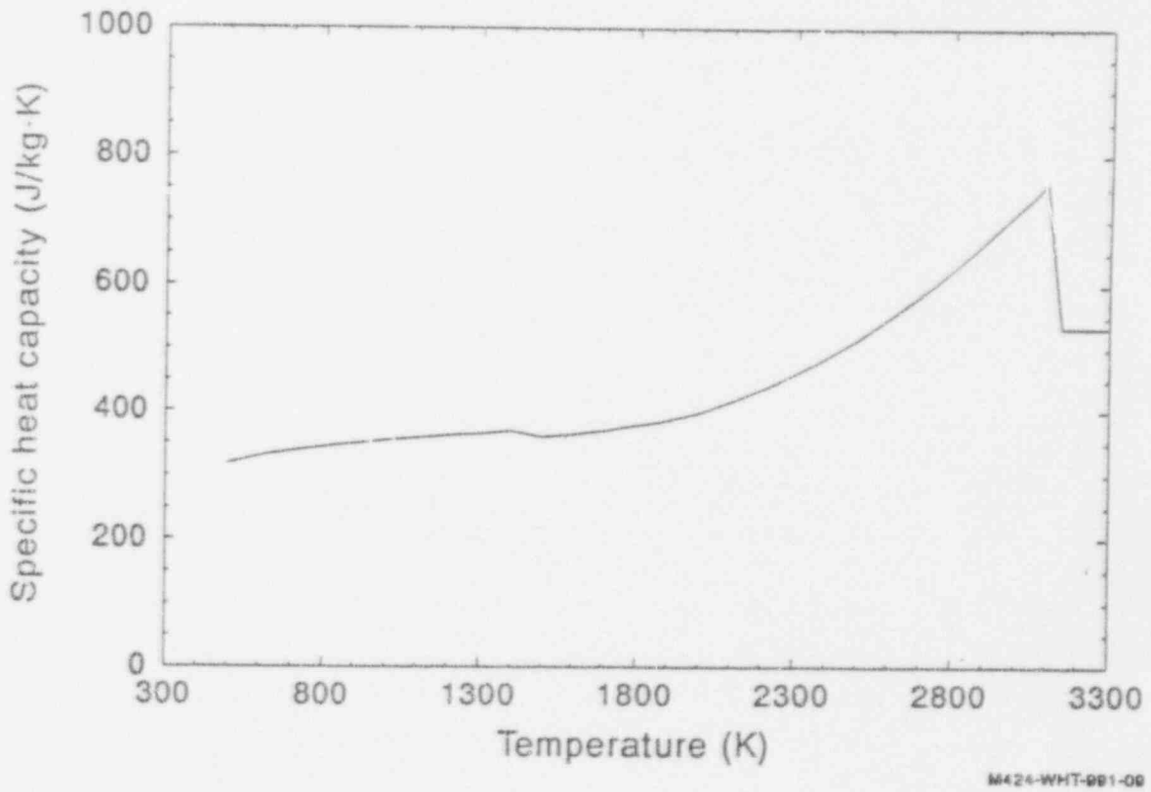

Figure F-1.1-13. Specific heat capacity for 80% UO_2 - 20% ZrO_2 weight fraction compound.[F-1]

F-1.2 Zircaloy and ZrO_2 Data

This section contains data for properties of zircaloy and zircaloy dioxide including thermal conductivity, theoretical density, enthalpy, and specific heat capacity, as summarized in Figures F.1.2-1 through F.1.2-8.

The viscosity of zircaloy at its liquidus temperature is 1.5×10^{-2} Pa-s.[F-4]

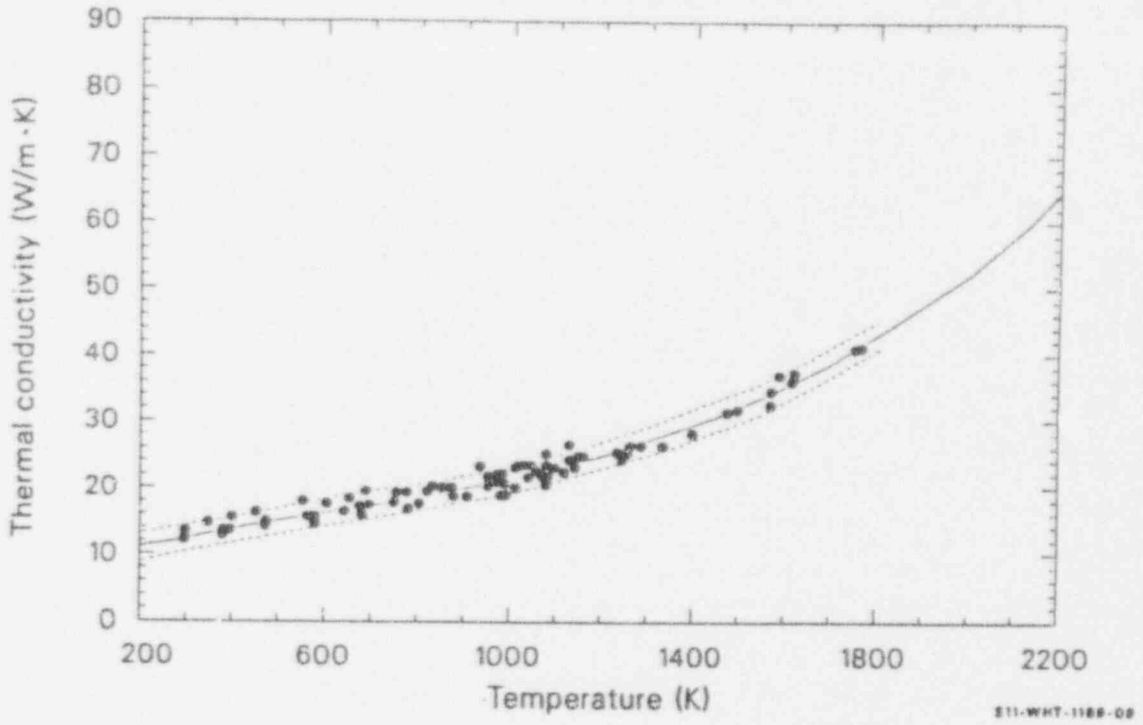

Figure F-1.2-1. Thermal conductivity data, least-squares fit, and the two standard deviation limits.[F-1]

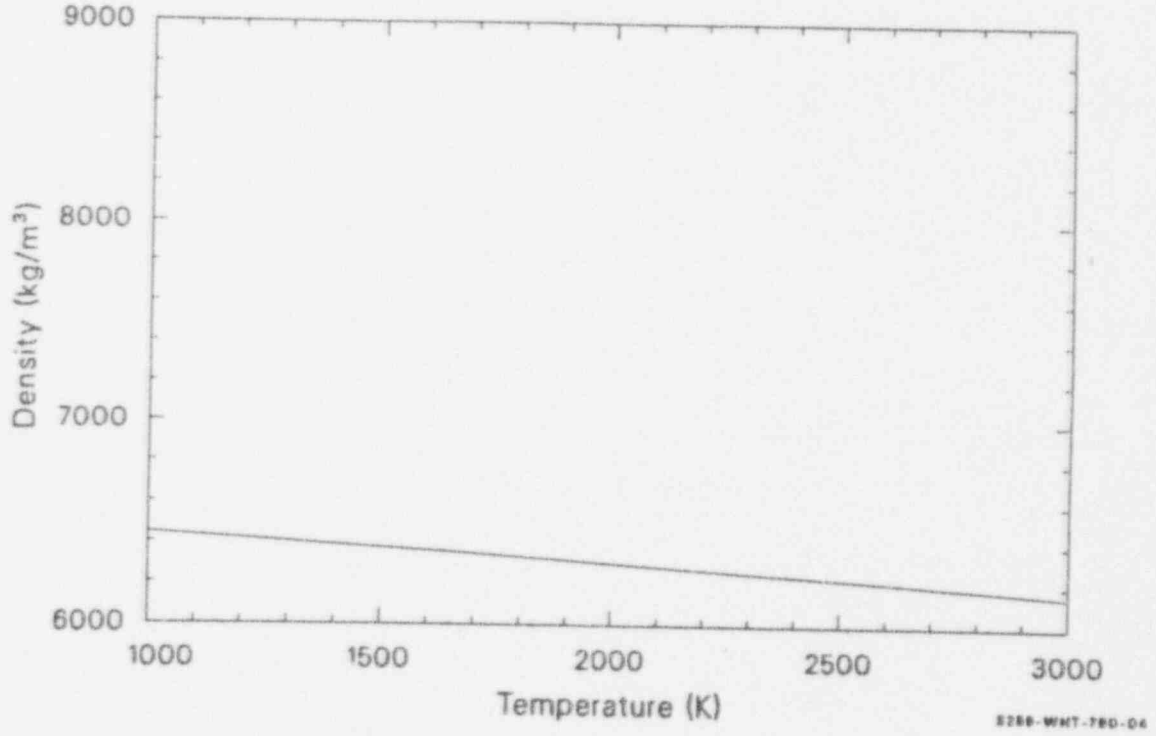

Figure F-1.2-2. Zircaloy density as a function of temperature.[F-1]

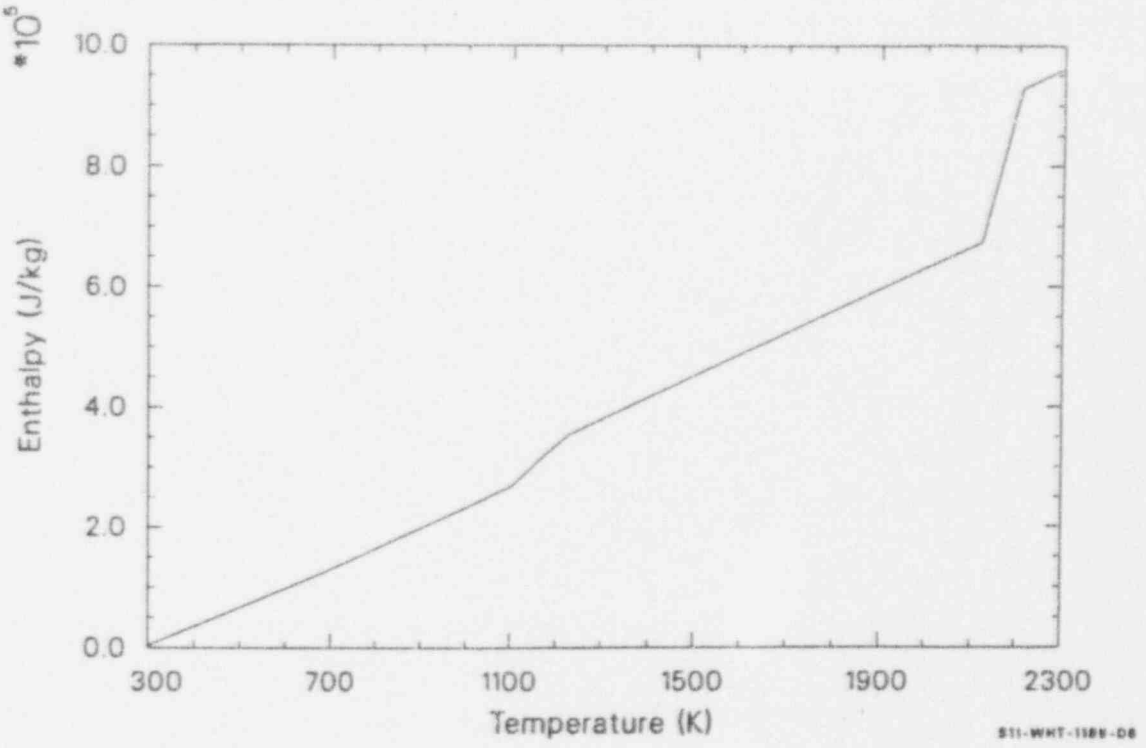

Figure F-1.2-3. Zircaloy enthalpy as a function of temperature.[F-1]

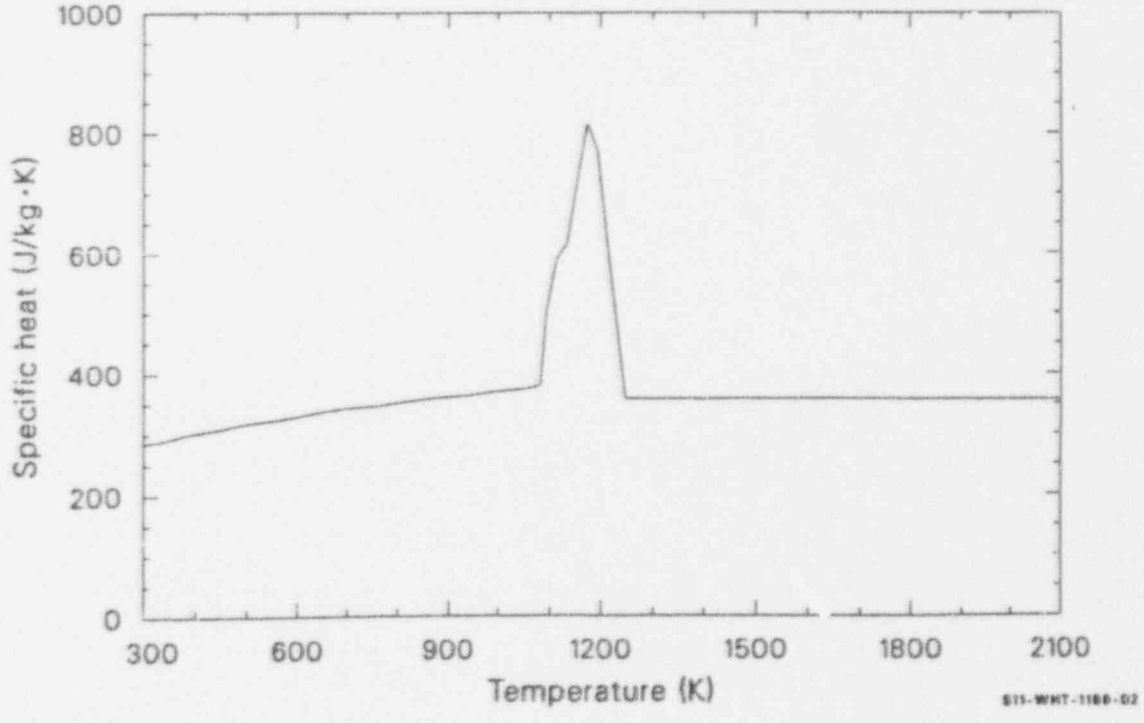

Figure F-1.2-4. Specific heat of zircaloy.[F-1]

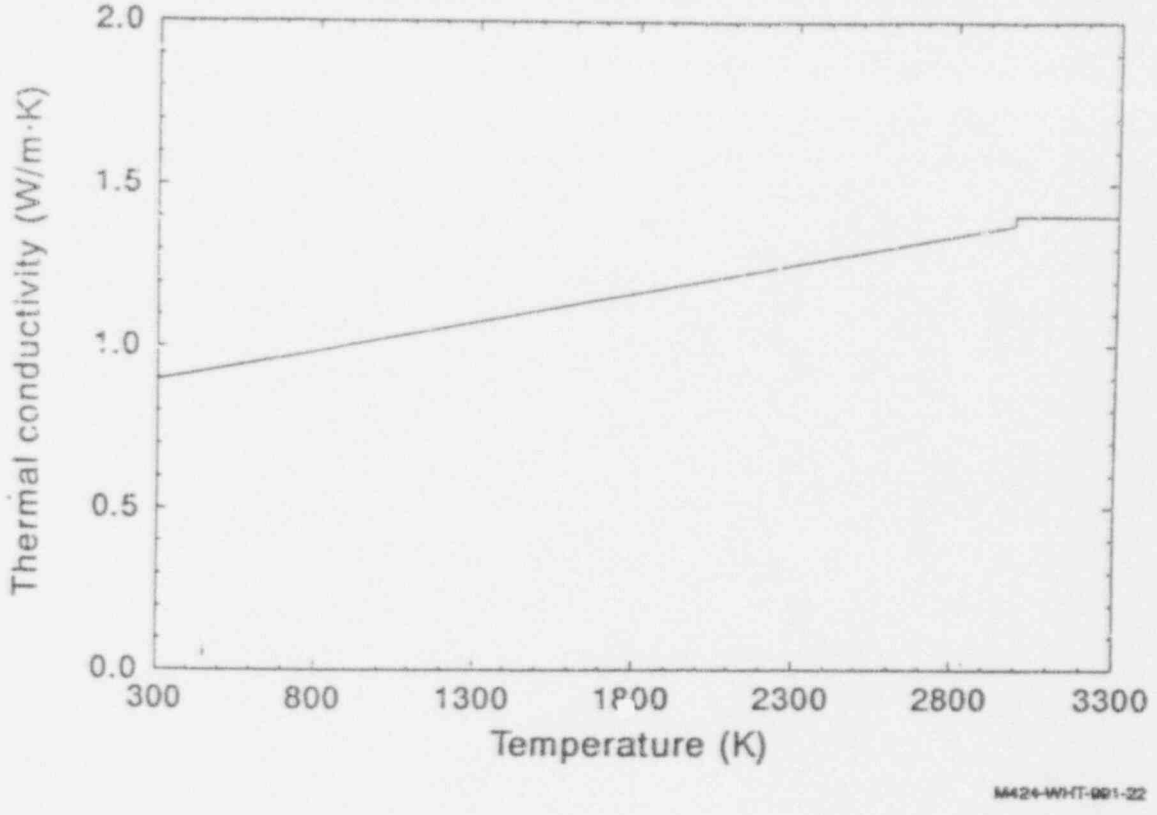

Figure F-1.2-5. Zircaloy oxide thermal conductivity as a function of temperature.[F-1]

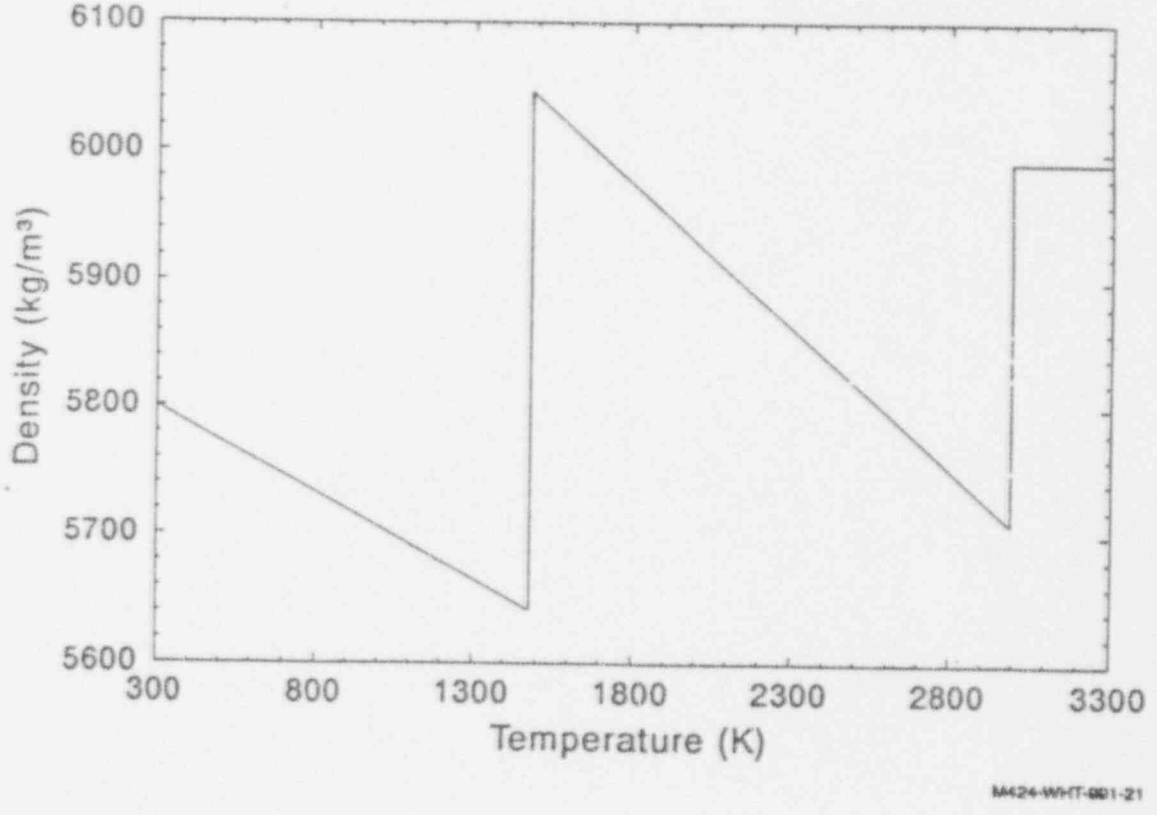

Figure F-1.2-6. Zircaloy oxide density as a function of temperature.[F-1]

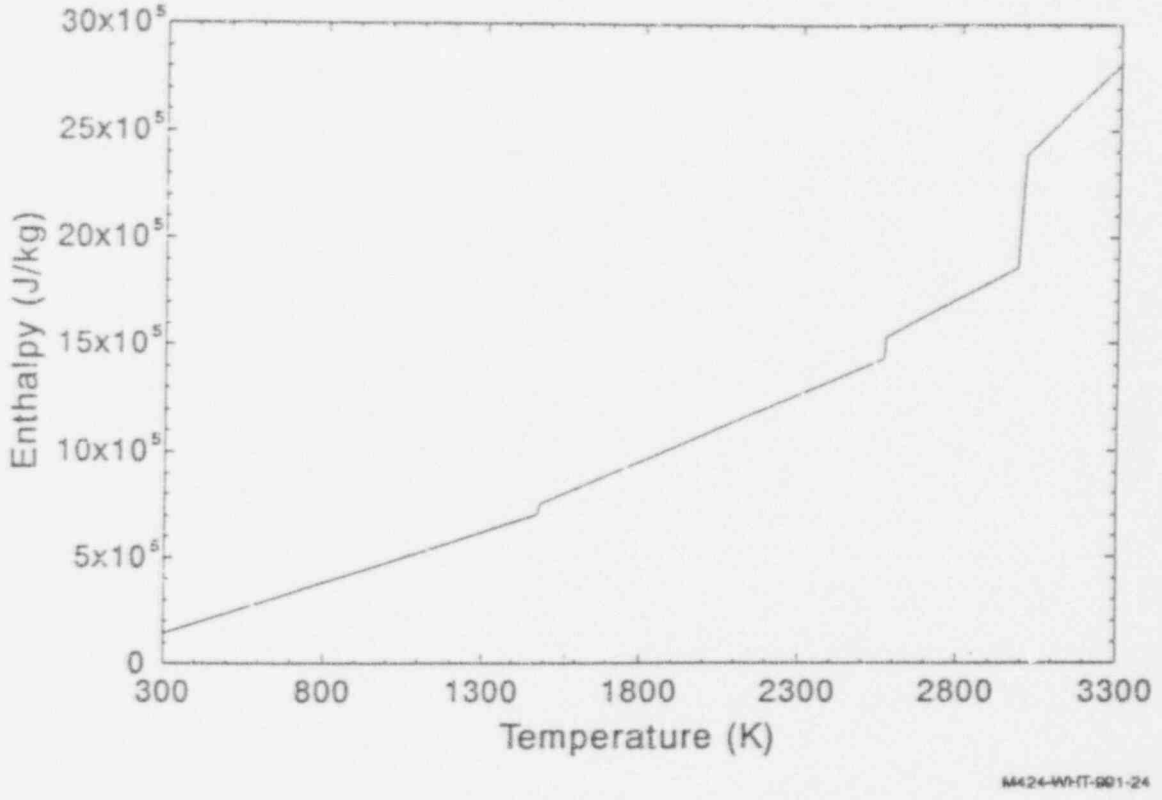

Figure F-1.2-7. Zircaloy oxide enthalpy as a function of temperature.[F-1]

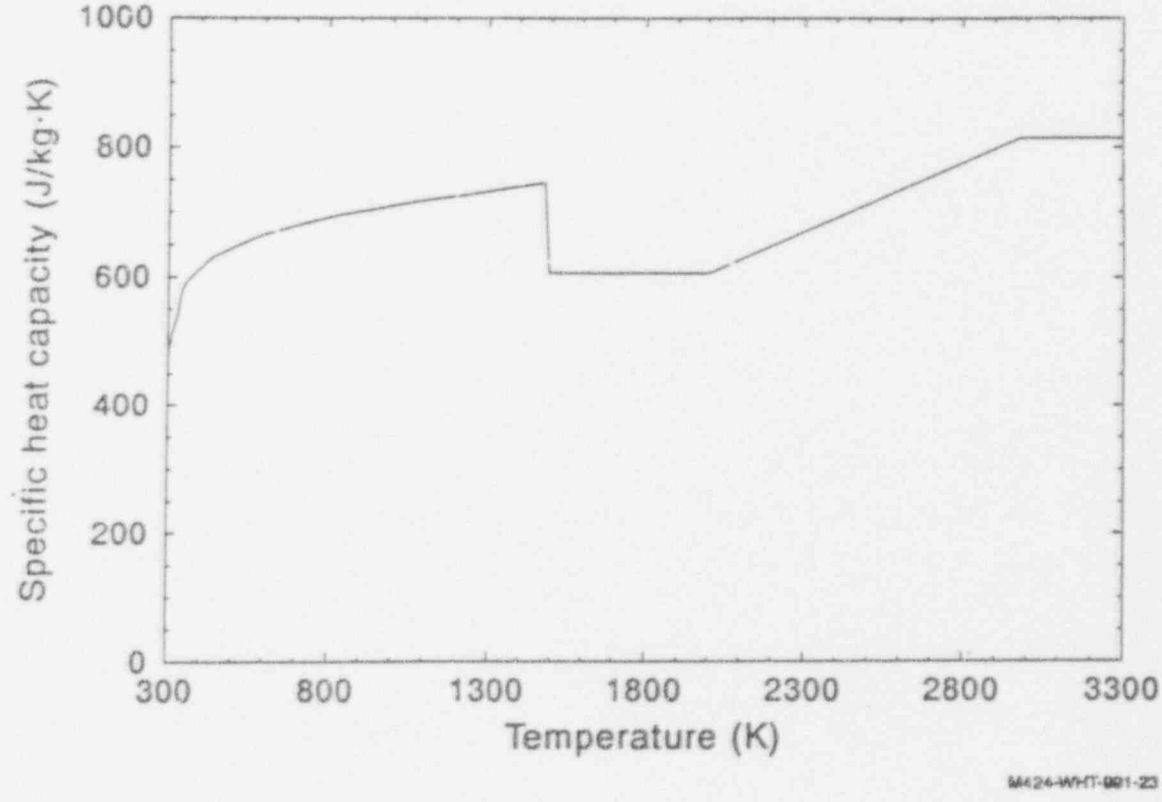

Figure F-1.2-8. Zircaloy oxide specific heat capacity as a function of temperature.[F-1]

F-1.3 Inconel-600 Data

This section contains data for properties of Inconel. Included for Inconel-600 are thermal conductivity, density, specific heat capacity, ultimate strength, thermal expansion coefficient, Young's modulus of elasticity, and emissivity. These data are summarized in Figures F-1.3-1 through F-1.3-7.

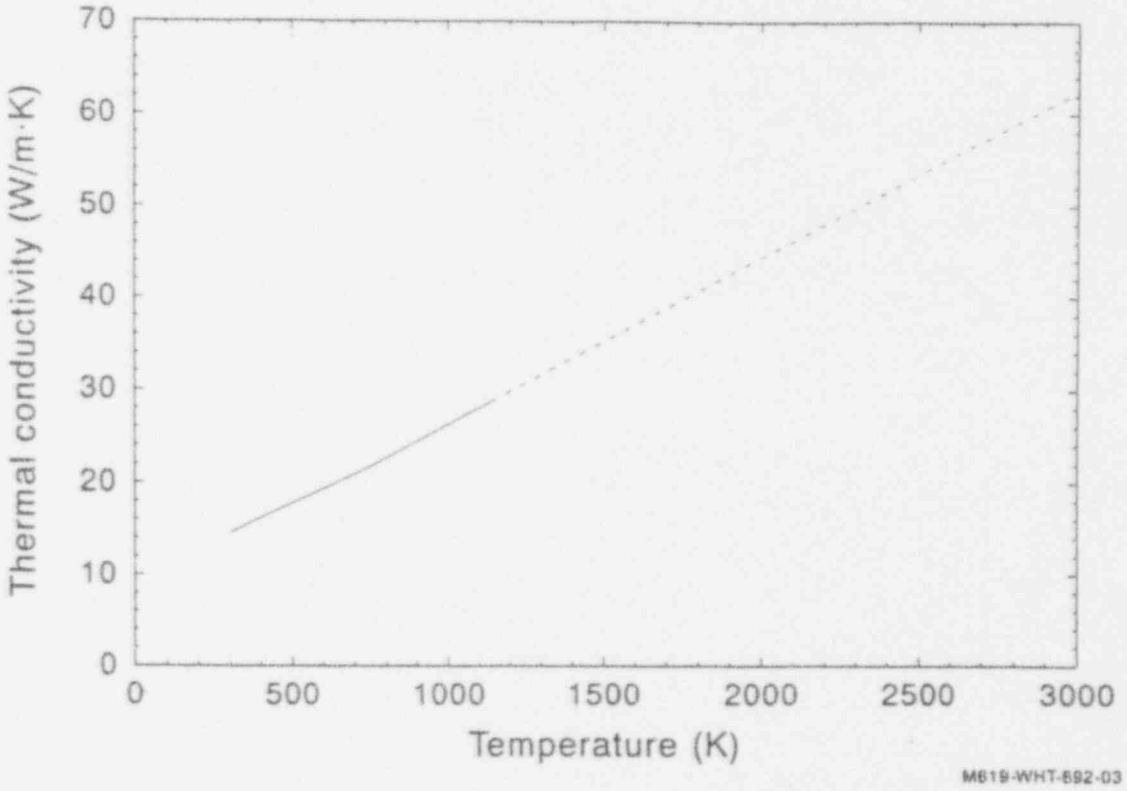

Figure F-1.3-1. Inconel-600 thermal conductivity as a function of temperature.[F-5]

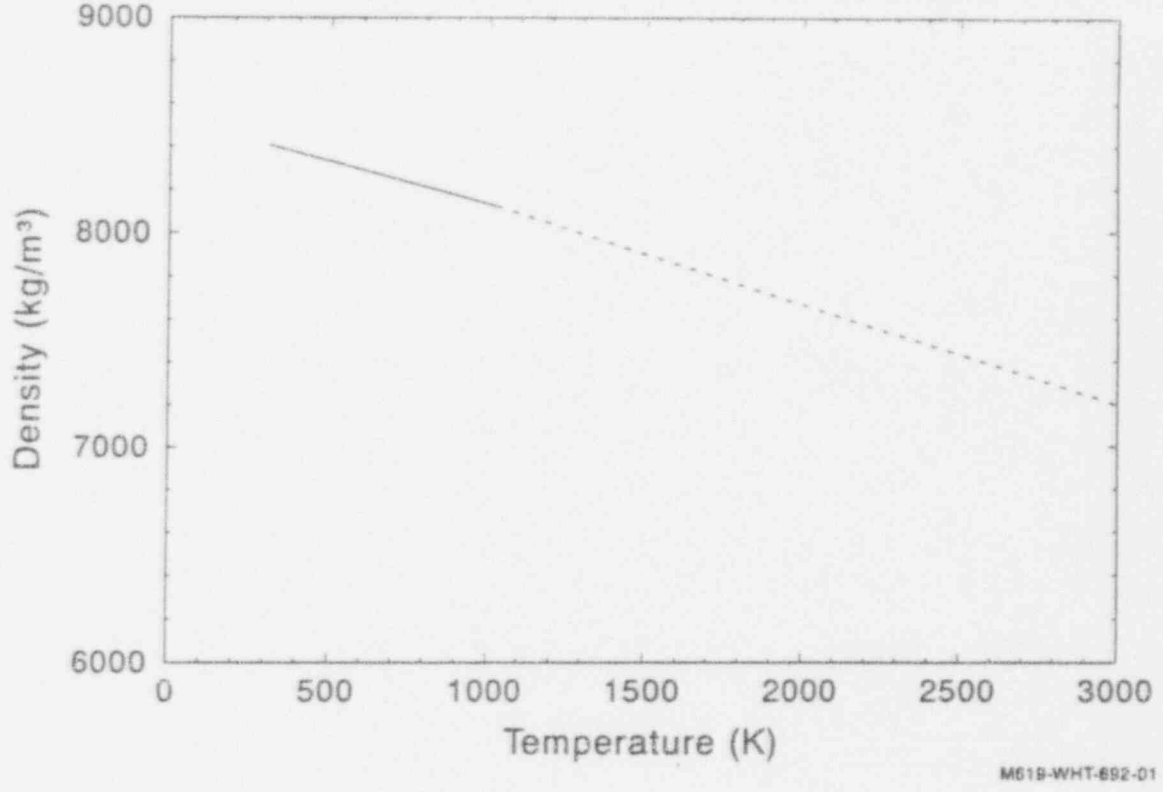

Figure F-1.3-2. Inconel-600 density as a function of temperature.[F-2]

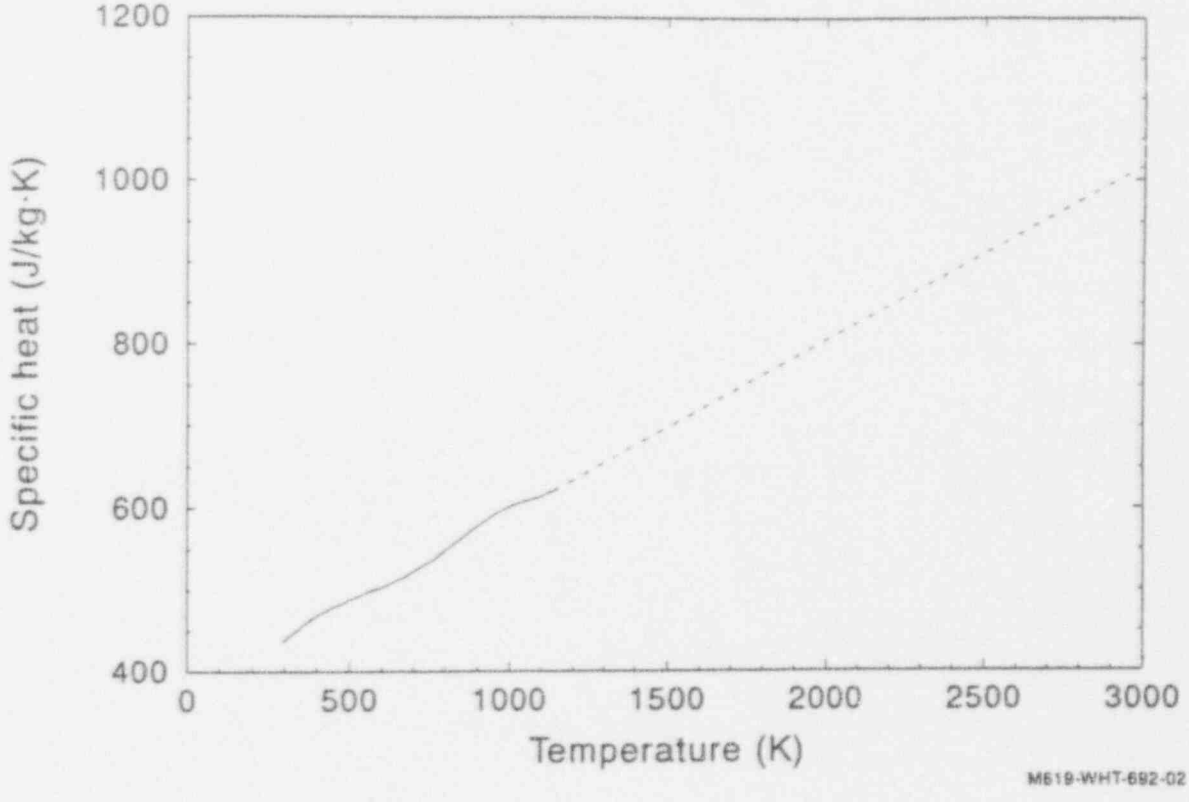

Figure F-1.3-3. Inconel-600 specific heat as a function of temperature.[F-5]

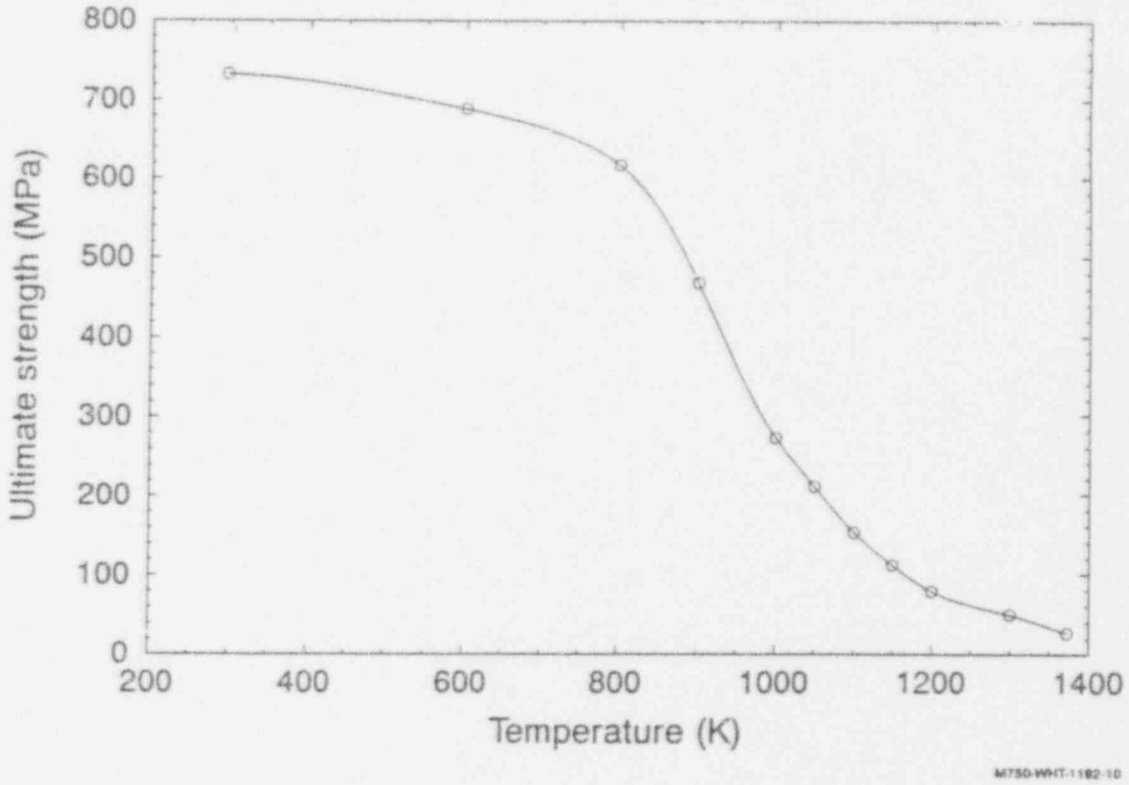

Figure F-1.3-4. Inconel-600 ultimate strength (see Appendix B).

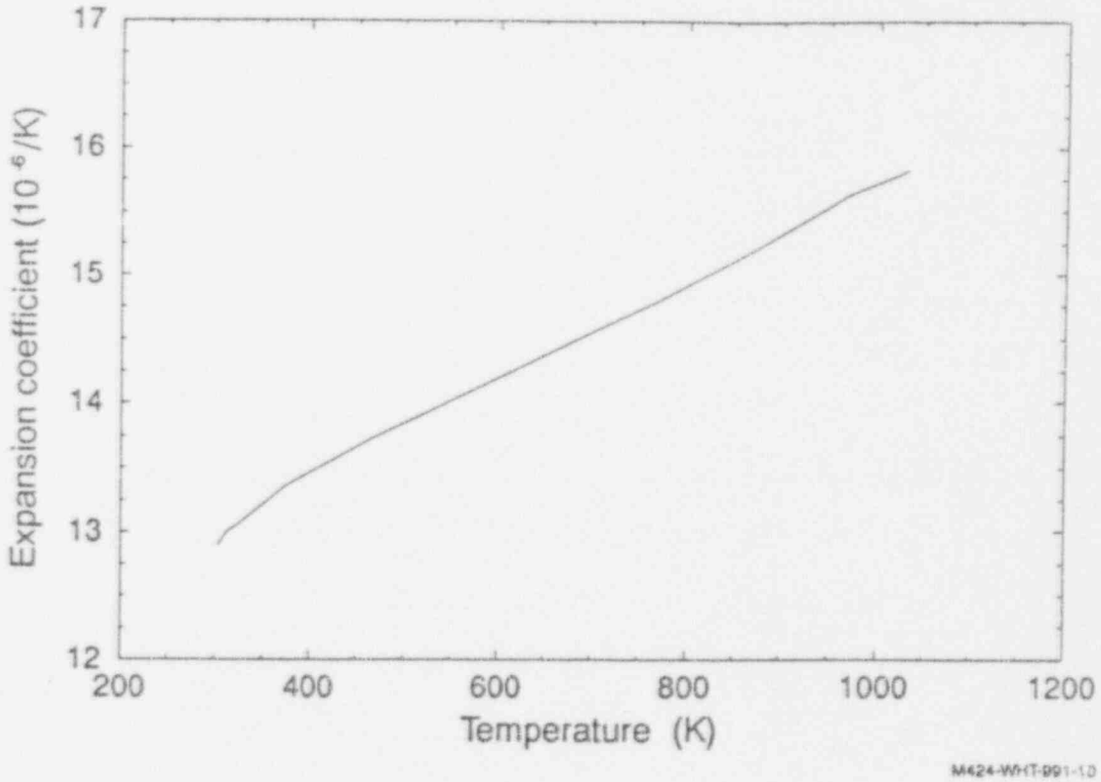

Figure F-1.3-5. Inconel-600 thermal expansion coefficient.[F-5]

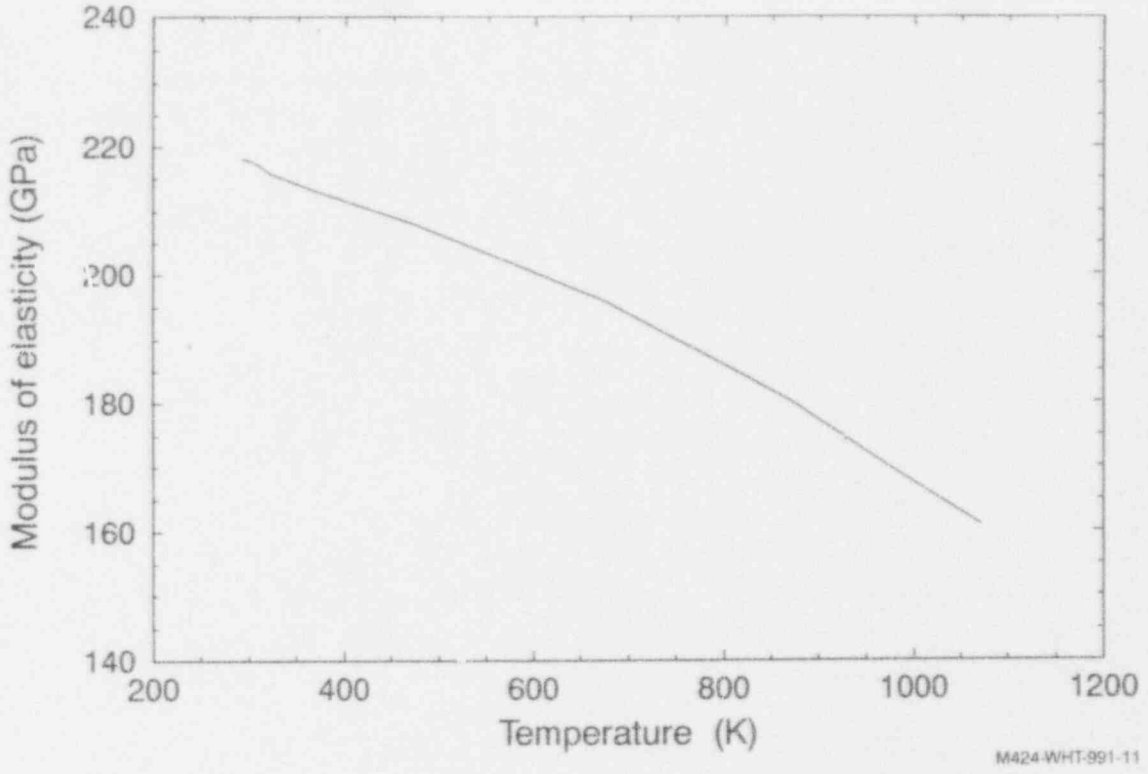

Figure F-1.3-6. Inconel-600 Young's modulus of elasticity.[F-5]

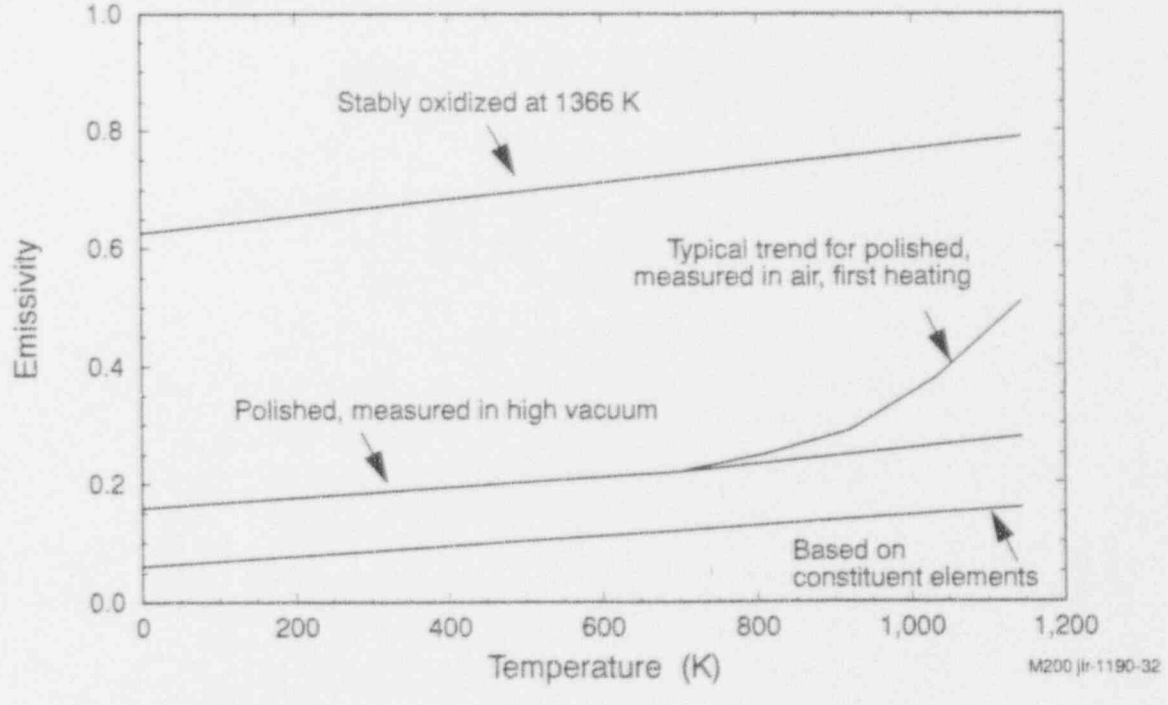

Figure F-1.3-7. Inconel-600 thermal emissivity.[F-6,F-7]

F-1.4 Stainless Steel Data

This section contains data for the following properties of stainless steel: thermal conductivity, density, enthalpy, specific heat capacity, ultimate strength, thermal expansion coefficient, and Young's Modulus. These data are summarized in Figures F-1.4-1 through F-1.4-7.

The viscosity of stainless steel at its liquidus temperature has been approximated using the viscosity of iron at its liquidus temperature, which is 2.2×10^{-3} Pa-s.[F-4]

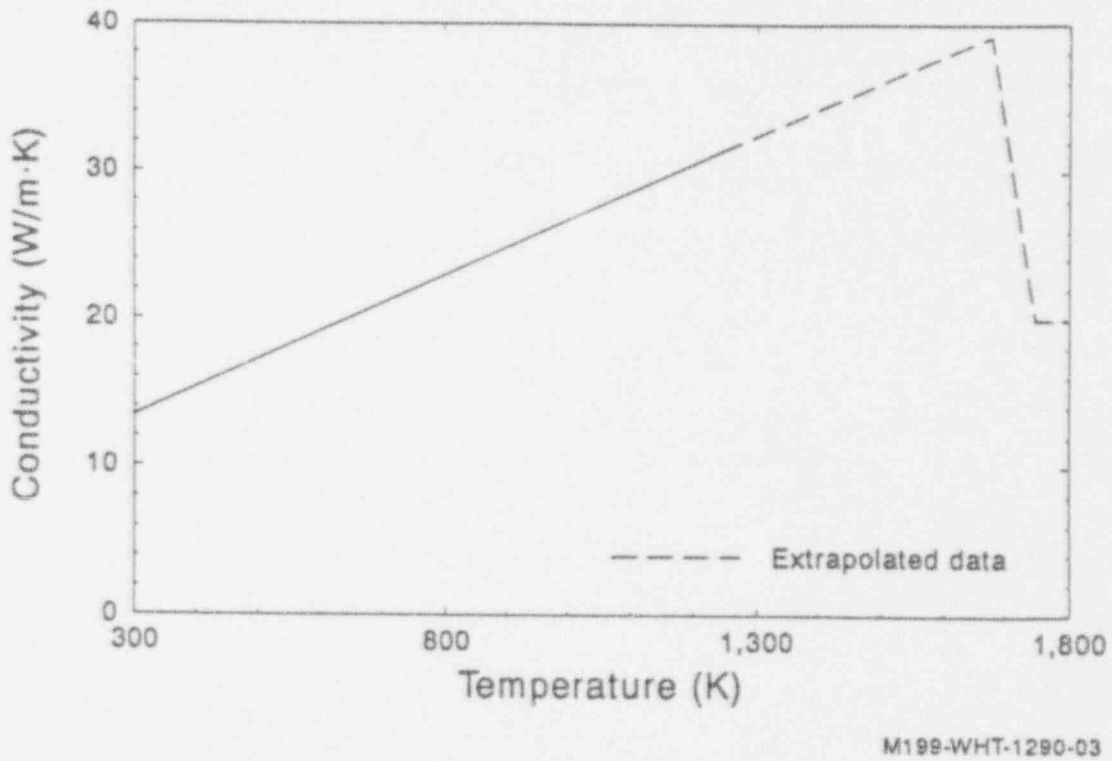

Figure F-1.4-1. Stainless steel thermal conductivity.[F-1]

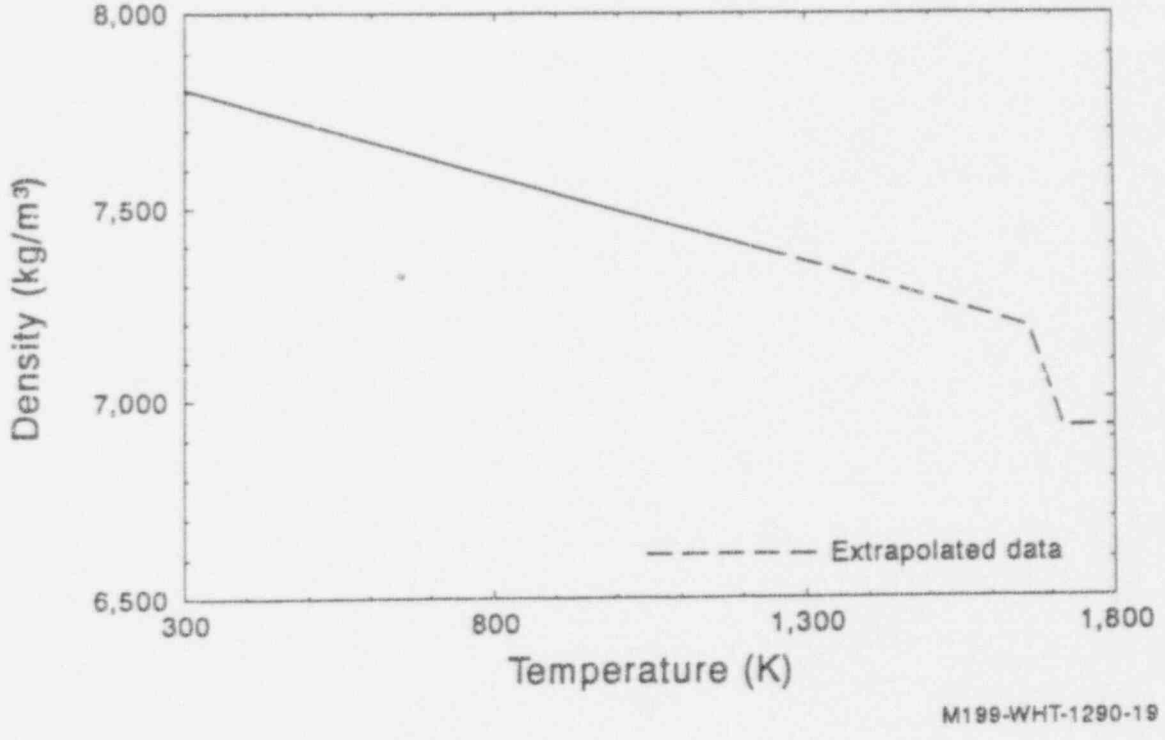

Figure F-1.4-2. Stainless steel density.[F-1]

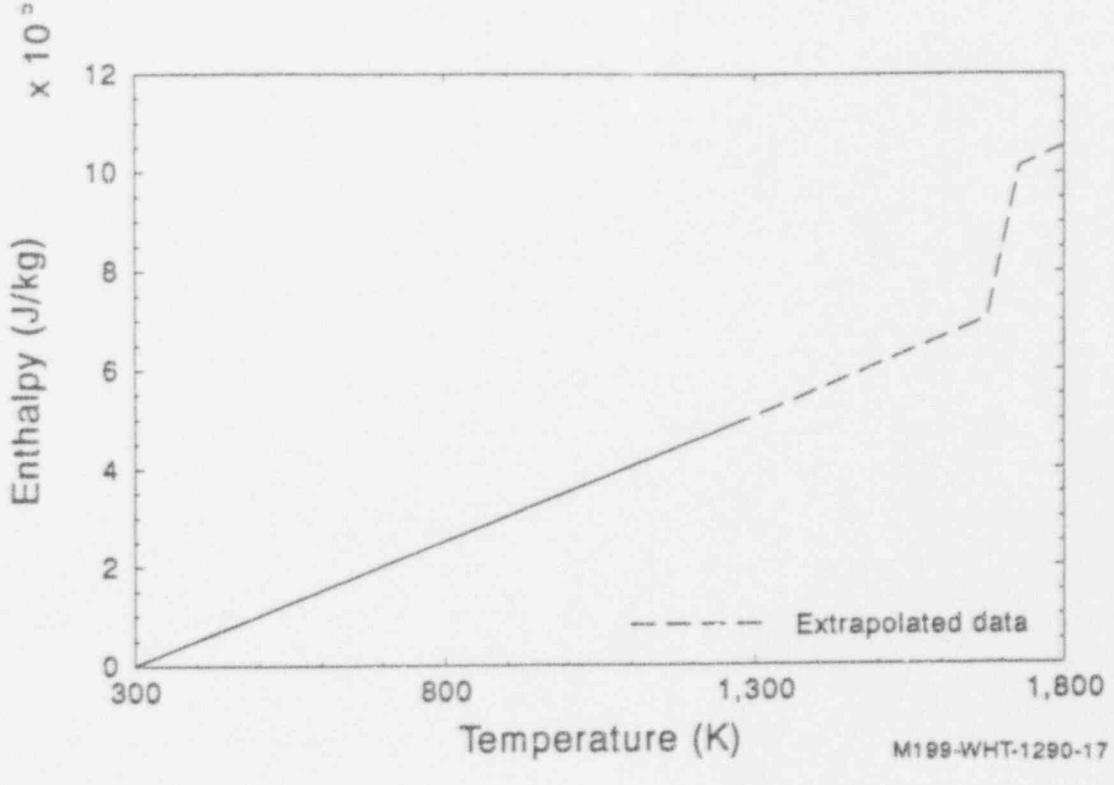

Figure F-1.4-3. Stainless steel enthalpy as a function of temperature.[F-1]

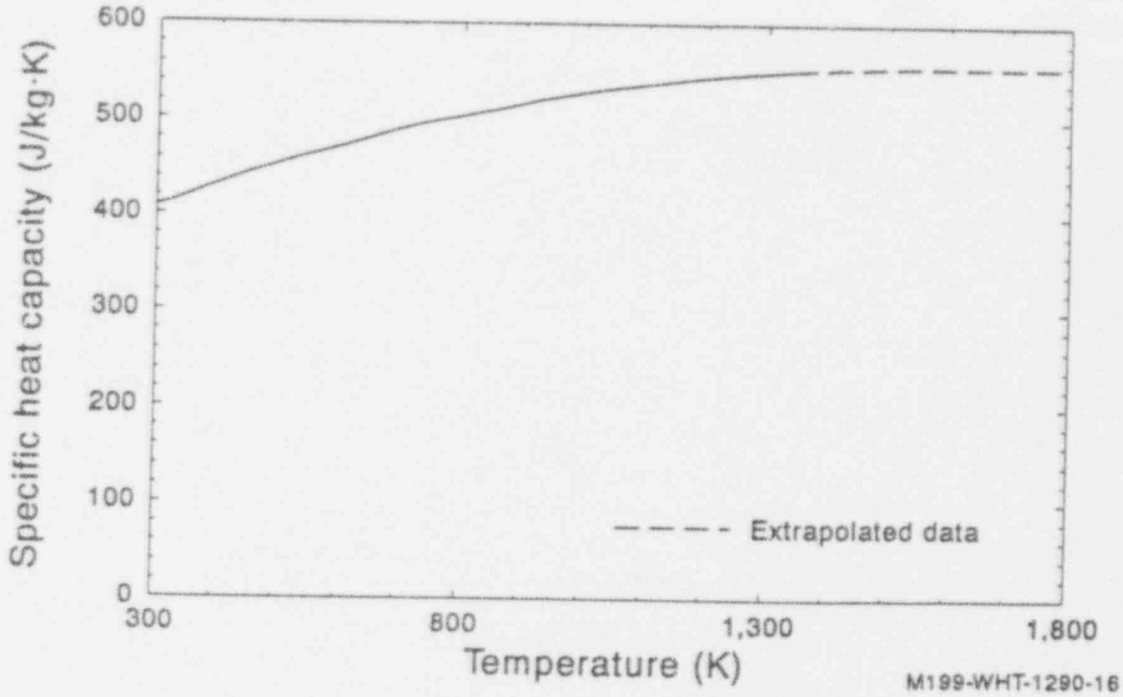

Figure F-1.4-4. Stainless steel specific heat capacity at constant pressure.[F-1]

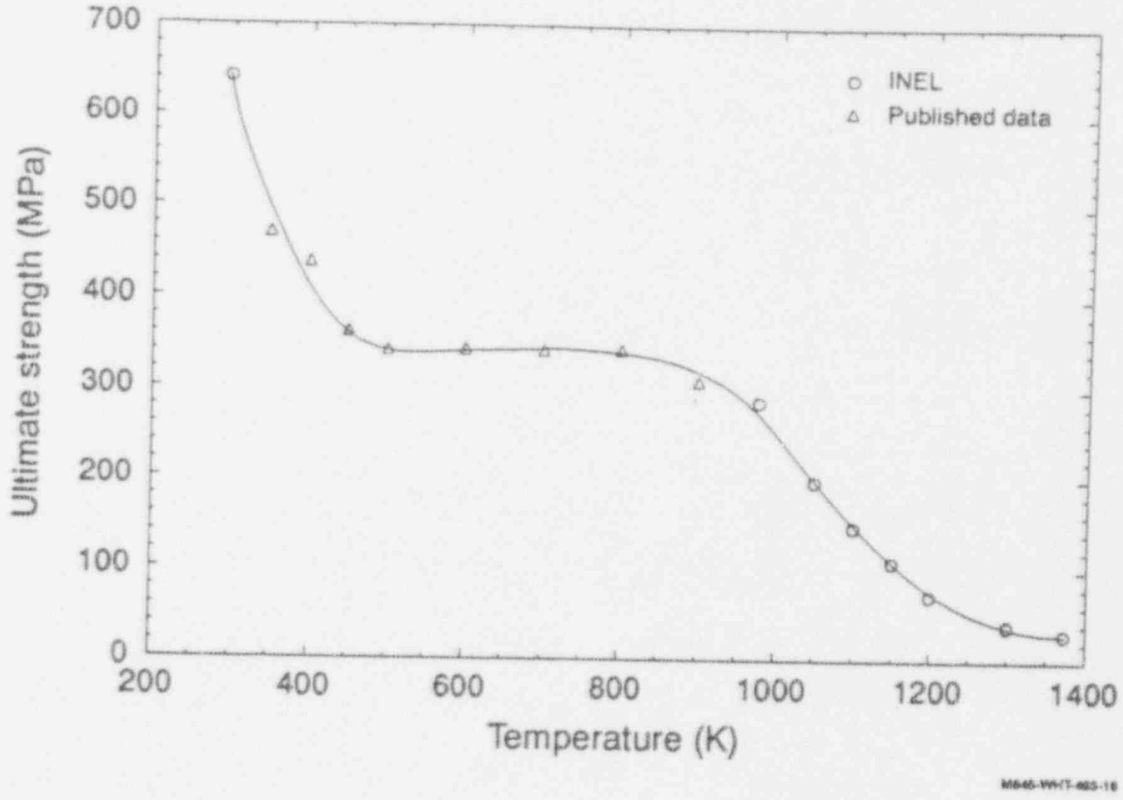

Figure F-1.4-5. Stainless steel ultimate strength, (References F-8 through F-11 and Appendix B).

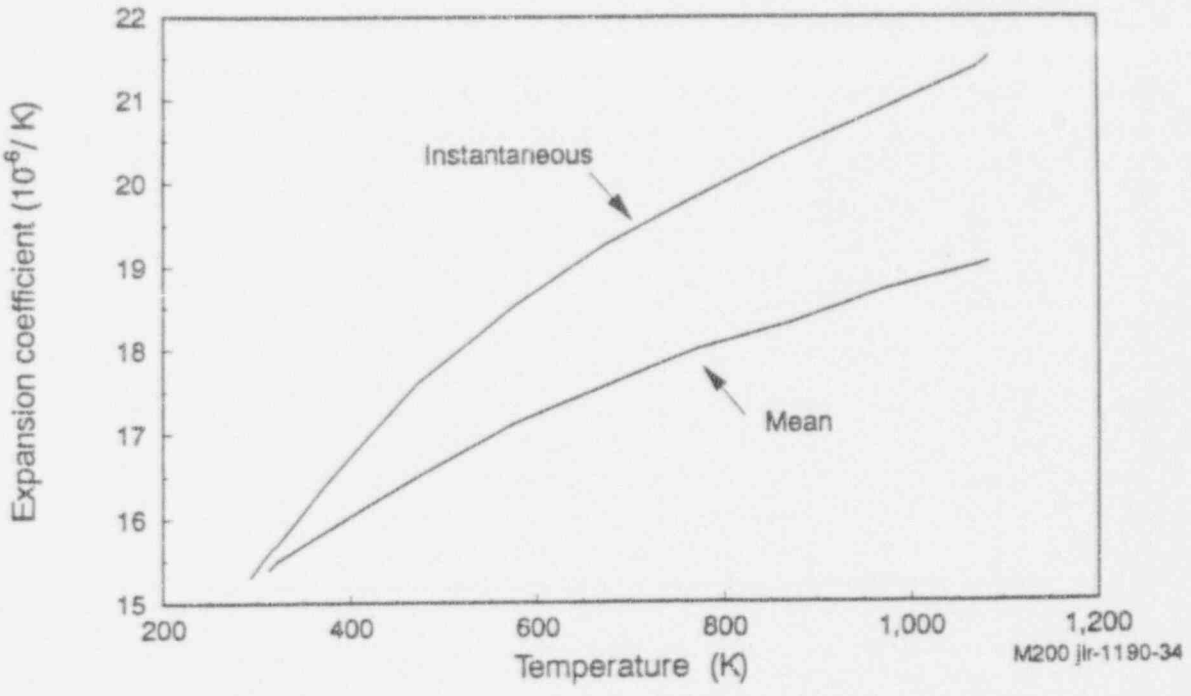

Figure F-1.4-6. Stainless steel mean and instantaneous thermal expansion coefficient.[F-12 through F-24]

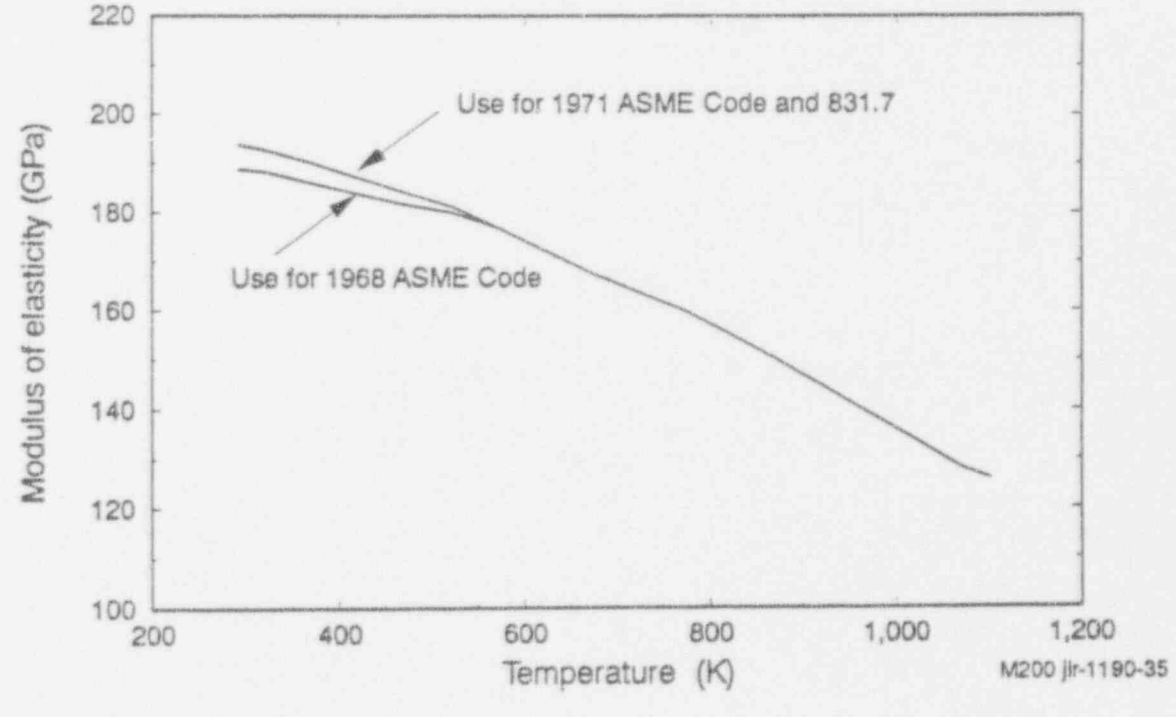

Figure F-1.4-7. Young's modulus of elasticity for stainless steel.[F-25 through F-27]

F-1.5 Silver-Indium-Cadmium Data

This section contains data for the following properties of silver-indium-cadmium: thermal conductivity, density, enthalpy, specific heat capacity, and viscosity. These data are summarized in Figures F.1.5-1 through F.1.5-5.

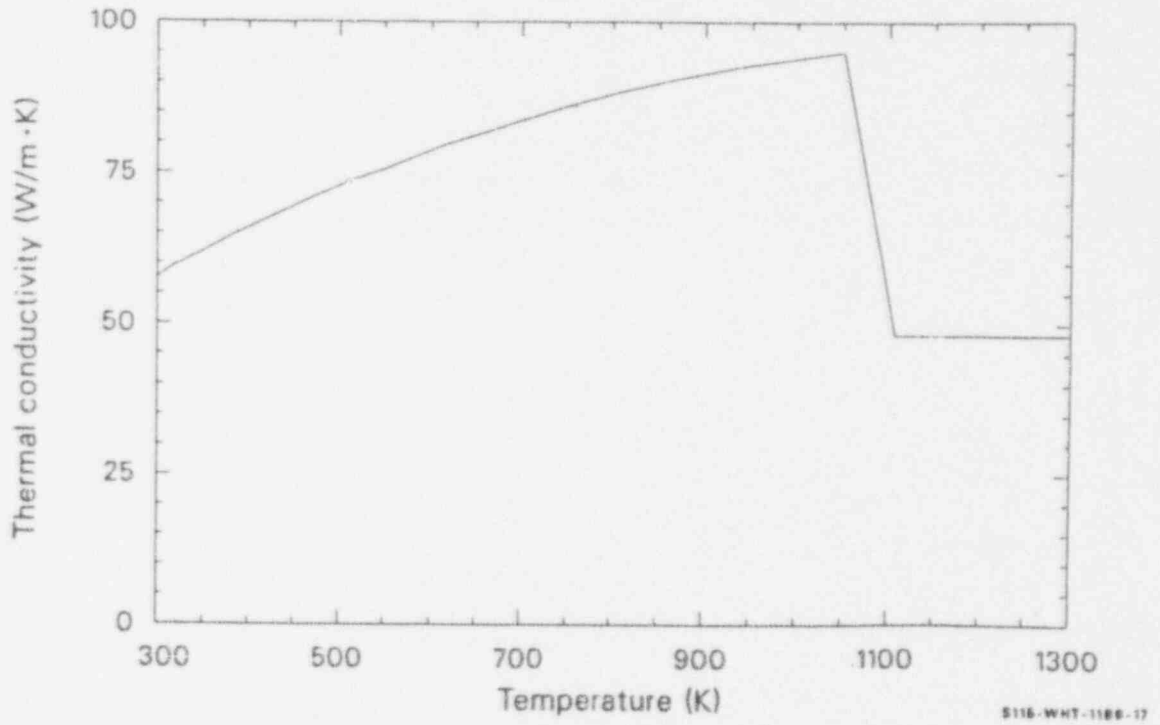

Figure F-1.5-1. Thermal conductivity of silver-indium-cadmium absorber.[F-1]

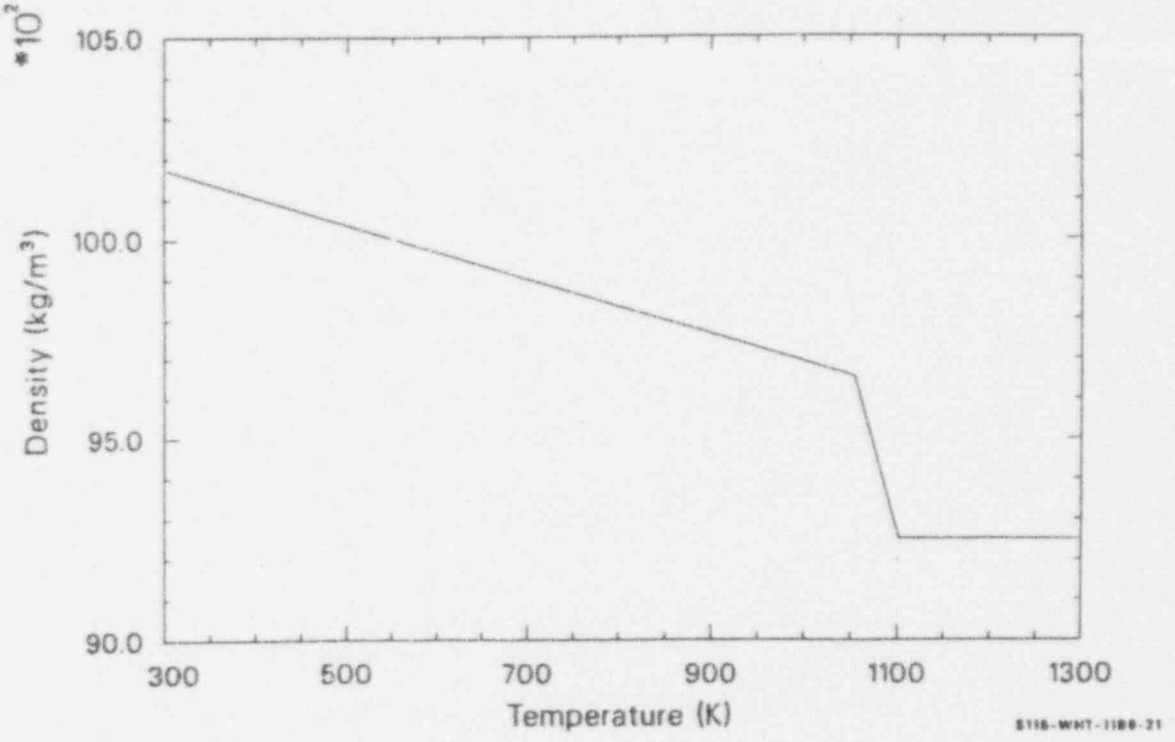

Figure F-1.5-2. Density of silver-indium-cadmium absorber.[F-1]

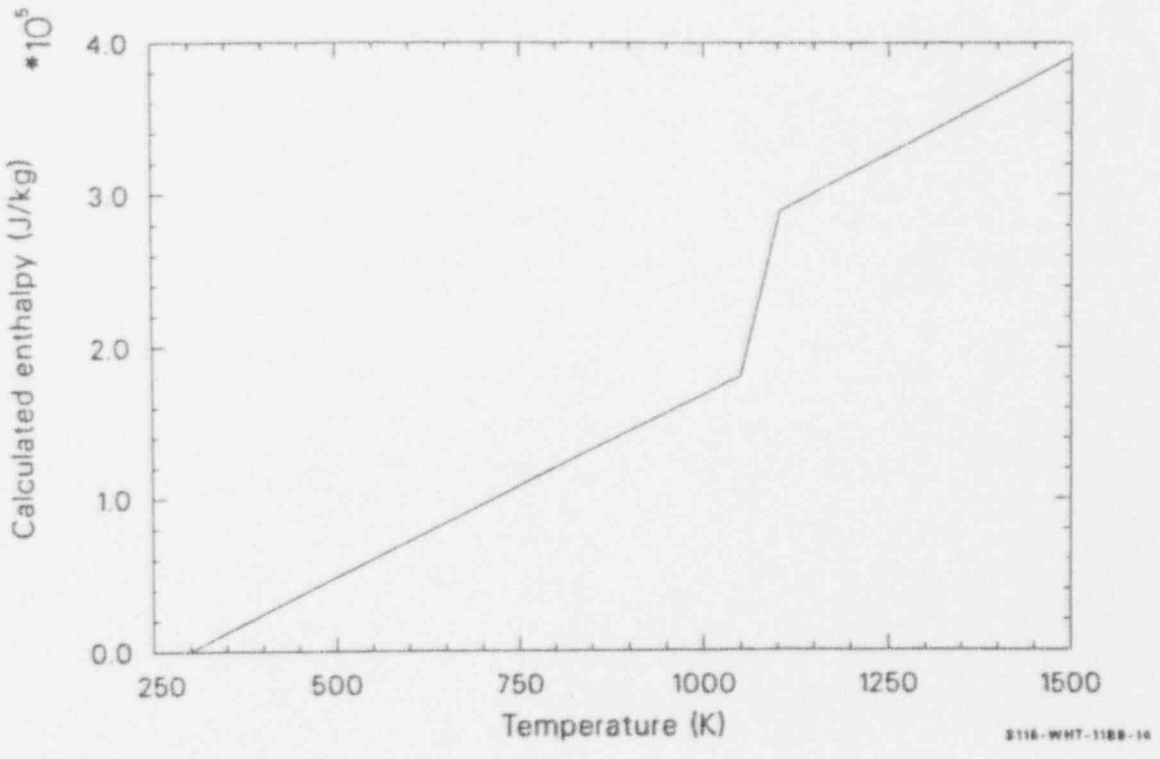

Figure F-1.5-3. Silver-indium-cadmium absorber enthalpy.[F-1]

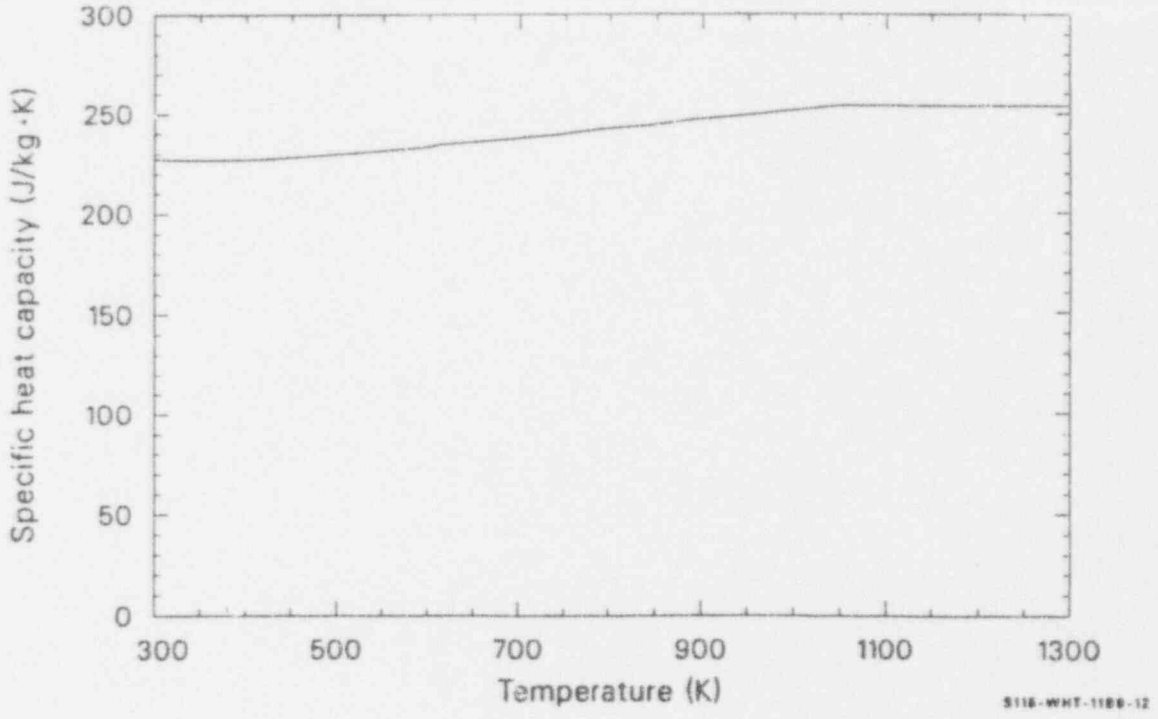

Figure F-1.5-4. Silver-indium-cadmium absorber heat capacity.[F-1]

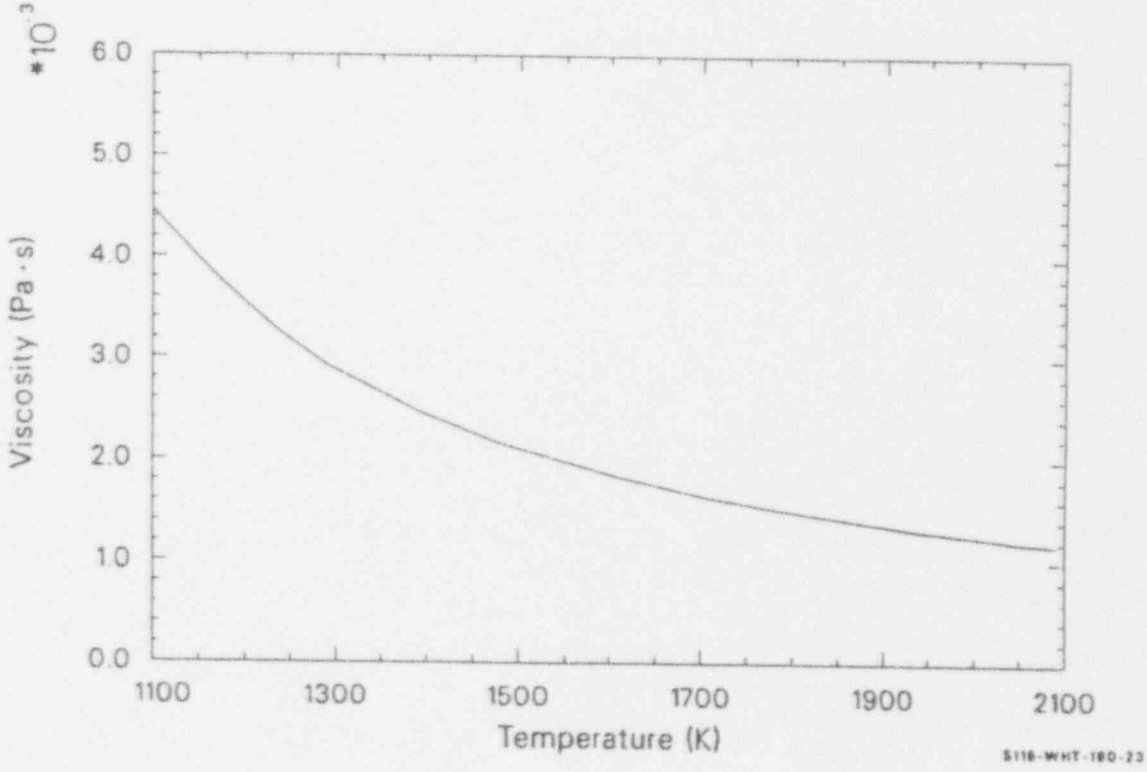

Figure F-1.5-5. Viscosity of silver-indium-cadmium absorber.[F-1]

F-1.6 Boron Carbide Data

This section contains data for the following properties of boron carbide: thermal conductivity, density, enthalpy, specific heat capacity, and viscosity. These data are summarized in Figures F.1.6-1 through F.1.6-5.

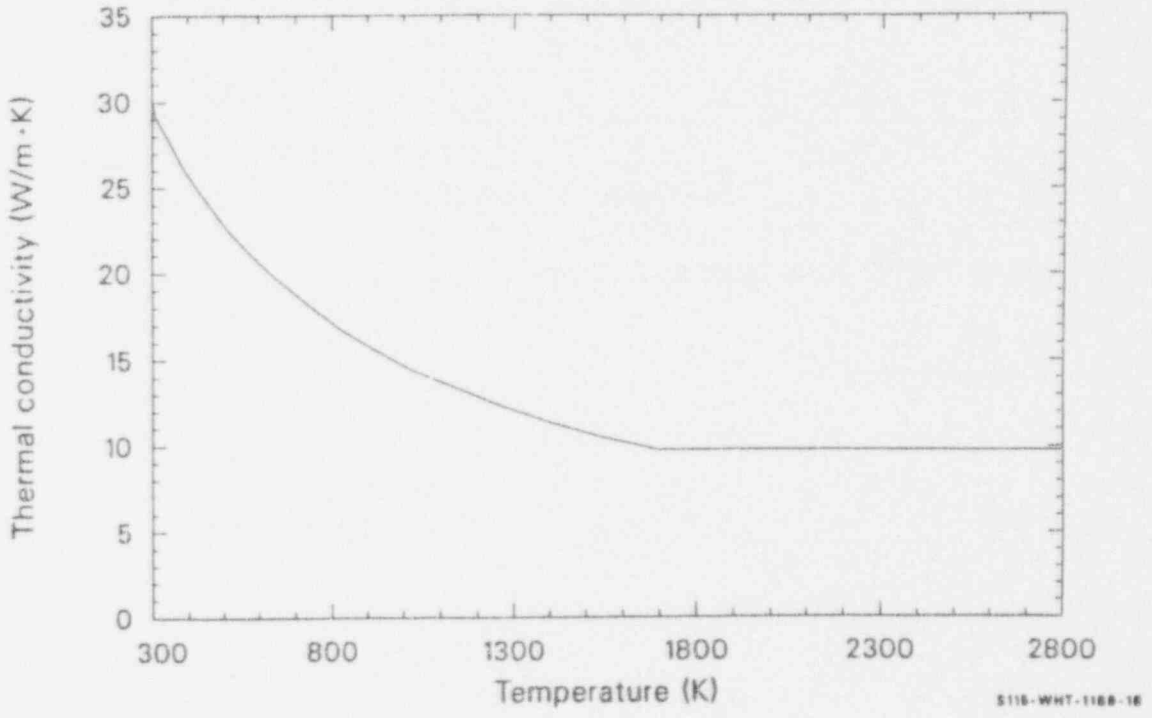

Figure F-1.6-1. Thermal conductivity of boron carbide absorber.[F-1]

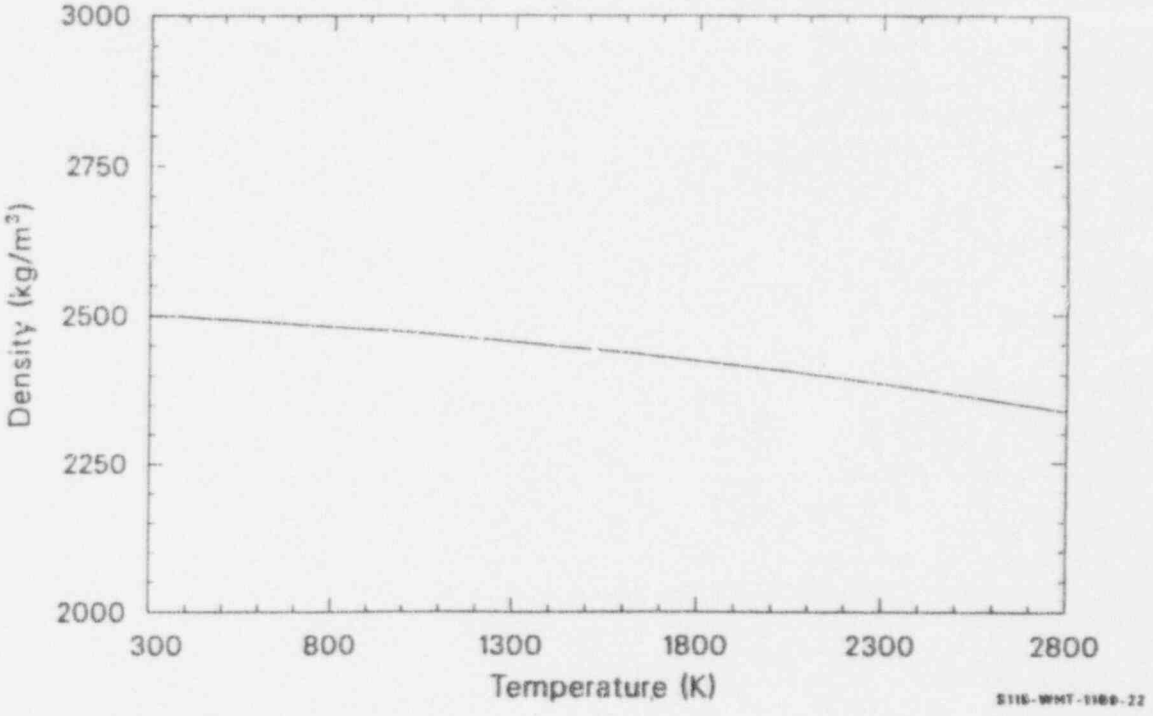

Figure F-1.6-2. Density of boron carbide absorber.[F-1]

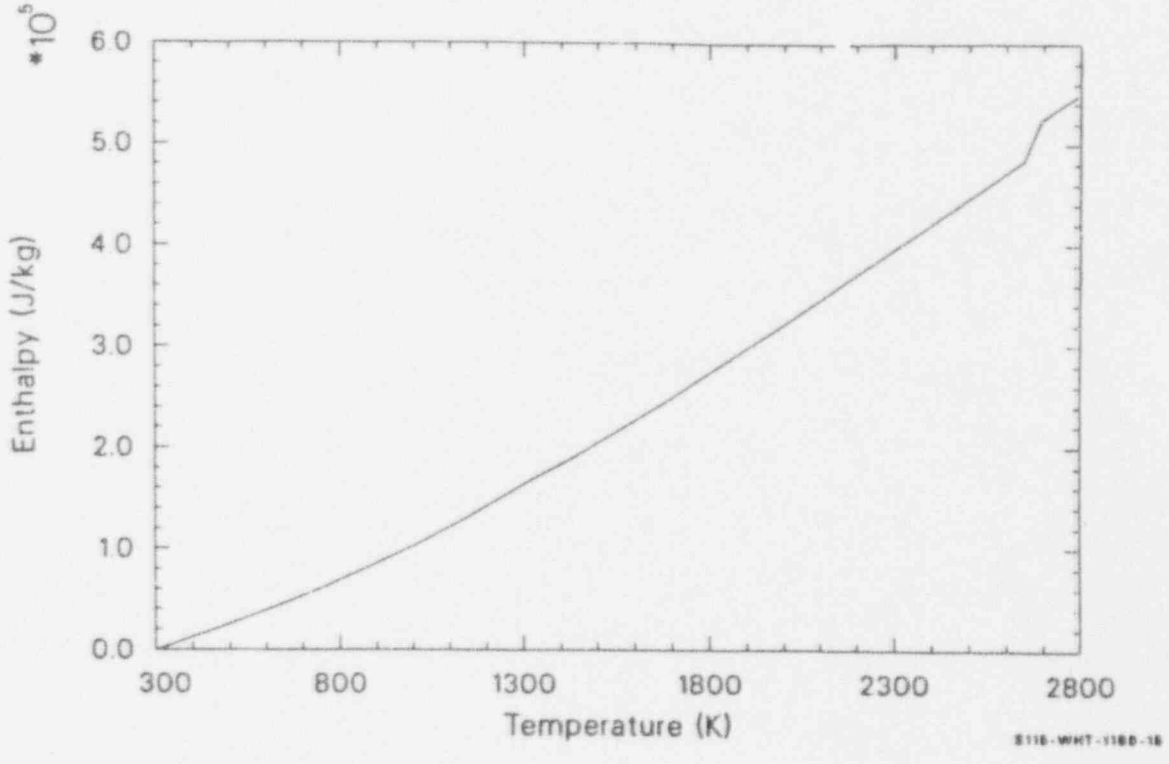

Figure F-1.6-3. Boron carbide absorber enthalpy.[F-1]

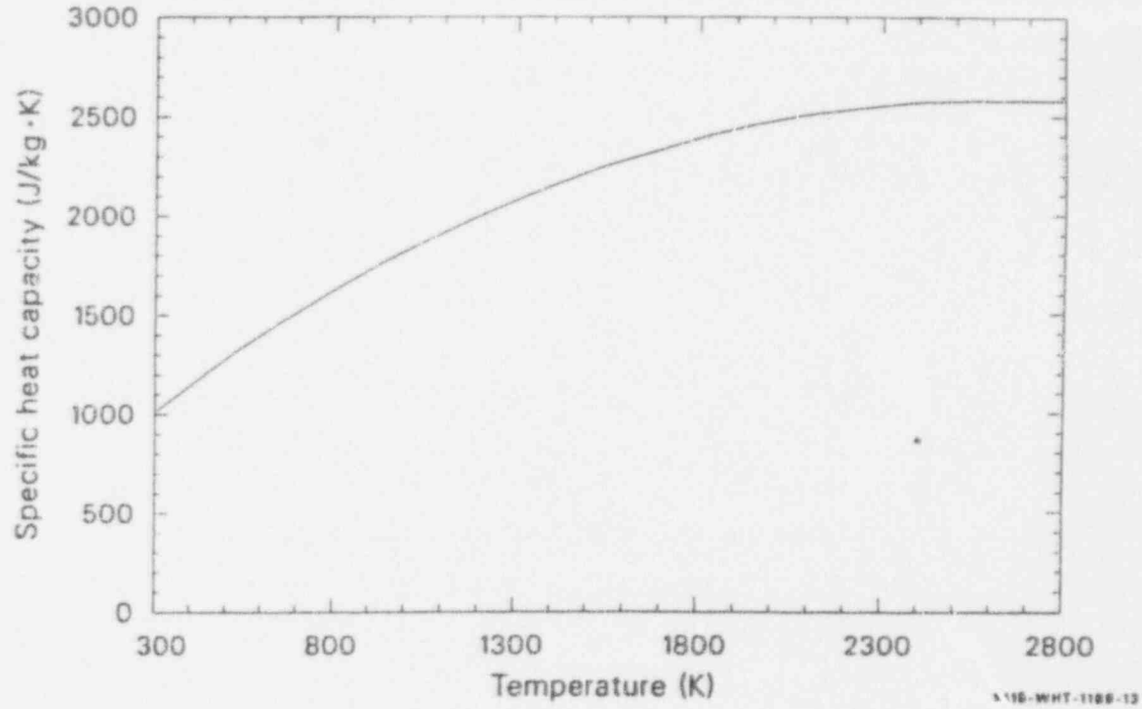

Figure F-1.6-4. Boron carbide absorber heat capacity.[F-1]

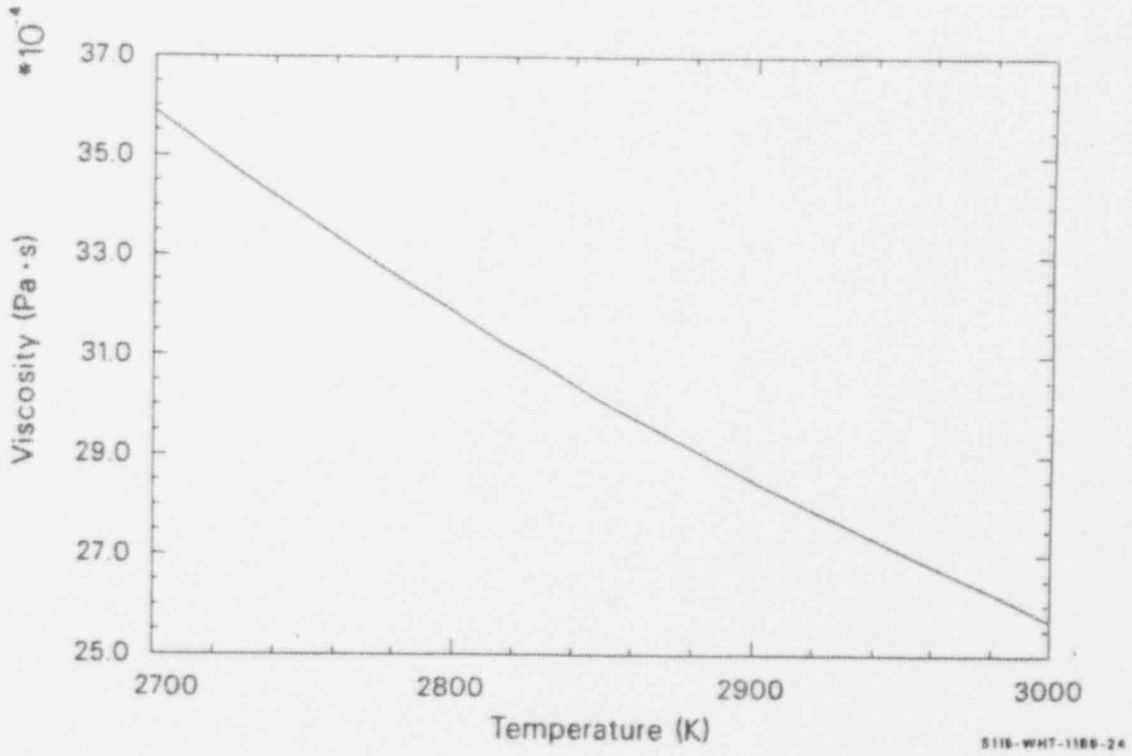

Figure F-1.6-5. Viscosity of boron carbide absorber.[F-1]

F-1.7 Carbon Steel Data

This section contains data for the following properties of carbon steel (SA533B1, SA105/SA106): thermal conductivity, density, specific heat capacity, ultimate strength, the coefficient of thermal expansion, thermal diffusivity, and Young's modulus. These data are summarized in Figures F-1.7-1 through F-1.7-9.

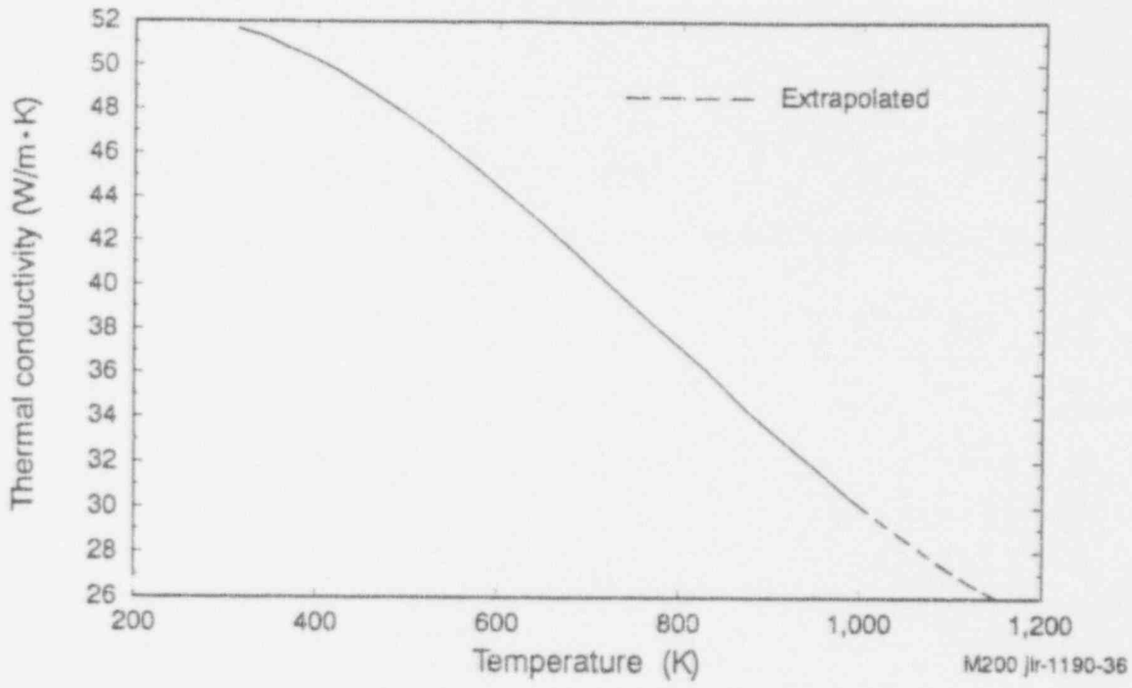

Figure F-1.7-1. Thermal conductivity of carbon steel (SA533B1).[F-28,F-29]

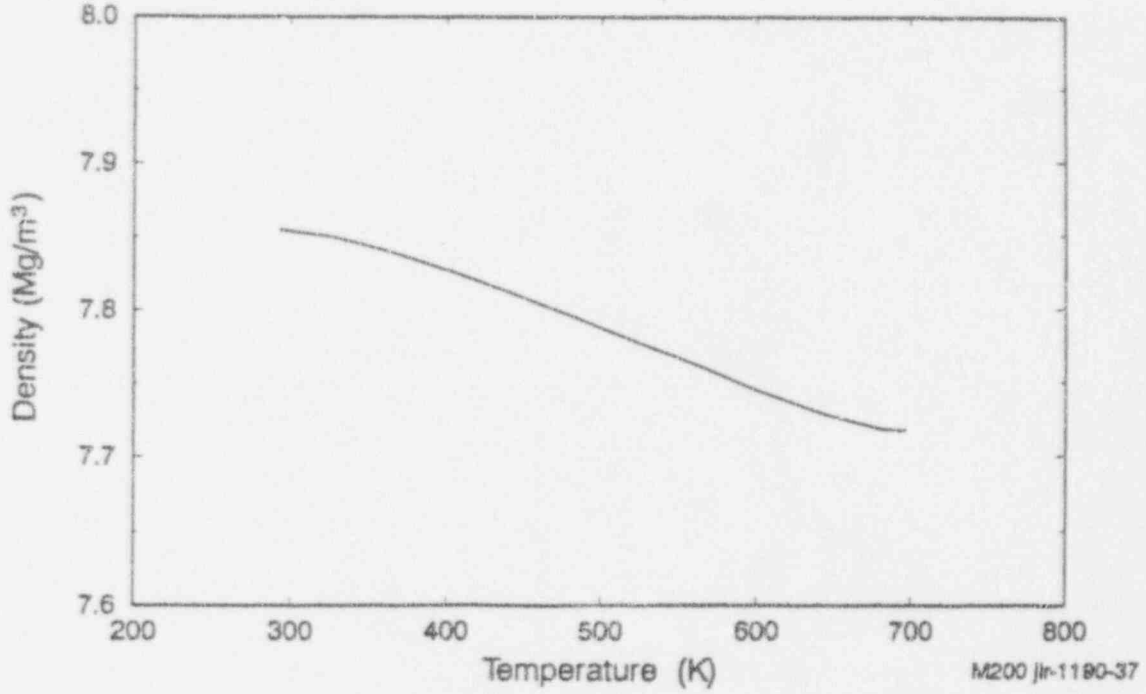

Figure F-1.7-2. Density of carbon steel (SA533B1).[F-30]

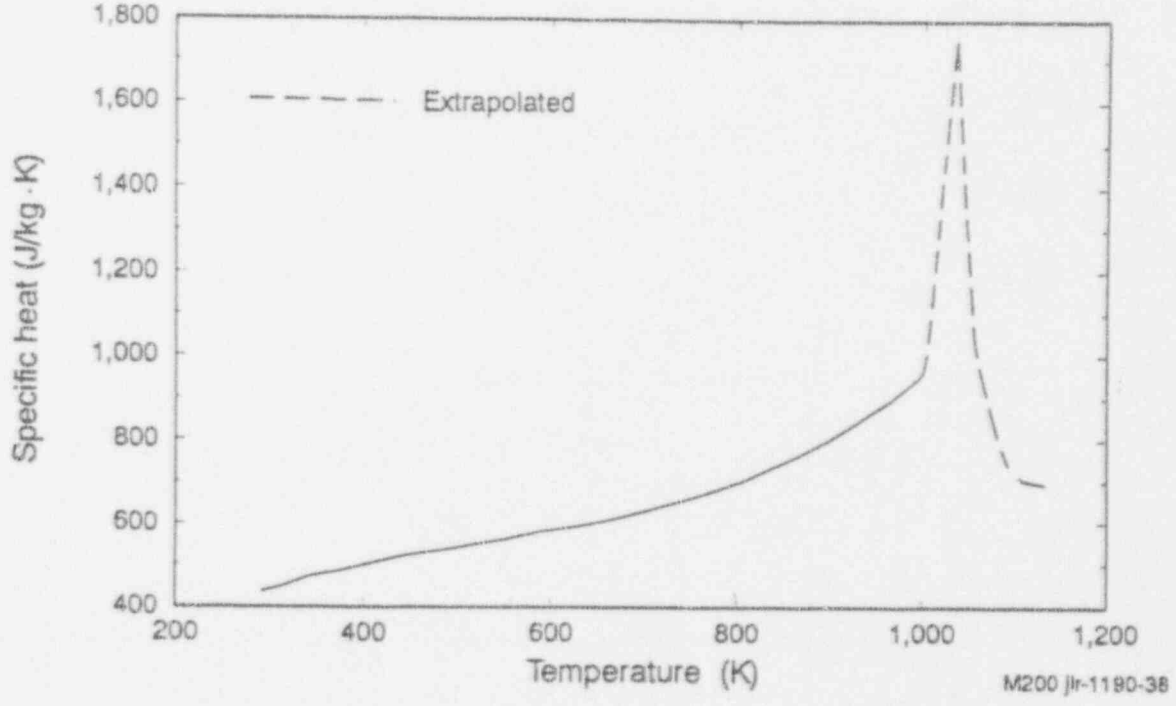

Figure F-1.7-3. Specific heat of carbon steel (SA533B1).[F-31 through F-36]

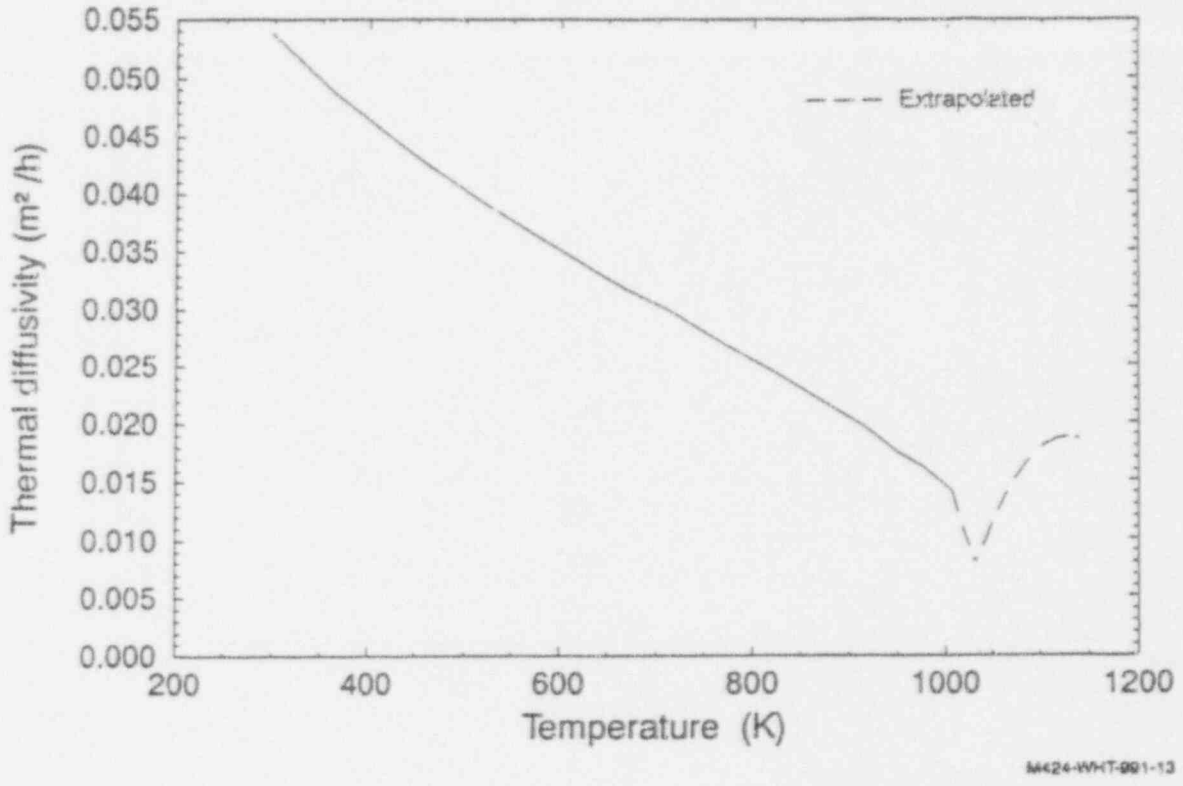

Figure F-1.7-4. Thermal diffusivity of carbon steel.[F-30, F-35]

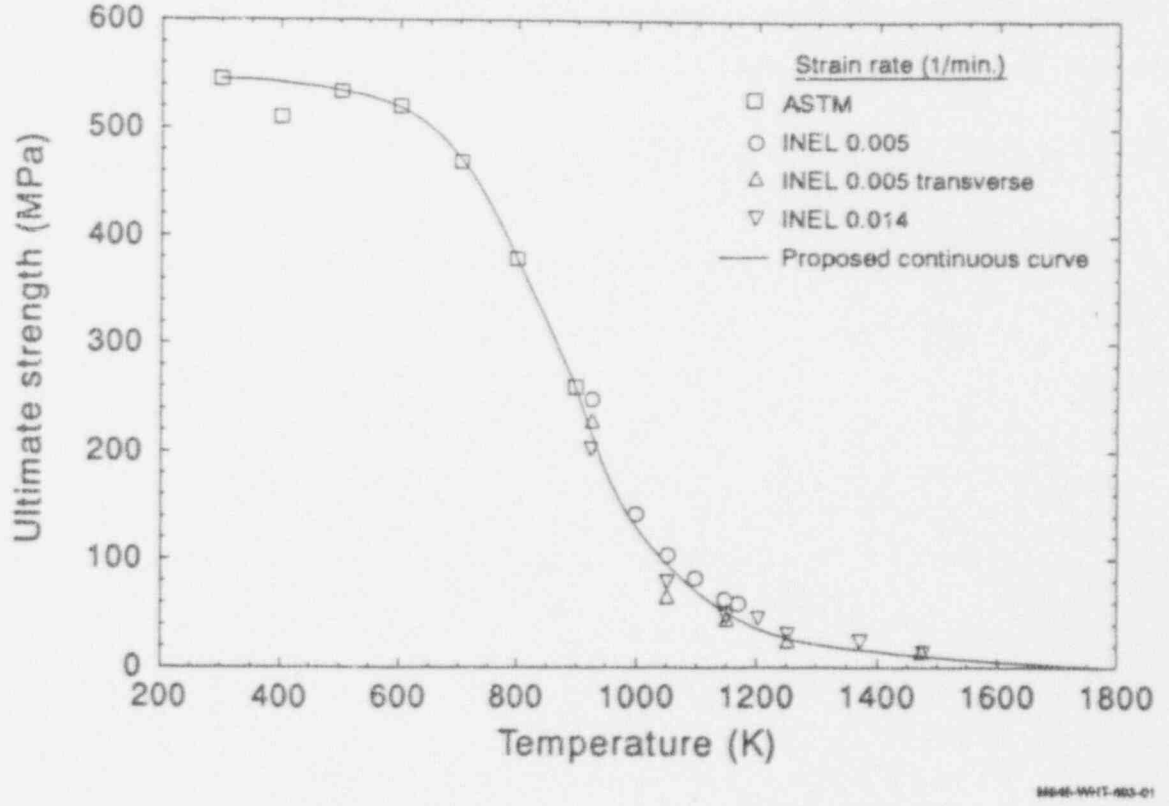

Figure F-1.7-5. Ultimate strength for carbon steel (SA533B1) (Reference F-36 and Appendix B).

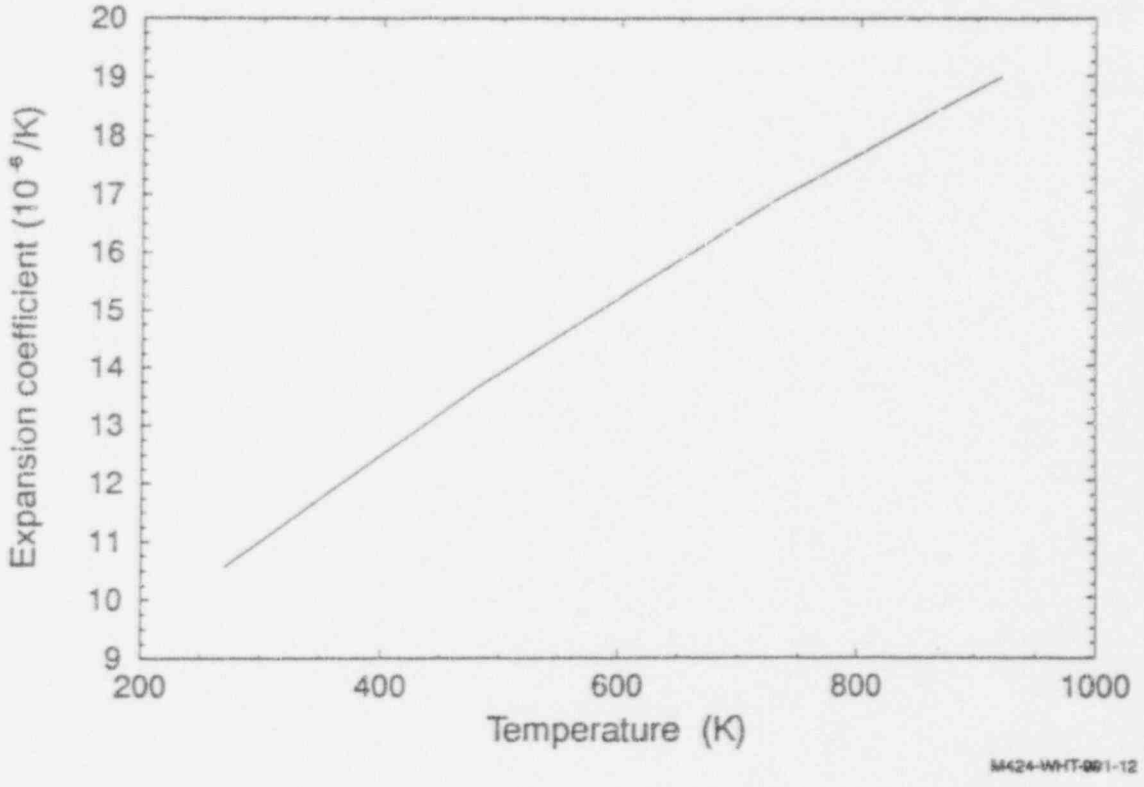

Figure F-1.7-6. Instantaneous coefficient of thermal expansion for carbon steel (SA533B1) at reference temperature of 294 K.[F-37]

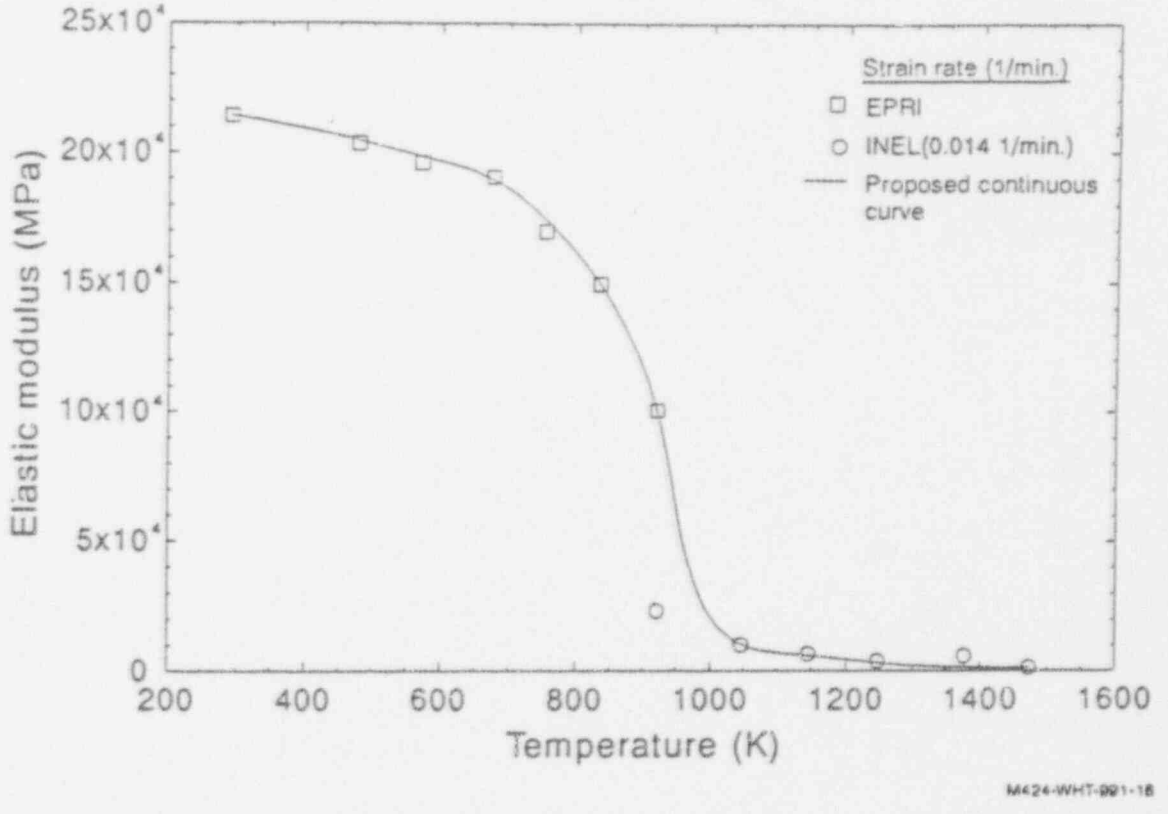

Figure F-1.7-7. Young's modulus for carbon steel (SA533) (Reference F-37 and Appendix B).

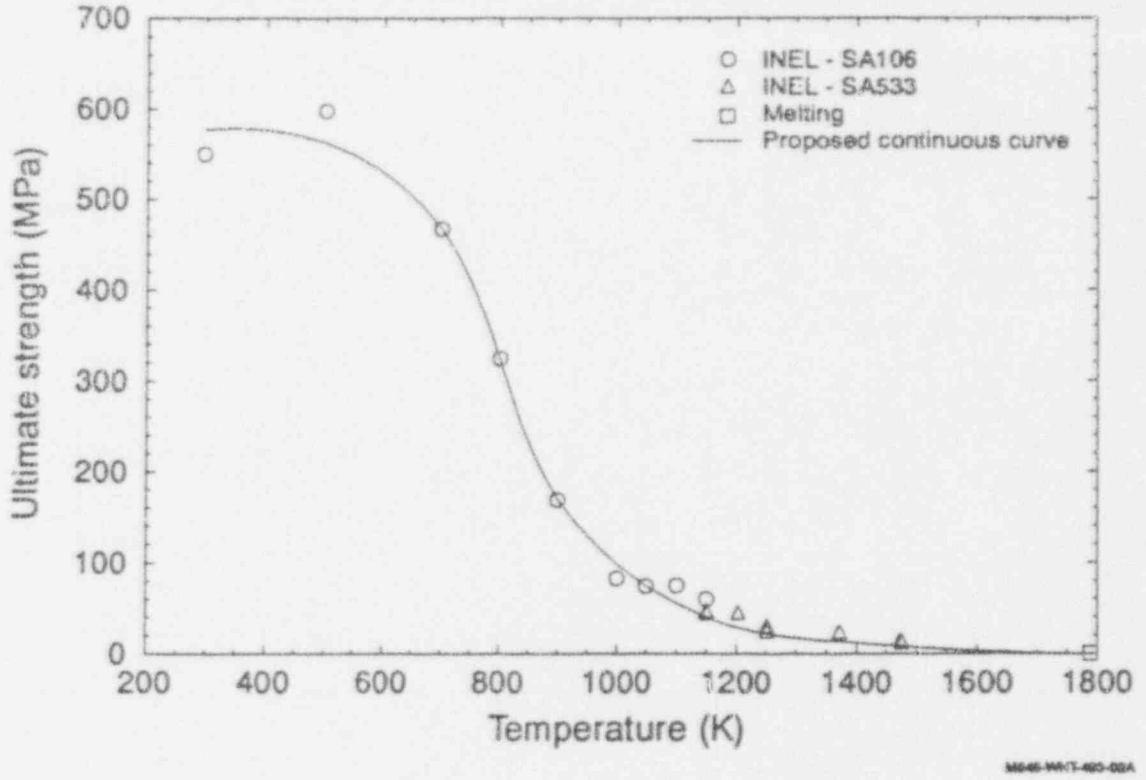

Figure F-1.7-8. SA106 B carbon steel ultimate strength (see Appendix B).

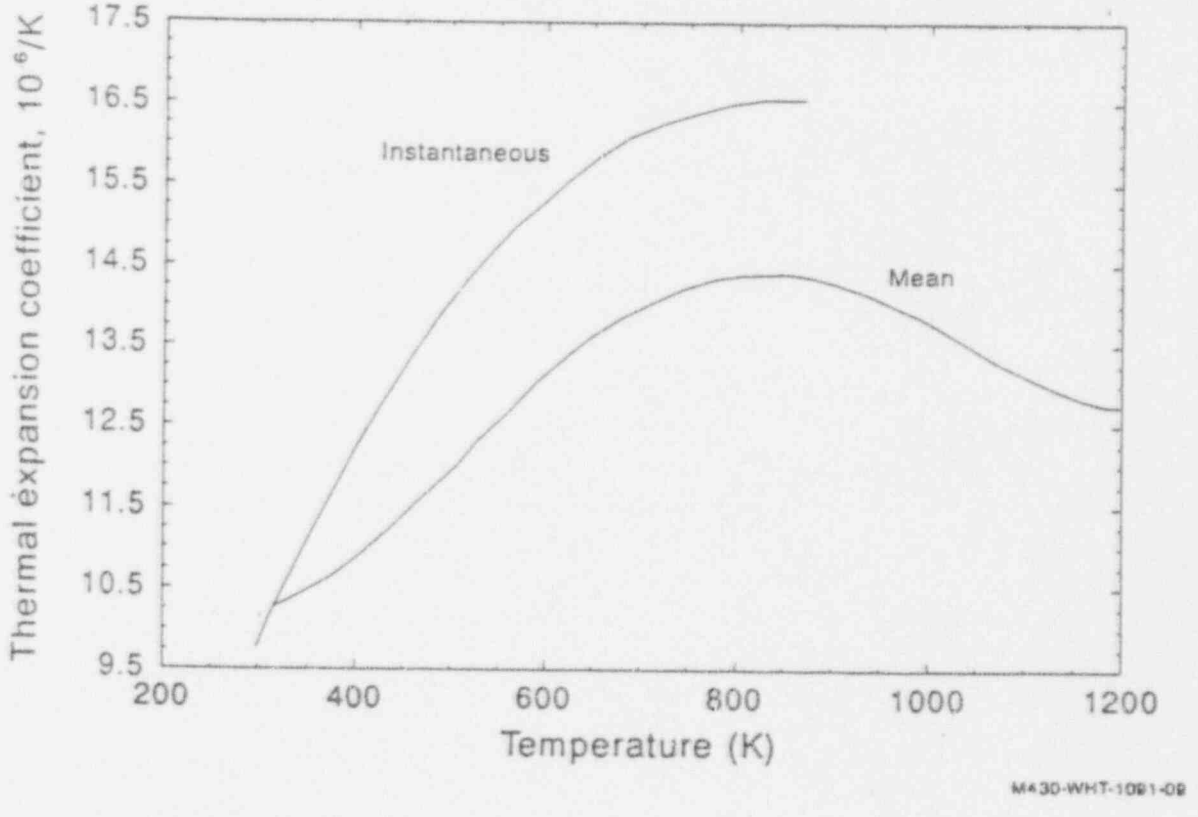

Figure F-1.7-9. Instantaneous and mean coefficient of thermal expansion for medium carbon steel.[F-34]

F-2. GEOMETRIC DATA

Calculations performed for the lower head failure analysis used the geometrical data summarized in Table F-2.1. Dimensioned component drawings in Section 3 clarify lower head and penetration data in this appendix. This information was compiled from plant component drawings, final safety analysis reports, discussions with plant personnel, and References F-39 and F-40.

Table F-2.1. Geometrical parameters used in lower head failure analysis.

Parameters	Reactor type (vendor)					
	PWR B&W	PWR CE	BWR/5 GE	PWR W2	PWR W1	BWR/4 GE
Power Level (MWt)	2772	3400	2440	3400	1825	3440
Vessel						
Material[a]	SA533B1	SA533B1	SA533B1	SA533B1	SA533B1	SA533B1 (SA302B)[b]
Lower head minimum thickness (m)	0.127	0.111	0.200	0.14	0.132	0.214
Lower head inner radius (m)	2.22	2.19	2.81	2.10	2.02	2.81
Cladding						
-Material[a]	SS	SS	INC	SS	SS	INC
-Minimum thickness (cm)	0.318	0.318	0.318	0.318	0.318	0.318
Design pressure (MPa)	17.2	17.1	8.6	17.1	17.1	8.6
Penetrations						
Instrumentation tube						
-Number	52	0	55	58	19	55
-Material[a]						
Tube	INC	NA[c]	304SS	INC	INC	304SS
Weld	INC	NA	SS/INC	INC	INC	SS/INC
-Radii (cm)						
Inside vessel:						

Table F-2.1. (continued).

Parameters	Reactor type (vendor) PWR B&W	PWR CE	BWR/5 GE	PWR W2	PWR W1	BWR/4 GE
-Thin upper nozzle						
Inner tube	0.78	NA	1.91	0.61	0.46	1.91
Outer tube	2.22	NA	2.51	1.37	1.90	2.51
-Thick lower nozzle						
Inner tube	0.78	NA	1.91	0.61	0.46	1.91
Outer tube	2.54	NA	2.51	1.37	1.90	2.51
Through vessel:						
Inner tube	0.78	NA	1.91	0.61	0.46	1.91
Outer tube	1.33	NA	2.51	1.37	1.90	2.51
-Tube-to-vessel	0.0064-		0.013-		0.002-	0.013-
Gap (cm)	0.013	NA	0.025	—[c]	0.008	0.025
Weld length (cm)	1.37[d]	NA	0.75[e]	1.40[e]	1.40[e]	0.75[e]
-Instrument string						
Outer radius (cm)	0.371	NA	0.89	0.385	0.371	0.89
Control rod guide tube housing						
-Number	0	0	185	0	0	185
-Material[a]						
Tube	NA	NA	304SS	NA	NA	304SS
Weld	NA	NA	SS/INC	NA	NA	SS/INC

Table F-2.1. (continued).

Parameters	Reactor type (vendor)					
	PWR B&W	PWR CE	BWR/5 GE	PWR W2	PWR W1	BWR/4 GE
-Radii (cm)						
Inner tube	NA	NA	6.17	NA	NA	6.17
Outer tube	NA	NA	7.59	NA	NA	7.59
-Tube-to-vessel gap (cm)	NA	NA	0.019-0.032	NA	NA	0.019-0.03[illegible]
-Guide tube pitch (cm)	NA	NA	30.48	NA	NA	30.48
-Control rod drive thermal sleeve outer radius	NA	NA	5.95	NA	NA	5.95
-Annular gap for flow between CR guide tube housing and thermal sleeve (cm)	—	—	0.20-0.23	—	—	0.20-0.23
Other lower head penetrations						
Drain nozzle						
-Number	0	0	1	0	0	1
-Material						
Tube	NA	NA	SA105II/ SA106B	NA	NA	SA105II/ SA106B
Weld	NA	NA	carbon steel	NA	NA	Carbon steel
-Tube radii (cm)						
Inner	NA	NA	2.50	NA	NA	2.50
Outer	NA	NA	3.20	NA	NA	3.20

Table F-2.1. (continued).

Parameters	Reactor type (vendor) PWR B&W	PWR CE	BWR/5 GE	PWR W2	PWR W1	BWR/4 GE
Core material masses (kg)						
304SS[f]	88,900	58,100	101,000	101,000	—	121,118
UO_2	93,000	102,000	118,000	101,000	—	172,500
Zircaloy	19,100	29,100	51,300	25,000	—	62,600
Inconel[g]	64	3630	3050	1870	—	0
Poison						
Ag-In-Cd	8200	14	0	1345	—	0
B_4C	—	146	644	1830[h]	—	1150
Insulation						
Minimum thickness (cm)	7.62	—	7.62	7.62	—	7.62
Material	SS	SS	SS	SS	SS	SS
Minimum distance from vessel lower head (cm)		—	3.80	2.40	—	3.80
Heat transfer surface area (m^2)	—	210	—	—	—	—
Coolant volume (m^3)[i]						
Volume below core	—	29.7	145.9	29.7	—	195.5
Volume to core top	—	67.1	263.1	61.2	—	351.1
Volume in vessel	115.0	143.7	309.3[j]	140.1	—	416.6[j]
Volume in RCS	335.4	314.4	309.3[j]	347.1	248.7	416.6[j]

Table F-2.1. (continued).

Parameters	Reactor type (vendor) PWR B&W	PWR CE	BWR/5 GE	PWR W2	PWR W1	BWR/4 GE
Lower plenum configuration						
Distance from bottom of fuel assemblies to reactor vessel lower head, core centerline/core periphery (m)	2.2/1.7	2.8/2.0[k]	—	3.1/2.5	—	5.3/4.0
BWR-specific:						
Tube radii (cm)						
Control rod guide tube	NA	NA	—	NA	—	14.0
Control rod drive housing	—	—	—	—	—	7.6
Control rod pitch (cm)	—	—	—	—	—	30.48
PWR-specific:						
Plate 1 name	Flat distributor plate	Core support assembly bottom plate	—	NA[l]	—	NA
Distance from plate underside to lower head, core centerline/core periphery (m)	1.8/1.4	1.8/1.0	—	NA[l]	—	NA
Plate thickness (m)	0.0254	0.0889	—	NA[l]	—	NA
Hole diameter (m)	0.089	0.0762	—	NA[l]	—	NA
Plate 2 name	Grid forging	Instrument guide tube support plate[m]	—	NA[l]	—	NA

Table F-2.1. (continued).

Parameters	Reactor type (vendor)					
	PWR B&W	PWR CE	BWR/5 GE	PWR W2	PWR W1	BWR/4 GE
Distance from plate underside to lower head, core centerline/core periphery (m)	1.3/0.86	1.1/0.3	–	–	–	NA
Plate thickness, (m)	0.4064	0.0508	–	–	–	NA
Hole diameter (m)	0.1651	0.254[n]	–	NA[l]	–	NA
PWR-specific	–	NA	–	–	NA[l]	NA
Plate 3 name	Elliptical flow distributor plate	NA	–	–	NA[l]	NA
Distance from plate underside to lower head, core centerline/core periphery (m)	0.74/0.63	NA	–	–	NA[l]	NA
Plate thickness (m)	0.051	–	–	–	–	–
Hole diameter (m)	0.1524	NA	–	–	NA[l]	NA

a. SA533B1 designates SA533 Grade B Class 1; SA302B designates SA302 Grade B; SA105 II designates SA105 Class II steel; SA106B designates SA106 Grade B steel; SS designates 304 stainless steel; INC designates Inconel-600.

b. Some older designs are composed of SA302B steel.

c. – designates information not available; NA designates information not applicable

d. B&W drawing, October 4, 1991.

Table F-2.1. (continued).

Parameters	Reactor type (vendor) PWR B&W	PWR CE	BWR/5 GE	PWR W2	PWR W1	BWR/4 GE

e. ASME Boilers and Pressure Vessel Code, Section III, 1989.[F-40]

f. Includes structural support steel (core barrels, support plates, etc.), and fittings, thermal shield pads (if applicable), and jet pumps (BWRs only).

g. Includes items such as radial support key, in-core support grids, flow skirts, etc.hAlthough not recorded in the FSAR, this Westinghouse Plant is designed to have the lower one-third of the absorber contain Ag-Cd-In, the upper two-thirds contains boron carbide pellets.

i. Preliminary estimates assume that reactor internals are in place.

j. To height of liquid during normal operation.

k. Dimension for CE lower plenum structures are based on the Maine Yankee plant configuration rather than a typical CE plant, which has no lower head penetrations.

l. Although several plates exist in the Westinghouse design, the configuration admits "straight-shot" relocation pathways that were assumed in Section 4 analyses.

m. Includes 0.0508-m-thick in-core guide support plate and 0.0127-m water gap.

n. Largest hole diameter.

F-3. REFERENCES

F-1. J. K. Hohorst, *SCDAP/RELAP5/MOD2 Code Manual, Volume 4: MATPRO - A Library of Materials Properties for Light-Water-Reactor Accident Analysis*, NUREG/CR-5273, EGG-2555, February 1990.

F-2. *Aerospace Structural Metals Handbook*, Air Force Materials Laboratory, 1990 Edition, Revised December 1989.

F-3. R. E. Bolz and G. L. Tuve (eds.), *CRC Handbook of Tables for Applied Engineering Science*, 2nd Edition, Boca Raton, Florida: CRC Press, 1973.

F-4. *Metals Handbook*, 2nd Printing, Metals Park, Ohio: American Society for Metals, 1985.

F-5. Huntington Alloy, *Inconel Alloy 600*, Technical Bulletin of The International Nickel Company, Inc., now Inco Alloys International, Inc., Huntington Alloy Products Division, Seventh Edition, Huntington, WV, 1987.

F-6. ASME Boiler and Pressure Vessel Code, Section II, "Nuclear Plant Components," 1971 Edition.

F-7. C. F. Lucks and H. W. Deem, *The Thermal Properties of Thirteen Metals*, ASTM Special Technical Publication No. 227, Philadelphia, PA, 1958.

F-8. W. F. Simmons and H. C. Cross, *The Elevated Temperature Properties of Stainless Steels*, ASTM STP-124, Philadelphia, PA, 1952.

F-9. W. F. Simmons and J. A. VanEcho, *The Elevated Temperature Properties of Stainless Steels*, ASTM DS5-S1, Philadelphia, PA, 1965.

F-10. United States Steel Corporation, *Mechanical and Physical Properties of Steels for Nuclear Applications*, ADUSS 92-1625, Section 3, 1967, pp. 20,43.

F-11. *Aerospace Structural Metals Handbook*, Code 1303 (Types 304 and 304L), extracts from Carpenter Steel (1962) and United States Steel (1956), March 1967 Revision.

F-12. National Aeronautic and Space Administration, *Technical Support Package for Technical Brief 69-1055-Thermal Expansion Properties of Aerospace Materials*, NASA Technology Utilization Division, PB 184 749, 1969.

F-13. H. L. Laquer, *Low-Temperature Thermal Expansion of Various Materials*, AECD-3706, U.S. Atomic Energy Commission Report, 1952.

F-14. J. M. Beenakker and C. A. Swenson, "Total Thermal Contractions of Some Technical Metals to 4.2 K," *Review of Scientific Instruments*, *26*, 1955, pp. 1204-1205.

F-15. F. L. Yaggee, E. R. Gilbert, J. W. Styles, "Thermal Expansivities, Thermal Conductivities, and Densities of Vanadium, Titanium, Chromium, and Some Vanadium-base Alloys," *Journal of Less Common Metals*, *19*, 1969, pp. 3-51.

F-16. W. R. Martin and J. R. Weir, *Dimensional Behavior of the Experimental Gas-Cooled Reactor Fuel Element at Elevated Temperatures*, ORNL-3103, 1961.

F-17. M. B. Loeb, "Thermal-Contraction Graphs for Cryogenic Temperatures," *Chemical Engineering*, 77, 1970, p. 194.

F-18. D. E. Furman, "Thermal Expansion Characteristics of Stainless Steels Between ~300 and 1000°F," *Transactions of Metals Society AIME*, *188*, 1962, pp. 230-235.

F-19. J. D. Lore, H. L. Richards, R. T. King, L. M. Greene, D. M. Darby, *Thermophysical Properties of a Type 308 Stainless Steel Weld*, Y-1967, Oak Ridge National Laboratory, April 30, 1975.

F-20. J. Valentich, "New Values for Thermal Coefficients," *Production Engineering*, 1965, pp. 63-71.

F-21. V. Arp, J. H. Wilson, L. Winrich, P. Sikora, "Thermal Expansion of some Engineering Materials from 20 to 293 K," *Cryogenics*, *2*, 1962, pp. 230-235.

F-22. B. Y. Neimark, "Influence of Cold Deformation and Aging on the Density and Coefficient of Linear Expansion of Chromium-Nickel Austenitic Steels," *Physical Metals Metalographer*, *14*, p. 126

F-23. H. S. Avery, C. R. Wilks, J. A. Fellows, "Cast Heat Resistant Alloys of the 21% Chromium-9% Nickel Type," *Transactions of the American Society of Metals*, *44*, 1952, pp. 57-80.

F-24. S. M. Makin, Jr., J. Standring, P. M. Hunter, *Determination of Coefficient of Linear Expansion of Metals*, RDB-(C)-TN-45, United Kingdom Atomic Energy Commission Report, 1953.

F-25. ASME Boiler and Pressure Vessel Code, Section III, "*Nuclear Power Plant Components*," 1971 Edition.

F-26. ANSI/ASME B31.7-69, *Nuclear Power Piping*, American National Standards Institute, 1969.

F-27. ASME Boiler and Pressure Vessel Code, Section III, *Nuclear Vessels*, 1968 Edition.

F-28. K. Honda and T. Simidu, "On the Thermal and Electrical Conductivities of Carbon Steels at High Temperature," *Science Reports of Tohoku University*, *6*, 1917-18, pp. 219-234.

F-29. D. L. Timrot, "Determination of Thermal Conductivity and Heat Capacity of Steels," *Zhurnal Tekhinicheskoi Fiziki*, *5*, 1935, pp. 1011-1036.

F-30. B. E. Neimark and V. E. Lynsternik, "Effect of Chilling on the Thermal Diffusivity of Carbon Steels," *Teploenergetika*, *7*, 1960, pp. 16-18.

F-31. J. H. Awbery, A. R. Challoner, P. R. Pallister, R. W. Powell, "The Physical Properties of a Series of Steels - Part II," *Journal of the Iron Steel Institute*, *154*, 2, London, 1946, pp. 83-111.

F-32. P. R. Pallister, "Specific Heat and Resistivity of Mild Steel," *Journal of the Iron Steel Institute, 185*, 4, London, 1957, pp. 474-482.

F-33. British Iron and Steel Research Association, *Physical Constants of Some Commercial Steels at Elevated Temperatures*, London: Butterworth's Scientific Publication, Ltd., 1953, p. 38.

F-34. E. Griffiths, R. W. Powell, M. J. Hickman, *The Physical Properties of a Series of Steels - I*, Special Report No. 24, London: Iron Steel Institute, 1939, pp. 215-251.

F-35. E. G. Shuidkovskii, "Measurement of the Thermal Conductivity of Metals by the Method of Angström," *J. Tech. Phys., 8,* USSR, 1938, pp. 935-947.

F-36. G. V. Smith, *Evaluations of the Elevated Temperature Tensile and Creep Rupture Properties of C-Mo, Mn-Mo, and Mn-Mo-Ni Steels*, Metal Properties Council, American Society for Testing and Materials, ASTM Data Series Publication DS47, 1971.

F-37. G. B. Reddy and D. J. Ayers, *High-Temperature Elastic-Plastic and Creep Properties for SA533 Grade B Class 1 and SA508 Materials*, EPRI NP-2763, Electric Power Research Institute, 1982.

F-38. G. Jaross, J. Maneke, and T. Stoodt, *A Study on the Configuration and Safety Features of U.S. Nuclear Power Plants*, ANL/LWR/SAF 82-2, I-IV, July 1982.

F-39. L. J. Ott, "Advanced Severe Accident Response Models for BWR Application," *Nuclear Engineering and Design, 115*, 1989.

F-40. "Boiler and Press Vessel Code," Section III, Appendices, July 1, 1989, American Society of Mechanical Engineers.

Appendix G

Summary of Peer Review Meeting

Appendix G

Summary of Peer Review Meeting

A meeting was held May 7, 1992, at the Bethesda Hyatt Hotel to discuss peer review comments on the draft report, *Light Water Reactor Lower Head Failure Analysis*. The draft report was prepared to integrate various individual failure studies made since TMI-2 into a single source that investigates the timing of various failure mechanisms. How well this objective and the more specific objectives noted below were met was the topic of this peer review meeting. The peer review committee had been invited by the U.S. Nuclear Regulatory Commission (USNRC). The following members of the committee submitted written comments and attended the meeting:

Dr. Harald Hirschmann, Paul Scherrer Institute (PSI)
Dr. Mati Merilo, Electric Power Research Institute (EPRI)
Dr. Hassein Nourbakhsh, Brookhaven National Laboratory (BNL)
Dr. Martin Pilch, Sandia National Laboratory (SNL)
Dr. Theo Theofanous, University of California-Santa Barbara (UCSB)
Dr. Brian Turland, AEA Technology

Although written comments were received from Dr. Charles Brinkman, Oak Ridge National Laboratory (ORNL), and Dr. Vladamir Asmolov, Kurchatov Institute, these reviewers were unable to attend the meeting.

The following representatives from the USNRC, the Idaho National Engineering Laboratory (INEL), and University of Wisconsin—Madison (UWM) were also present at the meeting:

Dr. Alan Rubin, USNRC
Dr. Thomas Walker, USNRC
Dr. Farouk Eltawila, USNRC
Dr. Robert Witt, UWM
Dr. Chris Allison, INEL
Mr. Gary Thinnes, INEL
Dr. Susan Chávez, INEL
Dr. Joy Rempe, INEL

Dr. H. Hashimoto, Japanese Atomic Energy Research Institute (JAERI), was also present at this meeting. Prior to this meeting, peer reviewers submitted written comments, and the INEL provided each peer reviewer with written responses to their comments. Minor comments, typographical errors, and areas where additional discussion was needed for clarification were corrected by the INEL in a revised version of the report that was distributed at the meeting.

At the beginning of the meeting, Drs. T. Walker and A. Rubin, USNRC, stated that the purpose of the meeting was to discuss reviewer comments about the research documented in the draft NUREG report rather than have the INEL make presentations of their work. In addition, the meeting should define revisions needed before the document is issued as a final report. To facilitate peer reviewer discussion, the INEL reviewed the following objectives of this research program:

- Identify dominant failure mechanisms

- Develop models for predicting dominant vessel failure mechanisms

- Apply models to determine which failure mechanisms are more likely to occur in different LWR designs for various debris and accident conditions.

One peer reviewer commented that the term "more likely" had risk connotations; whereas models in this report were used solely to predict the failure mechanism that occurs first during a particular scenario. The INEL agreed and suggested that the last objective should be reworded as follows:

- Apply models to determine which failure mechanisms are possible and the time when each mechanism occurs in different LWR designs for various debris and accident conditions.

Then, the INEL distributed Table G-1 that summarizes major comments from the peer reviewers. The table was organized according to the questions asked by Dr. B. Sheron, USNRC, in the letter requesting peer reviewers to serve on the committee. Although any additional comments were welcomed during the discussion, the peer review committee agreed to use the table as a basis for the discussion. Several items in the table required more detailed responses. The INEL prepared informal presentations to respond to these comments. The participants agreed to listen to these presentations after the items in the table were discussed. Topics for the presentations included the following:

- A flow diagram illustrating application of lower head failure models

- Potential flow paths for debris through lower head penetrations

- Appropriate boundary conditions for predicting vessel thermal response

- Revisions to tube ejection, tube rupture, and global vessel rupture failure maps and sensitivity of failure map results to thermal analysis assumptions

- Comparisons between finite element and analytical closed-form solution models and general guidelines for when finite element models are needed.

The remainder of this summary is organized according to the discussion that occurred from each question in Dr. Sheron's letter and comments raised during the informal INEL presentations.

Do the failure modes identified represent the dominant ones?

As noted in Table G-1, most reviewers felt that the dominant failure modes were considered. However, several reviewers suggested that the INEL should note that the research program initially considered other failure modes, such as ablation, thermal shock, and interactions between failure mechanisms and state the reason that these failure mechanisms were rejected. The INEL agreed that this was a good idea and could be incorporated easily into the final report.

Questions were raised regarding the adequacy of the THIRMAL code used for the jet impingement analysis. It was noted that ongoing FARO analyses indicate that the THIRMAL code is not conservative with respect to the potential for jet ablation. The INEL responded that because the FARO experiments are still being performed, it is premature to make definite

Table G-1. Summary of peer reviewer comments and INEL responses.

Comment	Number of reviewers	INEL response
Question 1: Do the failure modes identified represent the dominant ones?		
Dominant failure modes are considered	6	None required
Calculations should be continued to consider vessel/penetration behavior beyond initial failure so that the failure size can be determined as a function of time.	2	Although this information is useful in quantifying the consequences of a particular scenario, this task was not included in the current workscope for this project.
Initial failure by jet ablation should be considered.	1	Ablation was initially considered. However, results from our literature review indicate that it is not possible to get significant ablation in any of the reference plant designs for the range of accident conditions considered.
Thermal shock from external flooding, and thermal stresses during cooling by external flooding should be considered.	1	Thermal shock from external flooding was excluded from this project's workscope because it was not considered a dominant failure mechanism in existing LWR designs.
Interactions between failure mechanisms, such as wall thinning due to jet ablation, could lead to earlier creep rupture failure.	1	These failure modes were excluded from this project's workscope because they were not considered dominant failure mechanisms.
A failure mode in which vessel ballooning enhances the potential for tube ejection should be considered.	1	These failure modes were excluded from this project's workscope because they were not considered dominant failure mechanisms.
Additional work is needed to address debris conditions.	2	Potential debris conditions were reviewed as part of the literature search, and bounding values were obtained. Although detailed calculations of debris behavior are useful, they were excluded from this projects's workscope except in the Section 5 scenario-specific finite element calculations.

Table G-1. (continued).

Comment	Number of reviewers	INEL response
Question 2: Are the data and experiments from previous lower head failure analyses applied in a technically sound manner?		
Interpretation of previous data appears reasonable.	5	None required.
Validation calculations are needed using TMI-2 data.	1	Agree. This will be done as part of an ongoing OECD project. Additional validation calculations may also be performed as a follow-on program. We are considering existing data and any new data that may come from FAI, FARO, CORVIS, and RASPLAV.
More information is needed on debris behavior (e.g., timing of debris arrival, crust formation, and convection from a molten pool).	1	Potential debris conditions were reviewed as part of the literature search and bounding values were obtained.
Question 3: Are there additional data that could significantly affect the analysis or conclusions presented in the report?		
The literature review appears to be up-to-date and complete.	4	None required.
Review should consider MARCH models.	2	Agree, a review of the failure model in MARCH will be incorporated into the final report. A later presentation will discuss differences between MARCH and failure models used in this program.
Review should consider		
Results from MELCOR calculations and additional STCP calculation results	1	Will incorporate into the final report, provided that specific references are cited and references are available in the open literature.
New FARO and CORVIS data	1	
Papers by B. Turland and J. Morgan and paper by A. Cronenberg	1	
Recent KfK and CEN/ISPN results.	1	

Table G-1. (continued).

Comment	Number of reviewers	INEL response
Question 4: Are the analytical methodologies sound technically, clearly defined, and carried out in a consistent manner? Are the analytical assumptions reasonable and consistent with our current understanding of the underlying phenomena?		
Yes.	2	None required.
Assumptions and ranges of applicability for each failure analysis need to be clearly defined.	2	Failure analysis assumptions are stated in each section. However, a table could be added to emphasize assumptions in each failure analyses.
Melt penetration calculations should consider the presence of water in LWR penetrations.	2	As noted in Section 6 of the draft NUREG, the presence of water should be considered in certain cases. Work has been initiated to consider these cases. A later presentation will discuss this response in more detail.
The calculations for velocity of melt through a penetration tube at high pressure are not applicable to LWR penetrations.	3	Disagree. There are certain cases where it is possible to have a pressure head. A later presentation will discuss this response in more detail.
Temperature assumptions between different failure analyses should be consistent.	1	In general, failure maps were obtained for a range of temperature conditions. It would be difficult to determine one temperature distribution that is most representative because of uncertainties in debris conditions and vessel external heat removal conditions.
The heat transfer coefficient on the vessel outer surface in the one-dimensional analysis should be 1 W/m^2K.	1	A range of heat transfer coefficients is now being considered; temperature distributions and the corresponding tube ejection, tube rupture, and global vessel failure maps will be presented later.
The heat transfer coefficient on the vessel outer surface in the one-dimensional analysis should be between 20 and 40 W/m^2K.	1	
The one-dimensional temperature gradient is inconsistent with the presence of insulation around the vessel.	1	
The upper limit/lower limit lines in the tube ejection/tube rupture/global vessel rupture failure maps are confusing.	2	Agree. A later presentation will discuss how these maps have been revised.

Table G-1. (continued).

Comment	Number of reviewers	INEL response
The assumption of a nearly constant tube temperature distribution in the tube ejection/tube rupture/global vessel rupture failure maps is incorrect.	1	Disagree. However, other temperature distributions are now being considered, and results will be presented later.
Localized creep rupture analysis should be continued to characterize the heat fluxes and the generation rates of debris decay heat required to cause failure.	2	Although the objective for this analysis was to consider a broad range of conditions and determine the conditions needed to induce this failure mechanism, heat transfer conditions required to produce this type of failure could be considered in this section.
Eutectic formation between debris and vessel/penetration materials should be considered.	1	Eutectic formation would affect results for in-vessel tube melting because failure would be predicted at lower temperatures. However, ex-vessel tube failure analyses were based upon the temperature of the penetration material's failure. Hence, the results for these analyses are not expected to vary significantly.
Three-dimensional calculations are needed to model structural deformation and address the potential for lower head failure.	1	The INEL feels that the thermal conditions and structural material properties are too uncertain to warrant a scenario-specific three-dimensional calculation at this time.

Table G-1. (continued).

Comment	Number of reviewers	INEL response
Question 5: Are the following factors adequately considered in the report? • **Uncertainties in thermal hydraulic conditions and thermophysical properties.** • **Uncertainties in severe accident progression.** • **Plant design differences.**		
Uncertainties in the thermal-hydraulic conditions, properties, accident progressions, and plant differences are well addressed.	3	None required.
More information is needed on debris behavior (e.g., timing of debris arrival, crust formation, and convection from a molten pool).	1	Disagree; debris conditions were reviewed as part of the literature search and bounding values were obtained.
Uncertainties in modeling assumptions need to be addressed further.	2	INEL recommends that a list of uncertainties be included in the final report.
Question 6: Are the conclusions reasonable and technically supported by the analyses?		
Yes.	2	None required.
A flow chart illustrating the process used to arrive at conclusions would be helpful.	1	Agree. A later presentation will discuss a flow chart that would assist in integrating these analyses.
Analyses should be better integrated.	3	Agree. A later presentation will discuss results from work performed to address this comment.
Additional comparisons of analytical and finite element results should be provided.	3	
A summary is needed in each plant for dominant mechanisms over a wider range of conditions.	2	Agree. INEL recommends that a table summarizing the dominant failure mechanisms in different plants for different thermal-hydraulic conditions be added to the final report. Furthermore, Section 6.2 should be expanded to also consider a ceramic case.

conclusions about any code's ability to predict jet impingement phenomena. The INEL agreed that statements to this effect could be included in the text.

Questions were also raised about uncertainties in the INEL model predictions. The INEL noted that little information was available on high-temperature properties for SA105/SA106, Inconel, and SS304. Hence, it would be difficult to quantify uncertainties. One peer reviewer suggested that, as a minimum, the INEL should provide qualitative statements concerning their judgement of uncertainties in model results.

As noted in the table, several reviewers commented about the effect of debris conditions on vessel failure. The INEL responded that although the program included a literature search of previous analyses of debris properties (material composition, relocation temperature, porosity, particle size, thermal properties, etc.), detailed analyses of debris behavior was beyond the scope of the lower head failure project. However, the INEL agreed to add qualitative statements about debris conditions that correspond to heat load assumptions in these analyses.

Are the data and experiments from previous lower head failure analyses applied in a technically sound manner?

Most reviewers felt that the data were applied in a sound manner. However, one reviewer noted that validation calculations were needed. The INEL responded that TMI-2 calculations were being performed as part of ongoing OECD-sponsored TMI-2 VIP work and that the USNRC was currently sponsoring a task to identify other validation calculations using data from ongoing experiments at FAI, PSI (CORVIS), JRC Ispra (FARO), and the Kurchatov Institute (RASPLAV).

Dr. Merilo noted that FAI experimental data for melt transport through lower head penetrations will be available as soon as EPRI receives and reviews the final report.

Are there additional data that could significantly affect the analysis or conclusions presented in the report?

Most reviewers felt that the literature review was up-to-date and complete. Several reviewers requested that the literature review include the MARCH models. The INEL agreed and pointed out that Dr. Chávez would discuss the MARCH models later. Several other references, which are listed in Table G-1, were noted by reviewers. The INEL agreed to include these references in the document if specific references were cited and the references were available in the open literature.

Are the analytical methodologies technically sound, clearly defined, and carried out in a consistent manner? Are the analytical assumptions reasonable and consistent with our current understanding of the underlying phenomena?

Although several reviewers felt that the methods and assumptions were correct, other reviewers had comments and suggestions, as noted in Table G-1 and discussed in the following paragraphs.

Several reviewers requested that the assumptions and range of applicability for each failure analysis be more clearly defined. Although the assumptions used in each analysis were stated in each section, the INEL agreed to add a table to emphasize this information.

One reviewer pointed out that model assumptions neglect the effect of certain parameters for some cases. Hence, the resulting equations contain only the dimensionless groups that are considered important for that analysis. The reviewer felt that other dimensionless groups may be important in certain cases where the modeling assumptions are not valid. Hence, it was suggested that the INEL identify other dimensionless groups not currently included in the report. For example, BNL summarized the results from their contribution to a Committee on Safety at Nuclear Installations (CSNI) standard problem that might provide insight into other dimensionless groups. The INEL questioned the benefit of identifying these additional dimensionless groups. However, pending concurrence from the USNRC, the information in the BNL report could be added to the final report (if it is available in the open literature before the NUREG is published). *[Later, the USNRC chose not to include this task in the lower head failure program.]*

Several reviewers had questions about the presence of water in lower head penetration flow paths and the appropriateness of assuming pressure-driven heads for melt traveling though lower head penetrations. The INEL responded that additional information is needed in the text to clarify melt flow paths through lower head penetrations. The INEL also noted that there are pathways through lower head penetrations where water is not present and where pressure-driven flow may occur. However, additional discussion on this point was deferred to Dr. Rempe's informal presentation.

Several reviewers questioned the appropriateness of assumptions used in the simple one-dimensional vessel thermal response model. The INEL noted that the assumptions used in these sample calculations represented high values. The INEL acknowledged the need to discuss this point further with the peer review committee. The discussion was deferred to presentations by Dr. Rempe and Mr. Thinnes about the assumptions that were reasonable and the impact of these assumptions on failure map results.

Several reviewers had questions about the upper/lower limit lines in the tube ejection/tube rupture/global vessel rupture failure maps. One reviewer questioned the assumption of a nearly constant distribution of tube temperatures in these maps. The INEL agreed that the limit lines in the maps were somewhat confusing. A later presentation by Mr. Thinnes would discuss the revised maps and the impact of temperature assumptions on failure map results.

Several reviewers felt that additional work should be performed in the localized effects analysis to characterize the types of heat fluxes and debris decay heat generation rates required to cause failure. The INEL agreed that the additional work should be performed to determine the heat transfer conditions required to induce a localized creep failure.

One reviewer pointed out that three-dimensional calculations were needed to model structural deformation during lower head failure. The INEL replied that there was too much uncertainty in debris conditions to warrant three-dimensional structural response calculations. However, the INEL agreed that a qualitative review could be performed to determine the types of conditions that must occur before a three-dimensional response calculation would be needed.

Are the following factors adequately considered in the report:

- *Uncertainties in thermal hydraulic conditions and thermophysical properties*
- *Uncertainties in severe accident progression*
- *Plant design differences?*

Although several reviewers believed that uncertainties in the thermal-hydraulic conditions, properties, accident progress, and plant design differences were well addressed, other reviewers believed that additional work was needed to address uncertainties in modeling assumptions. One reviewer reiterated his concern that statements in the text indicating that a particular failure mode was "more likely" should be reworded to indicate that this failure mode was "predicted to occur earlier." Then, subsequent analysis should be performed to assess what other mechanism(s) might occur if the qualitative judgment of modeling uncertainties were included in the analysis. The INEL agreed that statements in the report citing a particular mechanism as being 'more likely to occur" should be reworded to "predicted to occur earlier." However, given the large amount of uncertainty present in certain models, the INEL was not certain that it would be useful to do more than list uncertainties present in each model and provide qualitative judgements related to uncertainties in model predictions.

Are the conclusions reasonable and technically supported by the analysis?

Some reviewers felt that the conclusions were reasonable and supported by the analysis. Several reviewers requested additional integration between analyses and additional finite element results. They also suggested that the final report include a flow chart illustrating the process used to arrive at conclusions and a table summarizing the failure mechanisms that may occur in each plant for a wider range of conditions. The INEL agreed with these comments. The INEL also suggested that Section 6.2 be expanded to consider a case with mostly ceramic debris. Discussion about the flow chart was deferred to Dr. Rempe's presentation. Further discussion about comparisons between finite element and closed-form analytical model results was deferred to Dr. Chávez' presentation.

Reviewers noted that failure maps do not contain timing. The INEL agreed that time-dependent temperature distributions must come from another analysis, either a simple one-dimensional calculation or a detailed finite-element calculation (examples of both types of analysis were included in the draft report). Reviewers also noted that interactions between mechanisms are not included. The INEL acknowledged that interactions between mechanisms were not considered because they believed that interactions would not play an important role in lower head failure.

A reviewer questioned whether the document's objective should be limited to describing methods. Noting that the document did not try to provide a comprehensive assessment of all debris conditions, the reviewer questioned whether the conclusions in the document were valid. Dr. Eltawila stated that reviewers could focus their discussion by noting the following USNRC objectives for this research program:

- Identify dominant failure mechanisms
- Develop models for predicting dominant vessel failure mechanisms
- Apply models to determine which failure mechanisms are possible and the relative time for each mechanism to occur in different LWR designs for various debris and accident conditions
- Formulate conclusions about lower head failure based on the analyses and identify conditions that would invalidate these results.

INEL Presentations to discuss issues requiring more detailed responses

1. Flow Chart Illustrating Application of Lower Head Failure Models

   The INEL presented a flow diagram illustrating the process that should be used to evaluate each failure mechanism. This diagram was based on a flow chart suggested by Dr. Pilch. The INEL agrees that a similar diagram should be included to illustrate the process that a user must follow to determine the first failure mechanism that would occur during a severe accident scenario. The diagram will provide a basis for the discussion of the metallic debris scenario and the ceramic debris scenario that will be included in this section. The INEL noted that the diagram was a draft and welcomed any reviewer comments for improving the content and usefulness of the diagram.

   Most reviewers agreed that the diagram would be a useful addition to the report. They suggested that the current notation on the diagram be made more detailed; all plant designs should be called out. (Currently, the map calls out only CE designs and assumes that all flow paths should be used for the remaining plant designs.) In addition, the draft report does not discuss any model for predicting weld failure. The INEL agreed, noting that they planned to use the vessel thermal response with the yield strength curve for the weld material to evaluate this failure mechanism.

2. Potential Pathways for Melt Through Lower Head Penetrations

   The INEL next presented information to illustrate possible pathways for melt flowing through lower head penetrations. This information was provided to address questions about the presence of water in these pathways and the appropriateness of assuming pressure driven heads for melt flowing through these pathways. Three types of penetrations were illustrated, and possible pathways through these penetrations were identified. Pressure heads are possible in all penetrations except the BWR drain line, and vapor, air, and liquid water interfaces near the debris are possible. Data pertinent to possible melt flow paths in lower head penetrations are primarily from TMI-2 instrument tubes, although ongoing FAI experiments are expected to provide additional information. Preliminary data indicate that it is possible for melt to flow down the air-filled channel in the instrument string and the water-filled annulus between the instrument string outer diameter and the instrument tube inner diameter.

   The INEL acknowledged that current models are not applicable to cases with a liquid water interface, which may occur in the annulus between the outside of an instrument string and the inside of an instrument tube and within the thermal sleeve and the annulus inside of the control rod guide tube. Existing models are being revised to consider cases where heat is lost to liquid that contacts the debris in the penetration.

   For the final report, reviewers suggested modifying the wording in the text to clarify possible pathways through lower head penetrations and including results from models that consider the effect of water in melt pathways. The INEL agreed to these changes.

3. Appropriate Boundary Conditions for One-Dimensional Thermal Analysis

   As noted in Table G-1, several reviewers questioned the appropriateness of boundary conditions used in the sample one-dimensional thermal analysis. The INEL agreed that the values used in the analysis represent a high value for the heat transfer coefficient at

the vessel outer surface and a midrange value for the debris heat flux. This combination of conditions yielded high temperature gradients through the vessel wall and high temperatures at the vessel inner surface when a steady state temperature distribution occurred.

The INEL suggested that several example temperature distributions should be included in the final report. However, noting the discrepancy in values suggested as appropriate by the reviewers, the INEL asked for reviewer input for the range of values that should be considered.

One reviewer stated that a constant temperature boundary condition would be more appropriate than a constant heat flux boundary condition. Two reviewers commented that a coupled debris/vessel thermal response analysis would be more appropriate. Another reviewer felt that it would be more appropriate to look at different detailed calculations that had been performed and reference these calculations.

The INEL noted that one-dimensional thermal analyses were used to provide bounding values. The temperature gradients from these calculations provided input to the failure maps for tube ejection, tube rupture, and global vessel rupture. The INEL would expect the user of this document to determine which temperature gradient was similar to the temperature gradient predicted in his or her detailed calculation and then select an appropriate failure map to determine which failure mechanism occurs first.

4. Revised Tube Ejection, Tube Rupture, and Global Vessel Failure Maps and Effect of Temperature Distribution Assumptions on Failure Map Results

As noted in Table G-1, several reviewers commented that the upper limit/lower limit lines in the tube ejection, tube rupture, and global vessel failure maps were confusing. Since upper limits for tube ejection are not viable in several cases, the INEL revised these failure maps by deleting the upper limit lines. The INEL presented the revised maps to the peer review committee.

Reviewers also expressed concern that the failure maps in the draft report depended on a nonrepresentative temperature distribution. As discussed above, the INEL plans to include several characteristic temperature distributions in the final report. Although the INEL is willing to incorporate any range of temperature distributions suggested by the peer review committee, some sample temperature distributions used to generate example tube ejection, tube rupture, and global vessel rupture failure maps were presented to the peer review committee.

Results illustrated that a lower heat flux assumption produces in lower peak temperatures at the vessel inner surface. Because it is assumed in most of these failure maps that the debris-filled tube temperature is approximately equal to the temperature at the vessel inner surface, the time until tube failure is delayed.

The heat transfer coefficient for the vessel outer surface primarily affects the vessel temperature gradient. If less heat is removed from the vessel, the temperature gradient through the vessel is decreased. Thus, failure maps assuming smaller heat transfer coefficients for the vessel outer surface indicate that for a given vessel inner surface temperature, global vessel rupture will occur at lower pressures (because a larger fraction of the vessel is at higher temperatures).

5. Additional Comparisons Are Needed Between Finite Element Results and Simpler Models in the NUREG and in the MARCH Code

   The INEL presented information comparing the simple models used in the draft report with the vessel failure model in the MARCH code. Both models consider plastic failure and assume that failure occurs when the forces in the vessel exceed the material's ultimate capacity. The MARCH model includes the dead weight of debris in the lower head. Although not included in the base case formulation of the draft NUREG model, the pressure within the vessel could be adjusted to include the debris dead weight for cases where this load is significant. The most significant difference between the MARCH and the INEL simple models lies in modeling the through thickness (radial) temperature distribution. The INEL model uses 20 temperature elements through the thickness; whereas, the MARCH model uses a bilinear distribution, with limitations on the outer vessel temperature distribution. Because ultimate strength is highly dependent on temperature between 600 and 1150 K, the INEL model is recommended.

   The INEL also presented information comparing the simple plastic model and the finite element creep and plastic models. Models differed primarily because the finite element model can account for thermal stresses and stresses associated with constraints (either from a structural support or a meridional temperature gradient). The finite element creep model also accounts for time-dependent creep behavior. Background information was included to describe the Larson-Miller parameter and the time damage model used in the finite element calculation. General rules of thumb were provided to identify when a creep analysis is necessary; and results from the creep and plastic analyses were compared.

General discussion

Several items were identified that the peer review group agreed should be included in the final report. These items are listed below:

- The final report should note the other failure mechanisms that were considered initially and state the reason that these mechanisms were not evaluated.

- Qualitative statements regarding uncertainties in debris/water interaction should be added to the section documenting the THIRMAL analysis.

- A flow diagram illustrating the process used to arrive at conclusions should be included in the final report.

- A second case, considering ceramic debris, should be considered in Section 6.2. These two cases should be used to define more specific conclusions related to the potential for vessel failure.

- Wording should be clarified that describes potential pathways for melt flow through lower head penetrations, and the results from models including the effects of water present in some melt pathways should be included in the final report.

- Additional assumptions for vessel and tube temperature distribution (resulting from vessel outer boundary conditions and tube-to-vessel contact) should be considered in

tube ejection, tube rupture, and global vessel rupture failure maps. Qualitative statements relating debris conditions to heat load assumptions should be added to the text.

- Failure maps considering tube ejection, tube rupture, and global vessel rupture should be revised to delete the upper limit lines for tube ejection.

- Tables should be included in the final report that summarize assumptions, range of applicability, and uncertainties for each failure analysis. (In some cases, only qualitative statements regarding uncertainties in models will be provided.)

- Tables should be included in the final report that summarize the failure mechanisms that occur in each plant over a wider range of conditions.

- Additional comparisons of finite element and analytical model results should be included. Where possible, general guidelines should be given for determining when finite element techniques are needed.

- MARCH models and other previous analyses/data (specific references cited by the reviewers and available in the open literature) should be included in the final report.

- Temperatures required to induce localized vessel failure should be linked to debris conditions.

- An analysis should be performed to indicate the maximum heat flux possible in a debris-filled penetration; the results should be used to indicate the feasibility for subsequent tube failure analyses.

- A comprehensive review should be performed to identify all dimensionless groups impacting vessel and debris behavior during severe accidents. *[The USNRC later chose not to include this large task in the lower head failure program.]*

- A qualitative review should be performed to determine the types of conditions that must occur to warrant a three-dimensional response calculation.

NRC FORM 335 (2-89) NRCM 1102, 3201, 3202

U.S. NUCLEAR REGULATORY COMMISSION

BIBLIOGRAPHIC DATA SHEET

(See instructions on the reverse)

1. REPORT NUMBER (Assigned by NRC, Add Vol., Supp., Rev., and Addendum Numbers, If any.)

NUREG/CR-5642
EGG-2618

2. TITLE AND SUBTITLE

Light Water Reactor Lower Head Failure Analysis

3. DATE REPORT PUBLISHED

MONTH	YEAR
October	1993

4. FIN OR GRANT NUMBER

D2029

5. AUTHOR(S)

J. L. Rempe, S. A. Chávez, G. L. Thinnes, C. M. Allison, G. E. Korth, R. J. Witt[1], J. J. Sienicki[2], S. K. Wang[3], L. A. Stickler, C. H. Heath, S. D. Snow

6. TYPE OF REPORT

Technical

7. PERIOD COVERED (Inclusive Dates)

8. PERFORMING ORGANIZATION – NAME AND ADDRESS (If NRC, provide Division, Office or Region, U.S. Nuclear Regulatory Commission, and mailing address; if contractor, provide name and mailing address.)

EG&G Idaho, Inc.
Idaho Falls, ID 83415

[1]University of Wisconsin–Madison, 1500 Johnson Drive, Madison, WI 53706
[2]Argonne National Laboratory, 9700 South Cass Avenue, Argonne, IL 60439
[3]Commonwealth Edison Company, One First National Plaza, Chicago, IL 60690–0767

9. SPONSORING ORGANIZATION – NAME AND ADDRESS (If NRC, type "Same as above"; if contractor, provide NRC Division, Office or Region, U.S. Nuclear Regulatory Commission, and mailing address.)

Division of Systems Research
Office of Nuclear Regulatory Research
U.S. Nuclear Regulatory Commission
Washington, D.C. 20555–0001

10. SUPPLEMENTARY NOTES

11. ABSTRACT (200 words or less)

This document presents the results from a U.S. Nuclear Regulatory Commission-sponsored research program to investigate the mode and timing of vessel lower head failure. Major objectives of the analysis were to identify plausible failure mechanisms and to develop a method for determining which failure mode would occur first in different light water reactor designs and accident conditions. Failure mechanisms, such as tube ejection, tube rupture, global vessel failure, and localized vessel creep rupture, were studied. Newly developed models and existing models were applied to predict which failure mechanism would occur first in various severe accident scenarios. So that a broader range of conditions could be considered simultaneously, calculations relied heavily on models with closed-form or simplified numerical solution techniques. Finite element techniques were employed for analytical model verification and examining more detailed phenomena. High-temperature creep and tensile data were obtained for predicting vessel and penetration structural response.

12. KEY WORDS/DESCRIPTORS (List words or phrases that will assist researchers in locating the report.)

vessel failure mechanisms; vessel; thermal and mechanical response

13. AVAILABILITY STATEMENT

Unlimited

14. SECURITY CLASSIFICATION

(This Page)
Unclassified

(This Report)
Unclassified

15. NUMBER OF PAGES

16. PRICE

Federal Recycling Program

UNITED STATES
NUCLEAR REGULATORY COMMISSION
WASHINGTON, D.C. 20555-0001

OFFICIAL BUSINESS
PENALTY FOR PRIVATE USE, $300

120555139531 1 IAN
US NRC-OADM
DIV FOIA & PUBLICATIONS SVCS
TPS-PDR-NUREG
P-211
WASHINGTON DC 20555

SPECIAL FOURTH CLASS RATE
POSTAGE AND FEES PAID
USNRC
PERMIT NO. G-67